IMPERIAL

Using the Ionic Liquid 1-Ethyl-3-Methylimidazolium Acetate as A Solvent for Fabricating Cellulose Lignin Composite Films

Farhana Othman
Department of Chemistry
Imperial College London

This dissertation is submitted for the degree of
Doctor of Philosophy

JULY 2026

To my son, Ibrahim al-Siddiq

Statement of Originality

This statement certifies that the content of this thesis is the product of my own work since December 2020 until September 2024, and that all experiments performed by collaborators are being clearly acknowledged. This thesis has not been submitted for any other degree or diploma at Imperial College London or any other educational institution.

Copyright Declaration

The copyright of this thesis rests with the author. Unless otherwise indicated, its contents are licensed under a Creative Commons Attribution-Non Commercial 4.0 International Licence (CC BY-NC). Under this licence, you may copy and redistribute the material in any medium or format. You may also create and distribute modified versions of the work. This is on the condition that: you credit the author and do not use it, or any derivative works, for a commercial purpose. When reusing or sharing this work, ensure you make the licence terms clear to others by naming the licence and linking to the licence text. Where a work has been adapted, you should indicate that the work has been changed and describe those changes. Please seek permission from the copyright holder for uses of this work that are not included in this licence or permitted under UK Copyright Law.

Acknowledgements

I have had my own unique PhD journey and been through series of life transition. These transitions brought challenges, but thanks to a supportive and conducive environment, I was able to reach the finishing line. I am deeply grateful to the many individuals and institutions who assisted me along the way, enabling me to finally bind this thesis.

I remember my first interview with my supervisor, Professor Tom Welton. He asked, “What will you do if you face difficulties and negative results?” Perhaps my answer convinced him to take me on as a student. I replied, “I will keep trying.” Indeed, perseverance is essential in a PhD. Professor Welton is not only a renowned scientist in the field of ionic liquids, but also an exceptionally efficient supervisor. I am truly thankful to him for shaping my scientific thinking and my attention to detail. Thank you for the opportunity to carry out this project and for guiding it to success. My sincere thanks also go to my co-supervisor, Dr. Agi Brandt-Talbot, who gave me opportunities to present my work, engage in scientific collaborations, and refine my research. She has been an understanding and supportive mentor, generously sharing her own experiences with me during my transition into motherhood; an important and challenging phase in my life.

This PhD journey would not have been possible without the crucial support from my government. I express my deepest gratitude to the Ministry of Higher Education, Malaysia, for fully sponsoring my tuition fees and stipend, and to my employer, Universiti Teknologi MARA, Malaysia, for granting me permission to pursue my studies. I am also thankful to Imperial College London for contributing to both my academic and personal growth. The advanced facilities, the postgraduate tutor support, and the understanding shown during interruptions in my studies and the extension of my submission deadline were invaluable.

I would like to thank my colleagues in the Welton group (Rickey, Nefeli, Gavin, Spiros, Frederik, Ana, and Julian) for their help, especially during my first year when I had no prior knowledge of ionic liquid synthesis, and during the restricted movements of my pregnancy. I am also grateful for the wonderful "girlfriends' bubble" I found in the Agi group. Thank you, Harriet, Maariyah, Zoyia, Priyanka, and Enny, for your continuous support and for always listening to my pep talks. Thanks also to Pedro and Suhaib from the Hallett group for their kindness and care, and to Dharu and Daniela from the Koon-Yang group for helping me with film fabrication. My appreciation also goes to the technical teams: Pete, for sharing his expertise in NMR and for our small but meaningful life chats, and Elena, who I treasure friendship with Senior Teaching Fellow after Global Fellowship Programme.

To my fellow Malaysian PhD fighters in the UK, Syazana, Suzi, Nik Alia, Liyana, and Izzah, thank you for being there whenever I doubted my decision to pursue a PhD. We were all in the same boat, and we all made it through. To my dear sister Rizana, thank you for always answering my calls and advising me to the very end. I cannot name everyone, but I am also thankful to my colleagues from UiTM, my Vellacott fellows, and my SMKAP friends. Thank you all for your encouragement. My heartfelt thanks also to the Sufa community for making our Friday spiritual gatherings meaningful, and to the Malaysian community at Malaysian Hall for the unforgettable moments we shared.

My deepest gratitude goes to the solace of my heart—my husband, Luqman Hakim for always motivating me and guiding me to the finishing line. Thank you to my parents, Asma and Othman, for your continuous support and prayers, and to my siblings, Fitrah, Cikna, and Abang, for always cheering me up.

I hope this work makes a small contribution to scientific knowledge.

"If you are grateful, I will certainly give you more." Quran [14:7]

Abstract

Plastic is lightweight and durable, making it suitable for many applications, including packaging. Nonetheless, its petroleum-based, non-biodegradable properties have resulted in significant global waste issues. Regenerated cellulose film, often referred to as cellophane, provides a sustainable alternative as it is produced from cellulose wood or cotton fibers. Lignin is a promising material because of its abundant functional groups, such as phenolic and aliphatic hydroxyls, carbonyls, which determine its reactivity and processing capabilities. This study aimed to substitute hazardous solvents for the dissolving of cellulose and lignin with the ionic liquid 1-ethyl-3-methylimidazolium acetate, $[C_2C_1im][OAc]$, together with DMSO as a co-solvent. $[C_2C_1im][OAc]$ was synthesized by several methods, and green metrics were assessed to evaluate sustainability. Films composed of cellulose-lignin (**cel-lig**) and cellulose-lignin-glycerol (**cel-lig-gly**) were produced using solution casting. Their physicochemical, thermal, and surface properties were determined, along with hydroxyl group quantification and compositional analysis (CA) to determine structure–property correlations. The ion-exchange synthetic method demonstrated the highest efficiency for synthesizing $[C_2C_1im][OAc]$, with an atom economy of 62.8% and an E-factor of 107.8. The NMR tests indicating that four and five washing cycles for **cel** and **cel-lig** film, respectively. ^{31}P NMR analysis indicated that hardwood lignins have a greater hydroxyl content compared to softwood lignins. Conversely, cellulose-softwood lignin (i.e. **10cel-4iSL**) films exhibited significant surface roughness, resulting in the greatest water contact angle of 88.7°. CA indicated that softwood lignin consisted of approximately 99.9% pure lignin, whereas ionosolv hardwood lignin (**iHL**) contained around only 60% lignin along with carbohydrate residues. Simultaneously, addition plasticiser of 5 wt.% glycerol produced optimal mechanical performance, increasing tensile yield by 120% in **cel-lig-gly**, with a tensile stress of 75.8 MPa. CA and hydroxyl content was essential for tailoring the properties of **cel-lig** films, enabling applications that require superior water-barrier or UV blocking capabilities.

Table of Contents

List of Figures xiii
List of Tables xviii
List of Abbreviations xx

Chapter 1: Introduction and Literature Review 1
1.1 Introduction 1
1.1.1 Plastics Problems 1
1.1.2 Biodegradable Biopolymers 3
1.1.2.1 Cellulose 7
1.1.2.2 Lignin 12
1.1.3 Ionic Liquids 16
1.1.4 Ionic Liquids in Biomass Processing 21
1.2 Literature Review 24
1.2.1 Green Chemistry and Sustainable Synthesis 24
1.2.1.1 Green Metrics Analysis 25
1.2.2 Synthesis of Ionic Liquids 29
1.2.3 Cellulose-Lignin Composite Films 36
1.2.3.1 Cellulose and lignin sources, fabrication techniques and key features in cellulose-lignin composites 36
1.2.3.2 Challenges with solubility, miscibility, and film uniformity 38
1.2.3.3 Solution casting parameters in cellulose-lignin processing 41
1.2.3.4 Summary of best practices for film fabrication 47
1.2.3.5 Gaps in understanding of structural-property relationships 47
1.2.4 Functionalization and Plasticization 48
1.2.5 Characterization Techniques 51
1.2.5.1 Thermal properties 51
1.2.5.2 Mechanical properties 53
1.2.5.3 Surface properties 57
1.2.5.4 Optical properties 60
1.3 Research Gaps and Rationale 64
1.4 Significance of Study 65

1.5 Objectives and Scope of Study....65
1.6 References....66

Chapter 2: Materials and Method....73
2.1 Preparation of dope solutions....73
2.1.1 Materials....73
2.1.2 Ionosolv lignin extraction method....74
2.1.2.1 Synthesis of *N,N*-dimethylbutylammonium hydrogen sulfate....74
2.1.3 Film fabrication technique of cellulose-lignin films....75
2.1.4 Analytical methods for dope solution characterisation....76
2.1.4.1 Optical Microscopy....76
2.1.4.2 Rheology....77
2.2 Characterisation....78
2.2.1 Fourier transform infrared spectroscopy....78
2.2.2 Thermogravimetric analysis....79
2.2.3 Tensile testing....80
2.2.4 Water contact angle....82
2.2.5 Ultraviolet-visible light spectrophotometry....84
2.2.6 Compositional analysis....85
2.2.7 Scanning electron microscopy....88
2.2.8 X-ray diffraction....88
2.2.9 Nuclear magnetic resonance spectroscopy of lignin....90
2.2.9.1 ^{31}P NMR....90
2.2.9.2 HSQC NMR....91
2.2.10 Gel Permeation Chromatography....92
2.3 References....92

Chapter 3: Synthesis of Ionic Liquids and Its Green Chemistry....94
3.1 Experimental....94
3.1.1 Reagents....94
3.1.2 Instrumentation....94

3.1.3 Synthesis of 1-ethyl-3-methylimidazolium bromide 95
3.1.4 Synthesis of 1-ethyl-3-methylimidazolium acetate via silver salt metathesis 96
3.1.5 Synthesis of 1-ethyl-3-methylimidazolium acetate using an ion exchange resin 96
3.1.6 Synthesis of 1-ethyl-3-methylimidazolium acetate via a one-pot method 97
3.17 Green chemistry metrics 98
3.2 Results and Discussion 99
3.2.1 Synthesis of 1-ethyl-3-methylimidazolium bromide 99
3.2.2 Synthesis of 1-ethyl-3-methylimidazolium acetate via silver salt metathesis 99
3.2.3 Synthesis of 1-ethyl-3-methylimidazolium acetate using an ion exchange resin 100
3.2.4 Synthesis of 1-ethyl-3-methylimidazolium acetate via a one-pot method 101
3.2.5 Green chemistry metrics and cost analysis of [C_2C_1im][OAc] synthesis 103
3.2.6 Cost Optimization and Industrial Scaling of [C_2C_1im][OAc] 105
3.2.7 Commercial [C_2C_1im][OAc] 106
3.3 References 106

Chapter 4: Development of Cellulose-Lignin Film Fabrication Method 108
4.1 The overall cellulose/lignin film fabrication protocol 108
4.1.1 *Solubility of cellulose and lignin in [C_2C_1im][OAc] / DMSO* 108
4.1.1.1 Cellulose solubility studies 109
4.1.1.2 Changing the cellulose dope solution temperature 112
4.1.1.3 Lignin Solubility Studies in [C_2C_1im][OAc] 113
4.1.1.4 Lignin Solubility Studies in [C_2C_1im][OAc]/DMSO 115
4.1.1.5 Studying the order of biopolymers addition in the cellulose-lignin dope solutions 119
4.1.2 *Drying the starting materials* 123
4.1.3 *Degassing the prepared dope solution* 124
4.1.4 *Cast the dope solution* 125
4.1.5 *Washing the prepared cellulose and lignin film* 129
4.1.6 *Drying the cellulose-lignin films* 133
4.2 Justification for increasing cellulose loading from 5 to 10 wt.% loading 137
4.3 A novel cellulose-lignin film fabrication contribution 139
References 140

Chapter 5: Cellulose-Lignin Film Characterisation 143
5.1 Cellulose and cellulose film characterisation 143
5.1.1 SEM 143
5.1.2 Crystallinity by XRD 145
5.1.3 Compositional Analysis 147
5.1.4 FTIR 149
5.1.5 Thermal Analysis 151
5.2 Lignin characterisation 153
5.2.1 GPC analysis 154
5.2.2 Compositional Analysis 157
5.2.3 FTIR 159
5.2.4 Establishment of ^{31}P NMR experimental setup for lignin characterisation 163
5.2.5 ^{31}P NMR 169
5.2.6 Heteronuclear Single-Quantum Correlation Spectroscopy (HSQC) NMR 172
5.2.7 Thermal analysis 177
5.3 Cellulose-lignin film characterisation 179
5.3.1 Cellulose-lignin film appearance and UV-Vis Spectroscopy 179
5.3.2 FTIR 182
5.3.3 Mechanical properties of cellulose-lignin films 188
5.3.4 Thermogravimetric analysis 201
5.3.5 Water contact angle 203
5.3.6 Compositional analysis for selected cel-lig films 205
5.3.7 SEM for selected cel-lig films 208
5.3.8 Crystallinity for selected cel-lig films 211
5.4 Conclusions 213
References 214

Chapter 6: Cellulose-Lignin-Glycerol Film Characterisation 218
6.1 Cellulose-glycerol film characterisation 218
6.1.1 Composition of plasticised cellulose films by FT-IR spectroscopy 219
6.1.2 Compositional analysis of cellulose-glycerol films 223

6.1.3 Tensile properties of the cellulose films 226
6.1.4 Choosing optimum glycerol concentration for film fabrication 230
6.2 Cellulose-lignin-glycerol film characterisation 231
6.2.1 Optical properties of cellulose-lignin-glycerol films 231
6.2.2 FTIR 237
6.2.3 Mechanical properties of cellulose-lignin-glycerol films 246
6.2.4 Thermogravimetric analysis 264
6.2.5 Water contact angle 270
6.2.6 Compositional analysis of cellulose-lignin-glycerol films 274
6.2.7 SEM for selected films 277
6.2.8 Crystallinity for selected films 282
6.3 Conclusions 285
References 286

Chapter 7: Conclusions and Outlook 289
7.1 Conclusions 289
7.2 Future work 300
7.3 References 305

Appendix 306
A1 ^{1}H NMR, ^{13}C NMR, MS and IR spectra of 1-Ethyl-3-methylimidazolium bromide 306
A2 ^{1}H NMR, ^{13}C NMR, MS and IR spectra of 1-Ethyl-3-methylimidazolium acetate via metathesis 309
A3 ^{1}H NMR, ^{13}C NMR, and IR spectra of 1-Ethyl-3-methylimidazolium acetate via ion exchange 312
A4 ^{1}H NMR, ^{13}C NMR, and IR spectra of 1-Ethyl-3-methylimidazolium acetate synthesised via one-pot method 314
A5 Green Metrics 316
A6 ^{1}H NMR, ^{13}C NMR, and IR spectra of commercial 1-Ethyl-3-methylimidazolium acetate 320
A7 ^{1}H NMR, ^{13}C NMR, and MS spectra of N,N-dimethylbutylammonium hydrogen sulfate, [DMBA][HSO_4] 323

List of Figures

Figure 1.1: Graphical representation of solid waste composition, important chronological events, plastic production by region, global plastic production and consumption, and per capita plastic waste generation. Images taken with permission from by Pilapitiya and Ratnayake, 2024.[6] 2
Figure 1.2: Routes for synthesizing polymers from fossil-based and bio-based sources. Adapted from Rosenboom et.al. (2022)[16] 5
Figure 1.3: Routes towards isolation of different components, i.e., cellulose, lignin, and hemicellulose from lignocellulosic biomass. Image adapted from Mujtaba et. al., 2023[18] 6
Figure 1.4: A cellulose polymer chain, n is typically 400-1000. Image adopted from Swatloski, et al. [24] 8
Figure 1.5: Different microstructure of cellulose derived from SEM images from different cellulose preparation method. Images adopted from Romão et. al [28] 9
Figure 1.6: Classification of cellulose regeneration processes showcasing the primary derivatizing (Gen 1) and direct dissolution pathways (Gen 2 and 3) for cellulose fiber production 11
Figure 1.7: Lignin monomers which are (S) syringyl units, (G) guaiacyl units, (H) p-hydroxyphenyl units. Images adopted from Zikeli et al.[44] 13
Figure 1.8: Representation of a lignin polymer from poplar, as predicted from NMR-based lignin analysis. Images adopted from Stewart et. al [45] 13
Figure 1.9: Some of cations and anions in ionic liquids commonly used for wood and cellulose dissolution and extraction. Image adapted from Abushammala and Mao, 2020[34] 17
Figure 1.10: Section through the phase diagram of cellulose and softwood kraft lignin in ([C_4C_1im][Chc]) and [C_2C_1im][OAc], respectively at a temperature of 95 °C: filled symbols represent experimental results, empty symbols are extrapolated. Image adapted from Protz et al., 2021[58] 18
Figure 1.11: Hydrogen bonding rupture is presented as the mechanism for cellulose dissolution. In this representation, 1-ethyl-3-methylimidazolium acetate is chosen to exemplify the hypothetical H-bond interactions between the solvent molecules and cellulose. 22
Figure 1.12: Synthesis of [C_2C_1im][OAc] using metathesis route 33
Figure 1.13: Synthesis of [C_2C_1im][OAc] using ion exchange resin route 34
Figure 1.14: Synthesis of [C_2C_1im][OAc] using one pot method 34
Figure 1.15: Synthesis of 1-ethyl-3-methylimidazolium methyl- carbonate. 35
Figure 1.16: Schematic illustration of multifunctional cellulose-lignin films. Image adopted from He et al. [90] 40
Figure 1.17: Glycerol incorporated in bacterial cellulose film. Image adopted from Jost et al. [114] 50
Figure 2.1: Overview of experimental workflow to obtain **cel-lig** films 73
Figure 2.2: Polarizing microscope operating principle [Picture taken from Microscopy Australia] [4] 76

Figure 2.3: Shear flow of a material [Picture taken from https://wiki.anton-paar.com/uk-en/basics-of-rheology/] [5] 77
Figure 2.4: Schematic representation of the working principle of ATR-FTIR spectroscopy. Image adapted from Bieberle-Hütter et. al 2021[6] 78
Figure 2.5: Diagram representing the measurement of T_{onset} using a temperature ramped TGA experiment with cellulose film sample. 80
Figure 2.6: Sample geometry of cellulose, cellulose-lignin and cellulose-lignin-glycerol specimens generated for tensile testing 81
Figure 2.7: Tensile stress strain curve material with linear behaviour (left) and non-linear behaviour (right). Images obtained from ASTMD882-10 standard protocol[12] 82
Figure 2.8: Illustrations of water contact angle measurements on hydrophilic and hydrophobic surface Image retrieve: https://www.nanoscience.com/blogs/what-probe-liquid-should-you-use-for-contact-angle-measurements/[13] 83
Figure 2.9: Schematic of Transmittance Measurement. Images retrieved from https://www.shimadzu.com/an/service-support/technical-support/uv/essential_knowledge/integratingspheres.html[14] 84
Figure 2.10: Schematic representation of the Bragg's equation. Image retrieved from https://www.jiamdiffraction.com/copy-of-videos[16] 89
Figure 2.11: Intensity values used in calculation of degree of crystallinity of cellulose. Image adopted from Shimadzu Corporation.[17] 90
Figure 3.1: Chemical reaction to synthesis $[C_2C_1im][OAc]$ using metathesis route 100
Figure 3.2: Ion exchange resin reaction synthesis 101
Figure 3.3: One-pot synthesis of $[C_2C_1im][OAc]$ 102
Figure 3.4: Chemical test for Pb in $[C_2C_1im][OAc]$ via one-pot method 102
Figure 4.1: Time frame for cellulose/lignin film fabrication 108
Figure 4.2: Cellulose solubilty and water content in different $[C_2C_1im][OAc]$ water ratio 112
Figure 4.3: The appearance of bubble gas diminished when a cellulose dope solution was prepared from 50 to 70 °C 113
Figure 4.4: Optical micrographs of lignin in $[C_2C_1im][OAc]$: **oHL** fully dissolved after 3 h (right); **iSL** remained undissolved after 12 h (left) 114
Figure 4.5: Optical micrographs of lignin **iSL** remains undissolved in $[C_2C_1im][OAc]$ (left) while completely dissolve in $[C_2C_1im][OAc]$ overnight stirring (right) 116
Figure 4.6: Schematic mechanism cellulose and lignin dissolution in $[C_2C_1im][OAc]$/DMSO adopted from Kuntapa et al. (2022)[4] 117
Figure 4.7: Comparison cellulose dissolution images in a brightfield microscope image (A) and polarised microscope image (B) using an optical microscope 119
Figure 4.8: Optical micrographs of pre-added cellulose under polarised light at different dissolution times 120
Figure 4.9: Mechanism representation of dissolution of cellulose fibers. Image adopted from Ghasemi et. al[24] 121
Figure 4.10: Optical micrographs of pre-added lignin under polarised light at different dissolution times 121

Figure 4.11: Optical micrographs of pre-added lignin and cellulose simultaneously under polarised light at different dissolution times 122
Figure 4.12: Viscosity over temperature at different cellulose-lignin weight percent ratio prepared in [C_2C_1im][OAc]/DMSO (a) at 25 to 100°C (b) at 70 to 100°C 127
Figure 4.13: Proposed mechanism of the shear-thinning behaviour semi-diluted polysaccharide–[C_2C_1im][OAc] solutions. Image adopted from the literature[5] 128
Figure 4.14: TGA thermogram of [C_2C_1im][OAc]/DMSO solvent mixture at 70°C 129
Figure 4.15: ^{1}H NMR spectra of cellulose film washed with deuterated water. Spectrum 1 and 5 indicate the first and the fifth washing cycle respectively. 130
Figure 4.16: ^{1}H NMR spectra of cellulose/lignin film washed with deuterated water. Spectrum 1 and 6 indicate the first and the fifth washing cycle respectively. 131
Figure 4.17: [C_2C_1im][OAc] recovery for five number of usage 132
Figure 4.18: FTIR spectra of [C_2C_1im][OAc] for each cycle used. The water content for the 2nd until the 5th use were 4.2% and 5.3% respectively 133
Figure 4.19: Drying cellulose film at different conditions setup. Left image is under static air in drying chamber and right image is at unregulated air flow. 134
Figure 4.20: Cellulose films were imaged after undergoing drying under various drying settings. The last row shows cellulose-lignin film formula of **10cel-1iSL** before and after drying. 136
Figure 4.21: Area recovered after drying cellulose film at different drying conditions 137
Figure 4.22: Physical appearance of neat cellulose (**5cel**) and cellulose-ionosolv lignin composite films with varying lignin contents (0.5 to 5 wt% **iSL**) against a background to illustrate transparency changes 137
Figure 4.23: Visual observation of cellulose/ionosolv lignin (**iSL**) dope solutions in [C_2C_1im][OAc] after overnight stirring. Incomplete dissolution is visible at higher lignin loadings of 2.5 wt.% and 5 wt.%. 139
Figure 5.1: SEM images of cellulose powder at different magnifications. The left image shows the overall particle morphology at ×330 magnification (scale bar: 50 μm), while the right image shows surface features at ×6500 magnification (scale bar: 2 μm) 144
Figure 5.2: SEM images of regenerated cellulose thin film (left on the surface at 1600 magnification) and (right on the cross section at 2200 magnification) 145
Figure 5.3: XRD patterns of cellulose powder and regenerated cellulose film 145
Figure 5.4: Compositional analysis of cellulose powder and regenerated cellulose 148
Figure 5.5: Fourier transform infrared spectroscopy of cellulose powder and regenerated cellulose (**10cel**) 150
Figure 5.6: Fourier transform infrared spectroscopy of **10cel** and **cel** indicating complete removal ionic liquid of [C_2C_1im][OAc] 151
Figure 5.7: Thermograms of cellulose (**cel**) and regenerated cellulose (**10cel**) 152
Figure 5.8: Original TGA curve of cellulose **(cel)** before modification of removing moisture content part at 105°C 152
Figure 5.9: Lignin subunits are denoted based on the methoxyl substitution on the aromatic ring as P, G and S units 154
Figure 5.10: Overlaid molecular weight distributions (MWD) of hardwood lignin (**oHL** and **iHL**) and softwood lignin (**kSL** and **iSL**) 155
Figure 5.11: Compositional analysis for different types of lignin which are softwood lignin (**kSL** and **iSL**) and hardwood lignin (**iHL** and **oHL**) 158

Figure 5.12: HSQC NMR identification β-D-glucopyranoside in hardwood lignin.....159
Figure 5.13: FTIR spectra for different types of lignin in softwood and hardwood lignin....161
Figure 5.14: HSQC NMR spectrum of **iSL** indicating the presence of residual [DMBA][HSO_4] in the extracted lignin.....163
Figure 5.15: The reaction lignin and phosphitylation reagent to produce phosphitylated products. Image credited to Meng, et. al.[39].....164
Figure 5.16: Overall ^{31}P NMR spectrum of phosphitylated lignin products (left) and a zoomed-in view of the main region of interest (right).....165
Figure 5.17: ^{31}P NMR spectrum of phosphitylated lignin products in different experimental setups.....167
Figure 5.18: Contents of different hydroxyl groups in lignin determined by ^{31}P NMR analysis 170
Figure 5.19: Quantitative ^{31}P NMR spectra of organosolv beech wood lignin, **oHL** (left) and ionosolv beech wood lignin, **iHL** (right) using cyclohexanol as the internal standard.....170
Figure 5.20: Quantitative ^{31}P NMR spectra of ionosolv spruce lignin, **iSL**(left) and kraft lignin, **kSL** (right) using cyclohexanol as the internal standard.....171
Figure 5.21: HSQC NMR of softwood lignin (**iSL** and **kSL**) and hardwood lignin (**oHL** and **iHL**).....174
Figure 5.22: Identified structural units of lignin in 2D HSQC NMR spectra.....175
Figure 5.23: TGA curves of hardwood lignin (**oHL** and **iHL**) and softwood lignin (**kSL** and **iSL**).....178
Figure 5.24: Cellulose-lignin composite film images with varying lignin content in different lignin types of softwood and hardwood.....180
Figure 5.25: UV−vis transmission spectra of cellulose-lignin films for hardwood (**iHL**, **oHL**) and softwood lignin (**kSL**, **iSL**) with various lignin concentrations.....181
Figure 5.26: FTIR spectra of cellulose-lignin composite films with hardwood lignin (a) and (b), and hardwood lignin (c) and (d) indicating the regenerated film is free from dissolution solvent mixture.....186
Figure 5.27: Structures of (a) 1-ethyl-3-methylimidazolium acetate ([C_2C_1im]OAc), (b) cellulose and (c) representative structure of lignin. Image adopted from Sun et.al[55].....187
Figure 5.28: Compilation representative tensile strength verses strain curves for cellulose-lignin films at different lignin weight percent (a)**10cel-iHL**, (b) **10cel-oHL**, (c) **10cel-kSL** and (d) **10cel-iSL**.....195
Figure 5.29: Tensile properties of cellulose–lignin composite films showing (a) tensile strength and strain at failure, (b) yield strength and yield strain, and (c) Young's modulus as a function of lignin type and content.....196
Figure 5.30: Thermogram of cellulose-lignin composite films at different weight percent ratio (a) for hardwood lignin and (b) softwood lignin.....202
Figure 5.31: Water contact angle of cellulose-lignin films which constitute from (a-b) hardwood lignin and (c-d) softwood lignin.....204
Figure 5.32: Compositional analysis of cellulose-softwood lignin films.....206
Figure 5.33: **10cel-2.5iSL** was initially dried under vacuum using a Schlenk line, followed by grinding to a 50-mesh powder for CA.....206
Figure 5.34: SEM images of **cel-iSL** films on the surface and cross sectional.....210
Figure 5.35: XRD patterns of thin films of cellulose-ionosolv softwood lignin at different weight percent ratio.....212
Figure 6.1: FTIR spectra of glycerol and regenerated cellulose films at different glycerol weight percent: (a) overall spectra; (b) zoomed-in region highlighting the –OH and –CH bands 221

Figure 6.2: Compositional analysis of fabricated **cel-gly** films.....224

Figure 6.3: HPL chromatograms from compositional analysis of fabricated **cel-gly** films...226
Figure 6.4: Representative stress-strain curves fabricated **cel-gly** films (a – e) at different glycerol weight content.....230
Figure 6.5: Physical appearance of **cel-lig** films with and without glycerol at varying lignin contents. (a, b) cellulose with hardwood lignin; (c, d) cellulose with softwood lignin.....234
Figure 6.6: UV−vis transmission spectra of cellulose-lignin-glycerol films for hardwood (a-b) (iHL, oHL) and softwood lignin (c-d) (kSL, iSL) with various lignin concentrations.....235
Figure 6.7: FTIR spectra of cel–lig and cel–lig–gly (4000–2800 cm^{-1}) (a) **10cel-oHL** and **10cel-oHL-5gly**, (b) **10cel-iHL** and **10cel-iHL-5gly**, (c) **10cel-iSL** and **10cel-iSL-5gly** and (d) **10cel-kSL** and **10cel-kSL-5gly** showing overlapping O–H and CH_2 stretching bands..238
Figure 6.8: FTIR spectra of fabricated cellulose-lignin-glycerol films with different lignin types (a) **cel-oHL-gly** (b) **cel-iHL-gly** (c) **cel-iSL-gly** (d) **cel-kSL-gly** overlapped with glycerol, $[C_2C_1im][OAc]$ and DMSO.....243
Figure 6.9: Tensile properties of cellulose-lignin-glycerol films at different various lignin and different weight percent (0, 0.5, 1, 2.5 and 4 wt.%) (a)**10cel-iHL-5gly** (b) **10cel-oHL-5gly** (c) **10cel-kSL-5gly** (d) **10cel-iSL-5gly**.....252
Figure 6.10: Average tensile properties of **cel-lig** and **cel-lig-gly** films at varying lignin contents (0, 0.5, 1, 2.5, and 4 wt.%), including **oHL**, **iHL**, **kSL**, and **iSL**.....254
Figure 6.11: Average tensile properties of cel-lig-gly films at various lignin content and weight percent ratio (**oHL**, **iHL**, **kSL** and **iSL**) at 0, 0.5, 1, 2.5 and 4 wt.%.....259
Figure 6.12: Tensile properties of **10cel-iHL** in comparison with **10cel-iHL-5gly**.....262
Figure 6.13: TGA curves of **cel-lig** and **cel-lig-gly** composite films at various lignin weight percent and different lignin types (a-b) hardwood lignin and (c-d) softwood lignin.....266
Figure 6.14: TGA curves of fabricated cellulose-lignin-glycerol films at various lignin weight percent and different lignin types (a-b) hardwood lignin and (c-d) softwood lignin.....269
Figure 6.15: Water contact angle of **cel-lig** and **cel-lig-gly** films at various weight percent and different lignin types (a -b) hardwood lignin and (c-d) softwood lignin.....271
Figure 6.16: Water contact angle of cellulose-lignin-glycerol films at various weight percent and different lignin types (a-b) hardwood lignin and (c-d) softwood lignin.....273
Figure 6.17: Compositional analysis for selected films for cellulose-organosolv hardwood lignin incorporated with 5 wt.% glycerol.....275
Figure 6.18: Surface morphology of all studied **10cel-iHL-5gly** films.....279
Figure 6.19: Proposed model to describe the location of the lignin within nanofibril suspensions and nanofibril after pressing. Image adopted from Rajo et. al[46].....280
Figure 6.20: SEM images comparison of surface morphology for films with (left) and without glycerol (right) (**cel-iSL** vs. **cel-iSL-5gly**). The glycerol-containing counterpart at 1 wt.% iSL was unavailable.....282
Figure 6.21: XRD patterns for (b) **10cel-iHL-5gly** films overlapped with (a) **cel** and **10cel-5gly**.....283

List of Tables

Table 1.1: Twelve principles in green chemistry 24
Table 1.2: Green metrics based on percentages and kg/kg analogous 27
Table 1.3: Synthetic routes to [C_2C_1im][OAc] 31
Table 1.4: Cellulose-lignin composite with various sources with key properties and potential applications 37
Table 1.5: Evaluation criteria of the solvent system for biomass processing 39
Table 1.6: Comparative review of film fabrication parameters and characteristics 42
Table 1.7: Glycerol as plasticiser in polysaccharide and protein-based films 49
Table 1.8: Heating rates and T_{onset} of cellulose, lignin and lignocellulosic film 52
Table 1.9: Aspects considered in determining mechanical properties of cellulose-lignin composite films 55
Table 1.10: Differences in experimental setups and studied parameters to determine water contact angle of fabricated cellulose-lignin films 58
Table 1.11: Reported optical properties of cellulose–lignin composite films, highlighting performance variations and common methodological gaps 62
Table 3.1: Green metrics analysis and cost for three different syntheses of [C_2C_1im][OAc] 103
Table 4.1: Solubility experiment of cellulose in [C_2C_1im][OAc] in different water content 111
Table 4.2: Lignin solubility in imidazolium-based ionic liquid 115
Table 4.3: Ionosolv softwood lignin (**iSL**) solubility test in [C_2C_1im][OAc] co-solvent with DMSO 118
Table 4.4: The experiment setup for different methods of degassing in a cellulose-lignin dope solution 124
Table 4.5: Lignin weight percent calculated according to the formula code 138
Table 4.6: Differences in thickness for 5 wt.% cellulose versus 10 wt.% cellulose 138
Table 5.1: Different type of lignins used in cellulose-lignin films 154
Table 5.2: Number Average Molecular Weight (Mn), Weight Average Molecular Weight (Mw), and Polydispersity Index (PDI) corresponding to the lignin 155
Table 5.3: FTIR assignments correspondence in hardwood and softwood lignin 161
Table 5.4: Different experimental setup for lignin hydroxyl quantifications 168
Table 5.5: Contents of different hydroxyl groups in lignin determined by ^{31}P NMR analysis 170
Table 5.6: Assignment for integral in HSQC NMR 176
Table 5.7: Range of maximum thermal decomposition temperature and unvolatilised weight fraction at 800°C of softwood and hardwood lignin 178
Table 5.8: Tensile properties of cellulose–lignin composite films at different lignin and content 197
Table 5.9: T_{onset} data of cellulose-lignin films from different types of wood 201
Table 5.10: Cellulose-lignin films measured and theoretical values 208

Table 6.1: Percent weight and glycerol concentration incorporated in cellulose dope solution ……218

Table 6.2: Assignments of FTIR bands in **10cel** and glycerol.....222
Table 6.3: Tensile properties of cellulose films at different glycerol quantities ranging from 2.5 to 15 wt.%.....226
Table 6.4: Tensile properties of cellulose–lignin-glycerol composite films at different lignin and content.....259
Table 6.5: Statistical significance criteria (Welch's t-test, n = 5) comparing the tensile properties of cellulose-ionosolv lignin composite films with and without glycerol incorporation (**cel-iHL** vs. **cel-iHL-5gly**).....262
Table 6.6: T_{onset} data of (a) cellulose-lignin-glycerol and (b) cellulose-lignin films from different types of wood.....264
Table 6.7: Cellulose-lignin-glycerol films measured and theoretical values.....277

List of Abbreviations

CO_2	carbon dioxide
HDPE	high-density polyethylene
LDPE	low-density polyethylene
PET	poly(ethylene terephthalate)
PLA	polylactic acid
ASTM	American Society for Testing and Materials
UV	ultraviolet
CS_2	carbon disulfide
NMMO	N-methylmorpholine-N-oxide
DMSO	dimethyl sulfoxide
DMF	dimethylformamide
DMAc	dimethylacetamide
ILs	ionic liquids
PILs	protonic ionic liquids
$[C_2C_1im]OAc$	1-ethyl-3-methylimidazolium acetate
$[C_1C_3im]Cl$	1-alkyl-3-methylimidazolium chlorides
$[C_2C_1im][Br]$	1-ethyl-3-methylimidazolium bromide
$[DMBA][HSO_4]$	*N,N*-Dimethyl-*N*-butylammonium hydrogen sulfate
AE	atom economy
E-factor	environmental factor
EMY	effective mass yield
NMR	nuclear magnetic resonance
TGA	thermogravimetric analysis
MS	mass spectrometry
FTIR	Fourier-Transform infrared
CA	compositional analysis
SEM	scanning electron microscopes

MCC	microcrystalline cellulose
CNF	cellulose nanofibre
RH	relative humidity
H	p-hydroxyphenyl
G	guaiacyl
S	syringyl
KL	kraft lignin
oHL	organsolv beech wood lignin
iHL	ionoslv beech wood lignin
iSL	ionsolv spruce lignin
kSL	kraft softwood lignin
WVP	water vapor permeability
WCA	water contact angle
PTFE	polytetrafluoroethylene
ASL	acid soluble lignin
AIL	acid insoluble lignin
cel	cellulose powder
10cel	regenerated cellulose film
cel-lig	cellulose-lignin film
cel-lig-gly	cellulose-lignin-glycerol film

Chapter 1: Introduction and Literature Review

1.1 Introduction

1.1.1 Plastics Problems

Large-scale manufacturing of plastic began in the 1950s, marking the initial widespread usage of plastic. In 1950, plastic production was around 2 million tons, which rose to 368 million tons by 2019, as depicted in Figure 1.1. Plastic constitutes roughly 5-12% of the overall material composition of global waste and 20-30% by weight. [1] Unfortunately, almost 80% of the produced waste reportedly accumulated in landfills or the natural environment, including the ocean. Merely 9% of the generated waste has been recycled.[2] Other waste management methods include incineration and biological treatment include composting and anaerobic digestion.[3] Incinerating plastic waste generates greenhouse gases (CO_2), air pollution, such as heavy metals, dioxins and particle matter. The accumulation of plastic waste adversely affects various ecosystem, threatening marine life in particular, while also posing several health concerns, including respiratory issues, increasing cancer risk, and hormonal irregularities resulting from the creation of microplastics.[4,5] This issue, also termed white pollution, occurs when plastic products such as packaging bags, agricultural mulch film, and polystyrene (PS), polypropylene (PP), and polyvinyl chloride (PVC) bottles contaminate the ecological environment and landscape.

Plastics are constituted of several synthetic and semi-synthetic chemicals, made up of monomers that are joined together in a repeating pattern, namely polymer and may be shaped into solid objects.[5] Since plastic originates from petrochemicals, the final product is typically non-biodegradable. Although plastics have downsides in terms of end-of-life management, plastics have numerous benefits such as being lightweight, high durability, chemical resistance and low production cost.[6] Numerous polymerization processes have been developed to fine tune the final properties, such as degrees of crystallinity, polarity, thermal stability, mechanical characteristics, gas permeability, optical properties, solubility, and functionalities.[7] Examples of plastics used in daily life are in the form of fibers, foams, films, adhesives, coatings and many more.

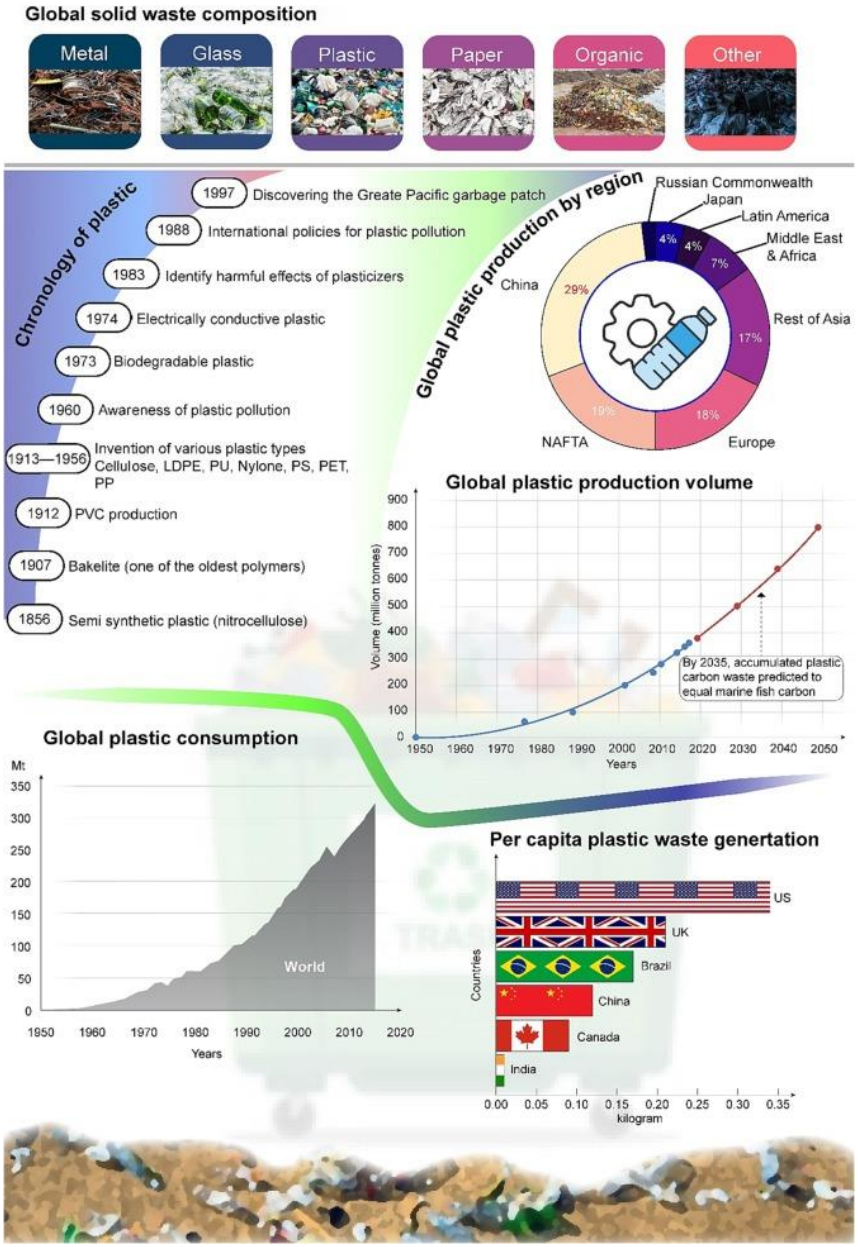


Figure 1.1: Graphical representation of solid waste composition, important chronological events, plastic production by region, global plastic production and consumption, and per capita plastic waste generation. Images taken with permission from by Pilapitiya and Ratnayake, 2024.[6]

Packaging offers a paramount and prevalent application of plastic materials. Approximately 40% of global plastic materials are utilized for the storage and packaging of final products from different companies. [2] The main polyethylene types utilized in the packaging industry are high-density polyethylene (HDPE) and low-density polyethylene (LDPE). Polyethylene possesses a low softening point, leading to reduced processing energy costs.[8] Others polymers that make up plastic packaging include polypropylene (PP) and poly(ethylene terephthalate) (PET). All

these polymers originate from diverse sources, including natural gas, petroleum, and coal, and are challenging to breakdown naturally, except through photodegradation, thermal degradation, and chemical degradation.[9] Inadequate photodegradation in landfills is both ineffective and contributes to secondary pollution. Secondary pollution refers to the formation of microplastics and the release of toxic chemical additives during partial photodegradation, which can then spread through soil and water systems.

In summary, petroleum-based plastics exhibit inherent limitations that pose serious environmental concerns. Their resistance to degradation leads to long-term accumulation of plastic waste, as these materials can persist in the environment for hundreds of years, contributing significantly to land and marine pollution and causing widespread ecological harm. Therefore, the necessity for biodegradable, bio-based polymers is vital.

1.1.2 Biodegradable Biopolymers

According to European standard EN13432, biodegradability is defined as the capability material to undergo rapid decomposition by microorganism facilitated by fungi and bacteria resulting in the conversion of the substrate into carbon dioxide, water, methane, and biomass.[10] A fundamental criterion of this process is that it must occur within both aerobic and anaerobic environments without leaving persistent toxic residues, thereby ensuring that the degradation products are not harmful to the environment. While biodegradation and dissolution are frequently conflated, they are mechanistically distinct.

Dissolution is a physical phenomenon characterized by the disentanglement and separation of polymer chains within a solvent. In the case of cellulose, for instance, the extent of dissolution is primarily governed by the effectiveness of the solvent in disrupting intermolecular forces to facilitate chain separation.[11] In contrast, biodegradation involves a fundamental chemical transformation. During this process, microbial enzymes act as biocatalysts that cleave the covalent bonds of the polymer backbone, effectively reducing long-chain polymers into smaller, transportable molecules. A prominent example is the polybutylene adipate terephthalate/polylactic acid (PBAT/PLA) film, which can be fully metabolized by soil microorganisms into CO_2 and H_2O.[12] Crucially, a prerequisite for this process is that the resulting degradation products must be non-toxic and pose no harm to the environment.

Biobased biodegradable polymers, such as PLA and polyhydroxybutyrate (PHB), can provide faster decomposition. However, a study showed that leachates from PLA and PHB exhibit toxicity comparable to that of extracts from traditional polymers.[13] While both polymers exhibit greater resistance to complete degradation in natural conditions (such as seawater and landfilling) than the standards set by International Organization for Standardization (ISO) tests for composting, their accelerated degradation relative to conventional polymers leads to a more efficient release of identified additives and microplastics into the environment.[13] Consequently, transitioning to lignocellulosic biomass, which is a highly abundant, cost-effective, and non-competitive source relative to the food chain, can be advantageous.

Biomass plastic, or bioplastic, refers to a category of polymers produced from renewable resources, including corn starch (e.g., PLA created from lactic acid sourced from corn), polysaccharides such as starch, cellulose, and protein, as well as some aliphatic polyesters, as seen in Figure 1.2. Certain types of bioplastics can be biodegradable, but others, such bio-PE, are not readily biodegradable. Polybutylene succinate (PBS) can undergo biodegradation by microbial activity on hydrolysis products. PBS exhibited a significant biodegradability of 48% weight reduction within 10 days utilising a lipase enzyme.[14] Among all biopolymers, lignocellulosic bioplastics have been receiving significant attention in recent years due to their exceptional biodegradability, recyclability by easy mechanical disintegration, natural abundance, and association with waste materials.[15]

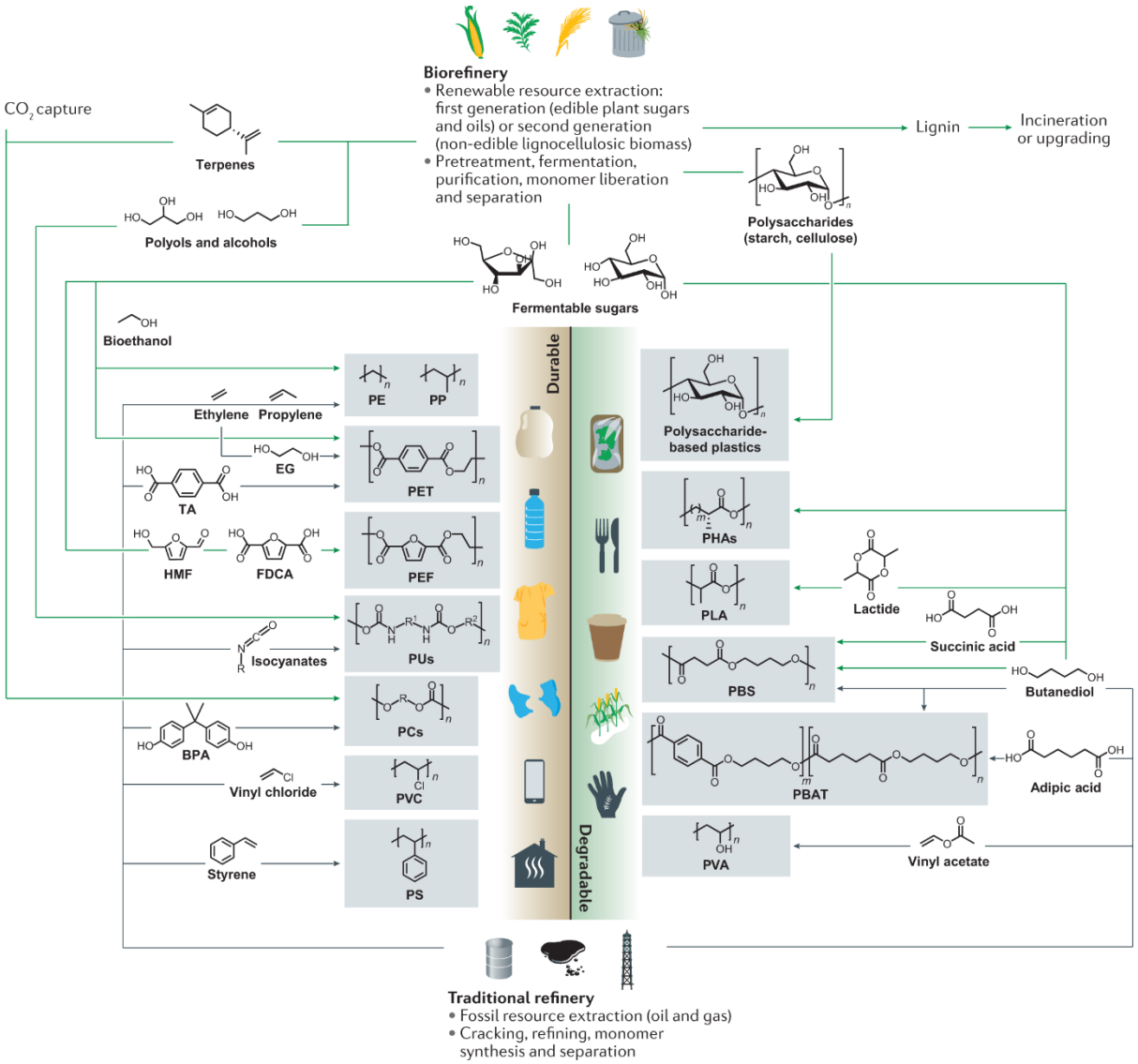


Figure 1.2: Routes for synthesizing polymers from fossil-based and bio-based sources. Adapted from Rosenboom et.al. (2022)[16]

Lignocellulosic biomass originates from plants and consists of polysaccharides (cellulose and hemicellulose) and an aromatic polymer (lignin). Lignocellulosic biomass is among the most plentiful renewable resources, with an estimated global yearly production of 200 billion tonnes.[17] Approximately 8.2 billion tonnes of lignocellulosic biomass is used throughout several application domains. Lignocellulosic biomass is derived from woody biomass, agricultural residues, and municipal solid waste, including pulp mill and timber mill wastes.[18] The utilisation of lignocellulosic wastes is believed to diminish reliance on petrochemical resources in the production of fuels and plastics. For the successful utilisation of substances recovered from lignocellulosic biomass (lignin, hemicellulose, cellulose, and other extracts),

they must be fractionated into marketable forms (biofuels and/or chemicals), as illustrated in Figure 1.3.

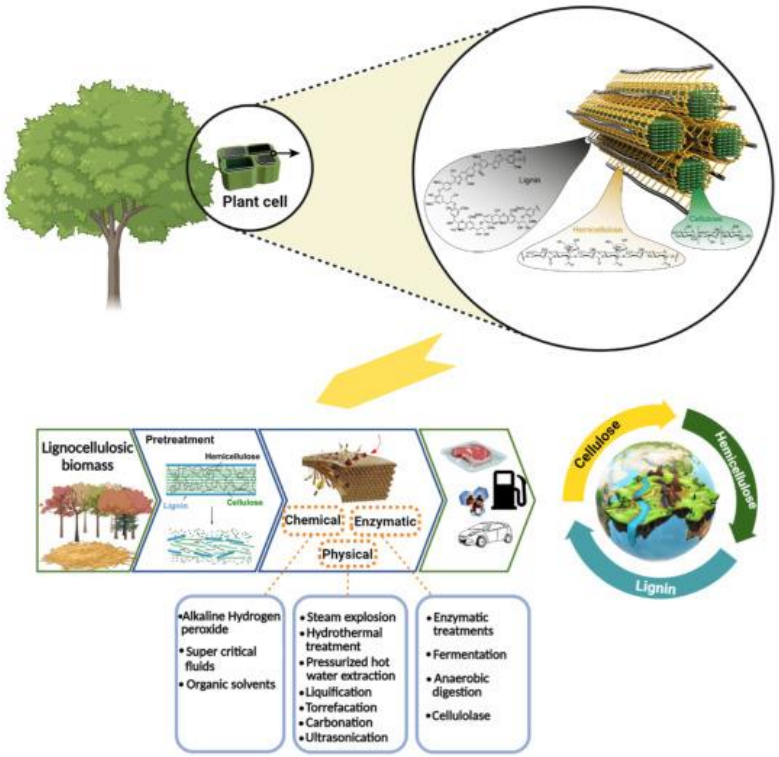


Figure 1.3: Routes towards isolation of different components, i.e., cellulose, lignin, and hemicellulose from lignocellulosic biomass. Image adapted from Mujtaba et. al., 2023[18]

Cellulose and lignin, prominent constituents of plant cell walls, have recently attracted considerable interest as biodegradable biopolymers with extensive application opportunities. These naturally occurring macromolecules have been thoroughly examined for their contributions to the advancement of sustainable materials, including fibers, hydrogels, composite films, and biomedical devices. Their attractiveness stems from their renewable characteristics, relative abundance, cost efficiency, and current underutilization in industrial applications.

Lignin is a major byproduct of the pulp and paper industry, with more than 70 million tons produced each year from the processing of lignocellulosic biomass.[19] Despite its intricate aromatic structure and inherent valuable attributes, lignin is predominantly underutilized and frequently regarded as waste or burnt for minimal energy recovery.[20] Conversely, cellulose is considered the most prevalent and extensively dispersed biopolymer on the planet which has

garnered increasing attention owing to its biodegradability, mechanical strength, and environmental friendliness. These characteristics make cellulose a particularly viable option for applications like biodegradable packaging materials, where environmental sustainability is important. Cellulose and lignin present a significant frontier in the search for bio-based materials, presenting substantial potential for value-added applications.[21]

Besides their distinct benefits, lignin and cellulose have advantageous chemical interactions, especially via hydrogen bonding, facilitating effective incorporation in composite materials. Multiple studies have shown that lignin can improve the wet strength of cellulose-based systems, principally through the establishment of intermolecular interactions and, in certain cases, covalent bonds between the two biopolymers.[22] These interactions enhance mechanical integrity and durability when exposed to moisture. However, the benefits of lignin incorporation are not uniformly beneficial; several studies suggest that the presence of lignin may diminish the overall mechanical strength of the composite. Nonetheless, these trade-offs frequently result in improvements in other functional attributes, such as ultraviolet (UV) blocking efficacy, which can be beneficial for particular applications.[23]

Despite these contradictory results, the synergistic combination of cellulose and lignin presents considerable potential for the creation of innovative of bio-based materials. To better utilize these natural polymers in various applications, it is essential to understand how they can be broken down and processed.

1.1.2.1 Cellulose

Cellulose is a polydisperse, linear homopolymer consisting of β-D-glucopyranose units linked by β-(1→4)-glycosidic linkages, as illustrated in Figure 1.4. Cellulose, the principal structural polysaccharide in the cell walls of plants and trees, is essential for preserving mechanical integrity and rigidity. The polymer chains arrange into supramolecular structures reinforced by significant intra- and intermolecular hydrogen bonding.[24] These interactions promote the simultaneous assembly of individual cellulose chains into primary fibrils, often 3–4 nm in diameter, which have a hierarchical structure consisting of alternating crystalline and amorphous domains along the fibril axis.[25] This hierarchical structure supports the exceptional mechanical strength inherent in native cellulose.

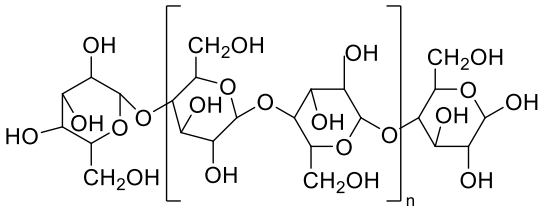


Figure 1.4: A cellulose polymer chain, n is typically 400-1000. Image adopted from Swatloski, et al. [24]

Cellulose can form both highly ordered (crystalline) and disordered (amorphous) domains due to its molecular structure. Crystalline cellulose comprises four distinct types, generally categorized into two primary types: cellulose I, the naturally occurring type present in plant fibers, and the regenerated or chemically modified forms with cellulose II, III, and IV typically generated through synthetic or post-treatment methods.[26] Cellulose I is the native polymorph consisting of two crystalline modifications: cellulose Iα and cellulose Iβ, which vary in unit cell symmetry and hydrogen bonding configurations. In cellulose I, the polymer chains exhibit a parallel alignment, and hydrogen bonding is restricted to individual molecular sheets. Conversely, cellulose II distinguished by an antiparallel chain configuration can be produced via the regeneration of native cellulose. This polymorph displays a more extensive hydrogen bonding network that encompasses both intra- and inter-sheet interactions, resulting in a three-dimensional (3D) structure. The conversion of cellulose I to cellulose II, III, or IV typically results in reduced overall crystallinity and crystallite dimensions, concurrently enhancing its inner surface area and modifying the physicochemical characteristics of the material. [27]

Cellulose can be categorized into distinct varieties according to the particular chemical or mechanical processes it experiences, like acid hydrolysis, oxidation, or high-shear mechanical disintegration. These treatments produce cellulose materials with distinct morphologies, dimensions, and structural characteristics, including nanocrystalline cellulose (NCC), nanofibrillated cellulose (NFC), and microcrystalline cellulose (MCC), as depicted in Figure 1.5.[28] Each shape displays distinct physicochemical characteristics due to variations in crystallinity, aspect ratio, and surface functioning. Alongside these structural variants, a diverse array of cellulose derivatives has been synthesized via chemical modification, yielding functionalized materials such cellulose acetate (CA), methylcellulose (MC), and

carboxymethyl cellulose (CMC), among others. These derivatives expand the applicability of cellulose by improving its solubility, processability, and compatibility with other materials. A wide range of studies has concentrated on the production of cellulose-based films employing NCC, MCC, and CA, demonstrating their applicability in advanced material applications.[29, 30,25, 31]

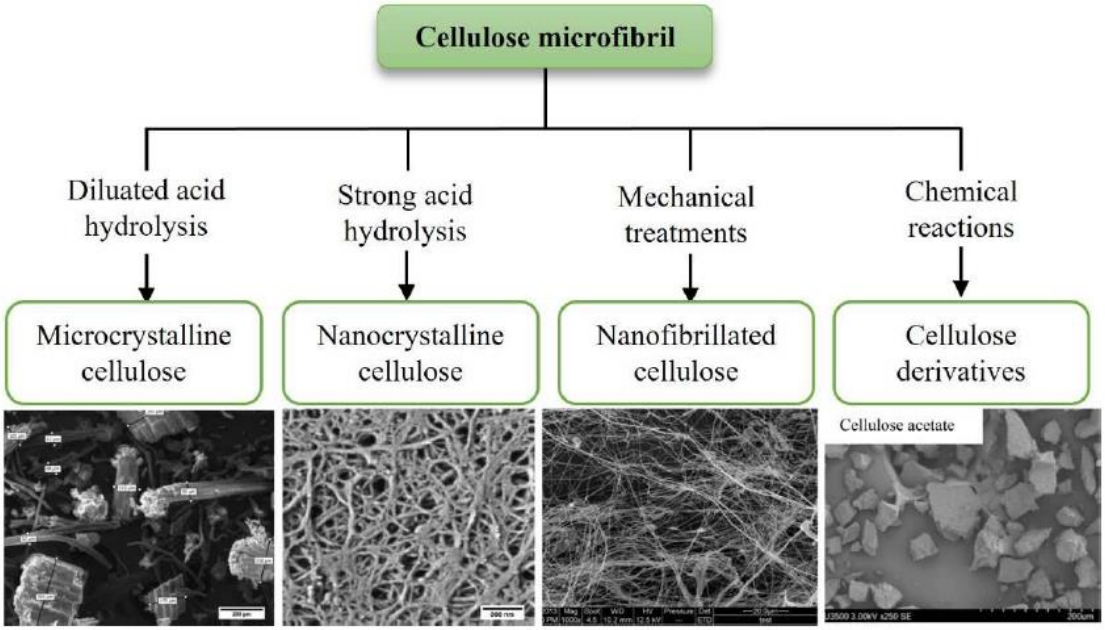


Figure 1.5: Different microstructure of cellulose derived from SEM images from different cellulose preparation method. Images adopted from Romão et. al [28]

The production of cellulose films often requires the regeneration of native cellulose I from solution via an antisolvent, such as water. Due to cellulose's inherently hydrophilic characteristics, water is essential in facilitating the breakdown and reformation of intra- and intermolecular hydrogen bonds, therefore prompting structural alteration. Amorphous cellulose can recrystallize into the thermodynamically stable cellulose II polymorph at ambient temperature when subjected to liquid water or water vapor under high relative humidity conditions (RH > 90%).[27] Nevertheless, despite water's function as a regeneration medium, cellulose remains insoluble in water because the extensive intermolecular hydrogen-bonding network and high crystallinity of cellulose stabilize the polymer chains more strongly than the hydrogen bonds that water molecules can form with them, preventing chain separation and dissolution. The regeneration of cellulose has numerous technical obstacles, with solvent selection being one of the most crucial. Effective dissolving usually demands solvents with

minimal water content and sometimes associates with non-green and environmental hazardous solvent. This poses an important challenge to the advancement of sustainable cellulose processing technologies and highlights the necessity for innovative, eco-friendly solvent systems that can effectively dissolve cellulose.

Dissolution is a process that disperses biopolymers in a solvent to create a homogeneous solution. Theoretically, this can occur via ideal dissolution, where the biopolymer completely dissociates into isolated, single chains uniformly dispersed throughout the medium. In practice, however, biopolymers typically exhibit non-ideal dissolution, characterized by the persistence of molecular aggregates rather than individual chains. This non-ideal behavior is driven by the dense network of intra- and intermolecular hydrogen bonding inherent to biopolymers.[32] Consequently, the dissolution of cellulose poses considerable difficulties owing to these distinct structural properties and chemical interactions. Each biopolymer therefore requires particular solvents and conditions capable of disrupting these hydrogen-bonded networks for efficient dissolution.

Cellulose is notably resistant to breakdown in water and most standard organic solvents. This resistance derives from the extensive structure of intra- and intermolecular hydrogen linkages, which enhance its high crystallinity and structural stiffness.[33] In the past, solvents including carbon disulfide (CS_2), N-methylmorpholine-N-oxide (NMMO), dimethyl sulfoxide (DMSO), dimethylformamide (DMF), and dimethylacetamide (DMAc), in conjunction with lithium chloride (LiCl), have been utilized to dissolve cellulose.[34, 35] Nevertheless, most of the studied solvents present environmental and safety issues. For example, carbon disulfide is recognized for emitting hazardous sulfide fumes, which may induce respiratory distress and chest pain with brief exposure.[36]

The industrial dissolution of cellulose for fiber regeneration has evolved through three distinct generations of solvent systems, transitioning from indirect chemical modification to direct dissolution as illustrated in Figure 1.6. Historically, carbon disulfide (CS_2) stands as the most globally dominant Generation 1 solvent system used for processing native cellulose into viscose rayon.[37] This traditional route is characterized by a low-cost yet chemically harsh two-step derivatization process, which are native cellulose is initially treated in sodium hydroxide

and reacted with with CS_2 that converts into sodium cellulose xanthate (viscose). The commercial production of cellulose began with the development of cellophane in 1903, generally derived from wood pulp or cotton linters.[38] This procedure entails the transformation of cellulose into viscose through treatment with alkali and CS_2 with a technique that, despite its industrial efficacy, produces dangerous consequences including poisonous sulfide gasses. As a result, there is an increasing demand to devise environmentally sustainable techniques for cellulose film production.

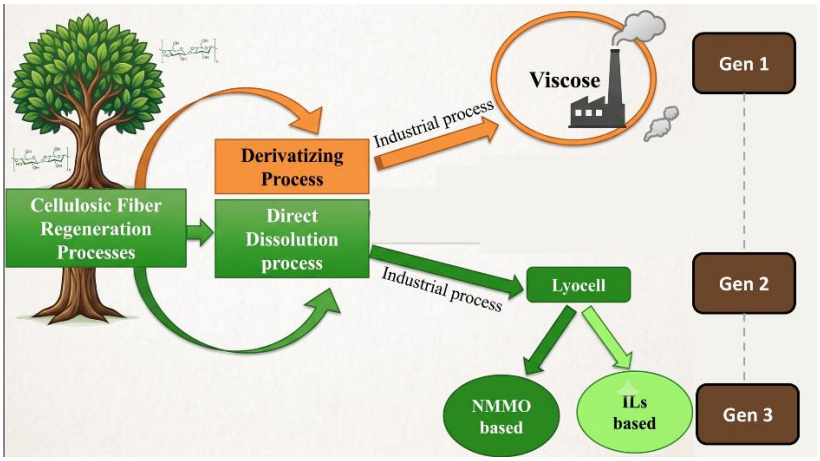


Figure 1.6: Classification of cellulose regeneration processes showcasing the primary derivatizing (Gen 1) and direct dissolution pathways (Gen 2 and 3) for cellulose fiber production

Next, generation 2 solvent systems introduced direct, non-derivatizing dissolution. NMMO is the only solvent presently utilized on an industrial basis, particularly in the manufacture of Lyocell fibers. Nonetheless, the NMMO-based approach has certain disadvantages, such as elevated energy consumption, thermal instability, and vulnerability to oxidative degradation during processing.[33] The dissolution process using NMMO is exothermic, generating concerns about potential runaway reactions and explosion threats that threaten operational safety.[37] Moreover, by-products produced during NMMO processing may contaminate the resultant cellulose fibers, thereby impacting material purity and performance. These constraints have stimulated continuous investigation into safer, more efficient, and ecologically friendly solvent systems for the dissolution and processing both of cellulose and lignin.

Generation 3 solvents are represented by ionic liquids (ILs). ILs is an organic liquid salts.[39] Renowned as highly tunable solvents, ILs like 1-butyl-3-methylimidazolium chloride,

([C_4C_1im]Cl) and 1-ethyl-3-methylimidazolium acetate, [C_2C_1im][OAc]) offer a highly stable platform for direct, non-derivatizing cellulose dissolution by disrupting hydrogen bonds via strong anion-hydroxyl interactions.[40] The primary advantages of ILs compared to other solvents from their negligible vapor pressure and excellent thermal stability. These properties completely eliminate the risk of volatile emissions (Gen 1) and hazardous exothermic runaway reactions (Gen 2) during high-temperature spinning. However, the main disadvantage of ILs compared to alternative solvents is that the synthesis and purification of high-quality ILs remain significantly more expensive than the low-cost reagents used in the viscose process or commercial NMMO.

1.1.2.2 Lignin

In contrast to cellulose, a linear and well-defined sequence of homopolysaccharide made up of β(1→4)-linked D-glucopyranose, lignin is an amorphous, three-dimensional, racemic aromatic heteropolymer characterized by a diverse array of interunit bonding configurations. Lignin is synthesized through the oxidative radical coupling of three principal monolignols: p-coumaryl, coniferyl, and sinapyl alcohols which vary in their extent of aromatic methoxylation and, when integrated into the polymer, yield p-hydroxyphenyl (H), guaiacyl (G), and syringyl (S) phenylpropanoid units as illustrated in Figure 1.7.[41] Lignins from dicotyledonous angiosperms (hardwoods) are predominantly composed of G and S units with minimal H content, while gymnosperm (softwood) lignins are primarily characterized by G units and low H levels. Grass (monocot) lignins generally possess similar quantities of G and S units, along with a greater fraction of H units compared to dicots. [42]

The phenylpropanoid units are interconnected via ether bonds (e.g., β-O-4, α-O-4, 4-O-5) and carbon–carbon bonds (e.g., β-β, β-5, β-1, 5-5), with the β-O-4 aryl–glycerol ether being the predominant connection as shown in Figure 1.8. The macromolecule exhibits many functional groups such as phenolic and aliphatic hydroxyls, carbonyls, methoxy substituents, and carboxyls that collectively dictate lignin's chemical reactivity and processing characteristics.[43]

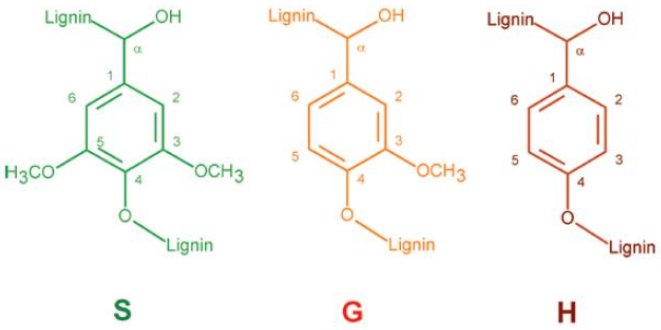


Figure 1.7: Lignin monomers which are (S) syringyl units, (G) guaiacyl units, (H) p-hydroxyphenyl units. Images adopted from Zikeli et al.[44]

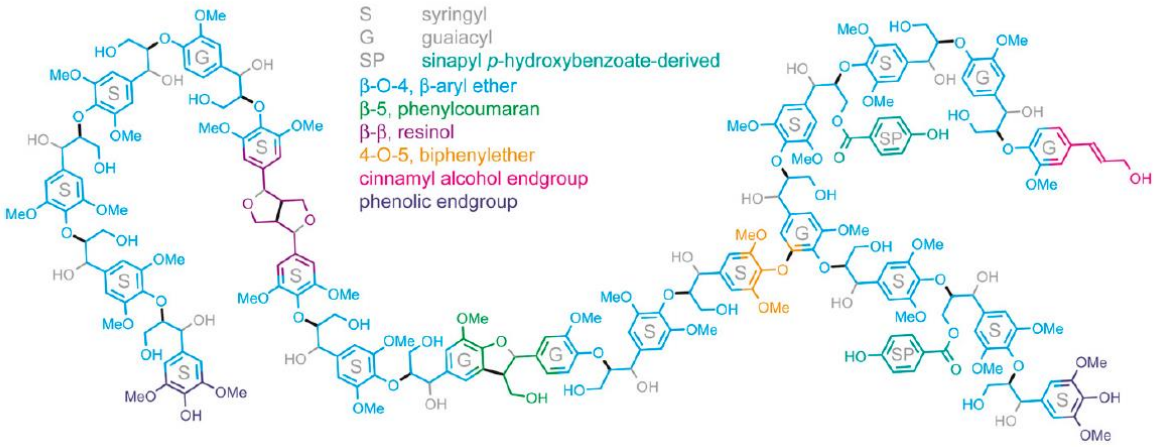


Figure 1.8: Representation of a lignin polymer from poplar, as predicted from NMR-based lignin analysis. Images adopted from Stewart et. al [45]

A wide variety of lignin extraction/fractionation techniques has been established, each affecting the physicochemical characteristics and subsequent utility of the obtained lignin. Attaining good homogeneity in lignin preparations generally requires post-isolation fractionation, predominantly using membrane filtering or solvent fractionation methods.[46] Fractionation methods are often classified according to the utilization of sulfur-containing or sulfur-free reagents. The majority of technical lignins are currently obtained as byproducts from industrial pulping processes, predominantly the kraft method. This method yields around 120 million tonnes of pulp annually, leading to the processing of nearly 70 million tonnes of lignin.[46] Kraft lignin (KL) is produced through the alkaline delignification of wood chips utilizing sulfur-based reagents, including sodium sulfide and sodium hydroxide. The kraft process while efficient, entails significant energy consumption and produces sulfur-laden waste streams, prompting environmental and economic issues.[47]

The organosolv pulping technique presents significant advantages, especially in producing sulfur-free lignin with minimum structural damage. Nonetheless, its extensive application is impeded by the thermal instability of numerous organic solvents and the substantial expenses related to solvent recovery and recycling.[47] Recently, ionic liquid (IL)-based pretreatment methods have been developed as viable alternatives, providing both economic and operational advantages. One technique, termed ionoSolv, employs aqueous protic ionic liquids to selectively solubilize lignin and hemicellulose, while maintaining a cellulose-rich solid fraction. Lignin precipitation is accomplished by introducing an anti-solvent, usually water, facilitating its effective extraction from the ionic liquid medium.[48] Lignin's high chemical versatility has led to a wide range of applications.

Lignin has many oxygen-containing functional groups, including phenolic and aliphatic hydroxyls, carboxyl, carbonyl, ether, and ester connections, which contribute to its significant reactivity and allow its use in numerous chemical and pharmaceutical applications.[49] These properties make lignin a viable precursor for the synthesis of bio-oils, adhesives, resins, and agrochemical transporters, including pesticide formulations. Furthermore, lignin's aromatic composition contains chromophoric groups that give ultraviolet (UV) absorption characteristics, enabling it to serve as a comprehensive UV-blocking agent. This attribute renders lignin a suitable component in sunscreens and other photoprotective substances. Amid rising environmental concerns and the demand for sustainable alternatives to petrochemical products, lignin-derived polymers present a renewable, biodegradable foundation for the creation of bio-based plastics, thus facilitating the shift towards a circular bioeconomy.

Although hydroxyl functionalities are crucial in influencing the reactivity and interfacial characteristics of lignin in composite materials, there is a lack of studies utilizing quantitative spectroscopy to evaluate the hydroxyl group content of lignin, especially concerning the physicochemical properties of cellulose–lignin film composites. Due to lignin's substantial presence of phenolic hydroxyl groups, in addition to aliphatic hydroxyls and carboxylic functionalities, ^{31}P NMR serves as an effective method for its structural characterisation. This technique is well-established for analyzing isolated lignins in fundamental lignin chemistry and valorization; nevertheless, its use in composite material research is still constrained.[43,50]

Guo et al. established a correlation between measured hydroxyl content and the antioxidant and UV-shielding efficacy of cellulose/technical lignin composites, underscoring the utility of ^{31}P NMR data for optimizing functional properties.[51] Nonetheless, a thorough comprehension of what types and concentration of hydroxyl groups affect composite properties, including film's mechanical strength, hydrophilicity, and thermal stability, remains elusive. Furthermore, a technical deficiency persists in the application of the ^{31}P NMR approach to a wider variety of technical lignins obtained from various processing methods (e.g., kraft, organosolv, ionic liquid extraction). This gap has restricted the extensive implementation of hydroxyl measurement in composite material design and has hindered the progress of lignin valorization technologies in bio-based functional films.

Dissolving lignin presents an additional hurdle. Lignin possesses a complex and heterogeneous structure characterized by multiple interunit connections, such as ether and carbon–carbon bonds. This structural complexity results in its inherent recalcitrance and diminished solubility in standard organic solvents.[52] Lignin isolation and processing generally necessitate severe conditions, including high temperatures and the application of strong acidic or alkaline solutions. Among the solvent systems investigated for lignin dissolving, ammonia especially in its liquid state has demonstrated notable efficacy. The utilization of liquid ammonia entails practical constraints, necessitating elevated pressures and reduced temperatures for safe and prolonged management, thereby complicating extensive applications.[53] These challenges have prompted the exploration of alternative solvent systems with improved efficiency and practicality.

Aprotic polar solvents, including dimethyl sulfoxide (DMSO) and dimethylformamide (DMF), together with ionic liquids, have exhibited differing levels of efficacy in lignin dissolution.[53] However, their efficacy is significantly influenced by the particular structural attributes of the lignin, which can differ based on its species origin and extraction process. For example, not all lignin types are completely soluble in DMSO, and the application of DMF presents considerable issues owing to its established toxicity.[53] Furthermore, none of these traditional solvents can concurrently dissolve both cellulose and lignin, which is a crucial prerequisite for the development of integrated biomass valorization processes. In this context, there is a critical need for the formulation and utilization of green solvent systems that satisfy essential criteria: low volatility, low toxicity, recyclability, and the capacity to dissolve both cellulose and lignin.

In summary, although aprotic solvents are effective for dissolving lignin, no conventional solvent can dissolve both lignin and cellulose simultaneously. This limitation highlights the advantage of ionic liquids, which possess tunable properties that enable the concurrent dissolution and processing of lignocellulosic biomass.

1.1.3 Ionic Liquids

Ionic liquids (ILs) are liquids exclusively constituted of ions, comprising a cation and an anion. In recent decades, ILs have garnered considerable attention owing to their distinctive physicochemical characteristics, such as minimal vapor pressure, thermal stability, and strong solvating capability. These attributes have made them as indispensable agents in both scholarly study and industrial applications, especially as catalysts and solvents.[54]

The initial report on the application of ionic liquids in cellulose processing was made by Swatloski et al. in 2002, who illustrated the ability of specific ionic liquids to successfully dissolve cellulose pulp.[34] This advancement created new opportunities for cellulose dissolution, regeneration, and chemical modification. The process via which ionic liquids dissolve cellulose mostly entails the breaking of its extensive hydrogen bonding network. The anions of ionic liquids interact with the hydroxyl groups of cellulose, displacing the native hydrogen bonds and resulting in molecular dissolution.[55] Figure 1.9 depicts common cation-anion pairings utilized in the dissolving and extraction of cellulose and lignin from lignocellulosic biomass.

The most efficient ionic liquids for cellulose dissolution include 1-alkyl-3-methylimidazolium chlorides, $[C_3C_1im]Cl$. Nonetheless, their application is frequently constrained by the corrosive nature and environmental issues related to halide anions. To resolve these challenges, BASF an innovator in industrial ionic liquid applications utilized 1-ethyl-3-methylimidazolium acetate ($[C_2C_1im][OAc]$) for cellulose dissolving. This ionic liquid demonstrates a beneficial array of characteristics, including low toxicity ($LD_{50} > 2000\ mg \cdot kg^{-1}$), minimal corrosiveness, a low melting point (< –20 °C), low viscosity (10 mPa·s at 80 °C), and excellent biodegradability.[56] Moreover, high-throughput screening methodologies, including quasi-

continuous dissolution profiling, have facilitated the comparative assessment of extensive libraries of ionic liquids up to 96 in a single investigation. These endeavours have consistently recognized [C_2C_1im][OAc] as one of the most efficacious solvents for cellulose dissolving, positioning it as a prime choice for subsequent advancement in biomass valorization strategies.[57]

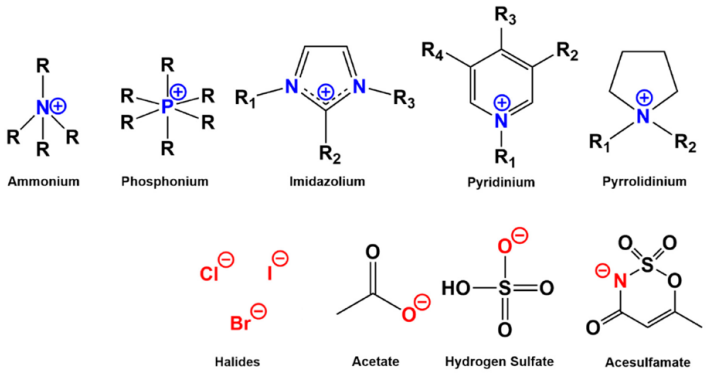


Figure 1.9: Some of cations and anions in ionic liquids commonly used for wood and cellulose dissolution and extraction. Image adapted from Abushammala and Mao, 2020[34]

Recent research has shown that specific ILs can dissolve lignocellulosic biomass, facilitating the partial or total dissolution of lignin as well. Investigations into ionic liquids for lignin dissolution have primarily concentrated on imidazolium-based ionic liquids, which have demonstrated significant efficacy in solubilizing lignin under very mild conditions. The most effective ILs documented for lignin dissolving include 1-butyl-3-methylimidazolium chloride ([C_4C_1im]Cl), 1,3-dimethylimidazolium methyl sulfate ([Mmim][$MeSO_4$]), and [C_2C_1im][OAc]. [Mmim][$MeSO_4$] has exhibited lignin solubility of 344 g/L, signifying its potent solvating capability.[52] The solubility of lignin in ionic liquids is predominantly influenced by the characteristics of the anion; anions exhibiting more basicity and hydrogen bond acceptor capacity typically disrupt lignin's hydrogen bonding and cleave ether connections, including β–O–4 bonds. The acetate anion is more effective than chloride in dissolving both lignin and wood due to its greater basicity and capacity to disrupt lignin's structure.[34] Conversely, ionic liquids with large, non-coordinating anions like tetrafluoroborate ($[BF_4]^-$) and hexafluorophosphate ($[PF_6]^-$) are typically inefficient as solvents for lignin because of their inadequate interaction with lignin's functional groups.[54] In contrast, certain ionic liquids with stronger interactions have demonstrated markedly higher dissolution capacities, as evidenced by comparative studies.

Protz et al. (2021) conducted a comparative analysis of various ionic liquid systems, revealing that the apparent solubility limit of softwood kraft lignin in [C_2C_1im][OAc] was around 25.4%, whereas that of cellulose was about 20.3%. The measured values were marginally greater than those for 1-butyl-3-methylimidazolium cyclohexyl carboxylate ([C_4C_1im][Chc]), which demonstrated a maximum solubility of 22.6% for lignin and 17.4% for cellulose (Figure 1.10).[58] These findings highlight that [C_2C_1im][OAc] has superior ability to dissolve both components. Building on the success of such conventional ionic liquids, recent attention has shifted toward protonic ionic liquids as promising candidates for lignin dissolution.

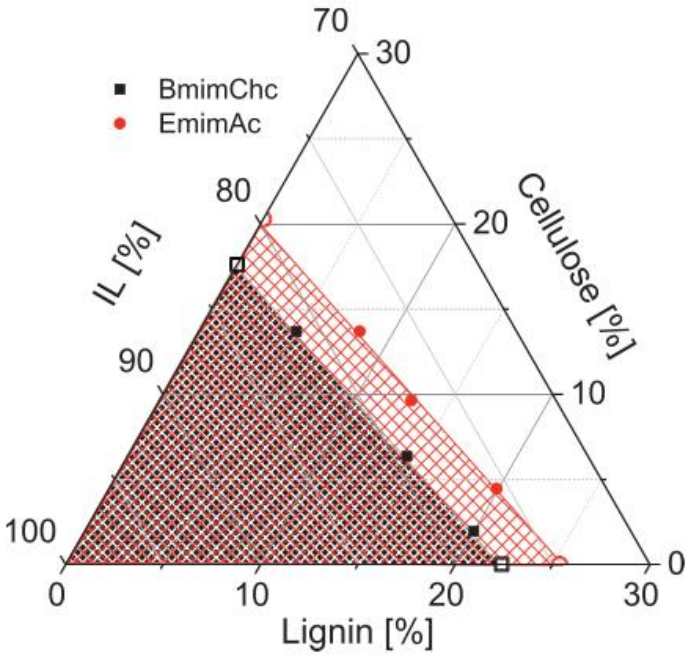


Figure 1.10: Section through the phase diagram of cellulose and softwood kraft lignin in ([C_4C_1im][Chc]) and [C_2C_1im][OAc], respectively at a temperature of 95 °C: filled symbols represent experimental results, empty symbols are extrapolated. Image adapted from Protz et al., 2021[58]

Protonic ionic liquids (PILs) have recently emerged as a viable alternative for the dissolving of lignin. PILs are often more economical than conventional ILs and have demonstrated effectiveness in altering lignin's structure via improved hydrogen bonding interactions with phenolic and aliphatic hydroxyl groups. PILs are often synthesised through a proton transfer process involving an organic acid and an organic base.[59] Nonetheless, a major restriction of PILs is their inability to dissolve cellulose; they are just useful for selective lignin extraction.[60]

This selectivity may benefit specific fractionation techniques but restricts their use in systems requiring simultaneous dissolution of both cellulose and lignin. To better evaluate their practical potential, it is important to examine how PILs perform in terms of lignin dissolution efficiency and processing times.

PILs containing the hydrogen sulfate anion ($[HSO_4]^-$) have been widely recognized for their effectiveness in processing lignocellulosic biomass, as extensively reported in the literature.[61] This efficiency arises from the ability of the $[HSO_4]^-$ anion to act as a strong hydrogen bond acceptor, facilitating the disruption of intermolecular hydrogen bonds within cellulose and lignin, thereby enhancing their dissolution. Among these, triethylammonium hydrogen sulfate ($[N_{2220}][HSO_4]$) has been one of the most frequently studied ionic liquids. In addition to its strong solvating capability, $[N_{2220}][HSO_4]$ is relatively inexpensive and enables facile recovery and recycling, making it a promising candidate for sustainable biomass pretreatment processes.

For instance, in the pretreatment of oil palm empty fruit bunches (OPEFB), $[N_{2220}][HSO_4]$ achieved optimal extraction performance at 85 wt.% composition and 120 °C. Under these conditions, the resulting biomass fractions contained 45.84% cellulose, 32.80% lignin, and 5.87% hemicellulose.[61] In a separate study, $[N_{2220}][HSO_4]$ was employed to dissolve willow biomass using the ionosolv pretreatment method to isolate lignin. [62] Furthermore, another ionosolv-based study utilizing $[N_{2220}][HSO_4]$ for cellulose pulp extraction from *Miscanthus* revealed that the process preserved the crystalline lattice structure of cellulose. Interestingly, an increase in Klason lignin content in overtreated pulp was associated with a moderate increase in particle size and a reduction in surface area, consistent with the deposition of pseudolignin on pulp surfaces.[63]

Building on these insights, subsequent studies have examined the kinetics of lignin dissolution in PILs under different operational conditions. Literature indicates that, under mechanical agitation, most types of PILs such as 2- hydroxyethylammonium malonate, 2-hydroxyethy-lammonium malate, 2-hydroxyethylammonium succinate, 2-hydroxyethylammonium glycolate require roughly 8 hours to attain saturation with lignin, except for lactate-based PILs, which require at least 24 hours. The utilization of ultrasound markedly expedited the process, lowering the saturation time to under 4 hours.[59] A separate investigation using nine distinct PILs demonstrated that ethanolamine acetate ([EOA][OAc]) could dissolve up to 35 wt% of enzymatic lignin at 90 °C.[64] Mechanistic insights obtained from model lignin dimer compounds

indicate that the increased solubility of lignin in PILs arises from a synergistic interaction between hydrogen bonding and electrostatic forces between the PIL constituents and lignin functional groups.

Considering the proven capacity of $[C_2C_1im][OAc]$ to efficiently dissolve both of cellulose and lignin, as indicated by phase diagram investigations, this ionic liquid presents itself as a highly promising solvent solution for the processing of lignocellulosic biomass. Its advantageous physicochemical characteristics such as low toxicity, moderate viscosity, and high hydrogen bond basicity render it especially effective in disrupting the intermolecular connections that support cellulose and lignin structures. Critical parameters, including dissolving duration and the highest attainable weight percentage of biomass in the ionic liquid, require careful optimization to guarantee effective and thorough solubilization. One strategy explored to address these optimization challenges is the incorporation of co-solvents, which can enhance overall dissolution efficiency.

A co-solvent is a secondary solvent added to a primary solvent system, often in smaller proportions to modify the system's physical and chemical properties, such as polarity, viscosity, or solubility capacity. The inclusion of a co-solvent has demonstrated efficacy in improving dissolving performance in various chemical processes. Several aprotic organic solvents, such as dimethylsulfoxide (DMSO), N,N-dimethylformamide (DMF), N,N-dimethylacetamide (DMA), and 1,3-dimethyl-2-imidazolidinone (DMI), have been employed as co-solvents to facilitate the dissolution of cellulose in ILs. DMSO has been shown to enhance the dissolving capacity of phosphonium-based ionic liquids by reducing the overall viscosity of the solvent system, facilitating mass transfer, and breaking the extensive hydrogen-bonding network of cellulose.[65] DMSO improves the kinetics and efficiency of biomass dissolving by promoting increased contact between the ionic liquid and the polymeric substrate. Consequently, including DMSO or similar co-solvents into $[C_2C_1im][OAc]$ may be an effective method for enhancing processability, especially in systems with complex biomass compositions. This co-solvent method has potential for facilitating more scalable, efficient, and adjustable biomass fractionation processes.

In conclusion, chloride-based ionic liquids such as $[C_3C_1im]Cl$ suffer from drawbacks including corrosivity and halide contamination, while inexpensive protic ionic liquids are

generally limited to dissolving lignin and are ineffective for cellulose. In contrast, [C_2C_1im][OAc], particularly when combined with DMSO, exhibits superior dissolution efficiency and reduced corrosive effects. Therefore, the following subsection focuses on a deeper understanding of the role of [C_2C_1im][OAc] in biopolymer processing.

1.1.4 Ionic Liquids in Biomass Processing

As previously mentioned, [C_2C_1im][OAc] was chosen as the ionic liquid (IL) for the dissolution of cellulose and lignin because of its ability to dissolve both lignin and cellulose and advantageous physicochemical characteristics. These characteristics encompass a low melting point, moderate viscosity, relatively low toxicity and adequate biodegradability. These properties provide [C_2C_1im][OAc] exceptionally suitable for the processing of lignocellulosic biopolymers while minimizing negative impacts on human health and the environment.[66]

Despite its benefits, concerns have emerged concerning the recyclability of [C_2C_1im][OAc], mainly due to its chemical interactions with lignocellulosic solutes and the possible degradation of dialkylimidazolium-based ionic liquids featuring basic anions.[67] Various investigations have proved the possibility of recovering high-purity [C_2C_1im][OAc] after its application in biomass processing. The acetate anion is acknowledged as a crucial factor in the dissolving mechanism of cellulose and lignin.[68] The function of the cation continues to be a topic of active debate. Computational modeling studies have enabled the evaluation of various ionic liquids (ILs) and indicate that cation structure may considerably affect solubility behavior.[69] These computational findings are complemented by experimental studies, particularly Nuclear Magnetic Resonance (NMR) spectroscopy, which provide direct evidence of the specific interactions occurring within such systems.

NMR spectroscopy data from investigations of the model system consisting of cellobiose and [C_2C_1im][OAc] indicate the establishment of hydrogen bonds involving both the anionic and cationic parts of the ionic liquid. The method specifically entails the interaction of free acetate anions, recognized for their strong hydrogen bond accepting capacity, with the hydroxyl groups of cellobiose. Simultaneously, the aromatic C–H protons of the bulky [C_2C_1im]$^+$ cation interact with the oxygen atoms of the hydroxyl groups, especially those that are less sterically obstructed.[69] This dual interaction effectively disrupts the vast hydrogen bonding network in

cellulose, enabling its breakdown. Figure 1.11 presents a schematic illustration of the suggested mechanism.

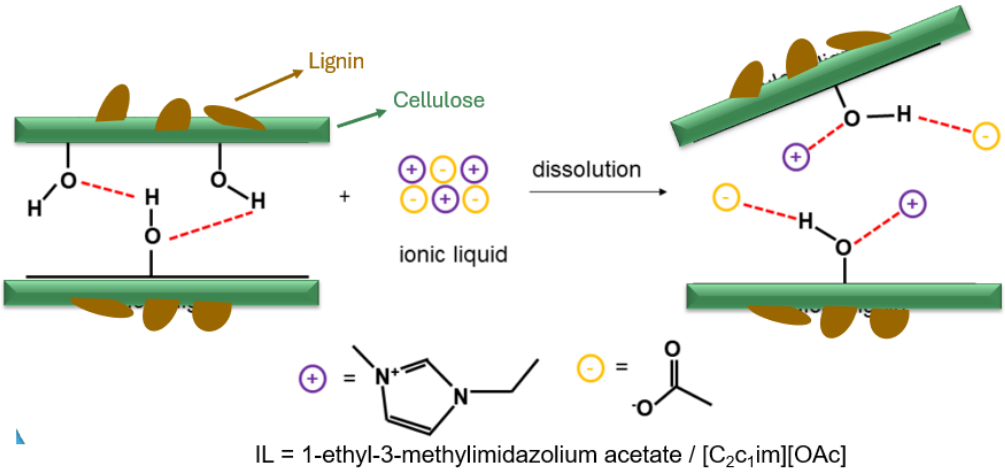


Figure 1.11: Hydrogen bonding rupture is presented as the mechanism for cellulose dissolution. In this representation, 1-ethyl-3-methylimidazolium acetate is chosen to exemplify the hypothetical H-bond interactions between the solvent molecules and cellulose.

Recent studies have shown that specific dialkylimidazolium-based ILs, notably [C_2C_1im][OAc], are exceptionally efficient in attaining near-total dissolution of entire lignocellulosic biomass, including southern yellow pine, bagasse, miscanthus, beech, poplar, and eucalyptus.[49] This results from a mixture of mechanisms: disruption of hydrogen bonding in cellulose, π–π interactions between the imidazolium cation and lignin aromatic structures, and the creation of electron donor–acceptor complexes between the ionic components of the IL and lignocellulosic substrates. These synergistic interactions enable the dissolution of cellulose and lignin inside a single medium.

Despite the established compatibility of cellulose and lignin in these solvent systems, the integration of lignin into cellulose-based composite materials has predominantly been restricted to low loading levels usually under 10% of total dry weight.[70] This conservative inclusion addresses challenges associated with lignin's structural heterogeneity and its effects on composite processability and performance. However, even minimal quantities provide beneficial intrinsic properties, including improved UV resistance, antioxidant activity, and mechanical reinforcement.

Several different ILs have been examined for their capacity to dissolve cellulose and lignin, such as [C_4mim]Cl and 1-allyl-3-methylimidazolium chloride ([C_3C_1im]Cl). Although these ionic liquids have shown success in solubilizing lignocellulosic biomass, the presence of halide anions poses issues regarding their possible corrosiveness, toxicity, and environmental implications. Notwithstanding these disadvantages, such ionic liquids may nonetheless present benefits compared to conventional caustic or organic solvents. [71]

Furthermore, a study examining the dissolving behavior of microcrystalline cellulose (MCC) in the ionic liquid [C_2C_1im][OAc] demonstrated a significant dependence on the water content within the solvent system. It was noted that increasing the water percentage in the [C_2C_1im][OAc] water mixture markedly diminished the solubility of MCC, with total dissolution inhibition happening when water concentration surpassed 20 wt%. While water is completely miscible with imidazolium-based ionic liquids, it fails to dissolve cellulose because of the latter's extensive hydrogen bonding network. Water preferentially interacts with [C_2C_1im][OAc] through hydrogen bonding, competing with cellulose for solvation sites and limiting the ionic liquid's capacity to effectively solubilize cellulose. Thus, the presence of water in the solution reduces cellulose solubility relative to that in pure [C_2C_1im][OAc]. Prior research has shown that, even for cotton linter, a structurally similar variant of cellulose, dissolving in [C_2C_1im][OAc]/water mixtures was restricted to a maximum water concentration of 15 wt%.[71] These findings highlight the necessity of maintaining low water content in [C_2C_1im][OAc] or analogous ionic liquids to facilitate effective cellulose dissolution.

In essence, the majority of existing literature has concentrated on the dissolution efficiency of ILs, highlighting elevated solubility yields and elucidating the mechanisms involved, especially the functions of cations and anions in promoting biomass dissolution. Nonetheless, very little focus has been directed towards the recyclability of ionic liquids, an essential determinant for their practical and economic feasibility in recurrent biomass processing. A notable deficiency persists in the literature about the utilization of green chemistry metrics to support the choice of particular ionic liquids for biomass dissolving. These gaps highlight the need for approaches that move beyond dissolution efficiency to assess the broader environmental sustainability of ILs in biomass processing.

1.2 Literature Review

1.2.1 Green Chemistry and Sustainable Synthesis

Green metrics emerged in the early 1990s as a reaction to chemists' increasing recognition of the necessity to reduce waste and the environmental impact of chemical processes. [72] A variety of strategies has been formulated to achieve this goal, focusing on the miniaturization of sample preparation methods and analytical instruments, the implementation of solvent-free or solvent-reducing extraction techniques, and the substitution of hazardous solvents with more environmentally friendly alternatives. [73] The Twelve Principles of Green Chemistry (12PGC) serve as a foundational framework, providing a comprehensive and widely accepted vision for attaining sustainability in the chemical sciences. The concepts outlined in Table 1.1 provide a fundamental framework for designing chemical processes that are safer, more efficient, and less harmful to the environment. [74]

Table 1.1: Twelve principles in green chemistry

• Waste prevention not remediation
• Less hazardous/toxic materials
• Innocuous solvents and auxiliaries
• Renewable rather than depleting raw material
• Catalytic rather than stoichiometric reagents
• Analytical methods for pollution prevention
• Atom efficiency
• Safer products by design
• Energy efficient by design
• Shorter synthesis (avoid derivatization)
• Design products for degradation
• Inherently safer processes

A range of green metrics has been established to objectively evaluate the environmental efficiency of chemical processes. The most commonly utilized metrics include reaction yield, atom economy (AE), Environmental factor (E-factor), Process Mass Intensity (PMI), and carbon efficiency (CE). [72] However, there is a deficiency of literature specifically utilizing these green metrics in the synthesis of $[C_2C_1im][OAc]$. This study seeks to assess suitable green metrics to determine the most sustainable, eco-friendly method and economically feasible for synthesizing $[C_2C_1im][OAc]$, aiming to reduce the environmental impact of solvent utilization in film production.

1.2.1.1 Green Metrics Analysis

Atom economy and the E-factor, established in the initial phases of green chemistry, continue to be the most essential and widely employed metrics owing to their conceptual clarity and practical relevance.[75] Table 1.2 outlines that green metrics can be primarily classified into two categories: percentage-based metrics (e.g., atom economy and carbon efficiency) and mass-based metrics (e.g., E-factor and PMI, quantified in kg/kg). These five indicators are especially important in organic synthesis, where enhancing material efficiency and reducing waste are essential for economic and environmental sustainability.

The Environmental factor (E-factor), proposed by Roger Sheldon, is an early and commonly utilized statistic for assessing the environmental impact of chemical processes. It is defined as the mass ratio of waste produced to the mass of product obtained, hence offering a direct measure of the material inefficiency of a reaction.[76] A lower E-factor signifies a more sustainable and ecologically friendly method. However, a significant drawback of this statistic is its failure to consider the environmental impact of the waste generated. To mitigate these constraints, the pharmaceutical industry established the Process Mass Intensity (PMI), which measures the total mass of all input materials (including reagents, solvents, and auxiliaries) in relation to the mass of the end product. Similar to the E-factor, a reduced PMI indicates a more material-efficient process. Nonetheless, PMI possesses several limitations: it fails to distinguish between waste categories (e.g., hazardous versus benign) and inadequately assesses multistep synthetic processes.[75] Notwithstanding these constraints, PMI has demonstrated

significant utility in pharmaceutical process development and management, functioning as an effective instrument for facilitating waste reduction and enhancing material efficiency.

Barry Trost established atom economy (AE) as a clear and theoretically sound tool for evaluating the efficiency of chemical syntheses.[73] AE is determined by dividing the molecular weight of the desired product by the total molecular weight of all reactants, hence calculating the fraction of starting materials integrated into the final product. This metric presumes optimal conditions, namely a 100% reaction yield, and excludes considerations of solvents or byproducts.[72] Lower AE values signify diminished efficiency and increased material waste, whereas higher values suggest greater atom efficiency and ecologically advantageous operations. Hudlicky and colleagues created the Effective Mass Yield (EMY), a metric that assesses the mass of the desired product in relation to the mass of non-benign reagents employed in the synthesis.[77] EMY offers a more pragmatic evaluation by factoring in the environmental acceptability of reagents and materials. Nevertheless, it omits elements classified as having little environmental impact such as saline water which in substantial quantities, may still impose significant ecological pressure. Carbon Efficiency (CE) is a significant environmental statistic that primarily emphasizes the utilization of carbon atoms.[74] It quantifies the proportion of carbon from the reactants that is preserved in the end product, therefore offering insight on carbon atom use and loss. In contrast to AE, CE frequently utilizes actual chemical formulas and reaction data, rendering it more indicative of real-world reaction synthesis. However, its scope is confined to carbon-containing species and does not consider the existence or influence of heteroatoms such as nitrogen, oxygen, or halogens, which are prevalent in numerous synthetic routes. To gain a more comprehensive understanding, it is essential to adopt an approach that considers the entire life cycle of the material.

Table 1.2: Green metrics based on percentages and kg/kg analogous

	Based on kg/kg analogous		Based on percentage analogous		
Metric Name	E factor	Process Mass Intensity (PMI)	Atom economy (AE)	Effective mass yield (EMY)	Carbon Efficiency (CE)
Formula	$\frac{total\ mass\ of\ waste}{mass\ of\ final\ product}$	$\frac{total\ mass\ in\ process}{mass\ of product}$	$\frac{mol\ wt\ of\ product}{sum\ of\ mol\ wts\ of\ reactants} x100$	$\frac{mol\ wt\ of\ product}{mass\ of\ hazardous\ reactants} x100$	$\frac{carbon\ in\ product}{total\ carbon\ reactants} x100$
Target value Advantageous	Ideally zero Widely recognised	Lower is better Simple	Lower is better Simple	Higher is better Intuitive % form	Higher is better Highlights carbon atom economy
Limitation	No info on waste severity	Does not differentiate waste type	Ignores the intermediates that are made in one stage	Reagents very low environment impact is excluded	Ignores non-carbon atoms
References	Sheldon, R. A. [75]	Sheldon, R. A. [75]	Constable, et al.[74]	Tobiszewski, et al. [72]	Tobiszewski, et al. [72]

A recent study conducted a life cycle assessment (LCA) of lignocellulosic films produced using the ionic liquid 1-ethyl-3-methylimidazolium acetate ([C_2C_1im][OAc]) using the ReCiPe 2016 framework to evaluate their environmental performance.[78] The discussion in this section focuses primarily on the global warming potential (GWP). The study revealed that the fabrication of lignocellulosic films imposes high environmental burdens, mainly due to energy-intensive processes such as ionic liquid synthesis and recovery, when compared with the production of commercial cellophane. The synthesis of [C_2C_1im][OAc] via the dimethyl carbonate route was identified as a significant contributor to the total GWP, with 1-ethylimidazole accounting for approximately 60% of the impact. During dope solution preparation, [C_2C_1im][OAc] contributed about 79% of the total GWP. In the film production stage, which includes a single ionic liquid recovery process, electricity consumption for freeze crystallisation was found to be the dominant contributor, representing 102 kg CO_2-eq per kilogram of film (56% of the total GWP). Freeze crystallisation facilitates selective water removal under low-temperature conditions, preserving the chemical integrity of both [C_2C_1im][OAc] and DMSO.

In the end, the green metrics examined are relatively easy to compute and provide valuable, though supplementary, insights into the environmental efficiency of chemical processes. In the laboratory-scale synthesis of [C_2C_1im][OAc] the most suitable metrics for assessing greenness were identified as the E-factor, Atom Economy (AE), and Effective Mass Yield (EMY). The Process Mass Intensity (PMI) was excluded from this study due to its conceptual overlap with the E-factor; both metrics pertain to material efficiency, with PMI concentrating on resource input and E-factor on waste production. Furthermore, PMI is widely adopted metric in the pharmaceutical industry for assessing the material efficiency of chemical processes. It can be applied to both laboratory and industrial scales to guide process optimization and sustainability improvements. Carbon Efficiency (CE), although beneficial in most organic transformations was considered inappropriate in this instance due to the inclusion of nitrogen atoms in the imidazolium ring structure, which CE fails to consider. Consequently, a comprehensive assessment utilizing E-factor, AE, and EMY offers a more accurate and contextually relevant evaluation of the sustainability of this synthetic pathway.

In summary, utilizing the E-factor, AE, and EMY is beneficial for selecting an appropriate synthetic method for ILs. Therefore, prior knowledge of IL synthesis efficiency such as yield, reaction conditions, and solvent usage is important in determining the chosen synthetic method.

1.2.2 Synthesis of Ionic Liquids

Ionic liquids (ILs) can be synthesized through a variety of pathways, with the choice of method often depending on whether the IL is miscible or immiscible in water.[39] The general strategy involves first constructing the cation framework and generating a suitable precursor, followed by incorporation of the desired anion. In many cases, the anions are obtained from commercial sources, since their direct synthesis can be challenging. Over the years, a wide range of synthetic approaches have been developed, including two-step synthesis, one-pot synthesis, solvent-free (fast) synthesis, ultrasound-assisted synthesis, ion exchange from halide precursors, high-pressure routes (e.g., dimethyl carbonate method), and metathesis reactions, among others.

ILs are predominantly produced using halide-containing precursors, such as chlorides or bromides, owing to the extensive availability of haloalkanes as initial materials for quaternization reaction.[79] The quaternization reaction, or quaternary ammonium salt production, is a nucleophilic substitution process where a tertiary amine or a structurally analogous base combines with an alkyl halide to produce a quaternary ammonium salt. This salt generally functions as the cation in the resultant ionic liquid. For instance, the production of $[C_2C_1im][OAc]$ often commences with the creation of 1-ethyl-3-methylimidazolium bromide ($[C_2C_1im]Br$) as an intermediate. The halide anion is then substituted via a metathesis reaction to get the desired product.

This halide-based method is well-established but has some disadvantages, including prolonged reaction times and the necessity for relatively expensive chemicals to enable anion exchange and isolate the final product.[80] Microwave-assisted synthesis considerably decreases reaction times from several hours to just minutes, and reduces the consumption of excess alkyl halides and organic solvents; yet, the subsequent purification process remains inefficient. To mitigate these limitations, alternate approaches such as one-pot synthesis and ion-exchange procedures have been suggested.[81,80] These considerations underscore the need for carefully optimized

synthetic routes, particularly in the case of [C_2C_1im][OAc], where purity and water content directly govern its performance in cellulose dissolution.

Synthesis of [C_2C_1im][OAc] with high purity and reduced water content is crucial for effective cellulose dissolution, given cellulose's greater susceptibility to moisture compared to lignin.[82] Multiple synthetic pathways have been established for the synthesis of [C_2C_1im][OAc], encompassing both halide-dependent and halide-independent approaches. Certain methodologies frequently necessitate extensive purification procedures, including recrystallization and vacuum distillation, to attain the requisite physicochemical characteristics. In recent years, synthetic methodologies have increasingly emphasized environmentally friendly, efficient, and economically feasible methods, in accordance with the principles of sustainable chemistry.

Table 1.3: Synthetic routes to [C_2C_1im][OAc]

Synthesis Method	Reagents and solvents	Purification method	Reaction conditions	Yield	Challenges	References
One-pot method	1-Methylimidazole, an excess of ethyl bromide, and propanetriol solution of lead acetate	The clear solution is washed with pure ethyl acetate (EtOAc) (30 ml) many times.	Reaction temperature at 60°C. After 20 hours, the white precipitated is removed by suction filtration. The product is obtained by vacuum rotary evaporation at 60°C for 2 hours.	87 %	Toxic from lead acetate was used. Extensive purification needed.	Zhu et. al, [80]
Ion exchange resin	Ambersep® 900 hydroxide form ion exchange resin, 1-ethyl-3-methylimidazolium ethyl sulfate, acetic acid, and deionised water	No purification needed	Aqueous 1-ethyl-3-methylimidazolium hydroxide is neutralized by careful addition of acetic acid at room temperature. The water is removed by rotary evaporation to yield 1-ethyl-3-methylimidazolium acetate.	95 %	Extensive water removal from the ionic liquid mixture.	Clough et. al,[83]
Ion exchange resin	1-butyl-3-methylimidazolium chloride, 2-butanone, sodium 4- tert-butylphenolate, Celite resin, acetic acid and deionised water	No purification needed	1-butyl-3-methylimidazolium chloride in dry 2-butanone is added to sodium 4- tert-butylphenolate. The reaction mixture is stirred for 12 h and filtered through Celite. An aqueous solution of acetic acid is added to the reaction mixture and stirred for half an hour. The organic phase is separated and washed with 50 mL of H_2O. The water is removed under vacuum to yield the product.	80 %	Sodium 4-tert-butylphenolate is harmful chemical and requires strict PPE and fume hood handling. Not suitable for the	Lethesh, et. al, [79]

					synthesis of ionic liquids with highly hydrophobic cations and choline cations.	
Metathesis	1-Ethyl-3-methylimidazolium bromide, silver acetate, and deionized water	Recrystallisation needed for $[C_2C_1im]Br$	1-Ethyl-3-methylimidazolium bromide, $[C_2C_1im]Br$ and silver acetate and deionized water were added, and the solution was stirred at room temperature for three days, during which time a yellow/green precipitate formed. The water is removed by rotary evaporation, and the product was dried at 50 °C under vacuum.	85 %	Prolonged reaction times	Clough et. al,[83]
Carbonate Based Ionic Liquid Synthesis (CBILS®)	1-ethyl-imidazole, and dimethyl carbonate	No purification needed	The formation of the quaternized alkylcarbonate intermediate, which is then reacted with Brønsted acids to obtain the final ionic liquid. Synthesis of 1-ethyl-3-methylimidazolium methyl-carbonate. Flow rates between 0.1 and 10-ml min^{-1} and pressures of up to 150 bar.	99.1 %	Elevated pressure	Kalb et. al, [84]

Two principal synthetic methods utilizing halide precursors have been extensively documented for the synthesis of [C_2C_1im][OAc], the traditional metathesis reaction and the ion-exchange resin method, as outlined in Table 1.3. For both methods require the preparation of halide precursor. The metathesis process entails the reaction of 1-ethyl-3-methylimidazolium bromide ([C_2C_1im]Br) with silver acetate under aqueous conditions, generally conducted over three days, as depicted in Figure 1.12. This approach is reasonably simple and has a high product output; however, it has notable disadvantages, such as extended reaction periods and the reliance on silver acetate. Unlike sodium or lithium acetate, which are more economical but ineffective in this transformation, silver acetate plays a role by delivering the acetate nucleophile. This necessity makes silver acetate indispensable, though it remains a costly and economically unfeasible reagent for large-scale synthesis.[83]

The ion-exchange resin approach employs either [C_2C_1im]Br or [C_2C_1im]Cl, which is passed through a column filled with an anion-exchange resin, as seen in Figure 1.13. The technique provides benefits including mild operating conditions (often at ambient temperature) and resin reusability, enhancing sustainability. Nevertheless, it is limited by low throughput, especially in batch column layouts.[83] A modified ion-exchange method utilizing phenolate anions has demonstrated the ability to yield [C_2C_1im][OAc] in moderate yields of up to 80%. However, this method is not universally applicable. Ionic liquids with cations that are unstable in strongly basic conditions, such as pyridinium-based ionic liquids, cannot be produced using this approach. Imidazolium-based ionic liquids demonstrate restricted stability in strong bases, as deprotonation may result in carbene generation. These carbenes can frequently be reverted to imidazolium salts through interaction with Brønsted acids. The production of choline-based ionic liquids is particularly difficult due to the very low solubility of choline phenolate salts in non-polar organic solvents.[79]

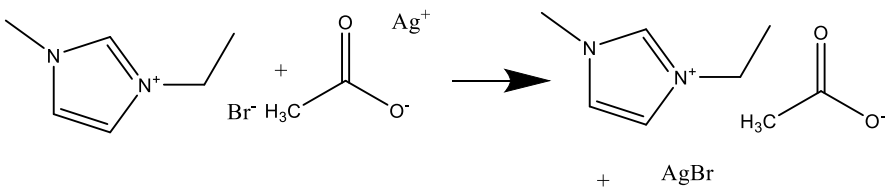


Figure 1.12: Synthesis of [C_2C_1im][OAc] using metathesis route

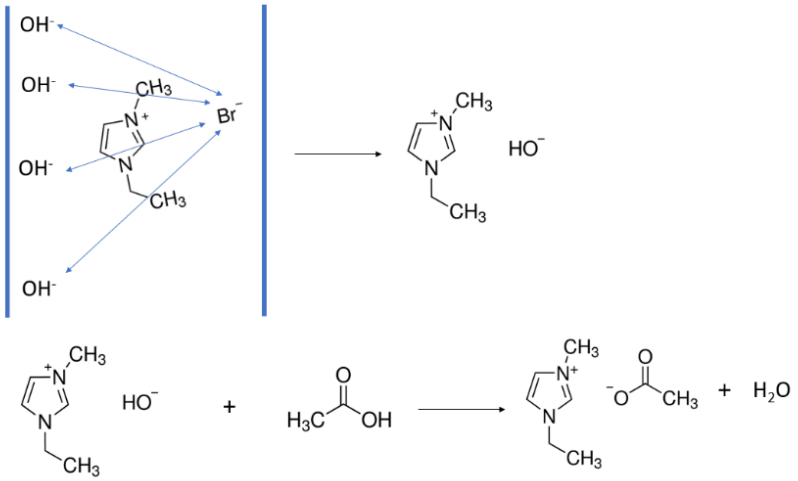


Figure 1.13: Synthesis of [C_2C_1im][OAc] using ion exchange resin route

A one-pot method has been developed to eliminate halide precursors and simplify multi-step synthesis, as depicted in Figure 1.14. This method streamlines the synthesis by combining all ingredients in one reaction vessel, producing [C_2C_1im][OAc] with an efficiency of roughly 87%.[80] Notwithstanding its operational simplicity, the technique exhibits some substantial flaws. It requires extensive purification with substantial quantities of ethyl acetate, which poses issues related to solvent waste and environmental consequences. The utilization of lead acetate as a reagent presents toxicity and sustainability concerns, hence constraining the green chemistry qualifications of the method. The one-pot approach, sometimes claimed as a more efficient and possibly environmentally friendly option, needs thorough assessment, especially for reagent toxicity, solvent usage, and overall ecological impact.

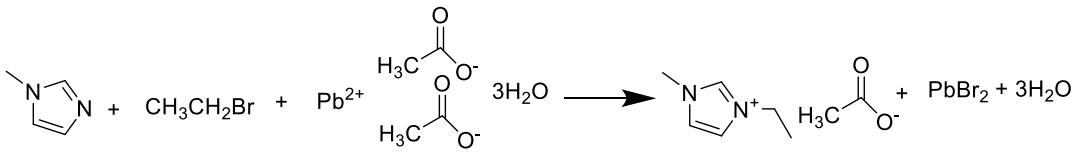


Figure 1.14: Synthesis of [C_2C_1im][OAc] using one pot method

A halide-free alternative involves the synthesis of ionic liquids by carbonate-based methods, signifying one of the most sophisticated and commercially feasible technologies for the environmentally friendly synthesis of ionic liquids. This approach depends on the formation of a quaternized alkylcarbonate intermediate, which then reacts with a Brønsted acid to produce

the required ionic liquid. In the instance of [C_2C_1im][OAc], 1-ethylimidazole undergoes a reaction with dimethyl carbonate to yield 1-ethylimidazolium carbonate as illustrated in Figure 1.15. The intermediate is subsequently processed with acetic acid and methanol yield [C_2C_1im][OAc] and carbon dioxide. It is important to note that many ionic liquid precursors, such as 1-ethylimidazole or dimethyl carbonate, are not directly available in high-purity form and must themselves be synthesized or purified prior to their use in ionic liquid preparation. These steps should be considered integral to the overall process, since the synthesis conditions and resulting purity of precursors directly influence the outcome of subsequent reactions and analyses. Experiments on continuous flow synthesis at different temperatures and residence durations revealed that a temperature of 200 °C for 120 minutes achieved a conversion efficiency of 99.1%.[84] A primary benefit of this approach is the utilization of methanol, a volatile solvent that can be easily eliminated from the end product, hence enhancing purification. This synthetic technique is utilized industrially due to its reduced environmental impact and elimination of halide waste; yet, it requires meticulously regulated reaction conditions, especially concerning temperature and CO_2 management.

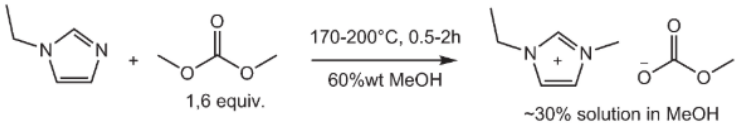


Figure 1.15: Synthesis of 1-ethyl-3-methylimidazolium methyl- carbonate.

To summarize, all the synthetic methods discussed achieved good yields (greater than 80%). Among them, three methods were selected for further study: (1) metathesis, (2) ion-exchange resin, and (3) the one-pot method. These methods were chosen because they all use halide precursors, making them suitable for comparative analysis. Once lignin and cellulose are successfully dissolved in the selected IL method, the technique used for film fabrication becomes crucial, as it directly influences the properties and characteristics of the resulting cellulose-lignin composite films.

1.2.3 Cellulose-Lignin Composite Films

Developing sustainable materials that combine strength, durability, and UV protection is increasingly important for next-generation coatings, packaging, and optical devices. Inspired by the structure of natural wood, cellulose–lignin composite films have emerged as a promising solution. Cellulose provides a strong and flexible framework, while lignin contributes hydrophobicity and inherent UV-blocking properties. Together, they form multifunctional materials that mimic the performance of natural fibers while enabling modern engineering applications such as coatings, vehicle windshields, architectural glazing, contact lenses, and specific biological sample containers.[23]

Considering the wide supply of cellulose and lignin as by-products of the pulp and paper industry, their incorporation into composite materials presents a sustainable and potentially biodegradable alternative to traditional materials. This review will examine the fabrication of cellulose-lignin composites, emphasizing the sources and varieties of cellulose and lignin, technical aspects in the processing methods, challenges in solubility of biopolymers and gaps in understanding of structural-property relationships.

1.2.3.1 Cellulose and lignin sources, fabrication techniques and key features in cellulose-lignin composites

Table 1.4 summarizes that the principal source of cellulose for the fabrication of cellulose–lignin composites has conventionally been cellulose pulp, with in the range of degree of polymerization between 650 and 680. Historically, cellulose pulp, easily obtained from wood and relatively inexpensive, had adequate structural integrity and bonding capacity to function as an appropriate matrix for bulk composite production with lignin.[85] Recent developments in processing techniques have redirected focus to more refined forms of cellulose, including microcrystalline cellulose (MCC) and cellulose nanofibrils (CNFs), derived from chemical or mechanical treatments. MCC and CNFs have markedly decreased particle sizes and thus enhanced surface area, which promotes a more uniform dispersion throughout a lignin matrix. The improved interfacial interaction significantly enhances the mechanical strength, thermal stability, and barrier characteristics of the resultant composites.[86] The integration of these enhanced cellulose forms signifies a prospective option for enhancing the efficacy of cellulose–lignin materials across many applications.

Table 1.4: Cellulose-lignin composite with various sources with key properties and potential applications

Cellulose source	Lignin types	Fabrication method	Key Properties	Applications	Authors
Cellulose pulp *Eucalyptus urograndis*	Softwood kraft lignin, Beechwood organosolv lignin	Dry-jet wet spinning	Improved strength properties, and reduced water adsorption	Precursors for carbon fibre production, and textile.	Ma, et al., 2015[87]
Cellionic™, degree of polymerization ~ 680	Softwood kraft lignin from pine	Spin-coated	Higher water resistance, and higher tensile strengths	Wood composite	Simmons et al., 2011[85]
Cellulose (bamboo pulp) with a degree of polymerization of 650	Lignin (not specified)	Solution casting	Good transparency, higher gas permeability	Fresh food packaging	Wu et al., 2009[88]
Microcrystalline cellulose (Advice HP-105)	Softwood kraft lignin	Solution casting	Increased UV absorption potential	UV light blocker film	Sadeghifar et al., 2017[23]
Hybrid poplar stem wood (*Populus trichocarpa* × *Populus maximowiczii*)	Hybrid poplar stem wood (*Populus trichocarpa* × *Populus maximowiczii*)	Solution casting	Induces water repellence, higher thermo-tolerance	Replace synthetic polymers	Rajan et al., 2022[89]
Dissolving wood pulp (DWP)	alkaline lignin (AL)	Solution casting	Excellent antibacterial ability, antioxidant activities, good UV-shielding, and reliable water vapor and oxygen barrier	Active food packaging	He at al., 2023[90]
Cellulose nanofibril	Softwood kraft lignin	Solution casting	Improved tensile strength, enhanced UV shielding, thermal stability, and biodegradability.	Various field	Ou et al., 2023[86]

Table 1.4 indicates that most cellulose–lignin composite films documented in recent literature utilize softwood kraft lignin as the primary lignin source. This choice is due to its broad industrial availability, clearly defined chemical structure, and comprehensive documentation in previous investigations.[46] Conversely, lignins obtained from alternate biomass sources such as poplar or organosolv-extracted beechwood have been utilized less often.[89,87] The restricted acceptance may arise from their reduced commercial availability and increased heterogeneity in molecular structure, which can negatively affect the homogeneity, reproducibility, and overall performance of the resultant composites. Ionosolv lignin is notably absent from the examined studies, presumably due to its restricted commercial availability and its early stage of industrial development and utilization.

Among the several fabrication procedures, solvent casting is one of the most prevalent methods for generating cellulose-lignin composite films. This method is preferred for its operational simplicity, cost-effectiveness, and ability to produce homogenous films while reducing thermal degradation of the biopolymers. The initial patent for cellophane production utilized a solvent casting method, highlighting its enduring significance.[91] This method is especially beneficial for achieving the dissolution or uniform dispersion of cellulose derivatives and lignin in suitable solvent solutions, thereby permitting comprehensive studies of composite interactions and the precise adjustment of film properties. A range of solvent systems has been utilized for this purpose, encompassing conventional organic solvent systems like dimethylacetamide/lithium chloride (DMAc/LiCl) and more recently formulated ionic liquids. For example 1,5-diazabicyclo[4.3.0]non-5-enium acetate and 1-allyl-3-methylimidazolium chloride.[87,88,23] These solvents provide improved solubilization of cellulose and lignin, expanding the variety of attainable film morphologies and functions.

1.2.3.2 Challenges with solubility, miscibility, and film uniformity

The shift from traditional solvents to ionic liquids signifies a groundbreaking development in lignocellulose processing. Table 1.5 summarises the criteria of solvent systems used in cellulose-lignin solubility. Dimethyl sulfoxide (DMSO) is known among conventional solvents for its exceptional solubilizing ability, especially for lignin. This is primarily ascribed to its

highly polar solvent, which has demonstrated a beneficial effect on the solubility of kraft lignin (KL) in organic solvents. [92] The polarity of solvents can be quantitatively described using the Hansen solubility parameter for polarity (δp). DMSO possesses a δp value of 16.4 $(MPa)^{1/2}$ markedly above that of 1-butanol, which is merely 5.7 $(MPa)^{1/2}$. The disparity in polarity underscores the essential importance of solvent choice in tackling issues associated with solubility, miscibility, and film uniformity.

Table 1.5: Evaluation criteria of the solvent system for biomass processing

Solvent system	Cellulose solubility	Lignin solubility	Miscibility	Volatility / Toxicity	Processing Temp	Recyclability
DMSO/ LiCl[93]	6 wt. % soluble	Excellent	High	High	High temp: 110 °C	Possible
DMAc/LiCl[23]	Excellent	Partial soluble	Moderate	High	High temp: 130 °C	Non-recyclable
$[C_3C_1im]Cl$[88,90]	6 wt. % soluble	6 wt. % soluble	Moderate	Moderate toxicity	80 °C	Recyclable
$[C_2C_1im][OAc]$[85,89]	Excellent	Good	High	Relatively benign	80 – 90 °C	Recyclable
IL/ DMSO[94,95,65,96]	Excellent	Excellent	High	Relatively benign	80 – 120°C	Recyclable

Binary solvent systems like DMSO/LiCl or DMAc/LiCl have been extensively studied for their superior solvating capabilities, eliminating the necessity for supplementary film-forming chemicals.[93] The DMAc/LiCl combination, initially documented in 1979, has now emerged as a recognized solvent for native cellulose.[23] Li^+ ions are pivotal as they effectively coordinate with electron-donating groups, especially the hydroxyl groups in cellulose, thereby breaking the extensive hydrogen bonding network and promoting disintegration. Nonetheless, films formed directly from cellulose dissolved in DMAc/LiCl sometimes exhibit a lack of uniformity. Conversely, when cellulose functionalized with azide groups is solubilized in this solution, up to 2% of propargyl-functionalized kraft lignin can be effectively integrated through click chemistry, leading to the creation of homogenous composite films.[23] Additionally, processing cellulose and lignin using this solvent system at temperatures exceeding 100 °C is undesirable. Although LiCl enhances reactivity and solubility, its inclusion affects the recovery and recyclability of DMSO, presenting a considerable obstacle for sustainable processing.

In recent years, imidazolium cation-based room-temperature ionic liquids (RTILs) have emerged as promising non-derivatizing solvents for lignocellulosic biomass. $[C_3C_1im]Cl$ has exhibited the capacity to dissolve both cellulose and lignin, achieving cellulose solubility of

around 6 wt.%. Although dissolution efficiency can be improved at higher temperatures, especially for lignin, the intrinsic solvation ability of $[C_3C_1im]Cl$ renders it appealing for integrated biomass processing.[88] Figure 1.16 illustrates a schematic representation of cellulose-lignin film manufacturing utilizing this solvent system. A primary feature of ionic liquids is their recyclability, due to their low volatility, thermal stability, and immiscibility with water or specific organic solvents, facilitating easy phase separation. Nonetheless, despite these advantages, $[C_3C_1im][Cl]$ raises concerns due to its mild toxicity and halide-based composition, potentially restricting its use in environmentally sensitive or large-scale industrial applications.

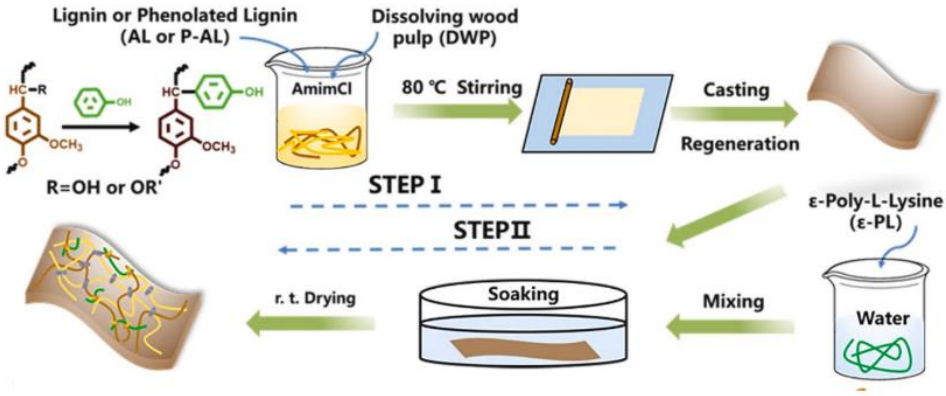


Figure 1.16: Schematic illustration of multifunctional cellulose-lignin films. Image adopted from He et al. [90]

Films produced with $[C_2C_1im][OAc]$ demonstrate exceptional homogeneity and superior surface characteristics, including increased hydrophobicity, as indicated by a water contact angle of around 108°.[89] The mild temperature used for dissolution at 80 to 90 °C is another advantage. These attributes render this ionic liquid an attractive option for the sustainable and efficient fabrication of lignocellulosic composite materials. To expand on this potential, investigations have turned toward combining ionic liquids with co-solvents such as dimethyl sulfoxide.

Recent developments have investigated the application of ionic liquids in conjunction with dimethyl sulfoxide (DMSO) as a binary solvent system. This method utilizes the remarkable solvating capacity of DMSO for organic molecules and its extensive miscibility with various

ionic liquids.[97] Adding DMSO leads to a substantial reduction in the viscosity of ionic liquids like [C_2C_1im][OAc], enhancing processability with negligible impact on the intrinsic interactions between cellulose and the ionic liquid.[96] A 60:40 w/w mixture of tetraoctylphosphonium acetate ([P_{8888}][OAc]) and DMSO dissolved up to 8 wt.% cellulose, while trioctyl(tetradecyl)phosphonium acetate ([P_{14888}][OAc]) attained a solubility of up to 3 wt.%.[65] Overall, the combination of ionic liquids and DMSO has shown great potential for enhancing the dissolution, processing, and regeneration of lignocellulosic materials.

Nefeli et al. (2025)[78] recently investigated lignocellulosic films regenerated from a mixture of [C_2C_1im][OAc] and DMSO, which serves as a green solvent system for lignocellulosic materials. The dissolution lignin up to 29 wt.%. The study also confirmed that the ionic liquid could be recovered and reused for up to five cycles without significant changes in its chemical composition or thermal stability. However, the cumulative residual yield decreased from 89% to 72%, reaching only 60.4% after the fifth cycle, which may limit its industrial feasibility. Thus, [C_2C_1im][OAc] can be effectively recycled up to four times to maximize solvent utilization and minimize chemical waste, aligning with the principles of green chemistry. The data clearly indicate that the integration of DMSO into ionic liquid systems like [C_2C_1im][OAc] significantly improves cellulose dissolution rates and overall process efficiency, presenting a viable pathway for scalable lignocellulosic material processing.

1.2.3.3 Solution casting parameters in cellulose-lignin processing

Several critical parameters affect the fabrication of biopolymer-based films, such as dissolution time and temperature, pouring temperature after the complete dissolution of the cellulose-lignin dope in the solvent system, and the drying technique, which is vital for attaining film homogeneity. The regeneration process utilizing an antisolvent is crucial for the effective incorporation and stabilization of biopolymers inside the film matrix. Table 1.6 summarises the methodologies for film preparation and the corresponding attributes as documented in recent research.

Table 1.6: Comparative review of film fabrication parameters and characteristics

Films types	Dissolution time and temp	Pouring Temp	Drying technique	Regeneration	Film features	Authors
Cellulose-lignin films	50 °C for 12 h in DMAc/LiCl	Not mention	Dried at room temperature	Acetone bath for 1 h followed by washing with a stream of cold water for 5 h	Homogeneous films, stable against elevated temperature at 120 °C and UV irradiation.	Sadeghifar et al. 2016[23]
Lignocellulosic thin films	12 to 18 days at 80 °C in $[C_2C_1im][OAc]$	80 °C	Stepwise humidity-controlled drying in chambers at: 100%, 95%, 85%, 75%, and finally 54% relative humidity (RH)	Anti-solvent bath of 100% methanol, then incubated in de-ionized water for 1 hour	Enrich cellulose and lignin and film yield.	Rajan et al. 2022[89]
Cellulose-lignin films	DWP were added into AmimCl solution at 80 °C for 1.5 hours	80 °C	Room temperature	Deionized water and thoroughly washed	The cellulose/phenolated lignin/ε-PL films with high lignin content of 30%.	He et al. 2023[90]
Lignin-containing cellulose films	20 min in $AlCl_3/ZnCl_2$	Room temperature	Dried at room temperature	Isopropanol steam bath for 24 hours	Lignin was homogeneously dispersed. The films were well-formed, bendable, foldable, and twistable.	Chun et al. 2023[98]

WCF/LNP/PVA films WCF (wood cellulose fibre) LNP (lignin nanoparticle)	Not mentioned	Room temp	Air-dried in a laboratory hood	No regeneration step	Good flexibility. LNP uniformly distribute.	Zhou et. al. 2023[99]
CNF/LNP/PVA composite films CNF (cellulose nanofibre) LNP (lignin nanoparticle)	2 hours at 90 °C	90 °C	Slow evaporation at room temperature	No regeneration step	Tightly packed composite structures formed by spherical LNPs to uniformly penetrate the pores of cellulose fibers.	Ou et. al, 2023[86]

1.2.3.3.1 Dissolution time

A significant deficiency in the literature is the absence of comprehensive data concerning the dissolving time of polymers in particular solvent systems. In certain studies, concerning polyvinyl alcohol (PVA), the time necessary for total dissolution in water at 95 °C is not clearly stated. A study indicates that 20 mL of the lignin nanoparticles (LNPs)/PVA mixture underwent microwave heating (2450 MHz, 800 W) with 1-minute heating and 5-minute cooling cycles until the volume was halved, without detailing the initial dissolution duration.[99]

The dissolution time is a crucial aspect, contingent upon the solvent's effectiveness in solubilizing both cellulose and lignin components. Alkaline lignin generally necessitates around 1.5 hours to dissolve in ionic liquid namely 1-ethyl-3-methylimidazolium chloride ($[C_2C_1im]Cl$) at 80 °C. This seems relatively brief it is because alkaline lignin undergoes phenolation with phenol and is then dissolved in sodium hydroxide solution.[90] Another study showed cellulose films containing lignin have been effectively produced with notably brief dissolution times around 20 minutes at ambient temperature utilizing a potent a molten binary mixture of $AlCl_3$ and $ZnCl_2$.[98] This combination generates a highly reactive ionic environment, wherein the potent Lewis acid characteristics of Zn^{2+} and Al^{3+} promote swift penetration and disruption of the biomass structure, hence facilitating efficient dissolving. Although shorter processing time and operation under moderate circumstances offer benefits for environmentally friendly processing methods, the intrinsic corrosiveness and ecotoxicity of $AlCl_3$ and $ZnCl_2$ pose considerable obstacles.

In contrast, microcrystalline cellulose and kraft lignin have been documented to dissolve in a DMAc/LiCl combination at 50 °C for an extensive duration of 12 hours, underscoring the necessity for prolonged dissolving periods even under moderate heating.[23] Besides, the dissolution of lignocellulosic biomass in the ionic liquid $[C_2C_1im][OAc]$ is markedly slower, necessitating a duration of 12 to 18 days at 80 °C for complete solubilization. The prolonged processing duration becomes a significant constraint for practical applications. Consequently, additional research is essential to optimize and ascertain the minimal dissolving period needed for the total miscibility of cellulose and lignin within these ionic liquid systems.

To address this issue, optical microscopy provides a swift and accessible technique for observing the dissolving process. A study utilizing a temperature-regulated microscope stage

revealed that a 4 wt.% blend of cellulose and lignin dissolved in [C_2C_1im][OAc] at 75 °C attained total dissolution in 60 minutes.[100] These strategies are essential for the real-time evaluation and enhancement of dissolving parameters, presenting considerable potential for increasing processing efficiency.

1.2.3.3.2 Pouring temperature

Upon preparation of the dope solution, meticulous attention must be paid to the pouring or casting temperature, as it directly affects the solution's flow characteristics and suitability with the film applicator. There is notable variability in casting procedures among research, accompanied by a lack of procedural uniformity. A majority method entails sustaining the dope solution at roughly 80 °C while employing a casting knife, hence promoting uniform distribution. One investigation indicated that the solution was cast at 80 °C onto a glass substrate to a thickness of 25 μm utilizing a pre-calibrated casting knife.[89] Nonetheless, other investigations lack this degree of specificity, simply indicating that the dope solution was uniformly applied to a heated glass plate at 80 °C, without detailing the film thickness.[90]

Very few studies conducted on rheological characterisation of cellulose dope solutions.[101] Meister and Kosan demonstrated that zero-shear viscosity serves as a highly sensitive parameter for determining polymer concentration; even a slight increase in pulp concentration from 11.8 wt% to 12.1 wt% resulted in a rise in viscosity from 8,211 Pa·s to 12,760 Pa·s at 85 °C.[102] Understanding the rheological properties, specifically the viscosity of cellulose-lignin dope solutions, is crucial for achieving consistent pouring and regulated film production with casting knives. A precise characterization of these characteristics would enhance reproducibility and scalability in film production techniques.

1.2.3.3.3 Drying technique

Most research in the literature indicate that biopolymer films are dried at ambient temperature, with less focus on the effects of evaporation rate and drying conditions. Several studies have emphasized the significance of gradual and regulated evaporation throughout the drying process.[86] Rajan et al. executed a systematic, humidity-regulated drying technique, systematically decreasing the relative humidity (RH) in a controlled chamber from 100% to

95%, 85%, 75%, and ultimately to 54% RH.[89] The progressive reduction in humidity was demonstrated to facilitate uniform film development.

Investigations into drying techniques for starch-based films indicated that natural convection, accomplished by drying the film in a petri dish under ambient circumstances, yielded high-quality, homogenous films, albeit the drying rate was slow. Conversely, forced convection drying without a cover caused fast moisture evaporation, resulting in the emergence of air bubbles and significant film distortion.[103] These findings emphasize the significance of regulated drying, especially for humidity and airflow, to guarantee the creation of flawless and uniform films.

1.2.3.3.4 Regeneration

Recent research on synthetic polymer-based systems has shown that composite films can be regenerated without employing antisolvent regeneration processes. A simple casting procedure is adequate, as demonstrated by wood cellulose fibre/lignin nanoparticle/poly(vinyl alcohol) (WCF/LNP/PVA) and cellulose nanofibre/lignin nanoparticle/poly(vinyl alcohol) (CNF/LNP/PVA) films. This is mainly because these systems do not necessitate dissolving in ionic liquids or alkaline solvents, as the lignin nanoparticles (LNPs) are already pre-formed and uniformly distributed within the polyvinyl alcohol (PVA) matrix. [86, 99]

Conversely, solvent systems utilizing ionic liquids or organic solvents generally necessitate a regeneration phase. The majority of documented techniques for regeneration cellulose from ionic liquids depend on antisolvent precipitation. In these systems, hydrogen bond-donating solvents, such as water or alcohols, exhibit strong interactions with the anions of the ionic liquid. Protic solvents, when included into the ionic liquid system, compete with cellulose for interactions with the anionic constituents of the ionic liquid. This competition hinders the solvation of cellulose, as protic solvents preferentially interact with the anions of the ionic liquid. Consequently, cellulose is precipitated from the mixture of ionic liquid and protic solvent.[104]

In two of the cited experiments, methanol and acetone were utilized as antisolvents, succeeded by a thorough water washing procedure afterwards.[23,89] Conversely, several studies employed solely deionized water as the antisolvent.[90] The range of potential suitable antisolvents is extensive; yet, it is firmly proven that polar protic solvents especially water can markedly

diminish cellulose solubility, even at minimal concentrations. This attribute defines a powerful antisolvent: a chemical that proficiently diminishes solubility and promotes precipitation.[104] Consequently, the utilization of water exclusively constitutes a remarkably efficient and practical option. The recyclability of ionic liquids using water as the antisolvent improves the sustainability and economic feasibility of the process.

1.2.3.4 Summary of best practices for film fabrication

The following are the important aspect to be considered when fabricating cellulose-lignin films in order to obtain a mechanically intact film that are crucial for further processing.

- Method Selection: Solution casting is an effective and versatile technique for fabricating films.
- The dissolution time of the polymer is largely independent of the solvent system, making it a reliable method across different solvents.
- Monitoring Dissolution: Optical microscopy provides a rapid and accessible approach to monitor the dissolution process, enabling real-time observation of polymer solubilization.
- Dissolution Conditions: For ionic liquids such as $[C_2C_1im][OAc]$, the optimal dissolution temperature is around 80 °C to ensure efficient solubilization without degrading the polymer.
- Polymer Viscosity Considerations: The biopolymer content strongly influences solution viscosity. Higher temperatures can reduce viscosity, facilitating better casting, while higher polymer concentrations increase viscosity, requiring careful control during processing.
- Drying Procedure: Films should be dried using a humidity-regulated drying technique to prevent defects such as cracking or uneven surfaces.
- Film Regeneration: The regenerated film achieves the best structural and mechanical properties when immersed in water.

1.2.3.5 Gaps in understanding of structural-property relationships

To fully understand the impact of lignin on composite performance, it is crucial to link various lignin sources with quantitative metrics, such as hydroxyl group quantification. Ou et al. revealed that the phenolation of softwood kraft lignin markedly elevated the phenolic hydroxyl

(Ph–OH) content from 4.33 mmol/g to 8.23 mmol/g. The increase in hydroxyl functionality promoted stronger hydrogen bonding interactions between lignin and cellulose nanofibrils (CNFs), consequently enhancing interfacial compatibility and producing composite films with significantly improved mechanical characteristics.[86] Given these encouraging results, a significant lack exists in the literature concerning the systematic measurement of lignin hydroxyl groups, especially regarding their influence on composite miscibility and phase compatibility. The absence of extensive data obstructs the capacity to forecast and enhance the mechanical performance of cellulose-lignin composites with various kinds of lignin and processing conditions.

Another crucial factor to address is the compositional analysis of both the starting materials and the resultant fabricated film. Compositional analysis yields quantitative data on essential biomass components, such as glucose, hemicellulose, acid-soluble lignin, acid-insoluble lignin, and ash concentration. This information is crucial for understanding how alterations in chemical composition affect the physical, mechanical, chemical, and thermal properties of the produced film. Compositional analysis is a recognized technique for biomass characterization and has been widely utilized to evaluate the impacts of different pre-treatment conditions, as reported in the literature.[105, 106,107] While this analysis does not directly measure the finished film's yield, it provides essential insights that can guide the strategic design of materials for specific applications, thus enhancing the originality and scientific importance of this research.

1.2.4 Functionalization and Plasticization

The development of flexible films is important for expanding the applications of cellulose-lignin systems. One common strategy to enhance flexibility is by adding plasticisers, which improve film attributes by increasing molecular mobility and thereby modifying physical and structural properties. Despite the importance of this subject, there exists a marked deficiency in research investigating the effects of plasticiser on the characteristics of cellulose-lignin composite films, indicating a considerable lack in the existing literature. Conversely, much research has investigated starch- and carboxymethyl cellulose (CMC)-based films concerning the integration of plasticizers, such as glycerol.[108,109,110] Table 1.7 summarizes the glycerol content and its impact, mainly on the mechanical properties of these biopolymer films.

Table 1.7: Glycerol as plasticiser in polysaccharide and protein-based films

Film types	Glycerol concentration (% w/w)	Tensile strength (MPa)	Elongation at break (%)	Water Vapor Permeability (WVP)	Authors
Cellulose	5	42 - 48	12.1	Increases with glycerol	Ahokas et al., 2015[111]
Wheat starch	33 – 50	Decrease from 3.29 to 2.10	Increase from 15.21 to 18.08	Increases with glycerol	Basiak et al., 2018[109]
Carboxy Methyl Cellulose	0.25 – 0.75	Decrease from 101.34 to 23.08	Increase from 2.5 to 72.3	Slight increase	Hidayati et al., 2021[108]
Zein	5 – 30	n/a	n/a	Suppressed the oxygen permeability.	Liang et al., 2015[110]
Maize starch	9.48 – 23.91	Decreases with high plasticiser content	Increases with high plasticiser content	Increases with plasticiser content.	Zhang et al., 2016[66]
Cellulose nanocrystals with extracted lignin from piassava fiber bagasses	20 (fix)	3.2 to 6.7	28.9 to 20.1	Improved barrier properties	Miranda et al., 2015[112]

In polymer science, plasticizers are primarily classified into two categories: internal and external. Internal plasticizers are chemically integrated into the polymer backbone by copolymerization or grafting. This structural alteration disrupts the tight arrangement of polymer chains, thus diminishing intermolecular interactions and decreasing the glass transition temperature (Tg) which enhances the material's flexibility. Conversely, external plasticizers are low-volatility, small-molecule additives that engage physically, rather than chemically with polymer chains. They promote polymer chain swelling and increase mobility by diminishing intermolecular pressures, without modifying the core chemical structure.[113]

Several theoretical frameworks have been suggested to elucidate the plasticization mechanism, with the most well recognized being: (i) the lubricity theory, (ii) the gel theory, and (iii) the free volume theory. Figure 1.17 demonstrates that glycerol functions as an efficient external

plasticizer by interrupting hydrogen bonding networks in bacterial cellulose. This disruption results in less intermolecular cohesion, augmented free volume, and increased molecular mobility. [114]

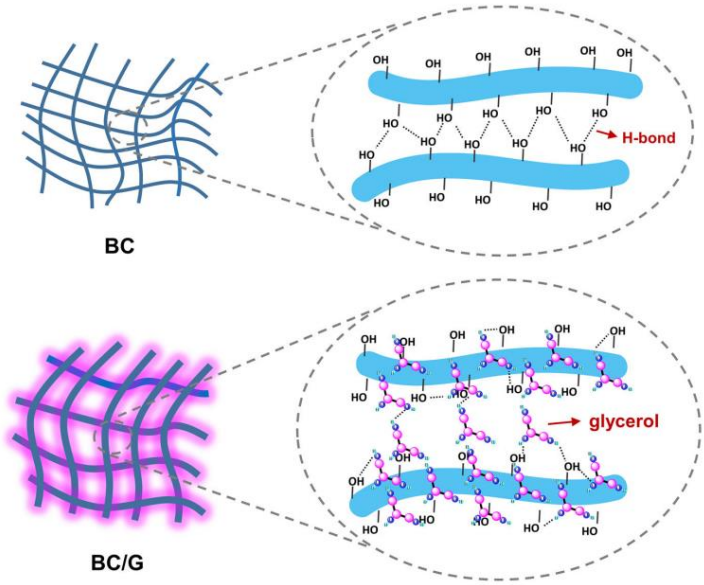


Figure 1.17: Glycerol incorporated in bacterial cellulose film. Image adopted from Jost et al. [114]

Based on Table 1.7, glycerol is one of the most often utilized plasticizers in biopolymer composites, owing to its low molecular weight, ease of integration, and role as an external plasticizer.[110] Its compatibility with polysaccharide-based systems makes it appropriate for altering the mechanical properties of biopolymer films. Increasing the content of plasticizer generally leads to a reduction in tensile strength.[108] This phenomenon is ascribed to the plasticizer interfering with intermolecular interactions among polymer chains, thereby diminishing the cohesive forces inside the matrix. In contrast, the incorporation of plasticiser typically results in an enhancement of elongation at break. This increase in flexibility also results from a decrease in intramolecular interactions among polymer chains, such as starch, due to the establishment of hydrogen bonds between glycerol and the biopolymer.[109] These interactions facilitate enhanced chain mobility and superior deformability.

It has been demonstrated that the plasticization of regenerated cellulose films modifies both their mechanical and barrier properties. In a study, control films showed high tensile strength (62–74 MPa), but exhibited low strain at break (5.1–5.5%), whereas plasticized films displayed diminished strength (~41 MPa) but dramatically enhanced elasticity (~12%).[111] The trade-off

between stiffness and flexibility aligns with the anticipated impact of plasticizers on breaking intermolecular connections within cellulose. The barrier characteristics were significantly influenced by the type of plasticizer used. Despite its widespread application, glycerol has been shown to enhance water vapor and oxygen permeability, hence weakening barrier efficiency. In contrast, polyols like sorbitol and particularly maltitol significantly enhanced barrier characteristics, with maltitol decreasing permeabilities by more than 90% relative to glycerol. The regenerated and plasticized cellulose films exhibited significantly reduced water vapor and oxygen permeabilities when compared to commercial viscose-based cellophane, underscoring their potential as renewable packaging materials.

Although plasticisers are extensively utilized in other biopolymer systems, the integration of glycerol into cellulose–lignin composite metrics are as yet inadequately investigated. Additional investigation is required to ascertain the ideal concentration of glycerol for these systems, as its impact may differ markedly based on the source, content, and structural properties of the associated biopolymers.

In summary, cellulose-lignin and cellulose-lignin-glycerol are expected to exhibit different characteristics, particularly due to the presence of a plasticizer. Therefore, thorough characterization techniques are necessary to confirm their performance.

1.2.5 Characterization Techniques

1.2.5.1 Thermal properties

Assessing the thermal characteristics of cellulose-lignin films is essential for determining their stability under elevated temperatures. Thermal characterization is generally conducted by thermogravimetric analysis (TGA) and differential scanning calorimetry (DSC).[23,115] TGA offers insights into thermal decomposition characteristics and residual mass analysis, whereas DSC is utilized to ascertain thermal transitions, including the glass transition temperature (Tg) and phase alterations during heating and cooling cycles. Table 1.8 summarizes the heating rates and onset breakdown temperatures (T_{onset}) for the starting materials and the produced lignocellulose thin films, mostly ascertained using TGA, which is more frequently employed for such analyses than DSC.

Table 1.8: Heating rates and T_{onset} of cellulose, lignin and lignocellulosic film

Compound(s)	Heating rate (°C/ min)	T_{onset} (°C)	References
$[C_2C_1im][OAc]$	10	214 - 216	Clough et al. 2013[116]
Cellulose nanocrystal	10	350	Acierno et. al 2020[117]
Microcrystalline cellulose	10	291	Liu et al. 2018[118]
Beech wood lignin	10	310	Margellou et al. 2021[119]
Acetosolv lignin	30	372	Zhou and Liu 2010[120]
Kraft lignin	10	377	Wannid et al. 2022[121]
Organosolv lignin	10	348	Wannid et al. 2022[121]
Poplar	10	300	Kim et al. 2014[122]
Lignocellulosic poplar thin film	10	330 - 338	Rajan et al 2022[123]

Thermogravimetric analysis (TGA) necessitates a regulated heating rate for the sample, which greatly affects the resolution and reproducibility of thermal phenomena. Table 1.8 illustrates that a heating rate of 10 °C/min is the most often utilized technique, providing a balance between analytical resolution and experimental length.

The thermal stability of cellulose is associated with its degree of crystallinity. The decomposition temperature for microcrystalline cellulose (MCC), is 291 °C, whereas for cellulose nanocrystals (CNC) it is reported as 350 °C.[118,117] X-ray diffraction analysis in both studies confirmed that CNC had a higher crystallinity index than MCC, at 80.0% and 72.1%, respectively. A study indicated that the extraction of hemicellulose and lignin from cellulose using acid hydrolysis results in a considerable decline in thermal stability, which correlates with a drop in crystallinity.[118]

Lignin typically demonstrates elevated T_{onset} values, varying from 300 °C to 377 °C, as documented in multiple investigations. [119, 120, 121] The improved stability is due to its intricate aromatic structure, abundant in C–C and C–O–C connections, and further reinforced by π–π interactions between aromatic units. In support of this, softwood lignin has been documented to maintain a residual mass of 38.8% during thermal degradation, signifying its elevated carbon content and char-forming potential.[121]

Lignocellulose films demonstrate superior thermal stability relative to their constituent components. A lignocellulose film from poplar biomass had a T_{onset} of 338 °C, while separated

lignin and cellulose from poplar displayed reduced thermal stabilities of roughly 300 °C and 260 °C, respectively, as indicated in prior investigations.[123, 122] The enhancement in thermal properties is ascribed to the synergistic interactions between lignin and cellulose in the composite matrix. These interactions, specifically hydrogen bonding and π–π stacking, enhance the development of a more thermally resilient network. Moreover, pretreatment with ionic liquids like 1-allyl-3-methylimidazolium chloride ($[C_3C_1]Cl$) has demonstrated an enhancement in cross-linking among the polymeric constituents, thereby augmenting the heat resistance of the resultant film.[123]

In well-integrated lignocellulose films, the homogeneous distribution of cellulose and lignin reduces the occurrence of phase-separated domains, which may otherwise act as beginning sites for premature thermal breakdown. The creation of a homogeneous and interconnected matrix facilitates the delay of decomposition beginning. The findings indicate that cellulose-lignin films, especially those treated with ionic liquids, have enhanced thermal stability, making them suitable for applications necessitating high-temperature resistance. Further research is necessary to understand the impact of various lignin types on cellulose mixtures, which may influence the thermal stability of the produced films.

1.2.5.2 Mechanical properties

Several critical aspects must be evaluated when assessing the mechanical properties of fabricated cellulose–lignin films. The primary consideration is the validation of the testing standard utilized, as compliance with an established standard guarantees the reliability and comparability of results. The selection of standard method directly affects parameters including specimen dimensions, crosshead speed, and the number of replications, all of which are essential for acquiring statistically valid results. Table 1.9 outlines common methodologies in the mechanical testing of cellulose-lignin composites, inclusive of those employing glycerol as a plasticizer and those that do not.

Table 1.9 summarizes that multiple standards are available for testing cellulose-lignin composites; however, it is important to note that not all are especially designed for cellulose-lignin thin films. Certain standards are established for carbon fibre applications, including

ASTM D2256 Standard Test Method for Tensile Properties of Yarns using the Single-Strand Method and SFS-EN 5079 Textile Fibres: Determination of Breaking Force and Elongation at Break of Individual Fibres.[87, 124] Although these methodologies may seem separate, they can offer valuable initial parameters for defining test conditions. The predominant standard for thin cellulose-lignin films is ASTM D882, which is extensively referenced in the literature and is essential for guaranteeing precise and repeatable mechanical testing.

It was noted that, despite the utilization of the same standard (ASTM D882), the dimensions of the specimens differed between studies. For instance, Wang et al. [112] employed specimens measuring 10 mm in width and 80 mm in gauge length, while Miranda et al.[125] utilized specimens measuring 25 mm in width and 80 mm in gauge length. Differences in specimen preparation can result from variations in material availability or sample limitations. The observed deviations in stress and strain values fell within acceptable limits, 1.0 to 5.9 for Wang et al. and 0.2 to 5.2 for Miranda et al. suggesting that these dimensional discrepancies did not materially impact the repeatability of the mechanical test outcomes.

Table 1.9: Aspects considered in determining mechanical properties of cellulose-lignin composite films

Sample Cellulose:lignin (wt:wt)	Glycerol (wt.%)	Width (mm)	Gauge (mm)	Crosshead speed (mm/min)	Temp (°C)	RH (%)	Load Cell (N)	Rep	ASTM	References
Cel: OS / kraft OS (organosolv lignin) Kraft (kraft lignin)	0	n/a	20	20	23	50	n/a	n/a	D2256	Ma et al. 2015[87]
E-BL /SL E (enocell pulp) BL (beech lignin) SL (spruce lignin)	0	n/a	20	20	20	65	0.2	20	SFS-EN 5079	Trogen et al. 2021[124]
Chitosan:lignin	0	25	100	1	21	35 and 75	100	3	EN ISO 527-1 standard	Crouvisier-Urion et al. 2016[126]
Li/cell Li (lignin) Cell (Cellulose)	0	n/a	20	2	Room temp	n/a	20	10	n/a	Vincent et al. 2018[62]
Regenerated cellulose film	0	10	80	25	n/a	n/a	200	3	D882	Wang et al. 2022[125]
FSGL Corn starch: glycerol: lignin	2.5	25	80	50 and 12.5	n/a	n/a	n/a	10	D882–00	Miranda et. 2015[112]
TPS + NC (plasticized starch and ordinary chitosan) & TPS + TPC (plasticized starch and plasticized chitosan)	2.5	n/a	50	100	n/a	n/a	n/a	5	D 882-91	Sun et al. 2019[127]
G:CH Glycerol: chitosan	50	n/a	n/a	10	25	57.7	1000	4	D 882–02	Maria V. et al. 2016[128]

A crucial element is the crosshead speed, as the testing rate directly affects both modulus and elongation. The literature indicates that crosshead speeds vary significantly, ranging from 2 mm/min to 100 mm/min, with the majority of research concentrated between 20 and 50 mm/min.[62, 127, 87] In films containing glycerol, elevated testing speeds are frequently utilized to accelerate measurement, as glycerol functions as a plasticizing and wetting agent, extending the time to failure. Miranda et al.[112] employed a crosshead speed of 50 mm/min for glycerol-containing films, in contrast to 12.5 mm/min for films devoid of glycerol. A desirable range of 20–50 mm/min is suggested for both glycerol-containing and glycerol-free cellulose–lignin films, compatible with most reported investigations and facilitating uniform, comparable assessments of mechanical properties.

Another key parameter is preconditioning. Preconditioning is frequently overlooked in the literature, despite its significance in guaranteeing accurate mechanical property assessments, especially for plasticized films, which exhibit considerable sensitivity to moisture. Preconditioning settings are generally reported to range from 21 to 25 °C and 50 to 65% relative humidity (RH).[128, 87, 124] It is advised that specimens be adapted for 24 hours at 23 °C ± 2 °C and 50 % ± 5 % relative humidity to reduce the impact of difference in moisture content on the assessed attributes.

The literature indicates a significant variation in the number of replications with reports ranging from triplicate measurements to as many as 20 replicates per sample.[126,125,124] Although augmenting the number of replicates improves statistical reliability, the optimal selection is contingent upon the study's aims and resource availability. For research-scale studies, a minimum of five replicates is advised to achieve satisfactory accuracy, whereas 10 or more replicates are optimal for rigorous comparisons of material attributes.

Considering the aforementioned factors, the ASTM D882 standard technique is the most suitable framework for assessing the mechanical properties of thin films. Specimen dimensions should adhere to the norm, but may be modified to align with material availability without undermining result reliability. Preconditioning for 24 hours at 50–55% relative humidity before testing is crucial to mitigate the effects of moisture. It is advisable to use a crosshead speed of 20–50 mm/min for both cellulose–lignin and cellulose–lignin–glycerol films, as this range fits

with most documented experiments and facilitates comparability. A minimum of five replicates per sample is recommended to obtain statistically significant findings.

The inherent properties of lignin, including its botanical source and chemical composition, substantially affect the mechanical performance of cellulose-lignin films. Kraft lignin and organosolv lignin may exhibit distinct mechanical characteristics when combined with cellulose. An investigation on lignocellulosic films regenerated from a mixture of $[C_2C_1im][OAc]$ and DMSO reported that the incorporation of organosolv softwood lignin did not significantly alter the mechanical properties of the regenerated films.[78] The neat cellulose film (F-0) exhibited a tensile strength of 80.03 MPa, while the addition of 8 wt.% lignin (F-2) achieved an optimum strength of 93.15 MPa. However, further increasing the lignin content to 29 wt.% (F-4) reduced the tensile strength to 72.31 MPa. These results indicate that excessive lignin loading can weaken the composite structure, emphasizing the importance of optimizing the processing window to this study for balanced performance. Given the sensitivity of the film composite to formulation parameters, attention has also turned to the role of plasticisers in adjusting mechanical flexibility and strength.

The addition of plasticisers, such glycerol, alters the mechanical properties by interfering with hydrogen bonding in the polymer matrix, resulting in enhanced elongation at break but typically diminishing tensile strength and modulus. Very few studies have investigated the role of plasticisers in lignocellulosic films. Thus, the right balance between lignin type and plasticizer concentration is essential to understand, as it governs the compromise between film strength and flexibility, eventually influencing appropriateness for particular applications.

1.2.5.3 Surface properties

In the examination of cellulose-lignin composite films, two principal yet fundamentally different performance characteristics are often assessed: surface properties and barrier properties. Surface wettability, often assessed using static water contact angle (WCA) tests, indicates the chemical composition and microstructural characteristics of the film's outermost layer. Conversely, barrier properties refer to the ability of the bulk material to impede the penetration of gases or vapors, commonly measured by water vapor transmission rate (WVTR) or oxygen transmission rate (OTR) testing.[129] While an increase in surface hydrophobicity is

occasionally qualitatively associated with improved moisture barrier performance, these two qualities are not directly interchangeable and should be evaluated separately.

The majority of research on lignin–cellulose composite thin films has mostly concentrated on WCA measurements. This focus arises from the aim of clarifying how lignin concentration, distribution, and molecular interactions affect surface hydrophobicity, without extending the research to bulk permeation behavior. Table 1.10 breaks down the principal parameters affecting the water contact angle of cellulose–lignin films as documented in the literature.

Table 1.10: Differences in experimental setups and studied parameters to determine water contact angle of fabricated cellulose-lignin films

Sample	Liquids	Droplet volume (µL)	Residence time (sec)	Temp and humidity	Surface energy calculation	References
LCNF-0 – LCNF-130 LCNF - lignin containing cellulose nanofibrils	Oil	2	Every 0.1	Not specified	Not specified	Xie et al.[130]
RM R100 – R160 RM (Eucalyptus grandis × E. urophylla) R100 -R160 (cellulose-rich residues and lignin)	Deionised water	Not specified	5	Not specified	Not specified	Sun et al. [131]
Chitosan / lignin	Water, ethylene glycol, glycerol, formamide, and diiodomethane	1	The initial very fast spreading step and the second step related to the evaporation of the liquid.	20°C	Young−Laplace equation	Crouvisier-Urion et al. 2016[126]
CNC/SKL cellulose nanocrystals/ softwood kraft lignin	Deionised water	Not specified	Automated	Not specified	Not specified	Parit et al. 2018[132]
Thin coating lignin films	Deionised water	1-4	20	23 °C and 50%	Not specified	Borrega et al. 2020[132]

In the majority of wettability investigations concerning cellulose–lignin films, the testing liquid used is deionized water.[131, 132] A limited number of studies, like the research by Crouvisier-Urion et al.[126], have utilized several liquids such as water, ethylene glycol, glycerol, formamide, and diiodomethane to facilitate the computation of surface energy. Surface energy, measured in $mJ \cdot m^{-2}$, serves as a fundamental indicator of the intermolecular forces present at a solid's surface. Nonetheless, considering that cellulose–lignin composites are primarily utilized in goods packaging, where water exposure is the predominant issue, deionized water is typically adequate for water contact angle evaluation.

The volume of the droplet is a crucial factor in WCA measurements and must be meticulously calibrated, as difference can profoundly affect the observed angle. Documented volumes for cellulose–lignin films vary from 1–2 μL[130,126] to 1–4 μL[132], demonstrating an inconsistency among investigations that hinders direct result comparison. Any volume within this range is permissible, depending upon continuous usage. The volume of a droplet is intricately linked to its residence time: immediately following deposition, a droplet swiftly transitions to its minimum-energy state. Chemical adsorption at the interface may persist for seconds to minutes, modifying the observable contact angle. Smaller droplets (e.g., 2 μL) are often assessed after approximately 5 seconds, but bigger droplets (e.g., 4 μL) may necessitate up to 20 seconds, partly owing to their reduced evaporation rates. The absence of established methods renders the direct comparison of WCA values among various research groups inaccurate, highlighting a substantial methodological deficiency in the field.

Environmental factors, including temperature and relative humidity, affect evaporation kinetics during WCA measurement. Limited research clearly documents these settings; yet, the prevailing opinion in the existing literature indicates that measurements should be conducted at 23 °C and 50% relative humidity, aligning with conventional laboratory ambient conditions.[132] The absence of uniform environmental reporting diminishes the transparency and repeatability of WCA measurements in various research.

In conclusion, whereas the sessile drop method is the standard approach for assessing static water contact angles, fluctuations in droplet volume, residency duration, and unreported environmental factors significantly undermine the reliability of cross-study comparisons. The absence of methodological standardization and the limited scope of property evaluation

highlight a significant gap in the existing literature. This research directly addresses the need to by develop reproducible WCA protocols under controlled environmental conditions.

1.2.5.4 Optical properties

The integration of lignin into a cellulose matrix markedly improves UV-blocking efficacy, mainly owing to the existence of phenolic, ketone, chromophoric, and auxochromic functional groups.[133] These structural characteristics allow lignin to serve a crucial function in UV resistance. The enhancements in the optical characteristics of cellulose-lignin composites significantly increase their value for commercial applications requiring UV resistance, hence potentially prolonging product longevity. Table 1.11 summarises the documented optical properties of cellulose–lignin composite films, specifying composition, measurement methodologies, and main findings. The data demonstrate discrepancies in UV-blocking efficiency, transparency, and methodological methods, while also highlighting enduring gaps especially in correlating instrumental techniques and UV-blocking performance with the fundamental structure–property correlations.

The literature frequently provides little detail regarding instrumentation techniques, compromising the credibility of stated results. The majority of investigations have utilized a standard UV–vis spectrophotometer lacking an integrating sphere, an essential accessory for precise measurement of both direct and scattered light, especially in translucent or opaque coatings. Of the examined studies, only He et al. (2023) employed an integrating sphere.[90] The lack of this component may cause scattering losses to be mistakenly perceived as absorption, resulting in an overstated assessment of UV-blocking efficacy, as demonstrated in various other studies.

Secondly, there is a significant gap in thickness control and documentation throughout the literature. Only Yang et al. (2020) specifically indicated that their samples were standardized to a thickness of 100 μm.[134] This absence is crucial, as optical absorbance and transmittance are directly dependent upon route pathlength, as delineated by the Beer–Lambert law. Variations in thickness may partially explain the differences in “complete" versus "partial" UV-blocking efficacy, even with similar lignin loadings. A cellulose film incorporating 2 wt.% propargylated kraft lignin (Cel-2% lignin), which blocked UVA = 90% and UVB = 100%,

demonstrated results practically equivalent to RCL10 (dissolving wood pulp with 10 wt.% alkaline lignin), which similarly exhibited UVA = 90% and UVB = 100%.[23, 90] Although differences may arise from variations in lignin type, extent of chemical modification or particle dispersion, all of which significantly affect the balance between UV-blocking and transparency, the likelihood of overestimation could be mitigated by maintaining uniform thickness and providing transparent reporting.

Table 1.11: Reported optical properties of cellulose–lignin composite films, highlighting performance variations and common methodological gaps

Film composition	Instrument	Wavelength range (nm)	Sample thickness	UV blocking	Visible light transmittance at 600 nm (%)	Method gaps	References
CNC nanocomposites containing LNPs (lignin nanoparticles)	UV–Visible Single Beam spectrophotometer	200–800	n/a	1wt.% LNP UVA= 92.1% UVB= 98.7% 5wt.% LNP UVA=99.5% UVB = 99.9%	40 - 15	Incomplete reporting	Lotfy and Basta, 2025[20]
PLA /PCL -3L PLA/PCL -12 L poly (lactic acid)-poly (ε-caprolactone)-nanolignin composite films	UV-vis spectrometer	250 to 900	normalized as 100 µm	PLA/PCL-12L UVA = 90% UVB= 100 %	70 - 40	No baseline correction	Yang et al. 2020[134]
Cellulose + (0.5 to 2.0% lignin) films	UV−vis spectrometer	200−600	n/a	Cel-2% lignin UVA = 90% UVB = 100%	70 - 55	Incomplete reporting	Sadeghifar et al. 2017[23]
RCL10 RCL30 RCL (dissolving wood pulp + alkaline lignin) LRCL-30-1 LRCL-30-6 (dissolving wood pulp + phenolated alkaline lignin + ε-polylysine)	UV–vis spectrophotometer, equipped with an integrating sphere accessory	200 - 800	n/a	RCL10 UVA= 90% UVB = 100% LRCL-30-1 Similar result with RCL-30 UVA= 99.9% UVB = 100%	60 - 40	Missing scan speed	He et al. 2023[90]

Moreover, numerous publications neglect to provide essential experimental parameters, including scan speed, slit width, and baseline correction.[20, 134, 23] These factors significantly affect spectral resolution and measurement precision, especially in the UV region, where lignin displays distinct absorption peaks. The exclusion of these characteristics compromises reproducibility and hinders the capacity to differentiate authentic material performance from possible measurement errors.

Much of the data demonstrates a clear trade-off, increased lignin concentrations typically enhance UV-blocking efficacy while concurrently diminishing visible-light transparency. Insufficient transparency can hinder commercial viability, especially in applications like product labelling where visual clarity is crucial. Incorporating 5 wt.% lignin nanoparticles (LNPs) into a cellulose nanocomposite achieves nearly total UVA and UVB blocking, although only attains 15% visible transparency.[20] In comparison, RCL-30 (dissolving wood pulp containing 30 wt.% alkaline lignin) attains 40% visible transparency, which is deemed acceptable for certain plastic applications.[90] Notwithstanding this trade-off, few systematic studies have examined the optimization of UV protection and visible transparency, as the majority of research has concentrated exclusively on enhancing UV blocking, sometimes disregarding visual aesthetics or functional transparency needs. Moreover, a significant disparity occurs in correlating lignin particle attributes such as lignin type, hydroxyl group content, or other chemical and morphological characteristics to the resultant optical performance.

In summary, this evaluation identifies numerous significant deficiencies in the existing literature. The absence of technical specificity and the employment of inadequate instrumentation have likely led to the overestimation of UV absorbance in numerous investigations. Moreover, a well-defined or commonly acknowledged standard for balancing UV-blocking efficiency with visible-light transparency remains absent, despite its significance for applications like packaging. The link between structure and optical properties is significantly underexplored, resulting in a lack of understanding of the fundamental variables that influence optical behavior. Due to the intrinsic heterogeneity in lignin structure, the majority of current studies cannot establish strong connections between lignin composition and the efficacy of lignin-based biodegradable UV-blocking coatings. Systematic characterisation, including the quantification of hydroxyl group content and comprehensive compositional

analysis, may yield significant insights into the impact of lignin's chemical and morphological properties on optical performance.

1.3 Research Gaps and Rationale

Notwithstanding the growing interest in sustainable material manufacturing, substantial deficiencies persist in the synthesis and characterisation of cellulose–lignin-based films. There is a significant deficiency of green synthetic approaches in solvent use that have been thoroughly assessed utilizing comprehensive environmental and economic performance measures. Notably, while ionic liquids have emerged as a prominent green solvent alternative, their widespread adoption is currently hindered by high production and acquisition costs. A critical research gap that necessitates the development of more economically lower-cost alternatives is crucial. Traditional assessments frequently exclude the integrated use of the E-factor, atom economy (AE), and environmental mass yield (EMY), which collectively offer a more sophisticated and contextually relevant appraisal of process sustainability. In the absence of a comprehensive green metrics analysis, benchmarking synthetic techniques and identifying process optimizations that reconcile environmental and cost factors becomes challenging.

The physicochemical characterization of cellulose–lignin and cellulose–lignin–glycerol films has not been adequately investigated concerning material purity, hydroxyl group concentration, and detailed compositional analysis. Specifically, comprehensive compositional characterization of both the source biomass and the produced films measuring glucose, hemicellulose, acid-soluble lignin, acid-insoluble lignin, and ash content remains limited. This data is crucial for clarifying the relation between feedstock composition and the resulting physical, mechanical, chemical, and thermal properties of the films. This study does not directly produce output measurements but offers essential insights into structure–property relationships, facilitating the precise design of materials for certain functional applications.

Third, the impact of plasticizer type and concentration on the performance of cellulose-lignin composite films is not well understood. Despite the extensive use of glycerol in many biopolymer systems, its incorporation into cellulose–lignin metrics has not been sufficiently

investigated. Optimal glycerol loading is likely dependent upon the biopolymer's origin, compositional characteristics, and structural arrangement. However, comprehensive studies evaluating these influences are absent. Addressing this deficiency is essential for creating application-specific formulations with customized flexibility, strength, and barrier wettability characteristics.

1.4 Significance of Study

This research significantly advances sustainable material development by creating a comprehensive process for fabricating cellulose-lignin composite films. This study innovatively develops cellulose–lignin and cellulose–lignin–glycerol films sourced exclusively from biodegradable and renewable ingredients, therefore adhering to circular economy principles and diminishing dependence on petroleum-based substances.

This work incorporates green metrics into the assessment of ionic liquid (IL) synthesis, a crucial element frequently neglected in current literature. This research clearly evaluates the environmental sustainability of the IL synthesis process, so addressing a methodological need and establishing a precedent for integrating green chemistry concepts into material creation processes.

Moreover, the bespoke cellulose–lignin composite films created in this research offer valuable perspectives for future bio-based packaging solutions intended to meet specific performance criteria. This study connects analytical characterisation with application-oriented research, providing both scientific and industrial avenues for the development of high-performance, sustainable bio-composite films.

1.5 Objectives and Scope of Study

This thesis aims to address significant deficiencies in the sustainable production of bio-based polymer composites film by pursuing the following objectives:

1. To develop and rigorously assess sustainable, low-cost synthesis pathways for [C_2C_1im][OAc] utilizing simple green chemistry metrics and economic viability, thereby offering a quantitative standard for the holistic sustainability of ionic liquid production.

2. To devise and enhance a novel fabrication technique for reliable cellulose–lignin and cellulose–lignin–glycerol composite films, aiming for producing high-quality films through a more sustainable process.

3. To enhance the fundamental understanding of cellulose-lignin interactions through accurate measurement of hydroxyl groups in lignin and comprehensive compositional analysis, facilitating structure-property correlations in the resultant films.

4. To systematically clarify the function of glycerol as a plasticizer in modifying the mechanical properties and surface attributes of cellulose-lignin composites.

1.6 References

1 A. A. Akinsemolu, A. M. Idowu and H. N. Onyeaka, *Polymers (Basel).*, 2024, **16**, 1–18.

2 N. Evode, S. A. Qamar, M. Bilal, D. Barceló and H. M. N. Iqbal, *Case Stud. Chem. Environ. Eng.*, 2021, **4**, 100142.

3 M. Shen, B. Song, G. Zeng, Y. Zhang, W. Huang, X. Wen and W. Tang, *Environ. Pollut.*, 2020, **263**, 114469.

4 F. Zhang, Y. Zhao, D. Wang, M. Yan, J. Zhang, P. Zhang, T. Ding, L. Chen and C. Chen, *J. Clean. Prod.*, 2021, **282**, 124523.

5 B. Jiang, C. Chen, Z. Liang, S. He, Y. Kuang, J. Song, R. Mi, G. Chen, M. Jiao and L. Hu, *Adv. Funct. Mater.*, 2020, **30**, 1–11.

6 P. G. C. Nayanathara Thathsarani Pilapitiya and A. S. Ratnayake, *Clean. Mater.*, 2024, **11**, 100220.

7 J. M. Millican and S. Agarwal, *Macromolecules*, 2021, **54**, 4455–4469.

8 P. Balakrishnan, M. Sara, L. A. Pothen, S. Thomas and M. S. Sreekala, *Encycl. Polym. Nanomater.*, 2014, 1–8.

9 Z. Yao, H. J. Seong and Y. S. Jang, *Ecotoxicol. Environ. Saf.*, 2022, **242**, 113933.

10 C. Campanale, S. Galafassi, F. Di Pippo, I. Pojar, C. Massarelli and V. F. Uricchio, *Trends Anal. Chem.*, 2024, **170**, 117391.

11 M. Ghasemi, P. Alexandridis and M. Tsianou, *Cellulose*, 2017, **24**, 571–590.

12 H. Zhang, S. Yu, W. Lv, X. Wang, P. Lu and H. Zhang, *J. Hazard. Mater.*, 2026, **506**, 141616.

13 L. G. Pinaeva and A. S. Noskov, *Sci. Total Environ.*, 2024, **947**, 174445.

14 J. Kim, S. Park, S. Jung, H. Yun, K. Choi, G. Heo, H. J. Jin, S. Park and H. W. Kwak, *Polym. Degrad. Stab.*, 2023, **216**, 110490.

15 X. Zhao, Y. Wang, X. Chen, X. Yu, W. Li, S. Zhang, X. Meng, Z. M. Zhao, T. Dong, A. Anderson, A. Aiyedun, Y. Li, E. Webb, Z. Wu, V. Kunc, A. Ragauskas, S. Ozcan and H. Zhu, *Matter*, 2023, **6**, 97–127.

16 J. G. Rosenboom, R. Langer and G. Traverso, *Nat. Rev. Mater.*, 2022, **7**, 117–137.

17 J. Liang, M. Nabi, P. Zhang, G. Zhang, Y. Cai, Q. Wang, Z. Zhou and Y. Ding, *Renew. Sustain. Energy Rev.*, 2020, **134**, 110335.

18 M. Mujtaba, L. Fernandes Fraceto, M. Fazeli, S. Mukherjee, S. M. Savassa, G. Araujo de Medeiros, A. do Espírito Santo Pereira, S. D. Mancini, J. Lipponen and F. Vilaplana, *J. Clean. Prod.*, 2023, **402**, 136815.

19 S. Barzegar, M. H. Aryaie Monfared and M. A. Hubbe, *Mater. Today Commun.*, 2022, **33**, 104617.

20 V. F. Lotfy and A. H. Basta, *Int. J. Biol. Macromol.*, 2025, **307**, 142124.

21 Y. Xie, Y. Pan and P. Cai, *Ind. Crops Prod.*, 2022, **176**, 114381.

22 H. Huang, C. Xu, X. Zhu, B. Li and C. Huang, *Green Chem.*, 2023, **25**, 4995–5009.

23 H. Sadeghifar, R. Venditti, J. Jur, R. E. Gorga and J. J. Pawlak, *ACS Sustain. Chem. Eng.*, 2017, **5**, 625–631.

24 R. P. Swatloski, S. K. Spear, J. D. Holbrey and R. D. Rogers, *J. Am. Chem. Soc.*, 2002, **124**, 4974–4975.

25 Z. Fang, B. Li, Y. Liu, J. Zhu, G. Li, G. Hou, J. Zhou and X. Qiu, *Matter*, 2020, **2**, 1000–1014.

26 C. Leng, K. Li, Z. Tian, Y. Si, H. Huang, J. Li and J. Liu, *Sci. Rep.*, 2021, 1–11.

27 S. Sun, J. R. Mitchell, W. MacNaughtan, T. J. Foster, V. Harabagiu, A. Yihu Song and Q. Zheng, *Biomacromolecules*, 2010, **11**, 126–132.

28 S. Romão, A. Bettencourt and I. A. C. Ribeiro, *Polymers (Basel).*, 2022, **14**, 4968.

29 S. Y. Park, H. L. Kim and J. Y. Her, *Carbohydr. Polym. Technol. Appl.*, 2024, **7**, 100423.

30 J. M. Andanson, E. Bordes, J. Devémy, F. Leroux, A. A. H. Pádua and M. F. C. Gomes, *Green Chem.*, 2014, **16**, 2528–2538.

31 S. M. Gonçalves, D. C. dos Santos, J. F. G. Motta, R. R. dos Santos, D. W. H. Chávez and N. R. de Melo, *Carbohydr. Polym.*, 2019, **209**, 190–197.

32 B. Medronho, L. Alves and C. Costa, *Phys. Chem. Chem. Phys*, 2017, **19**, 23704–23718.

33 X. Tan, X. Li, L. Chen and F. Xie, *Phys. Chem. Chem. Phys.*, 2016, **18**, 27584–27593.

34 H. Abushammala and J. Mao, *Polymers (Basel).*, 2020, **12**, 195.

35 S. Yousef, M. Tatariants, M. Tichonovas, Z. Sarwar, I. Jonuškienė and L. Kliucininkas, *Resour. Conserv. Recycl.*, 2019, **145**, 359–369.

36 C. H. Day, *Encycl. Toxicol.*, 2005, 420–423.

37 R. Li, C. Chang, J. Zhou, L. Zhang, W. Gu, C. Li, S. Liu and S. Kuga, *Ind. Eng. Chem. Res.*,

2010, **49**, 11380–11384.

38 R. S. Shutt and E. Mack, *Ind. Eng. Chem. Res.*, 1933, **25**, 687–692.

39 S. Koutsoukos, J. Becker, A. Dobre, Z. Fan, F. Othman, F. Philippi, G. J. Smith and T. Welton, *Nat. Rev. Methods Prim.*, 2022, **2**, 49.

40 Y. Liang, J. E. Hawkins, M. E. Ries and P. J. Hine, *Cellulose*, 2021, **28**, 715–727.

41 R. Vanholme, B. Demedts, K. Morreel, J. Ralph and W. Boerjan, *Plant Physiol.*, 2010, **153**, 895–905.

42 J. Ralph, K. Lundquist, G. Brunow, F. Lu, H. Kim, P. F. Schatz, J. M. Marita, R. D. Hatfield, S. A. Ralph, J. H. Christensen and W. Boerjan, *Phytochem. Rev.*, 2004, **3**, 29–60.

43 X. Meng, C. Crestini, H. Ben, N. Hao, Y. Pu, A. J. Ragauskas and D. S. Argyropoulos, *Nat. Protoc.*, 2019, **14**, 2627–2647.

44 F. Zikeli, V. Vinciguerra, A. R. Taddei, A. D'Annibale, M. Romagnoli and G. S. Mugnozza, *Holzforschung*, 2018, **72**, 961–972.

45 J. J. Stewart, T. Akiyama, C. Chapple, J. Ralph and S. D. Mansfield, *Plant Physiol.*, 2009, **150**, 621–635.

46 A. Duval, F. Vilaplana, C. Crestini and M. Lawoko, *Holzforschung*, 2016, **70**, 11–20.

47 T. Rashid, C. F. Kait, I. Regupathi and T. Murugesan, *Ind. Crops Prod.*, 2016, **84**, 284–293.

48 S. O. Anuchi, K. L. S. Campbell and J. P. Hallett, *Sci. Rep.*, 2022, **12**, 1–11.

49 A. Morales, M. Á. Andrés, J. Labidi and P. Gullón, *Ind. Crops Prod.*, 2019, **131**, 281–292.

50 Z. Zhang, R. Yang, W. Gao and X. Yao, *RSC Adv.*, 2017, **7**, 31009–31017.

51 Y. Guo, D. Tian, F. Shen, G. Yang, L. Long, J. He, C. Song, J. Zhang, Y. Zhu, C. Huang and S. Deng, *Polymers (Basel).*, 2019, **11**, 1–11.

52 D. Glas, C. Van Doorslaer, D. Depuydt, F. Liebner, T. Rosenau, K. Binnemans and D. E. De Vos, *J. Chem. Technol. Biotechnol.*, 2015, **90**, 1821–1826.

53 Z. Xue, X. Zhao, R. C. Sun and T. Mu, *ACS Sustain. Chem. Eng.*, 2016, **4**, 3864–3870.

54 Y. Pu, N. Jiang and A. J. Ragauskas, *J. Wood Chem. Technol.*, 2007, **27**, 23–33.

55 N. Sun, M. Rahman, Y. Qin, M. L. Maxim, H. Rodríguez and R. D. Rogers, *Green Chem.*, 2009, **11**, 646–65.

56 S. J. Haward, V. Sharma, C. P. Butts, G. H. McKinley and S. S. Rahatekar, *Biomacromolecules*, 2012, **13**, 1688–1699.

57 M. Zavrel, D. Bross, M. Funke, J. Büchs and A. C. Spiess, *Bioresour. Technol.*, 2009, **100**, 2580–2587.

58 R. Protz, A. Lehmann, J. Bohrisch, J. Ganster and H. P. Fink, *Carbohydr. Polym. Technol. Appl.*, 2021, **2**, 100041.

59 R. M. Dias, L. C. G. Petrin, F. H. B. Sosa, A. M. Da Costa Lopes, J. A. P. Coutinho and M. C. Da Costa, *Ind. Eng. Chem. Res.*, 2020, **59**, 18193–18202.

60 P. Y. S. Nakasu, P. Y. S. Nakasu, C. J. Clarke, S. C. Rabelo, A. C. Costa, A. Brandt-Talbot and J. P. Hallett, *ACS Sustain. Chem. Eng.*, 2020, **8**, 7952–7961.

61 M. Nurdin, H. Abimanyu, H. Putriani, L. O. M. I. Setiawan, M. Maulidiyah, D. Wibowo, A.

Ansharullah, M. Natsir, L. O. A. Salim, Z. Arham and F. Mustapa, *Sci. Rep.*, 2021, **11**, 1–11.

62 S. Vincent, R. Prado, O. Kuzmina, K. Potter, J. Bhardwaj, N. D. Wanasekara, R. L. Harniman, A. Koutsomitopoulou, S. J. Eichhorn, T. Welton and S. S. Rahatekar, *ACS Sustain. Chem. Eng.*, 2018, **6**, 5903–5910.

63 W. C. Tu, L. Weigand, M. Hummel, H. Sixta, A. Brandt-Talbot and J. P. Hallett, *Cellulose*, 2020, **27**, 4745–4761.

64 L. Zhang, D. Zhao, M. Feng, B. He, X. Chen, L. Wei, S. R. Zhai, Q. Da An and J. Sun, *ACS Sustain. Chem. Eng.*, 2019, **7**, 18593–18602.

65 A. J. Holding, A. Parviainen, I. Kilpeläinen, A. Soto, A. W. T. King and H. Rodríguez, *RSC Adv.*, 2017, **7**, 17451–17461.

66 B. Zhang, F. Xie, T. Zhang, L. Chen, X. Li, R. W. Truss, P. J. Halley, J. L. Shamshina, T. McNally and R. D. Rogers, *Carbohydr. Polym.*, 2016, **146**, 67–79.

67 A. W. T. King, J. Asikkala, I. Mutikainen, P. Järvi and I. Kilpeläinen, *Angew. Chemie - Int. Ed.*, 2011, **50**, 6301–6305.

68 F. Ibrahim, M. Moniruzzaman, S. Yusup and Y. Uemura, *J. Mol. Liq.*, 2015, **211**, 370–372.

69 B. Medronho and B. Lindman, *Curr. Opin. Colloid Interface Sci.*, 2014, **19**, 32–40.

70 O. Cusola, O. J. Rojas and M. B. Roncero, *ACS Appl. Mater. Interfaces*, 2019, **11**, 45226–45236.

71 X. Tan, X. Li, L. Chen and F. Xie, *Phys. Chem. Chem. Phys.*, 2016, **18**, 27584–27593.

72 M. Tobiszewski, M. Marć, A. Gałuszka and J. Namieśnik, *Molecules*, 2015, **20**, 10928–10946.

73 M. Tobiszewski, *Anal. Methods*, 2016, **8**, 2993–2999.

74 D. J. C. Constable, A. D. Curzons and V. L. Cunningham, *Green Chem.*, 2002, **4**, 521–527.

75 R. A. Sheldon, *ACS Sustain. Chem. Eng.*, 2018, **6**, 32–48.

76 W. Wang, J. Lü, L. Zhang and Z. Li, *Front. Chem. Eng. China*, 2011, **5**, 349–354.

77 T. Hudlicky, D. A. Frey, L. Koroniak, C. D. Claeboe and E. Larry, *Green Chem.*, 1999, 57–59.

78 R. Antonella, N. Pontillo, N. Mac Dowell, K. Lee, S. Chen, F. O. Diego and T. Welton, *RSC Sustain.*, 2025, **3**, 2301–2310.

79 K. C. Lethesh, D. Parmentier, W. Dehaen and K. Binnemans, *RSC Adv.*, 2012, **2**, 11936–11943.

80 H. X. Zhu, J. S. Li, R. Xu and S. Y. Yang, *J. Mol. Liq.*, 2012, **165**, 173–176.

81 S. B. Choi, S. W. Won and Y. S. Yun, *Chem. Eng. J.*, 2013, **214**, 78–82.

82 X. Tan, X. Li, L. Chen and F. Xie, *Phys. Chem. Chem. Phys.*, 2016, **18**, 27584–27593.

83 M. T. Clough, K. Geyer, P. A. Hunt, S. Son and T. Welton, *Green Chem.*, 2015, **17**, 1–12.

84 R. S. Kalb, M. Damm and S. P. Verevkin, *React. Chem. Eng.*, 2017, **2**, 432–436.

85 T. J. Simmons, S. H. Lee, J. Miao, M. Miyauchi, T. J. Park, S. S. Bale, R. Pangule, J. Bult, J. G. Martin, J. S. Dordick and R. J. Linhardt, *Wood Sci. Technol.*, 2011, **45**, 719–733.

86 J. Ou, S. Hu, L. Yao, Y. Chen, H. Qi and F. Yue, *Chem. Eng. J.*, 2023, **453**, 139770.

87 Y. Ma, S. Asaadi, L. S. Johansson, P. Ahvenainen, M. Reza, M. Alekhina, L. Rautkari, A.

Michud, L. Hauru, M. Hummel and H. Sixta, *ChemSusChem*, 2015, **8**, 4030–4039.

88 R. L. Wu, X. L. Wang, F. Li, H. Z. Li and Y. Z. Wang, *Bioresour. Technol.*, 2009, **100**, 2569–2574.

89 K. Rajan, K. Kim, T. J. Elder, A. K. Naskar and N. Labbé, *ACS Sustain. Chem. Eng.*, 2022, **10**, 8835–8845.

90 Y. He, H. C. Ye, T. T. You and F. Xu, *Food Hydrocoll.*, 2023, **137**, 108355.

91 J. Zhang, Xiaoyu Zhang, J. Yu and R. Li, *Regenerated Cellulose Film , Functional Film and Preparation Method Therefor*, United States Patent, 2017, vol. 2.

92 A. Dastpak, T. V. Lourençon, M. Balakshin, S. Farhan Hashmi, M. Lundström and B. P. Wilson, *Ind. Crops Prod.*, 2020, **148**, 112310.

93 M. Chen, X. Zhang, C. Liu, R. Sun and F. Lu, *ACS Sustain. Chem. Eng.*, 2014, **2**, 1164–1168.

94 W. Luo, C. Mao, P. Ji, J. Y. Wu, J. D. Yang and J. P. Cheng, *Chem. Sci.*, 2020, **11**, 3365–3370.

95 C. Zhu, A. F. Koutsomitopoulou, S. J. Eichhorn, J. S. van Duijneveldt, R. M. Richardson, R. Nigmatullin and K. D. Potter, *Macromol. Mater. Eng.*, 2018, **303**, 29–34.

96 L. Wu, S. H. Lee and T. Endo, *Bioresour. Technol.*, 2013, **140**, 90–96.

97 W. Luo, C. Mao, P. Ji, J. Y. Wu, J. D. Yang and J. P. Cheng, *Chem. Sci.*, 2020, **11**, 3365–3370.

98 C. Shi, L. Zhang, Z. Shi, M. Yan, Z. Wang and J. Ma, *Ind. Crops Prod.*, 2023, **193**, 116200.

99 Y. Zhou, Y. Han, J. Xu, W. Han, F. Gu, K. Sun, X. Huang and Z. Cai, *Int. J. Biol. Macromol.*, 2023, **232**, 123105.

100 M. Fitzpatrick, P. Champagne, M. F. Cunningham and C. Falkenburger, *Can. J. Chem. Eng.*, 2012, **90**, 1142–1152.

101 R. Sescousse, K. A. Le, M. E. Ries and T. Budtova, *J. Phys. Chem. B*, 2010, **114**, 7222–7228.

102 F. Meister and B. Kosan, *Nord. Pulp Pap. Res. J.*, 2015, **30**, 112–120.

103 K. Collier, A. Tovar, S. Goins, A. Chirgwin and A. Siegel, *J. Purdue Undergrad. Res.*, 2022, **12**, 21–28.

104 D. L. Minnick, R. A. Flores, M. R. Destefano and A. M. Scurto, *J. Phys. Chem. B*, 2016, **120**, 7906–7919.

105 M. Chen, F. Malaret, A. E. J. Firth, P. Verdía, A. R. Abouelela, Y. Chen and J. P. Hallett, *Green Chem.*, 2020, **22**, 5161–5178.

106 A. Brandt-Talbot, F. J. V. Gschwend, P. S. Fennell, T. M. Lammens, B. Tan, J. Weale and J. P. Hallett, *Green Chem.*, 2017, **19**, 3078–3102.

107 A. R. Abouelela, P. Y. S. Nakasu and J. P. Hallett, *ACS Sustain. Chem. Eng.*, 2023, **11**, 2404–2415.

108 S. Hidayati, Zulferiyenni, U. Maulidia, W. Satyajaya and S. Hadi, *Heliyon*, 2021, **7**, e07799.

109 E. Basiak, A. Lenart and F. Debeaufort, *Polymers (Basel).*, 2018, **10**, 412.

110 J. Liang, Q. Xia, S. Wang, J. Li, Q. Huang and R. D. Ludescher, *Food Hydrocoll.*, 2015, **44**, 94–100.

111 P. Ahokas, V. Kunnari, J. Majoinen, A. Harlin and M. Mäkelä, *ACS Sustain. Chem. Eng.*, 2025, **13**, 10771–10779.

112 C. S. Miranda, M. S. Ferreira, M. T. Magalhães, A. P. G. Bispo, J. C. Oliveira, J. B. A. Silva and N. M. José, *Mater. Today Proc.*, 2015, **2**, 134–140.

113 T. Mekonnen, P. Mussone, H. Khalil and D. Bressler, *J. Mater. Chem. A*, 2013, **1**, 13379–13398.

114 V. Jost, K. Kobsik, M. Schmid and K. Noller, *Carbohydr. Polym.*, 2014, **110**, 309–319.

115 C. S. Miranda, M. S. Ferreira, M. T. Magalhães, W. J. Santos, J. C. Oliveira, J. B. A. Silva and N. M. José, *Mater. Today Proc.*, 2015, **2**, 63–69.

116 M. T. Clough, K. Geyer, P. A. Hunt, J. Mertes and T. Welton, *Phys. Chem. Chem. Phys.*, 2013, **15**, 20480–20495.

117 F. D. Acierno, W. Y. Hamad, C. A. Michal and M. J. Maclachlan, *Bioenergy Res.*, 2020, **21**, 3374–3386.

118 Y. Liu, A. Liu, S. A. Ibrahim, H. Yang and W. Huang, *Int. J. Biol. Macromol.*, 2018, **111**, 717–721.

119 A. G. Margellou, P. A. Lazaridis, I. D. Charisteidis, C. K. Nitsos, C. P. Pappa, A. P. Fotopoulos, S. Van den Bosch, B. F. Sels and K. S. Triantafyllidis, *Appl. Catal. A Gen.*, 2021, **623**, 118298.

120 X. Zhao and D. Liu, *Ind. Crops Prod.*, 2010, **32**, 284–291.

121 P. Wannid, B. Hararak, S. Padee, W. Klinsukhon, N. Suwannamek, M. Raita, K. Khao-on and C. Prahsarn, *J. Polym. Environ.*, 2022, **30**, 2739–2750.

122 J. Y. Kim, H. Hwang, S. Oh, Y. S. Kim, U. J. Kim and J. W. Choi, *Int. J. Biol. Macromol.*, 2014, **66**, 57–65.

123 K. Rajan, K. Kim, T. J. Elder, A. K. Naskar and N. Labbé, *ACS Sustain. Chem. Eng.*, 2022, **10**, 8835–8845.

124 M. Trogen, N. D. Le, D. Sawada, C. Guizani, T. V. Lourençon, L. Pitkänen, H. Sixta, R. Shah, H. O'Neill, M. Balakshin, N. Byrne and M. Hummel, *Carbohydr. Polym.*, 2021, **252**, 117133.

125 X. Wang, W. Zheng, Z. Guo, H. Nawaz, T. You, X. Li and F. Xu, *Green Chem.*, 2022, **25**, 1597–1610.

126 K. Crouvisier-Urion, P. R. Bodart, P. Winckler, J. Raya, R. D. Gougeon, P. Cayot, S. Domenek, F. Debeaufort and T. Karbowiak, *ACS Sustain. Chem. Eng.*, 2016, **4**, 6371–6381.

127 K. Q. Sun, F. Y. Li, J. Y. Li, J. F. Li, C. W. Zhang, S. Chen, X. Sun and J. F. Cui, *RSC Adv.*, 2019, **9**, 24451–24459.

128 D. Maria V, C. Bernal and N. J. Francois, *J. Tissue Sci. Eng.*, 2016, **7**, 1000187.

129 M. Borrega, S. Päärnilä, L. G. Greca, A. S. Jääskeläinen, T. Ohra-Aho, O. J. Rojas and T. Tamminen, *Langmuir*, 2020, **36**, 9675–9684.

130 J. Xie, J. Xu, Z. Zhang, B. Wang, S. Zhu, J. Li and K. Chen, *Chem. Eng. J.*, 2023, **451**, 138591.

131 L. L. Sun, L. J. Zhao, S. Q. Yao, Y. Han, J. L. Wen, T. Q. Yuan, S. N. Sun and X. F. Cao, *Ind. Crops Prod.*, 2025, **229**, 120982.

132 M. Parit, P. Saha, V. A. Davis and Z. Jiang, *ACS Omega*, 2018, **3**, 10679–10691.

133 D. Wang, Y. Gu, S. Feng, W. Yang, H. Dai, H. Xiao and J. Han, *Green Chem.*, 2023, **25**, 9020–9044.

134 W. Yang, G. Qi, H. Ding, P. Xu, W. Dong, X. Zhu, T. Zheng and P. Ma, *Compos. Commun.*, , DOI:10.1016/j.coco.2020.100497.

Chapter 2: Materials and Method

This chapter presents the method of film fabrication and characterisations. The solution casting method for film fabrication was selected as the optimal approach due to its scalability from laboratory to pilot scale, its efficiency in dissolving cellulose and lignin into a homogenous dope solution, and its ability to yield smooth, transparent films. Figure 2.1 outlines the experimental workflow, starting from the acquisition and characterisation of raw materials, following to dope solution production, and finishing with film fabrication via the solution casting method to produce **cel-lig** films. The resultant films were further analysed utilizing analytical techniques to assess their physicochemical, thermal, and surface properties.

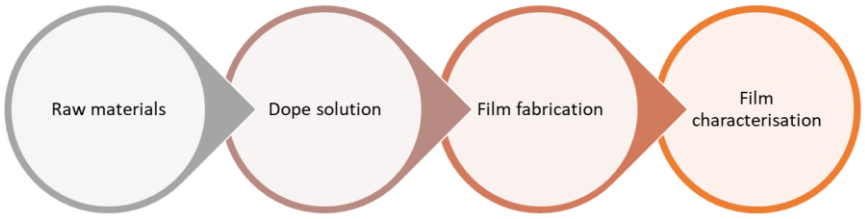


Figure 2.1: Overview of experimental workflow to obtain **cel-lig** films

2.1 Preparation of dope solutions

2.1.1 Materials

1-Ethyl-3-methylimidazolium acetate, ([C_2C_1im][OAc], >98%) was provided by Proionic GmbH (Raaba-Grambach, Austria). Dimethyl sulfoxide($(CH_3)_2SO$, ⩾99.9%) was purchased from VWR Chemical. Sigmacell Cellulose Type 101, $((C_{12}H_{22}O_{11})n)$ was purchased from Sigma-Aldrich. This material is a highly purified fibrous cellulose derived from cotton linters, characterized by an approximate molecular weight of 36,000 Da.[1] (i) Ionosolv spruce lignin, (Batch LB II) was supplied by Lixea Ou (Kristinehamn, Sweden), (ii) Organosolv beech wood lignin, U05-F5, was supplied by Netherlands Organisation for applied scientific research TNO, (iii) Kraft lignin, alkaline was purchased from Aldrich. The water contents in lignin and cellulose were 8 – 5 wt%; thus, cellulose and lignin were dried overnight via vacuum Schlenk line without any heating before conducting any experiments. Glycerol ($C_3H_8O_3$, 99.5%) was

purchased from VWR Chemicals. Beech chip (heat-treated) was purchased from Pettex company, *N,N*-Dimethyl-*N*-butylammonium hydrogen sulfate, [DMBA][HSO_4] was lab synthesised using starting materials of sulfuric acid (H_2SO_4, 95%) purchased from WVR Chemical and *N,N*-dimethyl-N-butylamine purchased from Aldrich.

2.1.2 Ionosolv lignin extraction method

2.1.2.1 Synthesis of *N,N*-dimethylbutylammonium hydrogen sulfate

[DMBA][HSO_4] was synthesised following Chen et al.'s work.[2] 5 M sulfuric acid (200 mL, 1 mol) was added dropwise into *N,N*-dimethylbutylamine (101.19 g, 1 mol) pre-cooled with an ice bath. The mixture was stirred for 3 h. The excess water was evaporated, and a transparent viscous liquid was obtained (199.27 g, 1.0 mol, 100%). The water content was adjusted to 20 wt.% by checking the acid/ratio and water content. A small amount of [DMBA][HSO_4] based on dry basis was titrated with 1 M NaOH to determine the acid/base ratio. The ideal acid to base ratio range shall be 1: 0.95 – 1.04. Its structure was confirmed by ^{1}H and ^{13}C NMR, IR and MS (see Appendix A7 for full characterization data).

^{1}H NMR: δ_H (400 MHz, DMSO-d_6)/ppm: 9.31 (s, 1H, N–H^+), 3.03 (m, J = 5.0 Hz, 2H, N–CH_2), 2.75 (s, 6H, N–$(CH_3)_2$), 1.61–1.53 (m, 2H, N–CH_2–CH_2), 1.30 (h, J = 7.4 Hz, 2H, N–CH_2–CH_2–CH_2), 0.89 (t, J = 7.4 Hz, 3H, N–CH_2–CH_2–CH_2–CH_3). ^{13}C NMR δC (101 MHz, DMSO-d6)/ppm: 56.92 (N–CH_2), 42.7 (N–$(CH_3)_2$), 26.18 (N–CH_2–CH_2), 19.63 (N–CH_2–CH_2–CH_2), 13.94 (N–CH_2–CH_2–CH_2–CH_3). MS (Magnet FB+) m/z: 102.13 ($[DMBA]^+$, 100%), (Magnet FB−) m/z: 96.96 ($[HSO_4]^-$, 100%).

Beechwood ionosolv lignin was isolated according to the method of Brandt et al. with slight modification.[3] 1.99 g beechwood was dried in the oven overnight at 105°C to determine the moisture content. The moisture content presented at 14.5 ± 1.2 %. The dry beech wood was placed in a 35 mL glass pressure tube (Aceglass) with teflone screw cap and front sealing rubber ring. [DMBA][HSO_4] with 20 wt.% water was added to the tube. Each lignin batch consisted of three pressure tubes. The tubes were sealed and samples incubated without stirring in an oven at 120 °C for 24 h. The samples were cooled to room temperature and washed with

ethanol (20 mL) followed by centrifuge 6000 rpm, 20 min for three times. The ethanol washes were concentrated by evaporating ethanol using a rotary evaporation with vacuum. After that, 20 mL water was added as an anti-solvent to precipitate the lignin. Lignin was washed with 20 mL water three times cycles to remove ionic liquid. The recovered lignin was dried using a freeze-dryer overnight. The lignin weight was recorded and calculated for the percentage yield. The lignin yield was ~ 22.39 % relative to biomass added.

2.1.3 Film fabrication technique of cellulose-lignin films

Cellulose powder, lignin powder, and glycerol were subjected to vacuum drying on a Schlenk line (without heating) for a duration of 24 hours. The ionic liquid $[C_2C_1im][OAc]$ was subjected to vacuum drying at 50–60 °C for a duration of two days. Dimethyl sulfoxide (DMSO) was utilised as supplied because to its minimal water content. Lignin (0.5 – 4.0 wt. %, depending upon the formulation) was initially dissolved in a $[C_2C_1im][OAc]$/DMSO (1:0.275, w/w) solvent mixture by stirring overnight at 70 °C. Thereafter, cellulose (10 wt%) was incorporated into the lignin solution and blended at 8000 rpm for 60 seconds with a vortex mixer. All the wt.% values are relative to weight of $[C_2C_1im][OAC]$. The cellulose-lignin solution was further heated at 70 °C for an additional 2 hours. In the second formulation, glycerol (5 wt%) was added, and the solution was stirred for a further hour.

Upon achieving complete dissolution, the dope solutions were degassed in an ultrasonic bath power of 80W at 70 °C for 20 to 30 minutes, contingent upon viscosity. The degassed dope solutions were kept at 70 – 100 °C (depending on the formulation) to enable casting. Approximately 2 g of solution was applied onto glass plates (300 mm × 300 mm × 15 mm) along with a casting knife with a 250 µm gap, operated at a velocity of 5.08 mm/s on an Elcometer 4340 Motorised Film Applicator. The use of a motorized film applicator ensures homogeneity by maintaining a constant casting velocity, which provides a uniform shear rate across the substrate. Unlike manual application, the motorized system eliminates variations in speed and downward pressure, ensuring that the 250 µm gap remains consistent throughout the application. This mechanical precision prevents thickness gradients and ensures the reproducibility of the film's physical properties.

The cast films were then promptly submerged in deionised water to restore cellulose–lignin or cellulose–lignin-glycerol thin films. Pure cellulose films necessitated a minimum of four water replacement (1 hour), while cellulose–lignin films required five replacement (1.25 hours). The films were ultimately dried in a controlled-humidity room (55 – 60% RH) with regulated airflow for three days to guarantee thorough drying. The desiccated films were preserved in airtight containers for subsequent examination.

2.1.4 Analytical methods for dope solution characterisation

2.1.4.1 Optical Microscopy

Dissolution of cellulose and lignin was observed by optical microscopy. Optical micrographs were recorded with a Leica DM2500 microscope equipped with Basler camera. Cross-polarisers were employed to monitor the dissolution of cellulose and lignin in $[C_2C_1im][OAc]$ and$[C_2C_1im][OAc]$ mixed with DMSO due to the birefringent nature of crystalline cellulose. Prior to all studies, the polarising lenses were adjusted to maximise their cross-polarisation and ensure that maximum extinction had been reached. All images were taken at different magnification 4x and 10× magnification. The operating principle of polarising microscope is shown in Figure 2.2.

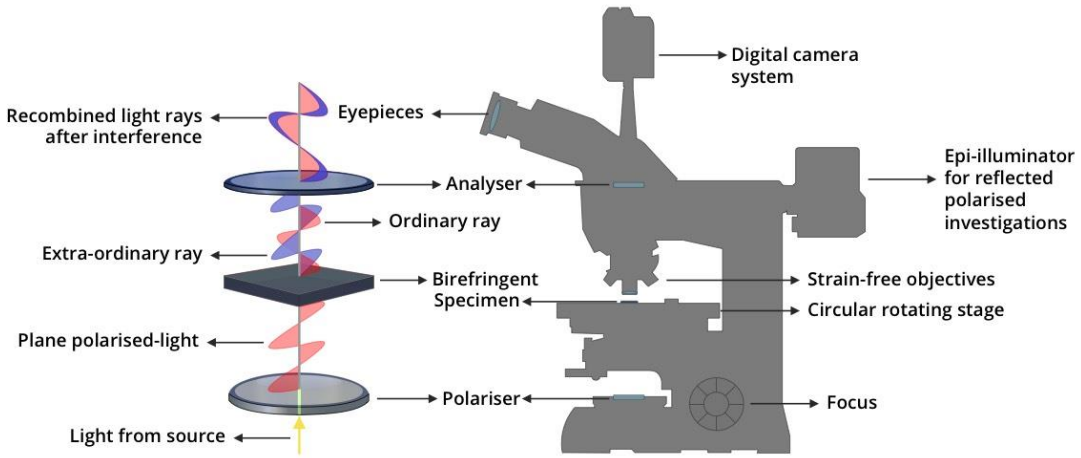


Figure 2.2: Polarizing microscope operating principle [Picture taken from Microscopy Australia] [4]

2.1.4.2 Rheology

The rheological measurements were performed using a HAAKE MARS 60 rheometer equipped with water bath-based temperature control system. A cone-plate geometry with 2° angle and 60 mm diameter (C60 2°/Ti - 02190045) was used. The steady-shear viscosity of cellulose-lignin dope solutions was measured at a shear rate of 10 s^{-1}, a similar to the casting rate used with the film casting machine. Temperatures ramp experiment was carried out ranging from 25 to 100°C, with measurements taken at 0.5°C intervals. Silicone oil was placed around the edge of the cone to prevent the absorption of water. The objective of the experiment is to ascertain the optimal temperature for casting the cellulose-lignin dope solutions.

There are two different kinds of flow: shear flow and extensional flow. Shear flow was employed in this experiment. Shear flow refers to the situation where the upper part of a fluid experiences a displacement resulting in maximum velocity, while the bottom part remains stationary, as seen in Figure 2.3. The formula for shear strain (γ) and shear rate (γ.) can be derived from this movement.

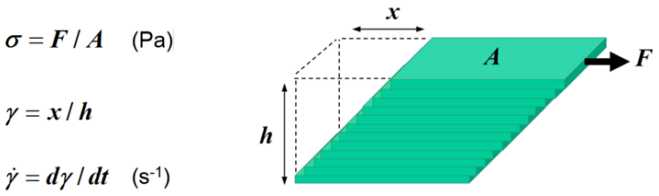


Figure 2.3: Shear flow of a material [Picture taken from https://wiki.anton-paar.com/uk-en/basics-of-rheology/] [5]

The relationship between shear stress and shear rate is defined as shear viscosity or dynamic viscosity (n), as represented by Equation 1. Pressure and temperature have a significant impact on viscosity.

$$\eta = \sigma / \dot{\gamma} \quad \text{(Pa.s)} \qquad \text{.....Equation 1}$$

2.2 Characterisation

Several testing instrumentations were used to characterise the physical, chemical, mechanical, and optical properties of starting materials, fabricated cellulose-lignin and cellulose-lignin-glycerol films.

2.2.1 Fourier transform infrared spectroscopy

The IR spectra were obtained using a Perkin Elmer 20 Spectrum 100 ATR-FTIR spectrometer with attenuated total reflectance (ATR) accessory. The ATR accessory had a diamond internal reflection element. The spectra were obtained with a resolution of 2 cm^{-1}, covering the range of 4000–650 cm^{-1} for all the samples. All the starting materials such as cellulose, different types of lignin, [C_2C_1im][OAc], DMSO, glycerol, fabricated **cel-lig** films were characterised using the same setup. The tests were conducted after calibration with the background.

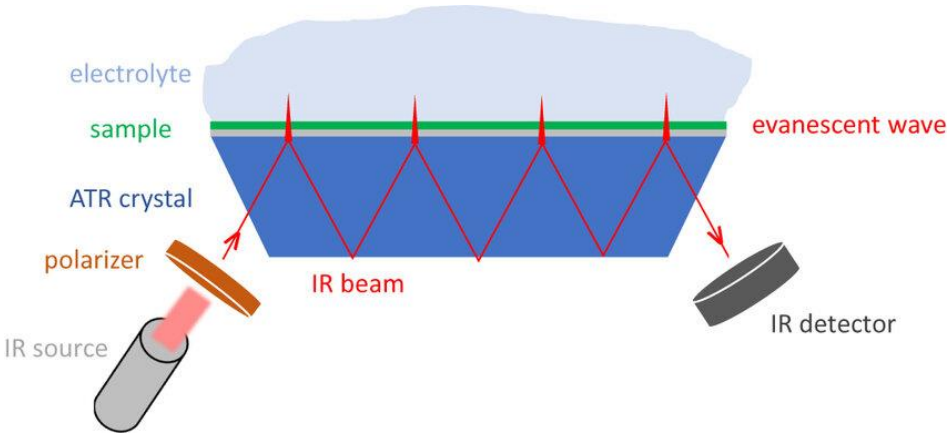


Figure 2.4: Schematic representation of the working principle of ATR-FTIR spectroscopy. Image adapted from Bieberle-Hütter et. al 2021[6]

Infrared light passes through a crystal, reflects beneath its surface, and interacts with a sample before making its way to the FTIR detector. When the light interacts with a sample where it can absorb, this phenomenon is known as an evanescent wave, as seen in Figure 2.4. The penetration depth of the evanescent wave into the sample is defined by the refractive index difference between the sample and the ATR crystal.

2.2.2 Thermogravimetric analysis

Thermogravimetric analysis, TGA of the cellulose-lignin and cellulose-lignin-glycerol films were performed on a Pyris 1 TGA Perkin Elmer. Samples (5–10 mg) were heated from room temperature to 105 °C, isothermal for 30 minutes, then temperature ramped to 800 °C at a rate of 10 °C/min. All the starting materials such as cellulose, different types of lignin, $[C_2C_1im][OAc]$, DMSO, glycerol, fabricated **cel-lig** films were characterised using the same set up. The two important temperature characteristics, namely, T_{onset} and residual weight were analysed. T_{onset} is the point in the TGA curve where a deflection is first observed from the established baseline prior to the thermal event. The solid weight that remains after furnace heating to maximum temperature is known as residual weight.

Thermogravimetric Analysis (TGA) measures the weight of a substance while it is exposed to a controlled temperature programme and atmosphere. The mass is measured as a function of either temperature or time. There are few use modes for TGA such as isothermal, quasistatic and temperature ramp. Isothermal TGA involves monitoring the change in sample weight over time at a constant temperature, while in quasistatic TGA the sample temperature is increased in a series of stages, with each step followed by a period of isothermal. During these periods, the sample mass is allowed to stabilise before the next temperature ramp. A temperature ramp refers to subjecting the sample to a continuous and controlled increase in temperature at a consistent heating rate. All these modes have been used to analyse the thermal analysis of cellulose-lignin films. The resulting thermogram is used to determine the residual weight and onset of the fabricated films.

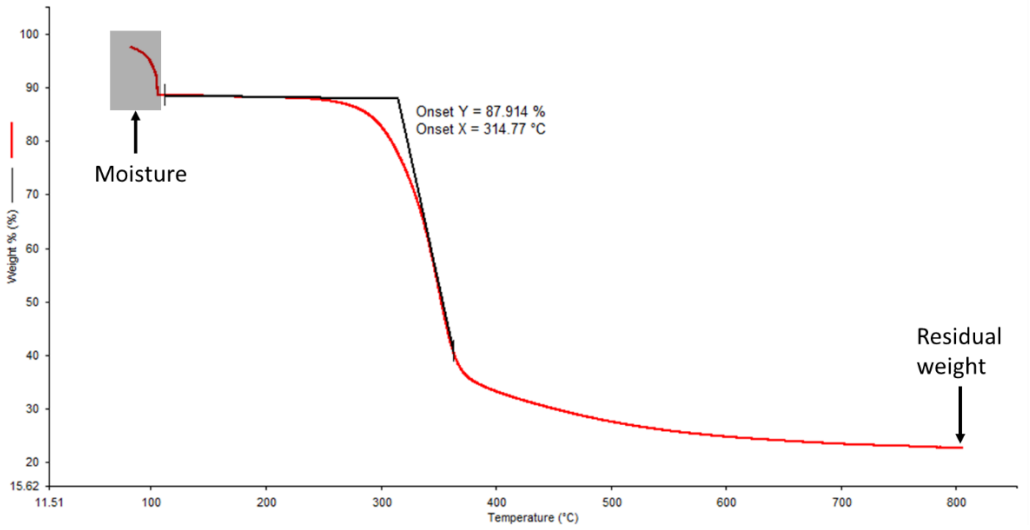


Figure 2.5: Diagram representing the measurement of T_{onset} using a temperature ramped TGA experiment with cellulose film sample.

The TGA data discussed in Chapters 5 and 6 are the modified data that eliminates moisture in the fabricated films. Figure 2.5 represents the initial thermogram of cellulose film, revealing the presence of moisture prior to a temperature shift above 105 °C. Eliminating moisture is crucial to guarantee the accuracy of the thermal characteristics of these bio-based polymer films.

2.2.3 Tensile testing

Tensile testing measures the maximum stress that a material can withstand before it fractures due to pulling forces that has been applied. The parameters determined by tensile testing are used to assess whether the film is strong and flexible or stiff enough for an application suitability for a particular tensile strength and strain at failure, which indicates its flexibility.[7]

There are several standard methods for tensile testing. This research used standard for plastic films is ASTM D882-10 that covers thickness less than 1000 µm. The cellulose-lignin and cellulose-lignin-glycerol films were tested using Linkam TST350 tensile tester with modular force stage and equipped with a 20 N load cell. Samples were mechanically cut in rectangular shapes of 50 mm length and 5 mm width; the effective distance between jaws (gauge length)

was 40 mm as shown in Figure 2.6. Temperature was controlled at 20 °C and conditioned at 45 -50 % relative humidity. The sample was tested at the rate of 20 mm min^{-1} and five specimens were tested for each film sample. Elongation at break (%), tensile strength (MPa), and Young's modulus (MPa) were calculated from the resulting stress-strain curves as average of five measurements according to ASTM D882-10.

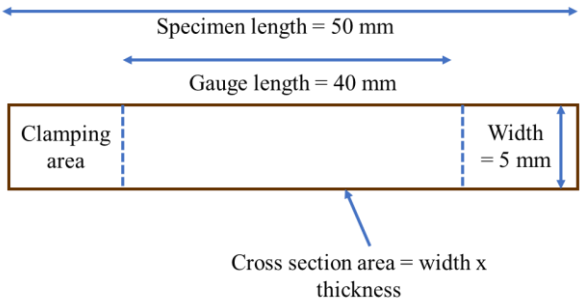


Figure 2.6: Sample geometry of cellulose, cellulose-lignin and cellulose-lignin-glycerol specimens generated for tensile testing

The specimens were prepared in accordance with ASTM D822-10, with a slight modification. The nominal width of the specimens has to be not less than 5.0 mm or greater than 25.4 mm. Test specimens were selected so that the thickness is uniform to within 10% of the thickness over the length of the specimen between the grips. When it is not possible to use a longer length, it is acceptable to use test sections as short as 100 mm provided it has been demonstrated that the results are not significantly impacted. However, due to the limited number of samples, a length of only 50 mm was utilised, consistent with what is reported in the literature.[7,8,9,10] Tensile tests were carried out at a crosshead speed of 20 mm/min, following the procedure reported by Ma et al,2015.[11] The gauge length was 40 mm.

The tensile strength and elongation at break can be determined using Equations 2 and 3, respectively.

$$\sigma max = \frac{P\ max}{A} \ldots\ldots\ldots \quad \text{Equation 2}$$

Where:

P_{max} = maximum load (N)

A = cross sectional area (mm^2)

A is determined by the thickness times with width as indicated in Figure 2.6.

Elongation at break, EB%

$EB\ \% = \frac{Lf-Lo}{Lo}$ x 100 …..… Equation 3

Where:

L_f = gauge length at fracture

L_0 = original gauge length

The Young's modulus is determined by fitting a tangent to the first linear section of the load-extension curve, choosing any point on this line, and dividing the tensile stress by the corresponding strain. The extension for "toe compensation" has to be corrected for according to the instructions provided in Figure 2.7. The unit for the tensile modulus is force per unit area N/m^2, and is often in given in megapascal (MPa).

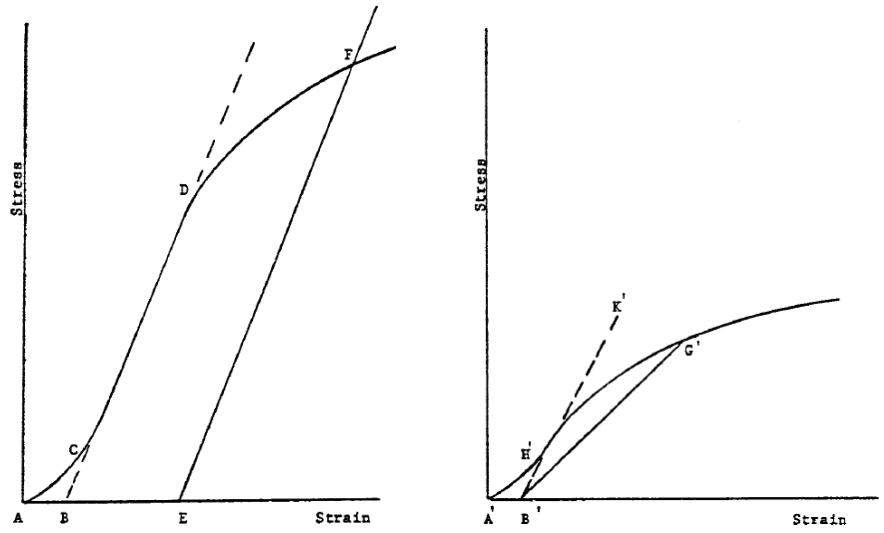


Figure 2.7: Tensile stress strain curve material with linear behaviour (left) and non-linear behaviour (right). Images obtained from ASTMD882-10 standard protocol[12]

2.2.4 Water contact angle

Several techniques known for quantifying contact angle are available. This study utilised the static sessile drop method. A contact angle goniometer measures the sessile drop contact angle using a high-resolution camera to capture the profile of water on a thin film. The contact angle is the angle formed at the interface between the liquid-solid and liquid-vapour phases. In general, a solid surface is classified as hydrophilic, or having good wettability, if the water

contact angle (WCA) is less than 90°. Conversely, a solid surface is considered hydrophobic, or having poor wettability, if the WCA is more than 90°. This information is illustrated in Figure 2.8.

The water contact angle (WCA) of cellulose-lignin and cellulose-lignin-glycerol was determined using a lux contact angle measuring equipment (Krüss, Germany) at room temperature and at range of 50 to 60% relative humidity. The water surface tension was approximately 72.8 mN m^{-1} provided by the software machine. Initially, film samples were cut into strips with 20 mm length and 10 mm width and mounted onto a level surface. Contact angles are highly susceptible to contamination; hence dust spray was employed to eradicate any solid particles. Next, a sessile 10 µL droplet of deionised water was placed on the surface of the samples, and the water contact angle was measured using a circular fitting at a constant residence duration of 2 seconds. At least, two droplets were dispensed in different regions.

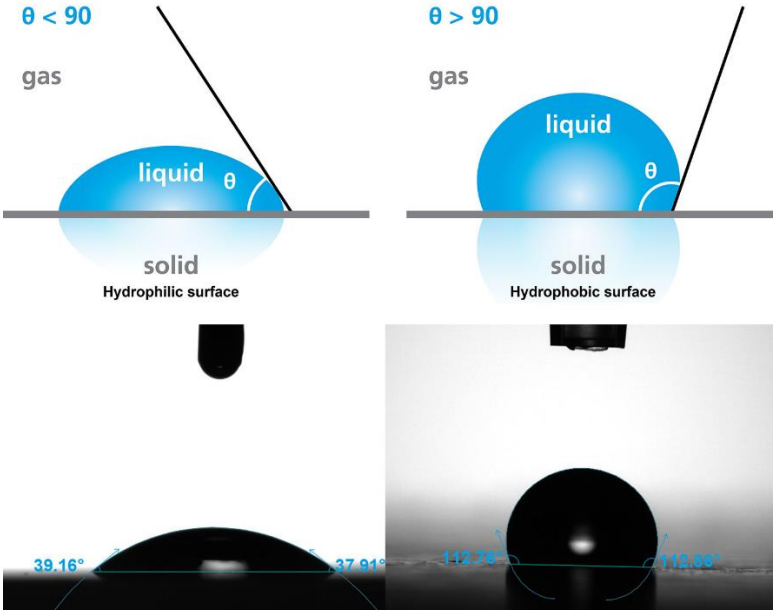


Figure 2.8: Illustrations of water contact angle measurements on hydrophilic and hydrophobic surface Image retrieve: https://www.nanoscience.com/blogs/what-probe-liquid-should-you-use-for-contact-angle-measurements/[13]

2.2.5 Ultraviolet-visible light spectrophotometry

Ultraviolet-visible light (UV-Vis) spectrophotometry measures absorption or reflectance of light in the ultraviolet and visible regions of the electromagnetic spectrum by a sample containing a chromophore in lignin, such as cellulose-lignin and cellulose-lignin-glycerol composite films. A chromophore is a molecule that selectively absorbs light at a certain wavelength and produces colour as a result. Equation 4 shows the correlation between absorbance (A) and transmittance (T).

$$A = -\log(\%T/100\%) \ldots\ldots\ldots \text{Equation 4}$$

A UV-Vis spectrophotometer typically measures the transmittance for a homogeneous and transparent liquid. In cases when materials such as suspended liquid or opaque substances like thin film scatter the light diffusely, only a fraction of the light reaches the detector. An integrating sphere efficiently collects most of the light emitted by the sample, resulting in a more accurate and representative measurement. When an integrating sphere is used for sample measurement, it ensures accurate results by diffusing all measuring lights inside the sphere and irradiating them onto the light-sensitive surface of the detector. This process occurs during both baseline correction and sample measurement. Figure 2.9 illustrates the schematic of transmittance measurement in UV-Vis with integrating sphere.

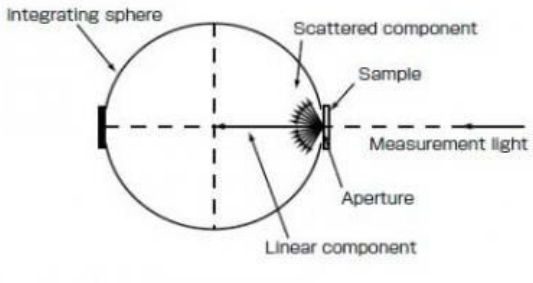


Figure 2.9: Schematic of Transmittance Measurement. Images retrieved from https://www.shimadzu.com/an/service-support/technical-support/uv/essential_knowledge/integratingspheres.html[14]

The absorption of UV-Vis light by the cellulose-lignin and cellulose-lignin-glycerol films were analysed using a UV-vis spectrophotometer (Lambda 356, PerkinElmer LAS Ltd., Beaconsfield, UK) equipped with a 50 mm diameter integrating sphere. A wavelength range of 250–700 nm and a scan speed of 240 nm/min were used. The film's transmittance was

measured using a wavelength accuracy (slit width) of 5 nm. The samples were directly placed into the solid sample holder and measured without further conditioning. The average of two scans was calculated and the resulting mean value was presented. The film thickness of the sample was kept constant in the range 18 to 22 micrometres. The film's UV-blocking properties were evaluated in the range of UV-B (280−320 nm) and UV-A (320−380 nm).

2.2.6 Compositional analysis

Compositional analysis (CA) quantifies the amounts of structural carbohydrates (glucose, xylose, galactose, arabinose, and mannose), lignin, extractives and ash present in solid samples. The compositional analysis in this work was carried out according to the standard laboratory analytical a protocol called "Determination of structural carbohydrates and lignin in biomass" published by National Energy Renewable (NREL).[15] It was used to determine the precise amounts of lignin and sugar that were present in the cellulose, different types of lignin, cellulose-glycerol, cellulose-lignin, and cellulose-lignin-glycerol films. This information compares the composition of the film with the composition of the dope. It is recommended to prepare the samples in three replications. However, due to the limited quantity of samples, they were made in duplicate. Below is the description step by step to execute CA.

Determination of total solids in biomass

The samples were dried in the oven at 105 °C overnight until they reached a constant weight. according to equation 5:

$$ODW = \frac{Weight\ of\ air\ dry\ sample\ x\ \%\ Total\ solids}{100} \quad \text{.....Equation 5}$$

This procedure measures the moisture content of the biomass or film samples.

Hydrolysis

300 mg (on an Organic Dry Weight (ODW) basis) of air-dry biomass and samples were placed into a 100-mL pressure tube. 3 mL of 72% sulfuric acid were added, then was placed to the pressure tubes into a preheated water bath at 30 °C. Samples were stirred every 15 minutes for an hour, then diluted them with 84 mL of distilled water. The pressure was tightly capped, and

the samples were autoclaved (Sanyo Labo Autoclave ML5 3020 U) for one hour at 121 °C and left to cool. The samples were then filtered through ceramic crucibles of a known weight. The filtrate was stored in two plastic tubes for further analysis.

Acid Insoluble Lignin and ash content

The crucibles were placed into a convection oven (VWR Venti-Line 115) at 105 °C for 24±2 h. They are placed in a desiccator for 15 min, and the weight is recorded to obtain acid insoluble lignin (AIL). The crucibles were then placed into a muffle oven (Nabertherm and controller P330) and ashed to a constant weight at 575 °C to obtain % ash.

$$\%\ AIR = \frac{Weight\ crucible\ plus\ AIR - Weight\ crucible}{ODW\ sample}\ x\ 100 \text{ …. Equation 6}$$

$$\%\ AIL = \frac{(Weight\ crucible\ plus\ AIR - Weight\ crucible) - (Weight\ crucible\ plus\ ash - Weight\ crucible)}{ODW\ sample}\ x\ 100\text{.. Equation 7}$$

$$\%\ Ash = \frac{Weight\ crucbile\ plus\ ash - Weight\ crucbile}{ODW\ sample}\ x\ 100\text{…… Equation 8}$$

% Acid soluble lignin (ASL)

The supernatant is used for the determination of acid soluble lignin content (ASL) by UV analysis at 240 nm (Equation 9 and 10) using a Perkin Elmer Lambda 650 UV/Vis spectrometer.

$$\%\ ASL = \frac{A}{l.\varepsilon.c}\ x\ 100 = \frac{A.Vfiltrate}{l.\varepsilon.ODW\ sample}\ x100\text{…… Equation 9}$$

$$\%\ ASL = \frac{UVabs\ x\ Volume\ filtrate\ x\ Dilution}{\varepsilon\ x\ ODW\ sample\ x\ Pathlength}\ x\ 100\text{…….Equation 10}$$

Where:

UV abs = average UV-Vis absorbance for the sample at appropriate wavelength (refer Table in the protocol[15])

Volume of hydrolysis liqour = 86.73 mL

ε = absorptivity of biomass at specific wavelength (refer Table in the protocol[15])

ODW_{sample} = weight of sample in milligrams

Pathlength = pathlength of UV-Vis cell in cm

$$Dilution = \frac{Volume\ sample + Volume\ diluting\ solvent}{Volume\ sample}\text{……. Equation 11}$$

The percentage of lignin is the summation of % AIL and % ASL.

Total sugar content

Calcium carbonate was added to the second liquid fraction until pH 5 is reached. The liquid is filtered through a 0.2 μm PTFE syringe filter and subsequently submitted to HPLC analysis using a Shimadzu with RI detector, equipped with an Aminex HPX-97P column (Bio-Rad). Purified water is used as the mobile phase at 0.6 mL/min, and the temperature of the column is 85 °C. De-ashing columns are used as pre-filters to find the total sugar content. Calibration standards with concentrations of 0.1, 1, 2, and 4 mg/mL of glucose, xylose, mannose, arabinose, and galactose are used. The sugar recovery coefficient (SRC) is determined according to Equation 12, and the sugar content of the analysed sample is determined using Equation 15:

$$\%\ R\ sugar = \frac{conc.detected\ by\ HPLC\ (\frac{mg}{mL})}{known\ conc.of\ sugar\ before\ hydrolysis\ (\frac{mg}{mL})}\ x\ 100 \text{ ….. Equation 12}$$

$$Cx = \frac{C\ hplc\ x\ dilution\ factor}{\%\ R\ average\ sugar\ /_{100}} \text{ …….. Equation 13}$$

Where:

C hplc = conc. of sugar as determined by HPLC, mg/mL

% R average sugar = average recovery of a specific SRC component

Cx = concentration in mg/mL of a sugar in the hydrolysed sample after correction for loss on 4% hydrolysis

$$C\ anhydro = C\ corr\ x\ Anhydro\ correction \text{….. Equation 14}$$

By using an anhydro correction of 0.88 (or 132/150) for C-5 sugars (xylose and arabinose) and a correction of 0.90 (or162/180) for C-6 sugars (glucose, galactose, and mannose). The percentage sugar can be determined as follow:

$$\%\ sugar\ extractive\ free = \frac{C\ anhydro\ x\ V\ filtrate\ x\ \frac{1\ g}{1000\ mg}}{ODW\ sample}\ x\ 100 \text{….. Equation 15}$$

Where: V filtrate = volume of filtrate, 86.73 mL

2.2.7 Scanning electron microscopy

Scanning electron microscopy (SEM) utilise a focussed beam of electrons to scan the surface of a material, resulting in high-resolution images. Electrons are generated from an electron source such as tungsten filaments or field emission guns and accelerated by the anode. The routes of the electrons are further adjusted by internal lenses. Upon reaching the surface of the imaged material, a variety of electrons are generated, with backscattered and secondary electrons being the most prevalent in SEM imaging. Backscattered and secondary electrons can offer valuable information on the subsurface and surface (topography) areas of a sample, respectively.

Cellulose powder, cellulose-lignin and cellulose-lignin-glycerol thin films are non-conductive samples. Thus, non-conductive samples need to be coated with electrically conductive materials such as gold. The application of the coating on the samples will prevent the accumulation of static electricity, preventing the production of artefacts in the SEM images and minimising beam damage. To facilitate SEM imaging, the cellulose films were affixed to specimen holders using carbon tape and subsequently coated with a layer of gold using spin-coating. The SEM images were obtained using a Zeiss Leo Gemini 1525 SEM equipped with a field emission gun (FEG). The microscope was operated in secondary electron imaging mode with a 5 kV accelerating voltage.

2.2.8 X-ray diffraction

X-ray diffraction refers to the phenomena that occur when X-ray beams change direction as a result of interacting with electrons surrounding the atoms. When X-ray encounters an atom, its energy absorbs by the electron, and the form of energy needs to re-emitted called as elastic scattering. In a crystal, the repeating arrangement of atoms forms distinct planes separated by well-defined distances. Strong amplification of the emitted signal occurs at very specific angle where scattered waves constructively interfere. If the wave is out of alignment, the signal will destroy and it is called destructive interferences. The angle between the incident and the scatted beam called 2-theta. The constructive interferences can be explained by the Bragg's Law equation as indicated in the Figure 2.10.

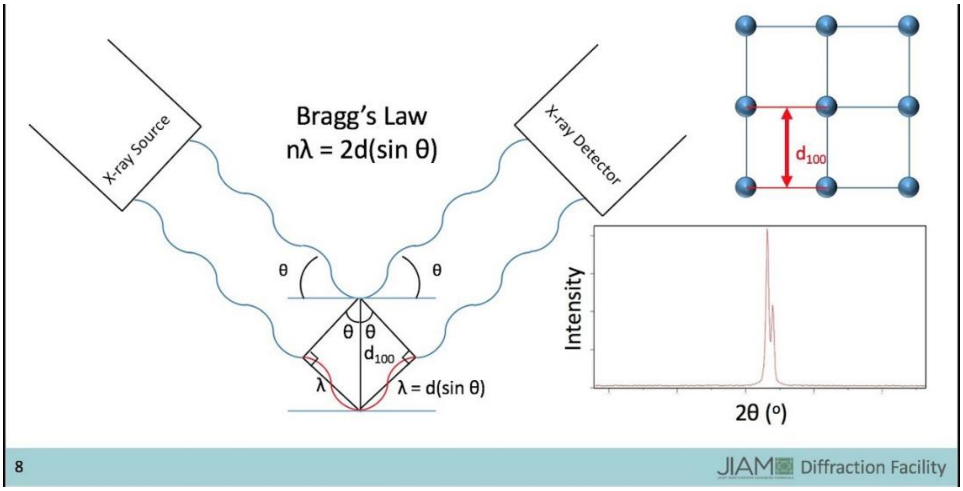


Figure 2.10: Schematic representation of the Bragg's equation. Image retrieved from https://www.jiamdiffraction.com/copy-of-videos[16]

The goal of using X-ray diffraction (XRD) in this study was to measure the order the regenerated films. The crystallinity index of cellulose and the regenerated cellulose-lignin and cellulose-lignin-glycerol films were measured using Bruker D2 Phaser XRD instrument. Specimens with a diameter of 3 cm were mounted flat onto a zero-background silicon plate. To ensure the samples remained stationery and level during rotation without the use of interfering adhesives, they were secured at the edges using a minimal amount of adhesive putty (Blue-Tac), ensuring the putty was outside the X-ray beam path.

Data collected using Cu Kα radiation over an angular range (2θ) of 5 to 50°, with a step size of 0.01° and the scanning speed was set at 10°/min. The crystallinity index (CI) was calculated as in Equation 16 according to Segal method using the following equation:

$$CI = \frac{I_{002} - I_{am}}{I_{002}} \; x \; 100\ \%$$ ….. Equation 16

where I_{002} represents the maximum intensity of the crystalline peak (located at approximately 2θ = 22.5° for cellulose I or 20° for cellulose II), and I_{am} denotes the intensity of the amorphous background (measured at approximately 2θ = 18° for cellulose I or 16° for cellulose II), as illustrated in Figure 2.11.

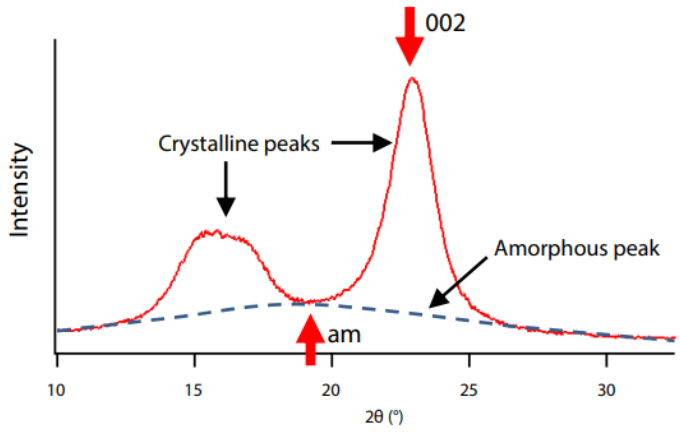


Figure 2.11: Intensity values used in calculation of degree of crystallinity of cellulose. Image adopted from Shimadzu Corporation.[17]

2.2.9 Nuclear magnetic resonance spectroscopy of lignin

2.2.9.1 ^{31}P NMR

^{31}P NMR spectroscopy is a technique used for characterising lignin, specifically to quantify the amount of hydroxyl (-OH) groups present. The procedures were adapted from Meng et al.[18] & Brandt et al.[3] with slight modifications such as all the preparation procedure were performed in the glove box with N_2 gas flushes to ensure success phosphitylated lignin in inert environment. The recommended relative humidity is below 15 %. The vials, NMR tubes, calibrated pipette, pipette tips, dried lignin and chemicals were placed in the glove box before opening the N_2 taps.

300 µl of a solvent solution made from 1.6:1 (v/v) of anhydrous pyridine and deuterated chloroform was prepared in the vial. The solvent solution is used to prepare a mixture solution containing 20.5 mg/ml of cyclohexanol (as internal standard) and a second 5.6 mg/ml solution of chromium (III) acetylacetonate solution (relaxation reagent). Dried lignin (ca. 10 mg) was accurately weighed and dissolved in 100 µl of anhydrous pyridine/ deuterated chloroform

solvent solution (1.6:1, v/v). 50 µL of the cyclohexanol solution, 50 µL of the chromium (III) acetylacetonate, 50 µL of 2-chloro-4,4,5,5-tetramethyl-1,3,2-dioxaphospholane (TMDP) were added to the to the lignin. Another 50 µL of solvent solution is added to give a total volume of 300 µL. The vial was mixed intensely until the solution is completely dissolved. The samples were transferred into Shigemi NMR tubes for subsequent ^{31}P NMR analysis.

The ^{31}P NMR experiments were carried out at 298 K on a Bruker Advance 500 MHz NMR spectrometer. To obtain quantitative spectra a relaxation delay of 25 s is used between 30° pulses, the number of scans was 2400 and an inverse gated decoupling pulse sequence was used. The acquisitions are performed at room temperature. Chemical shifts are calibrated relative to the internal standard (IS), i.e., the cyclohexanol peak signal centred at δ 144.2 ppm. This experimental setting runs for 14 hours to obtain a single NMR spectrum. Integrate the NMR peak regions with respect to the IS (cyclohexanol) peak based on the assignments.

2.2.9.2 HSQC NMR

The 2D ^{1}H–^{13}C HSQC NMR technique was employed to assign signals, identify inter-unit linkages, and characterize aromatic units in technical lignins (kraft, ionosolv and organosolv lignins). Approximately 15–20 mg of dried lignin was dissolved in 800–900 mg of DMSO-d6 (≈ 20 mg/0.7 mL) and transferred into a standard 5 mm NMR tube, ensuring complete dissolution. Spectra were acquired on a Bruker DRX-400 MHz spectrometer at room temperature using the standard Bruker pulse sequence hsqcetgpsisp.2. The acquisition time was ~3 h, with 16 scans collected per increment and an interscan delay (D1) of 1 s. Chemical shifts were referenced to the central DMSO-d6 solvent peaks (δ_H 2.49 ppm, δ_C 39.5 ppm). Data were processed using MestReNova software for linkage assignment, with standard phase and baseline corrections applied. The spectra presented in this study focus on the aliphatic region (δ_H 2.5–6.0 ppm; δ_C 50–90 ppm) and the aromatic region (δ_H 6.0–8.0 ppm; δ_C 100–150 ppm), which highlight characteristic correlations in lignin.

2.2.10 Gel Permeation Chromatography

GPC measurements were performed using an Agilent 1260 Infinity instrument equipped with a Viscotek column set (AGuard, A6000M and A3000M). The multi-detector (RID and viscometry) was used for detection. HPLC grade DMF containing LiBr (1 g/L) was used as eluent at a flow rate of 0.4 mL/min at 60 °C. Samples were prepared by dissolving 15 to 30 mg lignin in 1 mL eluent and filtering through a 0.45-µm hydrophilic polytetrafluoroethylene (PTFE) syringe filters. Polymethyl methacrylate consisting of 12 standards (Agilent, United Kingdom) in the molar mass range between 535 and 1,795,00 g mol^{-1} were used to calibrate the instrument.

2.3 References

1 D. S. Lodhi, G. Prasad, P. Ms, K. Chouksey and P. Golani, *J. Emerg. Technol. Innov. Res.*, 2022, **9**, 496–516.

2 M. Chen, F. Malaret, A. E. J. Firth, P. Verdía, A. R. Abouelela, Y. Chen and J. P. Hallett, *Green Chem.*, 2020, **22**, 5161–5178.

3 A. Brandt, L. Chen, B. E. Van Dongen, T. Welton and J. P. Hallett, *Green Chem.*, 2015, **17**, 5019–5034.

4 Microscopy Australia, Light & Fluorescence Mircoscopy, https://myscope.training/LFM_Polarised_light_microscopy.

5 A. P. GmbH, Basics Rheol., https://wiki.anton-paar.com/uk-en/basics-of-rheology/.

6 A. Bieberle-Hütter, A. C. Bronneberg, K. George and M. C. M. Van De Sanden, *J. Phys. D. Appl. Phys.*, 2021, **54**, 133001.

7 H. Kaur, T. S. Banipal, S. Thakur, M. S. Bakshi, G. Kaur and N. Singh, *ACS Sustain. Chem. Eng.*, 2013, **1**, 127–136.

8 Y. Xie, Y. Pan and P. Cai, *Ind. Crops Prod.*, 2022, **176**, 114381.

9 V. Jost, K. Kobsik, M. Schmid and K. Noller, *Carbohydr. Polym.*, 2014, **110**, 309–319.

10 E. Csiszár and S. Nagy, *Carbohydr. Polym.*, 2017, **174**, 740–749.

11 Y. Ma, S. Asaadi, L. S. Johansson, P. Ahvenainen, M. Reza, M. Alekhina, L. Rautkari, A. Michud, L. Hauru, M. Hummel and H. Sixta, *ChemSusChem*, 2015, **8**, 4030–4039.

12 ASTM D882-10, *Standard Test Method for Tensile Properties of Thin Plastic Sheeting*, 2014.

13 What Probe Liquid Should You Use for Contact Angle Measurements?, https://www.nanoscience.com/blogs/what-probe-liquid-should-you-use-for-contact-angle-measurements/.

14 Shimadzu, Integrating Sphere, https://www.shimadzu.com/an/service-support/technical-support/uv/essential_knowledge/integratingspheres.html.

15 A. Sluiter, B. Hames, R. Ruiz, C. Scarlata, J. Sluiter, D. Templeton and D. Crocker, *Natl. Renew. Energy Lab.*, 2008, 17.

16 IAMM Diffraction, Introduction to X-ray Diffraction, https://www.jiamdiffraction.com/copy-of-videos.

17 Shidmadzu Corporation, X-Ray Analysis Measurement of Degree of Crystallinity of Cellulose Nanofiber, https://www.shimadzu.com/an/sites/shimadzu.com.an/files/pim/pim_document_file/applications/application_note/13689/jpq319001.pdf.

18 X. Meng, C. Crestini, H. Ben, N. Hao, Y. Pu, A. J. Ragauskas and D. S. Argyropoulos, *Nat. Protoc.*, 2019, **14**, 2627–2647.

Chapter 3: Synthesis of Ionic Liquids and Its Green Chemistry

The objective of this chapter is to identify the greenest synthetic routes for synthesising [C_2C_1im][OAc] and the lowest cost ionic liquid production. The greenest synthetic route is greatly desired in chemical processes due to its ability to minimise waste and reduce the environmental impact. Green metrics were utilised to assess the most environmentally friendly synthetic method. The green metrics, such as E-factor, atom economy (AE), effective mass yield (EMY), and calculation cost material per grams, were extensively assessed for synthetic methods of [C_2C_1im][OAc]. Several techniques are available for the synthesis of [C_2C_1im][OAc], including metathesis, ion exchange resin, and a one-pot technique as documented in the literature. The final product of [C_2C_1im][OAc] will be synthesized from the commercially available starting materials 1-methylimidazole and 1-bromoethane.

3.1 Experimental

3.1.1 Reagents

1-Methylimidazole (>99%), 1-bromoethane (C_2H_5Br, 98%), acetic acid (CH_3COOH, 99.8%), dimethyl sulfoxide (DMSO, 99.8%), lead (II) acetate trihydrate (Pb $(CH_3CO_2)_2.3H_2O$, 99.5%), acetonitrile (C_2H_3N, ≥99.9%) and ethyl acetate ($CH_3COOC_2H_5$, 65 ≥99.5%) were purchased from VWR Chemicals. Silver acetate ($Ag(C_2H_3O_2)$, 99%) was purchased from Flurochem. Amberlyst™ A26, OH-form, ion-exchange resin was obtained from ACROS Organics.

3.1.2 Instrumentation

IR spectra were recorded on a Perkin Elmer 20 Spectrum 100 ATR-FTIR spectrometer with an attenuated total reflectance (ATR) accessory. The ATR accessory had a diamond internal reflection element. The spectra were obtained with a resolution of 2 cm^{-1}, covering the range of 4000–650 cm^{-1} for all the samples. ^1H spectra were recorded on a Brucker DRX-400 MHz spectrometer, with DMSO-d6 as the NMR solvent at room temperature. Electrospray ionisation (ESI) mass spectra were recorded on a Micromass LCT Premier instrument with mode of

ionization positive and negative. Data was acquired by a 4.0 GHz time-to-digital converter (TDC) and histogrammed in an embedded PC. Elemental analysis was performed by the London Metropolitan University Service using an acetanilide standard. The results showed only small deviations, all within the typical ±0.4% margin considered satisfactory for microanalysis. Each sample was analysed in duplicate to ensure reproducibility. The water content of the ILs dried under Schenk line vacuum before testing was determined using a volumetric Mettler Toledo Karl–Fischer titrator. The amount of IL tested was around 0.2 g with triplicate.

3.1.3 Synthesis of 1-ethyl-3-methylimidazolium bromide

30 mL 1-bromoethane was extracted with around 36.6 mL conc. H_2SO_4, followed by aqueous 4.8 grams of $NaHCO_3$, then washed with deionized water until pH 7. The 1-bromoethane was subsequently distilled from around 2 grams $MgSO_4$ in a dry nitrogen atmosphere. 15 mL 1-bromoethane was transferred via cannula in nitrogen atmosphere into 10 mL 1-methylimidazole, freshly distilled from 3.5 gram of KOH. The reaction was stirred vigorously at room temperature for two days until a white solid formed. The solid was recrystallized with 20:80 EtOAc/MeCN (30 mL:120 mL). The residual solution was decanted, and the white crystalline solid was vacuum dried for 12 hours. The yield was determined after the product was isolated and dried. This synthesis yielded a white crystalline solid with 65% isolated yield. Its structure was confirmed by ^{1}H and ^{13}C NMR, IR, MS, and elemental analysis (see Appendix A1 for full characterization data).

The characterization of $[C_2C_1im]Br$ was as follows: ^{1}H NMR (400 MHz, DMSO-d_6): δ 9.16 (1H, s), 7.81 (1H, t, J = 2 Hz), 7.72 (1H, t, J = 2 Hz), 4.20 (2H, q, J = 7 Hz), 3.86 (3H, s),1.42 (3H, t, J = 7 Hz). ^{13}C NMR (100 MHz, DMSO-d6): δ 136.2, 123.5, 122.0, 44.0, 35.7, 15.2. ν(neat)/cm^{-1} 3143, 3070 (aromatic C-H stretch, m), 2983 (aliphatic C-H stretch, m), 1570 (arom. ring def., m). m/z (LSIMS^{+}): 111 (100%) $[C_2C_1im]^{+}$. m/z (LSIMS^{-}): 80.9 (100%) $[^{81}Br]^{-}$, 78.9 (94%) $[^{79}Br]^{-}$. Calculation for $C_6H_{11}BrN_2$: C, 37.72; H, 5.80; N, 14.66%. Found: C, 36.44; H, 6.67; N, 14.24%.

3.1.4 Synthesis of 1-ethyl-3-methylimidazolium acetate via silver salt metathesis

Silver acetate (13.17 g, 79 mmol) and 30 mL of deionized water was added into a flask that was wrapped with aluminium foil to prevent photodegradation of the silver acetate. Then, 1-ethyl-3-methylimidazolium bromide (15.00 g, 79 mmol) was added slowly. The reaction was stirred vigorously for three days. A greenish grey precipitate formed which was filtered using a sintered funnel. The clear solution containing 1-ethyl-3-methylimidazolium acetate was tested for presence of Ag^+ and Br^-. Two drops of the ionic liquid solution were diluted with 1 mL of deionized water in two small vials each.

In the first vial, a drop of 1 M HCl was introduced to test for Ag^+, while a drop of 0.3 M $AgNO_3$ in 1 M HNO_3 was added to identify bromide ions in the second vial. Upon a positive test result, aqueous 1-ethyl-3-methylimidazolium bromide or, alternatively, aqueous silver acetate was incrementally added, and the silver and bromide test was repeated until no precipitate was observed. Upon obtaining negative findings for both tests, the water was eliminated via rotary evaporation, and the product was subjected to vacuum drying at 40 °C for 24 hours. The yield was ascertained subsequent to the isolation and desiccation of the product. The synthesis produced a colorless viscous liquid with an 85.6% yield. Its structure was confirmed by ^1H and ^{13}C NMR, IR and MS(see Appendix A2 for full characterization data).

The characterization of 1-ethyl-3-methylimidazolium acetate was as follows: ^1H NMR (400 MHz, DMSO-d6): δ 9.75 (1H, s), 7.84 (1H, t, J = 2 Hz) 7.75 (1H, t, J = 2 Hz), 4.21 (2H, q, J = 8 Hz), 3.87 (3H, s), 1.58 (3H, s), 1.41 (3H, t, J = 7 Hz). ^{13}C NMR (100 MHz, DMSO-d6): δ 173.5, 137.6, 123.9, 122.4, 44.5, 36.0, 26.4, 15.6. ν(neat)/cm^{-1} 3149, 3093 (aromatic C-H stretch, w), 2981 (aliphatic C-H stretch, m), 1560 (C=O stretch, s). m/z ($LSIMS^+$): 111 (100%) $[C_2C_1im]^+$, 56 (82%) $[C_2H_2N]^+$, m/z ($LSIMS^-$): 59 (100%) $[OAc]^-$.

3.1.5 Synthesis of 1-ethyl-3-methylimidazolium acetate using an ion exchange resin

A 150 mm diameter glass ion exchange column of 280 mm length with coarse fritted disc at the bottom was filled with approximately 1kg Amberlyst™ A26 (equivalence to 0.25 mol $[OH]^-$, ion-exchange resin. Water was flushed through the resin until the pH of the eluent

reached pH 7. The eluent was discarded in a waste container. Then, a minimal amount of water was added to 7.00 g (0.037 mol) 1-ethyl-3-methylimidazolium bromide, and the ionic liquid solution was dropped slowly on top of the resin using a syringe. The exchange reaction was allowed to complete and the stopcock valve was opened slowly, one drop in 30–40 seconds. The pH of the eluent was monitored carefully using a pH strip as the pH increased to pH 14 and then decreased to pH 7. In the meantime, the presence of halide ions in the eluent was tested regularly as stated in the previous section. The collected eluent was placed in a small container. The eluent containing the intermediate product, 1-ethyl-3-methylimidazolium hydroxide, was combined with 2.09 mL acetic acid. The remaining water was removed by rotary evaporation and the ionic liquid was vacuum dried for 24 hours. Since the product was slightly yellow, the ionic liquid was treated with 2 g of activated charcoal in 15 g of methanol to remove the coloration. The yield was determined after the product was isolated and vacuum dried. This synthesis yielded 85% as a colourless viscous liquid. Its structure was confirmed by ^{1}H and ^{13}C NMR, IR and MS (see Appendix A3 for full characterization data).

The characterization of $[C_2C_1im][OAc]$ was as follows. ^{1}H NMR (400 MHz, DMSO-d6): δ 9.74 (1H, s), 7.84 (1H, t, J = 2 Hz),7.75 (1H, t, J = 2 Hz), 4.21 (2H, q, J = 8 Hz), 3.87 (3H, s), 1.58 (3H, s), 1.40 (3H, t, J = 8 Hz). ^{13}C NMR (100 MHz, DMSO d6): δ 173.5, 137.6,123.9, 122.4, 44.5, 36.0, 26.4, 15.6. ν(neat)/cm^{-1} 3149, 3087 (aromatic C-H stretch, w), 2981 (aliphatic C-H stretch, m), 1561 (C=O stretch, s).

3.1.6 Synthesis of 1-ethyl-3-methylimidazolium acetate via a one-pot method

The method was adopted from Zhu et al.[1] with slight modification. Purification of the starting materials was carried out as described above before conducting this experiment. 1-Methylimidazole (4.11 g, 0.05 mol), an excess of bromoethane (9.81 g, 0.09 mol) and lead (II) acetate trihydrate (9.48 g, 0.025 mol) were added into the two-neck 25 mL flask under reflux with no solvent and stirred (180 rpm) at 60°C under atmospheric pressure. After 20 h, the solution was cooled to room temperature. A white precipitate was removed by suction filtration using Buchner funnel with filter paper. The clear solution was washed with ethyl acetate (EtOAc, 30 ml) repeatedly (see discussion below Section 3.2.4). The final product was obtained by vacuum rotary evaporation at 60°C. Further drying on the Schenk line with an external solvent trap cooled with liquid nitrogen was employed for water removal. The final product

was analysed with NMR spectroscopy, MS and testing for lead ions. The presence of lead was probed by preparing aqueous 0.35 M sodium hydrogen sulfide (NaHS). Three test tubes were filled with 5 mL water (as negative control), 5 mL lead (II) acetate trihydrate aqueous solution (positive control) and two drops of NaHS solution were added to aqueous samples of ionic liquid, respectively. All waste was collected in another flask for safe disposal. Percentage yield was determined after the product was isolated and dried. This synthesis generated a colourless viscous liquid with a yield of 84.7%. Its structure was confirmed by ^{1}H and ^{13}C NMR, IR and MS (see Appendix A4 for full characterization data).

The characterization of 1-ethyl-3-methylimidazolium acetate was as follows: ^{1}H NMR (400 MHz, DMSO-d6): δ 9.49 (1H, s), 7.81 (1H, t, J = 2 Hz) 7.72 (1H, t, J = 2 Hz), 4.21 (2H, q, J = 8 Hz), 3.876 (3H, s), 1.59 (3H, s), 1.41 (3H, t, J = 7 Hz). ^{13}C NMR (100 MHz, DMSO d6): δ 173.7, 137.2, 124.0, 122.4, 44.5, 36.0, 26.1, 15.6. m/z (LSIMS^{+}): 111 (100%) $[C_2C_1im]^{+}$, 56 (82%) $[C_2H_2N]^{+}$, N^{+}, H_2. m/z (LSIMS^{-}): 59 (100%) $[OAc]^{-}$.

3.17 Green chemistry metrics

All the synthetic routes to produce $[C_2C_1im][OAc]$ were evaluated to determine the greenest synthetic route. The following equations were used to calculate green metrics each of the routes:

$$E - factor = \frac{kg\ waste}{kg\ product} \quad \ldots\ldots \quad \text{Eq. 16}$$

$$Atom\ economy\ (AE) = \frac{Mw\ product}{\sum Mw\ starting\ materials} \quad \ldots\ldots \quad \text{Eq. 17}$$

$$Effective\ mass\ yield\ (EMY) = \frac{grams\ of\ product}{grams\ of\ non\ benign\ reagents}\ x\ 100 \quad \ldots\ldots \quad \text{Eq. 18}$$

Cost was determined by calculating the price of starting materials according to companies listed in the reagents section, in pounds per gram. The price unit per gram was then multiplied with the mass of starting materials used, regarding to each synthesis routes applied.

$$Cost = \sum \left(Price\ \left(\frac{£}{gram}\right) x\ weight\ of\ starting\ material\ (grams) \right) n \quad \ldots\ldots \quad \text{Eq. 19}$$

3.2 Results and Discussion

3.2.1 Synthesis of 1-ethyl-3-methylimidazolium bromide

1-ethyl-3-methylimidazolium bromide, $[C_2C_1im]Br$ was used as a starting material for synthesising $[C_2C_1im][OAc]$. The synthesis of 1-ethyl-3-methylimidazolium bromide, $[C_2C_1im]Br$ was performed to produce the intermediate since 1-bromoethane reacts with 1-methylimidazole quickly, forming a stable solid compound that can be purified by recrystallisation. Since purification of ionic liquids is difficult, it is preferred that the starting materials and intermediates are as pure as possible. After a few days of leaving a liquid mixture of 1-methylimidazole and 1-bromoethane at room temperature, a white solid formed. Nucleation is the step in which the ions start to gather into clusters, meanwhile, the crystal growth is the subsequent growth of the nuclei that succeed in achieving and surpassing the critical cluster size. This synthesis was conducted under nitrogen gas because $[C_2C_1im]Br$ is highly hygroscopic, thus it can absorb water from the air and even dissolve in it. This could prevent the $[C_2C_1im]Br$ from precipitating. Formation of the ionic liquid is due to this reaction being an exothermic process with $\Delta H_{f,\,liq}(298\ K)$ $[C_2C_1im]Br = -130 \pm 22$ kJ/mol.[2]

Elemental analysis indicated an increased hydrogen content and a decrease in carbon and nitrogen content compared to the theoretical value for $[C_2C_1im]Br$. The FTIR spectrum displayed distinct bands indicative of water, so proving the presence of moisture in the compound. The observations indicate that the synthesized ionic liquid easily absorbed moisture, perhaps due to exposure to air during the analytical methods. Therefore, $[C_2C_1im]Br$ should be dried thoroughly and preserved in an inert atmosphere to prevent additional moisture absorption, with storage in a glove box being the optimal method to guarantee its stability and reproducibility in future applications.

3.2.2 Synthesis of 1-ethyl-3-methylimidazolium acetate via silver salt metathesis

Four attempts to synthesise $[C_2C_1im][OAc]$ using metathesis with silver acetate, gave a positive result for the test for halide ions with 0.3 M $AgNO_3$ in 1M HNO_3 (white/pale cream precipitate) each time. The chemical reaction is shown in Figure 3.1. This test result strongly agreed with proton NMR spectra which indicated that the peak integration for the protons on the acetate anion was in the range of 2.23 - 2.43. Hence, the quality of the silver acetate reagent was

questioned, which was purchased in 2019. Silver acetate is known to be a light sensitive compound, and must be kept in a dry, cool and well-ventilated place. Silver acetate exposed to ambient oxygen decomposed the chemical, and generated silver oxides as in the following Equation 20:

$4CH_3COOAg + O_2 \rightarrow 2Ag_2O + 4CH_3COO^-$ ……Eq 20

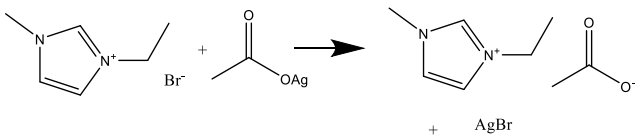


Figure 3.1: Chemical reaction to synthesis $[C_2C_1im][OAc]$ using metathesis route

The colour of silver acetate from 2019 was darker grey compared to a new bottle which has a light grey colour. This explanation is supported by a study on the thermal oxidative degradation of silver acetate, which reported that oxidation by air leaves residue of metal oxide salts, oxides and sulfides (in nanoparticle form).[3] Conducting the synthesis with a fresh bottle of silver acetate led to the desired product, free from halide contamination.

The failed synthesis led me to explore an alternative synthesis route reported by Zhu et al., 2012[1] which they called an "environmental friendly" one-pot synthesis, which is discussed below.

The characterization results were compared with literature[4] using the same starting material which is silver acetate. The NMR chemical shifts, FTIR peaks positions, $LSIMS^+$ yielded similar results, however $LSIMS^-$ was identified using fragmentation. The MS indicated that the synthesis in this project was better as in the literature indicated impurities were present in the form of sodium.

3.2.3 Synthesis of 1-ethyl-3-methylimidazolium acetate using an ion exchange resin

The synthesis of $[C_2C_1im][OAc]$ via the ion exchange resin route is depicted in Figure 3.2. The exchange of $[C_2C_1im]Br$ and $[OH]^-$ present in the resin provided the desired intermediate product which is $[C_2C_1im][OH]$, which is only stable in aqueous solution. $[C_2C_1im][OH]$ was

reacted with acetic acid immediately to prevent spontaneous generation of N-heterocyclic carbenes. N-heterocyclic carbenes are very reactive compounds and will form impurities in the IL product. A study suggested minimal amounts of neutral electrophile facilitate the formation of N-heterocyclic carbenes.[5] Therefore, the rapid neutralisation of the solution with acetic acid prevents the N-heterocyclic carbenes to occur. The amount of water consumed in this synthesis was high. Nearly 600 mL was used for the exchange of Br^- with $[OH]^-$.

The final $[C_2C_1im][OAc]$ product synthesized had a yellow tint, a less desirable colour appearance compared to the metathesis route. This colour usually does not affect the physical properties or performance of the IL, but from the point of view of commercial ionic liquid suppliers, colourless ILs may be preferable. The yellowish colour could have arisen from the higher temperature used during drying (water removal) which resulted in thermal degradation of $[C_2C_1im][OAc]$.[4] Discolouration can be removed by adding activated charcoal, acidic or neutral alumina.[6] This work has utilized activated charcoal with a ratio of 1:4 charcoal to $[C_2C_1im][OAc]$ in methanol, stirred for one day. The same synthesis method was applied and the results were compared in literature.[7] The chemical shift in ^1H NMR spectra were similar and slightly downfield due to different chemical environment as percentage water present was slightly different.

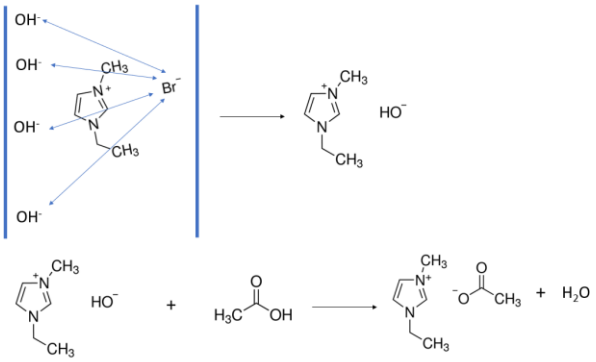


Figure 3.2: Ion exchange resin reaction synthesis

3.2.4 Synthesis of 1-ethyl-3-methylimidazolium acetate via a one-pot method

This reaction is depicted in Figure 3.3. Conducting this reaction required consultation with a safety officer since lead (II) acetate trihydrate is a harmful and toxic. After the reaction was refluxed and filtered, the $[C_2C_1im][OAc]$ was washed to remove contamination with $PbBr_2$.

The procedure states that "several" washings are needed.[1] The total number of washes with ethyl acetate was 20 times in this method. Since both $[C_2C_1im][OAc]$ and $PbBr_2$ are soluble in water, washing with ethyl acetate was used to remove $PbBr_2$ since it can be extracted in the organic layer.[8] 0.35 M NaHS was used to detect lead precipitate as shown in Figure 3.4. The test result indicated that Pb was present and formed a black precipitate as in the chemical scheme: $Pb^{2+} + S^{2-} \rightarrow PbS$

The MS spectra in positive mode showed a peak existed at 104 at 5% intensity, indicating the presence of Pb^{2+} which has an atomic weight of 208 atomic mass unit, a.m.u divided by two. NMR spectra also indicated the presence of unreacted alkylimidazole with signals at 7.56, 7.11, and 6.87 ppm, assigned to CH(2), CH(4,5), respectively. These values were slightly shifted downfield compared to reported common impurities.[9] The characterization results cannot be compared with the literature[1] since NMR and MS spectra were not provided, only FTIR spectra. FTIR spectroscopy was not conducted due to potential of contamination of the FTIR machine with lead.

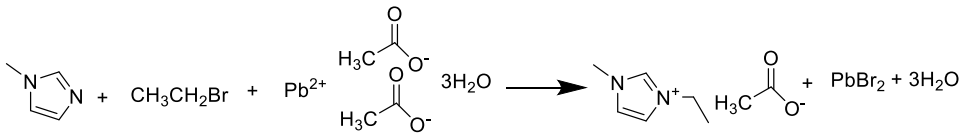


Figure 3.3: One-pot synthesis of $[C_2C_1im][OAc]$

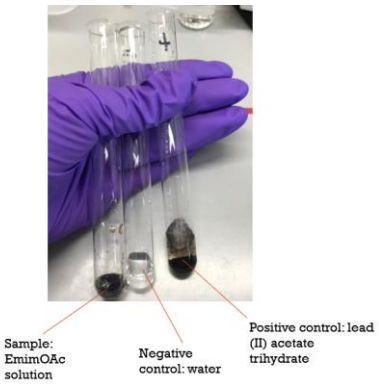


Figure 3.4: Chemical test for Pb in $[C_2C_1im][OAc]$ via one-pot method

3.2.5 Green chemistry metrics and cost analysis of $[C_2C_1im][OAc]$ synthesis

Green chemistry metrics were calculated for all synthesis routes used to produce $[C_2C_1im][OAc]$. The metathesis and ion-exchange column methods started with $[C_2C_1im]Br$, prepared from 1-methylimidazole. The one-pot synthesis method also employed 1-methylimidazole as the starting material. Consequently, all pathways utilize the identical precursor, facilitating a fair and consistent evaluation of the green chemistry metrics. Table 3.1 summarizes the key results for the green metrics analysis. Detailed calculations can be found in Appendix A5. Percentage yield of the final synthesized $[C_2C_1im][OAc]$ were almost equal for the three synthetic routes. Therefore, other metrics have to be taken into account to determine the best synthesis.

Table 3.1: Green metrics analysis and cost for three different syntheses of $[C_2C_1im][OAc]$

Synthesis Route	Yield (%)	Atom Economy (%)	E Factor	EMY (%)	Cost (£ / 1 g IL)
Metathesis	85.6	47.55	20.04	30.20	4.30
Ion Exchange	85.0	63.48	189.20	30.88	2.24
One-pot	84.7	29.84	69.59	30.77	3.06

Firstly, an atom economy of 100% is desirable since all the reactants are converted into desired product. The AE was the lowest for the one-pot reaction route, since this reaction is associated with a reagent that contains the heavy metal lead which has a higher molecular weight than other reagents used in the metathesis and ion exchange routes. AE does not count intermediate product or solvent use in purification and isolation product. Consequently, the molecular weight of $[C_2C_1im]Br$ and the materials used for purification of the starting compounds were not included in the calculation. Thus, ion exchange has the lowest total molecular weight which makes it have the highest AE counted 63.48%. This method is the simplest calculation, but ignores the use of solvent and excess reagent.[10] To address this limitation, the E-factor quantifies the ratio of waste mass to product mass.

E-factor is a measure of waste produced in a process and the process is greener and sustainable if the value is zero or nearly zero. The E-factor for the ion exchange route was the highest at 189.2 due to this route involving a number of washing steps[11], thus large amount of solvent was produced compared to other two synthetic methods. To synthesize about 5 grams $[C_2C_1im][OAc]$ using ion exchange method, around 200 mL of water is required for pre-washing the resin, and an additional 600 mL is needed for collecting the eluent. All of this water is included in the E-factor calculation, leading to a high value. Literature reports that this method offers several advantages, such as high conversion and the possibility of reusing or regenerating the resin. However, it requires large quantities of solvent, which increases the E-factor for the preparation of the ionic liquid. [12] Nonetheless, the E-factor can be significantly reduced if the water recovered from the product after vacuum drying is recycled and reused in subsequent syntheses. The one-pot route was identified by the second highest E-factor because washing with EtOAc to purify the final product caused a lot of solvent waste.

Effective mass yield (EMY) relates to the environmental impacts coming from the usage of reagents. In particular, EMY was used to quantify the formation of desired products against the amount of used reagents in the synthesis. However, compounds that have low environmental impact such as sodium chloride, acetic acid and water can be excluded in EMY calculation. [13] A high value is preferred. The metathesis method reported the lowest EMY (30.22 %) followed by one-pot synthesis (30.77 %) as it has a high mass of non-benign starting materials. Ion exchange has the highest percentage EMY (30.88 %) since acetic acid and water were benign chemicals which were excluded from the EMY calculation.

After considering all three green metrics, the one-pot method is the least green synthesis method. This method resulted in ionic liquid with the lowest purity and toxic lead metal contamination, which is unsuitable for solvent application. Chemical characterisation in section 3.2.4 revealed that the positive-mode MS spectrum displayed a peak at m/z 104 (5% relative intensity), which corresponds to a doubly charged Pb^{2+} ion. Additionally, NMR spectra indicated the presence of unreacted alkylimidazole.

The cost calculation included the expenses for purification chemicals and reaction synthesis in the preparation of $[C_2C_1im]Br$. All chemicals were accounted for, including solvents such as ethanol and water. Among the methods, metathesis had the highest cost, primarily due to the use of silver acetate, an expensive reagent priced at £68 per 25 g in 2021. In contrast, the ion-

exchange method was the most economical, as the resin can be recycled and has a lifespan of approximately up to six years, based on average data from recommendation usage.[14] The calculations were based on reactions performed at the lab scale, reflecting three years of PhD-level research. After considering all factors, including green metrics and the production cost of [C_2C_1im][OAc], the ion-exchange route emerges as the optimal synthesis method, being both environmentally friendly (with high AE and % EMY) and cost-effective.

3.2.6 Cost Optimization and Industrial Scaling of [C_2C_1im][OAc]

Based on the green metrics and economic evaluation conducted in this study, the ion-exchange method is identified as a technically viable route for the synthesis of [C_2C_1im][OAc]. At the laboratory scale, the production cost is calculated at £2,240/kg. While this is currently higher than the commercial benchmark set by BASF (£1,410/kg), which utilizes a high-pressure methyl carbonate route at 95% purity.[15] The ion-exchange method offers significant pathways for further cost optimization.

The transition from laboratory-grade reagents to bulk industrial procurement is projected to reduce material costs by 50–60%. Furthermore, the modular nature of ion-exchange resins allows for the implementation of continuous-flow column chromatography. This shift from batch to continuous processing enhances throughput and reduces the operational footprint, a critical factor in low-cost manufacturing.

The current process uses 800 mL of water for only 5.78 gram of product. This is extremely high water to product ratio (approx. 138 L per kg of [C_2C_1im][OAc]). The energy-intensive nature of evaporating this volume to recover [C_2C_1im][OAc] represents a significant economic hurdle. To mitigate this, a closed-loop water recycling system is proposed. By passing wash water through a secondary ion-exchange bed to remove residual halides, the aqueous phase can be recycled into subsequent batches, reducing both water consumption and the associated energy load of waste treatment.

While the initial cost analysis was modelled on a 36-month PhD timeframe, the hydroxide-functionalized resins employed in this study possess an operational lifespan of up to 6 years (72 months).[14] When the capital expenditure of the resin is amortized over its full functional life, the production cost is further reduced to £2,150/kg, representing an approximate 4–5%

reduction in the total unit cost. These strategies collectively bridge the gap between bench-scale synthesis and industrial commercialization.

3.2.7 Commercial [C_2C_1im][OAc]

We have gained a comprehensive understanding of how each synthetic route affects product purity, environmental impact, and cost. Although alternative synthesis routes were considered, ion exchange was identified as the most optimal method for producing [C_2C_1im][OAc]. However, for the development of lignin-cellulose films, [C_2C_1im][OAc] was sourced commercially from Proionic (Austria) due to sponsorship support. The dope solutions used in Chapters 4 to 6 were prepared using this commercial [C_2C_1im][OAc] without further purification. This product obtained was slight yellowish viscous liquid. Its structure was confirmed by ^{1}H and ^{13}C NMR, IR and MS (see Appendix A6 for full characterization data).

The characterization of 1-ethyl-3-methylimidazolium acetate was as follows: ^{1}H NMR (400 MHz, DMSO-d6): δ 9.86 (1H, s), 7.84 (1H, s, J = 2 Hz) 7.75 (1H, s, J = 2 Hz), 4.20 (2H, q, J = 8 Hz), 3.86 (3H, s), 1.57 (3H, s), 1.41 (3H, t, J = 7 Hz). ^{13}C NMR (100 MHz, DMSO d6): δ 173.46, 137.74, 123.96, 122.39, 44.43, 35.98, 26.41, 15.66. ν(neat)/cm^{-1} 3149, 3093 (aromatic C-H stretch, w), 2981 (aliphatic C-H stretch, m), 1560 (C=O stretch, s). m/z (LSIMS^{+}): 111 (100%) [C_2C_1im]$^{+}$, m/z (LSIMS^{-}): 59 (100%) [OAc]$^{-}$.

3.3 References

1 H. X. Zhu, J. S. Li, R. Xu and S. Y. Yang, *J. Mol. Liq.*, 2012, **165**, 173–176.

2 S. D. Chambreau, J. A. Boatz, G. L. Vaghjiani, C. Koh, O. Kostko, A. Golan and S. R. Leone, *J. Phys. Chem. A*, 2012, **116**, 5867–5876.

3 V. Logvinenko, O. Polunina, Y. Mikhailov, K. Mikhailov and B. Bokhonov, *J. Therm. Anal. Calorim.*, 2007, **90**, 813–816.

4 M. T. Clough, K. Geyer, P. A. Hunt, J. Mertes and T. Welton, *Phys. Chem. Chem. Phys.*, 2013, **15**, 20480–20495.

5 N. M. A. N. Daud, E. Bakis, J. P. Hallett, C. C. Weber and T. Welton, *Chem. Commun.*, 2017, **53**, 11154–11156.

6 A. Stark, P. Behrend, O. Braun, A. Müller, J. Ranke, B. Ondruschka and B. Jastorff, *Green*

Chem., 2008, **10**, 1152–1161.

7 M. T. Clough, K. Geyer, P. A. Hunt, S. Son and T. Welton, *Green Chem.*, 2015, **17**, 1–12.

8 S. Tabacco, 5.301 Chemistry Laboratory Techniques, January IAP 2004, http://dspace.mit.edu/handle/1721.1/75804%5Cnhttp://ocw.mit.edu/courses/chemistry/5-301-chemistry-laboratory-techniques-january-iap-2012/labs/MIT5_301IAP12_Work_Handout.pdf.

9 G. R. Fulmer, A. J. M. Miller, N. H. Sherden, H. E. Gottlieb, A. Nudelman, B. M. Stoltz, J. E. Bercaw and K. I. Goldberg, *Organometallics*, 2010, **29**, 2176–2179.

10 D. J. C. Constable, A. D. Curzons and V. L. Cunningham, *Green Chem.*, 2002, **4**, 521–527.

11 R. A. Sheldon, *ACS Sustain. Chem. Eng.*, 2018, **6**, 32–48.

12 M. Tiano, R. Clark and M. Costa, *Green Chem.*, 2023, **25**, 2541–2558.

13 M. Tobiszewski, M. Marć, A. Gałuszka and J. Namiešnik, *Molecules*, 2015, **20**, 10928–10946.

14 How Long Does Resin Last Before It Starts to Degrade, https://plaaastic.com/how-long-does-resin-last/.

15 A. W. T. King, J. Asikkala, I. Mutikainen, P. Järvi and I. Kilpeläinen, *Angew. Chemie - Int. Ed.*, 2011, **50**, 6301–6305.

Chapter 4: Development of Cellulose-Lignin Film Fabrication Method

4.1 The overall cellulose/lignin film fabrication protocol

This chapter will provide a detailed explanation of the framework, along with a step-by-step experimental procedure for producing a cellulose-lignin thin films. This research project introduces a novel framework that enhances our understanding by explaining the precise sequence of procedures and the underlying reasoning behind them, all aimed at producing a natural-based film. Overall, it takes one week to produce a single thin film, from the preparation of the starting materials to the final product, as depicted in Figure 4.1. After conducting multiple trials and experiments, and adjusting reaction parameters such as temperature and cellulose weight percent ratio, this is a reproducible protocol for making biodegradable cellulose-lignin films.

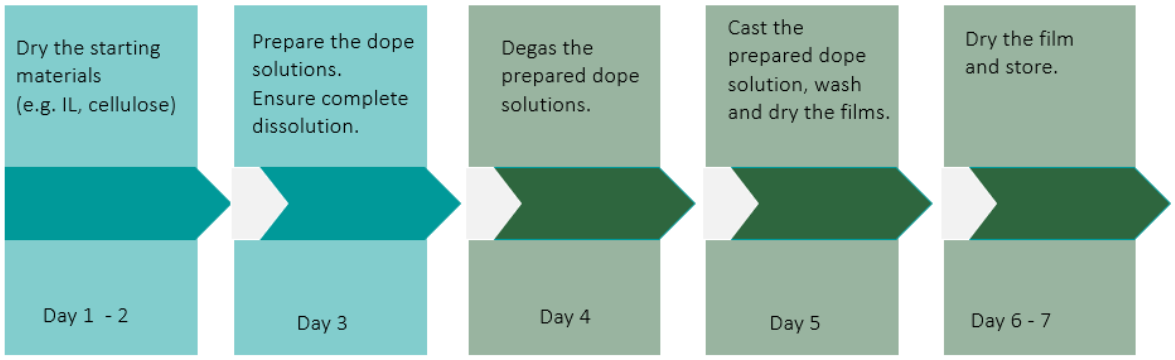


Figure 4.1: Time frame for cellulose/lignin film fabrication

4.1.1 *Solubility of cellulose and lignin in [C_2C_1im][OAc] / DMSO*

It is crucial to directly determine the solubility limits of cellulose and lignin in [C_2C_1im][OAc] in order to ascertain the range of conditions in which the system can be processed. In this study, the solubility of cellulose was investigated using [C_2C_1im][OAc], whereas the solubility of lignin was examined in a solvent mixture of [C_2C_1im][OAc]/DMSO. The finding of lignin

solubility using a solvent mixture including DMSO was made at a later time. The literature reported the efficacy of a mixture of ionic liquid in DMSO for biomass carbohydrates and lignin.[1,2,3,4] Consequently, the assessment of cellulose solubility and the investigation of the order of cellulose-lignin dope solution were carried out only in $[C_2C_1im][OAc]$ until the discovery of a solvent mixture containing $[C_2C_1im][OAc]$ /DMSO, which was then tested in lignin dope solutions.

4.1.1.1 Cellulose solubility studies

Cellulose is the main component in preparing a dope solution. Therefore, determination cellulose solubility studies are very important in determining the processing window of the cellulose-lignin dope solution. As previously stated, the cellulose can be precipitated into a regenerated form when there is a water content of up to 20%.[5] Thus, a study was done to identify the maximum point of cellulose solubility in $[C_2C_1im][OAc]$ in the presence of water.

Cellulose, $[C_2C_1im][OAc]$, and water were accurately measured as specified in Table 4.1. Water was introduced into the $[C_2C_1im][OAc]$ mixture at ratios (w/w) of 90:10, 85:15, and 80:20. The water content in $[C_2C_1im][OAc]$ was evaluated twice using volumetric Karl Fischer titration. Although no water was intentionally added ($[C_2C_1im][OAc]$: H_2O = 100:0), a water content of 0.38 w/w % was detected, indicating that $[C_2C_1im][OAc]$ absorbed moisture from the environment and during its preparation. Cellulose was dissolved in a combination of $[C_2C_1im][OAc]$ and water in a 25 mL round bottom flask under a flow of nitrogen gas. The experimental temperature was maintained at a constant 70 °C for a duration of 2 hours. The cellulose dope solution exhibited transparency and was subjected to examination under both polarised and non-polarized light using a light microscope. Subsequently, cellulose of a predetermined weight, ranging from approximately 0.01 to 0.03 grams, was incrementally added until the sample failed to dissolve within a 2-hour timeframe. Each ratio was replicated three times.

Generally, the solubility of cellulose decreased as the amount of water added to the ionic liquid increased, as seen in Figure 4.2. There is a sharp reduction of cellulose solubility at 15 wt.%

water content and cellulose becomes insoluble when there is more than 20% water in the ionic liquid. Water molecules hinder the interaction between acetate ions and cellulose, while $[C_2C_1im][OAc]$ forms a strong hydrogen bond with water. This rationale is supported by a molecular dynamics (MD) study investigating the regeneration of cellulose from $[C_2C_1im][OAc]$ at different water concentrations.[6] The study showed that increasing water content promotes the reformation of cellulose–cellulose hydrogen bonds. Specifically, the average number of hydrogen bonds within cellulose increased from 38.8 in the absence of water to 144.6 at 100 wt.% water. Concurrently, the interaction energy between cellulose and the ionic liquid (including both cation and anion) decreased significantly with increasing water content, dropping from 3407 kJ/mol at 20 wt.% water to 1250 kJ/mol at 40 wt.% water. These results indicate that water weakens cellulose–ionic liquid interactions while strengthening cellulose–cellulose hydrogen bonding, thereby facilitating cellulose regeneration.

The maximum solubility obtained in this study is supported by other literature using microcrystalline cellulose in $[C_2C_1im][OAc]$, which shows similar results that cellulose could not be dissolved when the water content reached 20 wt.%[5] The cellulose solubility observed in this dissolution experiment was slightly lower compared to their study, likely attributed to minor changes in the experimental conditions. This experiment was conducted by dissolving cellulose at a temperature of 70 °C for a duration of 2 hours. Meanwhile, their experiment was carried out at a temperature of 90 °C for the same duration of 2 hours. The process of dissolution is significantly influenced by temperature, as it is directly correlated with the amount of kinetic energy present in an ionic liquid. Hence, under the experimental conditions used in this research, it may be concluded that the maximum amount of water in the ionic liquid in which microcrystalline cellulose can dissolve is 15 weight percent.

Table 4.1: Solubility experiment of cellulose in $[C_2C_1im][OAc]$ in different water content

Ratio $[C_2C_1im][OAc]$: $[H_2O]$	100:0	90:10	85:15	80:20
Sample	1 g $[C_2C_1im][OAc]$ 0 g H_2O	0.9 g $[C_2C_1im][OAc]$ 0.1 g H_2O	0.85 g $[C_2C_1im][OAc]$ 0.15 g H_2O	0.8 g $[C_2C_1im][OAc]$ 0.2 g H_2O
Water content present in $[C_2C_1im][OAc]$ water mixture (wt.%)	0.38 ± 0.07	8.95± 0.09	13.17± 0.27	17.90± 0.60
Weight of $[C_2C_1im][OAc]$ in water (grams)	1.031 ± 0.06	0.913 ± 0.01	0.847 ± 0.01	0.8071 ± 0.01
Amount of cellulose able to be added into in 1 g $[C_2C_1im][OAc]$-water mixture (grams)	0.205 ± 0.005	0.126 ± 0.010	0.012 ± 0.001	0.000 ± 0.000
Cellulose solubility in $[C_2C_1im][OAc]/H_2O$	19.88 ± 0.71	13.86 ± 1.06	1.40 ± 0.13	0.00 ± 0.00

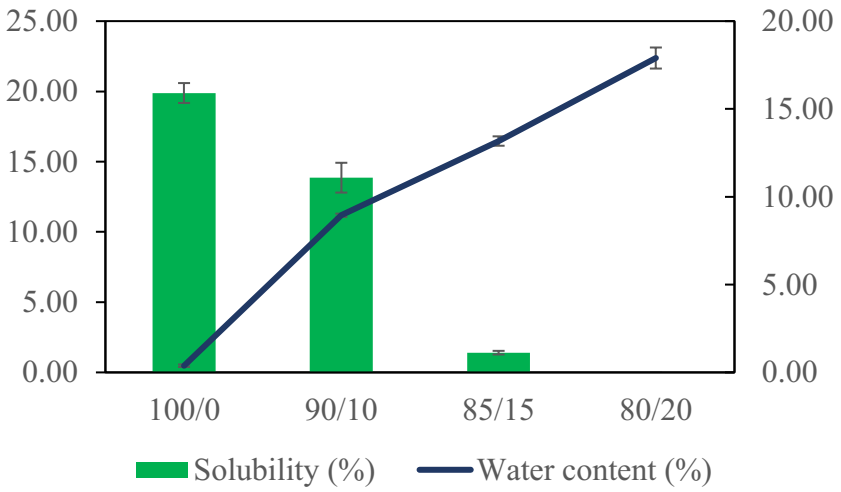


Figure 4.2: Cellulose solubilty and water content in different [C_2C_1im][OAc] water ratio

4.1.1.2 Changing the cellulose dope solution temperature

Cellulose can fully dissolve in [C_2C_1im][OAc] at a temperature of 50 °C.[7] However, dissolution at this temperature was slow requiring at least 2 hours. In most studies, lignocellulose dope solutions are prepared at higher temperatures, typically 80–90 °C, using [C_2C_1im][OAc].[8,9] To balance dissolution efficiency and energy consumption, cellulose in this study was initially prepared at 50 °C and compared with preparation at 70 °C.

The process of dissolving at a temperature of 70 °C exhibited a more rapid rate of dissolution completing in under 2 hours. The solubility of cellulose is significantly influenced by the temperature of the ionic liquid as a result of thermodynamic activity.[10] Raising the temperature will increase the kinetic energy and entropy of the cellulose molecule and the ionic liquid ions. The process of solute dissolution in solvents is influenced not only by changes in heat content (enthalpy) but also by changes in disorder (entropy). This is especially crucial for bulky solutes like polymers and has been examined in the context of cellulose solutions. In studies of ionic liquids such as [C_2C_1im][OAc], the viscosity of both the pure IL and cellulose/IL solutions decreases significantly with increasing temperature, consistent with reduced intrinsic viscosities as temperature rises. This reduction in viscosity at elevated temperatures enhances mass transfer and makes stirring easier, thereby shortening the time required for dissolution.[11] Transitioning from 50 °C to 70 °C reduced the overall energy consumption of the process, as

the higher temperature significantly shortened the time required for dissolution and homogenization. Furthermore, bubble formation during stirring was diminished due to the improved flowability of the dope solution at elevated temperature, as evidenced in Figure 4.3.

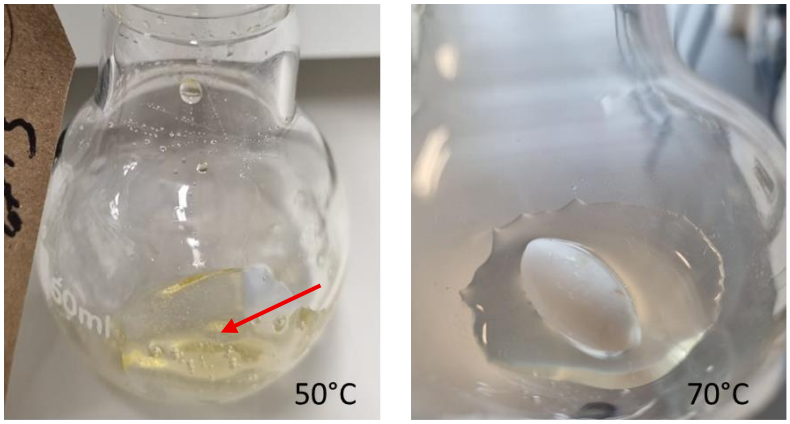


Figure 4.3: The appearance of bubble gas diminished when a cellulose dope solution was prepared from 50 to 70 °C

4.1.1.3 Lignin Solubility Studies in [C_2C_1im][OAc]

The solubility of lignin is challenging due to its complex structure, which includes many functional groups and many types of interlinkages such as α-O-4, β-O-4, β-β', and 4-O-5. Lignin is highly soluble in both organic solvents[12] and ionic liquids such as [C_2C_1im][OAc] and 1-butyl-3-methylimidazolium cyclohexyl carboxylate, [C_4mim][C_6H_{11}COO]. The solubility of lignin is primarily influenced by the anion components,[13,14] which disrupt the intramolecular hydrogen bonding network in lignocellulose.[15] This study introduces a combined IL-molecular solvent system for enhancing the solubility of lignin. The solvent system involves a blend of [C_2C_1im][OAc] and DMSO, which results in the efficient production of homogeneous lignin dope solutions. The initial section of this discussion will elucidate the solubility of lignin in [C_2C_1im][OAc], a process that requires a significantly longer duration for complete solubility. This will be followed by an examination of the solubility of lignin in a solvent mixture of [C_2C_1im][OAc]/DMSO. Lignin solubility can be assessed visually by employing an optical microscope, as lignin possesses a strong brown colour.

The results clearly demonstrate that lignin solubility in [C_2C_1im][OAc] is strongly dependent on the structural characteristics imparted by the lignin's botanical origin and extraction method. Although the same mass fraction of lignin (3.5 wt.%) was applied under identical dissolution conditions (70 °C), the two lignin types behaved markedly differently. Organosolv beechwood lignin (**oHL**) dissolved completely within 3 h, whereas ionsolv spruce lignin (**iSL**) remained partially undissolved even after 12 h as seen in Figure 4.4. This contrast indicates that hardwood-derived organosolv lignin interacts more favorably with the ionic liquid than softwood-derived ionsolv lignin, likely due to differences in molecular weight distribution, and functional group composition.

The difficulty in dissolving **iSL** aligns with broader trends reported in the literature: softwood lignins generally possess higher structural recalcitrance compared to hardwood lignins. Although direct comparison to prior studies is limited because most published work focuses on kraft lignins dissolved in protic ionic liquids (PILs), the general pattern is consistent.[15,16] For example, previous reports show that hardwood lignins, such as eucalyptus, achieve significantly higher solubility (31–39.9 wt.%) than softwood lignins, which often reach only ~25 wt.% under comparable conditions as indicated in Table 4.2.[17,18] These trends support the conclusion that the slower dissolution of **iSL** is inherent to softwood lignin's structural features. Overall, the results strongly support the argument that lignin botanical origin and extraction process are key determinants of solubility behavior in ionic liquids, with hardwood lignins generally displaying superior solubility and faster dissolution kinetics compared to softwood lignins.

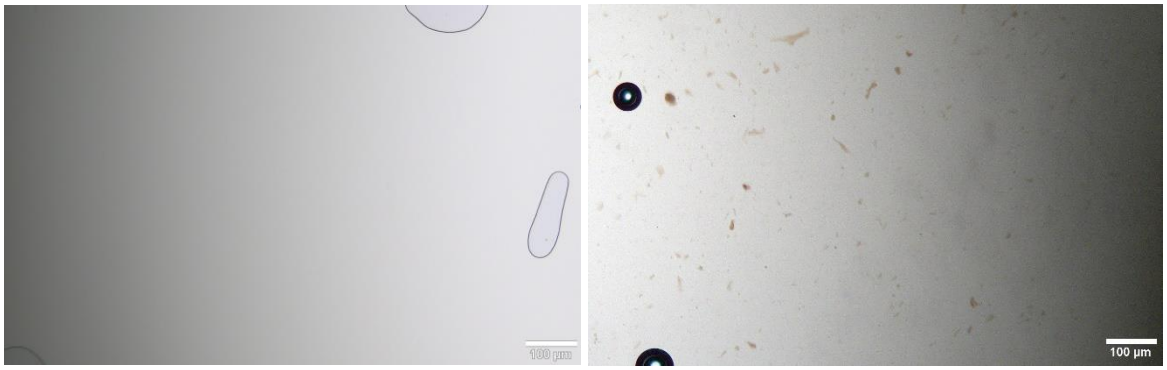


Figure 4.4: Optical micrographs of lignin in [C_2C_1im][OAc]: **oHL** fully dissolved after 3 h (right); **iSL** remained undissolved after 12 h (left)

Table 4.2: Lignin solubility in imidazolium-based ionic liquid

Ionic liquids	Lignin solubility (w/w %)	Reaction conditions	References
$[C_2C_1im][OAc]$	30	Indulin AT (kraft lignin) at 90°C after 24 h incubation	Lee et al. (2009)[19]
$[C_2C_1im][OAc]$	25.4	Lignoboost softwood centrifuged for 25 min	Protz et al. (2021)[17]
$[C_2C_1im][OAc]$	31 – 39.9	Eucalyptus alkaline lignin at 47 - 86°C for 2 hours	Yang et al. (2017)[18]

4.1.1.4 Lignin Solubility Studies in $[C_2C_1im][OAc]$/DMSO

Due to the lengthy dissolution process of lignin in the ionic liquid, the use of a co-solvent, specifically DMSO, helps to decrease the time required and reduce viscosity for complete lignin dissolution. The selection of DMSO as the co-solvent was based on its exceptional capacity to dissolve organic molecules and its miscibility with most ILs.[20]

A comparative analysis was performed using the identical experimental conditions to evaluate the dissolving rate of 35 mg of **iSL** at 70 °C in 1 g $[C_2C_1im][OAc]$ as compared to 1 g $[C_2C_1im][OAc]$ /DMSO (1:0.275, w/w). It was discovered that **iSL** fully dissolved when left overnight in a solvent consisting of DMSO and $[C_2C_1im][OAc]$. However, if only the $[C_2C_1im][OAc]$was present, **iSL** did not completely dissolve, as shown in Figure 4.5. DMSO decreases the viscosity of the solvent mixture, hence enhancing the movement of molecules between the solute and solvent.[7] Another contributing reason is that the presence of DMSO can enhance ion dissociation, leading to a greater abundance of active $[C_2C_1im]^+$ and $[OAc]^-$ ions. This, in turn, disrupts the hydrogen bond network of cellulose and lignin, ultimately enhancing their dissolution.[3] The dissolution mechanism of cellulose and lignin within the $[C_2C_1im][OAc]$ binary system relies on a synergistic interplay of hydrogen bonding disruption, hydrophobic interactions, and co-solvent-driven chemical attacks at 90°C as schematically outlined in Figure 4.6.

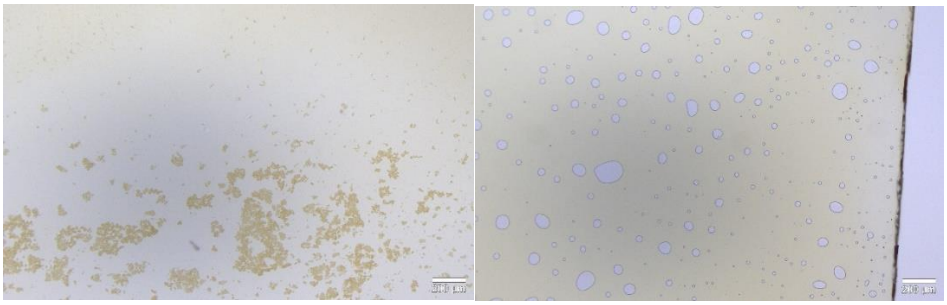


Figure 4.5: Optical micrographs of lignin **iSL** remains undissolved in $[C_2C_1im][OAc]$ (left) while completely dissolve in $[C_2C_1im][OAc]$ overnight stirring (right)

Lignin exists as a rigid, three-dimensional macromolecular network held together by dense networks of intra- and intermolecular hydrogen bonds among its aliphatic and phenolic hydroxyl (-OH) groups. The acetate anion possesses high hydrogen-bond basicity, enabling it to act as a powerful hydrogen-bond acceptor. The $[OAc]^-$ ions competitively target and form strong hydrogen bonds with the protons of the lignin and cellulose -OH groups. This competitive binding effectively breaks the native biopolymer-biopolymer hydrogen networks, causing the matrix to swell and individual polymer chains to separate.

While the anion disrupts the hydrogen bonds, the planar imidazolium ring of the $[C_2C_1im]^+$ cation simultaneously interacts with the electron-rich aromatic units of the lignin structure. These interactions comprising $\pi - \pi$ stacking, van der Waals forces, and hydrophobic dispersion which help stabilize the newly isolated lignin fragments in the solution phase and prevent them from re-aggregating.[21] The addition of DMSO further accelerates this process. Beyond physically reducing the viscosity of the ionic liquid to enhance mass transfer, the presence of DMSO promotes higher ion dissociation, increasing the availability of active $[C_2C_1im]^+$ and $[OAc]^-$ ions. Importantly, at an elevated temperature of 90°C (as proposed by Kuntapa et al., 2022), DMSO actively participates in a chemical mechanism where it targets specific linkages within the lignin matrix. This leads to a localized transition or covalent bonding interaction between the co-solvent and the lignin fractions. This targeted attack weakens the primary structural integrity of the lignin polymer, rendering it highly susceptible to complete solvation by the surrounding ionic liquid pairs.

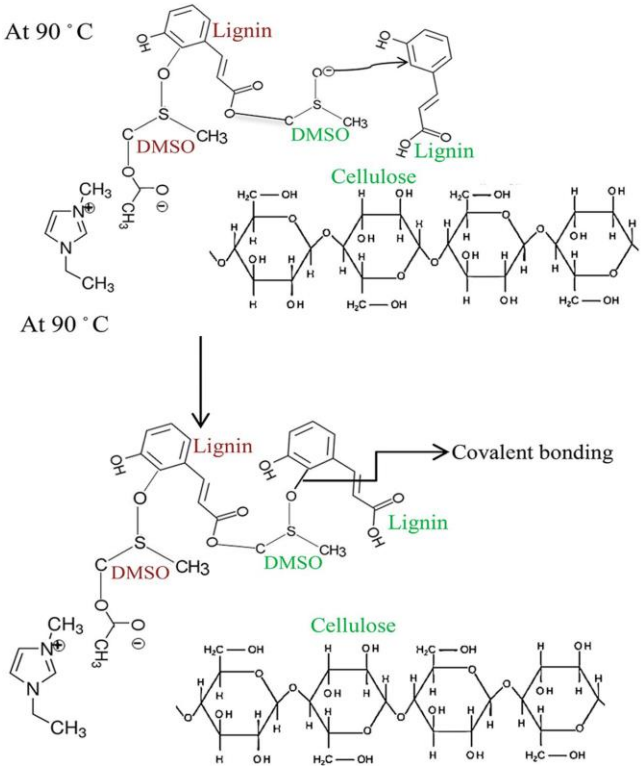


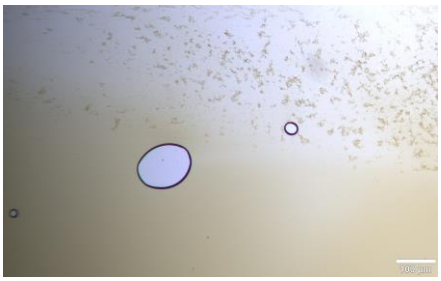
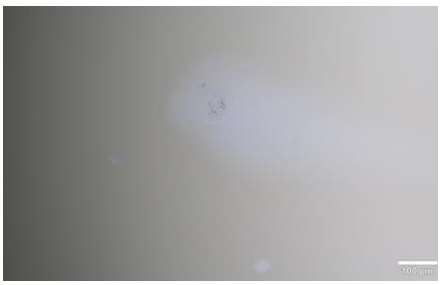
Figure 4.6: Schematic mechanism cellulose and lignin dissolution in [C_2C_1im][OAc]/DMSO adopted from Kuntapa et al. (2022)[4]

Furthermore, the optimal weight percentage of DMSO obtained at 27.5 w/w% relative to IL weight, or the mole ratio χ = 0.35 DMSO/[C_2C_1im][OAc] was determined by a series of experiments conducted at different DMSO weight percentages. The lignin dissolution was kept at 70°C, stirred at 600 rpm for overnight. The lignin solubility in DMSO/[C_2C_1im][OAc] was selected based on literature reports showing that only 0.8 wt% lignin dissolves in pure DMSO (90 mg in 11 g DMSO) for softwood kraft lignin.[22] The results of **iSL** solubilities are presented in Table 4.3.

The results showed that when only DMSO was utilised, the **iSL** was only partially dissolved, with small lignin particles remaining observable under the optical microscope. The concentration (0.72 wt%) observed was lower than that documented in the literature for the same type of softwood lignin; nevertheless, differences in extraction techniques may result in changes in solubility thresholds.[23] The combination of equal parts [C_2C_1im][OAc] and DMSO exhibited low efficiency. Although the incorporation of DMSO reduces viscosity that enhance the mixture's stirring and dissolving efficiency, but this is not the case for this mixture. This conclusion is consistent with prior research, which indicated that DMSO did not significantly interact with cellulose in equimolar mixes of [C_4C_1im][OAc] and DMSO.[7] Consequently,

optimizing the DMSO concentration as a co-solvent can improve the solvation capacity of the ionic liquid by promoting mass transport through viscosity reduction, while minimally impacting the specific interactions among cations, anions, or between the ionic liquid and the polymer.

Table 4.3: Ionosolv softwood lignin (**iSL**) solubility test in [C_2C_1im][OAc] co-solvent with DMSO

Lignin weight (mg)	DMSO (g)	[C_2C_1im][OAc] (g)	DMSO/ [C_2C_1im][OAc] (w/w %)	Lignin conc. (w/w %)	Observation
20	2.750	0.000	100.00	0.72	Partially soluble 
20	0.92	1.83	50.02	0.72	Partially soluble 
20	0.59	2.16	27.50	0.72	Completely soluble 

4.1.1.5 Studying the order of biopolymers addition in the cellulose-lignin dope solutions

A study was done to investigate the sequence of biopolymers incorporation in the preparation of cellulose-lignin dope solutions in order to determine the optimal order based on micrograph evidence. A solution of **5cel-0.5kSL** was prepared by adding cellulose and lignin biopolymers in a certain order to $[C_2C_1im][OAc]$ at a temperature of 70 °C. The first set of cellulose was allowed to dissolve for a duration of 30 minutes, after which the lignin was added. This set was referred to as pre-added cellulose. The second set of lignin was left to dissolve for a duration of 30 minutes, after which cellulose was added. This batch was referred to as pre-added lignin. The final set is referred to as added lignin and cellulose, as it was involved the simultaneous dissolution of cellulose and lignin. A small quantity of the sample was promptly collected at regular intervals of 2, 10, 28, 37, 91, and 100 minutes for optical microscope examination. The polarised pictures were taken to facilitate the observation of cellulose and lignin dissolution.

The polarising microscope allows to visualise and characterise birefringent samples. In case of cellulose dissolution, the application of cross-polarised light microscopy can visualise a greater contrast between cellulose and the solvent. Example of cellulose dissolution images in a bright field and polarised lenses is shown in Figure 4.7.

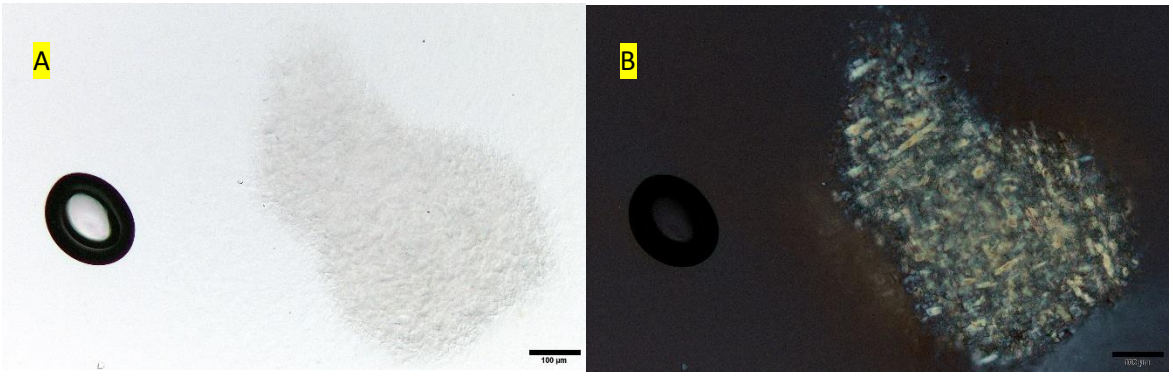


Figure 4.7: Comparison cellulose dissolution images in a brightfield microscope image (A) and polarised microscope image (B) using an optical microscope

Figure 4.7 depicts contrasting images obtained through different optical microscopy techniques. Image A illustrates the presence of undissolved cellulose in $[C_2C_1im][OAc]$ using

brightfield microscopy. Cellulose can be observed by a white accumulation, whereas a trapped gas is indicated by a black circle ring. On the other hand, with cross-polarized optical microscopy, the light-colored region corresponds to cellulose that has not dissolved, while the dark regions indicate the presence of a solvent.

In the pre-added cellulose dissolution, a small quantity of cellulose remains undissolved after 100 min, as depicted in Figure 4.8. Cellulose formed hydrogen bonds with IL, making the IL more viscous. Cellulose formed gel-like structures, taking much time to disentangle into bulk solution. Therefore, it is ineffective and disrupts solvent capability. The mechanism of cellulose dissolving in solvent supported by literature is depicted in Figure 4.9. [24] Dissolution of cellulose begins with the diffusion of solvent into both amorphous and crystalline parts of the fiber, with the amorphous regions being more easily penetrated due to their disordered structure. The fiber swells into a gel-like consistency when crystalline structures are changed and transformed into amorphous forms. Ultimately, cellulose chains dissolve and disperse into the bulk solution, completing the dissolving process.

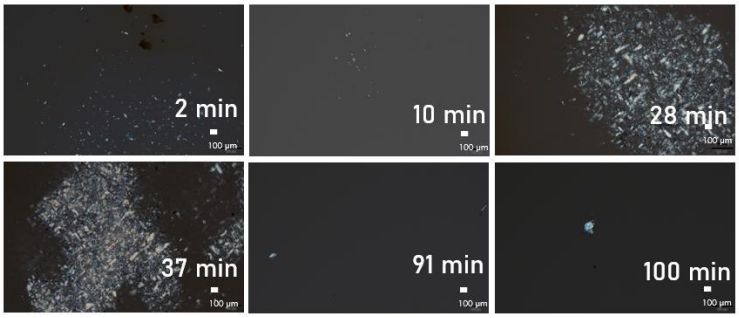


Figure 4.8: Optical micrographs of pre-added cellulose under polarised light at different dissolution times

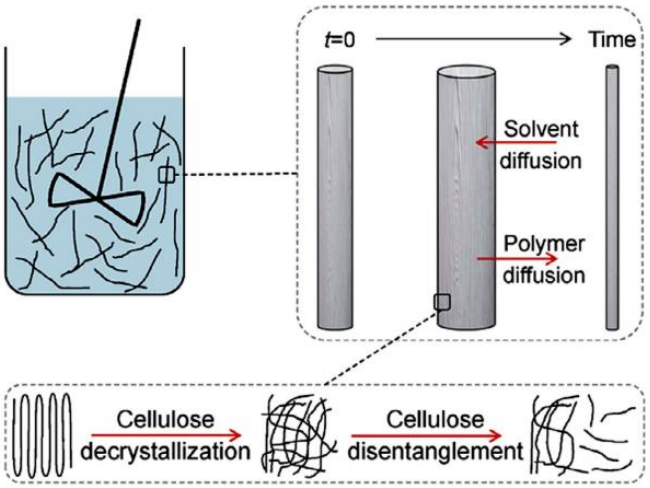


Figure 4.9: Mechanism representation of dissolution of cellulose fibers. Image adopted from Ghasemi et. al[24]

During pre-added lignin dissolution, cellulose almost fully dissolves within 37 minutes. Because lignin is an amorphous polymer, it interacts more readily with the IL.[25] This interaction decreases the effective viscosity of the IL system, which promotes cellulose chain disentanglement and accelerates dissolution. Therefore, the presence of pre-existing lignin improves and expedites cellulose dissolution, as shown in Figure 4.10. A similar viscosity reducing effect has been reported in other polymer systems. For example, incorporating 40–60 wt.% lignin into acrylonitrile-butadiene-styrene (ABS) unexpectedly decreased the melt viscosity.[26] This behavior was attributed to the structure of organosolv hardwood lignin, which is rich in syringyl units. These units introduce steric hindrance and increase the free volume within the lignin phase, enhancing molecular mobility and lowering melt viscosity. Although this system differs from IL–cellulose dissolution, the underlying mechanism supports the observation that lignin can reduce viscosity and facilitate polymer mobility.

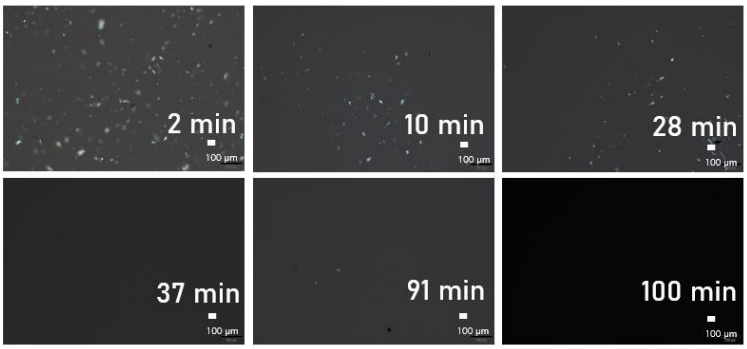


Figure 4.10: Optical micrographs of pre-added lignin under polarised light at different dissolution times

In the cellulose–lignin mixture, amorphous lignin and crystalline cellulose are simultaneously introduced into the solvent, resulting in competition for dissolution. Figure 4.11 illustrates that the disentanglement of the mixed dope solutions began at approximately 37 minutes, with total dissolving of both polymers achieved by 100 minutes. There is an absence of literature regarding the concurrent dissolution of cellulose and lignin. One study indicated that a blend of 20 wt.% kraft lignin and 80 wt.% cellulose necessitated a temperature of 71–73 °C for complete dissolution in the ionic liquid 1,5-diazabicyclo[4.3.0]non-5-enium acetate within 1.5 hours, circumstances similar to those needed for dissolving 100% cellulose (75–80 °C).[27] The similar temperature indicates that the incorporation of lignin does not significantly modify the overall dissolution conditions; nonetheless, it could hinder the process due to competing solvent interactions. Cellulose and lignin specifically compete to establish hydrogen bonds with the ionic liquid, whereas the steric hinderance associated with lignin reduces cellulose's accessibility to the solvent. Therefore, the observed dissolution sequence in this system, initial disentanglement followed by complete dissolution is consistent with the expected competition between cellulose and lignin for solvent accessibility and may be regarded as an effective dissolution pathway.

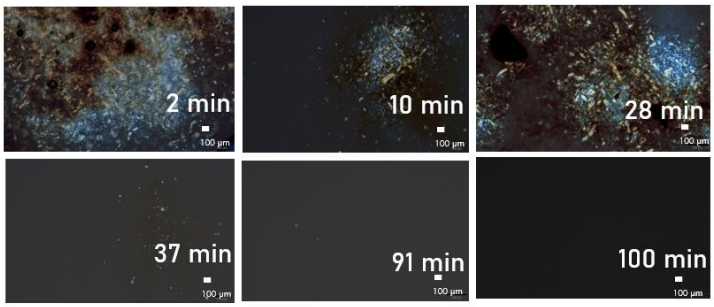


Figure 4.11: Optical micrographs of pre-added lignin and cellulose simultaneously under polarised light at different dissolution times

In conclusion, pre-added lignin and lignin and cellulose simultaneously have benefits to the solvent system. Pre-added lignin was adopted in the cellulose-lignin dope solutions preparation in this project because the biopolymer components have almost dissolved in a short time at 37 minutes.

The final verdict

Thus, the standard protocol for preparing the dope solution was chosen to be that the lignin was first dissolved in the solvent mixture $[C_2C_1im][OAc]$/DMSO overnight. Next, the cellulose was dissolved in the lignin dope solution for an additional 2 hours at a temperature of 70 °C. The specified sequence of adding the components, reaction duration, and temperature is the optimal reaction setup for obtaining a fully soluble cellulose-lignin dope solution.

4.1.2 *Drying the starting materials*

The three primary components utilised in the fabrication of composite films are as follows: (i) biopolymers, which are cellulose powder and lignin powder; (ii) solvent systems, namely DMSO and $[C_2C_1im][OAc]$; and (iii) plasticiser, which is glycerol for another formulation, which will be discussed further in Chapter 6.

All the mentioned starting materials require drying, as they usually contain moisture. Cellulose and lignin typically have a water content of approximately 8-10%. DMSO has an extremely low moisture content of 0.03 parts per million (ppm) as supplied, whereas $[C_2C_1im][OAc]$ has about 0.25 – 0.35% water and it is strongly hygroscopic. The amount of moisture absorbed depends on the storage condition. The water concentration in $[C_2C_1im][OAc]$ increased up to 973 ppm during a period of 8 days when stored in a closed environment. The moisture absorption is expected to be less susceptible if a capped container with nitrogen gas is used. The presence of water will have a substantial inhibitory effect on the dissolution of cellulose because water is an anti-solvent that causes cellulose to coagulate from the ionic liquid.

Cellulose powder, lignin powder, and glycerol were dried under Schlenk line vacuum without any heating for a day. This allowed sufficient duration for the sample to dry. $[C_2C_1im][OAc]$ was subjected to vacuum Schlenk line drying at a temperature of 50-60 °C for a duration of two days. The DMSO was used in its original state without any modifications, as its water content was very low. Ensuring a low moisture level is crucial, particularly for cellulose. The ability of the hydrogen bond network in cellulose to regenerate with water is the reason for this behaviour. Furthermore, the presence of water hampers the effectiveness of $[C_2C_1im][OAc]$ due to the formation of hydrogen bonds between water and the acetate ion.[28] This interaction prevents the acetate ion from making hydrogen bonds with the cellulose-OH groups.

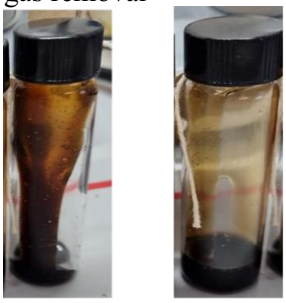
4.1.3 *Degassing the prepared dope solution*

Removing gas from the prepared solution is an important step to create a thin film without any trapped bubbles. Dope solution degassing is required in many cases to prevent air bubbles being formed during the film forming process.[29] The film's mechanical properties are significantly influenced by the presence of gas, as it has a significant impact on the film surfaces. The objective is to fabricate the film with minimal presence of bubbles. Thus, a few approaches have been done to ensure the dope solution is nearly bubble free.

An experimental setup was performed on cellulose-lignin dope solutions using two different approaches to remove gas: an ultrasonic bath and a gravitational technique. 2 g of cellulose-lignin dope solutions with a content of **10cel-0.5kSL** were subjected to ultrasonic treatment in a bath with a power of 80W at a temperature of 70°C for a duration of 20-30 minutes. Another 2 g of a solution with a concentration of **10cel-0.5kSL** were left overnight in the laboratory at the ambient temperature. The observation was recorded in Table 4.4.

Both dope solutions, after degassing, showed almost identical results, with nearly no bubbles observed. The advantage of using an ultrasonic water bath over gravitational degassing is the significantly shorter processing time, as sonication achieves bubble removal much faster than overnight settling. Although sonication requires a small amount of energy to maintain the desired temperature and current, this is compensated by the substantial reduction in degassing time.

Table 4.4: The experiment setup for different methods of degassing in a cellulose-lignin dope solution

Method of degassing	Conditions	Time	Results
Ultrasonic water bath	Temperature: 70°C Power: 80 Watt	20 – 30 minutes	Nearly complete bubble gas removal  Before degassing After degassing

Gravitational forces	Temperature: room temperature (20 - 25°C)	Overnight	Nearly complete bubble gas removal  Before degassing After degassing

There is limited literature discussing degassing methods, as the focus is generally on obtaining bubble-free dope solutions rather than the degassing process itself. For example, a pilot study on preparing cellulose dope solutions for fiber spinning used vacuum degassing for 3.5 hours to produce fibers with bright surfaces at an industrial scale.[30] Similarly, in a laboratory-scale study, a nanofibrillated cellulose–graphite flake dope solution was degassed under vacuum for 20 minutes until no bubbles were observed.[31] Therefore, sonication can be considered an efficient and sufficient method for preparing bubble-free cellulose–lignin dope solutions.

4.1.4 *Cast the dope solution*

Solution casting allows production of technical films for packaging applications in order to achieve thickness below 0.2 mm.[32] The solution casting method is often regarded as the most common, straightforward, and reliable approach for casting the film.[33] However, it comes with challenges to get a stable film. A stable film is a thin sheet of film that maintains its integrity and functional properties under mechanical stress, and remains unchanged when exposed to variations in moisture, temperature, or other environmental conditions.

Several factors must be considered in solution casting, including the biopolymer rheology and drawing distance ratio for film application.[32] Drawing distance is important for industrial scale for the order of magnitude of the radius of the calendering rolls which give rise to adhesion

between the polymer film and the substrate. However, this factor is irrelevant for this lab-scale project, as a straightforward method using a film applicator machine was employed. The solution casting approach was as follows.

The casting speed on the Elcometer 4340 Motorised Film Applicator was fixed at 5.08 mm/s. The casting medium used was glass with dimensions of 300 mm × 300 mm and a thickness of 15 mm, and films were spread evenly using a casting knife set to 250 micrometres. Both casting medium and casting knife were kept constant in this project.

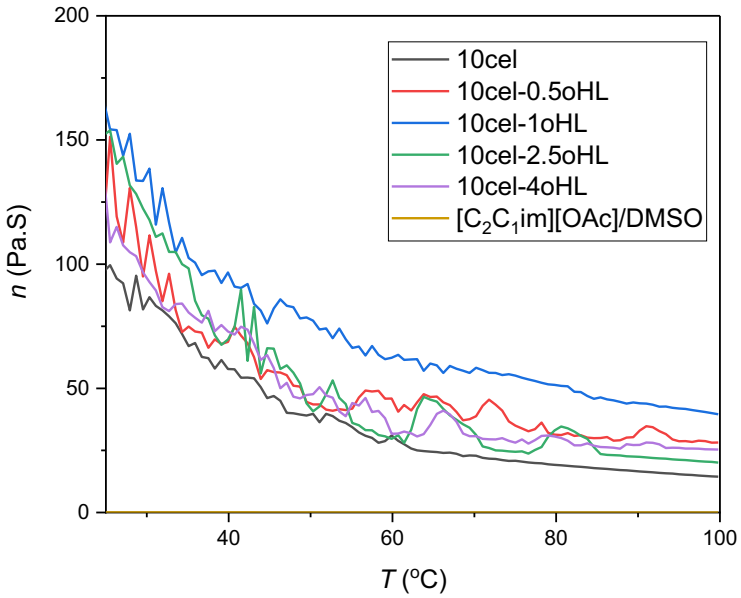
Cellulose dope solution and **10cel-oHL** varying lignin content dope solutions were prepared in $[C_2C_1im][OAc]$/DMSO. These solutions were then subjected to a temperature ramp viscosity experiment, ranging from 25 to 100 °C at a constant shear rate of 10 s^{-1}. The viscosity of the dope solutions was evaluated by taking measurements at intervals of 0.5°C.

Viscosity increases with an increase lignin content, and decreases with rising temperature, as expected in a classical polymer solution. The $[C_2C_1im][OAc]$/DMSO solvent system exhibits a Newtonian plateau, similar to that reported in the literature for $[C_2C_1im][OAc]$ alone.[34] At 80 °C, the viscosity $[C_2C_1im][OAc]$ of is slightly higher (0.02 Pa·s) in the literature compared to mixing the two solvents in this study resulted in a lower viscosity (0.01 Pa·s) at the same temperature. Observations of cellulose-lignin dope solutions provide valuable insights into the optimum casting temperature.

The cellulose-lignin dope solutions demonstrate shear-thinning behavior, as illustrated in Figure 4.12, which is consistent with prior studies. [35,5] Within the temperature range of 20–40 °C, the flow curves exhibit a staggered pattern. The shear-thinning mechanism is elucidated by the model suggested for semi-diluted polysaccharides in $[C_2C_1im][OAc]$, as depicted in Figure 4.13.[36] Polysaccharides tend to entangle due to steric hindrance and hydrogen-bonding interactions with $[C_2C_1im][OAc]$. Under applied shear, these networks are disrupted, leading to a reduction in viscosity.[36] Furthermore, research indicates that the addition of 50 wt.% organosolv softwood lignin leads to an increased complex viscosity, comparable to that of pure cellulose solutions. [27] The current investigation likewise demonstrates this trend, since the formulation with the highest lignin content, **10cel-4oHL** displays a viscosity similar to that of

10cel. The findings indicate that the viscoelastic characteristics of the dope solutions are influenced by both the cellulose-to-lignin ratio and the general consistency of the solvent system. Moreover, increasing the temperature significantly reduces the solution viscosity.

(a)



(b)

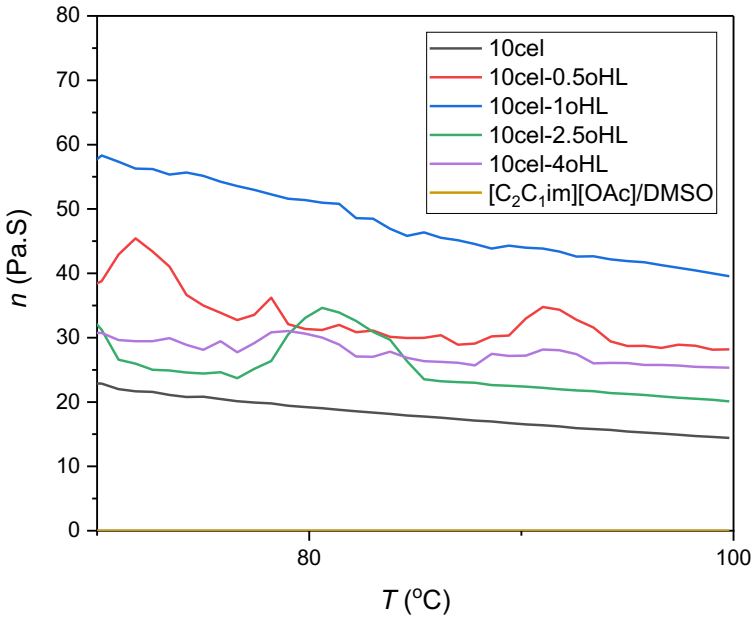


Figure 4.12: Viscosity over temperature at different cellulose-lignin weight percent ratio prepared in [C₂C₁im][OAc]/DMSO (a) at 25 to 100°C (b) at 70 to 100°C

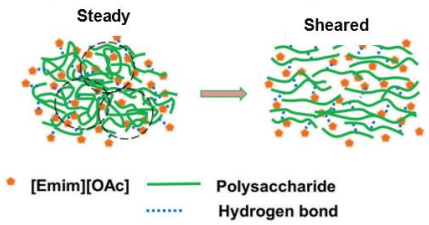


Figure 4.13: Proposed mechanism of the shear-thinning behaviour semi-diluted polysaccharide–$[C_2C_1im][OAc]$ solutions. Image adopted from the literature[5]

As the temperature rises to 70 °C and above, the curve changes into a more linear form. The viscosity of the majority of dope solutions decreases to < 50 Pa·s during the temperature range of 70–100 °C. Modifying temperature or the solution viscosity can transition the dope solution from an elastic to a more fluid state, hence enabling easier pouring. This trend aligns with the reported reduction in viscosity as temperature rises for cellulose weight percentage in superbase ionic liquids.[37] The increase in temperature enhances molecular thermal motion and reduces intermolecular contacts, facilitating more molecular mobility.[37] These results suggest that temperatures between 70 °C and 100 °C are optimal for pouring the dope solution onto the glass casting medium.

To ascertain that the solvent mixture employed in film preparation remains stable during the preparation of dope solutions, a freshly prepared $[C_2C_1im][OAc]$/DMSO mixture was assessed for its long-term thermal stability. The experiment was performed utilizing an isothermal TGA equipment at 70 °C for a duration of 12 hours. The initial water content of the combination was quantified at 0.52 ± 1.33 wt.%, and the associated moisture contribution was deducted from the TGA thermogram, as outlined in Section 2.3.2. A negligible weight loss of 0.33% was recorded over the 12-hour duration, as illustrated in Figure 4.14, signifying insignificant decomposition. This outcome aligns with the observations of Clough et al., who indicated that $[C_2C_1im][OAc]$ commences degradation at around 105 °C with little weight loss.[38] The ideal operating temperature range for this solvent system is 70 °C to 100 °C, depending upon the weight ratio of cellulose to lignin in the dope solutions.

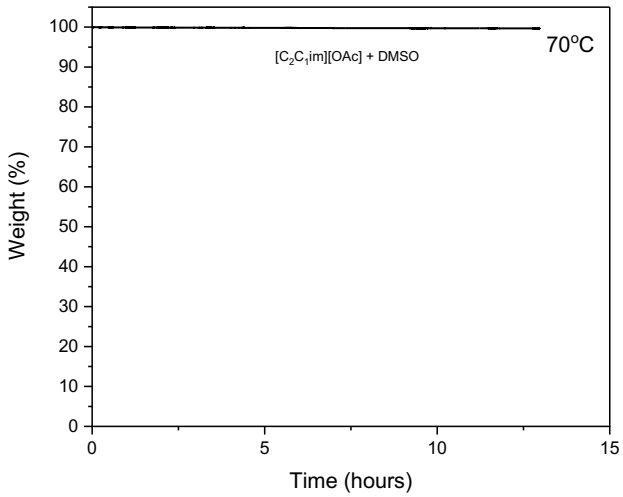


Figure 4.14: TGA thermogram of $[C_2C_1im][OAc]$/DMSO solvent mixture at 70°C

4.1.5 *Washing the prepared cellulose and lignin film*

Cellulose and lignin can be regenerated into composite thin films by dissolving them in an ionic liquid, followed by precipitation in a coagulant bath. Typical coagulants employed in this procedure comprise water, ethanol, and ethanol/water mixtures.[37] Water is the primary coagulation medium used in the industry, despite its substantial volume demands. Nevertheless, it is recyclable following solvent extraction from the coagulation bath. The standard protocol for regenerated cellulose films states that the coagulation temperature should be between 20 and 60 °C.[39] This study utilized deionized water at ambient temperature to minimize energy consumption during film production. The washing stage is designed to guarantee the thorough elimination of the ionic liquid.

A study was conducted to determine the number of washing cycles needed and the duration required to extract ionic liquid from the coagulation bath. Proton NMR spectra were recorded at 15-minute intervals. The freshly casted regenerated cellulose (**10cel**) and cellulose-lignin films (**10cel-2.5oHL**) were cut into 10 mm x 10 mm pieces and immersed in 1 mL of deuterated water to mimic the washing process during the film's fabrication.

Figures 4.15 and 4.16 show that the **10cel** film required a minimum of four washing cycles, totalling to one hour, while the **10cel-2.5oHL** film required five washing cycles, totalling 1.25 hours. Further washing was required for the cellulose–lignin films owing to the intricate structure of lignin, which possesses several active binding sites. The methoxyl groups in lignin obstruct the penetration of water molecules into its hydroxyl regions, where hydrogen bonding generally occurs. Thus, the existence of hydrogen-bonded water reduces the average diffusion constant.[40] To our knowledge, no existing research has documented the number of washing steps required, preventing any direct comparisons. Many literature approaches only modify washing protocols from prior studies, frequently omitting critical variables such as washing volume or duration.

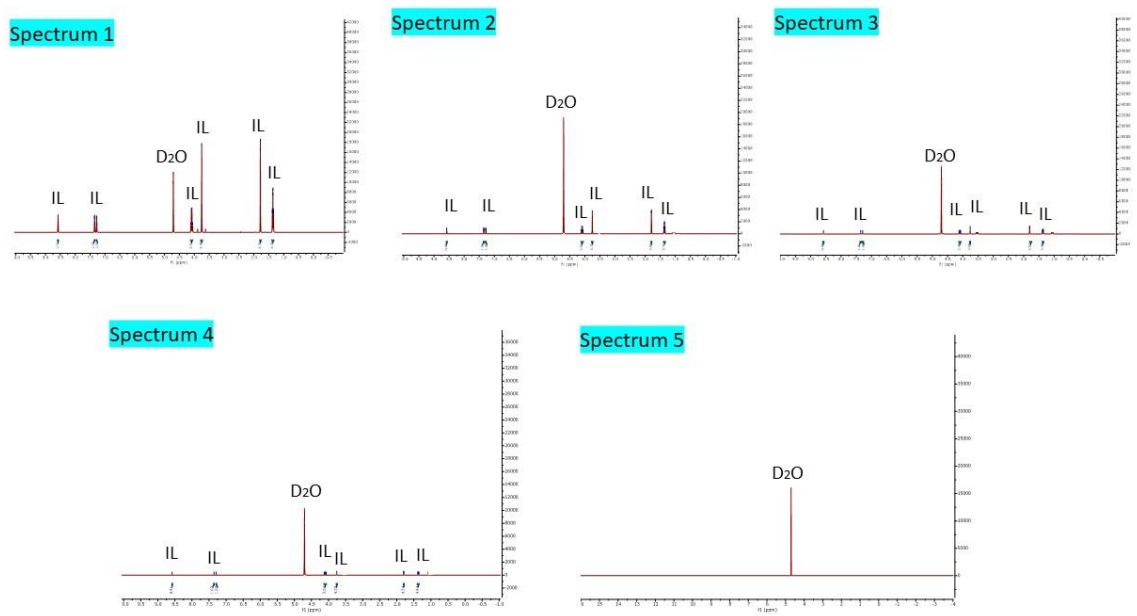


Figure 4.15: ^{1}H NMR spectra of cellulose film washed with deuterated water. Spectrum 1 and 5 indicate the first and the fifth washing cycle respectively.

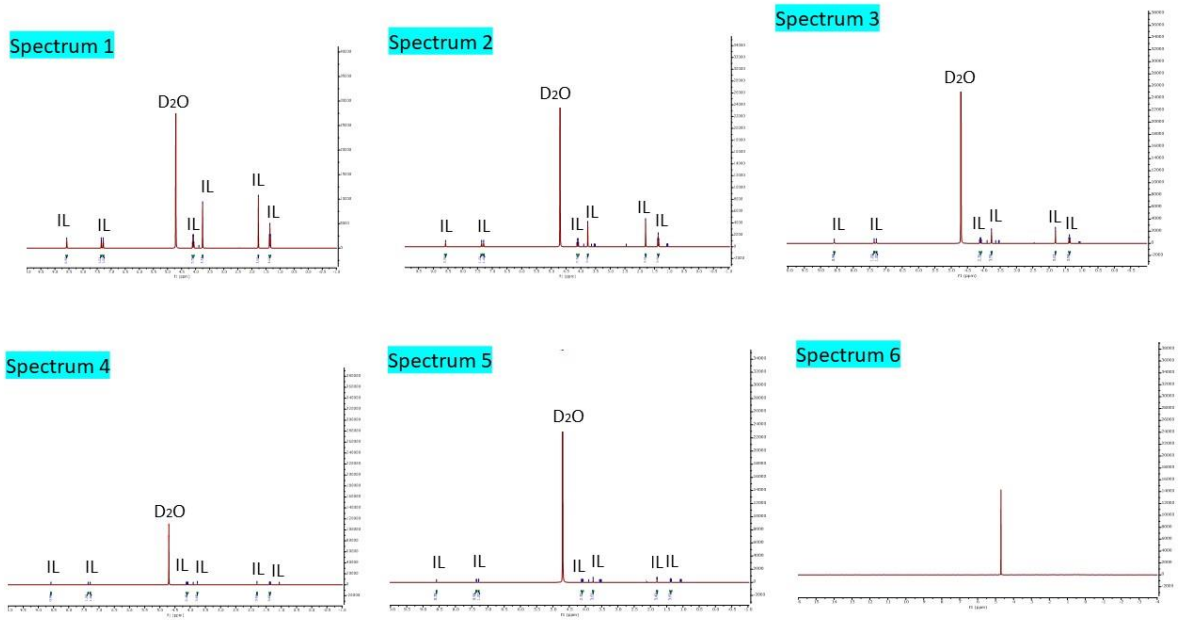


Figure 4.16: ^{1}H NMR spectra of cellulose/lignin film washed with deuterated water. Spectrum 1 and 6 indicate the first and the fifth washing cycle respectively.

Therefore, this experiment indicates the optimal washing cycles and duration required to effectively remove ionic liquid from cellulose and cellulose-lignin films. The experiment utilised solely [C_2C_1im][OAc] (designated as IL in the previously provided figures), so the formulation of a [C_2C_1im][OAc]/DMSO solvent system was excluded from this research phase. However, all composite films were examined using FTIR to ascertain the presence of any residual DMSO. The laboratory-produced regenerated cellulose, cellulose–lignin, and cellulose–lignin–glycerol films were verified to be devoid of both [C_2C_1im][OAc] and DMSO, as demonstrated by the FTIR spectra presented in Chapters 5 and 6. The subsequent two chapters present a comprehensive analysis of this part. Recycling water from the ionic liquid is very important from a technoeconomic perspective.

[C_2C_1im][OAc] and DMSO can be efficiently recycled through rotary evaporation of water and DMSO, but residual trace amounts may persist, largely yielding the ionic liquid.[41] The reutilization of the ionic liquid as a solvent offers economic advantages and a more sustainable methodology. Published techno-economic models indicate that a recovery rate of at least 96% is necessary, even if the ionic liquid is inexpensive; ideally, the recovery rate should be far

greater.[42] [C_2C_1im][OAc] was effectively recovered from **10cel** films for a maximum of five usage cycles.

Figure 4.17 illustrates that [C_2C_1im][OAc] is recyclable for a maximum of five cycles, exhibiting recovery rates between 88% and 95%. This experiment was conducted exclusively in [C_2C_1im][OAc], absent of DMSO. A study on recyclable phosphonium ionic liquids with DMSO in regenerated cellulose achieved a total ionic liquid recovery of 97 %, comparable to the first and fourth cycles found in this investigation.[41] Correspondingly, studies on lignocellulosic films utilizing the same solvent system of [C_2C_1im][OAc]/DMSO indicated ionic liquid recycling yields of over 90% for the initial two cycles, declining to 86.4% and 84% for the subsequent third and fourth cycles, respectively. [43] The reduced recovery yields are mainly attributed to the isolation technique, which may not be ideal for this system, together with mechanical losses intrinsic to the multistep process. The results indicate that the recovery of [C_2C_1im][OAc] is more efficient in **10cel** films compared to **cel-lig** composite thin films.

To confirm the recovery of [C_2C_1im][OAc], FTIR was employed to detect any structural changes. The FTIR spectra indicate that the chemical bonding remains unchanged when [C_2C_1im][OAc] is reused as shown in Figure 4.18. The widening OH band observed at 3200 cm^{-1} suggests the existence of water within the range of 4.2 to 5.3 wt.%, indicating that additional vacuum drying is required.

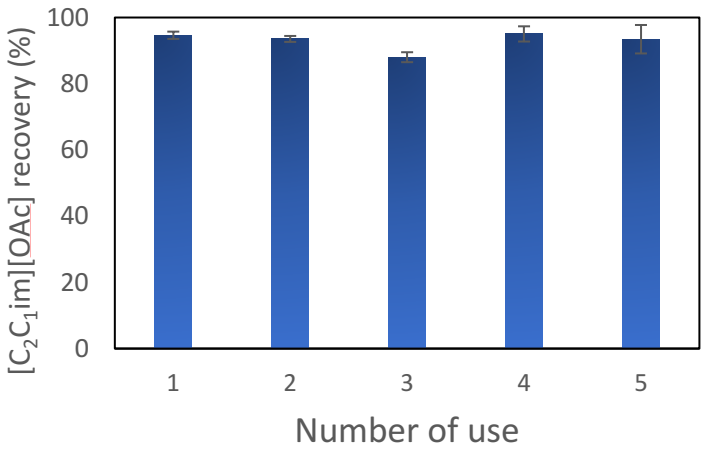


Figure 4.17: [C_2C_1im][OAc] recovery for five number of usage

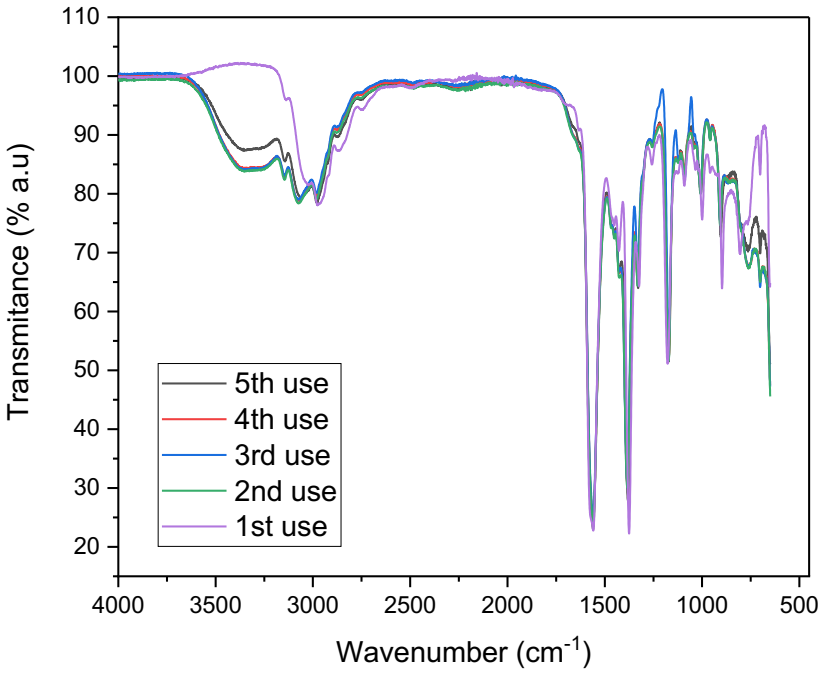


Figure 4.18: FTIR spectra of $[C_2C_1im][OAc]$ for each cycle used. The water content for the 2nd until the 5th use were 4.2% and 5.3% respectively.

4.1.6 *Drying the cellulose-lignin films*

Drying is a technique that transforms a cellulose-lignin film from a gel state to a stable dry film at room temperature. Obtaining smooth and flat surfaces for a film is crucial as this physical characteristic significantly impacts property measurement, such as mechanical characteristics and water contact angle. The drying efficiency is dependent upon external factors such as temperature, airflow, agitation, and the median area of the exposed surface area.[44] This study evaluated the role of substrate material in the drying process.

The regenerated cellulose films were precisely cut to dimensions of 25.4 mm by 25.4 mm. The films were dried on several substrates, including aluminium foil, glass, PTFE board, and parafilm applied to the glass. Each drying surface was exposed to two different environments, resulting in varying levels of humidity at room temperature. An enclosed drying chamber was maintained at a constant relative humidity (RH) of 55-60% using a solution of $Mg(NO_3)_2$ salt, as described in the literature.[45] The second sample was stored in a standard laboratory

environment with a relative humidity of around 60%. The films' measurements were obtained in triplicate over a span of two days. The experimental setup is presented in Figure 4.19. In order to assess the efficacy of each drying technique, the recovery area was computed utilising Equation 21.

$$\%\ recovery\ area = \frac{width\ after\ drying\ (mm)\ x\ length\ after\ drying\ (mm)}{width\ before\ drying\ (mm)\ x\ length\ before\ drying\ (mm)}\ x\ 100 \ldots\ldots \text{Eq 21}$$

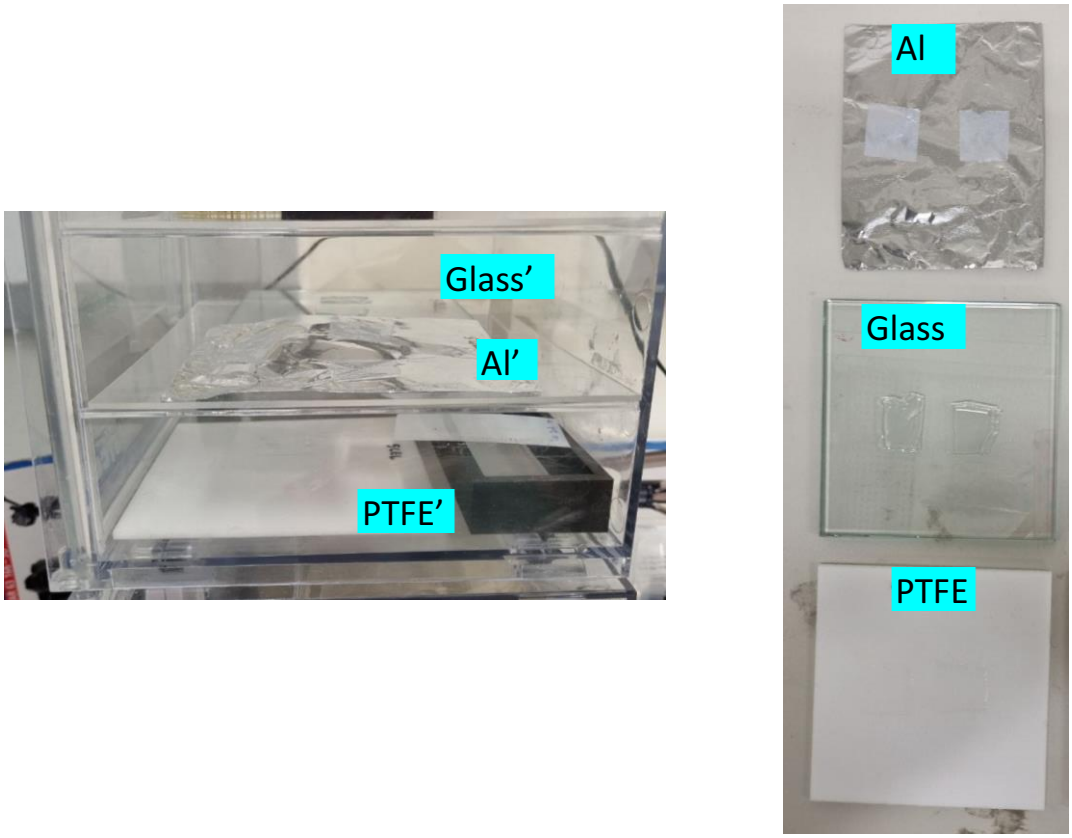


Figure 4.19: Drying cellulose film at different conditions setup. Left image is under static air in drying chamber and right image is at unregulated air flow.

The controlled environment resulted in a significantly larger recovery area as compared to the ambient condition. Films left in drying chamber leads to less shrinking as depicted in Figure 4.20. This is because static airflow in the drying chamber enables the cellulose molecules to reorganise in a controlled manner.[46] Whereas, unregulated environments are susceptible to shrinking at the edges. This conclusion is further supported by the existing research on the drying out process of cellulose nanocrystal films.[47] Controlling humidity in confined space with various humidity range during the drying process slows down capillary flow, resulting in

increased homogeneity. Meanwhile, the process of fast drying such as air dried induces kinetic arrest, resulting in a thermodynamically non-equilibrium state, likely due to capillary flow.[47]

Aluminium has the largest recovery area for **10cel** film at 98 % recovery area in drying chamber, followed by glass and PTFE median as shown in Figure 4.21. Unfortunately, aluminium resulted in the cellulose film sticking to its surface. No current studies document the drying of cellulose films on aluminium; prior research has mainly used borosilicate glass, soda-lime glass, or Teflon (PTFE) plates.[33] The possible explanation is that aluminium foil has a very thin oxide layer namely aluminium oxide, Al_2O_3. The oxide surface possesses negatively charged sites that can interact strongly with the –OH groups in cellulose, resulting in significant adhesion between the cellulose film and the aluminium. Therefore, aluminium is not a suitable medium for recovering **cel** and **cel-lig** composite films. Glass is the second-best substrate for fabricating these films.

Drying conditions	Unregulated airflow	Regulated airflow
Aluminium		
Glass		



Figure 4.20: Cellulose films were imaged after undergoing drying under various drying settings. The last row shows cellulose-lignin film formula of **10cel-1iSL** before and after drying.

Glass exhibited a recovery area of 82% under controlled airflow conditions. This outcome aligns with literature demonstrating that glass plates produce smooth cellulose acetate films, while PTFE substrates provide patterned films that contain concentric micro-sized channels.[33] As a result, films placed on glass were clear, whereas those created on PTFE were translucent. In summary, glass demonstrated the highest suitability as a substrate for the fabrication of cellulose films. However, a difficulty arose when films made from a cellulose-lignin composite stuck excessively to the glass surface. This problem resulted in the creation of a novel method: positioning a strip of superhydrophobic Parafilm beneath the film edge on the glass substrate (refer to the last row in Figure 4.20). Employing the parafilm-on-glass method, all cellulose-lignin films were simply detached. This approach is evidently innovative, lacking prior documentation in the current literature.

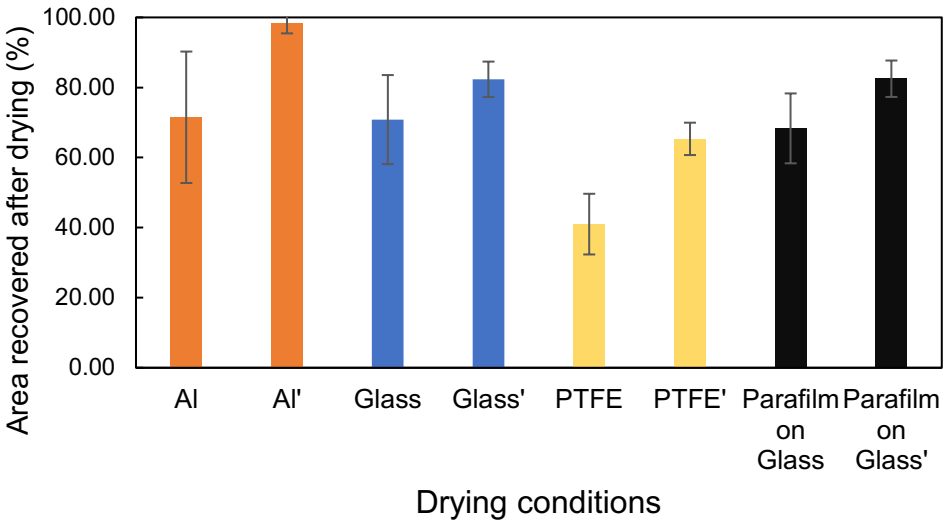


Figure 4.21: Area recovered after drying cellulose film at different drying conditions

4.2 Justification for increasing cellulose loading from 5 to 10 wt.% loading

The cellulose content was increased from 5 to 10 wt.% due to several challenges encountered in producing high-quality composite thin films. The failure of the 5 wt.% cellulose films to form a continuous structure can be attributed to excessive volumetric shrinkage during the regeneration and drying phases. At low polymer concentrations, the high solvent-to-solid ratio results in significant internal tensile stress as the solvent is replaced by the non-solvent. Because the polymer network at 5 wt.% was too sparse to withstand these stresses, the films underwent structural collapse, manifesting as the brittleness and discontinuity observed in Figure 4.22.

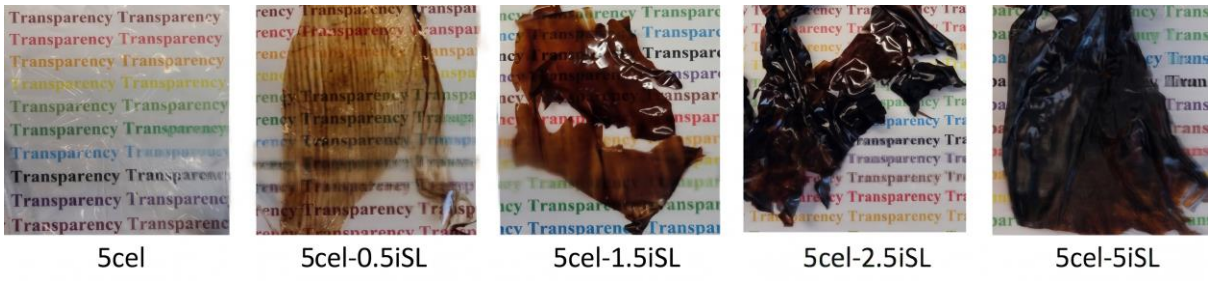


Figure 4.22: Physical appearance of neat cellulose (**5cel**) and cellulose-ionosolv lignin composite films with varying lignin contents (0.5 to 5 wt% **iSL**) against a background to illustrate transparency changes

To limit this shrinkage and improve film integrity, the cellulose content was increased to 10 wt.%. This increase effectively raised the nucleation density of the cellulose chains, creating a more robust framework capable of resisting capillary pressures during drying. Furthermore, the higher solids content reduces the total volume of solvent displaced, thereby minimizing the total dimensional contraction of the composite.

The thickness of the film fabricated with 5 wt.% cellulose fell outside the recommended range. Two formulations containing different cellulose contents, 5 wt.% and 10 wt.% (**5cel-0.5iSL** and **10cel-1iSL**) were compared because they contained the same lignin content (9.09 wt.%), allowing for a meaningful comparison, as shown in Table 4.5. The thickness was determined by averaging three measurements taken at different locations on the film. As indicated in Table 4.6, the thickness of **5cel-0.5iSL** was insufficient, falling below the minimum required value of 15 microns when compared with **10cel-1iSL**.[48] Previous studies have shown that the amount of polysaccharide incorporated strongly influences the final film thickness.[49]

Example: **5cel-0.5iSL**

Lignin weight percent = $\frac{0.5}{5+0.5}\ x\ 100 = 9.09\%$

Table 4.5: Lignin weight percent calculated according to the formula code

Cellulose weight percent ratio	Formula code	Lignin weight percent (%)
5 wt.%	**5cel**	0.00
	5cel-0.5iSL	9.09
	5cel-1.5iSL	23.08
	5cel-2.5iSL	33.33
	5cel-5iSL	50.00
10 wt.%	**10cel**	0.00
	10cel-0.5iSL	4.76
	10cel-1iSL	9.09
	10cel-2.5iSL	20.00
	10cel-4iSL	28.57

Table 4.6: Differences in thickness for 5 wt.% cellulose versus 10 wt.% cellulose

Formula code	Thickness (μm)
5cel-0.5iSL	9.0 ± 1.2
10cel-1iSL	22.3 ± 0.7

Additionally, the lignin content in the 5 wt.% cellulose formulation exceeds the levels commonly reported in the literature, as discussed in Section 4.1.1. For lignocellulose film fabrication, the working maximum lignin weight percent was 29 to 29.9.[9,43] In contrast, the formulations **5cel-2.5iSL** and **5cel-5iSL** contain 33.33 wt.% and 50.00 wt.% lignin, respectively. At these levels, the lignin could not be fully dissolved in [C_2C_1im][OAc]. As shown in Figure 4.23, residual undissolved lignin remained after overnight mixing in both formulations, indicating that longer dissolution times would be required. To avoid unnecessary experimental time and inefficiency, a cellulose–lignin dope solution with approximately 30 w/w% lignin is considered a more practical and effective range. Based on all the factors discussed, the formulation containing 10 w/w % cellulose was selected as the most suitable for this study.

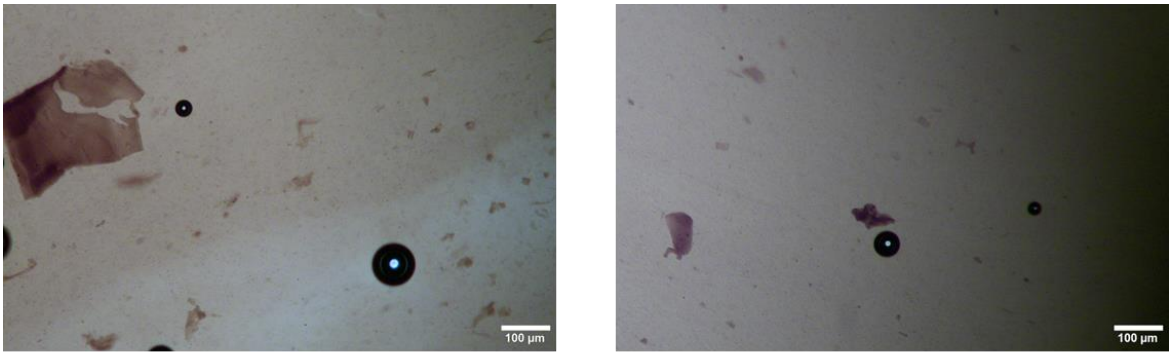


Figure 4.23: Visual observation of cellulose/ionosolv lignin (**iSL**) dope solutions in [C_2C_1im][OAc] after overnight stirring. Incomplete dissolution is visible at higher lignin loadings of 2.5 wt.% and 5 wt.%.

4.3 A novel cellulose-lignin film fabrication contribution

In summary, the comprehensive workflow for the fabrication of cellulose-lignin films is presented in Section 4.1. In this work, the developed method adheres to a more sustainable and systematic approach. The selected solvent system is environmentally benign, and the application of a moderate heating temperature of 70 °C guarantees that the procedure is not energy-intensive. The regenerated films were meticulously washed with a specified number of rinses using fresh deionised water to guarantee the thorough removal of solvents, allowing for

potential solvent recovery and recycling. The application of static airflow in drying chamber during drying facilitated the attainment of films with enhanced and consistent characteristics.

References

1 W. Luo, C. Mao, P. Ji, J. Y. Wu, J. D. Yang and J. P. Cheng, *Chem. Sci.*, 2020, **11**, 3365–3370.

2 T. A. Bioni, M. L. de Oliveira, M. T. Dignani and O. A. El Seoud, *New J. Chem.*, 2020, **44**, 14906–14914.

3 C. Zhu, A. F. Koutsomitopoulou, S. J. Eichhorn, J. S. van Duijneveldt, R. M. Richardson, R. Nigmatullin and K. D. Potter, *Macromol. Mater. Eng.*, 2018, **303**, 29–34.

4 M. Kuntapa, K. Sudaprasert and C. Tachaapaikoon, *Biomass Convers. Biorefinery*, 2023, **13**, 13037–13050.

5 X. Tan, X. Li, L. Chen and F. Xie, *Phys. Chem. Chem. Phys.*, 2016, **18**, 27584–27593.

6 Z. Ju, Y. Yu, S. Feng, T. Lei, M. Zheng, L. Ding and M. Yu, *Materials (Basel).*, 2022, **15**, 1–12.

7 J. M. Andanson, E. Bordes, J. Devémy, F. Leroux, A. A. H. Pádua and M. F. C. Gomes, *Green Chem.*, 2014, **16**, 2528–2538.

8 T. J. Simmons, S. H. Lee, J. Miao, M. Miyauchi, T. J. Park, S. S. Bale, R. Pangule, J. Bult, J. G. Martin, J. S. Dordick and R. J. Linhardt, *Wood Sci. Technol.*, 2011, **45**, 719–733.

9 K. Rajan, K. Kim, T. J. Elder, A. K. Naskar and N. Labbé, *ACS Sustain. Chem. Eng.*, 2022, **10**, 8835–8845.

10 D. L. Minnick, R. A. Flores, M. R. Destefano and A. M. Scurto, *J. Phys. Chem. B*, 2016, **120**, 7906–7919.

11 A. Brandt, L. Chen, B. E. Van Dongen, T. Welton and J. P. Hallett, *Green Chem.*, 2015, **17**, 5019–5034.

12 L. Zhang, D. Zhao, M. Feng, B. He, X. Chen, L. Wei, S. R. Zhai, Q. Da An and J. Sun, *ACS Sustain. Chem. Eng.*, 2019, **7**, 18593–18602.

13 A. Potthast, S. Radosta, B. Saake, S. Lebioda, T. Heinze, U. Henniges, A. Isogai, A. Koschella, P. Kosma, T. Rosenau, S. Schiehser, H. Sixta, M. Strlič, G. Strobin, W. Vorwerg and H. Wetzel, *Cellulose*, 2015, **22**, 1591–1613.

14 W. E. S. Hart, J. B. Harper and L. Aldous, *Green Chem.*, 2015, **17**, 214–218.

15 T. Rashid, C. F. Kait, I. Regupathi and T. Murugesan, *Ind. Crops Prod.*, 2016, **84**, 284–293.

16 R. M. Dias, L. C. G. Petrin, F. H. B. Sosa, A. M. Da Costa Lopes, J. A. P. Coutinho and M. C. Da Costa, *Ind. Eng. Chem. Res.*, 2020, **59**, 18193–18202.

17 R. Protz, A. Lehmann, J. Bohrisch, J. Ganster and H.-P. Fink, *Carbohydr. Polym. Technol. Appl.*, 2021, **2**, 100041.

18 Z. Zhang, R. Yang, W. Gao and X. Yao, *RSC Adv.*, 2017, **7**, 31009–31017.

19 S. H. Lee, T. V. Doherty, R. J. Linhardt and J. S. Dordick, *Biotechnol. Bioeng.*, 2009, **102**, 1368–1376.

20 W. Luo, C. Mao, P. Ji, J. Y. Wu, J. D. Yang and J. P. Cheng, *Chem. Sci.*, 2020, **11**, 3365–3370.

21 I. Hasanov, M. Raud and T. Kikas, *Energies*, 2020, **13**, 1–24.

22 A. Dastpak, T. V. Lourençon, M. Balakshin, S. Farhan Hashmi, M. Lundström and B. P. Wilson, *Ind. Crops Prod.*, 2020, **148**, 112310.

23 D. Glas, C. Van Doorslaer, D. Depuydt, F. Liebner, T. Rosenau, K. Binnemans and D. E. De Vos, *J. Chem. Technol. Biotechnol.*, 2015, **90**, 1821–1826.

24 M. Ghasemi, M. Tsianou and P. Alexandridis, *Bioresour. Technol.*, 2017, **228**, 330–338.

25 M. Ghasemi, P. Alexandridis and M. Tsianou, *Cellulose*, 2017, **24**, 571–590.

26 N. A. Nguyen, S. H. Barnes, C. C. Bowland, K. M. Meek, K. C. Littrell, J. K. Keum and A. K. Naskar, *Sci. Adv.*, 2018, **4**, 1–16.

27 Y. Ma, S. Asaadi, L. S. Johansson, P. Ahvenainen, M. Reza, M. Alekhina, L. Rautkari, A. Michud, L. Hauru, M. Hummel and H. Sixta, *ChemSusChem*, 2015, **8**, 4030–4039.

28 J. Ou, S. Hu, L. Yao, Y. Chen, H. Qi and F. Yue, *Chem. Eng. J.*, 2023, **453**, 139770.

29 U. Siemann, *Prog. Colloid Polym. Sci.*, 2005, **130**, 1–14.

30 R. Li, C. Chang, J. Zhou, L. Zhang, W. Gu, C. Li, S. Liu and S. Kuga, *Ind. Eng. Chem. Res.*, 2010, **49**, 11380–11384.

31 Y. Zhou, C. Chen, S. Zhu, C. Sui, C. Wang, Y. Kuang, U. Ray, D. Liu, A. Brozena, U. H. Leiste, N. Quispe, H. Guo, A. Vellore, H. A. Bruck, A. Martini, B. Foster, J. Lou, T. Li and L. Hu, *Mater. Today*, 2019, **30**, 17–25.

32 Y. Demay and J. F. Agassant, *Int. Polym. Process.*, 2021, **36**, 264–275.

33 A. Kramar, I. Rodríguez Ortega, G. González-Gaitano and J. González-Benito, *Cellulose*, 2023, **30**, 2037–2052.

34 R. Sescousse, K. A. Le, M. E. Ries and T. Budtova, *J. Phys. Chem. B*, 2010, **114**, 7222–7228.

35 W. Liu and T. Budtova, *Polymer (Guildf).*, 2012, **53**, 5779–5787.

36 X. Tan, X. Li, L. Chen and F. Xie, *Phys. Chem. Chem. Phys.*, 2016, **18**, 27584–27593.

37 X. Wang, W. Zheng, Z. Guo, H. Nawaz, T. You, X. Li and F. Xu, *Green Chem.*, 2022, **25**, 1597–1610.

38 M. T. Clough, K. Geyer, P. A. Hunt, J. Mertes and T. Welton, *Phys. Chem. Chem. Phys.*, 2013, **15**, 20480–20495.

39 J. Zhang, Xiaoyu Zhang, J. Yu and R. Li, *Regenerated Cellulose Film , Functional Film and Preparation Method Therefor*, United States Patent, 2017, vol. 2.

40 T. Vu, A. Chaffee and I. Yarovsky, *Mol. Simul.*, 2002, **28**, 981–991.

41 A. J. Holding, A. Parviainen, I. Kilpeläinen, A. Soto, A. W. T. King and H. Rodríguez, *RSC Adv.*, 2017, **7**, 17451–17461.

42 A. Brandt-Talbot, F. J. V. Gschwend, P. S. Fennell, T. M. Lammens, B. Tan, J. Weale and J. P. Hallett, *Green Chem.*, 2017, **19**, 3078–3102.

43 R. Antonella, N. Pontillo, N. Mac Dowell, K. Lee, S. Chen, F. O. Diego and T. Welton, *RSC Sustain.*, 2025, **3**, 2301–2310.

44 S. Sinquefield, P. N. Ciesielski, K. Li, D. J. Gardner and S. Ozcan, *ACS Sustain. Chem. Eng.*, 2020, **8**, 9601–9615.

45 K. Rajan, K. Kim, T. J. Elder, A. K. Naskar and N. Labbé, *ACS Sustain. Chem. Eng.*, 2022, **10**, 8835–8845.

46 K. Collier, A. Tovar, S. Goins, A. Chirgwin and A. Siegel, *J. Purdue Undergrad. Res.*, 2022, **12**, 21–28.

47 M. H. Chang and M. Oh-e, *Sci. Rep.*, 2022, **12**, 1–12.

48 ASTM D882-10, *Standard Test Method for Tensile Properties of Thin Plastic Sheeting*, 2014.

49 V. Jost and C. Stramm, *J. Appl. Polym. Sci.*, 2016, **133**, 42513.

Chapter 5: Cellulose-Lignin Film Characterisation

The aim of this chapter is to characterise the properties of cellulose and lignin as starting materials, as well as the resulting cellulose-lignin films that are formed by combining cellulose with various types of lignin. Compositional analysis will be determined on the starting materials and cellulose-lignin films to measure the proportions of structural carbohydrates, lignin, extractable components, and ash, enabling a clear understanding of how compositional variations influence the properties of the different films. Furthermore, hydroxyl content in lignin will be quantified using ^{31}P NMR to observe direct impact on the film's properties. Finally, the cellulose-lignin composite films will be thoroughly characterised in terms of their physical, chemical, mechanical, and thermal properties.

5.1 Cellulose and cellulose film characterisation

Cellulose was the main component used in the film fabrication, maintained at a constant content of 10 wt.% relative to the total amount of ionic liquid in the dope solution. The cellulose used in this project was Sigmacell Cellulose Type 101 ($(C_{12}H_{22}O_{11})_n$), purchased from Sigma-Aldrich. A comparative analysis was performed to examine how the chemical, physical, and thermal properties of the cellulose powder (**cel**) changed after it was dissolved in [C_2C_1im][OAc], and recovered as a regenerated cellulose film (**10cel**) using water as an antisolvent.

5.1.1 SEM

Scanning electron microscopy (SEM) is a useful technique for examining materials, analysing their texture, and studying their topography due to its ability to provide high-resolution images. **Cel** powder exhibits an indefinite and heterogeneous morphology in terms of its shape and size, as depicted in Figure 5.1. The mean size of **cel** is approximately 50 micrometres. **Cel** is a type of microcrystalline cellulose (MCC) and its morphology matches previously reported structures for MCC. A literature article presented an SEM image of MCC, with a significant quantity of cellulose microcrystals mixed with amorphous regions.[1] This claim is supported by

the MCC observed in the sample at x330 magnification (left) and at x6500 magnification (right). In the left image, the amorphous portion exhibits an uneven, porous, and disorganised texture, while the right image reveals this morphology in greater detail, highlighting the increased surface roughness and irregular pore structure. The XRD results in section 5.1.2 indicate that a portion of the MCC exhibits crystalline characteristics, with peaks at 16.0°, 22.5°, and 32.8°.

Meanwhile, the **10cel** exhibits a predominantly smooth surface with some indentations, as shown in Figure 5.2 (left), while the cross-sectional image (right) reveals a relatively dense and uniform internal structure across the film thickness. The indentations likely occur when drying at a controlled relative humidity of 50%. Despite the use of controlled and slow drying, the semi-crystalline nature of cellulose may cause the amorphous regions to experience greater shrinkage during film formation, leading to surface indentations. This observation closely resembles the one described in the literature for cellulose nanofibril (CNF) film.[2] Carboxymethyl cellulose (CMC) films in the literature had a smooth and dense surface at 0% lignin present.[3] Although both **cel** and **10cel** are solid materials, effective dissolution followed by regeneration allows the cellulose to be processed into a uniform, thin sheet film. This transformation is achieved through the film-fabrication method detailed in Chapter 4.

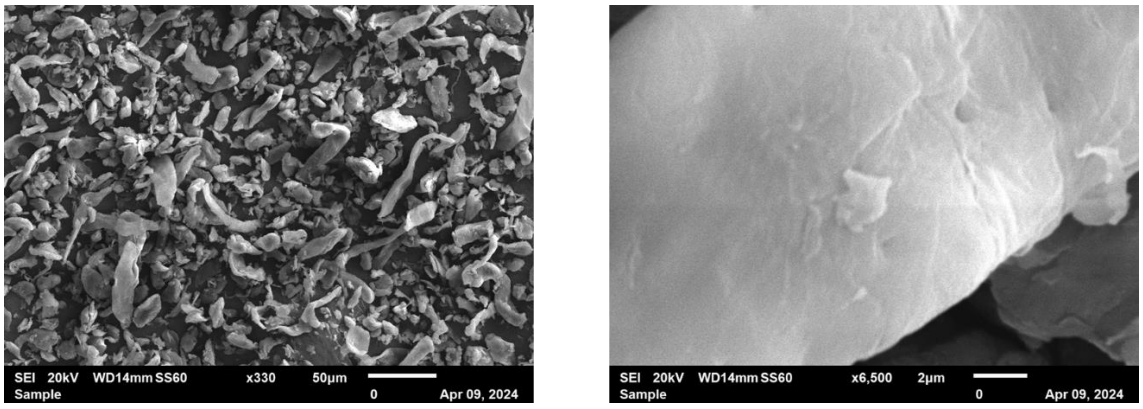


Figure 5.1: SEM images of cellulose powder at different magnifications. The left image shows the overall particle morphology at ×330 magnification (scale bar: 50 µm), while the right image shows surface features at ×6500 magnification (scale bar: 2 µm)

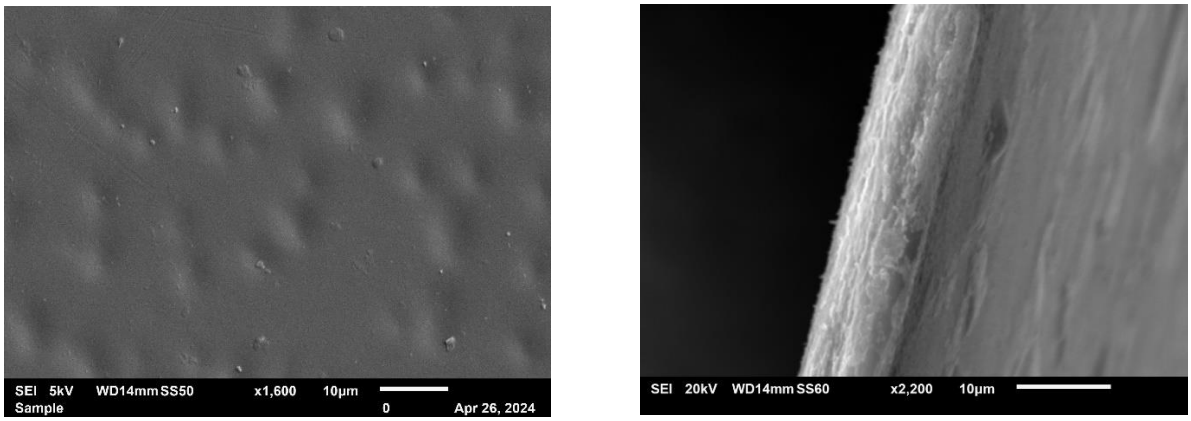


Figure 5.2: SEM images of regenerated cellulose thin film (left on the surface at 1600 magnification) and (right on the cross section at 2200 magnification)

5.1.2 Crystallinity by XRD

Cellulose contains both crystalline and amorphous regions, as shown in the SEM images in Section 5.1.1, which makes it suitable for analysis using X-ray diffraction (XRD). XRD analysis was employed to evaluate the crystallinity of **cel** and **10cel**, as well as to investigate how the dissolution process with [C_2C_1im][OAc] and DMSO modifies their structure.

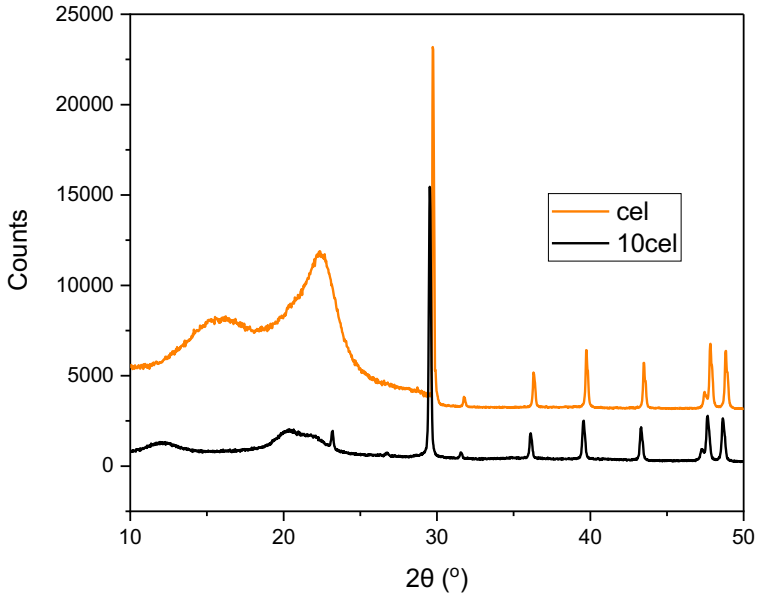


Figure 5.3: XRD patterns of cellulose powder and regenerated cellulose film

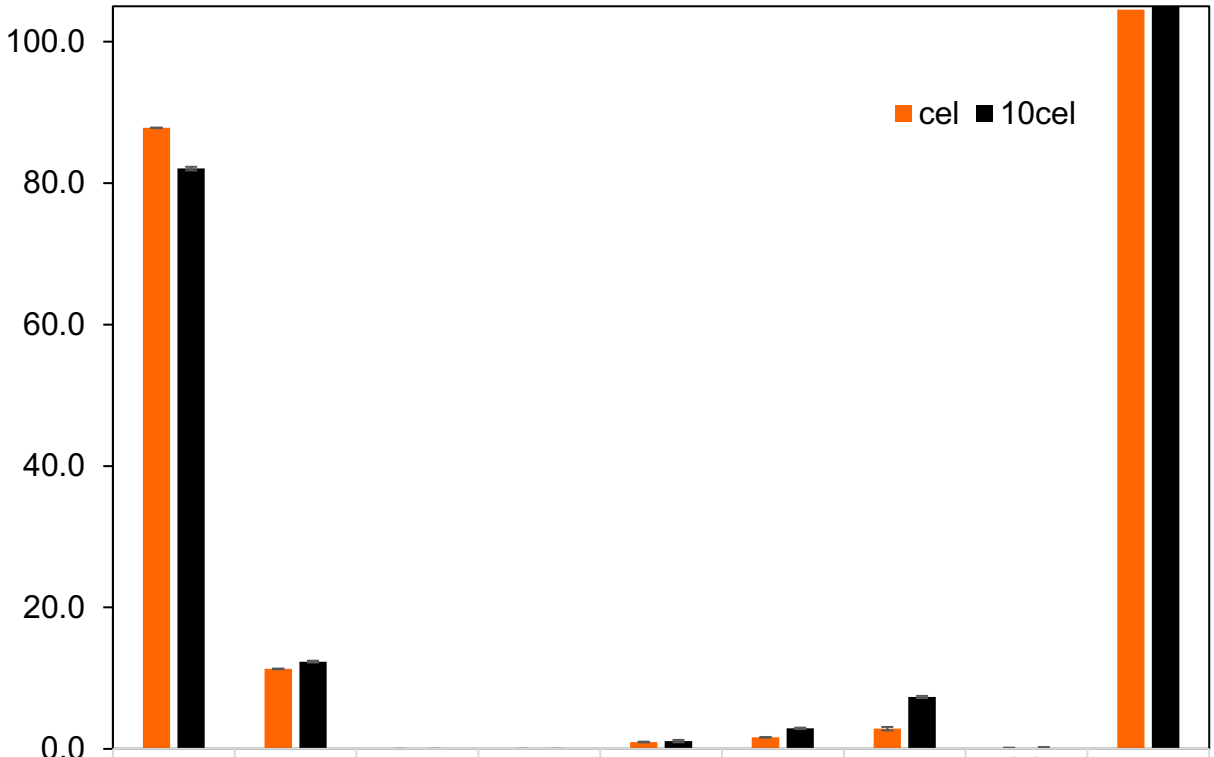
Cellulose exhibits different polymorphic forms, mainly cellulose I (native cellulose) and cellulose II (regenerated or mercerized cellulose), each displaying unique crystalline structures. XRD analysis can distinguish between these types by their distinct diffraction peaks. Cellulose I generally exhibits peaks at around 2θ = 16.0°, 22.5°, and 32.8°, which correspond to the (101), (002), and (040) planes, respectively. Conversely, cellulose II displays characteristic diffraction patterns at 2θ = 20.1° and 21.2°. To verify the crystalline structure of **cel** and **10cel**, the XRD results have been compared with literature-reported patterns of authenticated cellulose I and cellulose II samples.[4,5,6] The noticeable disappearance of peaks at 16.0° and 21.2° in Figure 5.3 suggests a rearrangement of cellulose macromolecules during the processes of dissolution and regeneration of cellulose II. The transition from cellulose I to cellulose II is associated with a relative decrease in crystallinity and an increase in amorphous content. The XRD pattern indicates that **10cel** remains in crystalline form, suggesting that the regenerated film consists of a mixture of cellulose I and cellulose II. This conclusion is supported by a dissolution study of microcrystalline cellulose (MCC) in varying amounts of DMSO and pure tetraoctylphosphonium acetate ([P_{8888}][OAc]), an ionic liquid. With an excess of cellulose (10 wt.%), a portion of the cellulose swells rather than dissolves, resulting in an intermediate mixture of cellulose I and cellulose II polymorphs.[7]

The XRD pattern of the **10cel** sample exhibits multiple strong diffraction peaks missing in the majority literature on **cel** pattern.[4,5,6] The peaks are situated at roughly 23.1°, 29.5°, 36.1°, 39.4°, 43.2°, and 47.5° 2θ. These do not align with the crystalline reflections of cellulose I or II. Comparison with typical diffraction patterns from the crystallography open database indicates that these peaks correspond closely to the calcite form of calcium carbonate ($CaCO_3$) which similar pattern found in literature,[8] suggesting the existence of an extra inorganic crystalline phase. This molecule likely originates from the cellulose extraction process, maybe due to the inadequate removal of mineral fillers typically utilised in industrial paper manufacture.[9] The presence of $CaCO_3$ highlights the necessity for enhanced washing or purification in cellulose recovery. The overlap of the carbonyl in $CaCO_3$ with the C-O in cellulose in FTIR (Section 5.1.4) was confirmed at the pronounced C-O stretching peaks around 1420 cm^{-1}.

5.1.3 Compositional Analysis

The compositional analysis (CA) was performed in this section to quantitatively evaluate the proportions of sugars, lignin, extractable components, and ash in **cel** and **10cel**. Both substances contain the same cellulose, although they have different physical forms and structural arrangements. Cellulose is a fine loose powder and consists of small particles with no cohesive structure, whereas **10cel** is a continuous thin film and restructured into a dense and cohesive matrix. However, for the purpose of sample preparation in this analysis, the regenerated cellulose must be in the form of a powder. The samples were prepared at a particle size of 50 mesh (300 microns) for regenerated films, whereas the cellulose powder was used as per supplied by the manufacturer with an average particle size of 50 microns (refer to SEM images in subtopic 5.1.1, Figure 5.1). This is because the analysis is highly sensitive to the size of the particles.

An overly large particle is not effective for analysis as the concentrated sulphuric acid is unable to break down the substance. This requirement creates a challenge for sample preparation, as the CA Laboratory Analytical Procedure is primarily designed for biomass materials, which naturally exist in powder or easy to grind forms.[10] High particle size can lead to a lower accuracy in measuring carbohydrate content and a higher bias towards lignin due to the inadequate breakdown of complex sugars into simpler sugars. The CA of **cel** and **10cel** is shown in Figure 5.4.



	Glucose	Xylose	Galactose	Arabinose	Mannose	% ASL	% AIL	Ash residue	Total
cel	87.8	11.3	0.0	0.0	1.0	1.6	2.9	0.1	104.5
10cel	82.1	12.3	0.0	0.0	1.1	2.9	7.3	0.1	105.9

Figure 5.4: Compositional analysis of cellulose powder and regenerated cellulose

The CA for **cel** and **10cel** exhibited a high degree of similarity, particularly in terms of their sugar composition. The primary sugar detected in both samples was glucose, accounting for approximately 82.1% to 87.8% of the total sugar content. Glucose is a hexose monosaccharide containing six carbon atoms and is the most abundant monosaccharide in the samples. The 5.7% reduction in glucose content observed in **10cel** suggests less efficient hydrolysis of regenerated cellulose in sulfuric acid, likely because **10cel** was not originally in powder form, unlike **cel**. The outcome for the total sugar concentration in both **cel** and **10cel** was 101.1 ± 0.02% and 95.5 ± 0.04%, respectively. According to Raza et al. (2022), the composition of cellulose nanocrystal (CNC) was found to be 94.3% sugars, while the remaining 5.7% of CNC is believed to consist of chemical contaminants such sodium hydroxide, sodium sulphate, and small amounts of other minerals.[5] This literature employs an alternative approach for doing compositional analysis. The method T 204-cm-97, established by the Technical Association of

Pulp and Paper Industry (TAPPI) was employed which can be found in their paper. Therefore, a direct comparison could not be made.

Mannose, is a C-2 epimer of glucose, meaning it differs from glucose in the position of the hydroxyl group at one carbon. Mannose was present albeit in lower quantities for **cel** and **10cel** at 0.9 and 1.1 %, respectively. Xylose was the second most abundant sugar in both celluloses accounted 11.3 and 12.3 %. Xylose is a monomer of hemicelluloses,[11] meaning the presence of xylose indicates that the celluloses still contains some hemicellulose. Bleached hardwood kraft pulp can be upgraded to dissolving pulp by selectively removing hemicelluloses, particularly xylan. Although techniques like cold alkaline extraction are well studied, they may not completely remove hemicellulose.[9]

Moreover, small percentages acid soluble lignin (ASL) (1.6 % and 2.9%) and acid insoluble lignin (AIL) (2.8 and 7.3%) were found in **cel** and **10cel**, respectively. ASL denotes lignin components solubilised through acid hydrolysis, measured via UV-Vis spectrophotometry. AIL represents the portion of lignin that remains insoluble during acid hydrolysis and is generally quantified gravimetrically. The sole distinction between **cel** and **10cel** is in the composition of ASL and AIL, which is only slightly impacted. **10cel** has a greater amount of ASL and AIL compared to **cel**, with increases of around 1.3% and 4.4%, respectively. The ASL and AIL probably indicate trace lignin or lignin-like contaminants that persisted during the cellulose extraction process. It is essential to eliminate lignin and other constituents to obtain pure cellulose.[12] Lignin functions as an adhesive that binds hemicellulose and cellulose; hence, for the successful extraction of cellulose, the removal of other components such as lignin, hemicelluloses, and undesired impurities must be meticulously controlled.[13] Minor aromatic or lignin-derived molecules might persist and be identified as ASL and AIL in CA analysis. The FTIR spectra in Figure 5.5 exhibited substantial absorption of CH vibrations at 892 – 896 cm^{-1}, suggesting the presence of a minor quantity of aromatic compounds.

5.1.4 FTIR

Fourier Transform Infrared Spectroscopy (FTIR) is a straightforward and precise method for identifying the chemical bonds that exist within a molecule. This investigation aims to

determine whether there are differences in the functional groups present in **cel** and **10cel**. Figure 5.5 illustrates the superimposed FTIR spectrum for **cel** and **10cel**.

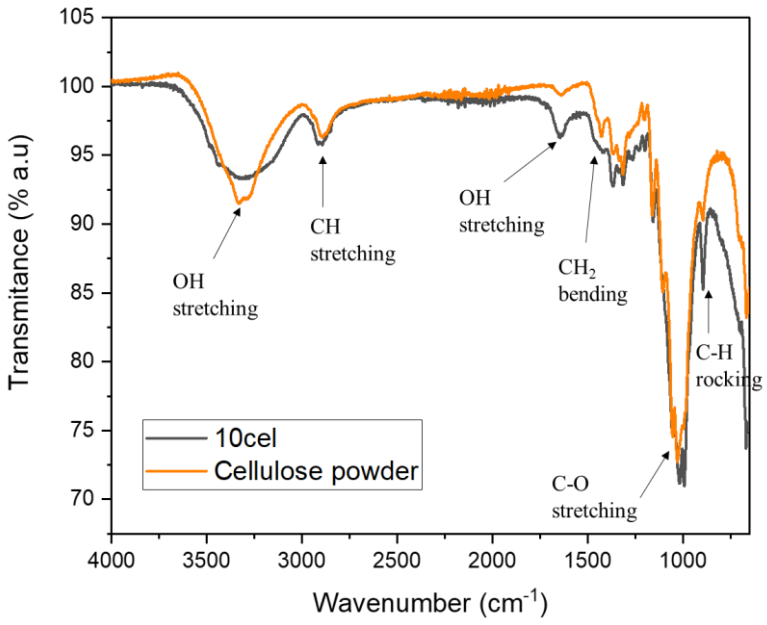


Figure 5.5: Fourier transform infrared spectroscopy of cellulose powder and regenerated cellulose (**10cel**)

In general, the spectra of **10cel** and **cel** are almost identical, except for the widened OH stretching observed in **10cel**, which is attributed to its greater moisture content in comparison to **cel**. The TGA data confirms that **10cel** has a moisture content that is 5.3 wt.%, more than **cel**, which has a moisture content of only 2.8 wt.%, as shown in Figure 5.8. The **cel** and **10cel** FTIR spectrum was discovered to be comparable to the ones documented in the literature for α- and β-cellulose.[14] The distinction lies in their crystalline structure and alignment of polymer chains, with cellulose I being the native form and cellulose II being the processed form. Cellulose I has higher crystallinity, while cellulose II is more stable and less crystalline. The absorbance bands observed at 3440–3443 cm^{-1} (O–H stretching), 2910–2920 cm^{-1} (C–H stretching), 1650 cm^{-1} (O–H bending of absorbed water), 1430–1420 cm^{-1} (C–H bending), 1026–1050 cm^{-1} (C–O–C stretching), and 892–896 cm^{-1} (C–H rocking) are characteristic of cellulose and are common to both cellulose I and cellulose II. The findings of this study indicate that the regenerated cellulose possesses a molecular structure that closely resembles the original form. This suggests that the process of fabricating cellulose film has been executed

accurately, with the complete removal of the ionic liquid in the coagulation bath as indicated in Figure 5.6.

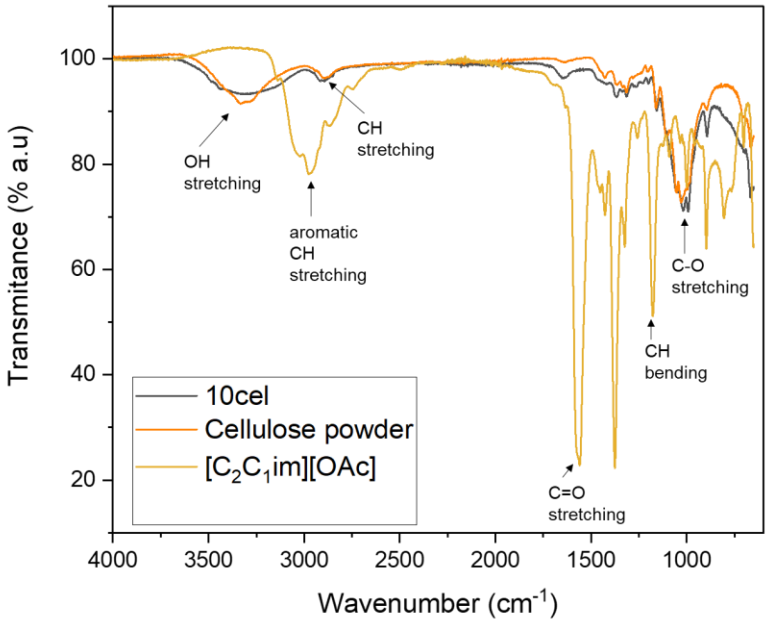


Figure 5.6: Fourier transform infrared spectroscopy of **10cel** and **cel** indicating complete removal ionic liquid of $[C_2C_1im][OAc]$

5.1.5 Thermal Analysis

A thermogravimetric analysis (TGA) was performed to examine the thermal stability of **cel** and thin film **10cel**. While plastic packaging is commonly utilised for domestic purposes at normal room temperatures, it is important to understand the thermal resistance of cellulose thin films, especially in extreme condition. This information can be employed when the thin film comes into touch with a heated object or during a sterilisation procedure. The TGA curves of **cel** and **10cel** were analysed, as shown in Figure 5.7. A temperature ramp was conducted at 105°C to eliminate any moisture present in the compounds as indicated in Figure 5.8. The moisture content in cellulose typically ranges from 3% to 7% for the majority of commercially available MCC products. The **cel** and **10cel** samples comprise 2.83% and 5.29% water, respectively.

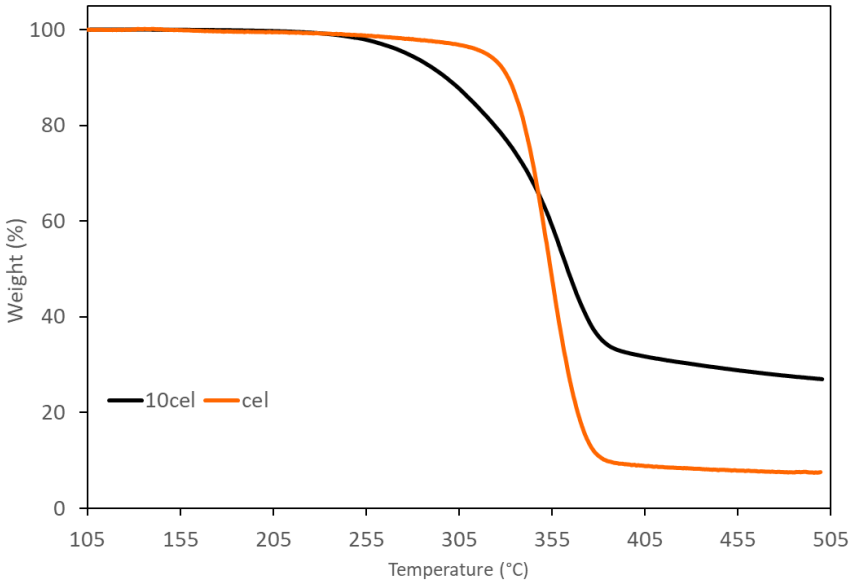


Figure 5.7: Thermograms of cellulose (**cel**) and regenerated cellulose (**10cel**)

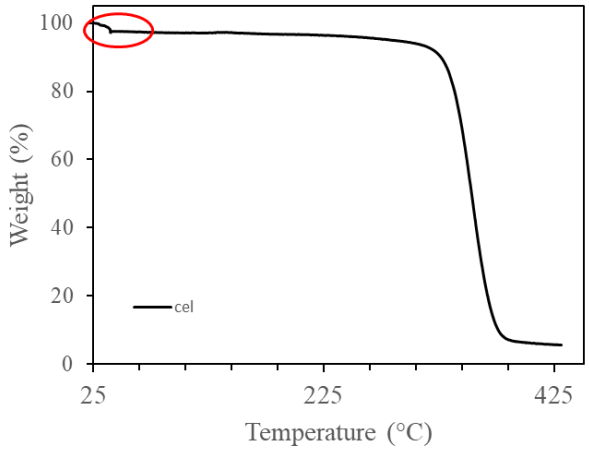


Figure 5.8: Original TGA curve of cellulose **(cel)** before modification of removing moisture content part at 105°C

The thermal degradation of **cel** and **10cel** occurred in a single step, with the maximum decomposition temperatures observed at 314.7°C and 250.4°C, respectively. The T_{onset} temperatures for **cel** and **10cel** were 340.0°C and 317.5°C, respectively. The T_{onset} temperature indicates the initiation of a thermal event or reaction. The T_{onset} **cel** is consistent with the literature, which exhibited a weight loss at a maximum temperature of 358 °C, using the same microcrystalline material as in this project.[15] The superior thermal stability of **cel**, in comparison to **10cel**, can be attributed to the inherent characteristics of MCC, which possesses a greater proportion of crystalline regions compared to the more amorphous regions of **10cel**, as indicated in section 5.1.2. Consequently, the crystalline regions exhibit a higher degree of

order and require increased energy for breakdown during thermal degradation.[5] Moreover, the extensive hydrogen bond networks within the crystalline regions of **cel** provide enhanced heat resistance compared to **10cel**; nevertheless, solvent dissolution during regeneration compromises and disrupts these hydrogen bonds, resulting in reduced thermal stability.[16]

The main difference between **cel** and **10cel** was the residual weight at 500 °C, with **cel** and **10cel** yielding 7.59 wt.% and 27.34 wt.%, respectively. This significant difference indicates that the dissolving process prompted structural reconfiguration in **10cel**, resulting in an increased yield of thermally stable residue. Literature indicates that the commercial microcrystalline cellulose (MCC) Avicel PH101 leaves a char residue weighing 12.23 wt.% at 400 to 700°C.[17] This literature value is slightly higher than that observed in this study, likely because part of the moisture content in the material was not eliminated during the TGA measurement. Another research on regenerated cellulose films indicated that the residual weight at 600°C is claimed to range from 18 to 23 wt.%.[18] This finding is supported by the discovery of thermal stability in regenerated cellulose film following the incorporation of DMSO and $CaCl_2$, resulting in a residual weight of 22 wt.%.[19]

5.2 Lignin characterisation

Lignin is a biopolymer that acts as a binder for cellulose and hemicellulose fibres, giving plants their rigidity.[13] Multiple techniques exist for isolating lignin from biomass. This project involves the utilization of two different types of wood, namely hard wood and soft wood, with varying extraction methods to fabricate cellulose-lignin films, as depicted in Table 5.1. The main difference between hardwood and softwood lignin lies in its sources, compositions and structure, which result in varied applications. Hardwood lignin, shown by beech, consists of syringyl (S) and guaiacyl (G) monolignols together with a minor proportion of p-hydroxyphenyl (H) units, whereas softwood lignin, represented by spruce, is comprised solely of G monomers.[20, 21] The elevated ratio of S units in hardwood results in a more linear and less cross-linked structure in comparison to softwood lignin.[22] The major subunits present in lignin are illustrated in Figure 5.9.

Table 5.1: Different type of lignins used in cellulose-lignin films

Sources	Hardwood		Softwood	
Extraction processes	organosolv	ionosolv	kraft	ionsolv
Wood species	Beech	Beech	Unknown	Spruce
Suggested symbol	**oHL**	**iHL**	**kSL**	**iSL**

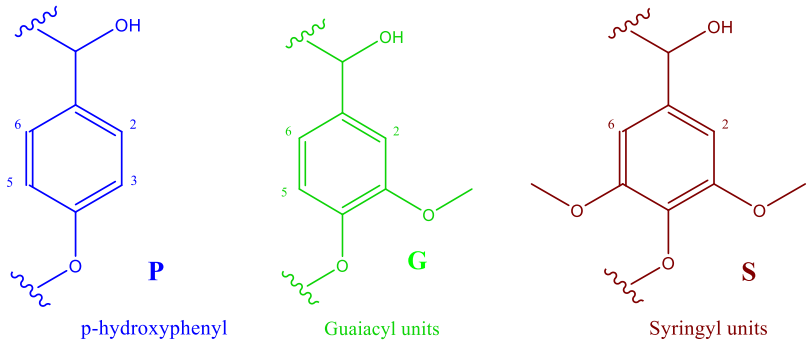


Figure 5.9: Lignin subunits are denoted based on the methoxyl substitution on the aromatic ring as P, G and S units

A comprehensive grasp of lignin characterisation is crucial for accurately assessing its purity, molecular structure, and thermal properties. It is also necessary to determine whether there will be a major or negligible difference in lignin characterisation when comparing the same species but different extraction methods. This study utilised several analytical techniques, such as ^{31}P NMR, 2D HSQC NMR, GPC, FTIR, CA, and TGA, to comprehensively characterise lignin.

5.2.1 GPC analysis

Gel permeation chromatography (GPC) facilitates the characterisation of polymeric molecular constituents by size and separates sample molecules in the mobile phase. Larger molecules elute more rapidly than smaller ones due to the ability of tiny molecules to diffuse into or out of the pore, while larger molecules are largely excluded. [23] Before discussing the GPC results, GPC analysis of lignin conducted in this study was performed under certain instrumental limitations. At the time of measurement, the major GPC system in use lacked a functional refractive index (RI) detector, which is generally the most appropriate for lignin due to its low UV absorbance and comparatively short polymer chain length. A viscometer detector was utilised as an alternative. Nevertheless, owing to lignin's weak signal response in the viscometer and its reduced inherent viscosity relative to cellulose, an increased sample loading was

necessary to achieve a detectable signal. This increased concentration presents a recognised risk of promoting lignin aggregation, instead of quantifying isolated polymer chains.

DMSO combined with LiBr was employed as the eluent to diminish intermolecular interactions. Despite these precautions, some level of aggregation cannot be completely avoided; hence, the molecular weight data acquired should be read carefully. Although these limitations impact the definitive accuracy of the results, the data nonetheless offer significant comparative insights into the patterns and relative alterations in lignin properties under varying settings. Optimal molecular weight determination would ideally require a fully functional RI detector, currently accessible in the upgraded analytical suite.

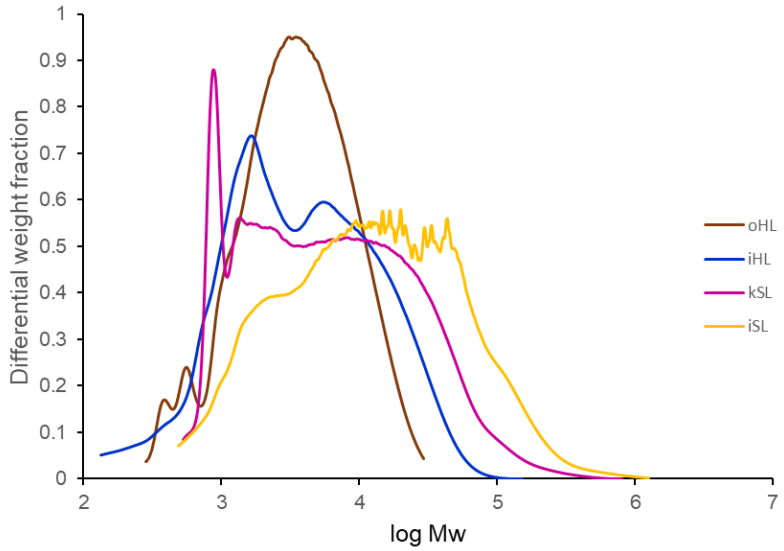


Figure 5.10: Overlaid molecular weight distributions (MWD) of hardwood lignin (**oHL** and **iHL**) and softwood lignin (**kSL** and **iSL**)

Table 5.2: Number Average Molecular Weight (Mn), Weight Average Molecular Weight (Mw), and Polydispersity Index (PDI) corresponding to the lignin

Lignin samples	Mn (g/mol)	Mw (g/mol)	PD
oHL	2135	4989	2.34
iHL	1062	7385	6.95
kSL	2790	15690	5.62
iSL	4613	32635	7.07

Utilizing GPC with molar mass-sensitive detectors, such as a viscometer, enables the calculation of absolute molar mass and molar mass distribution, independent of the chemical properties of calibration standards. Lignin concentration was assessed with a UV-Vis detector

at 340 nm, and the sample's molecular weight distribution was evaluated via GPC utilizing a calibration curve (refractive index detector). In lignin samples, low molecular weight (mw) was seen for hardwood lignin, whereas high molecular weight (mw) was noted for softwood lignin, as illustrated in the molar mass distribution in Figure 5.10 and Table 5.2. The elevated molecular mass of softwood results in a more stable, condensed, and maintained structure owing to an increased amount of guaiacyl (G).[24] Concurrently, hardwood lignin exhibits a more linear or less condensed structure owing to a greater number of syringyl (S) units, potentially influencing its compatibility with cellulose.

Literature values for spruce milled wood lignin, show Mn = 4640 g/mol, Mw = 29,580 g/mol, and PD = 6.37.[25] The spruce lignin extracted with the ionosolv method (**iSL**) in this study exhibited Mn = 4613 g/mol, Mw = 32,635 g/mol, and PD = 7.07, indicating comparable molecular weight properties. **iSL** significantly higher than that of all other isolated lignins (**oHL**, **iHL**, and **kSL**). This elevated molecular weight is attributed to both the botanical origin of the feedstock and the extraction mechanism. Softwood lignin consists almost exclusively of G units, which possess an unsubstituted C5 position on the aromatic ring. This permits extensive cross-linking via recalcitrant carbon–carbon bonds, which are highly resistant to cleavage during processing. Unlike the severe cleavage of β-O-4 ether bonds observed in Kraft pulping **kSL**, the ionic liquid system used in ionosolv extraction selectively dissolves intact macromolecular fragments from the plant matrix with minimal depolymerization.[26]

Furthermore, these findings may be compared across different sample types of hardwood lignin, elucidating clear trends where softwood lignin consistently exceeds hardwood lignin in molecular weight. Hardwood contains a mixture of G and S units; the steric hindrance from methoxy groups on the S units limits C-C cross-linking, making hardwood lignin inherently easier to depolymerize into lower molecular weight fractions. The beechwood lignin isolated using organosolv (**oHL**) in this study has Mn of 2135 g/mol, Mw of 4989 g/mol, and a PD of 2.34. This is contrasted with literature values for the same isolation process and species, which indicate Mn as 640 g/mol, Mw as 2350 g/mol, and PD as 3.67.[27] The elevated Mw and Mn in this study suggest altered extraction conditions relative to the literature. The solvent, temperature, and reaction duration employed in organosolv extraction can substantially influence lignin characteristics.

Low polydispersity index (PDI) values signify a more uniform distribution of molecular weights across lignin fragments, indicating that the fragments exhibit more size homogeneity. Lignin with a low PDI in hardwood lignin is typically highly stable and exhibits a narrow molecular weight distribution, making it especially appropriate as a polymer additive.[28] A greater PDI indicates a wider distribution of molecular weights, which can be beneficial in specific value-added applications such as polymer composites, where it enhances melt processability and mechanical performance.

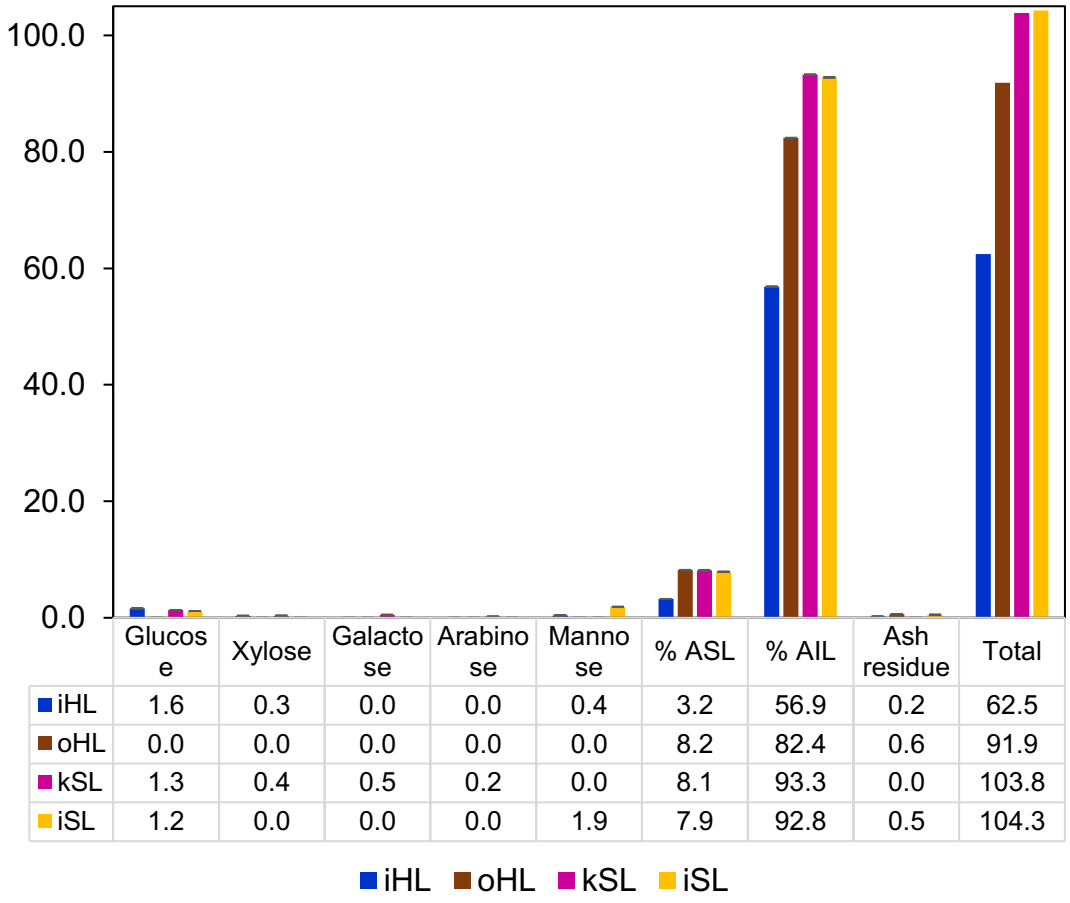
5.2.2 Compositional Analysis

Compositional analysis (CA) reliably determines the content of sugars and lignin present in biomass.[10] In this context, all lignin samples were quantified by CA method to determine their purity. Soluble lignin (ASL) and acid soluble lignin (AIL) are expected to be the majority composition in all lignin samples. ASL is quantified after hydrolysis with concentrated sulphuric acid using spectrophotometric absorbance measurements, while AIL is determined by drying the residue at 105°C. The approved value for CA is from 95 to 105% given that this method inherent uncertainties, as discussed in Section 5.1.2. Analytical apparatus and machine errors involved in CA, such as chromatographs or spectrometers, include inherent precision limits and may exhibit minor variations due to detector sensitivity. Minor variations in sample preparation result from human error.

Softwood lignins, **kSL** and **iSL** were reported to have total lignin (ASL plus AIL) counted as 101.4% and 100.7 %, respectively as indicated in Figure 5.11. Both lignins exhibited minimal residual carbohydrates in the extracted lignin, ranging from 2.4 to 3.0%. A review study explained lignin in plant cell walls is covalently bonded to hemicellulose and other polysaccharides via lignin-carbohydrate complexes.[29] The connections are difficult to fully break during isolation, resulting in residual carbohydrates which cannot simply diminished. Overall, both **kSL** and **iSL** contain high purity lignin.

Conversely, hardwood lignin, specifically **iHL** and **oHL**, exhibits total lignin (ASL plus AIL) percentages of 60.3% and 91.9%, respectively. **iHL** is the self-synthesized ionosolv lignin.

Meanwhile, **oHL** is the commercial product from the organosolv extraction. Several reasons contribute to the low lignin content especially for **iHL**. **iHL** was proven to have residual polymeric carbohydrates which may interfere with the determination in CA. This is evident at C2/H2, C3/H3, and C5/H5 in β-D-glucopyranoside, as illustrated in Figure 5.12. This sugar exists in a bonded state as lignin-carbohydrate complexes (LCC)[29], likely representing glycosidic links rather than free monomeric sugars detectable by HPLC. **oHL** is not impacted by this interference as seen in Figure 5.12 which contributes to increased lignin output than **iHL**. The low lignin contributed from LCC or carbohydrates related product.



	Glucose	Xylose	Galactose	Arabinose	Mannose	% ASL	% AIL	Ash residue	Total
iHL	1.6	0.3	0.0	0.0	0.4	3.2	56.9	0.2	62.5
oHL	0.0	0.0	0.0	0.0	0.0	8.2	82.4	0.6	91.9
kSL	1.3	0.4	0.5	0.2	0.0	8.1	93.3	0.0	103.8
iSL	1.2	0.0	0.0	0.0	1.9	7.9	92.8	0.5	104.3

Figure 5.11: Compositional analysis for different types of lignin which are softwood lignin (**kSL** and **iSL**) and hardwood lignin (**iHL** and **oHL**)

Ionosolv extraction typically produces lignin of high purity, as reported in previous studies.[30] However, the **iHL** obtained in this work exhibited a comparatively low purity of only 60.3%, indicating that the extraction conditions were not fully optimised for this feedstock. Two factors likely contributed to this outcome. First, the beech wood chips supplied for the study

had undergone prior heat-treatment, meaning the biomass was no longer in its native state. Such thermal preprocessing can promote lignin condensation, particularly under severe pretreatment conditions, where the β-O-4 ether linkages being the most labile and cleave subsequently form condensed structures.[31] Second, the optimisation strategy followed was based on the method of Brandt, A. et al.[32] which was developed for *Miscanthus giganteus*, a perennial grass. Because hardwood lignin differs substantially from grass lignin in structure and reactivity, these parameters were not directly transferable, likely leading to suboptimal fractionation of the beech-derived lignin.

Another cause, could be due to an incomplete hydrolysis of **iHL** lignin in the sulfuric acid. Some lignin components might remain in a partially degraded or chemically changed form such as LCC that is not accounted for in either the soluble or insoluble fractions. Consequently, **iHL** lignin exhibited a lower weight percent ratio than the anticipated value. A mild pretreatment, such as pretreatment, such as specific enzymatic hydrolysis as suggested by literature[29], could serve as a method to cleave lignin-carbohydrate complexes linkages.

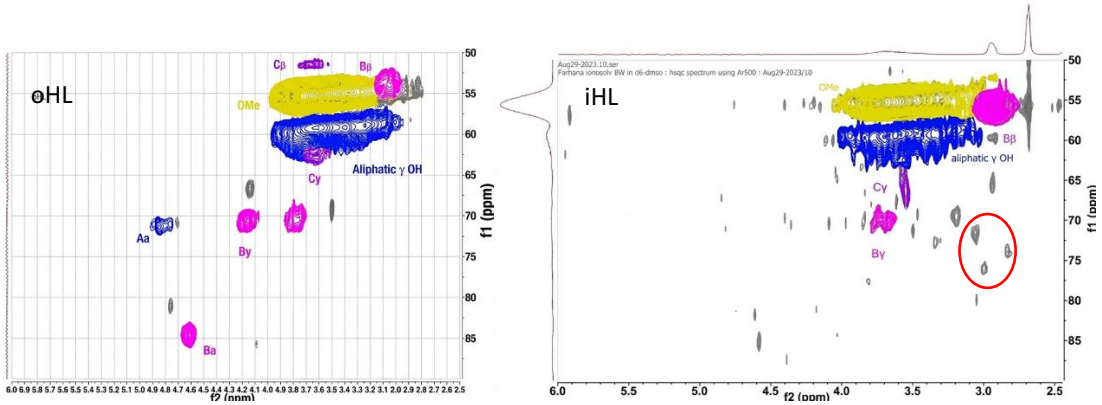
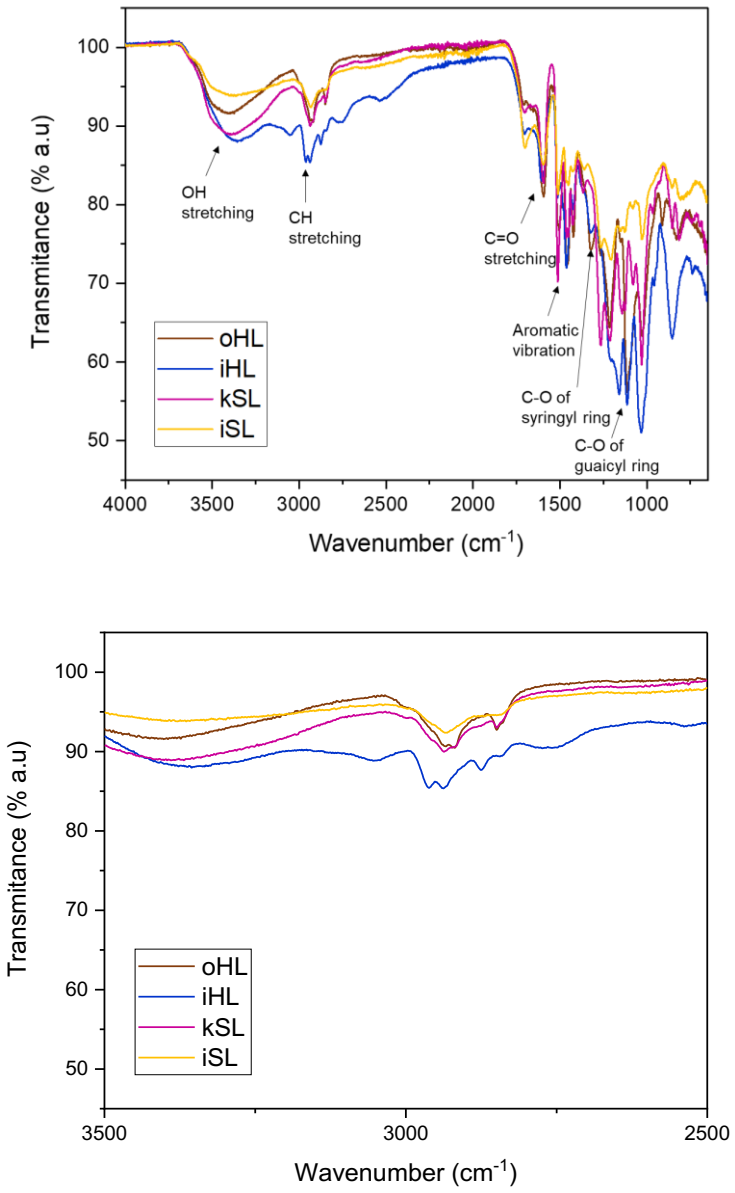


Figure 5.12: HSQC NMR identification β-D-glucopyranoside in hardwood lignin

5.2.3 FTIR

FTIR was employed for the molecular characterisation of the predominant functional groups in softwood and hardwood lignin at different extraction methods which are **iSL**, **kSL**, **iHL** and **oHL**. Softwood and hardwood lignin can be distinctly identified in the fingerprint region at specific wavenumbers, [33] as identical wood types exhibit the same absorption-band patterns, as shown in Figure 5.13. The main vibrational modes observed in lignin include O–H stretching of associated hydroxyl groups (3450–3380 cm^{-1}), C–H stretching of CH_2 and CH_3 groups in

aliphatic side chains (2932–2842 cm^{-1}), and various skeletal vibrations of aromatic rings (1607–1515 cm^{-1}),[16] as summarised in Table 5.3. In addition to these general features, more specific absorptions provide detailed information about the lignin subunits. The asymmetric bending of methyl and methylene groups around 1460 cm^{-1} displays a consistent absorption band pattern across all samples. The band at 1269 cm^{-1}, characteristic of the G unit, is observed in all lignin samples.[34] The C–O bond of the syringyl ring is detected exclusively in hardwood lignin and is absent in softwood lignin, consistent with HSQC NMR results, which confirm that the syringyl unit occurs only in hardwood lignin.



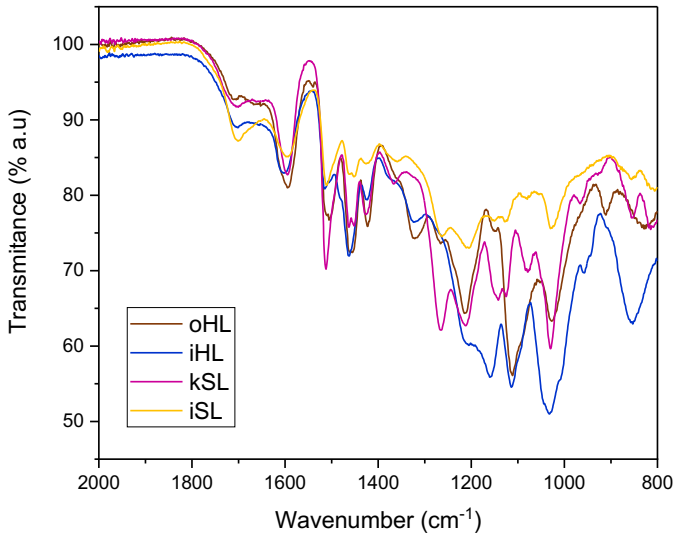


Figure 5.13: FTIR spectra for different types of lignin in softwood and hardwood lignin

Table 5.3: FTIR assignments correspondence in hardwood and softwood lignin

Band (cm^{-1})		Assignments
Softwood lignin	Hardwood lignin	
3450	3450 – 3380	O-H stretching
2930	2930	C-H asymmetric stretching
2842	2875 - 2842	C-H symmetric stretching
1700	1700	C=O stretching
1600; 1520	1600; 1512	Aromatic skeletal vibration
1459	1460	Asymmetric bending deformation of methyl and methylene groups
1425	1425	C-H in-plane deformation with aromatic ring stretching
1370	1370	Symmetric bending deformation of methyl group
-	1326	C-O of syringyl ring
1269	1269	C-O of guaicyl ring
1215	1215	C-C and C-O stretch
1127	1116	C-O deformation in ester bond
1030	1030	Aromatic C-H in-plane deformation (G>S)
856	856 - 839	C-H out-of-plane (2,5,6 in G units)

The most common types lignin such **kSL** and **oHL**, which are widely available because of commercial extraction, could be compared with existing literature. The FTIR spectra results of **kSL** and **oHL** align with existing literature,[35,33] and no new bands are observed in the spectrum. The band resemblance is noted within a broad band ranging from 3200 to 3500 cm^{-1}, attributed to the stretching vibrations of -OH in alcoholic and phenolic hydroxyl groups. The bands at 2935 and 2842 cm^{-1} correspond to C–H asymmetric stretching vibrations in methoxy groups ($-OCH_3$) and symmetrical vibrations of $-CH_2-$ in the side chains of lignin moieties,

respectively. The bands within the range of 1604−1425 cm^{-1} are attributed to the vibrations of the aromatic rings, indicating that the aromatic characteristics of lignin from various extractions correspond with those of organosolv lignin and kraft lignin.[33] The signal at 1709 cm^{-1} corresponds to the stretching vibration of C—O bonds in carboxylic esters, conjugated aldehydes, or non-conjugated ketones within the aromatic ring. The signal at 1326 cm^{-1} is attributed to C–O in alcohols, ethers, or carboxylic esters and is associated with syringyl units. The band at 1031 cm^{-1} is indicative of the aromatic C–H in-plane deformation predominantly in G aromatic units of lignin.[33,27]

The scarcity of literature regarding softwood lignin extracted via the ionosolv makes FTIR spectral analysis for our **iSL** samples difficult to compare with other studies. Much of the literature characterises lignin structure by 2D HSCQ NMR, which provides comprehensive proton and carbon correlations to elucidate the links present in lignin. The nearest reference is to the comparison with grass species *Miscanthus* subjected to ionosolv pretreatment utilising the protic ionic liquid triethylammonium hydrogen sulphate, $[N_{2220}][HSO_4]$.[36] The discourse focusses solely to the fingerprint region. The bands identified in **iSL** had nearly identical values and a minor shift from the FTIR spectra. The similar band at 1700 cm^{-1} can be ascribed to the stretching of carbon-oxygen double bonds, as observed in carboxylic acids and esters. The band at 1215 cm^{-1} is characteristic of C-O single bond stretches in esters, while alkyl-aryl C–O single bond stretches also absorb at this wavenumber. Alkyl-aryl C–O single bonds exist in lignin as methoxyl groups attached to the aromatic rings. The spectra for Miscanthus and **iSL** exhibited significant bands at 1600 and 1515 cm^{-1}, indicating carbon–carbon bond stretches in aromatic rings, which are prevalent in lignin.[36]

Self-synthesized lignin, **iHL**, was obtained using the same ionosolv extraction method, for which there is limited literature available for comparison. In the FTIR spectrum, the –OH absorption band of **iHL** is shifted to a lower wavenumber (3380 cm^{-1}) compared to other technical lignins such as **oHL**, **kSL**, and **iSL** (3450 cm^{-1}). This shift is attributed to the presence of residual ionic liquid $[DMBA][HSO_4]$ associated with the lignin as indicated in Figure 5.14. The displacement of the -OH absorption band to a lower wavenumber result from stronger hydrogen bonding interactions. The decrease in wavenumber arises from stronger hydrogen-bonding interactions, which elongate the O–H bond and lower its vibrational frequency.[37] This

suggests increased hydrogen bonding with the hydrogen sulfate anion in [DMBA][HSO_4].[38] The broad –OH signal observed in FTIR qualitatively indicates the presence of hydroxyl groups, consistent with the high hydroxyl content quantified by ^{31}P NMR (Section 5.2.5).

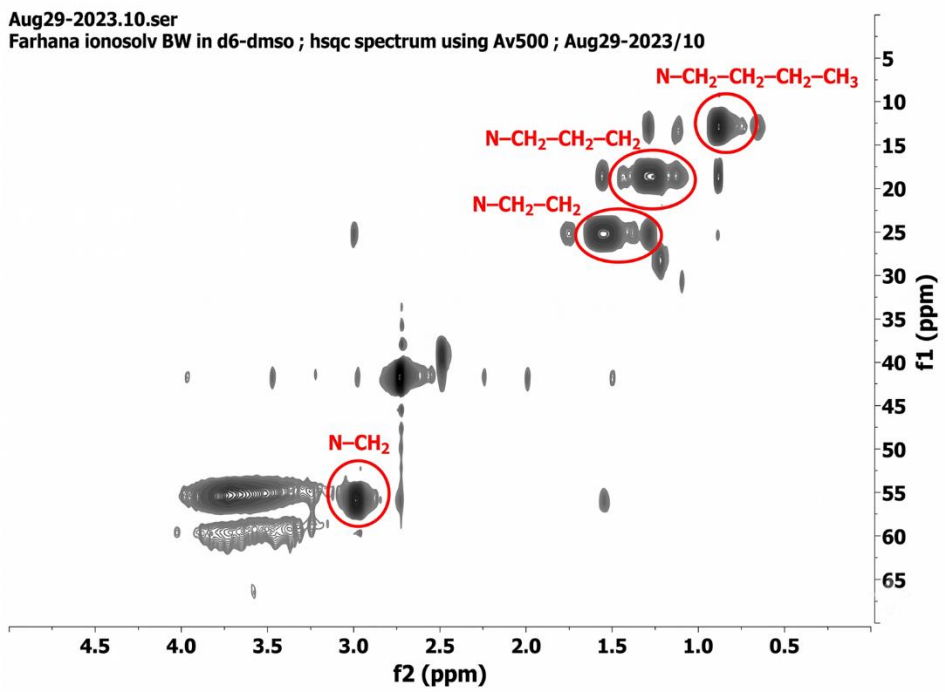


Figure 5.14: HSQC NMR spectrum of **iSL** indicating the presence of residual [DMBA][HSO_4] in the extracted lignin

5.2.4 Establishment of ^{31}P NMR experimental setup for lignin characterisation

^{31}P NMR spectroscopy is a technique employed for characterising lignin, specifically to measure the amount of hydroxyl (-OH) groups present in a quantitative manner. The -OH contents value is crucial to determine as -OH from lignin forms hydrogen bonds to cellulose, which is the shared interaction found in both biopolymers. The -OH contents are obtained using a single NMR spectrum. Lignin, which is dense in -OH groups, undergoes a reaction with 2-chloro-4,4,5,5-tetramethyl-l,3,2-dioxaphospholane (TMDP), acting as a phosphitylation reagent. This reaction results in the formation of phosphitylated products, as illustrated in Figure 5.15. Subsequently, the quantity of -OH can be ascertained using software analysis based on the integration of the phosphitylated products versus an internal standard.

Figure 5.16 depicts the complete range of lignin phosphitylated in the ^{31}P NMR spectrum, with an emphasis on the region between 133 and 149 ppm. The TMDP and TMDP hydrolysis product, exhibited peaks at 175.0 and 130.0 p.p.m., respectively, while the internal standard cyclohexanol displayed a single peak at 144.0 p.p.m.. All lignin samples were dissolved in solvent of pyridine:d-chloroform with ratio 1.6:1. The NMR spectra for all lignins were compared to previously documented literature.[39,32] The presence of a chlorine group in TMDP makes it highly reactive towards moisture. This is because chlorine is a chemically favourable leaving group, which promotes the formation of the TMDP complex. Figure 5.16 on the right illustrated the ^{31}P NMR spectra of lignin which can be divided into three primary regions: 138.80–140.24, 147.86–145.01, and 135.07–133.00 p.p.m. These regions correspond to the phenolic -OH group, aliphatic -OH, and carboxylic group -COOH, respectively.

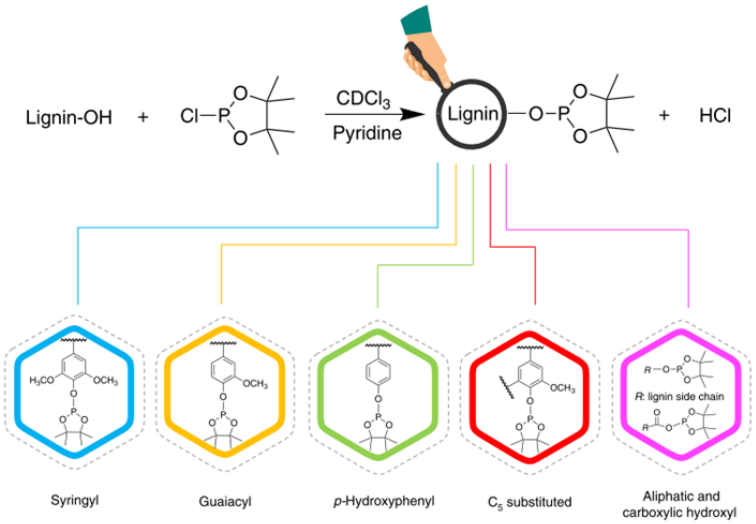


Figure 5.15: The reaction lignin and phosphitylation reagent to produce phosphitylated products. Image credited to Meng, et. al.[39]

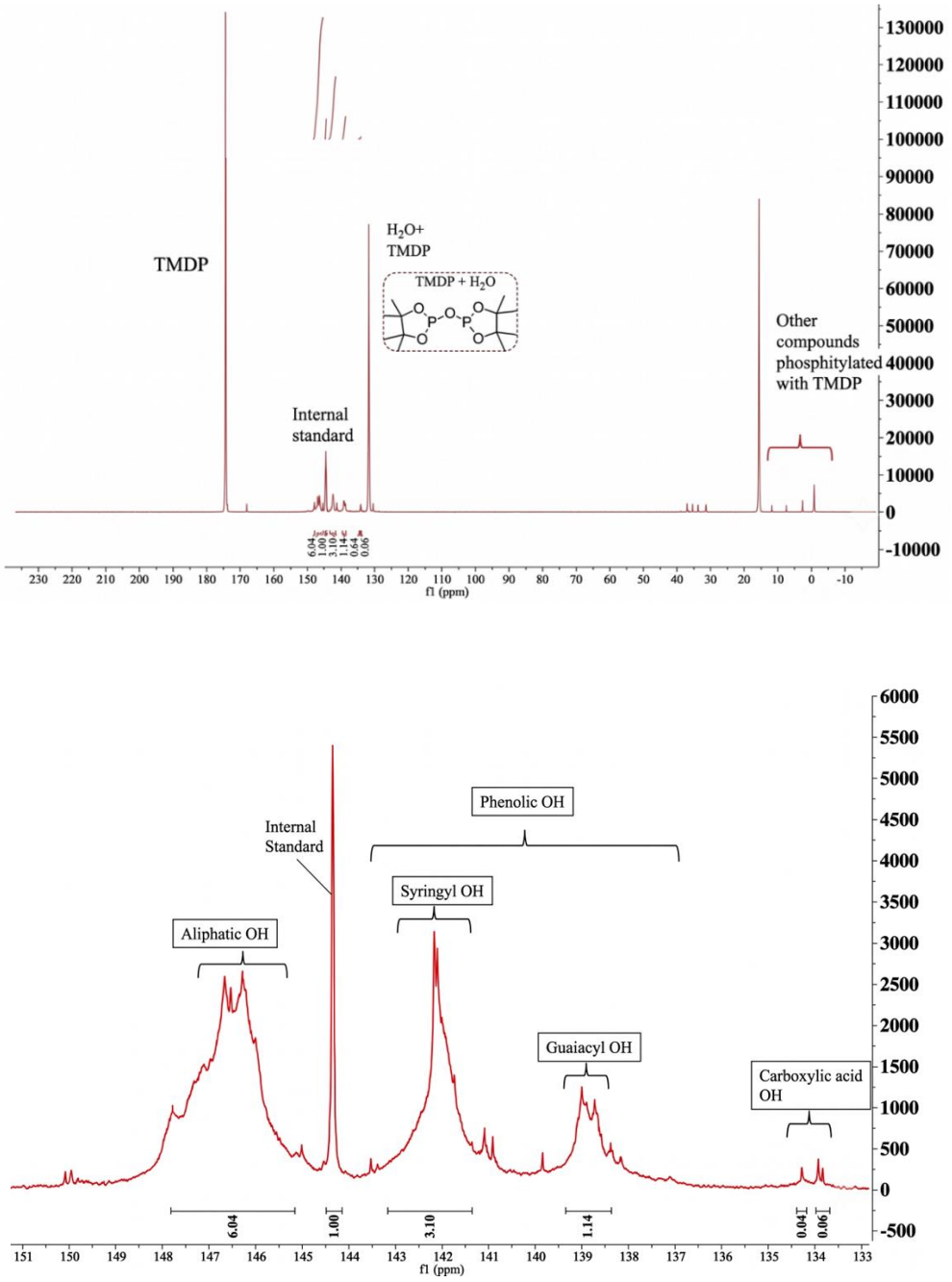


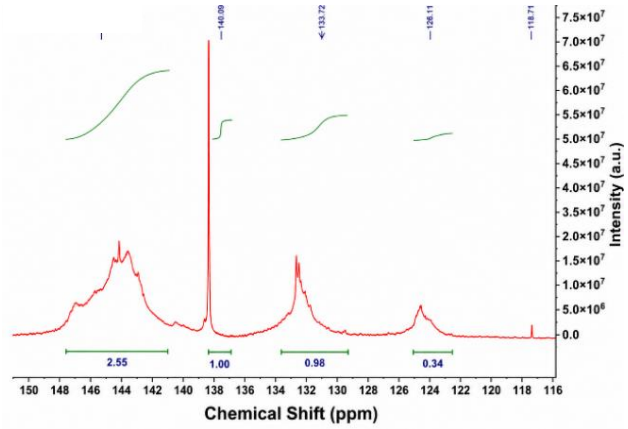
Figure 5.16: Overall ^{31}P NMR spectrum of phosphitylated lignin products (left) and a zoomed-in view of the main region of interest (right)

The initial ^{31}P NMR experiment was carried out according to the procedure described in literature[32] without any modification. The experiment, referred to as experiment 1a, was conducted under standard laboratory conditions as indicated in Table 5.4. The NMR spectra were analysed quantitatively as indicated in Figure 5.17, and the outcome was found to be inconsistent with the specifications of the company's product. According to the result of experiment 1a, **oHL** has a total OH content of 1.34 mmol/g, whereas this lignin has a total OH

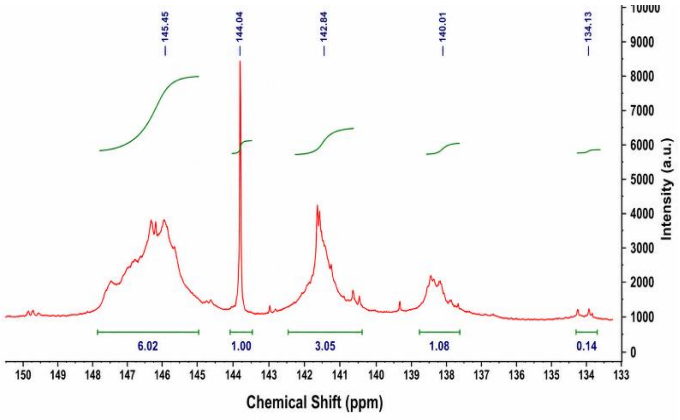
content of 4.80 mmol/g from the company's specification (based on internal company data), which is further broken down into aliphatic OH (1.85 mmol/g), syringyl (0.93 mmol/g), guaicyl (0.84 mmol/g) and carboxylic acid (0.21 mmol/g). The findings of experiment 1a exhibit significant inconsistencies relative to the company's specifications. The quantified aliphatic OH content (0.91 mmol/g) is markedly lower than the documented 1.85 mmol/g. The syringyl (0.31 mmol/g) is significantly lower than what is needed, 0.93 mmol/g, and no carboxylic acid groups were identified, contrary to the reported 0.21 mmol/g. Furthermore, guaiacyl OH (0.12 mmol/g) was significantly lower than the documented 0.84 mmol/g.

Following this, the same ^{31}P NMR method was carried out under completely inert conditions and in a closed system. This experiment is designated as experiment 1b, indicating that it has been carried out within the confines of a glovebox with an atmosphere of dry nitrogen. The chemicals were meticulously arranged in the glovebox one day prior to the commencement of the experiment. In this controlled environment, all compounds were protected from the absorption of moisture from the surroundings, particularly TMDP. Therefore, TDMP could effectively convert into phosphitylated products. The NMR spectrum yielded a result that was in line with the company's specifications. Experiment 1b yielded a total OH of 3.66 mmol/g, compared to 3.92 mmol/g with the company's report: the distribution among the different –OH types is shown in Table 5.4.

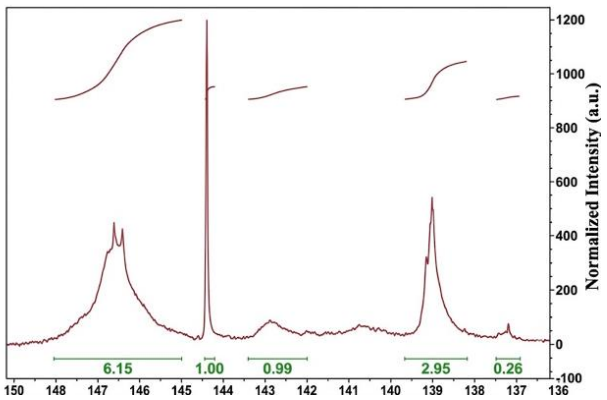
Method 1a (oHL)



Method 1b (oHL)



Method 1b (kSL)



Method 2 (kSL)

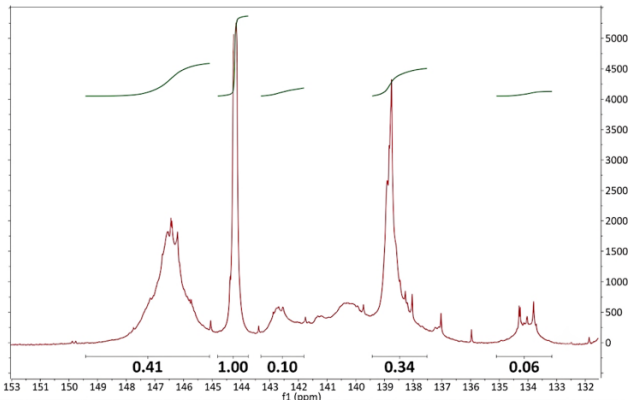


Figure 5.17: ^{31}P NMR spectrum of phosphitylated lignin products in different experimental setups

Due to the extended duration of scans in the experiment, an attempt was made to decrease the number of scans by increasing the concentration of the relaxation agent and TMDP as indicated in Table 5.4. Utilising the appropriate concentration of the relaxation agent know as $Cr(ac)_3$, NMR spectra obtained through real-time with a flow system yield superior data, attributed to markedly diminished polarisation and relaxation durations, without excessive peak broadening or compromise of 2D methodologies.[40] The experiment was executed as described in the literature[39] with minor modifications, using **kSL** as the sample. This modified procedure is referred to as Method 2. The quantity of $Cr(ac)_3$ and the number of scans were replicated precisely as documented in the literature. While excess phosphitylating agent can theoretically be converted into the product efficiently, the experimental results for **kSL** varied significantly between the two methods. To assess which method is more reliable, the results were compared to existing literature data on softwood lignin. Method 1b demonstrated superior conformity with the literature. Consequently, Method 1b is the optimal practice, demonstrating high precision for softwood and hardwood with minimum and maximum standard deviations of 0.47% and 4.72%, respectively.

Table 5.4: Different experimental setup for lignin hydroxyl quantifications

Samples	Quantity of sample (mg)	Method	Parameters									Results (mmol/g)				
			Relaxation agent (Cr(ac)3) (mg/ml)	solvent mixture	volume of solvent mixture (mL)	weight of relaxation agent (Cr(ac)3) (mg)	weight of cyclohexane (mg)	volume of TMDP (µL)	Time of relaxation delays (s)	Number of scans	Time of experiment (h)	Aliphatic	Syringyl	Guaiacyl	p–Hydroxyphenyl	Carboxylic
oHL	30	Method 1a (normal ambient)	5	pyridine: $CDCl_3$ 1.6:1	0.7	0.5	1.085	50	25	≈ 2000	12	0.91	0.31	0.12	0.00	0.00
oHL	30	Method 1b (in the glovebox)	5	pyridine: $CDCl_3$ 1.6:1	0.7	0.5	1.085	50	25	≈ 2400	14	2.15	1.08	0.38	0.00	0.05
kSL	30	Method 1b (in the glovebox)	5	pyridine: $CDCl_3$ 1.6:1	0.7	0.5	1.085	50	25	≈ 2400	14	2.19	0.35	1.05	0.00	0.09
kSL	30	Method 2	18	pyridine: $CDCl_3$ 1.6:1	0.7	1.8	1.085	100	10	256	< 2	0.14	0.03	0.12	0.00	0.02
Company's oHL	-	-	-	-	-	-	-	-	-	-	-	1.85	0.93	0.84	0.09	0.21

5.2.5 ^{31}P NMR

The overall total -OH contents are higher in hardwood lignin compared to softwood lignin, as indicated in Table 5.5 and Figure 5.18. Hardwood lignins, specifically **iHL** and **oHL** lignin, had the highest concentrations of total hydroxyl groups, measuring 10.37 mmol OH/g and 5.50 mmol OH/g, respectively. Softwood lignins, such as **iSL** and **kSL**, exhibited a low total amount of hydroxyl groups (OH), with values of 3.21 mmol/g and 4.26 mmol/g respectively. However, the –OH content reported for **iHL** is likely overestimated because the sample did not meet the required sample specifications.

The protocol states that lignin used for hydroxyl quantification must be moisture-free, sulfur- and ash-free, and contain minimal carbohydrate contamination.[39] As discussed in Section 5.2.2, **iHL** contains a high amount of sugar, and these sugars are present as lignin–carbohydrate complexes, which artificially increase the apparent hydroxyl content. Because **iHL** does not comply with the sample protocol and because relevant literature on ionosolv hardwood lignin is limited, **iHL** cannot be reliably compared with literature values and will not be further discussed in this section.

The second-highest concentration of total hydroxyl groups was observed in the **oHL** sample. **oHL** is a hardwood lignin typically consisting of both syringyl (S) and guaiacyl (G) subunits as indicated in Figure 5.19. Although the **oHL** sample contained some ash contamination (Section 5.2.2), this lignin is still considered to be of high purity, with a total lignin content of 91.9%. Therefore, the ^{31}P NMR quantification remains reliable. The results obtained here are comparable to data reported in the literature for silver birch wood (*Betula pendula* L.) lignin extracted using an organosolv/steam-explosion process under varying treatment conditions.[41] For example, lignin prepared at 60% v/v ethanol for 15 min with 1% w/w H_2SO_4 at 200 °C showed an aliphatic OH content of 1.34 mmol g^{-1}, a total phenolic OH content of 2.89 mmol g^{-1}, and a carboxylic OH content of 0.17 mmol g^{-1}, values that are close to those obtained for **oHL**. The lower aliphatic OH content reported in the literature compared with the technical **oHL** sample can be attributed to the addition of acid and the resulting increase in treatment severity. Under these conditions, lignin side chains undergo oxidation and dehydration reactions, which commonly remove or transform aliphatic hydroxyl (–OH) groups.[41]

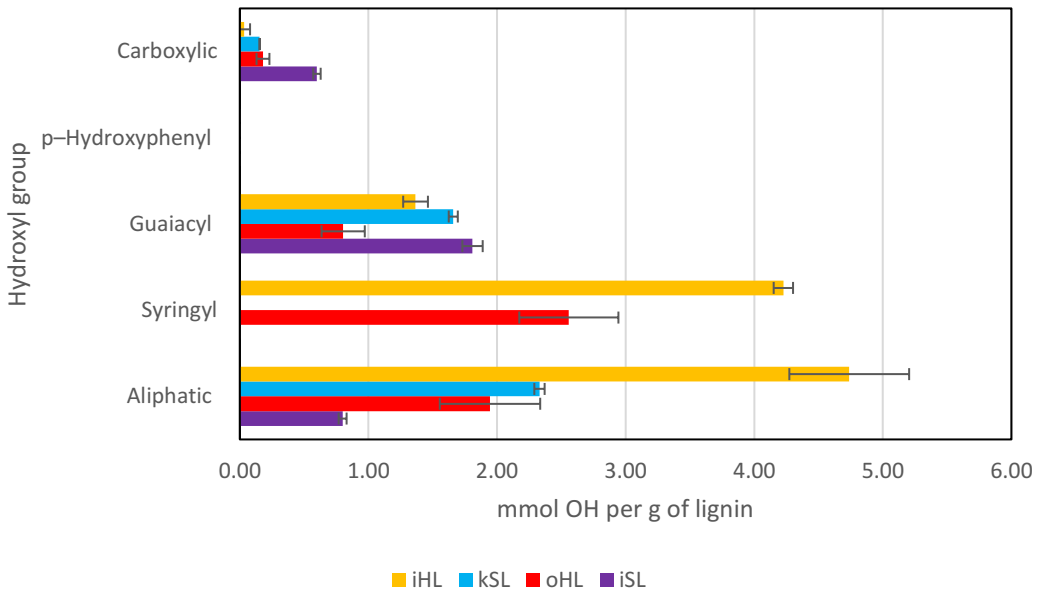


Figure 5.18: Contents of different hydroxyl groups in lignin determined by ^{31}P NMR analysis

Table 5.5: Contents of different hydroxyl groups in lignin determined by ^{31}P NMR analysis

	Type of lignin			
Lignin OH group	oHL	iHL	kSL	iSL
Aliphatic	1.96 ± 0.39	4.74 ± 0.47	2.33 ± 0.04	0.80 ± 0.03
Phenolic	3.36 ± 0.56	5.60 ± 0.18	1.78 ± 0.04	1.81 ± 0.08
Carboxylic	0.18 ± 0.56	0.03 ± 0.05	0.15 ± 0.00	0.60 ± 0.03
Total OH	5.50 ± 0.26	10.37 ± 0.22	4.26 ± 0.02	3.21 ± 0.03

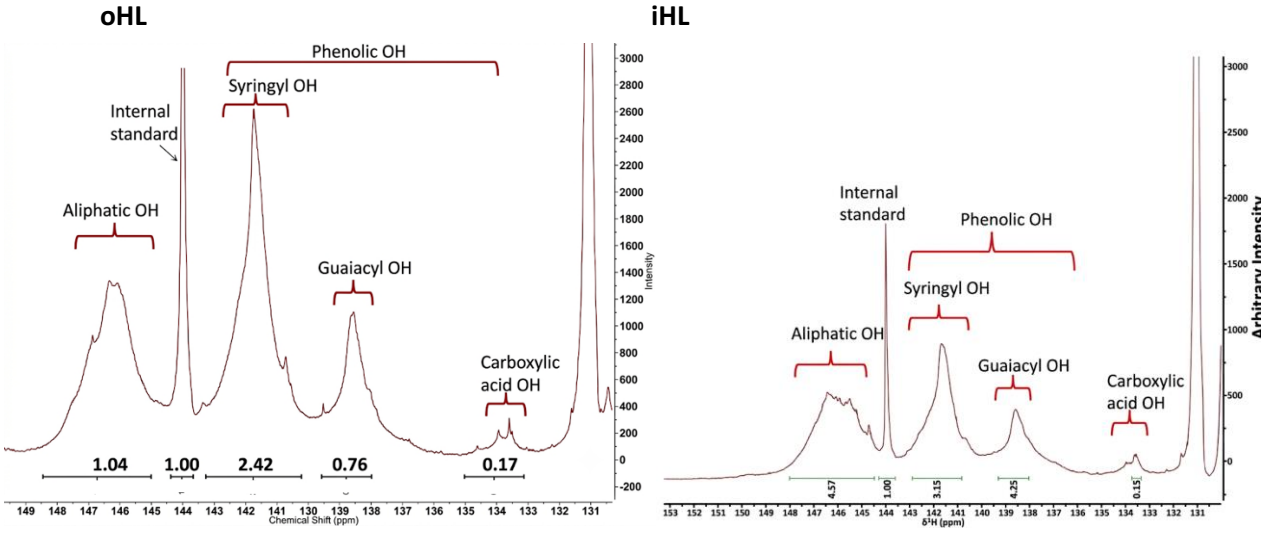


Figure 5.19: Quantitative ^{31}P NMR spectra of organosolv beech wood lignin, **oHL** (left) and ionosolv beech wood lignin, **iHL** (right) using cyclohexanol as the internal standard

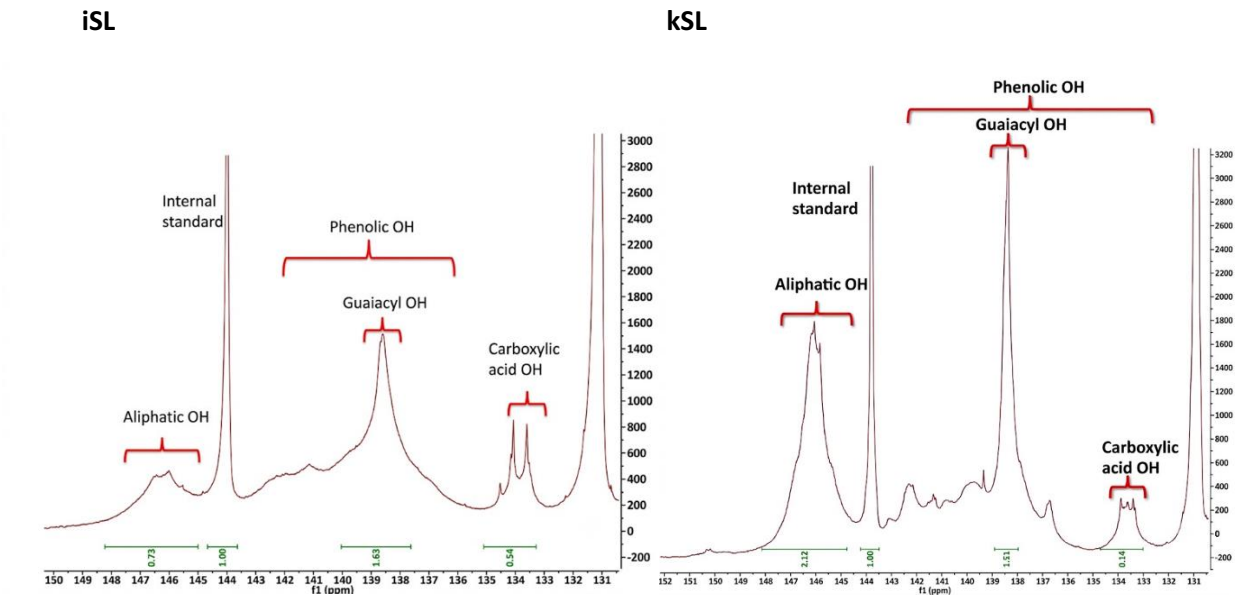


Figure 5.20: Quantitative ^{31}P NMR spectra of ionosolv spruce lignin, **iSL**(left) and kraft lignin, **kSL** (right) using cyclohexanol as the internal standard

Both **kSL** and **iSL** are softwood lignins but differ in their extraction processes. As shown in Figure 5.20, both samples contain exclusively G units. The **kSL** sample exhibits a broader peak between 145.5 and 149.5 ppm, which corresponds to aliphatic OH groups, indicating the presence of hydroxyls on aliphatic lignin side chains and carbohydrate-derived hydroxyl groups.[42] Kraft lignins with varying lignin content are known to remain partially bound to polysaccharides in the form of lignin–carbohydrate complexes and residual carbohydrates.[43] The **kSL** sample was compared with literature values for a commercial softwood Kraft lignin (Indulin AT).[42] Reported values for Indulin AT include aliphatic OH (1.79 mmol/g), total phenolic OH (2.77 mmol/g), and carboxylic groups (0.33 mmol/g). The functional-group content of **kSL** is broadly comparable, although it shows slightly higher aliphatic OH and quite lower phenolic and carboxylic contents. These variations likely arise from differences in processing conditions. Although both materials are Kraft-type lignins produced by alkaline sulfide pulping, suppliers use different pulping and isolation parameters, i.e., liquor-to-wood ratio, alkali charge, cooking temperature, and purification step. Consequently, commercial Indulin AT and Sigma-Aldrich's "Kraft lignin, alkaline" are not chemically identical.

A similar trend was observed in **iSL**, consistent with previous reports on willow and pine softwood processed via ionosolv extraction coupled with vanadium-based polyoxometalates under oxygen-rich conditions.[44] In all cases, the abundance of aliphatic hydroxyl groups decreased while phenolic

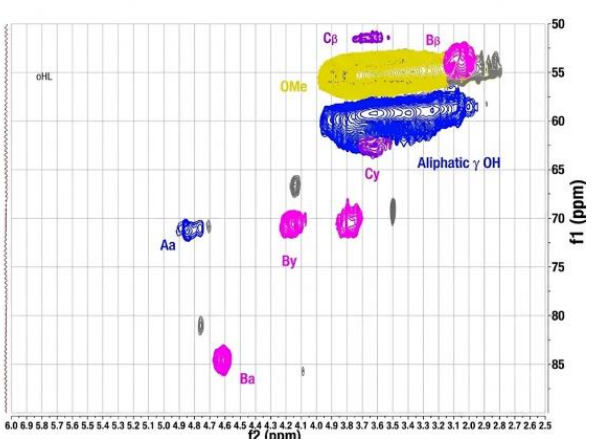
hydroxyl groups increased. This shift has been attributed to dehydration reactions occurring prior to β-O-4 hydrolysis, and the removal of hemicellulose moieties linked to the lignin backbone. The concentration of carboxylic acids in **iSL** was 0.60 mmol g^{-1} the highest among the lignin samples which aligns with literature proposing that these groups originate from aromatic units bound to lignin through intra- or intermolecular ester linkages.[45,25] An increased phenolic hydroxyl content will enhance cellulose-lignin film fabrication by strengthening intermolecular hydrogen bonding.

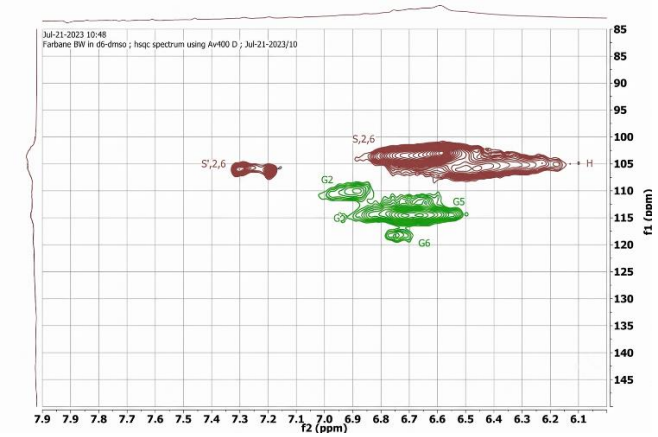
This study of hydroxyl content correlates with lignin purity, as the presence of residual carbohydrates or lignin-bound carbohydrates can lead to an overestimation of total hydroxyl content. These findings indicate that variations in hydroxyl content may affect the interaction between cellulose-lignin films, potentially impacting mechanical qualities in future studies. The overall presence of phenolic OH groups, carboxylic groups, or aliphatic OH groups is expected to have an impact on the ability of the two biopolymer components to interact with each other and mix together, and will directly influence their mechanical properties. These effects will be extensively explored in the next section.

5.2.6 Heteronuclear Single-Quantum Correlation Spectroscopy (HSQC) NMR

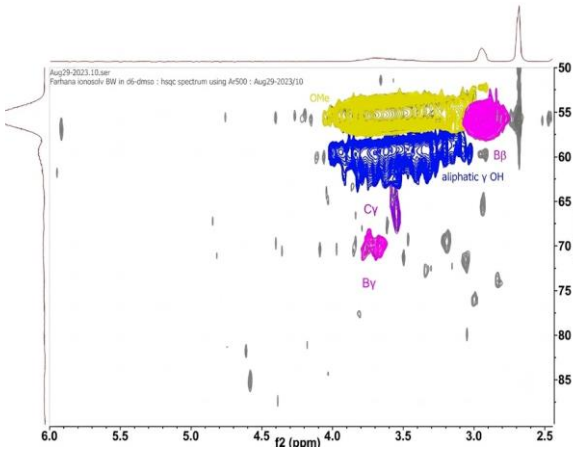
The Heteronuclear Single-Quantum Correlation (HSQC) experiment demonstrates the correlations between resonances of two nuclei that are connected and separated by a single bond. Typically, one of the nuclei is a hydrogen atom (^{1}H) while the other is a heteroatom, specifically either carbon-13 (^{13}C) or nitrogen-15 (^{15}N). The 2D HSQC NMR technique provides a highly informative method for determining signal assignments, as well as identifying inter-unit connections and the types of aromatic units. The objective of HSQC NMR experiment is to ascertain the individual carbon atoms in the lignin molecule that are connected to particular protons through chemical bonds. The NMR spectra displayed in this study specifically emphasise the aliphatic region, which spans from 2.5 to 6.0 ppm horizontally and 50 to 90 ppm vertically. Additionally, it also showcases the aromatic region, ranging from 6.0 to 8.0 ppm horizontally and 100 to 150 ppm vertically. All the HSQC NMR spectra for lignin samples are illustrated in Figure 5.21.

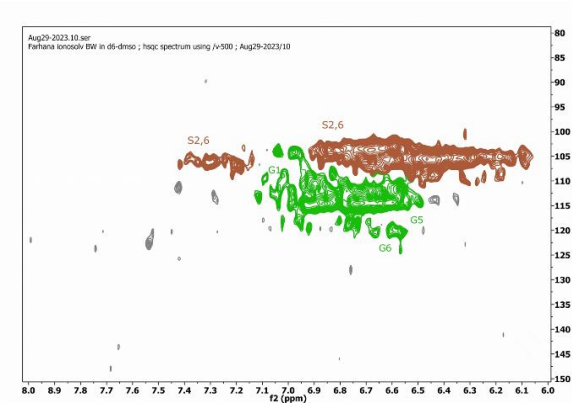
oHL


oHL
Cβ
Bβ
OMe
Aliphatic γ OH
Cγ
Aa
Bγ
Ba
f2 (ppm)
f1 (ppm)

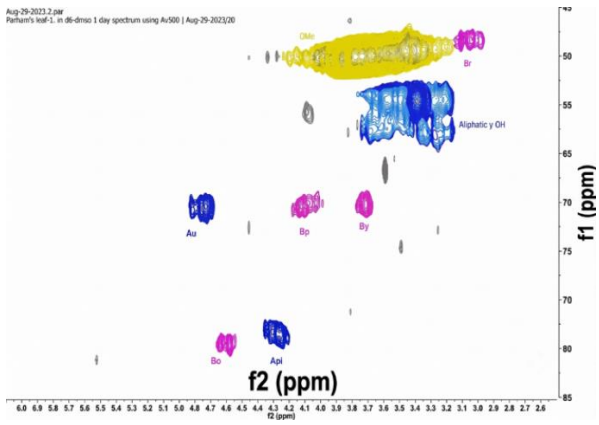

S',2,6
S,2,6
G2
G5
G6
H
f2 (ppm)
f1 (ppm)

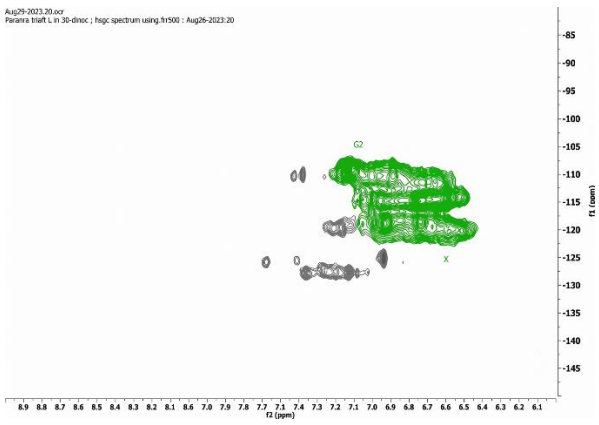
iHL


OMe
Bβ
aliphatic γ OH
Cγ
Bγ
f2 (ppm)


S2,6
S2,6
G1
G5
G6
f2 (ppm)

kSL


OMe
Br
Aliphatic γ OH
Au
Bp
By
Bo
Api
f2 (ppm)
f1 (ppm)


G2
X
f2 (ppm)
f1 (ppm)

iSL

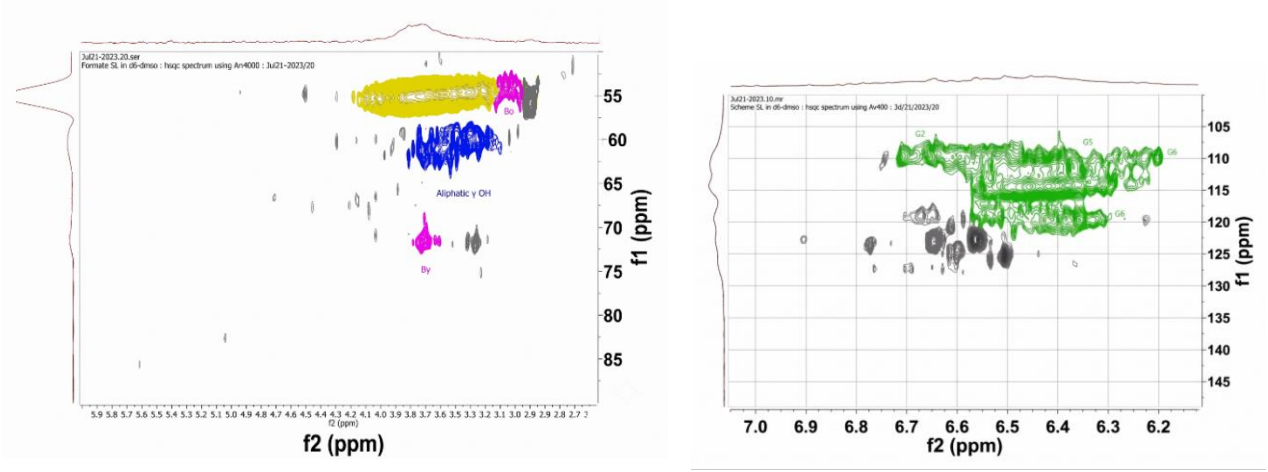


Figure 5.21: HSQC NMR of softwood lignin (**iSL** and **kSL**) and hardwood lignin (**oHL** and **iHL**)

In the aliphatic region, all lignins typically exhibit the major interunit linkages characteristic of native structures, including β-aryl ethers (β-O-4), β–β, and β–5 bonds. The chemical structures of these linkages are shown in Figure 5.22. Notably, the **oHL** sample contained more complete interunit structures than the **iHL** sample, particularly the full β–β derived substructures (highlighted in pink), which include β–β, β–α, and β–γ units. This difference is attributed to the substantially higher purity of **oHL** (91.9%) relative to **iHL** (60.3%), as indicated by the compositional analysis. The higher purity of **oHL** facilitated the preservation of most major lignin linkages. The presence of the glucose unit in **iHL** was confirmed by HSQC NMR analysis, which showed the characteristic β-D-glucopyranoside cross-peaks at C2/H2 (74.8/2.88 ppm), C3/H3 (76.7/3.06 ppm), and C5/H5 (70.3/3.18 ppm), all of which are circled in red in the spectrum. This is consistent with the compositional analysis result showing 0.6% glucose monomer unit. The spectral features of **oHL** align well with literature reports for beechwood lignin obtained via acetone-based organosolv fractionation.[46] Clear signals corresponding to phenylcoumaran-type (β–5) linkages, marked in purple, were also observed in the **oHL** spectrum.[47]

In the aromatic region, characteristic hardwood lignin signals arising from both syringyl (S) and guaiacyl (G) units were identified, and their structural representations are provided in Figure 5.22. A rough estimation of the S/G ratios in both **oHL** and **iHL** indicates values consistent with the typical composition of beechwood lignin (approximately S 60%, G 40%).[46] As expected,

beechwood is richer in syringyl-type structures than in guaiacyl units. Equal S/G distributions have also been widely reported for other hardwood species, such as oak.[27] This interpretation is further supported by the ^{31}P NMR data, which confirms the high abundance of phenolic OH groups in **oHL** and provides an accurate quantitative determination of its hydroxyl functionality.

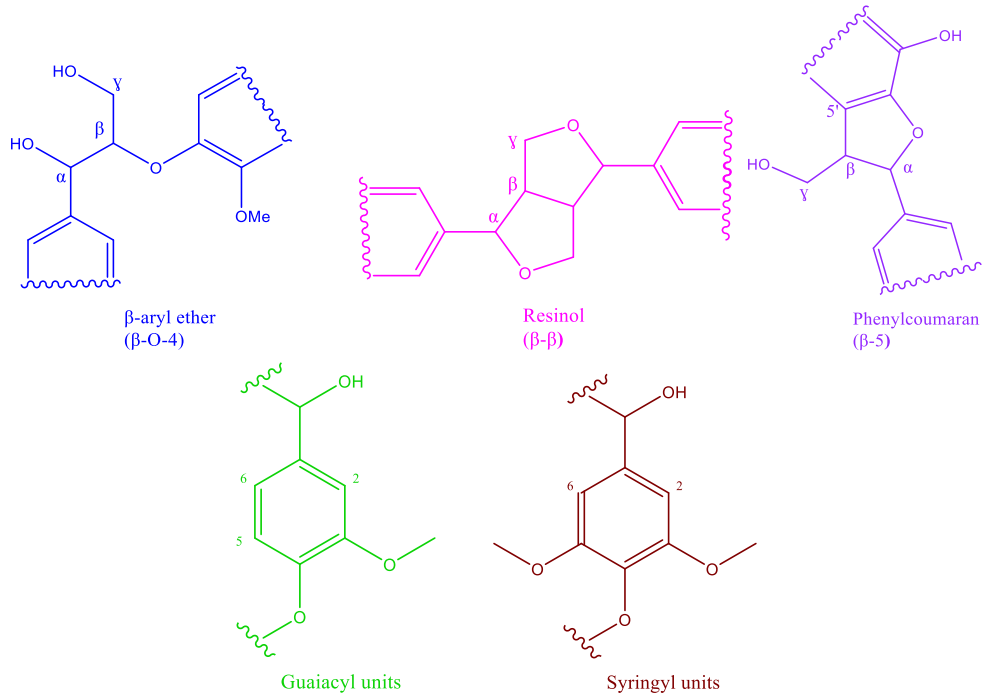


Figure 5.22: Identified structural units of lignin in 2D HSQC NMR spectra

In the aliphatic region of the HSQC spectra, presence methoxy signals were observed for both **iSL** and **kSL**. The dominant interunit linkages β-aryl ether (β-O-4), phenylcoumaran (β-5), and resinol (β–β) were consistently present in both samples. For **kSL**, the relative abundance of these motifs closely resembled that of commercial Indulin kraft lignin,[42] indicating that the kraft-derived material retained a structural profile typical of this process. In contrast, the **iSL** sample exhibited subtle structural differences, notably the absence of several sub-correlations such as Aα/Aβ and Bγ/Bβ, when compared with previous observations for pine-derived ionosolv lignin.[48] These differences can be attributed to variations in biomass species as well as the characteristic β-O-4 cleavage occurring during ionosolv pulping, which promotes the formation of more condensed lignin structures.

This interpretation of the HSQC spectra is further supported by the quantitative ^{31}P NMR analysis: kraft lignin (**kSL**) contained 2.33 mmol/g of aliphatic hydroxyl groups, whereas the ionosolv lignin

(**iSL**) contained only 0.80 mmol/g. The reduced aliphatic hydroxyl content in **iSL** is consistent with enhanced condensation and loss of native ether linkages during the ionosolv process.

In the aromatic region, both **kSL** and **iSL** predominantly exhibit guaiacyl (G) units, which is consistent with the typical composition of softwood lignins. As expected for softwood, no syringyl (S) units are detected in either sample, confirming the absence of S2/6 correlations in the aromatic region. The observed cross-peaks corresponding to G2, G5, and G6 agree with literature-reported on ionosolv and kraft softwood lignin.[48,42] Several additional cross-peaks appear in the aromatic region that remain unassigned, as they do not correspond to commonly reported lignin substructures. These unassigned signals may originate from new or modified aromatic structures formed during the different extraction processes: ionic-liquid pretreatment in **iSL**, and the alkaline kraft pulping process in **kSL**, which is known to generate more condensed structures.[48] A summary of all interunit linkages commonly reported for softwood and hardwood lignins is provided in Table 5.6.

Table 5.6: Assignment for integral in HSQC NMR

Labels	δ_C/δ_H	Assignment
OMe	56.0/3.74	C-H in methoxyls
Aα	71.8/4.86	Cα-Hα in β-O-4' (A) and γ-acetylated β-O-4'
$A_{\beta(G/H)}$	83.9/4.28	Cβ-Hβ in β-O-4' (A) linked to G and H
$A_{\beta(S)}$	85.9/4.12	Cβ-Hβ in β-O-4' (A) linked to S
A_{γ}	59.8/3.61	Cγ-Hγ in β-O-4’ (A)
C_{α}	86.8/5.46	Cα-Hα in β-5’ and α-O-4’ phenylcoumaran (C)
C_{β}	53.4/3.45	Cβ-Hβ in β-5’ and α-O-4’ phenylcoumaran (C)
C_{γ}	62.5/3.73	Cγ-Hγ in β-5’ and α-O-4’ phenylcoumaran (C)
B_{α}	84.8/4.67	Cα-Hα in β-β’ and α-O-γ’ resinol (B)
B_{β}	53.5/3.06	Cβ-Hβ in β-β’ and α-O-γ’ resinol (B)

B_γ	71.0/3.82-4.20 71.45/4.10,3.72	Cγ-Hγ in β-β' and α-O-γ' resinol (B)
$S_{2,6}$	104.3/6.71	C2-H2 & C6-H6 in syringyl (S)
$H_{3,5}$	114.2/6.68	C3-H3 & C5-H5 in *p*-hydroxyphenyl(H)
$H_{2,6}$	128.2/7.19	C2-H2 & C6-H6 in *p*-hydroxyphenyl (H)
G_2	111.8/6.98	C2-H2 in guaiacyl (G)
G_5	115.3/6.75&6.93	C5-H5 in guaiacyl (G)
G_6	119.3/6.90	C6-H6 in guaiacyl (G)

5.2.7 Thermal analysis

Thermogravimetric analysis (TGA) can assess the thermal behaviour and stability of lignin. The thermal degradation curves can characterise the content of lignin, including hemicellulose and α-cellulose, in biomass. The TGA curves for all lignins, as depicted in Figure 5.23, exhibit anticipated patterns characteristic for most common lignins. For example, the **oHL** TGA curve apparently exhibits a thermogram nearly identical to that of beech wood organosolv lignin documented in other publications.[27] The thermal behaviour is typically categorised into three distinct phases: (i) the first stage, (ii) the intermediate stage, and (iii) the final stage characterised by flattened curves.

The lignins exhibit lower onset temperatures for hardwood lignin and much higher for softwood lignin as indicated in Table 5.7. This observation is consistent with literature on the thermal characteristics of lignoforce kraft lignin, which showed T_{onset} values of 212.8°C for LFHL (hardwood lignin) and 232.6°C for LFSL (softwood lignin). Softwood lignins often exhibit greater thermal resistance than hardwood lignins, regardless of the extraction method employed. GPC result showed that softwood lignins with higher molecular mass degrade at higher temperatures, indicating the presence of more thermally stable substructures in their chemical composition.

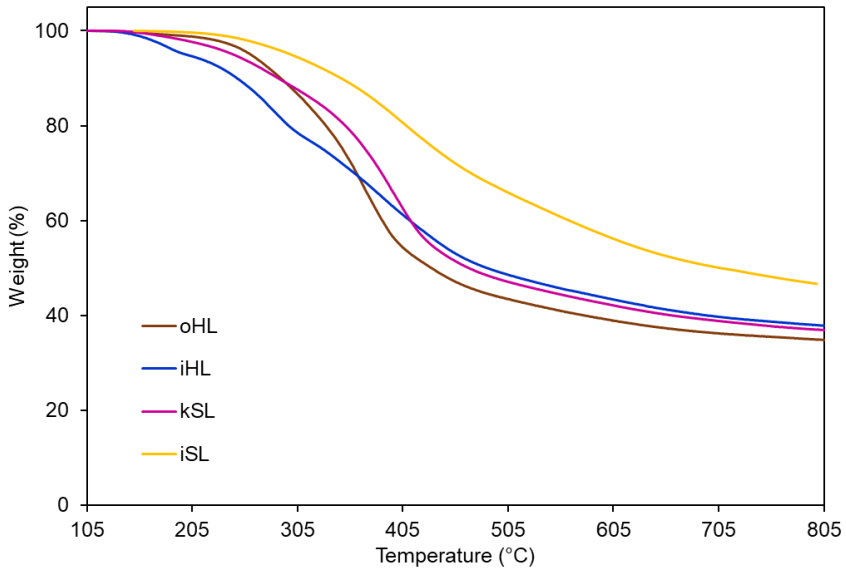


Figure 5.23: TGA curves of hardwood lignin (**oHL** and **iHL**) and softwood lignin (**kSL** and **iSL**)

Guaiacyl (G) found in the HSQC NMR units tend to condense at the free C5 position, resulting in C–C linkages (e.g., 5−5' and β-β') that exhibit greater thermal stability. In contrast, hardwood lignins possess greater quantities of less stable β-O-4′ substructures compared to softwood lignins.[49] A significant weight loss of 40–60% occurs within the temperature range of maximum decomposition rate (T_{max}) from 170−500 °C, associated with lignin decomposition.

Table 5.7: Range of maximum thermal decomposition temperature and unvolatilised weight fraction at 800°C of softwood and hardwood lignin

Samples	Types of lignin	T onset (°C)	Range of T max (°C)	Residue (%)
oHL	Hardwood	258.9	240.0 – 396.0	34.9
iHL	Hardwood	198.6	170.0 – 484.0	37.9
kSL	Softwood	308.7	215.0 – 440.0	37.0
iSL	Softwood	318.6	268.0 – 500.0	50.3

Thermal degradation within this range is attributed to the fragmentation of inter-unit linkages such as β-O-4′, β-β′, and related bonds. During the intermediate decomposition phase (370–400 °C), the aliphatic side chains of lignin begin to degrade, accompanied by the cleavage of more stable carbon–carbon linkages.[24] This intermediate stage may also arise from the concurrent degradation of hemicellulose and lignin, indicating the presence of lignin–carbohydrate complexes. Among the samples, **kSL** and **iSL** exhibit the highest lignin purity, which explains their comparatively slower thermal degradation, as lignin decomposes more gradually than carbohydrate-rich fractions.

However, at approximately 400 °C, **iHL** degrades more slowly than **oHL** despite having lower lignin purity. This thermal behavior suggests that **iHL** contains lignin–carbohydrate complexes that were underestimated in the compositional analysis, leading to the observed slower degradation at this stage.

In the final stage, the TGA curves flattened between 600−800 C, attributed to the additional condensation of the previously generated carbonaceous material, resulting in a residual char of around 34.9 –50.3 % at 800 ◦C. The highest percentage of residues among all lignin was **iSL**. Residual yield is an indicator for char formation potential, which directly influences its applicability in material sciences (i.e. carbon fibre or activated carbon). The residual mass, associated with non-volatile residues such as ashes, is thought to rise with increasing molecular mass. The GPC results indicated that **iSL** possesses the largest molecular weight compared to other lignins. Previous researchers have noted that increasing molecular weight correlates with increased residue weight in the context of kraft lignin fractionation through serial extraction with organic solvents.[24] Additionally, softwood lignin predominantly comprises resinol (β-β), which contributes to the formation of stable intermediate structures during pyrolysis. This structural feature contributes to a higher char yield at elevated temperatures. Although lignin undergoes carbonization above 500 °C, the nature of its native linkages influences the degradation pathway and final residue formation.[49]

5.3 Cellulose-lignin film characterisation

5.3.1 Cellulose-lignin film appearance and UV-Vis Spectroscopy

The physical appearance of **10cel** and **cel-lig** films were captured using a digital camera to observe variations in brown intensity hue resulting from the incorporation of various lignin types and differing weight percentage ratios as indicated in Figure 5.24. The films' appearance was analyzed in relation to their transparency using UV-Vis spectroscopy. The transmittance of the cellulose-lignin films was measured to evaluate their ultraviolet (UV)-blocking properties, given that lignin is rich in phenolic compounds. These phenolic compounds strongly absorb UV light, enabling π–π* electronic transitions in UV-Vis spectroscopy. The relevant UV transmittance region includes UV-A (320–400 nm) and UV-B (280–320 nm).

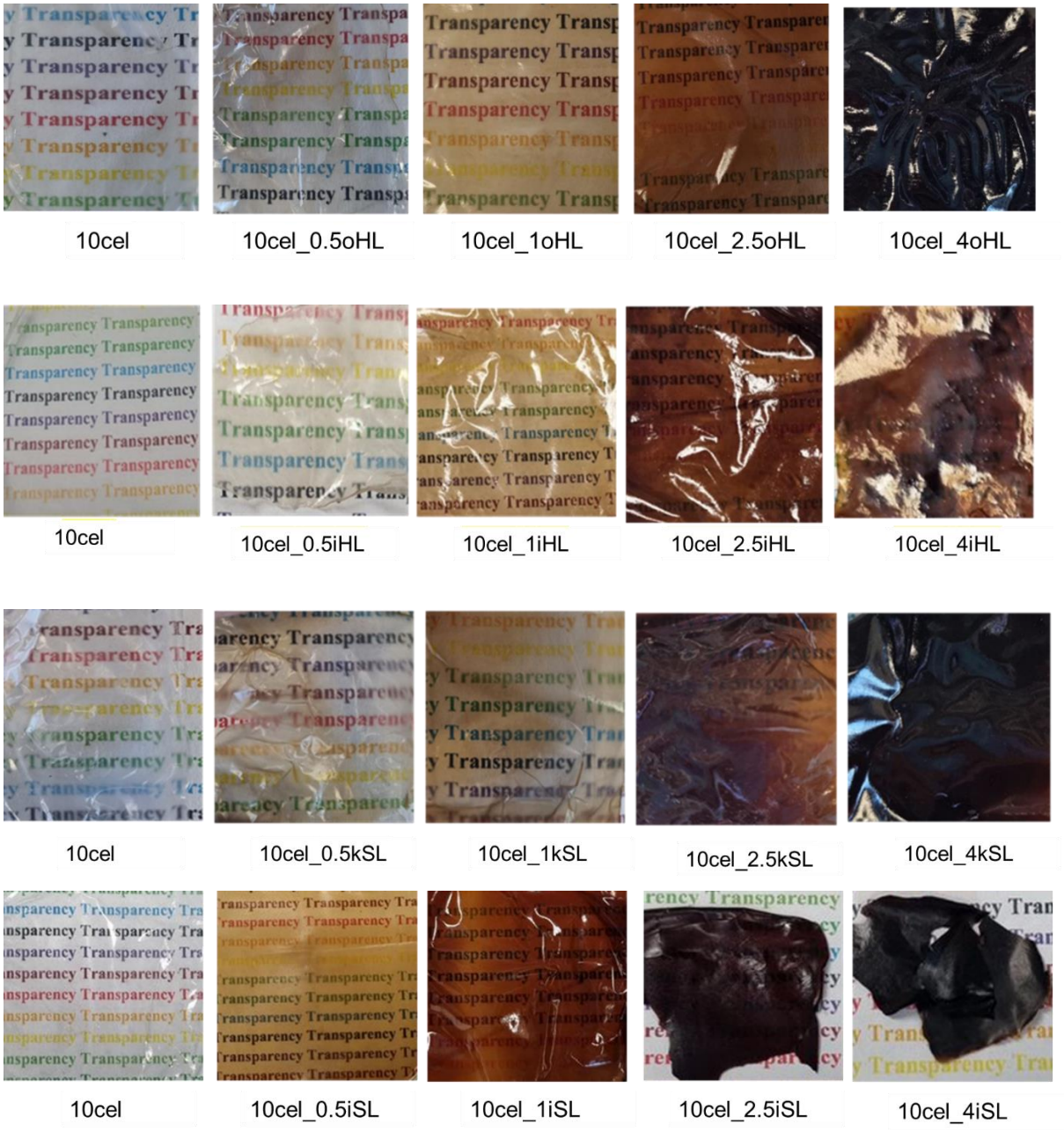


Figure 5.24: Cellulose-lignin composite film images with varying lignin content in different lignin types of softwood and hardwood

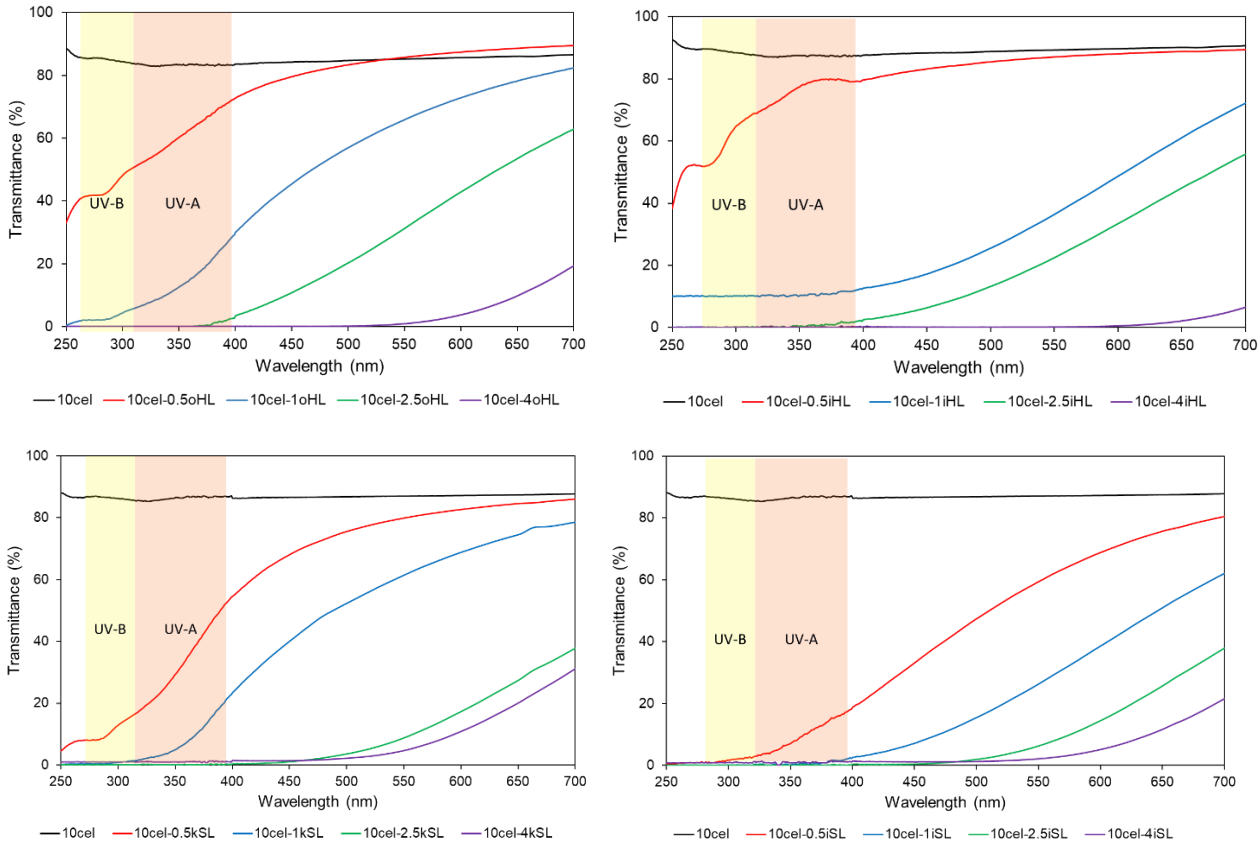


Figure 5.25: UV−vis transmission spectra of cellulose-lignin films for hardwood (**iHL**, **oHL**) and softwood lignin (**kSL**, **iSL**) with various lignin concentrations

10cel without lignin exhibited a remarkable transparency ranging from 92.7% to 86.7% over the visible to UV wavelengths as indicated in Figure 5.25. This result is corroborated by the literature, which indicates that cellulose acetate (CA) film exhibits a high transparency of 90.06%.[50] Both **cel** and **cel-lig** films exhibited flat and smooth surfaces, with lignin uniformly dispersed throughout the film, a common observation noted in the literature on cellulose-lignin films.[51,52] The yellowish-brown hue intensity increased with higher lignin content, corroborating findings in the literature on cellulose wood-alkaline lignin films.[53]

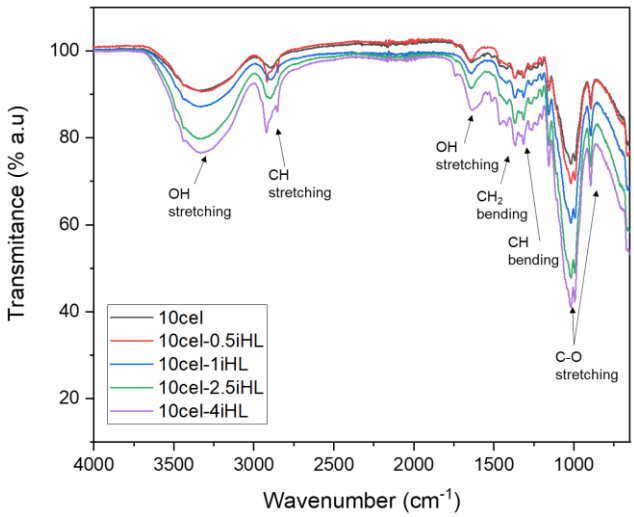
Transparency was distinctly observable in films containing 1 wt.% lignin, except for **10cel-1iSL**, facilitating easy visual inspection of underlying objects. In the visible light spectrum, at 550 nm, it was observed that **10cel-1iSL** exhibited the lowest transmittance at 26.35%, whereas other films with 1 wt.% lignin demonstrated transmittance values much higher ranging from 36.35% to 65.87%. Thus, this physical appearance film corresponds to the transmittance value. The variation in light absorption among cellulose-lignin films is attributed to their light scattering properties.[53]

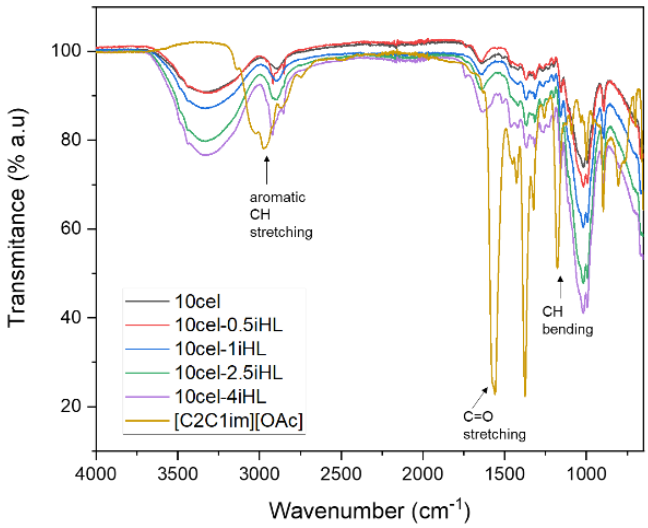
The incorporation of lignin at concentrations of 2.5 and 4 wt.% demonstrated comprehensive UV-blocking capabilities against both UV-A and UV-B radiation in **10cel-iSL** and **10cel-kSL**. This result is analogous to literature indicating that only 2 wt.% bonded lignin in cellulose demonstrates light absorption in the UV-A range.[52] The complete UV-blocking observed at low lignin content is particularly advantageous, as it preserves both transparency and UV resistance in the composite films. This UV-blocking behavior corroborates the validity of the phenolic hydroxyl quantification obtained via ^{31}P NMR. The apparent overestimation of hydroxyl content in **iHL** can be attributed to contamination with carbohydrates and lignin–carbohydrate complexes. This interpretation is consistent with the UV-blocking results, where complete UV shielding was achieved only at a lignin content of 4 wt% in **iHL**. All **cel-lig** films exhibit complete UV-blocking characteristics only when 4 wt.% lignin is included. This results from the homogeneous dispersion of lignin within the cellulose-lignin film.[51]

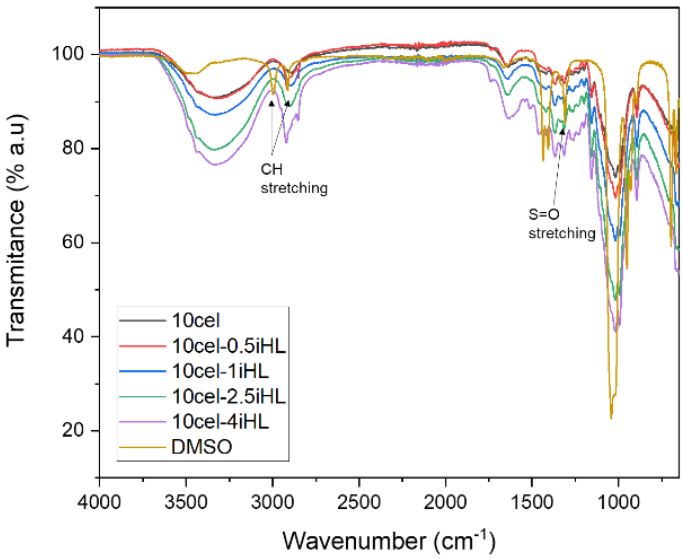
5.3.2 FTIR

The presence of primary functional groups indicated in FT-IR spectra of **10cel** and **cel-lig** films at various lignin weight percent ratios are illustrated in Figure 5.26. All films exhibited an apparent absorption band in the 3450-3000 cm^{-1} range, indicating O–H stretching vibrations among the biopolymers. The introduction of lignin causes the O-H bond to shift to a lower wavenumber, signifying the formation of intermolecular hydrogen bonds between cellulose and lignin.[2] The bands at 2910 and 2842 cm^{-1} correspond to C–H asymmetric and symmetric stretching, respectively; 1425 cm^{-1} is indicative of CH_2 symmetric bending; 1360 cm^{-1} represents C–H bending commonly found in cellulose and lignin. 1017 cm^{-1} and 897 cm^{-1} are associated with ether bonds in the aliphatic chain (C–O antisymmetric stretching) and alicyclic groups in polysaccharide molecules (C1–H deformation with ring vibration contribution). All **cel-lig** films displayed a significant band at around 1466 cm^{-1} and within the range of 1511 to 1600 cm^{-1}, corresponding to aromatic backbone vibrations in lignin, similar to literature cellulose-lignin films.[53]

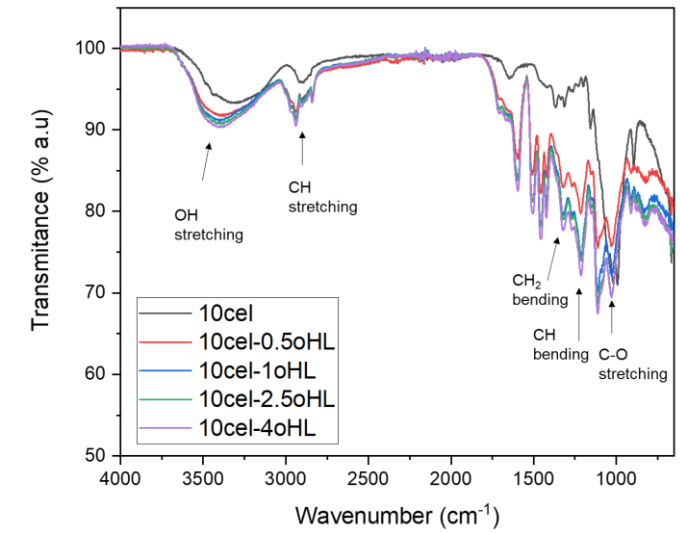
(a) iHL

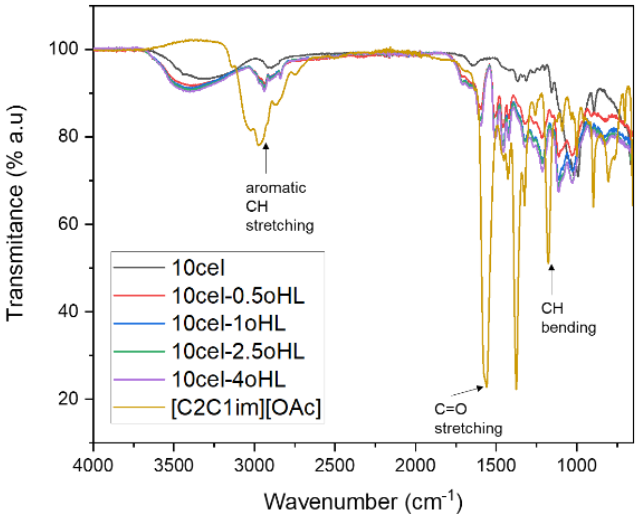

Transmitance (% a.u)
Wavenumber (cm-1)
OH stretching
CH stretching
OH stretching
CH2 bending
CH bending
C-O stretching
10cel
10cel-0.5iHL
10cel-1iHL
10cel-2.5iHL
10cel-4iHL

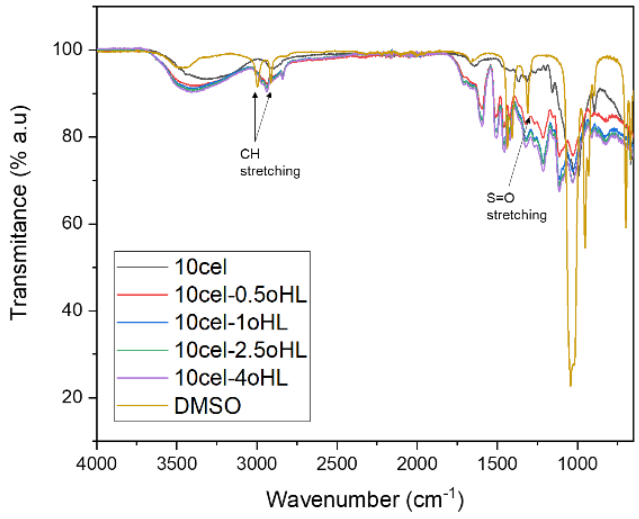

Transmitance (% a.u)
Wavenumber (cm-1)
aromatic CH stretching
CH bending
C=O stretching
10cel
10cel-0.5iHL
10cel-1iHL
10cel-2.5iHL
10cel-4iHL
[C2C1im][OAc]


Transmitance (% a.u)
Wavenumber (cm-1)
CH stretching
S=O stretching
10cel
10cel-0.5iHL
10cel-1iHL
10cel-2.5iHL
10cel-4iHL
DMSO

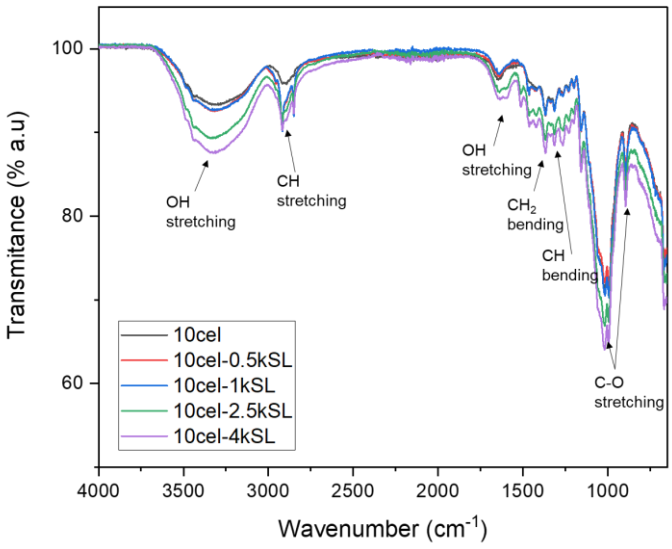
(b) oHL

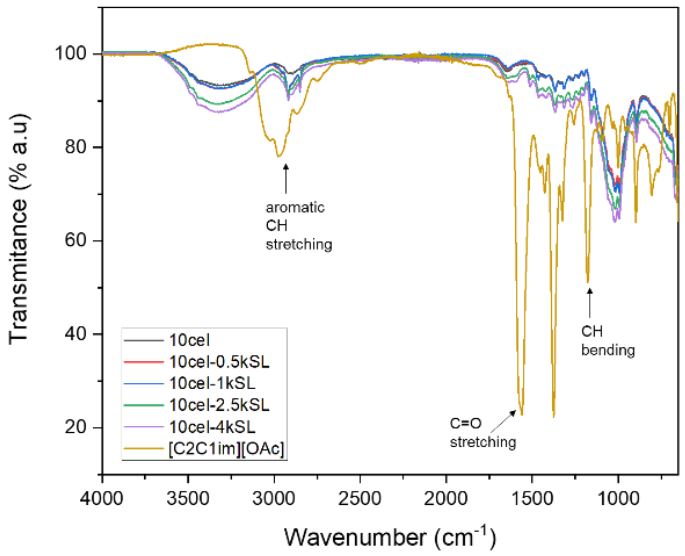

Transmitance (% a.u)
Wavenumber (cm-1)
OH stretching
CH stretching
CH2 bending
CH bending
C-O stretching
10cel
10cel-0.5oHL
10cel-1oHL
10cel-2.5oHL
10cel-4oHL

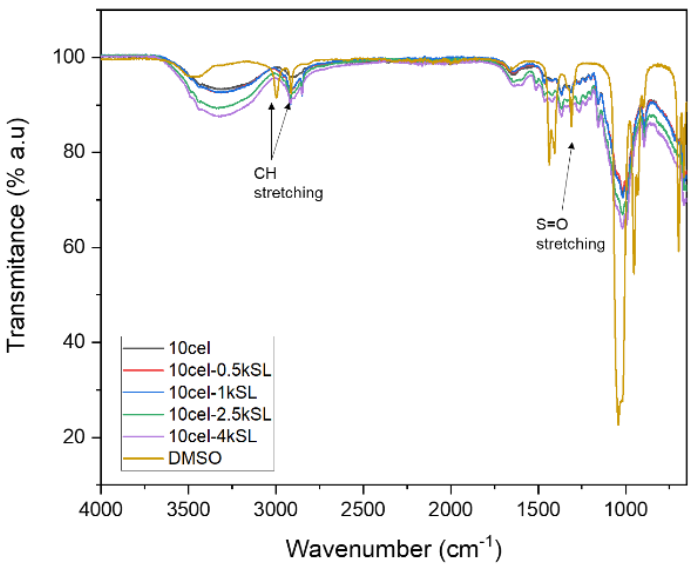

Transmitance (% a.u)
Wavenumber (cm-1)
aromatic CH stretching
CH bending
C=O stretching
10cel
10cel-0.5oHL
10cel-1oHL
10cel-2.5oHL
10cel-4oHL
[C2C1im][OAc]


Transmitance (% a.u)
Wavenumber (cm-1)
CH stretching
S=O stretching
10cel
10cel-0.5oHL
10cel-1oHL
10cel-2.5oHL
10cel-4oHL
DMSO

(c) kSL


Transmitance (% a.u)
Wavenumber (cm-1)
OH stretching
CH stretching
OH stretching
CH2 bending
CH bending
C-O stretching
10cel
10cel-0.5kSL
10cel-1kSL
10cel-2.5kSL
10cel-4kSL


Transmitance (% a.u)
Wavenumber (cm-1)
aromatic CH stretching
CH bending
C=O stretching
10cel
10cel-0.5kSL
10cel-1kSL
10cel-2.5kSL
10cel-4kSL
[C2C1im][OAc]


Transmitance (% a.u)
Wavenumber (cm-1)
CH stretching
S=O stretching
10cel
10cel-0.5kSL
10cel-1kSL
10cel-2.5kSL
10cel-4kSL
DMSO

(d) iSL

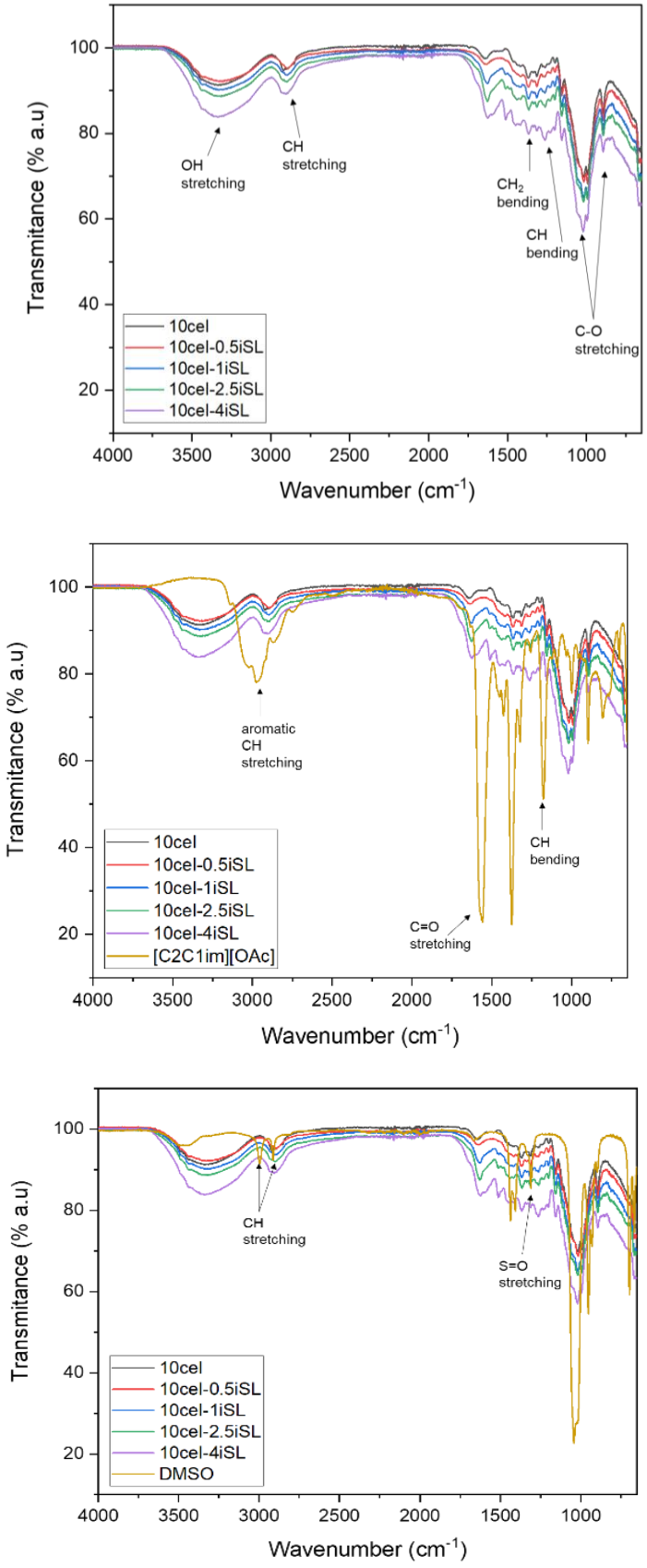


Figure 5.26: FTIR spectra of cellulose-lignin composite films with hardwood lignin (a) and (b), and hardwood lignin (c) and (d) indicating the regenerated film is free from dissolution solvent mixture

The FTIR spectra show overlapping bands for cellulose and lignin, signifying their dispersion. FTIR cannot effectively assess the degree of dispersion between cellulose and lignin; it can only detect interactions between the biopolymer components. Cellulose dominates all spectra, with lignin bands present, corresponding to aromatic skeletal vibrations and guaiacyl and syringyl subunits. Details cellulose and lignin FTIR characterisation has been discussed in the previous section.

$[C_2C_1im][OAc]$ and DMSO promote uniform blending during dissolution and regeneration by improving solubility. The high ionic strength of the ionic liquids disrupts the inter- and intramolecular hydrogen-bonding connections within cellulose chains and lignin as illustrated in the chemical structures shown in Figure 5.27. The dissolution of lignin involves a synergistic mechanism driven by both the IL's anion and cation. The strongly basic acetate anion acts as a powerful hydrogen bond acceptor, directly interacting with the aliphatic and phenolic hydroxyl groups of lignin to break its self-associated network. Simultaneously, the planar imidazolium ring of the $[C_2C_1im]^+$ cation engages in non-covalent π- π stacking interactions with the electron-rich aromatic rings of the guaiacyl and syringyl subunits in lignin. Additional weak hydrogen bonding occurs between the acidic ring protons of the imidazolium cation and the oxygen atoms of the methoxy and ether linkages in lignin. These multi-site interactions support the finding that the anion's characteristics are pivotal for dissolution,[54] enabling both softwood lignin (southern yellow pine) and hardwood lignin (red oak) to completely dissolve in $[C_2C_1im][OAc]$ following light grinding, in contrast to 1-butyl-3-methylimidazolium chloride($[C_4C_1im]Cl$).[55]

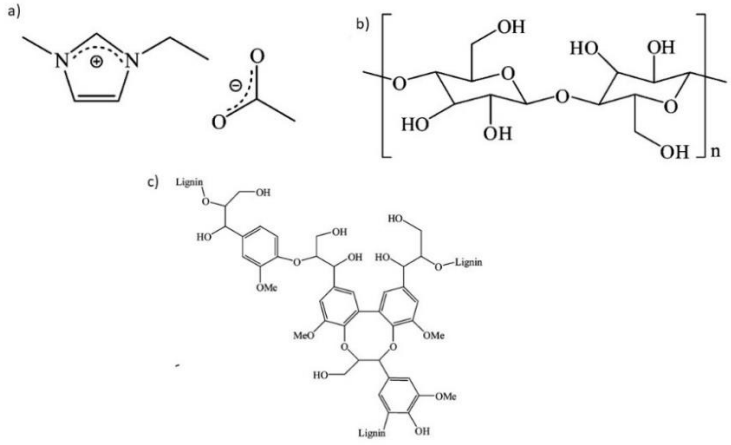


Figure 5.27: Structures of (a) 1-ethyl-3-methylimidazolium acetate ($[C_2C_1im]OAc$), (b) cellulose and (c) representative structure of lignin. Image adopted from Sun et.al[55]

All cellulose-lignin films were thoroughly washed until no evidence of the ionic liquid, $[C_2C_1im][OAc]$ or DMSO remained. Some literature claims that solvent removal occurs either by incubation in deionized water or prolonged washing with running water, as well as through evaporation in an oven.[56, 6,57] In this study, solvent removal was achieved by five times washing with fresh deionised water each time. The number of washings was established by experimental studies using NMR spectra to quantify ionic liquid present and was described details in method development chapter. The absence of wavebands at 3093 and 2981 cm^{-1} (aromatic C-H stretch and aliphatic C-H stretch, respectively), 1560 cm^{-1} (C=O), and 1375 cm^{-1} (C-H bending) in **10cel** and **cel-lig** films confirms the films are free from residual ionic liquid. The absence of bands at 3000 and 2915 cm^{-1} (C-H stretch) and 1400 cm^{-1} (S=O stretch) confirms the effective removal of DMSO from the cellulose-lignin films. The purity of this cellulose-lignin film may influence its mechanical, thermal, and optical properties.

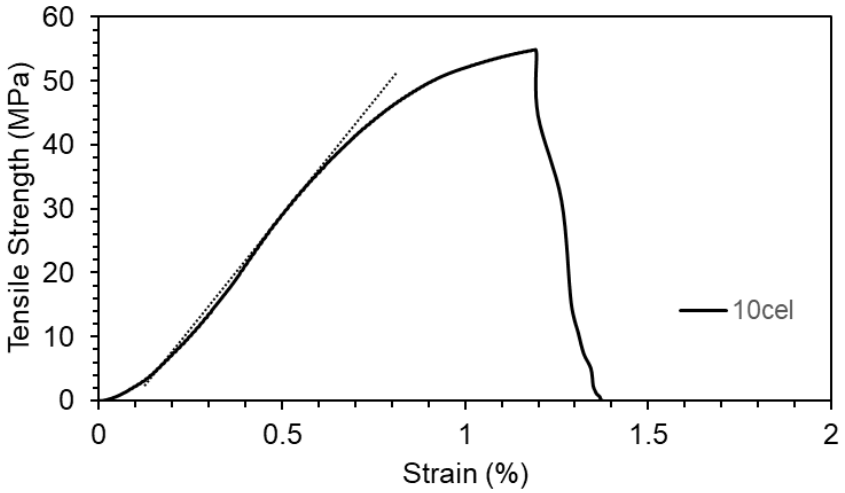
A study on the impact of residual ionic liquids on thermal stability and electrochemical behavior revealed that the concentration of residual $[C_2C_1im][OAc]$, ranging from 2.68 to 0.75 wt.%, in regenerated cellulose correlates with the lowest decomposition temperature, which is attributed to the entrapment of large quantities of residual ionic liquid.[58] Imidazolium-based ionic liquids can react with cellulose, resulting in the breakdown of polymer chains and side reactions.[59] This will affect the mechanical properties of the film.

5.3.3 Mechanical properties of cellulose-lignin films

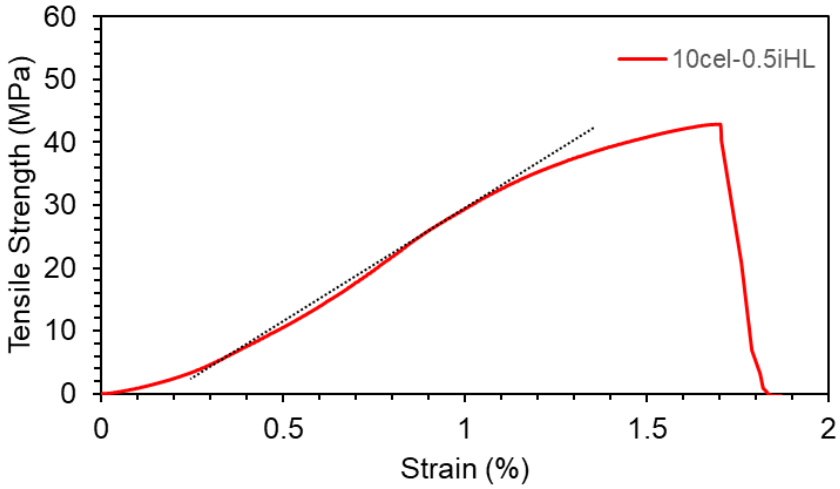
The tensile properties of a material are crucial, as tensile stress (TS) indicates the force a material can withstand before deformation, percentage strain measures the extent of material elongation, and Young's Modulus (YM) essentially reflects the material's stiffness. Representative stress-strain curves for the all **cel-lig** films with the offset value on strain-stress correction adjusted in accordance with the criteria of standard protocol D882-10 are depicted in Figure 5.28.[60] This off-set adjustment not only minimizes standard deviation for accurate results but also allows direct determination of YM from the graph. For the developed cellulose-lignin composite films, the mechanical properties at the yield point are also critical for determining their practical application limits, as plastic deformation marks the onset of structural failure. The tensile properties extracted from these curves are summarized and discussed in Figure 5.29.

(a) 10cel-iHL

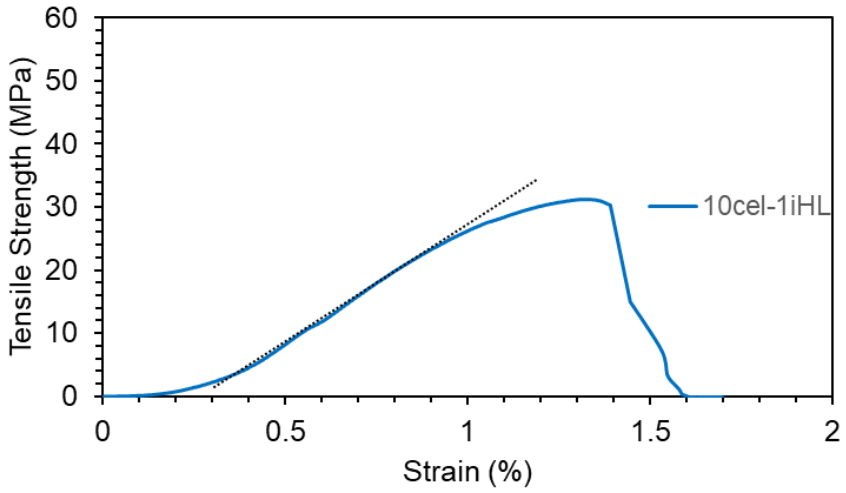
10cel



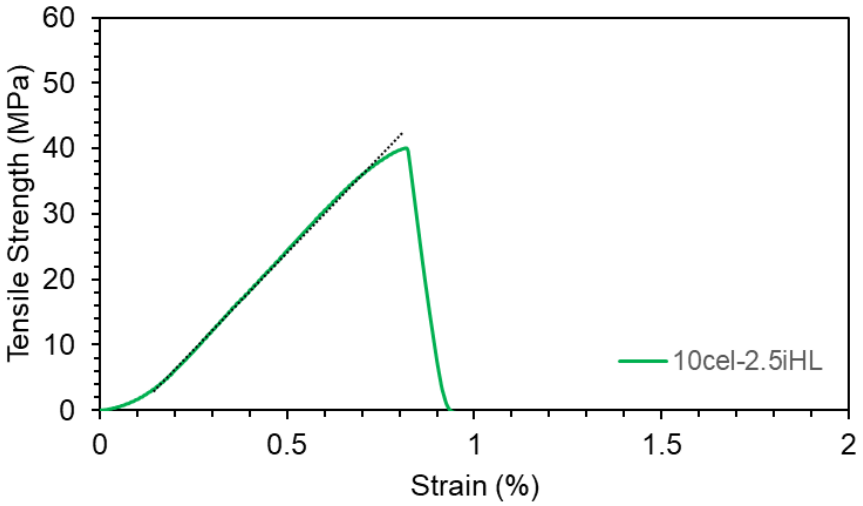
10cel-0.5iHL



10cel-1iHL

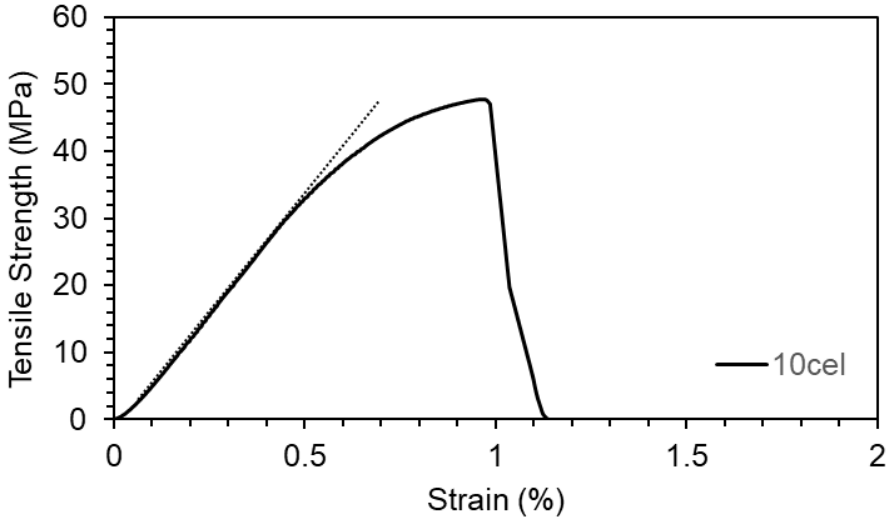


10cel-2.5iHL

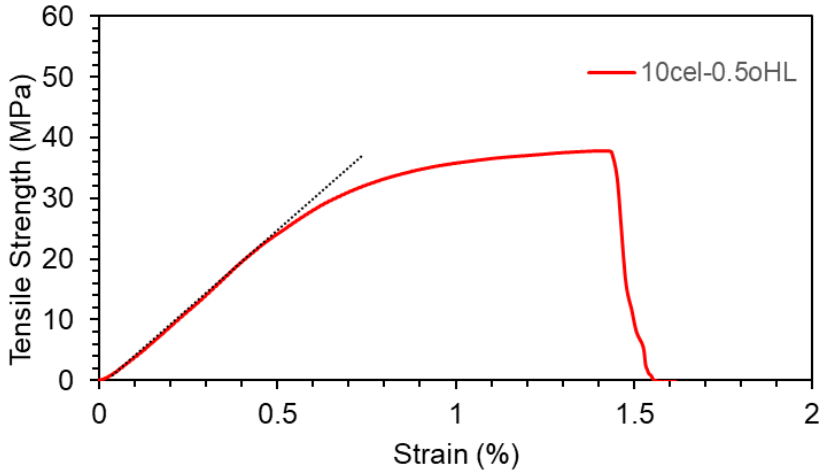


(b) 10cel-oHL

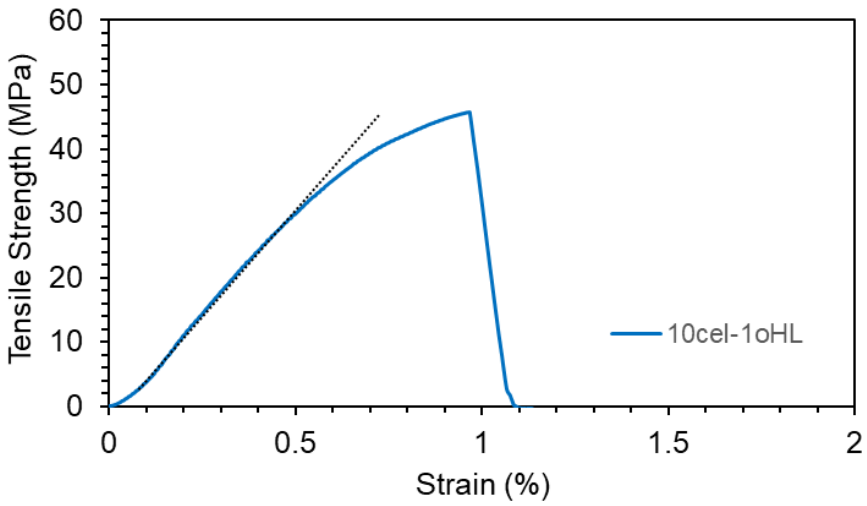
10cel



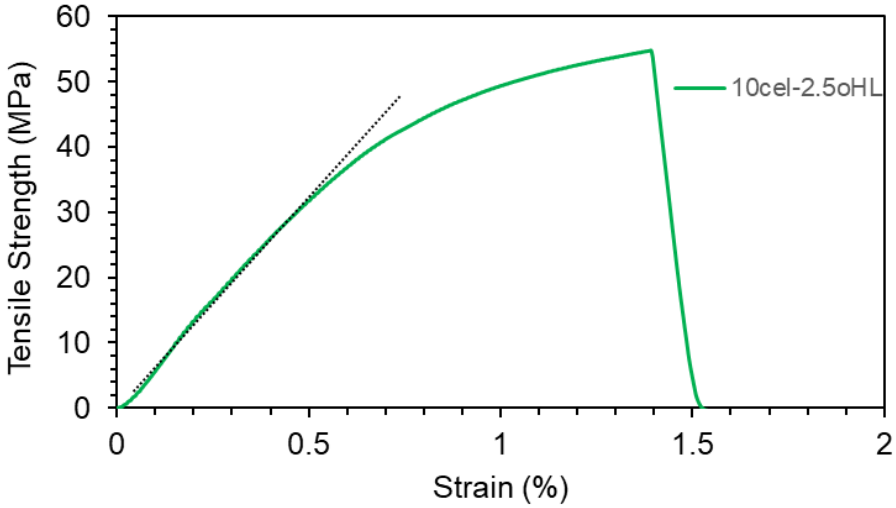
10cel-0.5oHL



10cel-1oHL

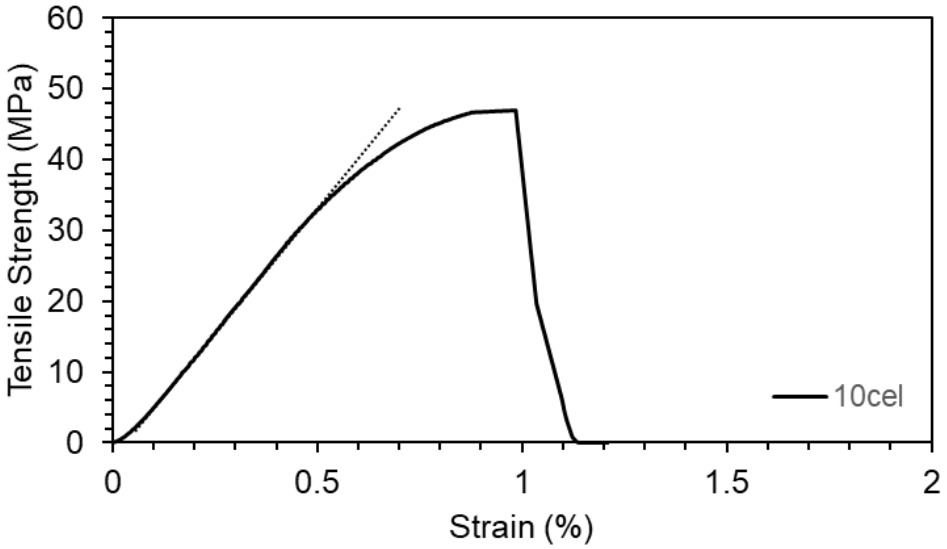


10cel-2.5oHL

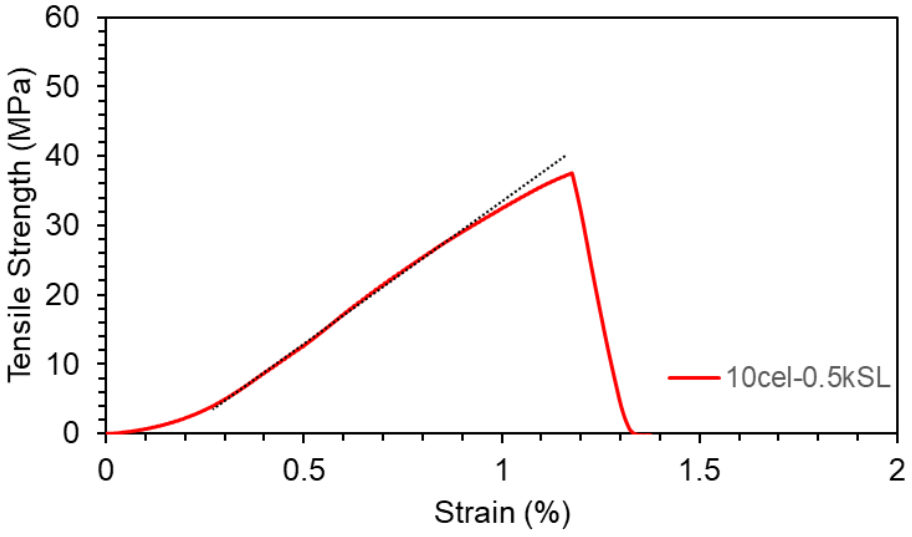


(c) 10cel-kSL

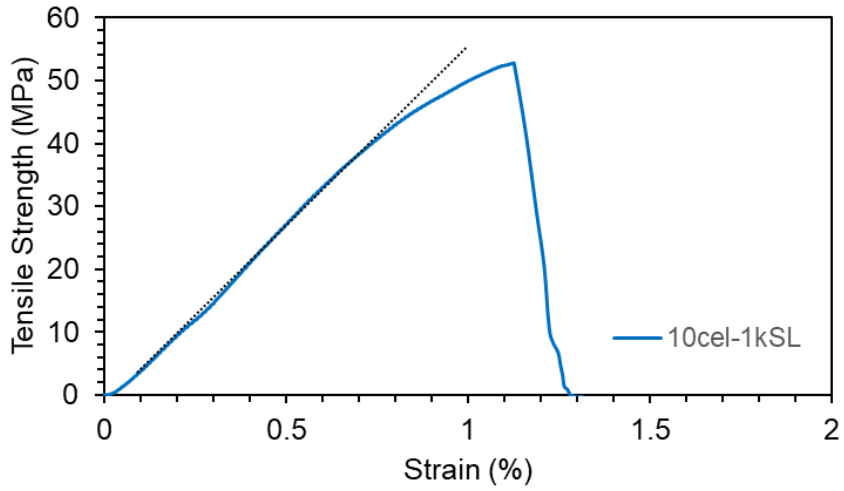
10cel



10cel-0.5kSL

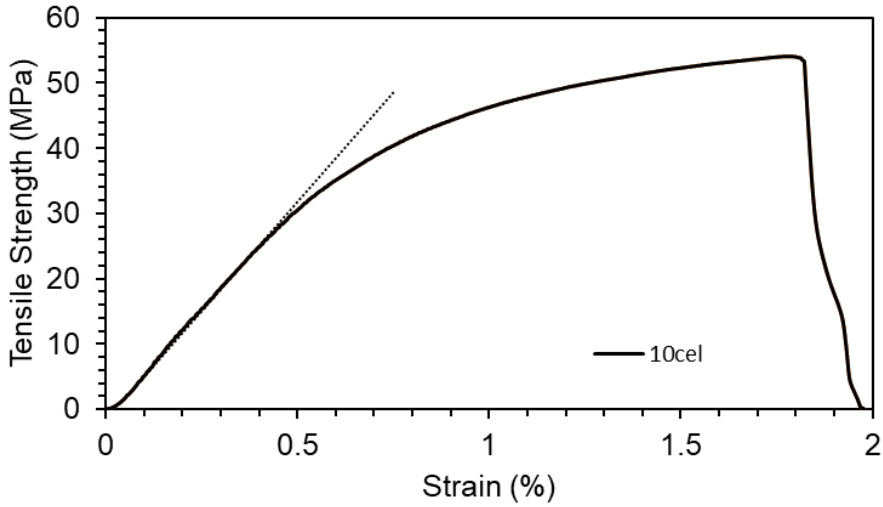


10cel-1kSL

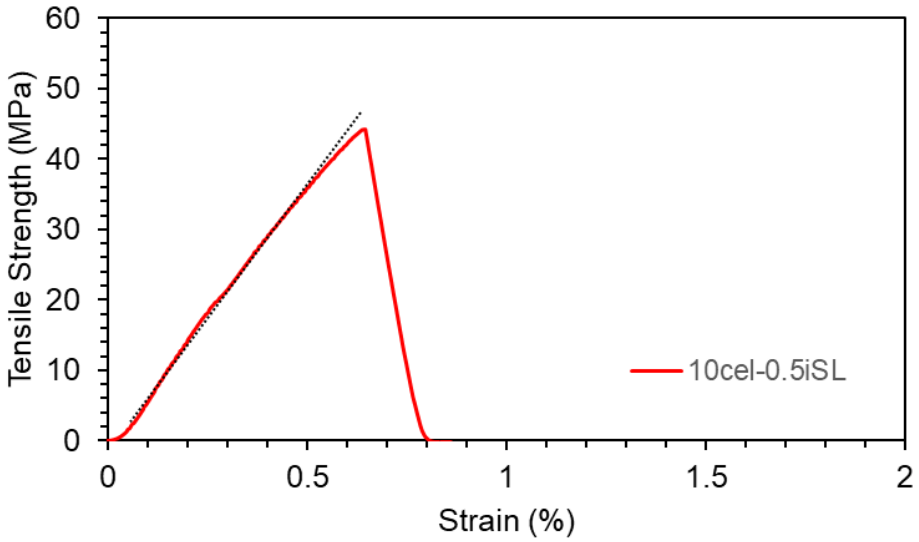


(d) 10cel-iSL

10cel



10cel-0.5iSL



10cel-1iSL

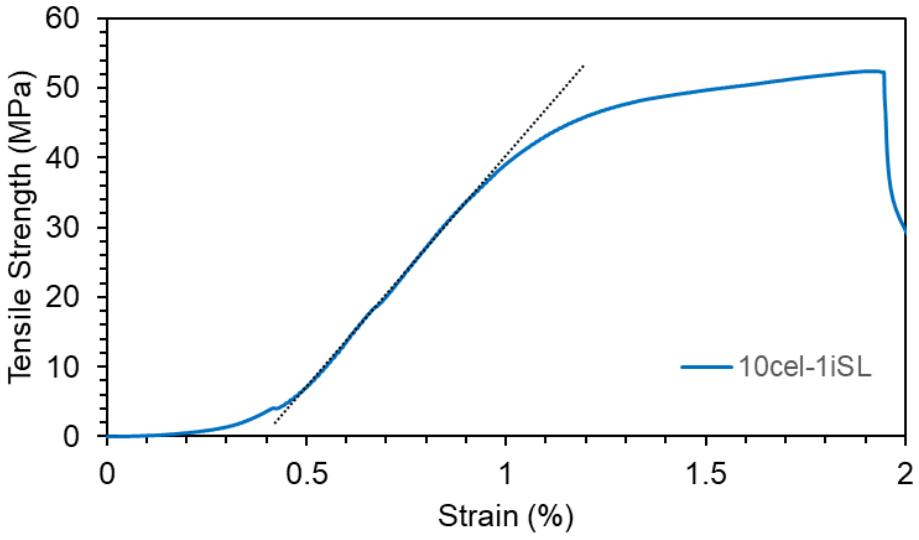


Figure 5.28: Compilation representative tensile strength verses strain curves for cellulose-lignin films at different lignin weight percent (a)**10cel-iHL**, (b) **10cel-oHL**, (c) **10cel-kSL** and (d) **10cel-iSL**

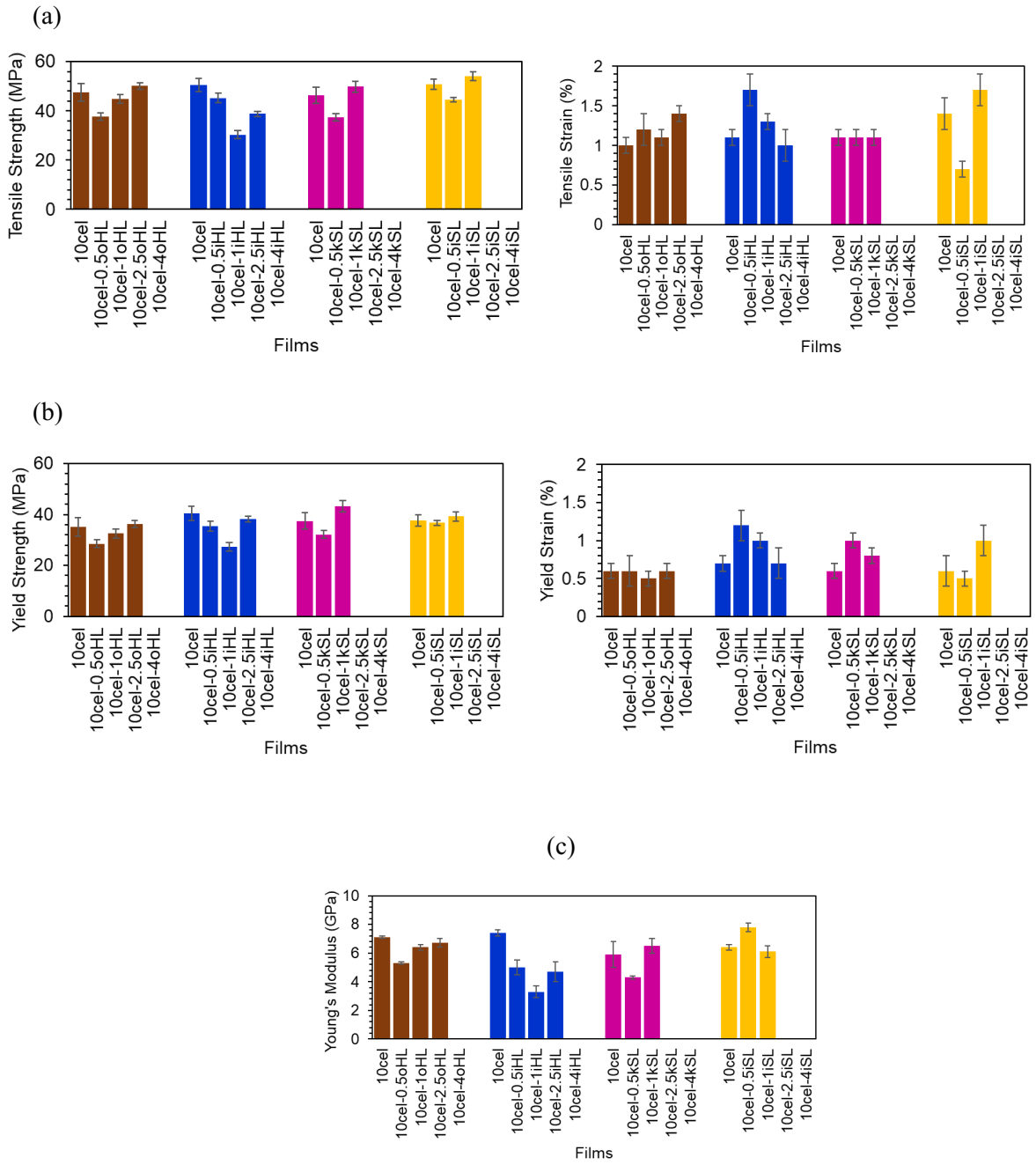


Figure 5.29: Tensile properties of cellulose–lignin composite films showing (a) tensile strength and strain at failure, (b) yield strength and yield strain, and (c) Young's modulus as a function of lignin type and content

For engineering and packaging applications, the yield point is technically more critical than the properties at break. The yield point defines the elastic limit of the material beyond this threshold, the film undergoes permanent plastic deformation, rendering it functionally compromised even before physical rupture occurs. The experimental data reveals a highly rigid and narrow plastic region across all cellulose-lignin composite films formulations. The average difference between ultimate tensile strength and yield strength is only 9.2 MPa, while the average difference between

tensile strain at break and yield strain is a minimal 0.46%. These composite films display a rigid, relatively brittle nature which characterized by high Young's modulus and total strains under 2%, the onset of yielding is rapidly followed by total structural fracture. Therefore, while the yield point marks the true functional limit of the films, both metrics must be evaluated together to capture the complete deformation profile. The exact value for the yield and break points for all films are comprehensively detailed in Table 5.8.

Table 5.8: Tensile properties of cellulose–lignin composite films at different lignin and content

Lignin type	Formula	Tensile Strength (MPa)	Strain at Failure (%)	Yield Strength (MPa)	Yield Stress (%)	Young's Modulus (GPa)
oHL	**10cel**	47.6 ± 3.6	1.0 ± 0.1	35.1 ± 2.6	0.6 ± 0.1	7.1 ± 0.1
	10cel-0.5oHL	37.8 ± 1.5	1.2 ± 0.2	28.5 ± 1.4	0.6 ± 0.1	5.3 ± 0.1
	10cel-1oHL	44.9 ± 1.8	1.1 ± 0.1	32.5 ± 1.7	0.5 ± 0.1	6.4 ± 0.2
	10cel-2.5oHL	50.11 ± 1.2	1.4 ± 0.1	36.5 ± 1.1	0.6 ± 0.1	6.7 ± 0.3
	10cel-4oHL	-	-	-	-	-
iHL	**10cel**	50.5 ± 2.8	1.1 ± 0.1	40.4 ± 2.6	0.7 ± 0.1	7.4 ± 0.2
	10cel-0.5iHL	45.2 ± 2.0	1.7 ± 0.2	35.4 ± 1.8	1.2 ± 0.1	5.0 ± 0.5
	10cel-1iHL	30.3 ± 1.7	1.3 ± 0.1	27.3 ± 1.5	1.0 ± 0.1	3.3 ± 0.4
	10cel-2.5iHL	38.8 ± 1.1	1.0 ± 0.2	38.1 ± 1.0	0.7 ± 0.1	4.7 ± 0.7
	10cel-4iHL	-	-	-	-	-
kSL	**10cel**	46.3 ± 3.2	1.1 ± 0.1	37.4 ± 2.8	0.6 ± 0.1	5.9 ± 0.9
	10cel-0.5kSL	37.5 ± 1.5	1.1 ± 0.1	32.1 ± 1.4	1.0 ± 0.1	4.3 ± 0.1
	10cel-1kSL	49.8 ± 2.3	1.1 ± 0.1	43.3 ± 2.2	0.8 ± 0.1	6.5 ± 0.5
	10cel-2.5kSL	-	-	-	-	-
	10cel-4kSL	-	-	-	-	-
iSL	**10cel**	50.8 ± 2.2	1.4 ± 0.2	37.7 ± 2.1	0.6 ± 0.1	6.4 ± 0.2
	10cel-0.5isL	44.5 ± 0.9	0.7 ± 0.1	36.7 ± 0.9	0.5 ± 0.1	7.8 ± 0.3
	10cel-1isL	54.0 ± 1.8	1.7 ± 0.2	39.2 ± 1.6	1.0 ± 0.1	6.1 ± 0.4
	10cel-2.5isL	-	-	-		-
	10cel-4isL	-	-	-		-

TS and percentage tensile strains are typically reported for cellulose-based films, with some work also addressing YM.[61,18,62] The **10cel** film exhibits a tensile strength of 46.3 ± 3.2 to 50.8 ± 2.2 MPa as illustrated in Figure 5.28. Other studies using regenerated cellulose films derived from modified microcrystalline cellulose report tensile strengths between 110–150 MPa, significantly higher than the values observed in this study. This is likely due to differences in cellulose source and processing conditions.[52,53] In contrast, studies on films composed of pure microcrystalline

cellulose report a tensile strength of 44.3 MPa, which closely aligns with the results obtained in this study. [63]

Overall, the trend was non-linear for all mechanical properties in this study. The TS and YM values of the **cel-lig** film decreased relative to **10cel** as the lignin content increased, reaching a minimum before increasing again, as shown in Figure 5.29 and Table 5.8. This observation aligns with the studies conducted by He et al.[53] on cellulose-lignin films, where this behaviour was attributed to the internal void inside the films. Although the film did not exhibit internal voids, as confirmed by the SEM images, aggregated regions were present in the cross-section, as shown in Section 5.37 for the **10cel-0.5iSL** film. Phase separation or aggregation, indicating poor intermixing and non-uniform distribution at the microstructural level. At this low weight percent, lignin may not form a continuous phase within the cellulose matrix, functioning instead as a weak spot that hinders stress transfer during mechanical testing.[64] Lignin can exert multiple effects at varying concentrations within the cellulose matrix, thereby influencing the mechanical properties through mechanisms beyond the formation of internal voids alone.

To enable a fair comparison among different lignin types, the tensile properties of films containing 1 wt.% lignin were evaluated, as this was the only lignin loading at which all films could be successfully measured. At 1 wt.% lignin loading, the tensile performance of the composite films followed the order: **10cel-1iSL** > **10cel-1kSL** > **10cel-1oHL** > **10cel-1iHL**, where **10cel-1iSL** exhibited the highest tensile strength (54 MPa) and flexibility (1.7%), while **10cel-1iHL** showed the lowest Young's modulus (3.3 GPa), indicating lower resistance to elastic deformation under applied load. The reasons underlying the superior performance of the **10cel-1iSL** composite film are discussed in the following paragraph.

This mechanical performance trend **10cel-1iSL** greater than **10cel-1iHL** correlates directly with the molecular weight profiles of the respective lignin samples shown in Table 5.2 (Section 5.2.1). The **iSL** sample possesses the highest weight-average molecular weight (M*w* = 32,635 g/mol) and number-average molecular weight (M*n* = 4,613 g/mol). In polymer composite systems, a higher molecular weight promotes extensive chain entanglement and enhances interfacial hydrogen bonding between the lignin molecules and the cellulose matrix.[65] This well-integrated network allows for more efficient stress transfer across the matrix, resulting in superior tensile strength and flexibility. In contrast, the poor mechanical performance of the **10cel-1iHL** film can be attributed to the significantly lower molecular weight of **iHL** (M*n* = 1,062 g/mol). The abundance of shorter

polymer chains and oligomers in **iHL** introduces a high density of chain ends, which act as structural defects and stress concentration points within the composite.[27] While the high-molecular-weight cellulose provides the fundamental structural backbone across all film variants, the molecular weight of the incorporated lignin acts as a critical modulating factor; higher molecular weight fractions consistently provide more effective structural reinforcement

Lignin serves as a stiffening agent, occupying voids and reinforcing the matrix when available in adequate amounts.[3] For instance, Liu et al. (2009) also reported an increment in TS of carboxylated cellulose nanofibril (CNF) with the incorporation of kraft lignin and lignosulfonates lignin.[66] SEM images of **10cel-1iSL** (Figure 5.34) demonstrated that lignin is uniformly dispersed inside cellulose matrix, and the compact cross-sectional images showed lignin homogeneous blend withing cellulose matrix. At this weight percent, lignin comprises aromatic rings and functional groups capable of interacting effectively with cellulose through hydrogen bonding, which is the main interaction in this system. This may result in enhanced stress transfer and elevated stiffness, leading to increased tensile strength and Young's Modulus.[67]

There are two notable observations in the trend of mechanical properties. First, at 1 wt.% softwood lignin (**iSL** and **kSL**), both films exhibit superior mechanical properties compared to the **10cel** and cellulose-hardwood films. Second, cellulose–softwood lignin films cannot be reliably tested for mechanical properties above 1 wt.%, which is supported by the hydroxyl quantification presented in Section 5.2.5. Overestimation of hydroxyl content in **iHL** is excluded from this discussion. While literature on the correlation between hydroxyl content and mechanical properties is limited, the number of hydroxyls and their influence are thoroughly discussed in the context of existing findings.

The addition of small amounts of softwood lignin can enhance interfacial interactions in cellulose–lignin composite films when the lignin is finely dispersed without agglomeration and is preferentially located at the cellulose–lignin interface. **kSL** with aliphatic OH content (2.33 mmol/g), provides flexible side-chain hydroxyls that can form hydrogen bonds without excessive rigid aromatic stacking.[52] This promotes local adhesion at very low loadings, resulting in strength gains relative to the **10cel** film. At 1 wt.% loading, both **kSL** and **iSL** improve tensile strength; however, the **10cel-1iSL** film exhibits the highest tensile strength and strain, indicating superior mechanical performance compared to **kSL** at the same loading. The lower aliphatic (0.8 mmol/g in

iSL), but similar phenolic OH content of **iSL** relative to **kSL** may contribute to these enhanced properties at low lignin contents.

At 2.5 wt.%, cellulose–softwood lignin films become brittle, whereas hardwood (**oHL**) films remain workable. Softwood lignins, particularly G-rich and condensed types, tend to self-associate through aromatic interactions. At low loadings, fine dispersion is beneficial, but above a threshold (~2.5%), they can form rigid, lignin-rich domains that act as crack initiation sites, resulting in overall brittleness. In contrast, hardwood **oHL** has high overall hydroxyl content, which allows continued hydrogen bonding with cellulose at higher loadings, improving compatibility and preventing the formation of large brittle lignin-rich domains. This observation is consistent with studies on CNF–starch films that quantified hydroxyl content, addition of hardwood lignin increased tensile stress, while softwood lignin reduced it.[68] This difference may be related to the uniformity of lignin dispersion in the composite films.

Exceeding 2.5 wt.% and 4 wt.% for hardwood lignin and softwood lignin may result in the film becoming brittle due to phase separation or excessive rigidity.[67] This phenomenon is evident in the SEM images (Figure 5.34), where phase separation appears as lignin deposited on both the surface and cross-section of the **10cel-4iSL** sample. Increasing the lignin concentration reduces the film's elasticity and diminishes the inherent ductility of cellulose. Because lignin is intrinsically brittle and exhibits low crystallinity, higher lignin content decreases the film's ability to deform under stress, resulting in reduced mechanical performance and practical challenges during measurement, such as premature sample failure.

Studies on composite films containing cellulose, starch, and lignin have shown that these films display pronounced amorphous characteristics after dissolution and blending in ionic liquids. This behavior arises from phase separation within the cellulose–starch matrix induced by the addition of amorphous lignin, which consequently compromises tensile properties.[67] XRD analysis further supports these findings, indicating that the **10cel-2.5iSL** and **10cel-4iSL** films exhibit low crystallinity.

5.3.4 Thermogravimetric analysis

Thermogravimetric analysis (TGA) is a technique to assess the thermal stability of materials, including mostly reported on **cel-lig** films.[67,53] The primary application of **cel-lig** film is in plastic packaging, typically utilised for commercial purposes at ambient or external temperatures; however, its thermal stability makes it a viable candidate for use in extreme environmental conditions such as at high temperature. A key parameter in TGA analysis is the degradation curves specifically at beginning of thermal degradation (T_{onset}) and the residual weight after a dynamic thermal event occurs in the sample.

Table 5.9: T_{onset} data of cellulose-lignin films from different types of wood

Types of lignin	Samples	T_{onset} (°C)
oHL	**oHL**	285.0
	10cel	310.7
	10cel-0.5oHL	314.3
	10cel-1oHL	314.3
	10cel-2.5oHL	306.2
	10cel-4oHL	304.9
iHL	**iHL**	198.6
	10cel	308.6
	10cel-0.5iHL	317.8
	10cel-1iHL	314.8
	10cel-2.5iHL	307.0
	10cel-4iHL	306.9
kSL	**kSL**	308.7
	10cel	317.5
	10cel-0.5kSL	320.1
	10cel-1kSL	314.2
	10cel-2.5kSL	294.8
	10cel-4kSL	294.0
iSL	**iSL**	318.6
	10cel	309.9
	10cel-0.5isL	309.8
	10cel-1isL	307.9
	10cel-2.5isL	307.5
	10cel-4isL	307.5

T_{onset} for most lignin commences at 300 °C, when aliphatic side chains begin to disintegrate, progressing to the cleavage of more thermally stable C−C bonds between 300 and 400 °C.[30, 27] In this study, the T_{onset} temperatures of **10cel** films varied between 309 °C and 317 °C, with a mean of 311 °C as indicated in Table 5.9. The T_{onset} of **cel-lig** films varied between 294 °C and 320 °C, with a mean of 315 °C. Some **cel-lig** films exhibited T_{onset} values as high as 320 °C, while others were lower than those of pure cellulose. The observed T_{onset} trend closely mirrors the mechanical

properties: low lignin content increases T_{onset}, but beyond a certain point, further increases in lignin content reduce T_{onset}.

The integration of lignin into cellulose matrices in literature is frequently linked to enhanced thermal stability owing to lignin's aromatic nature.[2] This behaviour only occurred for low lignin content at 0.5 and 1 wt.%. At low concentrations, lignin can integrate well into the cellulose matrix, forming strong hydrogen bond interactions with cellulose chains. This reinforces the overall structure, stabilizing cellulose against initial thermal degradation. However, at high lignin content, T_{onset} reduces. The integration of lignin into the cellulose matrix may disrupt the crystalline domains of cellulose, hence diminish its thermal decomposition rate. A study demonstrated that the addition of organosolv lignin hinders the formation of a uniformly ordered structure in cellulose-lignin blends, resulting in a reduction in percent crystallinity and reduced T_{onset}.[69] The same trend observed in all **cel-lig** films this study especially for high lignin content at 2.5 wt.% and 4 wt.%.

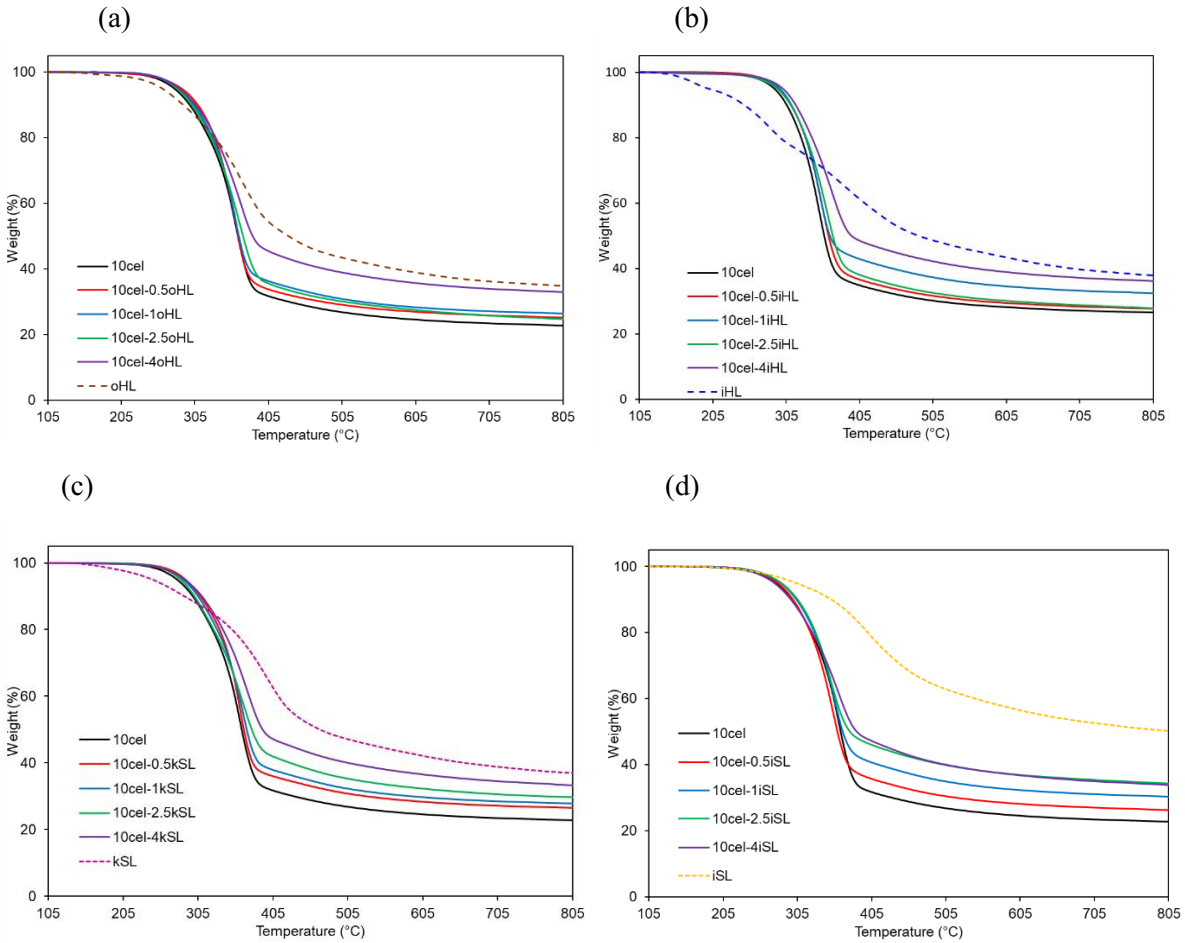


Figure 5.30: Thermogram of cellulose-lignin composite films at different weight percent ratio (a) for hardwood lignin and (b) softwood lignin.

The TGA curves of all films stabilized at 800°C, indicating a constant residual weight corresponding to thermal stable char formation as illustrated in Figure 5.30. A clear difference was observed between cellulose-softwood lignin and cellulose-hardwood lignin films. Cellulose-softwood lignin films exhibit a more pronounced increase in residual weight compared to hardwood lignin films. Specifically, the residual weight of cellulose-hardwood lignin films showed only minor variations between 0.5 and 2.5 wt.% lignin, with noticeable increase only at 4 wt.%. In contrast, the increase in residual weight with cellulose-softwood lignin film was more linear and significant across all lignin concentrations.

At comparable lignin loadings and at temperature of 800 °C, the residual weights for **10cel-4kSL**, **10cel-4iSL**, **10cel-4iHL**, and **10cel-4oHL** were reported as 33.3 %, 33.9 %, 36.2 %, and 33.0 %, respectively. These results indicate broadly similar residual weights across the samples, with the cellulose–hardwood lignin film exhibiting the highest residue. This enhanced thermal stability can be attributed to the syringyl units in hardwood lignin, which possess additional methoxyl groups that hinder radical condensation, thereby promoting higher char yield and greater thermal stability compared with softwood-derived lignins.[70]

5.3.5 Water contact angle

The water contact angle (WCA) is a commonly used parameter for evaluating the wettability and surface hydrophobicity of materials. Elevated lignin weight percent ratio has substantially enhanced the WCA of **cel-lig** films from the control film (**10cel**) of 43.5° to an impressive (**10cel-4iSL**) 88.7° as indicated in Figure 5.31. **10cel** has a water contact angle similar to that of regenerated cellulose derived from kraft pulp, reported in the literature as 46.2°.[71] In cellulose-rich films (**10cel**), the hydroxyl groups in cellulose readily form hydrogen bonds with water, resulting in a lower WCA. This finding is further corroborated by a study indicating that cellulose nanofibril (CNF) nanocomposite films exhibit great hydrophilicity.[72] In contrast, cellulose films incorporating with lignin exhibit a significant higher water contact angle.

Elevating the lignin content in **cel-lig** films reduces -OH groups on the surface available for hydrogen bonding, leading to an increased WCA. The incorporation of lignin interferes with the

hydrogen-bonding network by introducing the steric hindrance and reducing accessibility of lignin hydroxyl groups for water interaction. The total hydroxyl (–OH) group content of softwood (**kSL**, **iSL**) and hardwood (**oHL**) lignins determined by ^{31}P NMR was 4.26 ± 0.02, 3.21 ± 0.03, and 5.50 ± 0.26 mmol OH g^{-1} lignin, respectively. **iHL** was excluded due to overestimation, as discussed in Section 5.2.4. Although the bulk hydroxyl content follows the order **oHL** > **kSL** > **iSL**, the measured water contact angles follow a different trend (**iSL** > **kSL** > **oHL**). This indicates that wettability is not governed solely by the total hydroxyl content but rather by the surface-accessible hydroxyl groups and their chemical nature. The effective hydroxyl–water interactions at the lignin surface, thereby affecting the observed WCA.

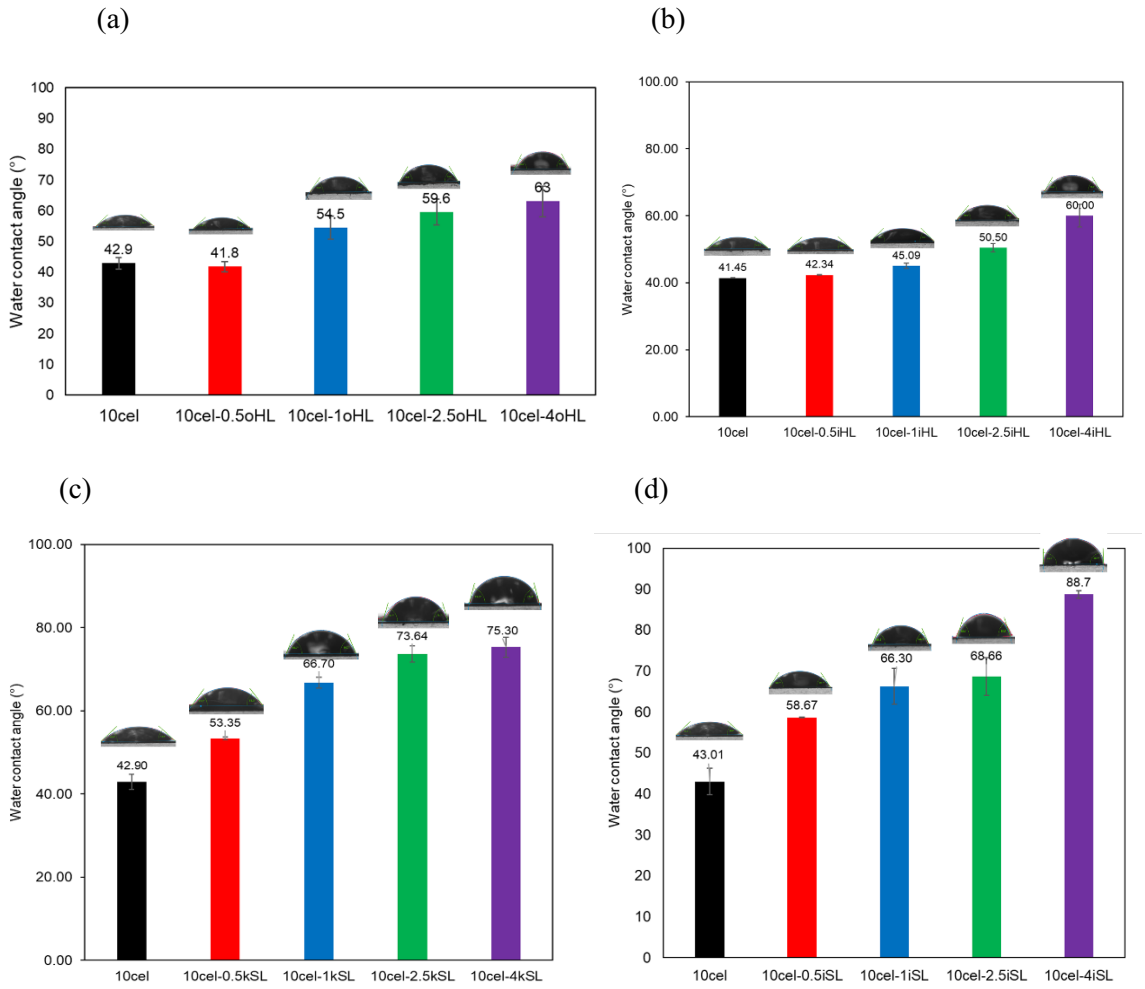


Figure 5.31: Water contact angle of cellulose-lignin films which constitute from (a-b) hardwood lignin and (c-d) softwood lignin

The WCA improved significantly, reaching its maximum at 4 wt.% lignin content. This trend can be attributed to the reduced hydroxyl group content in the lignin-containing films, which reduces

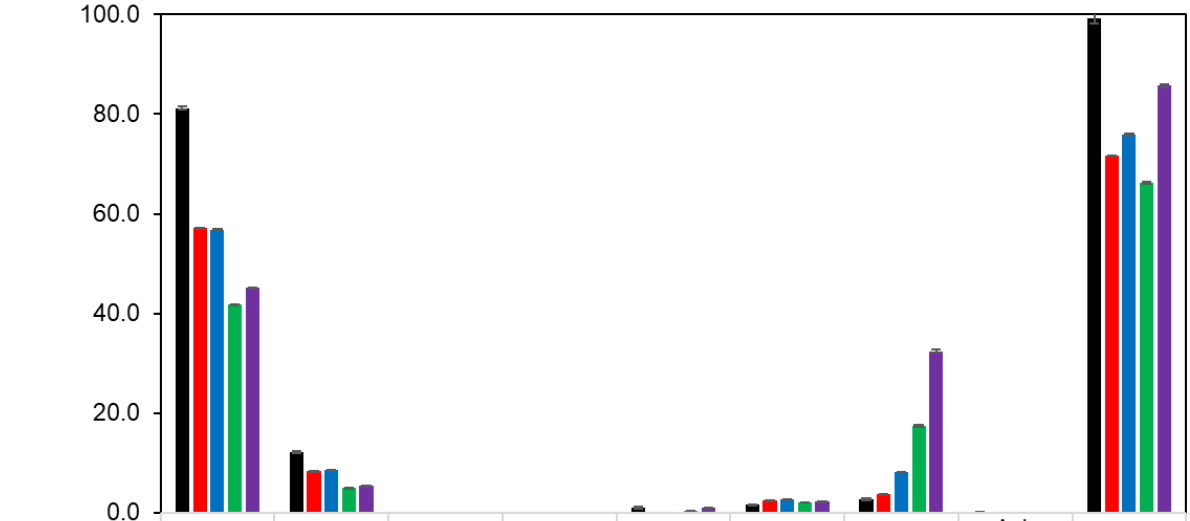
hydroxyl–water interactions and enhances surface hydrophobicity. Notably, **cel-kSL** and **cel-iSL** lignin films showed WCAs of 73.5° and 88.7°, respectively, exceeding values reported in the literature for similar systems. Both **isL** and **kSL** has the lowest total hydroxyl contents as indicated by ^{31}P NMR experiment. For comparison, lignocellulose nanofibrils (LCNF) containing 2, 4 and 14 wt.% softwood lignin reported increase WCA at 49°, 61° and 78°, respectively. Another secondary reason could contribute to high WCA is methoxy group. The positive correlation between methoxyl group content and roughness indicates that hardwood lignins possessing a greater degree of methoxylation than those derived from softwoods and grasses, would yield rougher thin films.[73]

Lignin's irregular distribution leads to agglomeration, resulting in micro-roughness on the surface. The Wenzel and Cassie-Baxter models indicate that surface roughness can enhance hydrophobicity by capturing air pockets or increasing the water-repellent surface area.[74] Section 5.3.7 presents SEM pictures indicating that **10cel-4iSL** exhibited surface roughness due to lignin aggregation. This explains why **10cel-4iSL** exhibited the highest WCA among the films. This finding further supports that the elevated surface roughness of HWE-90, a form of lignocellulosic film, contributed to its hydrophobicity. Its high lignin content and deficiency in hemicellulose likely enhanced its hydrophobic properties. [75]

5.3.6 Compositional analysis for selected cel-lig films

The primary aim of the compositional analysis (CA) conducted on cellulose-lignin films is to ascertain the precise percentages of cellulose and lignin in relation to theoretical values. This analysis is useful for biomass as the compositional analysis methods of the National Renewable Energy Laboratory (NREL) provide reliable and reproducible results, leading to its widespread acceptance across several industries.[10] **cel-iSL** films were chosen to quantify CA due to their high TS and YM (particularly in the **10cel-1iSL** film), stable thermal behavior, and high water contact angle. Nonetheless, the measured value fell below the accepted range as indicated in Figure 5.32. An effort was made in sample preparation aimed at reducing particle size through grinding and sieving to 50 mesh (approximately 300 microns) to enhance surface area for efficient acid hydrolysis as seen in Figure 5.33; however, an incomplete acid hydrolysis contributes to the suboptimal predicted value of the results. To my knowledge, the determination of CA in a cellulose

and lignin mixture has not been addressed in any literature. The CA method is primarily performed only on lignocellulose biomass or lignin.[76,77]



	Glucose	Xylose	Galactose	Arabinose	Mannose	% ASL	% AIL	Ash residue	Total
10cel	81.2	12.1	0.0	0.0	1.0	1.6	2.7	0.0	99.3
10cel-0.5iSL	57.2	8.4	0.0	0.0	0.0	2.5	3.6	0.0	71.7
10cel-1iSL	56.7	8.5	0.0	0.0	0.0	2.7	8.1	0.0	75.9
10cel-2.5iSL	41.7	4.9	0.0	0.0	0.4	2.1	17.4	0.0	66.3
10cel-4iSL	45.1	5.3	0.0	0.0	0.9	2.2	32.4	0.0	85.7

Figure 5.32: Compositional analysis of cellulose-softwood lignin films



Figure 5.33: **10cel-2.5iSL** was initially dried under vacuum using a Schlenk line, followed by grinding to a 50-mesh powder for CA

The underestimated measured value resulted from low sugar content. This is caused by the slow conversion of cellulose to sugar through acid hydrolysis due to the protective matrix of lignin and hemicellulose surrounding the crystalline cellulose fragment. Consequently, the pretreatment of these materials is essential to enhance the hydrolysis rate of cellulose into fermentable monomeric sugars, which may be quantified using HPLC instrumentation.[78] Analytical parameters such as

calibration curves, and moisture content in biomass can be disregarded, as these elements have been meticulously accounted for in the sugar concentration. A control sample, **10cel**, was analysed to verify the efficacy of the acid hydrolysis process in releasing all sugars. Pure cellulose powder achieved 100% in CA, however **10cel** ranged from 94.27% to 95.50%. The **10cel** experienced incomplete acid hydrolysis, resulting in roughly 5% incomplete conversion of cellulose to monomeric sugars. This finding lacks comparative literature as the analysis is mostly applicable to lignocellulose and lignin. The presence of lignin in **cel-lig** films further obstruct the detection of sugars. Lignin acts as a structural barrier in these films, and effective pretreatment may be required to overcome this issue.

Pretreatments work by deconstructing the structural and chemical barriers that lignin and other components pose to cellulose accessibility. Enzymes such as laccases can oxidise lignin and reduce its physical barrier effect on cellulose. The literature indicates that an effective pretreatment procedure involves reducing the particle size to 0.2 mm through milling or grinding, which enhances the specific surface area and subsequently improves cellulose accessibility to enzymes. The removal of solvents from the system is essential, since they may hinder enzymatic hydrolysis and fermentative microorganisms.[79] By taking this action, the CA evaluation of **cel-lig** films will be more accurate.

Ultimately, this CA cannot ascertain the theoretical value due to the underestimation of cellulose for all **cel-lig** films. Nevertheless, lignin exhibited a surprisingly tighter agreement with the measured value, differing by only 0.5 to 6.0% as shown in Table 5.10. This indicates that the incorporated lignin wt.% in the cellulose matrix is accurate and well-mixed. Although a small amount of lignin may have been washed out during the coagulation bath especially at higher lignin contents, the final formulation remains within an acceptable range. According to Sluiter et al. (2010), who created the NREL approach, this procedure is essential for quantifying the structural carbohydrates and lignin in a solid biomass sample.[10] In contrast to these investigations, cellulose and lignin were separated and subsequently combined physically. Utilising the appropriate pretreatment as recommended, CA would yield precise results and produce more accurate cellulose and lignin quantification.

Table 5.10: Cellulose-lignin films measured and theoretical values

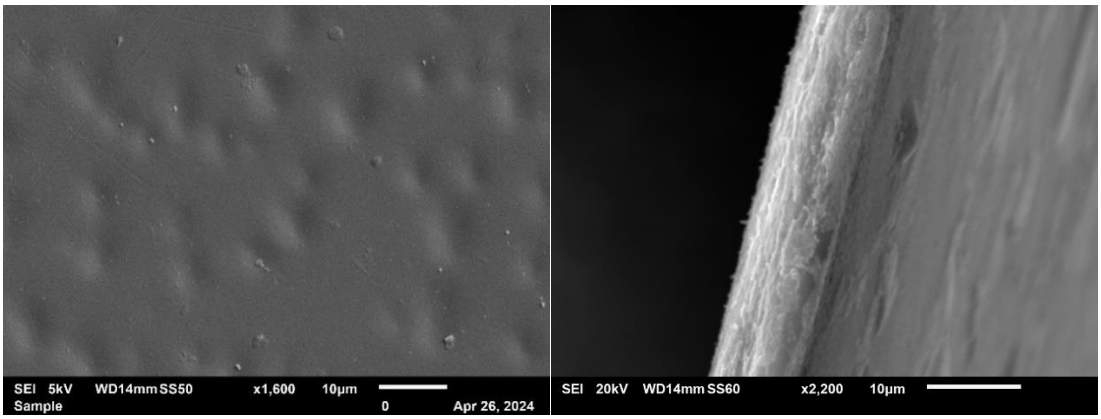
Sample	Measured		Theoretical	
	Cellulose (%)	Lignin (%)	Cellulose (%)	Lignin (%)
10cel	93.3	4.3	100.0	0.0
10cel-0.5iSL	65.5	6.1	95.2	4.8
10cel-1iSL	65.1	10.6	90.9	9.1
10cel-2.5iSL	46.9	19.5	80.0	20.0
10cel-4iSL	51.3	34.6	71.4	28.6

5.3.7 SEM for selected cel-lig films

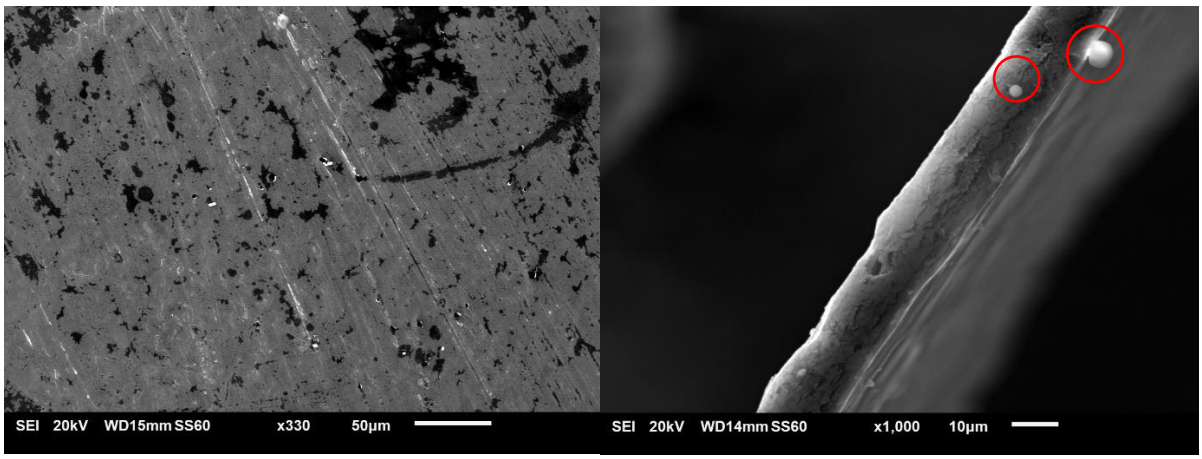
Scanning electron microscopy (SEM) generates high-resolution images and allows for the examination of surface morphology. Nonetheless, the various mechanical properties in cellulose-lignin films, including tensile strength (TS) and Young's modulus (YM), can be correlated with SEM surface appearance. The surface morphology observed using SEM can enhance the understanding of mechanical properties; for instance, a study on carboxymethyl cellulose with lignin film revealed small aggregation structures that significantly affect the TS of the composite film.[3] A series of cellulose-ionosolv softwood lignin films with varying weight percent ratios were examined due to their superior tensile stress and Young's modulus.

The **10cel** film appearance distinct from the **cel-lig** film as the surface appeared patches, signifying miscibility between cellulose and lignin, while the **10cel** film appeared uniform. Even at low lignin loadings (**10cel-0.5iSL**), the presence of black regions suggested that lignin was well integrated within the cellulose matrix, as shown in Figure 5.34. In this formulation, an actual lignin content of 4.8% was successfully incorporated, as confirmed by the CA results. From a top-surface perspective, all **cel-iSL** films appeared rough and exhibited phase separation, particularly at **10cel-4iSL**. Phase separation or aggregation can be interpreted differently when evaluating films incorporated with lignin.

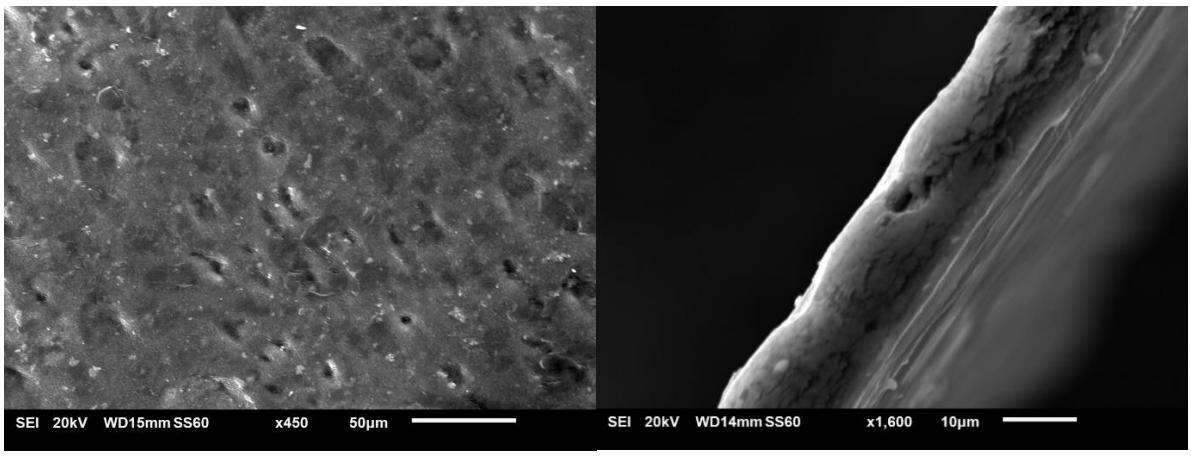
a) 10cel (left – surface morphology and right – cross section morphology)



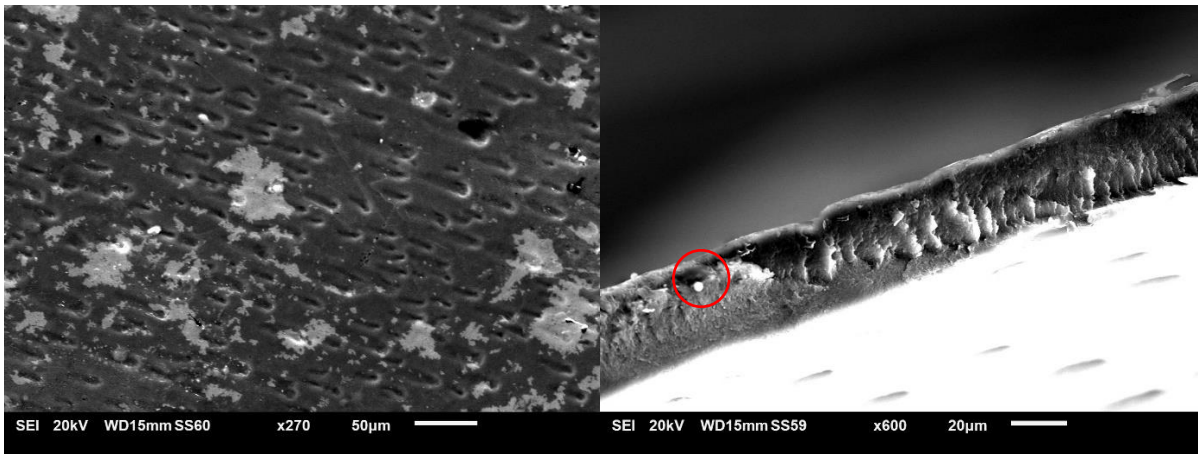
b) 10cel-0.5iSL (left – surface morphology and right – cross section morphology)



c) 10cel-1iSL (left – surface morphology and right – cross section morphology)



d) 10cel-2.5iSL (left – surface morphology and right – cross section morphology)



e) 10cel-4iSL (left – surface morphology and right – cross section morphology)

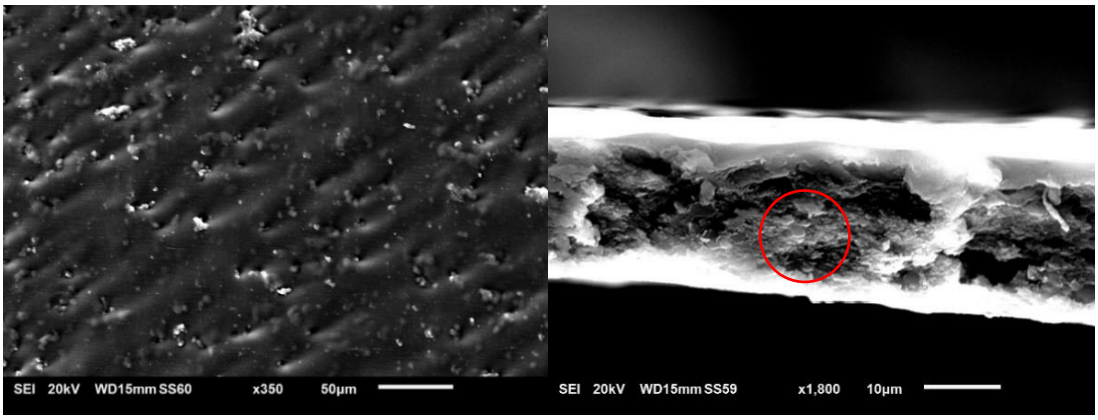


Figure 5.34: SEM images of **cel-iSL** films on the surface and cross sectional

There are various reviews regarding the incorporation of lignin in the film composite. A study utilising poly(butylene adipate-co-terephthalate) (PBAT) with technical lignin identified that the production of larger lignin particles was due to the self-aggregation of lignin.[80] Whereas, no visible aggregation of lignin nanoparticles or phase separation were seen in the fibrous matrix of carboxylated cellulose nanofibrils (CNF) with industrial kraft lignin and lignosulfonates.[66] Lignin aggregates arise from the self-assembly of lignin, propelled by weak interactions among aromatic rings and hydroxylated groups. The lignin aggregations are promoted by several parameters, including low acidic pH and surfactant dependency.[81] **iSL** lignin is obtained using the ionosolv process, wherein lignin is chemically modified to be acidic, since this biomass uses an acidic protonic ionic liquid for extraction.

Another factor was micropores are observable on the surface of **10cel-2.5iSL** and **10cel-4iSL** films. These micropores exist at a significantly greater lignin weight percent ratio. This is because, prior to the film casting process, heat treatment was applied to the dope solution to facilitate smooth pouring. The heating-induced dehydration of moisture leads to the removal of hydroxyl groups from lignin, resulting in increased foam densities and the formation of microbubbles. [82] A cross-sectional analysis of the film provides further insight into its properties and lignin aggregation.

The fracture on the cross-section becomes more pronounced with the addition of lignin, as illustrated in Figure 5.34. At low lignin loadings (0.5 and 1 wt.%), the cross-sections remained relatively dense, displaying only limited fracture formation. However, as the lignin content increased to 4 wt.%, the fractures became substantially more distinct and developed into layered structures. This trend is consistent with previous reports, which documented that a 35 wt.% lignin–cellulose nanofibril (LNFC) epoxy composite exhibited a homogeneous dispersion of fibrils and fibril aggregates within the polymer matrix, with the aggregates displaying strong interfacial adhesion.[83] A small number of lignin aggregates highlighted in red were detected in all **cel-iSL** films except for **10cel-1iSL**.

The resulting morphology of the cellulose–lignin films, characterised by both lignin aggregation and pronounced fracture formation at 2.5 and 4 wt.% lignin, led to excessive film brittleness, rendering tensile strength measurements unobtainable. In contrast, **10cel-1iSL** demonstrated markedly higher TS and YM. This improvement is attributed to its compact, aggregation-free morphology, which arises from extensive hydrogen bonding within the cellulose matrix, as also reported by Zhou et al.[67]

5.3.8 Crystallinity for selected cel-lig films

X-ray diffraction (XRD) analysis elucidates the crystalline and amorphous domains of materials. **10cel** film was differed from **cel-lig** films because it exhibited a massive reduction in crystallinity with increasing lignin content especially at crystalline region at 21.3°, indicating loss of ordered regions inside the **10cel** films as depicted in Figure 5.35. The **10cel–0.5iSL** film exhibited a negligible difference (only 28 counts) between the crystalline and amorphous peak intensities, indicating a high degree of amorphous in the sample. In such cases, the Segal method's reliability

declines to calculate crystallinity index (CI), and the determined CI of approximately 4% requires careful interpretation. The low signal-to-noise ratio can conceal any significant differentiation between crystalline and amorphous regions.

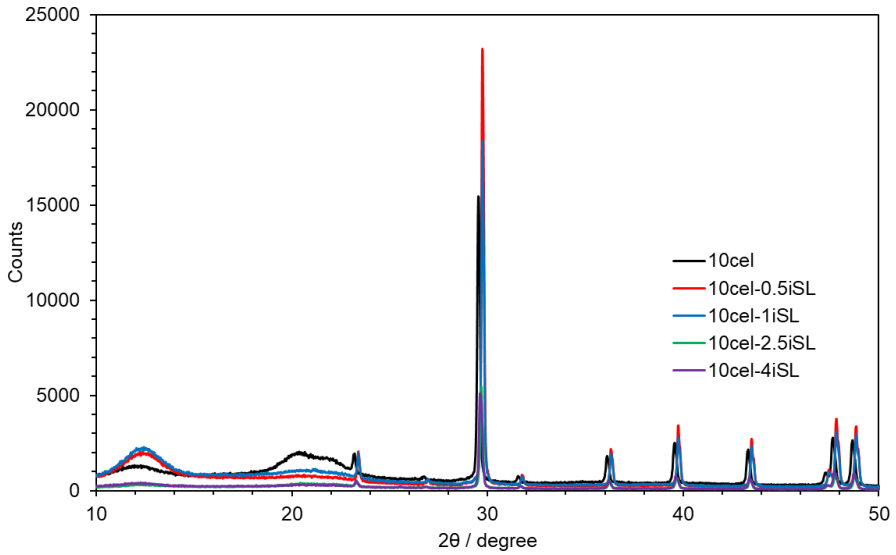


Figure 5.35: XRD patterns of thin films of cellulose-ionosolv softwood lignin at different weight percent ratio

The incorporation of lignin into the films disturbs the hydrogen-bonding network, hence decreasing the number of crystalline areas. This disruption accounts for the apparent gradual reduction in peak intensity with increased lignin content. This finding has been supported by literature on composite films, became significantly amorphous upon dissolution in IL, likely due to the strong dissolving effect of [$C_nC_1$im]]Cl and the formation of intermolecular hydrogen bonds among cellulose, starch, and lignin, which impede the crystallization of cellulose and starch.[6] Consequently, the incorporation of lignin suppresses the overall intensity of the diffracted X-rays due to increased disorder, leading to reduced counts throughout the spectrum.

Peak broadening in the XRD pattern was clearly evident with an increase in lignin concentration, particularly at 2.5 and 4.0 wt.% lignin ratios. The broadening can be ascribed to a decrease in the size of crystalline domains and increased disorder within the cellulose-lignin structure through disrupted hydrogen bonding. This observation is corroborated by literature indicating that the cellulose film with 2 wt.% bound lignin showed weakening and broadening peaks. The branching structure of lignin inhibited the rearrangement and organisation of cellulose chains into structured

formations.[52] This same effect is consistent with the characteristics of regenerated Cellulose II, which typically exhibits higher amorphous content compared to native cellulose as indicated in literature the untreated microcrystalline cellulose and regenerated cellulose derived from the ionic liquid tetraoctylphosphonium acetate combined with DMSO. The overlap of cellulose peaks with the amorphous halo of lignin may further obscure peak sharpness, contributing to the observed broadening.[7]

The reduction in crystallinity associated with elevated lignin content significantly impacts the physical properties of cellulose-lignin films, particularly their thermal stability. Amorphous substances such as lignin demonstrate distinct thermal degradation characteristics compared to crystalline cellulose, potentially affecting the film's thermal properties by increasing its degradation rates. The observed trend aligns with prior investigations, indicating that the introduction of lignin into cellulose composites leads to reduced crystallinity. Research on lignin-cellulose films has consistently demonstrated that lignin interferes with the crystalline structure of cellulose, resulting in a more amorphous substance. This agreement confirms the structural impact of lignin in the present study as indicated in literature the presence of amorphous lignin and hemicelluloses, which may prevent cellulose macromolecules from forming cellulose II in the regeneration process.[84]

5.4 Conclusions

This chapter established the compositional analysis and hydroxyl content functionalities of the lignin samples and demonstrated how these parameters influence the performance of **cel-lig** composite films. High-purity lignins (**iSL**, **kSL**, and **oHL**) provided a reliable basis for structure–property correlations, whereas the presence of residual ionic liquid and carbohydrate impurities in **iHL** affected both its measured hydroxyl content and its relevance to film properties. The ^{31}P NMR analysis confirmed that softwood lignin possesses a lower total hydroxyl content than hardwood lignin, which was shown to be advantageous for mechanical and surface performance.

Overall, a reduced hydroxyl content, particularly due to a lower aliphatic OH content could enhance a film's tensile strength and increased its water contact angle. Incorporating lignin was also shown to disrupt cellulose hydrogen bonding sufficiently to modify crystallinity, surface morphology, UV transmittance, and other functional properties, enabling films with strong UV-blocking capacity and

improved water repellence. Among the formulations evaluated, the **10cel-1iSL** film exhibited the best overall balance of properties, combining improved mechanical strength, complete UVA/UVB blocking, uniform lignin dispersion, and acceptable thermal stability.

The insights gained in this chapter clarify how lignin composition and hydroxyl functionality govern film properties and provide a foundation for the next stage of this work. The following chapter will extend these relationships by examining the role of glycerol as a plasticizer and assessing its influence on the physical, chemical, mechanical, and thermal behaviour of the **cel-lig** films.

References

1 L. Petersson and K. Oksman, *Compos. Sci. Technol.*, 2006, **66**, 2187–2196.

2 J. Ou, S. Hu, L. Yao, Y. Chen, H. Qi and F. Yue, *Chem. Eng. J.*, 2023, **453**, 139770.

3 M. Michelin, A. M. Marques, L. M. Pastrana, J. A. Teixeira and M. A. Cerqueira, *J. Food Eng.*, 2020, **285**, 110107.

4 X. Sun, C. Lu, W. Zhang, D. Tian and X. Zhang, *Carbohydr. Polym.*, 2013, **98**, 405–411.

5 M. Raza, B. Abu-Jdayil, F. Banat and A. H. Al-Marzouqi, *ACS Omega*, 2022, **7**, 25366–25379.

6 R. L. Wu, X. L. Wang, F. Li, H. Z. Li and Y. Z. Wang, *Bioresour. Technol.*, 2009, **100**, 2569–2574.

7 A. J. Holding, A. Parviainen, I. Kilpeläinen, A. Soto, A. W. T. King and H. Rodríguez, *RSC Adv.*, 2017, **7**, 17451–17461.

8 S. Basfar and S. Elkatatny, *Sci. Rep.*, 2023, **13**, 18295.

9 B. Yang, X. Qin, H. Hu, C. Duan, Z. He and Y. Ni, *Cellulose*, 2020, **27**, 9653–9661.

10 A. Sluiter, B. Hames, R. Ruiz, C. Scarlata, J. Sluiter, D. Templeton and D. Crocker, *Natl. Renew. Energy Lab.*, 2008, 17.

11 F. H. B. Sosa, R. M. Dias, A. M. d. C. Lopes, J. A. P. Coutinho and M. C. da Costa, *Sustainability*, 2020, **12**, 3358.

12 M. Rajinipriya, M. Nagalakshmaiah, M. Robert and S. Elkoun, *ACS Sustain. Chem. Eng.*, 2018, **6**, 2807–2828.

13 L. Chopra and Manikanika, *Mater. Today Proc.*, 2021, **48**, 1265–1270.

14 D. M. S. A. Salem and M. M. Ismail, *Egypt. J. Aquat. Res.*, 2022, **48**, 307–313.

15 D. Loof, M. Hiller, H. Oschkinat and K. Koschek, *Materials (Basel).*, 2016, **9**, 1–14.

16 W. Ji, Z. Ding, J. Liu, Q. Song, X. Xia, H. Gao, H. Wang and W. Gu, *Energy and Fuels*, 2012, **26**, 6393–6403.

17 S. Y. Park, H. L. Kim and J. Y. Her, *Carbohydr. Polym. Technol. Appl.*, 2024, **7**, 100423.

18 X. Liu, J. Pang, X. Zhang, Y. Wu and R. Sun, *Cellulose*, 2013, **20**, 1391–1399.

19 H. Xu, L. Huang, M. Xu, M. Qi, T. Yi, Q. Mo, H. Zhao, C. Huang, S. Wang and Y. Liu, *ACS Omega*, 2020, **5**, 23743–23754.

20 J. Ralph, K. Lundquist, G. Brunow, F. Lu, H. Kim, P. F. Schatz, J. M. Marita, R. D. Hatfield, S. A. Ralph, J. H. Christensen and W. Boerjan, *Phytochem. Rev.*, 2004, **3**, 29–60.

21 N. Obrzut, R. Hickmott, L. Shure and K. A. Gray, *RSC Sustain.*, 2023, **1**, 2328–2340.

22 Z. Börcsök and Z. Pásztory, *Eur. J. Wood Wood Prod.*, 2021, **79**, 511–526.

23 and K. Q. Leonard, R G, *Chem. Week*, 2005, **172**, 28.

24 T. V. Lourençon, F. A. Hansel, T. A. Da Silva, L. P. Ramos, G. I. B. De Muniz and W. L. E. Magalhães, *Sep. Purif. Technol.*, 2015, **154**, 82–88.

25 M. Balakshin, E. A. Capanema, X. Zhu, I. Sulaeva, A. Potthast, T. Rosenau and O. J. Rojas, *Green Chem.*, 2020, **22**, 3985–4001.

26 L. Weigand, S. Mostame, A. Brandt-Talbot, T. Welton and J. P. Hallett, *Faraday Discuss.*, 2017, **202**, 331–349.

27 A. G. Margellou, P. A. Lazaridis, I. D. Charisteidis, C. K. Nitsos, C. P. Pappa, A. P. Fotopoulos, S. Van den Bosch, B. F. Sels and K. S. Triantafyllidis, *Appl. Catal. A Gen.*, 2021, **623**, 118298.

28 Q. Ma and X. Zhang, *Sci. Rep.*, 2022, **12**, 1–10.

29 N. Giummarella, Y. Pu, J. Ragauskas and M. Lawoko, *Green Chem.*, 2019, **21**, 1573–1595.

30 C. L. Chambon, V. Fitriyanti, P. Verdía, S. M. Yang, S. Hérou, M. M. Titirici, A. Brandt-Talbot, P. S. Fennell and J. P. Hallett, *ACS Sustain. Chem. Eng.*, 2020, **8**, 3751–3761.

31 M. Chen, F. Malaret, A. E. J. Firth, P. Verdía, A. R. Abouelela, Y. Chen and J. P. Hallett, *Green Chem.*, 2020, **22**, 5161–5178.

32 A. Brandt, L. Chen, B. E. Van Dongen, T. Welton and J. P. Hallett, *Green Chem.*, 2015, **17**, 5019–5034.

33 T. Rashid, C. F. Kait, I. Regupathi and T. Murugesan, *Ind. Crops Prod.*, 2016, **84**, 284–293.

34 F. Zikeli, V. Vinciguerra, A. R. Taddei, A. D'Annibale, M. Romagnoli and G. S. Mugnozza, *Holzforschung*, 2018, **72**, 961–972.

35 L. Serrano, E. S. Esakkimuthu, N. Marlin, M. C. Brochier-Salon, G. Mortha and F. Bertaud, *Energy and Fuels*, 2018, **32**, 5969–5977.

36 W. C. Tu, L. Weigand, M. Hummel, H. Sixta, A. Brandt-Talbot and J. P. Hallett, *Cellulose*, 2020, **27**, 4745–4761.

37 T. Fornaro, D. Burini, M. Biczysko and V. Barone, *J. Phys. Chem. A*, 2015, **119**, 4224–4236.

38 S. Kudo and S. Nakashima, *Spectrochim. Acta Part A Mol. Biomol. Spectrosc.*, 2020, **228**, 117779.

39 X. Meng, C. Crestini, H. Ben, N. Hao, Y. Pu, A. J. Ragauskas and D. S. Argyropoulos, *Nat. Protoc.*, 2019, **14**, 2627–2647.

40 A. Bara-Estaún, M. C. Harder, C. L. Lyall, J. P. Lowe, E. Suturina and U. Hintermair, *Chem. - A Eur. J.*, 2023, **29**, 1–13.

41 P. P. Thoresen, H. Lange, C. Crestini, U. Rova, L. Matsakas and P. Christakopoulos, *ACS Omega*, 2021, **6**, 4374–4385.

42 W. J. J. Huijgen, R. J. A. Gosselink, P. C. A. Bruijnincx, B. M. Weckkhusyen, R. J. H. Grisel, D. S. van Es, R. Boelens, P. de Peinder, A. E. Frissen, H. L. J. Wienk and S. Constant, *Green Chem.*,

2016, **18**, 2563–2910.

43 M. Lawoko, G. Henriksson and G. Gellerstedt, *Biomacromolecules*, 2005, **6**, 3467–3473.

44 G. F. De Gregorio, R. Prado, C. Vriamont, X. Erdocia, J. Labidi, J. P. Hallett and T. Welton, *ACS Sustain. Chem. Eng.*, 2016, **4**, 6031–6036.

45 C. Crestini and D. S. Argyropoulos, *J. Agric. Food Chem.*, 1997, **45**, 1212–1219.

46 A. T. Smit, M. Verges, P. Schulze, A. Van Zomeren and H. Lorenz, *ACS Sustain. Chem. Eng.*, 2022, **10**, 10503–10513.

47 R. Rinaldi, R. T. Woodward, P. Ferrini and H. J. E. Rivera, *J. Braz. Chem. Soc.*, 2019, **30**, 479–491.

48 F. J. V. Gschwend, C. L. Chambon, M. Biedka, A. Brandt-Talbot, P. S. Fennell and J. P. Hallett, *Green Chem.*, 2019, **21**, 692–703.

49 M. J. Suota, T. A. da Silva, S. F. Zawadzki, G. L. Sassaki, F. A. Hansel, M. Paleologou and L. P. Ramos, *Ind. Crops Prod.*, 2021, **173**, 114138.

50 J. Xie and Y. C. Hung, *LWT Food Sci. Technol.*, 2018, **96**, 307–314.

51 C. Shi, L. Zhang, Z. Shi, M. Yan, Z. Wang and J. Ma, *Ind. Crops Prod.*, 2023, **193**, 116200.

52 H. Sadeghifar, R. Venditti, J. Jur, R. E. Gorga and J. J. Pawlak, *ACS Sustain. Chem. Eng.*, 2017, **5**, 625–631.

53 Y. He, H. C. Ye, T. T. You and F. Xu, *Food Hydrocoll.*, 2023, **137**, 108355.

54 F. Hermanutz, M. P. Vocht, N. Panzier and M. R. Buchmeiser, *Macromol. Mater. Eng.*, 2019, **304**, 1–8.

55 N. Sun, M. Rahman, Y. Qin, M. L. Maxim, H. Rodríguez and R. D. Rogers, *Green Chem.*, 2009, **11**, 646–65.

56 K. Rajan, K. Kim, T. J. Elder, A. K. Naskar and N. Labbé, *ACS Sustain. Chem. Eng.*, 2022, **10**, 8835–8845.

57 S. M. F. Silva, H. L. Ribeiro, A. L. A. Mattos, M. de F. Borges, M. de F. Rosa and H. M. C. de Azeredo, *J. Food Sci. Technol.*, 2021, **58**, 1979–1986.

58 S. K. Mahadeva and J. Kim, *Fibers Polym.*, 2012, **13**, 289–294.

59 E. González Carmona, I. Schlapp-Hackl, S. Jääskeläinen, M. Järvinen, K. Nieminen, D. Sawada, M. Hummel and H. Sixta, *Cellulose*, 2023, **30**, 11633–11648.

60 ASTM D882-10, *Standard Test Method for Tensile Properties of Thin Plastic Sheeting*, 2014.

61 H. Kaur, T. S. Banipal, S. Thakur, M. S. Bakshi, G. Kaur and N. Singh, *ACS Sustain. Chem. Eng.*, 2013, **1**, 127–136.

62 M. G. Coscia, J. Bhardwaj, N. Singh, M. G. Santonicola, R. Richardson, V. K. Thakur and S. Rahatekar, *Ind. Crops Prod.*, 2018, **111**, 536–543.

63 L. Zhang, W. Shi, H. Sheng, S. Feng, M. Yao, P. Chen, Q. Zheng and H. Xie, *Green Chem.*, 2021, **23**, 5856–5865.

64 S. Vincent, R. Prado, O. Kuzmina, K. Potter, J. Bhardwaj, N. D. Wanasekara, R. L. Harniman, A. Koutsomitopoulou, S. J. Eichhorn, T. Welton and S. S. Rahatekar, *ACS Sustain. Chem. Eng.*, 2018, **6**, 5903–5910.

65 F. Meister and B. Kosan, *Nord. Pulp Pap. Res. J.*, 2015, **30**, 112–120.

66 Y. Liu, *ACS Sustain. Chem. Eng.*, 2018, **6**, 5524–5532.

67 Y. Zhou, Y. Han, J. Xu, W. Han, F. Gu, K. Sun, X. Huang and Z. Cai, *Int. J. Biol. Macromol.*, 2023, **232**, 123105.

68 Y. Zhao, G. Dobele, M. E. Lindstrom and O. Sevastyanova, *Polymers (Basel).*, 2019, **11**, 538.

69 Y. Ma, S. Asaadi, L. S. Johansson, P. Ahvenainen, M. Reza, M. Alekhina, L. Rautkari, A. Michud, L. Hauru, M. Hummel and H. Sixta, *ChemSusChem*, 2015, **8**, 4030–4039.

70 M. Trogen, N. D. Le, D. Sawada, C. Guizani, T. V. Lourençon, L. Pitkänen, H. Sixta, R. Shah, H. O'Neill, M. Balakshin, N. Byrne and M. Hummel, *Carbohydr. Polym.*, 2021, **252**, 117133.

71 R. Tian, C. Wang, W. Jiang, S. Janaswamy, G. Yang, X. Ji and G. Lyu, *Small*, 2024, **20**, 1–13.

72 M. Farooq, T. Zou, G. Riviere, M. H. Sipponen and M. Österberg, *Biomacromolecules*, 2019, **20**, 693–704.

73 M. Borrega, S. Päärnilä, L. G. Greca, A. S. Jääskeläinen, T. Ohra-Aho, O. J. Rojas and T. Tamminen, *Langmuir*, 2020, **36**, 9675–9684.

74 H. Yildirim Erbil and C. Elif Cansoy, *Langmuir*, 2009, **25**, 14135–14145.

75 K. Rajan, K. Kim, T. J. Elder, A. K. Naskar and N. Labbé, *ACS Sustain. Chem. Eng.*, 2022, **10**, 8835–8845.

76 A. Brandt-Talbot, F. J. V. Gschwend, P. S. Fennell, T. M. Lammens, B. Tan, J. Weale and J. P. Hallett, *Green Chem.*, 2017, **19**, 3078–3102.

77 A. R. Abouelela, P. Y. S. Nakasu and J. P. Hallett, *ACS Sustain. Chem. Eng.*, 2023, **11**, 2404–2415.

78 M. J. Taherzadeh and K. Karimi, *BioResources*, 2007, **2**, 707–738.

79 P. Alvira, E. Tomás-Pejó, M. Ballesteros and M. J. Negro, *Bioresour. Technol.*, 2010, **101**, 4851–4861.

80 S. J. Xiong, B. Pang, S. J. Zhou, M. K. Li, S. Yang, Y. Y. Wang, Q. Shi, S. F. Wang, T. Q. Yuan and R. C. Sun, *ACS Sustain. Chem. Eng.*, 2020, **8**, 5338–5346.

81 M. H. Sipponen, H. Lange, M. Ago and C. Crestini, *ACS Sustain. Chem. Eng.*, 2018, **6**, 9342−9351 Research.

82 Q. Yan, T. Ketelboeter, W. Fan, C. Wan and Z. Cai, *Green Chem.*, 2024, **26**, 5194.

83 S. S. Nair, P. Y. Kuo, H. Chen and N. Yan, *Ind. Crops Prod.*, 2017, **100**, 208–217.

84 M. Chen, X. Zhang, C. Liu, R. Sun and F. Lu, *ACS Sustain. Chem. Eng.*, 2014, **2**, 1164–1168.

Chapter 6: Cellulose-Lignin-Glycerol Film Characterisation

This chapter expands on the findings found in previous chapter on cellulose-lignin (**cel-lig**) films, emphasising the integration of glycerol as a plasticiser. The glycerol was added into the formulation to improve the flexibility of films, therefore improving their applicability in plastic packaging applications. The aim of the work presented in this chapter is to determine the optimum glycerol concentration (by weight) in **cel-lig** films. Cellulose-lignin-glycerol (**cel-lig-gly**) films were subsequently produced with optimum glycerol concentrations utilising two distinct forms of lignin: softwood and hardwood lignins. These films underwent thorough characterisation, on their physical, chemical, mechanical, structural and thermal properties. The resulting data provide essential insights into how glycerol affects the characteristics of the **cel-lig** films. It elucidates the interaction between glycerol and **cel-lig** matrix and identifying enhancements in mechanical performance that result from these interactions.

6.1 Cellulose-glycerol film characterisation

This section examines the influence of glycerol wt.% on cellulose films, with the objective of identifying the optimal mechanical properties. The mechanical properties were selected as the primary criterion for determining the appropriate glycerol concentration, as they reflect changes in flexibility and tensile strength, a crucial characteristic for functional materials. Percent formulation of dope solutions used to prepare composite films is detailed in Table 6.1. The glycerol content yielding optimal mechanical performance was subsequently utilised in the production of **cel-lig** films.

Table 6.1: Percent weight and glycerol concentration incorporated in cellulose dope solution

Formula code	% w/w (relative to $[C_2C_1im][OAc]$)	Concentration glycerol in cellulose dope solution (mg/mL)
10cel-0gly	0.0	0.00
10cel-2.5gly	2.5	26.88
10cel-5gly	5.0	52.65
10cel-10gly	10.0	101.05

10cel-15gly	15.0	145.80

Example: **10cel-2.5gly**

Glycerol weight percent = $\frac{0.05\ grams\ glycerol}{2.00\ gram\ [C_2\ C_1 im][OAc]}$ x 100 % = 2.5 %

Cellulose weight percent = $\frac{0.20\ grams\ glycerol}{2.00\ gram\ [C_2\ C_1 im][OAc]}$ x 100 % = 10.0 %

** The weight of $[C_2C_1im][OAc]$ reported here has been corrected to exclude the water content.

Concentration glycerol (mg/mL) = $\frac{50\ mg}{1.82\ mL\ [C_2\ C_1 im][OAc] + 0.04\ mL\ glycerol}$ = 26.88 mg/mL

** The volumes of $[C_2C_1im][OAc]$ and glycerol were determined based on their respective densities of 1.10 $g \cdot mL^{-1}$ and 1.26 $g \cdot mL^{-1}$.

6.1.1 Composition of plasticised cellulose films by FT-IR spectroscopy

Glycerol was incorporated into the cellulose films because of its significant plasticizing effect.[1] Glycerol reduces frictional forces among polymeric chains, acting as a lubricant for chains to slide along each other, increasing flexibility. Prior research has illustrated the plasticizing effect of glycerol in cellulose films, indicating significant enhancements in their elasticity.[2]

Initially, the incorporation of glycerol into the film needed to be confirmed. FTIR spectroscopy was utilized to characterize the **cel-gly** films as illustrated in Figure 6.1. The detailed bands assignment for **10cel** and glycerol can be found in Table 6.2. In the control sample, **10cel**, cellulose without glycerol (Figure 6.1 (b)), the significant absorption band at 3340–3330 cm^{-1} was attributed to O–H stretching vibrations and is typical for polysaccharides. The absorption band seen between 2910–2920 cm^{-1} is ascribed to the C–H stretching vibrations which are also present in polysaccharides. The band about 1650 cm^{-1} corresponds to vibrations of water molecules physically adsorbed to cellulose. Additional bands were seen at 1430–1420, 1026, and 992 cm^{-1}, corresponding to the stretching and bending vibrations of $–CH_2$, –CH, –OH, and C–O functional groups, respectively. These bands align with previously documented FTIR spectra of cellulose obtained from wood pulp and cotton.[3]

The FTIR spectrum of glycerol (Figure 6.1, Table 6.2) exhibited a broad absorption band with a band at about 3290 cm^{-1}, again indicative of O–H stretching vibrations linked to hydroxyl groups. The aliphatic C–H stretching vibrations were seen at 2936 cm^{-1} and 2880 cm^{-1}, indicating the presence of saturated hydrocarbon chains. Moreover, absorption bands within the range of 1024–990 cm^{-1} are due to C–O stretching vibrations, hence affirming the existence of alcohol functional groups. These bands align with prior studies that describe commercial-grade glycerol.[4] The anticipated band around 1653 cm^{-1}, generally linked to O–H bending vibrations of water, was not found in the present research. The absence is ascribed to the remarkably low water content of the glycerol sample utilized in this study, which was measured to be 0.1% by using Karl Fischer titration.

The addition of glycerol to **10cel** led to significant changes, particularly in the C–H stretching region highlighted in yellow in Figure 6.1(b). Two separate bands at 2921 cm^{-1} and 2849 cm^{-1}, representing asymmetric and symmetric stretching of $–CH_2$ groups, respectively, exhibited increased intensity with elevated glycerol content (2.5 to 15 wt.%). This is due to the C–H band from glycerol being more intense and increased molecular mobility resulting from its plasticizing impact. Glycerol interferes with the hydrogen bonding network in cellulose, resulting in a less ordered structure and enhanced infrared activity of specific vibrational modes.[5]

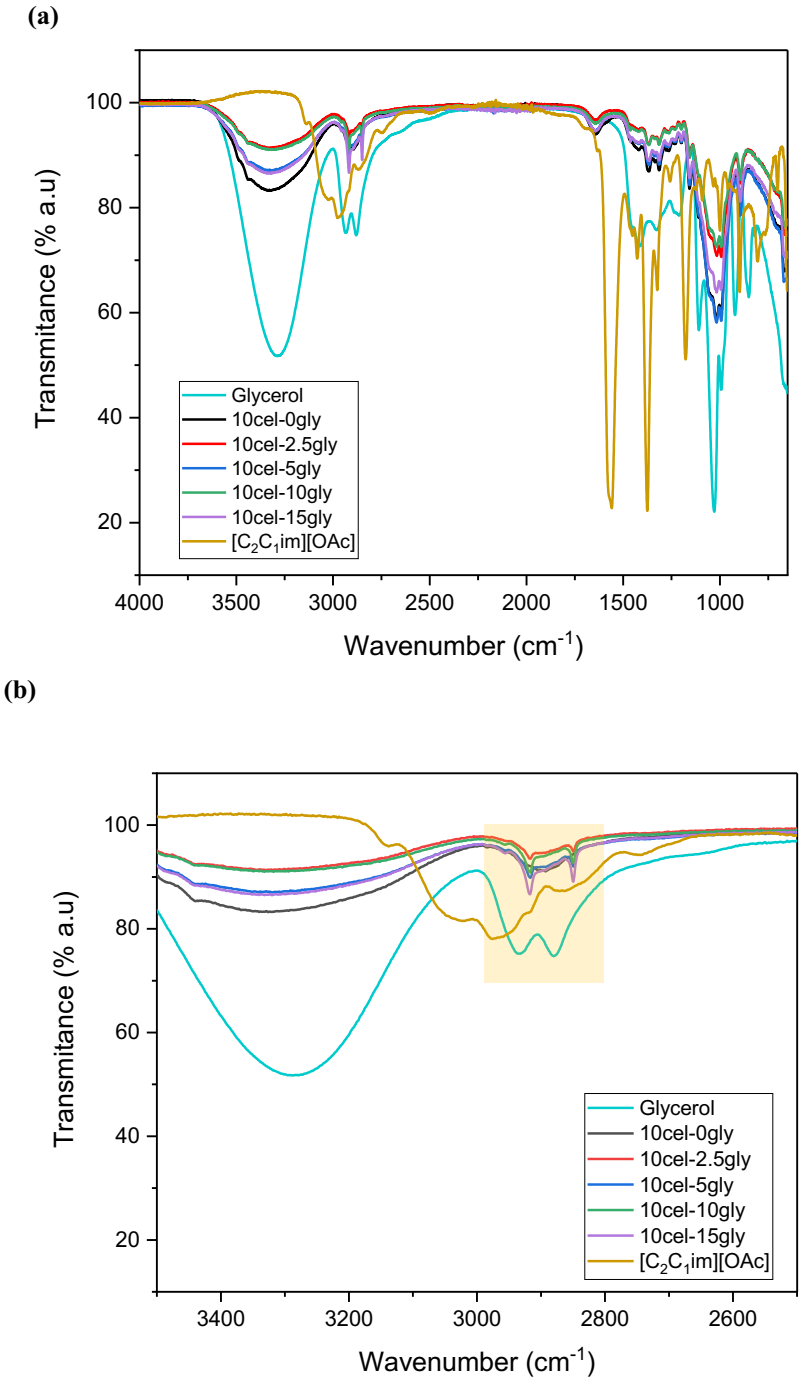


Figure 6.1: FTIR spectra of glycerol and regenerated cellulose films at different glycerol weight percent: (a) overall spectra; (b) zoomed-in region highlighting the –OH and –CH bands

This is corroborated by another study on the fabrication of cellulose acetate with glycerol concentrations of 5, 10, 20, 30, and 50% (w/v). The incorporation of glycerol resulted in an enhancement of the bands at 2936 cm^{-1} (CH stretching), 3478 cm^{-1} (OH stretching), 1232 cm^{-1}, and 1045 cm^{-1} (carbonyl stretching).[6] The C=O stretching band was not observed in **cel-gly** films. This absence is attributed to the extensive washing of the films conducted four times to ensure complete removal of the ionic liquid. Also, glycerol, which preferentially forms strong hydrogen bonds with water, was largely removed and only a small amount was left in the film. Studies have shown that water molecules preferentially donate hydrogen atoms to glycerol rather than to other water molecules, leading to a strong interaction between water and glycerol molecules.[5]

In conclusion, FTIR analysis confirms the presence of glycerol in the cellulose films, indicating interactions primarily via hydrogen bonding. However, FTIR is not a quantitative technique and therefore lacks the sensitivity to accurately determine the amount of residual glycerol present in the samples. The results of tensile testing and compositional analysis reveal notable differences between the films, suggesting variations in glycerol retention that cannot be fully resolved by FTIR alone. To confirm and quantify the glycerol content more precisely, complementary analytical techniques such as HPLC should be employed in future studies.

Table 6.2: Assignments of FTIR bands in **10cel** and glycerol

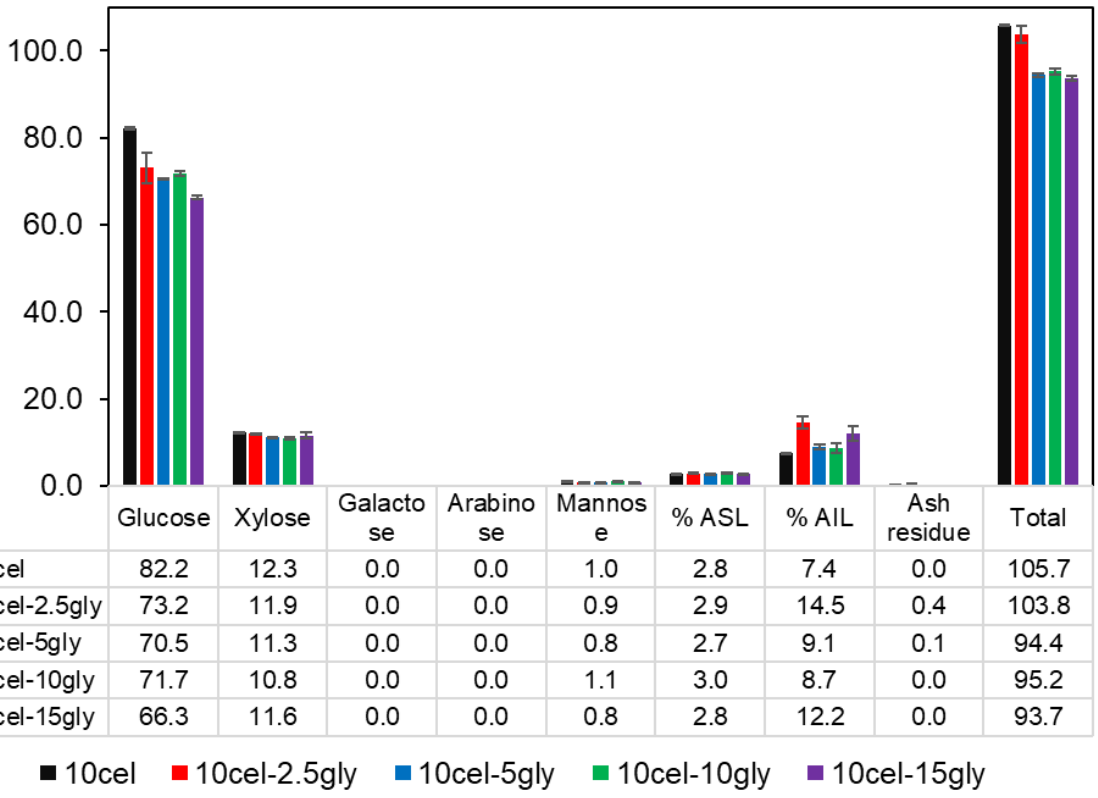
Band (cm^{-1})		Assignments
10cel	Glycerol	
3340 - 3330	3290	O-H stretching
2910 - 2920	2921; 2849	C-H asymmetric stretching
1650	-	O–H bending
1430-1420	1420	C–H bending
1026	1024	C–O–C stretching
992	990	C–O–H out-of-plane bending
892 – 896	850	C-H rocking

6.1.2 Compositional analysis of cellulose-glycerol films

A compositional analysis (CA) of **cel-gly** films was performed to determine the film composition and glycerol content as an alternative to FT-IR spectroscopy. The concentration of glycerol was measured in the hydrolysate obtained during CA via HPLC separately. Figure 6.2 illustrates that the predominant sugar identified was glucose, the principal monomer of cellulose. The measured glucan content decreased as the glycerol concentration increased, reducing from 82.2% to 66.3%. Other sugars detected included xylose and mannose, which are major components of softwood hemicellulose, a polysaccharide found with cellulose in plant cell walls. The xylose content remained constant (10.8–12.3%), while mannose exhibited moderate variation (0.8–1.1%). The existence of these sugars signifies that hemicellulose is not entirely separated from cellulose during extraction.[7]

The acid-soluble lignin (ASL) content, the portion of lignin that dissolves in dilute acid, was consistent among samples (2.7–3.0%). However, the acid-insoluble lignin (AIL), the insoluble residue obtained during compositional analysis, was high and fluctuated, it was highest in the **10cel–2.5gly** sample (14.5%) and **10cel-15gly** sample (12.5%) and decreased in other formulations. The ash content was negligible. The maximum total CA value was recorded in the **10cel** sample (105.7%), whilst the minimum was found in **10cel–15gly** (93.4%). The mass closure was good, but falling at the top or bottom of the anticipated range (95-105%),[8] particularly at 5 wt.% and 15 wt.% glycerol.

The primary observation indicated that elevated glycerol levels reduced glucan content. The variation in AIL, such as spike at **10cel-2.5gly,** may result from sample variability in samples, as the protocol is not designed for cellulose films. Ash and minor sugars are insignificant in this context. Glycerol may induce the development of insoluble lignin derivatives or sugar-glycol adducts that are not identified in routine assays or it may not be present in the films. [9]



	Glucose	Xylose	Galactose	Arabinose	Mannose	% ASL	% AIL	Ash residue	Total
10cel	82.2	12.3	0.0	0.0	1.0	2.8	7.4	0.0	105.7
10cel-2.5gly	73.2	11.9	0.0	0.0	0.9	2.9	14.5	0.4	103.8
10cel-5gly	70.5	11.3	0.0	0.0	0.8	2.7	9.1	0.1	94.4
10cel-10gly	71.7	10.8	0.0	0.0	1.1	3.0	8.7	0.0	95.2
10cel-15gly	66.3	11.6	0.0	0.0	0.8	2.8	12.2	0.0	93.7

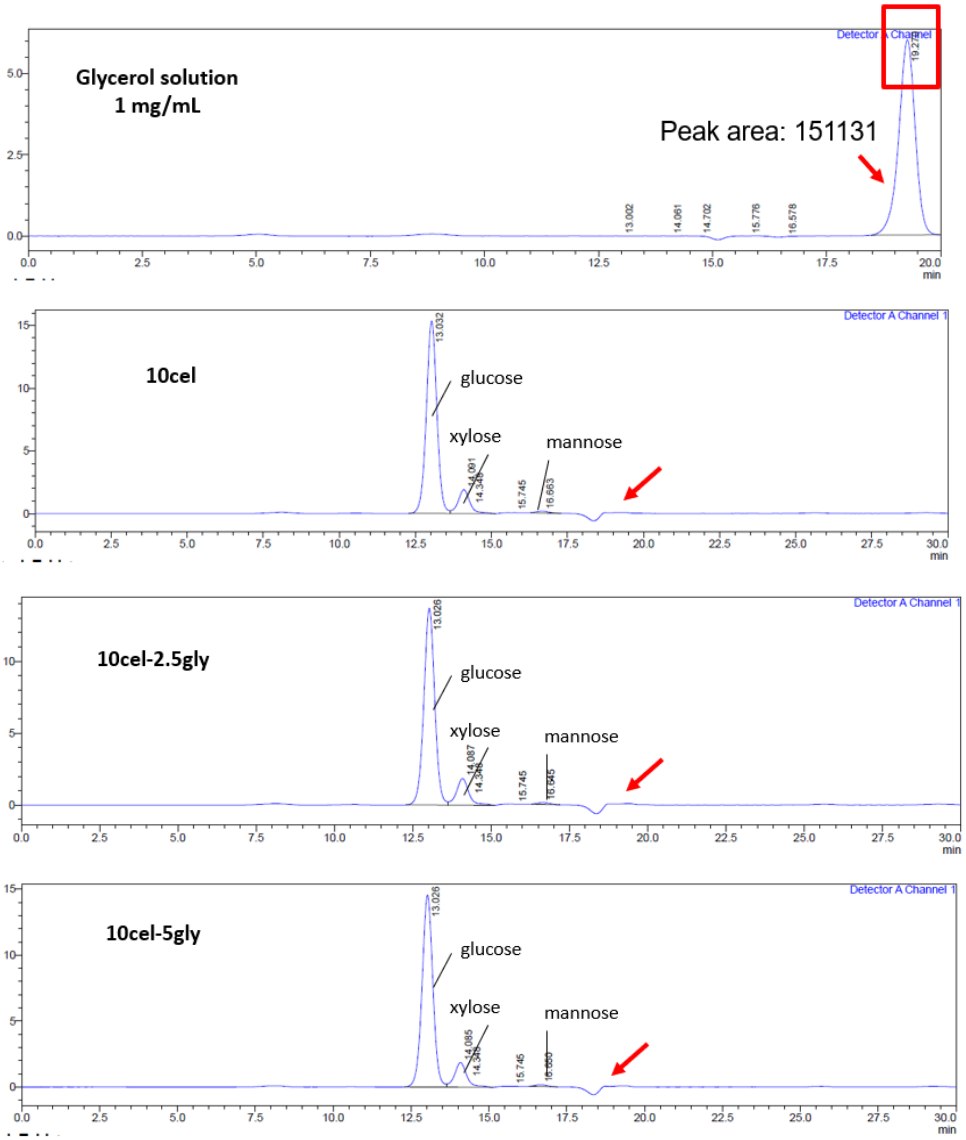
Figure 6.2: Compositional analysis of fabricated **cel-gly** films

Glycerol was not directly observed in the compositional analysis. However, glycerol is suspected to interfere with sample evaluation, particularly in the quantification of sugars and lignin. As shown in Figure 6.3, glycerol is readily detected by HPLC– Refractive Index (RI) in a standard solution (1 mg/mL) that has not undergone acid hydrolysis. In contrast, only trace glycerol peaks were observed in the hydrolysates of film samples containing 10 and 15 wt.% glycerol. This is primarily attributed to the harsh conditions of concentrated sulfuric acid hydrolysis, which promote dehydration and extensive degradation of glycerol. Under these conditions, glycerol is largely converted into degradation products, potentially including acrolein, rather than remaining as intact glycerol detectable by RI.

Sample preparation further reduces the detectable glycerol concentration. During film formation, glycerol is partially removed during washing with deionized water for cellulose coagulation. Following acid hydrolysis, the samples are further diluted with 84 mL of deionized water as part of the CA procedure, resulting in a substantial reduction in glycerol concentration. For example, the **10cel–2.5gly** sample initially contains 26.88 mg/mL glycerol in the dope

solution; however, washing and subsequent dilution reduce the concentration to levels below the reliable detection limit of the RI detector. Because dilution after acid treatment does not restore degraded glycerol, the RI response becomes increasingly unreliable at lower glycerol loadings.

At higher glycerol contents (10 and 15 wt.%), small peaks may still be observed, likely arising from residual unreacted glycerol or minor amounts of glycerol mono- or di-sulfates, which exhibit weak RI responses. Therefore, glycerol quantification in **cel-gly** composite films should be conducted in a separate experiment using a glycerol-specific analytical method that avoids concentrated acid hydrolysis.



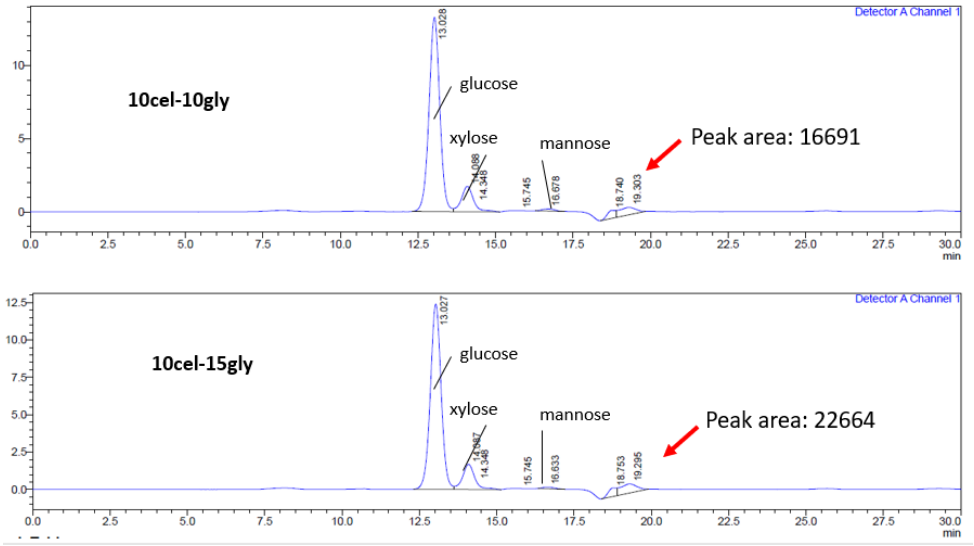


Figure 6.3: HPL chromatograms from compositional analysis of fabricated **cel-gly** films

6.1.3 Tensile properties of the cellulose films

Tensile testing is important for assessing the performance of materials under stress, providing information on the films' strength and flexibility. Tensile properties values of **cel-gly** films in terms of stress (MPa), strain (%) and Young's modulus (GPa) is tabulated in Table 6.3, and stress-strain curves for all **cel-gly** films are shown in Figure 6.4.

Table 6.3: Tensile properties of cellulose films at different glycerol quantities ranging from 2.5 to 15 wt.%

Films	Tensile Strength (MPa)	Yield Strength (MPa)	Strain at failure (%)	Yield Strain (%)	Young's Modulus (GPa)
10cel-0gly	48.8 ± 4.0	43.2 ± 3.8	1.0 ± 0.2	0.8 ± 0.2	7.2 ± 0.3
10cel-2.5gly	51.2 ± 2.5	42.5 ± 2.4	1.7 ± 0.2	1.0 ± 0.2	5.7 ± 0.5
10cel-5gly	54.5 ± 2.8	40.0 ± 2.8	2.3 ± 0.2	1.0 ± 0.2	6.4 ± 0.6
10cel-10gly	41.5 ± 3.6	32.4 ± 3.2	2.1 ± 0.4	0.9 ± 0.2	4.0 ± 0.6
10cel-15gly	32.9 ± 2.2	30.8 ± 2.0	1.6 ± 0.4	1.0 ± 0.3	3.2 ± 0.5

Tensile strength (TS) initially increased with glycerol content in the dope, peaking at 54.5 MPa at 5 wt.% glycerol. At high glycerol contents of 10 wt.% and 15 wt.%, tensile strength decreased markedly to 41.5 MPa and 32.9 MPa, respectively. The literature reports diverse

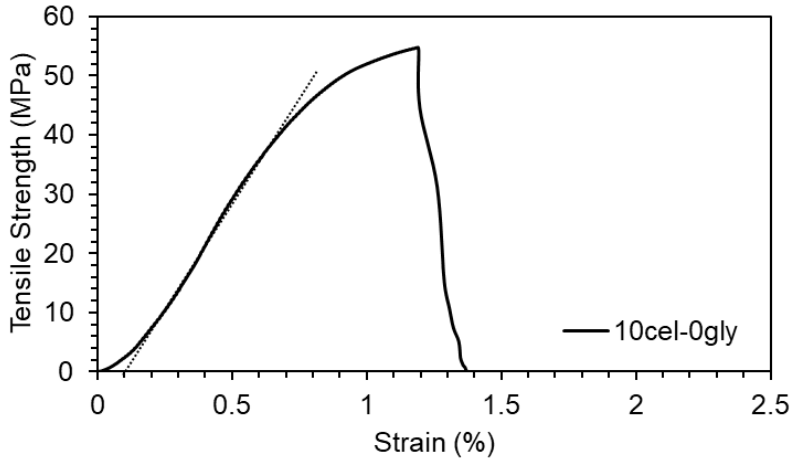
effects of glycerol on cellulose film tensile properties, some indicate no measurable change, while others indicate a reduction in TS. For example, the differences in tensile strength among glycerol-plasticized starch films was negligible at low (9.5 wt. %) glycerol content.[10] A study on cellulose film incorporating different plasticizers, specifically glycerol and maltitol, revealed that the addition of 5 wt.% plasticizer to 6.7 wt.% softwood sulfite pulp reduced the film strength from 62.3 MPa to an average of 41 MPa, while markedly enhancing the film elasticity from 5.1% to 12%.[1] At a low weight percentage of glycerol facilitates improved stress distribution within the cellulose matrix, resulting in increased tensile strength. **10cel-2.5gly** showed improved TS than **10cel**. As glycerol concentration increases, excessive plasticization disrupts intermolecular interaction between cellulose polymers, thereby weakening the film. This conclusion aligns with most of literature data, indicating that elevated glycerol content diminishes the mechanical strength of polysaccharide films, as the plasticiser weakens intermolecular interactions between neighbouring molecules.[11,12]

Strain or the elongation at break (EAB) measures of how much a material can stretch before it breaks. **10cel** EAB of 1.0% increased to a peak of 2.3% at a glycerol concentration of 5 wt.%, demonstrating glycerol's plasticising effect. At elevated quantities (15 wt.%), the EAB dropped to 1.6%, indicating that an excess of glycerol weakens the film's performance. At low to moderate concentrations, glycerol significantly improved the film's elasticity by breaking intermolecular connections within the cellulose matrix, thus reducing its rigidity. Conversely, at high concentrations, the excessively plasticised matrix becomes structurally compromised, either due to phase separation or the emergence of discontinuities, which reduces its elastic characteristics. This trend is supported by literature on sugarcane bagasse-based biocomposites, where higher concentrations of glycerol and sorbitol resulted in a decrease in EAB.[13]

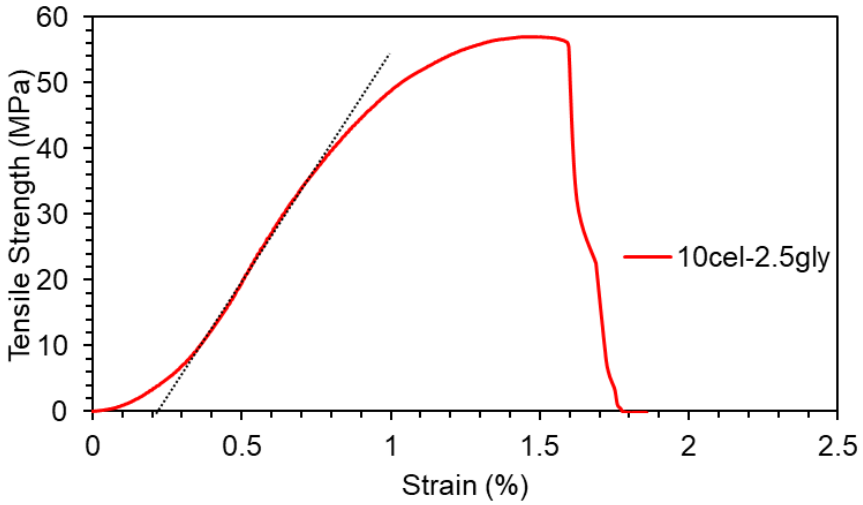
The Young's modulus (YM) measures material’s stiffness. YM of **cel** films reduced progressively with increasing glycerol concentration, varying from 7.2 GPa without glycerol to 3.2 GPa at 15 wt.% glycerol. The modulus without glycerol is similar to the modulus documented in a study on cornhusk-derived cellulose treated with 1-allyl-3-methylimidazolium chloride, which demonstrated a Young's modulus of approximately 6

GPa.[14] The decrease in mechanical stiffness aligns with expectations, as the incorporation of poly(glycerol succinate-co-maleate) (PGSMA) into cellulose nanocrystals has been shown to create an amorphous component into the semicrystalline polymer matrix, thereby disturbing crystallinity and weakening rigidity.[12]

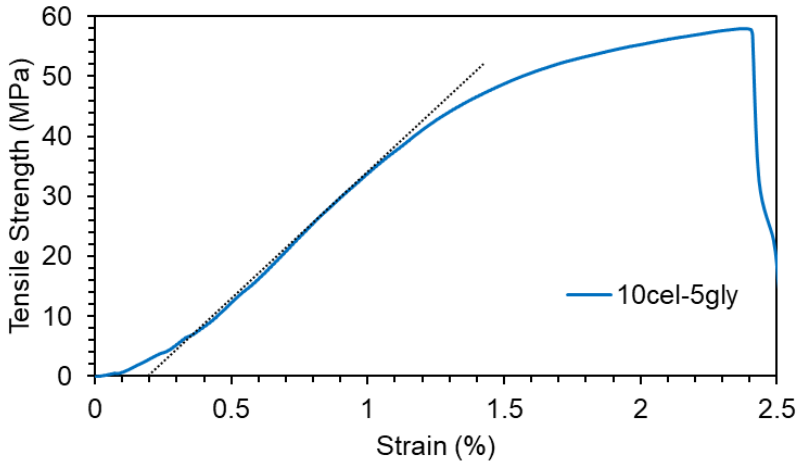
(a) 10cel-0gly



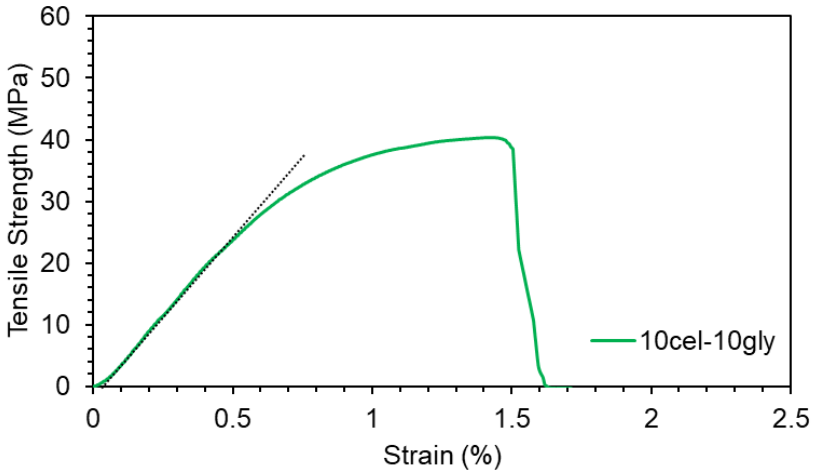
(b) 10cel-2.5gly



(c) 10cel-5gly



(d) 10cel-10gly



(e) 10cel-15gly

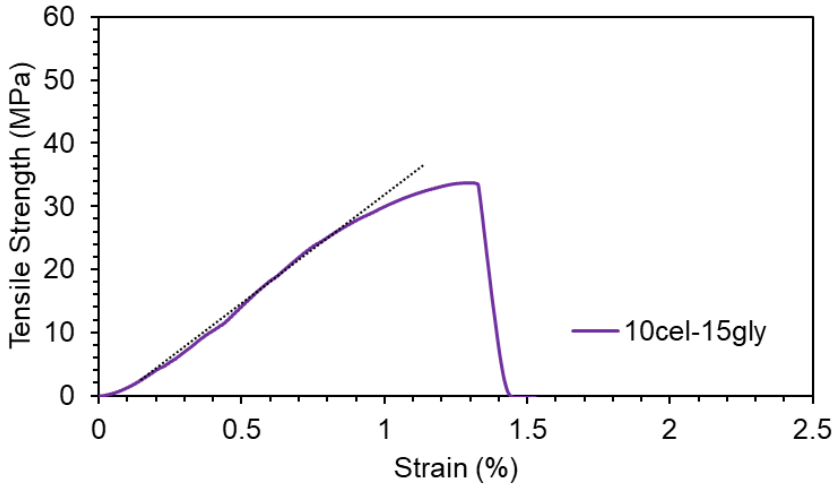


Figure 6.4: Representative stress-strain curves fabricated **cel-gly** films (a – e) at different glycerol weight content

6.1.4 Choosing optimum glycerol concentration for film fabrication

The mechanical properties were the primary performance indicator for determining the optimum glycerol concentration, since flexibility and tensile strength are crucial elements for material performance in practical applications. The data suggest that a 5 wt.% glycerol content in the dope provided the optimal balance of mechanical properties, even though detection was challenging. The **10cel-5gly** formulation demonstrated the improved TS (54.5 MPa), and moderate strain at break (2.3%) and Young's modulus (6.4 GPa) indicating an ideal blend of stiffness during elastic deformation. Conversely, films with elevated glycerol contents (10 wt.% and 15 wt.%) exhibit excessive softness and mechanical instability, therefore restricting their applicability in load-bearing applications.

FTIR findings demonstrate molecular interactions between glycerol and the cellulose matrix, especially in the C–H stretching region as indicated in Section 6.1.1 (Figure 6.1). Two distinct bands at 2921 cm^{-1} and 2849 cm^{-1}, representing the asymmetric and symmetric stretching

vibrations of $–CH_2$ groups, respectively, exhibit heightened intensity with increasing glycerol concentrations. This trend signifies improved interaction between glycerol and cellulose, reinforcing the conclusion that 5 wt.% glycerol in the dope facilitates effective structural alteration in the resulting cellulose film without excessive plasticization or compromising matrix integrity. However, it should be noted that FTIR evidence suggests the proportion of glycerol retained within the final film is considerably lower than that present in the initial dope solution.

6.2 Cellulose-lignin-glycerol film characterisation

The incorporation of glycerol at constant 5 wt.% into **cel-lig** dope solutions is expected to produce significant impacts on the film's properties. This section will elucidate the characterization of **cel-lig-gly** films regarding their optical, chemical, mechanical, thermal, and structural properties. To my knowledge, there is a deficiency of study on cellulose-lignin films incorporating glycerol. The hydroxyl quantification of lignin presented in the previous chapter is directly related to the resulting film properties.

6.2.1 Optical properties of cellulose-lignin-glycerol films

The transparency of the cellulose-lignin-glycerol films was assessed by ultraviolet-visible (UV-Vis) spectroscopy, quantifying transmittance in the 250–700 nm range. Figure 6.5 presents digital images illustrating that the incorporation of lignin leads to a pronounced reduction in film transparency. Owing to the intrinsic coloration of both softwood and hardwood lignin, transparency progressively decreases as the lignin content increases. In comparison with the all **cel–lig** films without glycerol presented in Figure 5.24 (Chapter 5), the films in Figure 6.5 generally exhibited a comparable reduction in transparency with increasing lignin content, indicating that lignin remained the dominant factor governing optical attenuation.

Nevertheless, a notable deviation from this trend was observed for **10cel-4oHL-5gly**, which displayed a visibly lighter brown appearance than **10cel-4oHL** at an equivalent lignin loading. This qualitative observation is corroborated by UV–Vis measurements, where the transparency at 700 nm increased markedly from 19.3% for **10cel-4oHL** to 54.9% for **10cel-4oHL-5gly**.

Importantly, compositional analysis (Table 6.6) confirmed a measured lignin content of 33.2% for **10cel-4oHL-5gly**, in close agreement with the theoretical value of 28.6%, thereby excluding reduced lignin incorporation as the primary cause of the lighter coloration. The observed colour attenuation is therefore more plausibly attributed to glycerol-induced changes during coagulation, potentially involving enhanced lignin–water interactions through hydrogen bonding, which may alter lignin distribution within film matrix.

(a)





(b)


10cel-5gly
10cel-0.5iHL-5gly
10cel-1iHL-5gly
10cel-2.5iHL-5gly
10cel-4iHL-5gly


10cel
10cel_0.5iHL
10cel_1iHL
10cel_2.5iHL
10cel_4iHL

(c)


10cel-5gly
10cel-0.5kSL-5gly
10cel-1kSL-5gly
10cel-2.5kSL-5gly
10cel-4kSL-5gly


10cel
10cel_0.5kSL
10cel_1kSL
10cel_2.5kSL
10cel_4kSL

(d)

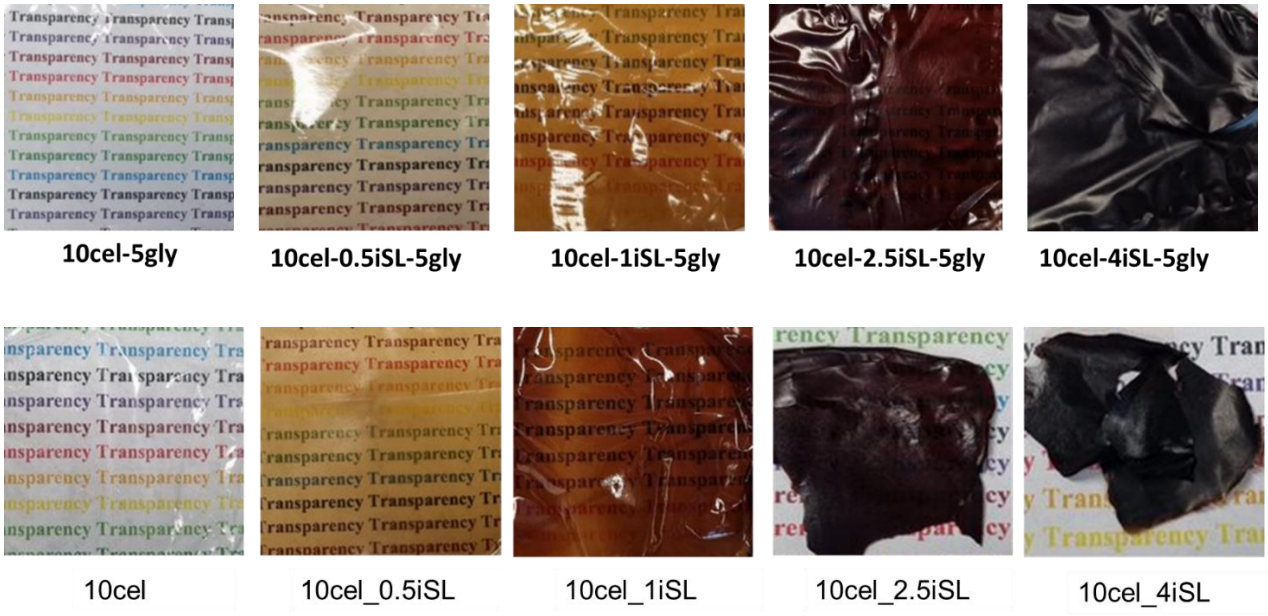


Figure 6.5: Physical appearance of **cel-lig** films with and without glycerol at varying lignin contents. (a, b) cellulose with hardwood lignin; (c, d) cellulose with softwood lignin.

The optical transparency of the **cel–lig–gly** films is presented in Figure 6.6. Although no previous studies have explicitly reported the UV–Vis transparency of **cel–lig–gly** systems, transmittance data for **cel–lig** films in the literature provide a useful benchmark for comparison. When directly compared with the **cel–lig** films in Figure 5.25 (Chapter 5), the majority of samples exhibited similar wavelength-dependent transmittance trends, indicating that the incorporation of glycerol did not fundamentally alter the UV–Vis absorption behaviour of the **cel–lig** matrix. This suggests that the optical response remains predominantly governed by lignin-associated chromophores rather than by glycerol addition. Given that glycerol has no conjugated double bonds or UV-active functional groups, its influence on optical properties is expected to be indirect. Consequently, the comparable UV–Vis profiles observed between **cel–lig** and **cel–lig–gly** films support the conclusion that glycerol acts mainly as a plasticizing agent without introducing new optically active transitions.

At 600 nm, the transmittance of the **10cel** was 88 ± 1.3 %, while the **10cel–5gly**, used as the control, exhibited a similar transmittance between 88 and 89%. The close agreement between these values indicates that the incorporation of glycerol had little effect on the optical transparency of the film, which may suggest a relatively low glycerol content in the **10cel–5gly** film. In contrast, a cotton cellulose nanocrystal film containing glycerol reported in the

literature showed a significantly lower transmittance of 74% at 600 nm.[15] This marked reduction in transparency suggests notable structural or compositional differences compared to the films prepared in this study, potentially indicating differences in glycerol proportion and dispersion within the matrix.

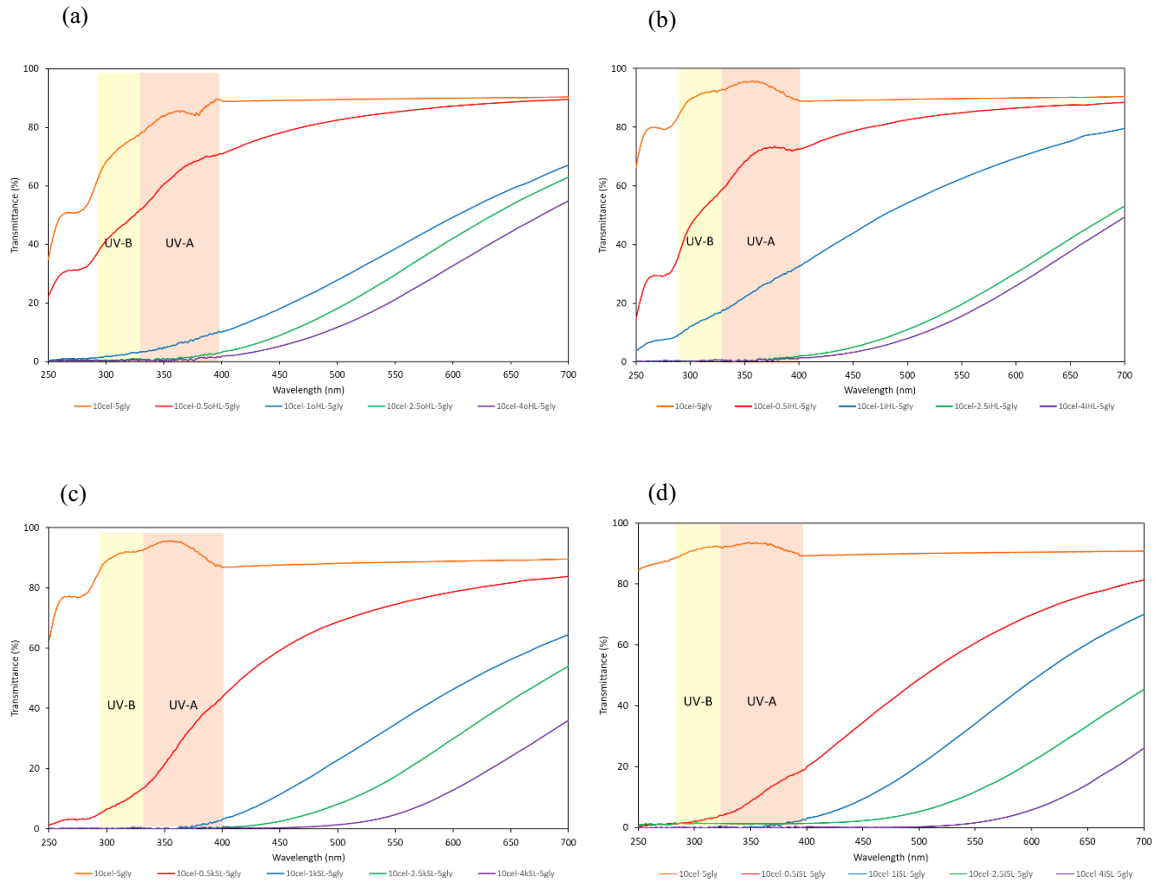


Figure 6.6: UV−vis transmission spectra of cellulose-lignin-glycerol films for hardwood (a-b) (iHL, oHL) and softwood lignin (c-d) (kSL, iSL) with various lignin concentrations

As the lignin content reached 1 wt.% and higher, the transparency of the **cel-lig-gly** films declined markedly, resulting in a substantial reduction in visible light transmission, as shown in Figure 6.6. Films without lignin exhibited high transparency, with minimal light scattering and negligible colouration, indicating that the cellulose-glycerol matrix alone does not significantly impede light transmission. In contrast, films containing softwood-derived lignins (**10cel-iSL-5gly** and **10cel-kSL-5gly**) showed a comparable decrease in transparency with increasing lignin content, consistent with the digital images at 4 wt.%. Notably, films incorporating softwood lignin appeared darker brown than those containing hardwood lignin.

This behaviour aligns with the well-established light-absorbing properties of lignin, which arise from its phenolic structural units.[16] As reported in Section 5.2.5, the phenolic acid contents of **kSL** and **iSL** are 1.78 and 1.81 mmol g^{-1}, respectively, while **10cel-oHL-5gly** films displayed a similar trend due to their higher phenolic acid content (3.36 mmol g^{-1}). The observed reduction in transmittance is attributed to enhanced light absorption and scattering, which collectively diminish the amount of light transmitted through the sample and detected by the instrument.

With respect to UV absorption, films based on softwood lignin exhibited exceptional performance, particularly the 2.5 wt.% and 4 wt.% **10cel-iSL-5gly** and **10cel-kSL-5gly** films, which completely blocked both UVA (320–400 nm) and UVB (280–320 nm) radiation. This enhanced UV-blocking capability can be attributed to the high content of phenolic hydroxyl groups in softwood lignin, which, along with other chromophoric structures, effectively absorb UV light. Previous studies have similarly reported that the incorporation of phenolic-rich compounds, such as tannic acid or sodium lignosulfonate, into PVA-based films significantly enhances their UV-shielding properties across UVA, UVB, and UVC regions.[17] These observations are consistent with literature findings indicating that cellulose-lignin films containing more than 20 wt.% lignin can block nearly 100% of UVB and approximately 99.9% of UVA.[18] Notably, both **10cel-2.5iSL-5gly** and **10cel-2.5kSL-5gly** films contain 20 wt.% lignin, corroborating their superior UV-blocking performance.

In contrast, films containing 2.5 wt.% and 4 wt.% lignin from **10cel-iHL-5gly** and **10cel-oHL-5gly** exhibited complete UVB blocking and nearly complete UVA attenuation. Theoretically, hardwood lignin comprises both syringyl (S) and guaiacyl (G) units, as evidenced by the HSQC NMR analysis presented in Section 5.2.6. In addition to the UV-absorbing contributions of phenolic hydroxyl groups, ketone and chromophoric structures also enhance UV resistance, while the number of methoxyl substituents further modulates this effect.[19] S-type lignin units, in particular, are known to exhibit enhanced UV resistance due to their higher methoxyl content, which increases the availability of free electron pairs capable of absorbing and dissipating UV radiation.[19] This mechanistic understanding would suggest superior UV-shielding performance for S-rich lignin; however, the current results deviate from this expectation. The phenolic hydroxyl content in **iHL** may have been overestimated, precluding a direct correlation between structure and UV absorption. The observed slight decrease in UV-

blocking performance is likely attributable to the lower purity of the lignin, which reduces the number of active sites available for UV absorption.

6.2.2 FTIR

FTIR spectroscopy was performed to detect the chemical functional groups in **cel–lig–gly** films, highlighting the incorporation of lignin into the cellulose–glycerol matrix. Significant absorption bands were observed at 3370, 2909, 1450, 1635, 1320, and 1245 cm^{-1}, corresponding to O–H stretching, C–H stretching, C–H bending, O–H bending, C–O stretching, and C–O–C stretching, respectively (Figure 6.8). In cellulose–glycerol films, characteristic C–H stretching bands are typically observed at 2921 and 2849 cm^{-1}, corresponding to the asymmetric and symmetric stretching of CH_2 groups. In the lignin-containing films, these bands were either slightly shifted or partially overlapped with the broad band at 2909 cm^{-1}, which can be attributed to the combined C–H stretching vibrations from cellulose, glycerol, and lignin. This indicates that the incorporation of lignin does not eliminate the characteristic CH_2 vibrations of cellulose and glycerol, but may slightly alter their exact position due to interactions within the composite matrix.

The effect of glycerol to **cel-lig** film were observed to detect changes of functional groups specifically at 3478 to 3300 cm^{-1} and 2936 cm^{-1} as illustrated in Figure 6.7. These specific wavelengths were targeted because previous studies reported similar observations: starch films crosslinked with citric acid and incorporated with glycerol showed a widening of the OH band at 3478–3300 cm^{-1}, indicating increased OH vibration and hydrogen bonding formation.[20,6] Additionally, cellulose acetate films containing 5–50 wt% glycerol exhibited an increase in the 2930 cm^{-1} band, corresponding to CH stretching, with higher glycerol content.[6] Since glycerol is a simple triol molecule with prominent O-H stretching a band is observed at 3300 cm^{-1}, signifying strong hydrogen bonding and aliphatic C-H stretching is detected at 2930 and 2880 cm^{-1}.

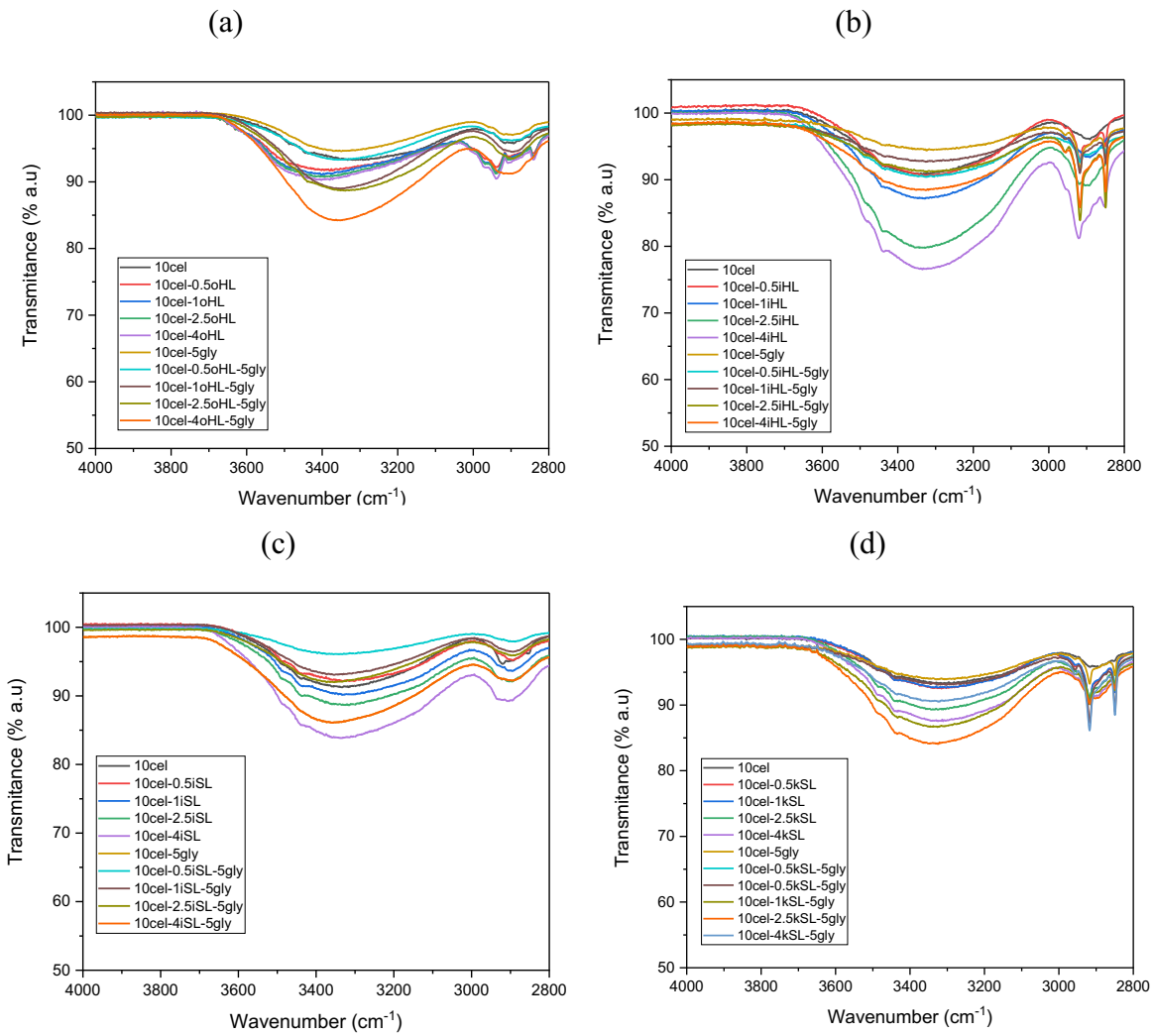


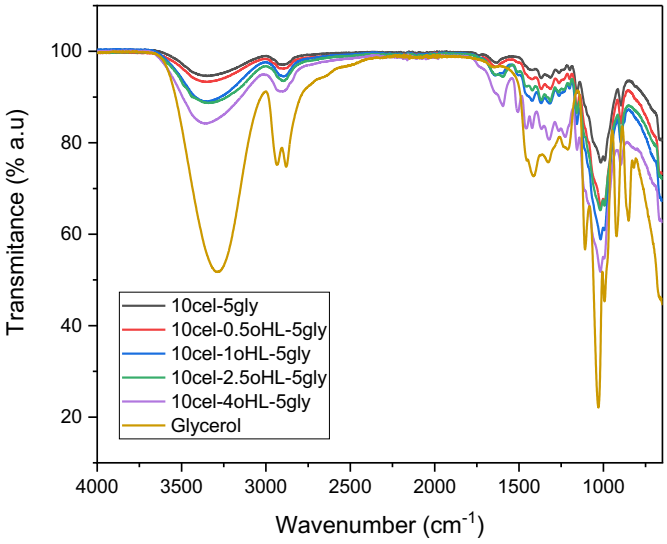
Figure 6.7: FTIR spectra of cel–lig and cel–lig–gly (4000–2800 cm^{-1}) (a) **10cel-oHL** and **10cel-oHL-5gly**, (b) **10cel-iHL** and **10cel-iHL-5gly**, (c) **10cel-iSL** and **10cel-iSL-5gly** and (d) **10cel-kSL** and **10cel-kSL-5gly** showing overlapping O–H and CH_2 stretching bands.

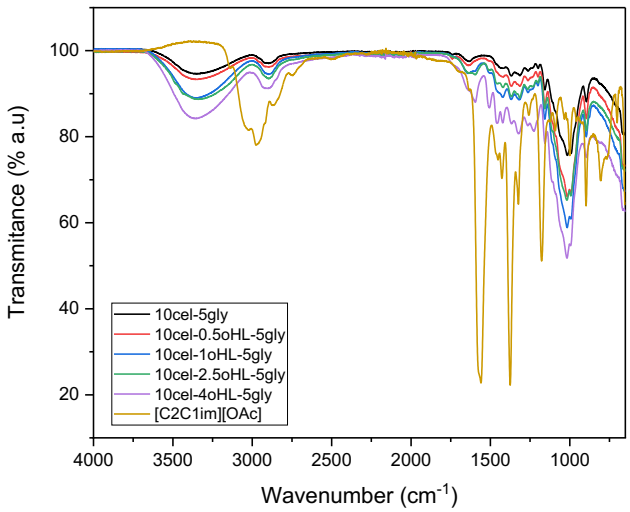
The observations revealed clear distinctions between lignin types, particularly between ionosolv, kraft, and organosolv lignins. In all films containing ionosolv lignin (**10cel-iHL-5gly** and **10cel-iSL-5gly**) in Figure 6.7 (b) and (c), the OH and CH_2 regions did not show the band widening reported in the literature, indicating that glycerol was not fully incorporated into these lignins. This is likely due to the steric hindrance of the condensed softwood lignin structure, which impedes glycerol integration. The highly condensed nature of ionosolv softwood lignin especially half of the G2 units has been documented in several studies.[21]

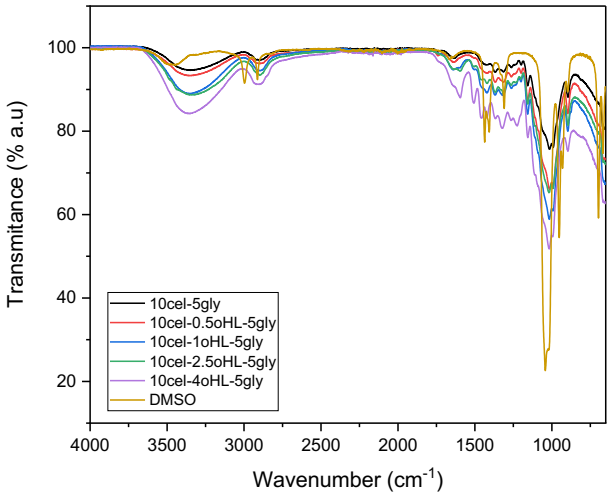
Meanwhile, for cellulose films containing kraft and organosolv lignin, such as **10cel-oHL-5gly** and **10cel-kSL-5gly** (Figure 6.7 (a) and (d)), higher lignin content promoted successful glycerol integration, as indicated by broadening of the OH band and intensification of the CH_2

band. For organosolv lignin, OH broadening was observed in films from **10cel-1oHL-5gly** to **10cel-4oHL-5gly**, while CH_2 intensification occurred only in **10cel-4oHL-5gly**. For kraft lignin, the OH band widened in **10cel-1kSL-5gly** and **10cel-2.5kSL-5gly**, whereas CH_2 intensification was observed only in **10cel-0.5kSL-5gly** and **10cel-4kSL-5gly**. These results suggest that kraft and organosolv lignins, which have fewer branches and more linear structures compared to ionosolv lignin, allow glycerol to more easily integrate into the cellulose–lignin matrix. [22,23]

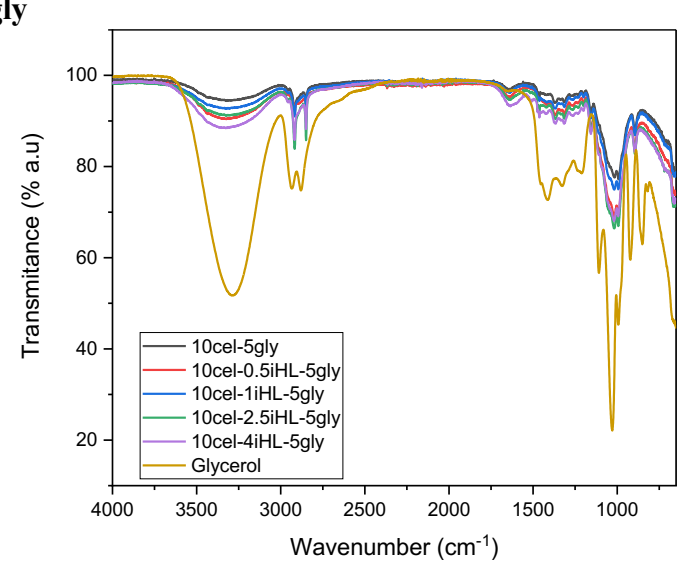
(a) 10cel-oHL-5gly

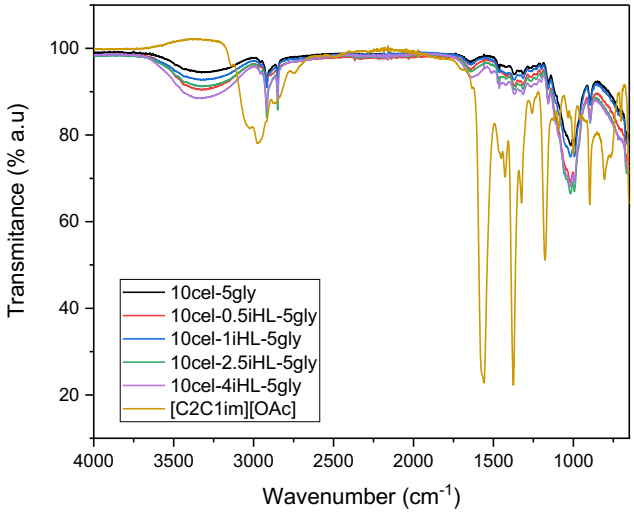


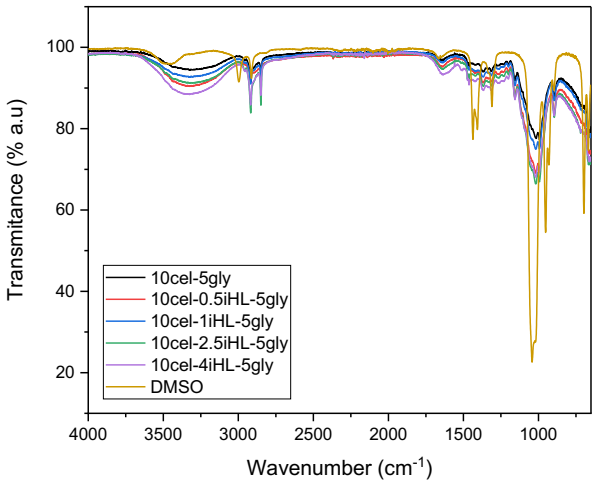




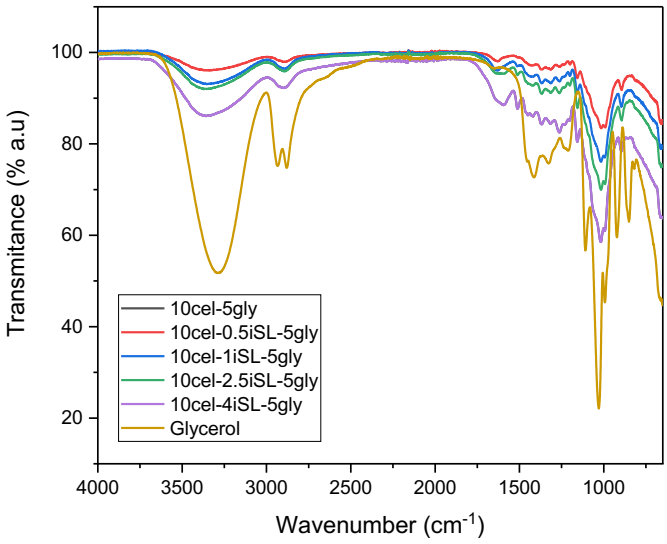
(b) 10cel-iHL-5gly

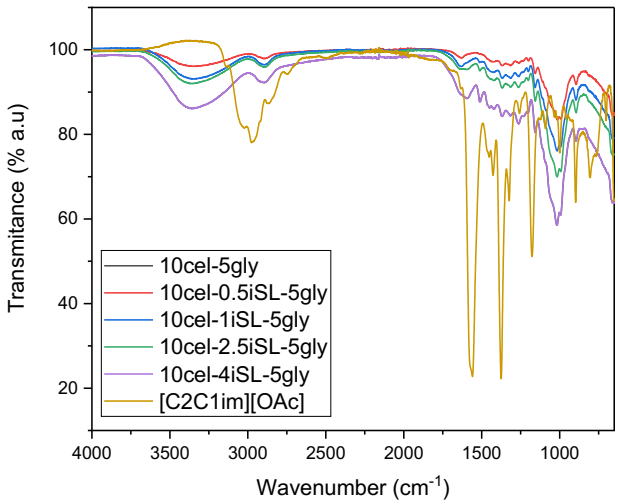


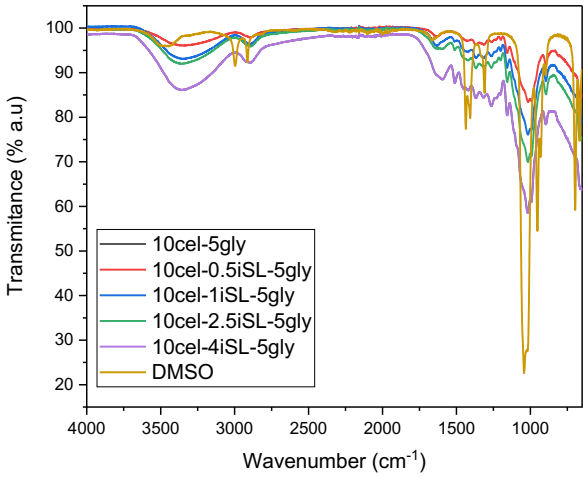




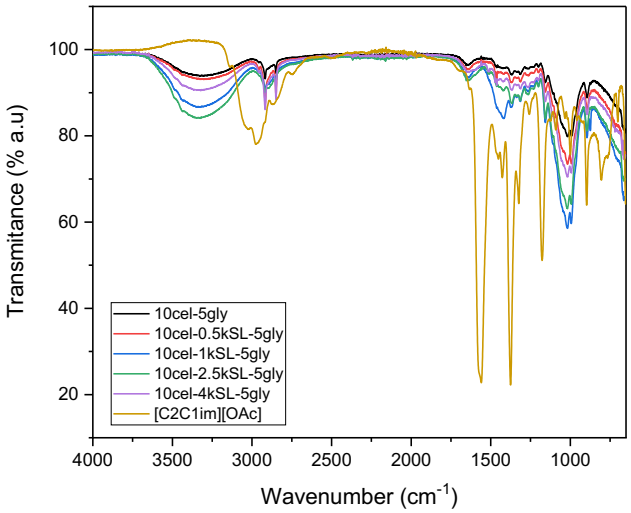
(c) 10cel-iSL-5gly

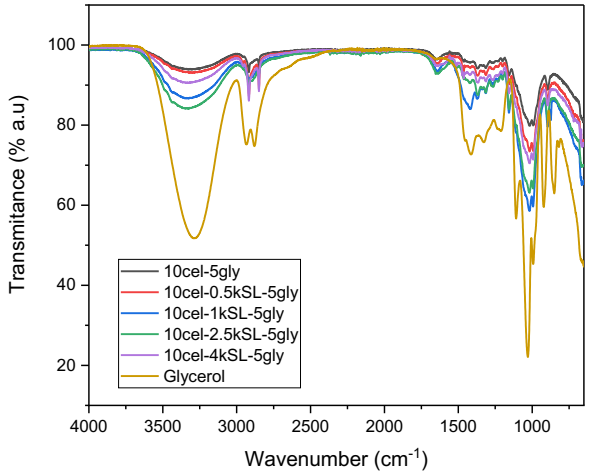






(d) 10cel-kSL-5gly





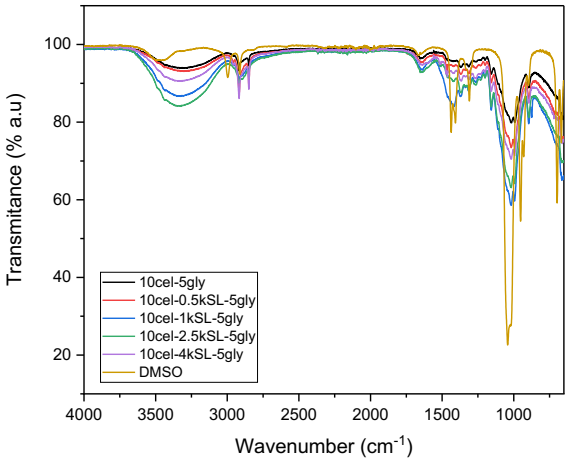


Figure 6.8: FTIR spectra of fabricated cellulose-lignin-glycerol films with different lignin types (a) **cel-oHL-gly** (b) **cel-iHL-gly** (c) **cel-iSL-gly** (d) **cel-kSL-gly** overlapped with glycerol, $[C_2C_1im][OAc]$ and DMSO

Other than that, integration glycerol can be observed at the bending vibration of C-O-H occurs within the range of 1334 - 1416 cm^{-1}, whereas the C-O stretching of primary alcohol is commonly observed at 1033 cm^{-1}. Analysis of the fingerprint region reveals clear evidence of effective glycerol integration within the **cel-lig** films.

The fingerprint region between 1100 and 1400 cm^{-1} can disclose distinctive patterns associated with glycerol. Numerous studies have investigated the incorporation of glycerol into polymer matrices. A study noted the appearance of a band within the range of 1030–1070 cm^{-1} when gelatin films were plasticized with glycerol; this band is associated with glycerol and exhibited greater intensity with higher glycerol concentrations.[24] The band has shifted within the range 1023 to 1030 cm^{-1} intensify that glycerol integrated in all **cel-lig** films.

At this stage, I will focus exclusively on the **cel-lig-gly** film in Figure 6.8. The shifting broad band OH from high to low transmittance at 3378 to 3374 cm^{-1} for majority of **cel-lig-gly** films indicates enhanced hydrogen bonding due to elevated lignin content. Glycerol does not contribute to this effect because it is a small molecule present in low relative amounts compared to lignin which has numerous hydroxyl groups on each polymer chain. Lignin comprises phenolic and aliphatic hydroxyl groups that exhibit significant absorption in the OH stretching

region.[25] The phenolic and aliphatic hydroxyl groups for all lignin were presented in Section 5.2.5, which contribute to shifting broad band. The range of 1636 cm^{-1} to 1645 cm^{-1} corresponds to the OH bending mode, which exhibited a similar change to a lower band with the addition of more lignin. The fingerprint region spans from 1500 to 400 cm^{-1}, where the presence of lignin and cellulose were identified in the spectra.

In addition to that, a notable shift to a lower frequency was seen in the C-H stretching at 2909 cm^{-1}. Various vibrational modes of C-H bending (scissoring) were seen at 1450–1420 cm^{-1}, signifying the presence of methyl ($–CH_3$) and methylene ($–CH_2$) groups. This band signifies the presence of methylene side chains in cellulose and lignin.[26] In the spectra of **10cel-iHL-5gly** and **10cel-kSL-5gly**, two distinct bands were seen at 2915 cm^{-1} and 2848 cm^{-1}, corresponding to the asymmetric and symmetric stretching vibrations of a C-H bond in a methylene (CH_2) group, confirming the presence of aliphatic side chains characterised by methylene structures. This corroborated with a literature examining hardwood (*Eucalyptus sp*.) and softwood (*Pinus sp*.) extracted using the same kraft method, revealing two prominent bands at 2932 and 2842 cm^{-1}, which correspond to C-H axial deformation of CH_2 and CH_3 in aliphatic side chains.[27] In contrast, a singular broad CH stretching (~2909 cm^{-1}) was observed for **10cel-oHL-5gly** and **10cel-iSL-5gly**. A single broad band can result from environmental effects; in some molecules, overlapping CH_2 and CH_3 stretches may produce a broad absorption instead of two distinct bands.

The C-O stretching of phenolic compounds was seen at 1320 and 1265 cm^{-1} indicating monomer units in lignin. The literature on orgonsolv beech wood lignin identifies a band at 1326 cm^{-1}, attributable to C–O bonds in alcohols, ethers, or carboxylic esters, associated with syringyl units.[28] The C–O–C stretching in aryl ethers was found at 1158 cm^{-1}, corresponding to the anticipated lignin–carbohydrate bonds. This finding supported by a review work on lignin-carbohydrate complexes (LCC) indicates that the band at 1170 cm^{-1} corresponds to the C–O stretching in the C–O–C bond of phenyl glycoside linkages. This band may also indicate the presence of acetyl groups in cellulose or hemicellulose.[29] Wavenumbers of 1010 cm^{-1} and 990 cm^{-1} are frequently linked to the vibrations of C-O bonds in diverse functional groups, especially within the fingerprint area.

The FTIR spectral analysis was utilized to confirm the total removal of the solvent system, which consisted of [C_2C_1im][OAc] and DMSO, employed in the dissolution process. The FTIR spectrum of pure [C_2C_1im][OAc] displays prominent absorption bands, featuring C–H stretching vibrations at 2975 cm^{-1} linked to methyl (–CH_3) groups, and at 2745 cm^{-1}, associated with aliphatic or aromatic C–H stretching. The absence of these bands in all **cel-lig-gly** films indicated the successful elimination of the ionic liquid. Moreover, a significant signal at 1558 cm^{-1}, associated with N–H bending and C–N stretching typical of imidazolium-based compounds, was not observed in the films, signifying the lack of amide functionalities, thus confirming the removal of [C_2C_1im][OAc]. Correspondingly, the pronounced absorption band at 1375 cm^{-1}, characteristically linked to alkyl chains or methyl-substituted aromatic rings, was absent in the spectra of all fabricated films. A significant band at 1178 cm^{-1}, representative of C–O stretching in C–O–C ether linkages or ester functionalities (such as those found in the acetate anion), exhibited a substantial reduction in strength across all samples, suggesting no residual acetate content. The absorption band between 800–820 cm^{-1}, associated with out-of-plane C–H bending vibrations in the imidazolium ring, was completely eliminated, further substantiating that the ionic liquid was not preserved in the final **cel-lig-gly** composite films.

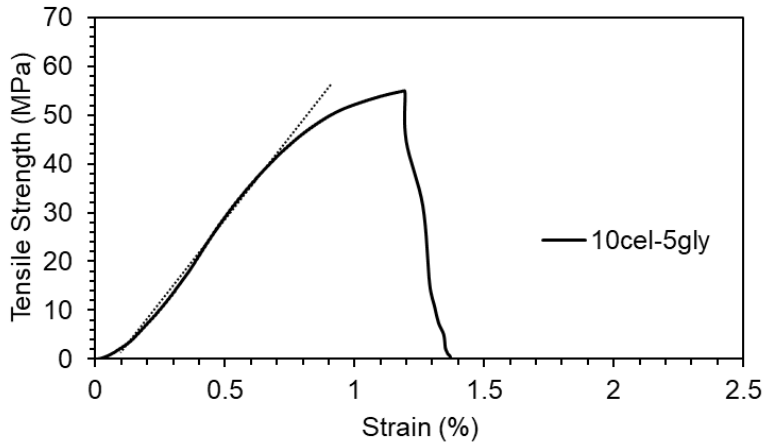
The characteristic FTIR absorption bands of the DMSO co-solvent used in the dissolution process were examined. The FTIR spectrum of pure DMSO has bands at 2998 cm^{-1} and 2915 cm^{-1}, which are indicative of the asymmetric and symmetric stretching vibrations of methyl (CH_3) groups attached to sulfur, respectively. Both bands were absent in all **cel-lig-gly** films, signifying the effective elimination of DMSO. Furthermore, deformation modes related to CH_3 groups specifically the asymmetric bending at 1436 cm^{-1} and symmetric bending at 1405 cm^{-1} were also absent in the spectra of the produced films. Likewise, the CH_3 wagging vibration at 1308 cm^{-1}, affected by the sulfur atom in DMSO, was not observed. Significantly, the pronounced absorption band at 1041 cm^{-1}, associated with the S=O stretching vibration was not observed in all film samples. These observations collectively verify that DMSO was successfully eliminated during the film production process. With both solvents removed, the composite films pose no safety concerns for end users.

6.2.3 Mechanical properties of cellulose-lignin-glycerol films

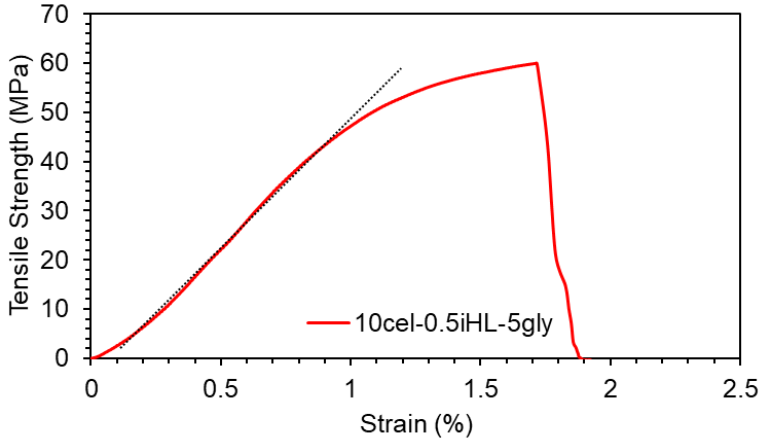
The mechanical properties of **cel-lig-gly** films are essential for assessing their potential use as plastic packaging materials. Critical measurements like tensile strength (TS), stiffness Young's modulus (YM), and ductility (% strain) were evaluated to understand the response of these films to mechanical stress. The representative stress-strain curves, produced from five replicates for each sample, are illustrated in Figure 6.9. A Hookean line was drawn for each curve to adjust for initial offsets, adhering to the standardised procedure ASTM D882-10.[30] Because there is limited literature on lignocellulosic films incorporating glycerol, composite films containing lignin will be used for comparison instead.

(a) 10cel-iHL-5gly

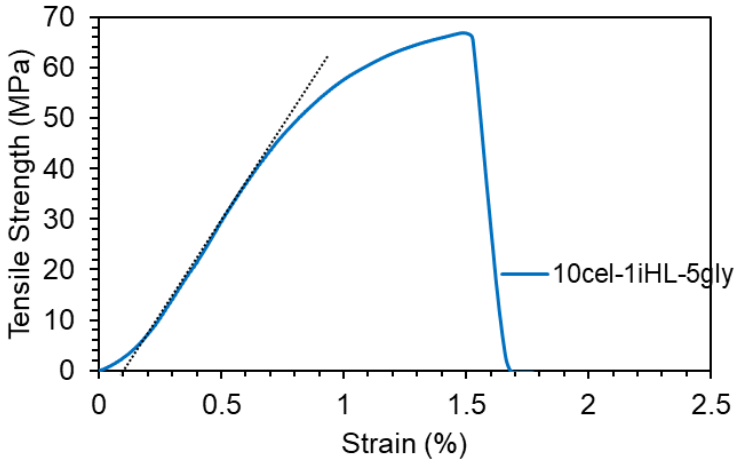
10cel-5gly



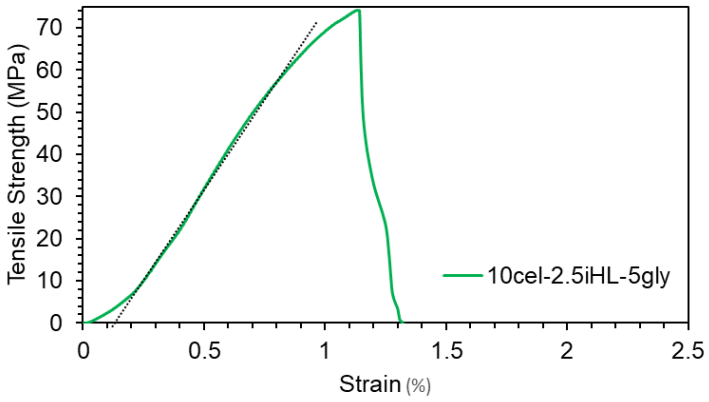
10cel-0.5iHL-5gly



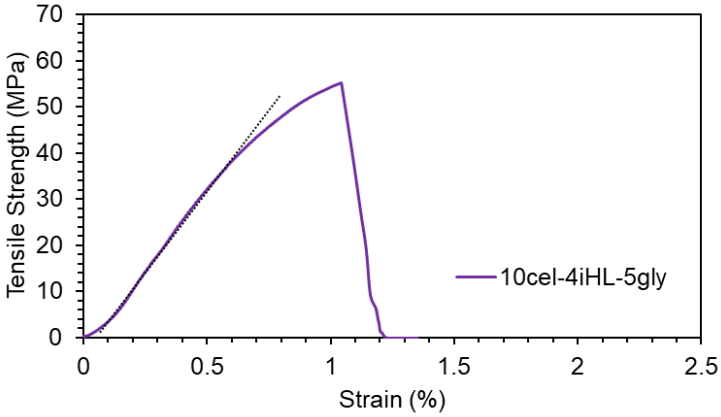
10cel-1iHL-5gly



10cel-2.5iHL-5gly

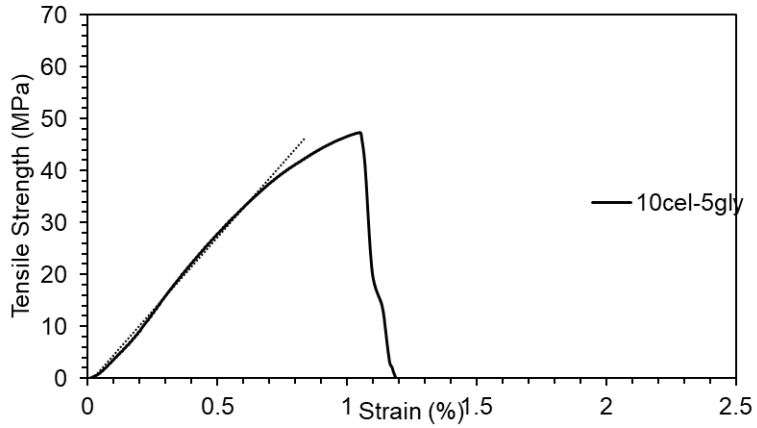


10cel-4iHL-5gly

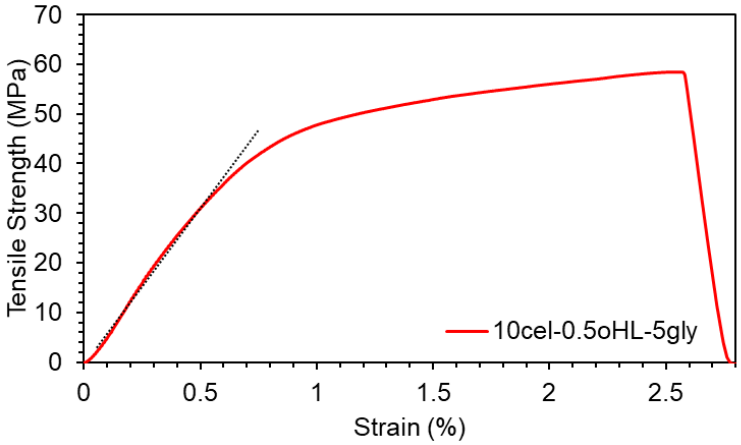


(b) 10cel-oHL-5gly

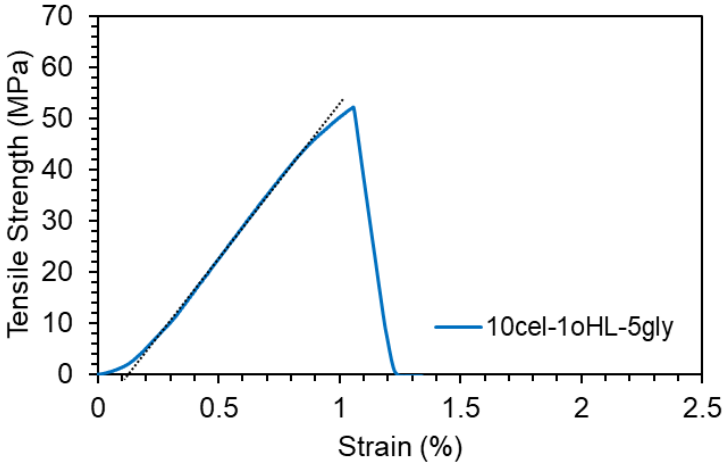
10cel-5gly



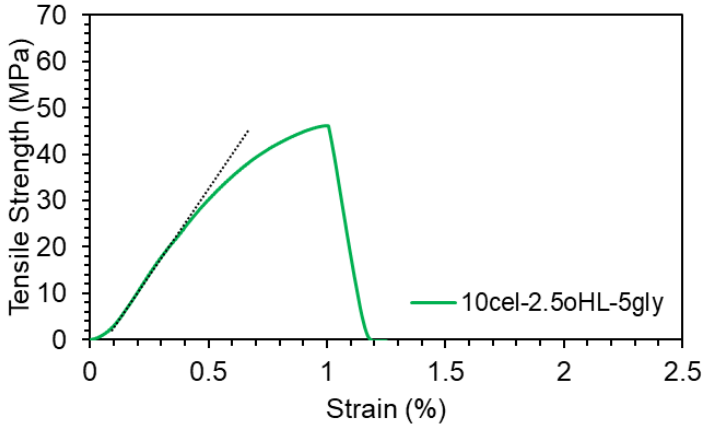
10cel-0.5oHL-5gly



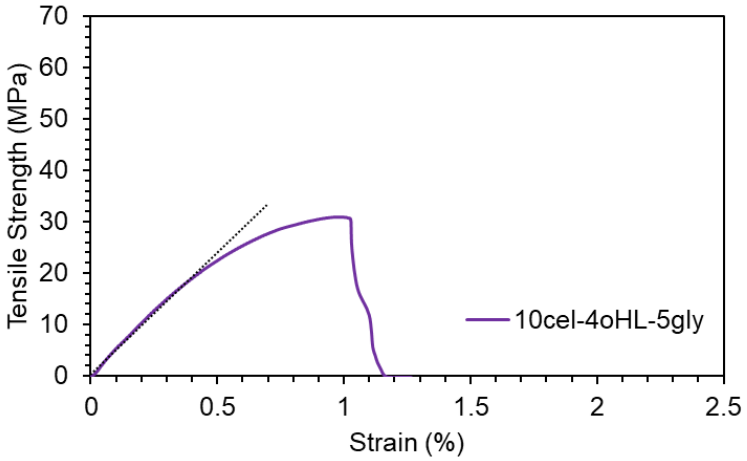
10cel-1oHL-5gly



10cel-2.5oHL-5gly

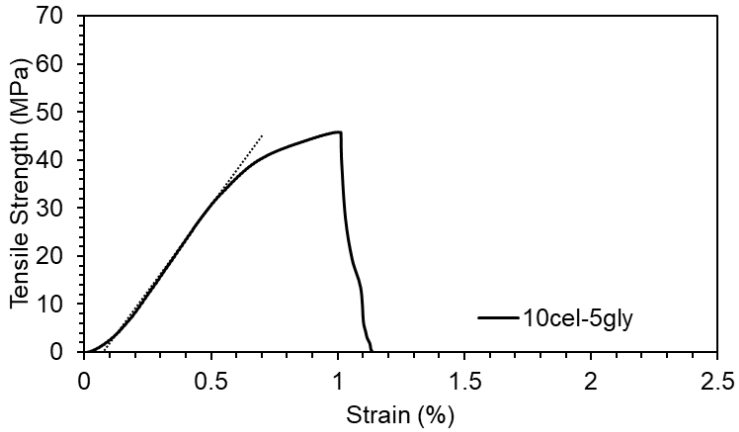


10cel-4oHL-5gly

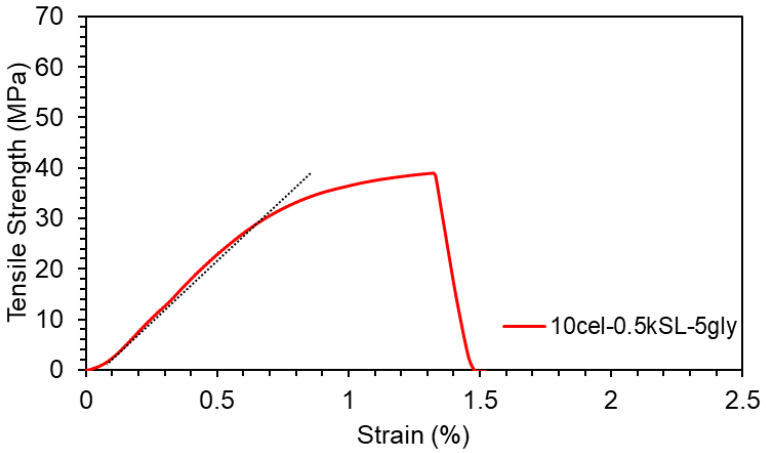


(c) 10cel-kSL-5gly

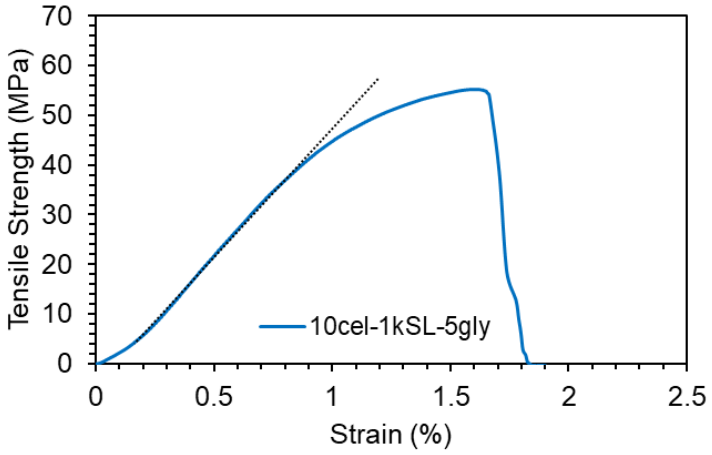
10cel-5gly



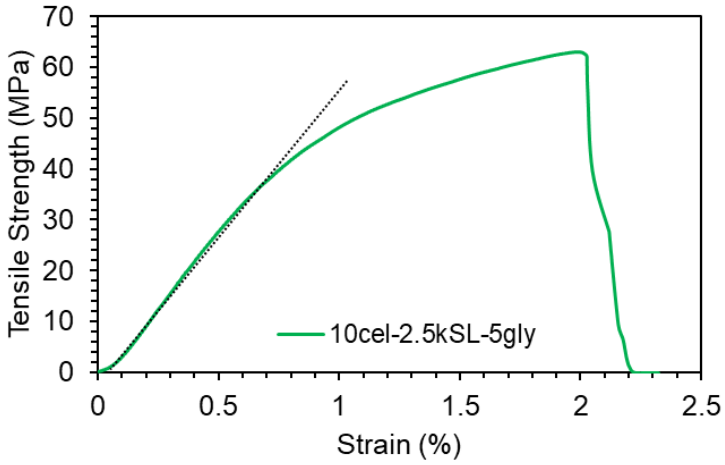
10cel-0.5kSL-5gly



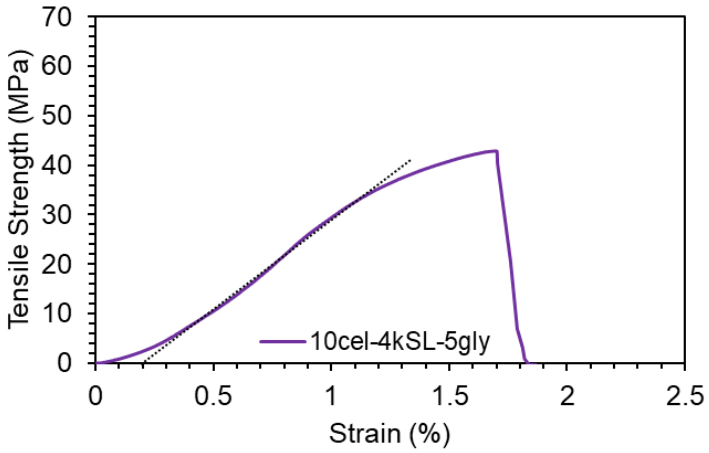
10cel-1kSL-5gly



10cel-2.5kSL-5gly

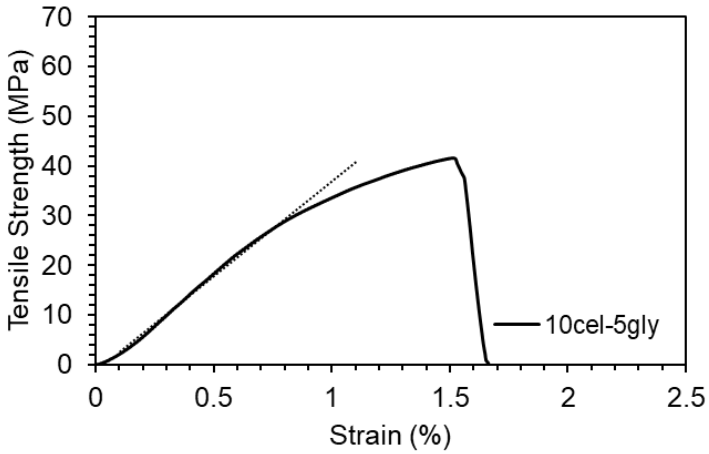


10cel-4kSL-5gly

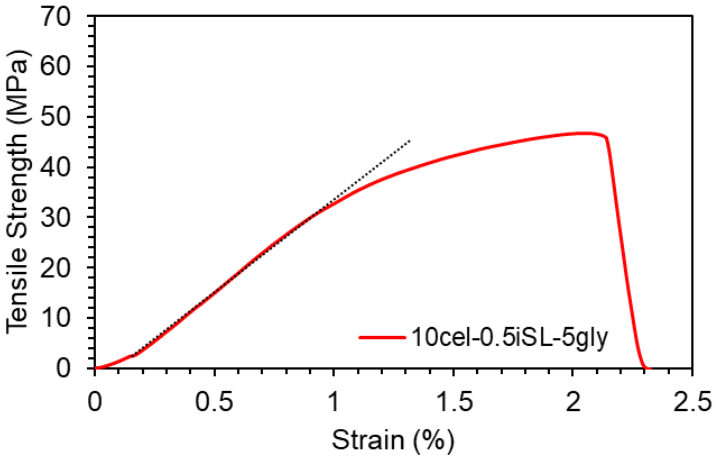


(d) 10cel-iSL-5gly

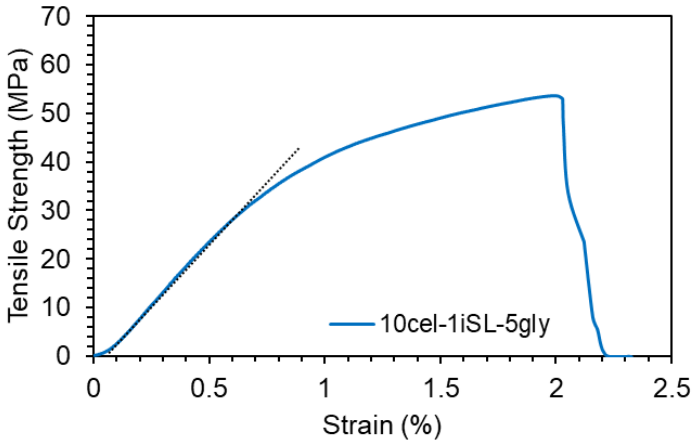
10cel-5gly



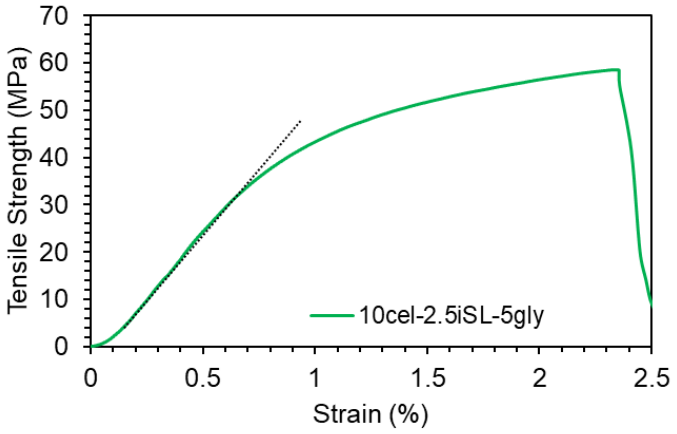
10cel-0.5iSL-5gly



10cel-1iSL-5gly



10cel-2.5iSL-5gly



10cel-4iSL-5gly

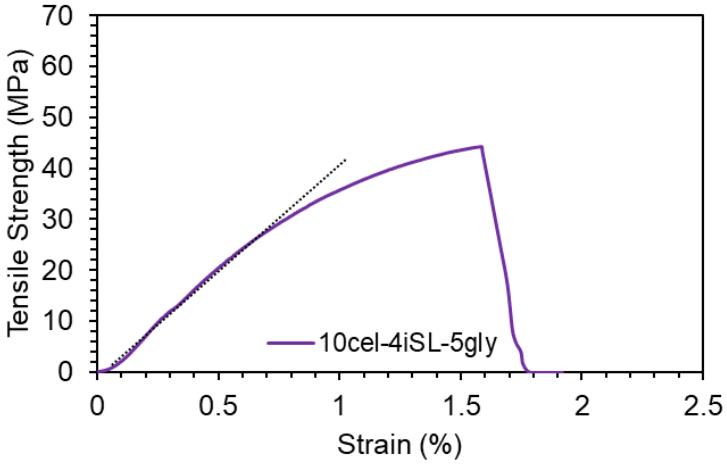
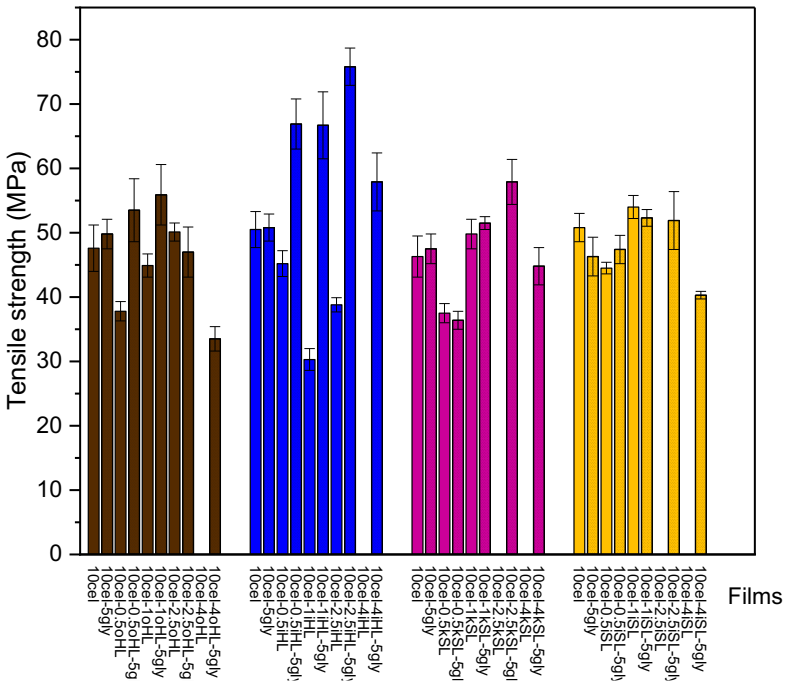


Figure 6.9: Tensile properties of cellulose-lignin-glycerol films at different various lignin and different weight percent (0, 0.5, 1, 2.5 and 4 wt.%) (a)**10cel-iHL-5gly** (b) **10cel-oHL-5gly** (c) **10cel-kSL-5gly** (d) **10cel-iSL-5gly**

Figure 6.10 compares the mechanical properties of **cel-lig** and **cel-lig-gly** films at equivalent lignin loadings. For each lignin type, the addition of glycerol resulted in higher tensile strength compared to the corresponding **cel-lig** films without glycerol. For example, **10cel-0.5oHL-5gly** exhibited a gradual increased TS than **10cel-0.5oHL**, while a more pronounced increase was observed for the **iHL**-containing films. A slight improvement was noted for the **10cel-kSL-5gly** formulation compared to **10cel-kSL**. However, within the **cel-lig-gly** series, increasing lignin content led to a reduction in TS, consistent with the trend observed in the **cel-lig** films. FTIR analysis confirmed that glycerol was effectively incorporated into cellulose-organoslv and cellulose-kraft lignin composite films (Section 6.2.2), but was absent in the ionosolv lignin group.

The increased TS observed in **10cel-iHL-5gly** compared to the corresponding film without glycerol (**10cel-iHL**) is notable, given that glycerol is traditionally associated with a reduction in TS.[6] The significant improvement can be attributed to the absence of glycerol molecules, which allows more homogeneous mixing between the cellulose and lignin matrices, thereby strengthening the composite material. In contrast, the slight improvement observed in composite films containing kraft and organosolv lignin is likely due to effective hydrogen bonding among glycerol, cellulose, and these lignin types, which helps the material withstand applied loads more effectively.



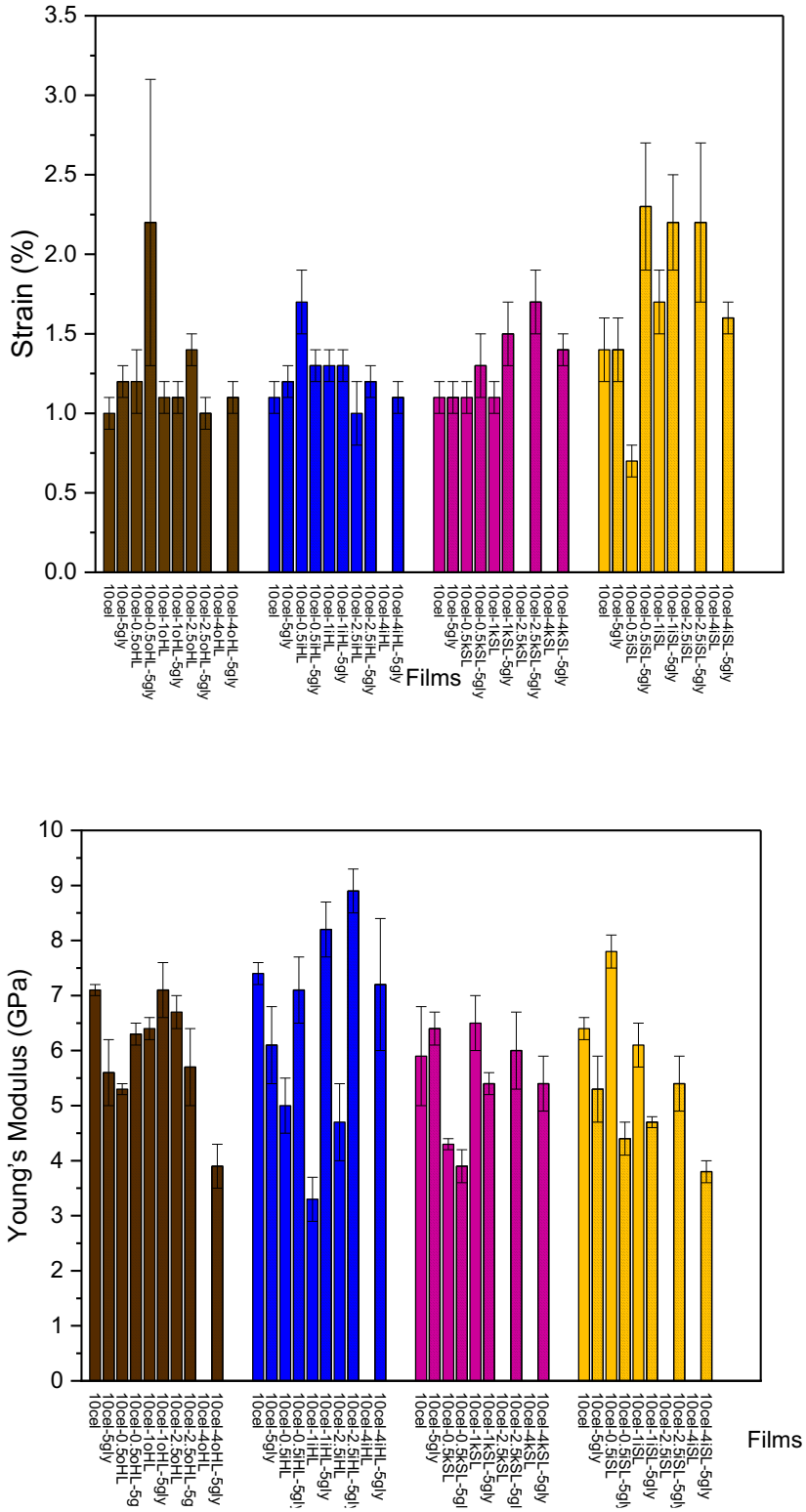


Figure 6.10: Average tensile properties of **cel-lig** and **cel-lig-gly** films at varying lignin contents (0, 0.5, 1, 2.5, and 4 wt.%), including **oHL**, **iHL**, **kSL**, and **iSL**

The effective interaction of glycerol with cellulose and lignin was demonstrated by the measurable mechanical properties in all the **cel-lig-gly** composite films. In the absence of glycerol, **cel–lig** films could only be mechanically characterized at compositions of **10cel–**

1iSL, **10cel–1kSL**, **10cel–2.5oHL**, and **10cel–2.5iHL**, as films with other compositions were too brittle to be measured. In contrast, the incorporation of glycerol enabled all composite films to be mechanically tested, indicating a substantial improvement in flexibility and mechanical integrity. Glycerol acts as a plasticizer, loosening the compact structure, weakening inter- and intramolecular hydrogen bonding, and enhancing lignin accessibility. [31]

Within both the **cel-lig** and **cel-lig-gly** series, increasing lignin content resulted in a reduction in tensile strength at higher lignin loadings, consistent with the trend previously reported in Chapter 5. This trend is consistent with previous reports in the literature. For example, composite films based on poly(butylene adipate-co-terephthalate) (PBAT) blended with 50–60 wt.% lignin exhibited a severe decrease in TS.[32] The deterioration in mechanical performance was attributed to the formation of large lignin agglomerates, insufficient interfacial adhesion between lignin and the polymer matrix, and a reduction in the continuous phase of the PBAT matrix, as evidenced by scanning electron microscopy (SEM) analysis.

In terms of ductility, no statistically significant difference in percent strain was observed between the **cel-lig** and **cel-lig-gly** films, indicating that glycerol did not substantially enhance elongation in these systems. A slight improvement was observed for the **cel-iSL-5gly** films compared to their glycerol-free counterparts. Specifically, the percent strain increased from approximately 1.0% to 1.3% for the **cel-oHL-5gly** and **cel-iHL-5gly** films relative to the corresponding films without glycerol, and from 1.5% to 2.2% for the **cel-iSL-5gly** and **cel-kSL-5gly** films. Despite this modest increase, the elongation at break of the glycerol-containing films remains significantly lower than values commonly reported in the literature for similar **cel-lig** films. For example, pure cellulose films have been reported to exhibit a maximum strain of 10%, which decreased to 6% upon addition of 2 wt.% lignin.[16] The discrepancy between that study and the present work is likely due to the use of chemically modified materials in the former research. Specifically, azide-functionalized cellulose and lignin conjugated via highly efficient click chemistry, which enhances interfacial compatibility and mechanical performance.

An increase in percentage strain was observed for the **10cel-iSL-5gly** sample compared to the corresponding glycerol-free **10cel-iSL** film, indicating enhanced flexibility; however, this finding appears to contradict the FTIR results, which did not show noticeable O–H or CH_2 band

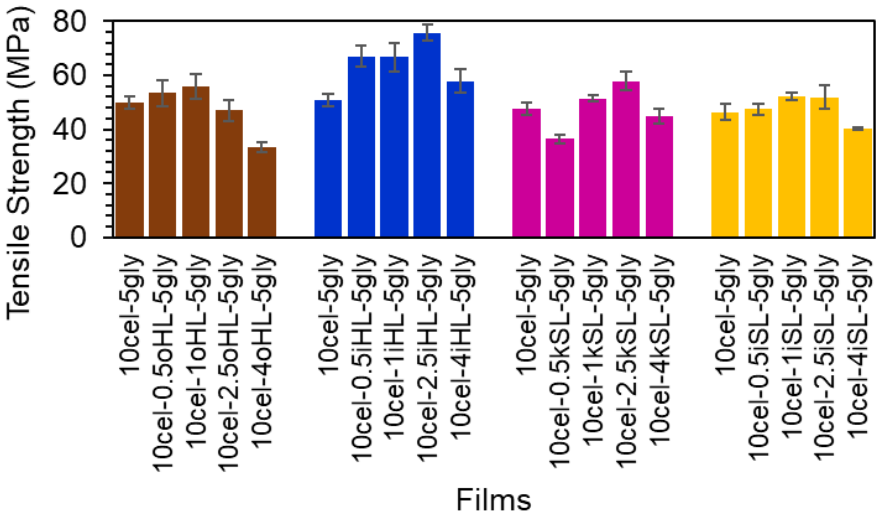
broadening that would confirm the presence of glycerol. The inability of FTIR spectroscopy to detect glycerol incorporation can be attributed to several factors. Glycerol contains O–H and C–O functional groups, whose characteristic absorption bands often overlap with those of the cellulose-lignin matrix, particularly in systems already rich in hydroxyl, ester, or ether groups. Furthermore, when glycerol acts as a physical plasticizer, it interacts with cellulose and lignin primarily through hydrogen bonding rather than forming new covalent bonds with the polymer chains; therefore, no new infrared absorption bands are expected. In addition, the relatively low glycerol content may result in signals that are too weak to be distinguished from the dominant polymer backbone. Independent evidence supporting the presence of glycerol is provided by water contact angle measurements, which show increased surface hydrophilicity (Section 6.2.5).

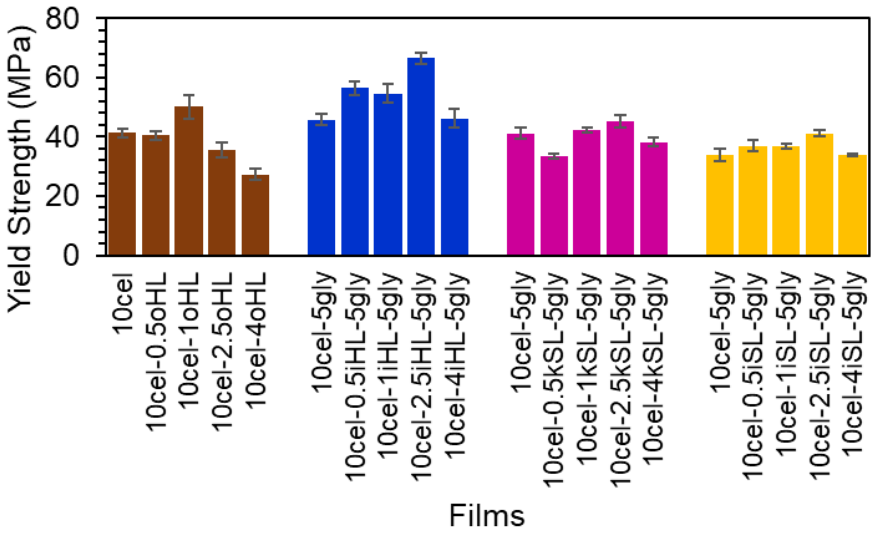
A lower YM indicates higher deformability, while a higher YM reflects a stiffer material. In this study, YM generally decreased for **10cel-kSL-gly** and **10cel-iSL-gly** in comparison to **10cel-iHL-gly** and **10cel-oHL-gly** group, which can be attributed to their higher strain values. The increased strain suggests enhanced flexibility, resulting in lower resistance to elastic deformation and, consequently, a reduced YM. In contrast, **10cel-iHL-5gly** exhibited a low strain value, indicating limited flexibility and a more rigid structure. FTIR analysis chemically confirmed the absence of significant glycerol interaction in this formulation. As a result, this film showed a high YM, meaning it required greater stress to produce a small amount of elastic deformation. This stiffness explains why **10cel-iHL-5gly** also demonstrated a higher TS, as stronger intermolecular interactions within the polymer matrix contribute to both higher YM and TS.

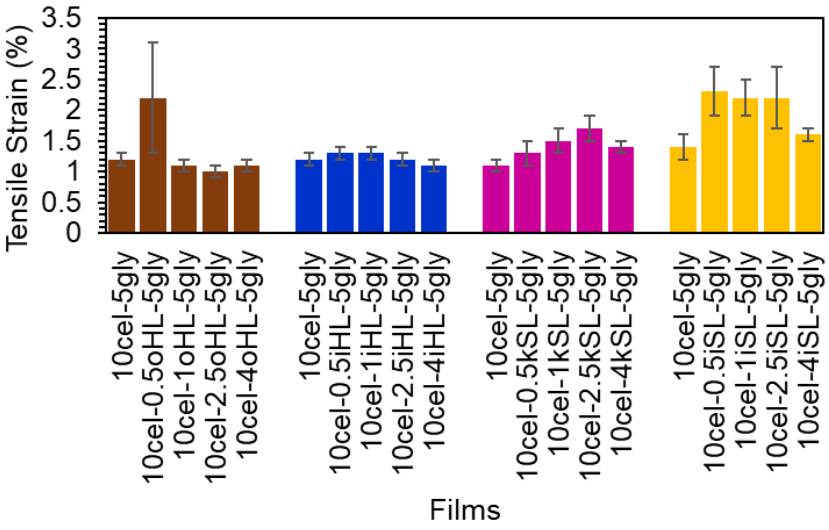
Overall, most **cel-lig-gly** films exhibited relatively high YM values compared to **cel-lig** composite films. In these systems, glycerol does not primarily function as a plasticizer to improve flexibility. Instead, it likely acts as a physical plasticizer, occupying free volume within the polymer matrix and forming hydrogen bonds with cellulose and lignin hydroxyl groups; however, these interactions appear insufficient to significantly increase chain mobility. This behavior restricts elastic deformation and contributes to increased stiffness rather than enhanced flexibility.

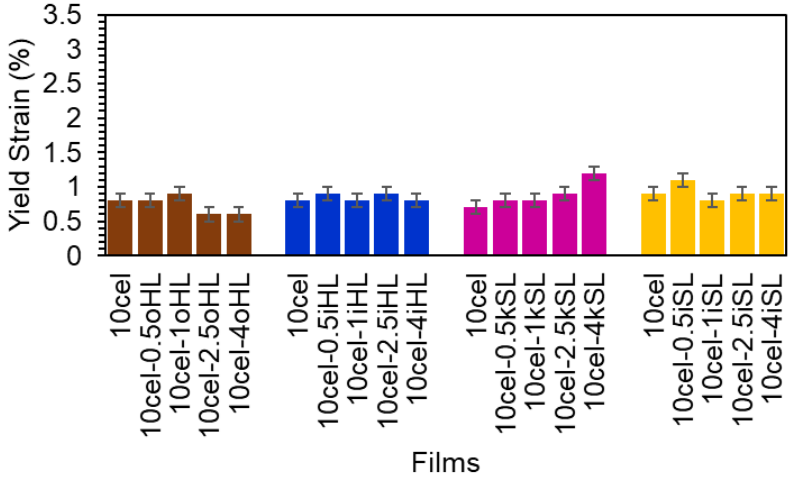
The following section discusses the TS, YM, and strain of the **cel–lig–gly** films in detail indicated in Figure 6.11 and Table 6.4. Overall, tensile yield strength follows a trend consistent with TS, consistently remaining approximately 20% lower across formulations. Characterizing the yield point is critical for industrial translation, as it marks the upper boundary of the linear elastic region prior to irreversible plastic deformation. Furthermore, yield strain exhibited minimal variation across all **cel–lig–gly** formulations, underscoring the limited inherent ductility of the composite matrix. Consequently, these materials are better suited for rigid or semi-rigid single-use applications, such as sustainable packaging, rather than end-uses requiring high elastomeric flexibility.

To begin with, the **10cel-5gly** film exhibited an average TS of 48.6 MPa, which is very close to the previously reported value of 48.8 MPa for the **10cel** film without glycerol. A slight increase in strain at break (from 1.0% to 1.2%) and a decrease in Young's modulus (from 7 GPa to 5.8 GPa) were observed when comparing **10cel** to **10cel-5gly**. These changes indicate slight improved flexibility in the **10cel-5gly** film. The TS measured in this study is also consistent with values reported in the literature for cellulose films containing 5 wt.% glycerol and maltitol, which typically show tensile strengths of around 48 MPa.[1]




Yield Strength (MPa)
80
60
40
20
0
10cel
10cel-0.5oHL
10cel-1oHL
10cel-2.5oHL
10cel-4oHL
10cel-5gly
10cel-0.5iHL-5gly
10cel-1iHL-5gly
10cel-2.5iHL-5gly
10cel-4iHL-5gly
10cel-5gly
10cel-0.5kSL-5gly
10cel-1kSL-5gly
10cel-2.5kSL-5gly
10cel-4kSL-5gly
10cel-5gly
10cel-0.5iSL-5gly
10cel-1iSL-5gly
10cel-2.5iSL-5gly
10cel-4iSL-5gly
Films


Tensile Strain (%)
3.5
3
2.5
2
1.5
1
0.5
0
10cel-5gly
10cel-0.5oHL-5gly
10cel-1oHL-5gly
10cel-2.5oHL-5gly
10cel-4oHL-5gly
10cel-5gly
10cel-0.5iHL-5gly
10cel-1iHL-5gly
10cel-2.5iHL-5gly
10cel-4iHL-5gly
10cel-5gly
10cel-0.5kSL-5gly
10cel-1kSL-5gly
10cel-2.5kSL-5gly
10cel-4kSL-5gly
10cel-5gly
10cel-0.5iSL-5gly
10cel-1iSL-5gly
10cel-2.5iSL-5gly
10cel-4iSL-5gly
Films


Yield Strain (%)
3.5
3
2.5
2
1.5
1
0.5
0
10cel
10cel-0.5oHL
10cel-1oHL
10cel-2.5oHL
10cel-4oHL
10cel
10cel-0.5iHL
10cel-1iHL
10cel-2.5iHL
10cel-4iHL
10cel
10cel-0.5kSL
10cel-1kSL
10cel-2.5kSL
10cel-4kSL
10cel
10cel-0.5iSL
10cel-1iSL
10cel-2.5iSL
10cel-4iSL
Films

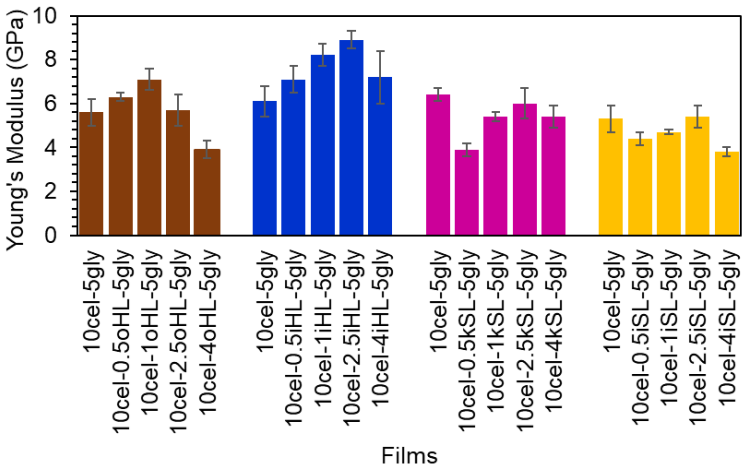


Figure 6.11: Average tensile properties of cel-lig-gly films at various lignin content and weight percent ratio (**oHL**, **iHL**, **kSL** and **iSL**) at 0, 0.5, 1, 2.5 and 4 wt.%

Table 6.4: Tensile properties of cellulose–lignin-glycerol composite films at different lignin and content

Lignin type	Formula	Tensile Strength (MPa)	Yield Strength (MPa)	Strain (%)	Yield Strain (%)	Young's Modulus (GPa)
oHL	**10cel-5gly**	49.8 ± 2.3	41.3 ± 1.5	1.2 ±0.1	0.8 ±0.1	5.6 ± 0.6
	10cel-0.5oHL-5gly	53.5 ± 4.9	40.4 ± 1.5	2.2 ± 0.9	0.8 ±0.1	6.3 ± 0.2
	10cel-1oHL-5gly	55.9 ± 4.7	50.1 ± 3.9	1.1 ± 0.1	0.9 ±0.1	7.1 ± 0.5
	10cel-2.5oHL-5gly	47.0 ± 3.9	35.7 ± 2.5	1.0 ± 0.1	0.6 ±0.1	5.7 ± 0.7
	10cel-4oHL-5gly	33.5 ± 1.9	27.3 ± 1.8	1.1 ± 0.1	0.6 ±0.1	3.9 ± 0.4
iHL	**10cel-5gly**	50.8 ± 2.1	45.8 ± 2.0	1.2 ± 0.1	0.8 ±0.1	6.1 ± 0.7
	10cel-0.5iHL-5gly	66.9 ± 3.9	56.4 ± 2.3	1.3 ± 0.1	0.9 ±0.1	7.1 ± 0.6
	10cel-1iHL-5gly	66.7 ± 5.2	54.6 ± 3.2	1.3 ± 0.1	0.8 ±0.1	8.2 ± 0.5
	10cel-2.5iHL-5gly	75.8 ± 2.9	66.5 ± 2.0	1.2 ± 0.1	0.9 ±0.1	8.9 ± 0.4
	10cel-4iHL-5gly	57.9 ± 4.5	46.2 ± 3.2	1.1 ± 0.1	0.8 ±0.1	7.2 ± 1.2
kSL	**10cel-5gly**	47.5 ± 2.3	41.2 ± 1.7	1.1 ± 0.1	0.7 ±0.1	6.4 ± 0.3
	10cel-0.5kSL-5gly	36.4 ± 1.4	33.4 ± 1.0	1.3 ± 0.2	0.8 ±0.1	3.9 ± 0.3

	10cel-1kSL-5gly	51.5 ± 1.0	42.3 ± 1.0	1.5 ± 0.2	0.8 ±0.1	5.4 ± 0.2
	10cel-2.5kSL-5gly	57.9 ± 3.5	45.4 ± 2.1	1.7 ± 0.2	0.9 ±0.1	6.0 ± 0.7
	10cel-4kSL-5gly	44.8 ± 2.9	38.2 ± 1.5	1.4 ± 0.1	1.2 ± 0.1	5.4 ± 0.5
iSL	**10cel-5gly**	46.3 ± 3.0	33.9 ± 2.1	1.4 ± 0.2	0.9 ±0.1	5.3 ± 0.6
	10cel-0.5isL-5gly	47.4 ± 2.2	37.0 ± 1.8	2.3 ± 0.4	1.1 ±0.1	4.4 ± 0.3
	10cel-1isL-5gly	52.3 ± 1.3	36.7 ± 0.8	2.2 ± 0.3	0.8 ±0.1	4.7 ± 0.1
	10cel-2.5isL-5gly	51.9 ± 4.5	41.2 ± 0.9	2.2 ± 0.5	0.9 ±0.1	5.4 ± 0.5
	10cel-4isL-5gly	40.3 ± 0.6	33.8 ± 0.5	1.6 ± 0.1	0.9 ±0.1	3.8 ± 0.2

Significant variations in TS were observed among the **cel-lig-gly** formulation films. Among all the samples, the **10cel-iHL-5gly** film exhibited the highest TS. However, this differs from the glycerol-free films reported in Chapter 5, where **10cel-1iSL** exhibited the highest TS, indicating that glycerol influenced the relative mechanical performance of the formulations. The **10cel-iHL-5gly** formulation contains a higher proportion of cellulose compared to the other lignin type in **cel-lig-gly** formulations, as indicated by the increased carbohydrate signal intensity observed in the HSQC NMR spectra (Figure 5.12). This higher cellulose content is likely to contribute to the improved mechanical properties observed for this film. This conclusion is consistent with previous findings in fiber-spinning studies, which report that increasing cellulose polymer concentration is associated with higher tensile strength.[33]

The **10cel-2.5iHL-5gly** film achieved the highest tensile strength (75.8 MPa). In contrast, the glycerol-free samples reported in Chapter 5 showed the highest tensile strength for the **10cel-1iSL** formulation, indicating that glycerol influences the relative contribution of **iHL**-derived lignin–carbohydrate complexes (LCCs) to the mechanical performance. The presence of LCCs enables additional hydrogen bonding with cellulose, thereby enhancing the film's mechanical strength. This behaviour is consistent with findings from the literature on lignin–polyvinyl alcohol (PVA) composite films.[34] For example, P2L-PVA films exhibit more than double the tensile strength of pure PVA due to strong hydrogen bonding interactions and the filler effect of P2-lignin nanoparticles. Further studies also show that the tensile strength of composite films increases with rising lignin nanoparticle (LNP) content, reaching a maximum of 85.9 ± 5.1 MPa at 4 wt.% LNPs, followed by a decline at higher concentrations.

Across the 0.5–2.5 wt.% lignin range, the **10cel-oHL-5gly**, **10cel-kSL-5gly**, and **10cel-iSL-5gly** films exhibited similar overall trends in tensile strength, with TS values spanning from 36.4 to 57.9 MPa. In general, TS increased with increasing lignin content and reached a maximum at 2.5 wt.% lignin for most formulations. The only exception was the **10cel-oHL-5gly** film, which showed a TS maximum at 1 wt.% lignin before declining at higher loadings. Notably, these TS values were generally higher than those observed for the corresponding **cel-lig** films discussed in the previous chapter, although this trend was not observed for all compositions. Among all samples, the **10cel-4oHL-5gly** formulation exhibited the lowest TS.

YM provides insight into the stiffness and ductility of **cel-lig-gly** composite films, with variations in YM values reflecting differences in mechanical behaviour among the samples. For example, the **10cel-iHL-5gly** group, which exhibits high TS low strain at break, and a YM of 8.9 GPa, indicates that the resulting composite film is robust, stiff, and brittle. In contrast, the **10cel-iSL-5gly** group has a lower YM (3.8 GPa), reflecting reduced stiffness. The presence of **iSL** is thought to enhance interfacial adhesion and improve overall matrix cohesion, potentially mitigating the effects of plasticization and contributing to the observed mechanical behavior. These findings align with previous reports on willow-lignin–cellulose composites, where a formulation containing 75% lignin and 25% cellulose produced a YM of 3.0 GPa, while reversing the ratio (25% lignin, 75% cellulose) increased the modulus to 5.9 GPa.[35]

A specific comparison was made between the **cel-iHL-5gly** and **cel-iHL** films due to the remarkable increase in TS. To establish statistical significance criteria for the changes observed in the mechanical properties of the composite films, a two-sample Welch's t-test was conducted assuming a sample size of $n = 5$ ($p < 0.05$) as tabulated in Table 6.5.

The TS increased by up to 120.1% for the **10cel-1iHL-5gly** film, with further improvements observed up to 4 wt.% lignin loading, as illustrated in Figure 6.12. This behaviour can be explained by considering glycerol as a temporary processing aid rather than a permanent plasticiser. For the 2.5% **iHL** blend, the incorporation of glycerol (**10cel-2.5iHL-5gly**) resulted in an extremely significant improvement in tensile stress from 38.8 ± 1.1 MPa to 75.8 ± 2.9 MPa ($p < 0.0001$). During film fabrication, glycerol likely enhances the dispersion of lignin and cellulose chains, promoting improved molecular alignment and interfacial contact. However, it is subsequently removed during coagulation in the water bath due to strong

hydrogen bonding. Previous studies have reported similar findings, showing that processing aids such as glycerol can temporarily modify hydrogen-bonding networks and crystallinity during regeneration, resulting in films with enhanced tensile properties, despite the later accumulation of excess glycerol on the surface of sericin films, a protein derived from silkworm cocoons.[36]

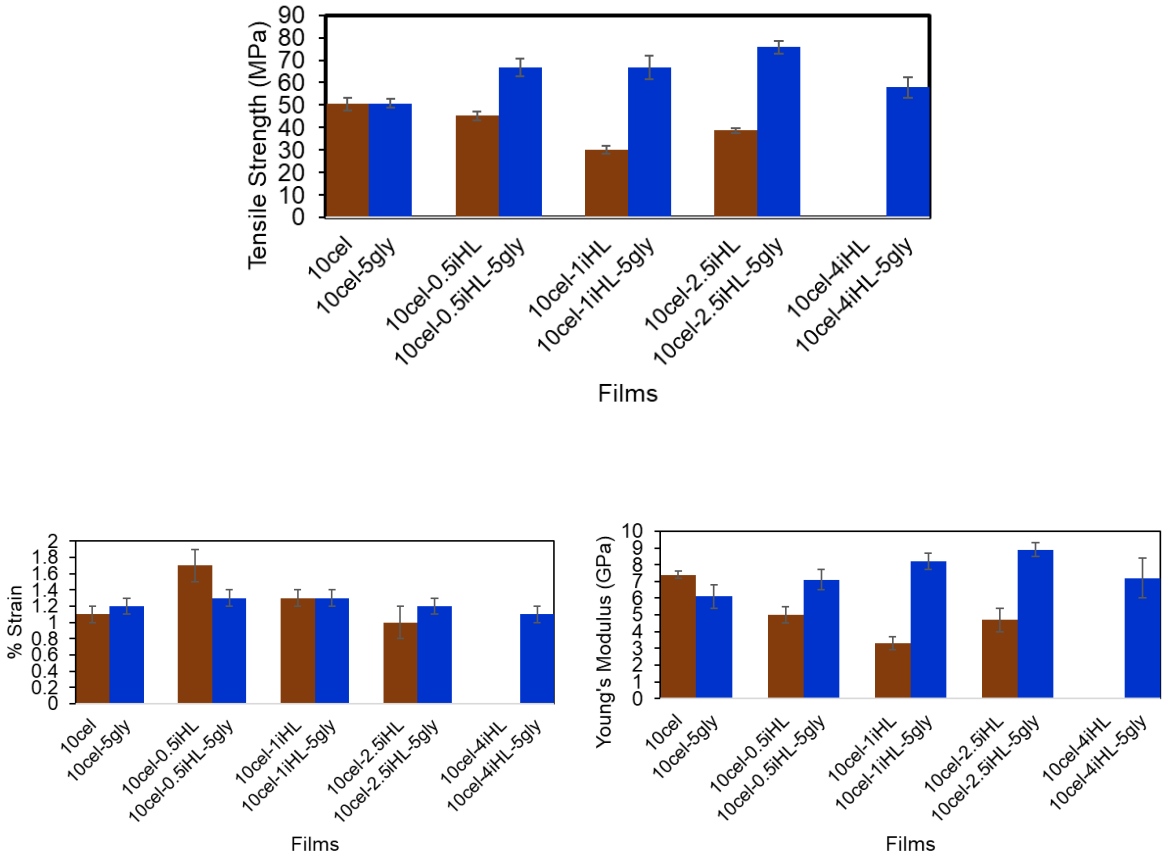


Figure 6.12: Tensile properties of **10cel-iHL** in comparison with **10cel-iHL-5gly**

Table 6.5: Statistical significance criteria (Welch's t-test, n = 5) comparing the tensile properties of cellulose-ionosolv lignin composite films with and without glycerol incorporation (**cel-iHL** vs. **cel-iHL-5gly**)

Mechanical property	Film without glycerol	Film with glycerol	Exact p-value	Statistically significant
Tensile stress (MPa)	10cel	10cel-5ly	0.85315	No
	10cel-0.5iHL	10cel-0.5iHL-5gly	0.00003	Yes ($p < 0.001$)
	10cel-1iHL	10cel-1iHL-5gly	0.00003	Yes ($p < 0.001$)

	10cel-2.5iHL	10cel-2.5iHL-5gly	< 0.00001	Yes ($p < 0.001$)
Young's Modulus (GPa)	10cel	10cel-5ly	0.01204	Yes ($p < 0.05$)
	10cel-0.5iHL	10cel-0.5iHL-5gly	0.00036	Yes ($p < 0.001$)
	10cel-1iHL	10cel-1iHL-5gly	< 0.00001	Yes ($p < 0.001$)
	10cel-2.5iHL	10cel-2.5iHL-5gly	0.00002	Yes ($p < 0.001$)
Strain (%)	All other pairs	All other pairs	$p > 0.05$	No

Data presents calculated t-statistics, exact p-values, and explicit significance designations, where *$p < 0.05$, $p < 0.01$, $p < 0.001$, and ns indicates no statistically significant difference ($p > 0.05$).

The minimal difference in % strain between **10cel-iHL** and **10cel-iHL-5gly** indicates that glycerol was not fully retained in the final film matrix, as the presence of a plasticiser would generally lead to significant increased elongation at break. This hypothesis is strongly supported by the independent t-test results for percent strain. The lack of statistical significance upon adding glycerol to the matrix evidenced by p-values > 0.05.

The elevated YM reported for **10cel-iHL-5gly** aligns with the increased TS, signifying a more rigid and mechanically resilient structure. This implies that glycerol's effect during the initial gelation or regeneration phases may have resulted in a more crystalline or tightly connected cellulose-lignin network, even after its removal. For the 2.5 wt. % **iHL** blend, the incorporation of glycerol (**10cel-2.5iHL-5gly**) resulted in an enhancement in Young's Modulus to 8.9 GPa ($p = 0.00002$)

In conclusion, the addition of 5 wt.% glycerol enhances the TS of selected cel-lig-gly films, particularly those containing **10cel-iHL-5gly** composite films, producing mechanically resilient materials with TS values approaching those of commercial bioplastics. The temporary effect of glycerol enhances the dispersion of lignin and cellulose chains. Of the formulations examined, **10cel-2.5iHL-5gly** demonstrated the most significant mechanical properties, with a tensile stress of 75.8 MPa, a strain of 1.2%, and a Young's modulus of 8.9 GPa. These characteristics highlight its possible use in plastic films, where great strength and rigidity are crucial. Subsequent research will entail comprehensive morphological and structural

characterisation, using scanning electron microscopy (SEM) and X-ray diffraction (XRD), to clarify the correlation between microstructure, crystallinity, and the mechanical properties exhibited by the **10cel-iHL-5gly** films.

6.2.4 Thermogravimetric analysis

Thermogravimetric analysis (TGA) was performed on **cel-lig-gly** films to assess their thermal properties when **cel-lig** incorporated with glycerol. A direct comparison with the current literature is limited, as thermal property data for glycerol-incorporated films are largely available for natural polysaccharides, including starch and chitosan, as well as for semi-synthetic polymers like cellulose acetate. Consequently, the present results were evaluated in relation to these representative systems reported in the literature.

The thermogram was obtained within a temperature range from 105 to 800 °C. Moisture loss below 105 °C was ascribed to the removal of residual water from the film, with moisture content varying between 6.2% and 9.5% for the **cel-lig-gly** films, slightly higher than that of the **cel-lig** films, which ranged from 2.5% to 9.1% suggesting that glycerol enhances water retention. This behavior is consistent with previous studies on cellulose and chitosan films, where the strong interactions between water molecules and the –OH groups of glycerol require higher energy for removal, leading to a shift or increase in the first thermal event temperature.[15,37]

The thermogram is categorised into three distinct regions: initial thermal stability, main degradation, and the post-decomposition plateau. Table 6.6 tabulated T_{onset} value for **cel-lig** in comparison with **cel-lig-gly** film at different lignin contents and types. Figure 6.13 illustrates the overlapping TGA thermograms of **cel–lig** and **cel–lig–gly**.

Table 6.6: T_{onset} data of (a) cellulose-lignin-glycerol and (b) cellulose-lignin films from different types of wood

(a)

Types of lignin	Samples	T onset (°C)
oHL	**oHL**	285.0
	10cel-5gly	309.1

	10cel-0.5oHL-5gly	321.1
	10cel-1oHL-5gly	320.8
	10cel-2.5oHL-5gly	314.9
	10cel-4oHL-5gly	303.8
iHL	**iHL**	198.6
	10cel-5gly	308.8
	10cel-0.5iHL-5gly	311.5
	10cel-1iHL-5gly	311.9
	10cel-2.5iHL-5gly	316.5
	10cel-4iHL-5gly	315.3
kSL	**kSL**	308.7
	10cel-5gly	311.9
	10cel-0.5kSL-5gly	315.3
	10cel-1kSL-5gly	305.3
	10cel-2.5kSL-5gly	311.6
	10cel-4kSL-5gly	307.6
iSL	**iSL**	318.6
	10cel-5gly	317.4
	10cel-0.5isL-5gly	314.6
	10cel-1isL-5gly	303.2
	10cel-2.5isL-5gly	289.2
	10cel-4isL-5gly	285.1

(b)

Types of lignin	Samples	T_{onset} (°C)
oHL	**oHL**	285.0
	10cel	310.7
	10cel-0.5oHL	314.3
	10cel-1oHL	314.3
	10cel-2.5oHL	306.2
	10cel-4oHL	304.9
iHL	**iHL**	198.6
	10cel	308.6
	10cel-0.5iHL	317.8
	10cel-1iHL	314.8
	10cel-2.5iHL	307.0
	10cel-4iHL	306.9
kSL	**kSL**	308.7
	10cel	317.5
	10cel-0.5kSL	320.1
	10cel-1kSL	314.2
	10cel-2.5kSL	294.8
	10cel-4kSL	294.0
iSL	**iSL**	318.6
	10cel	309.9
	10cel-0.5isL	309.8
	10cel-1isL	307.9

10cel-2.5isL	307.5
10cel-4isL	307.5

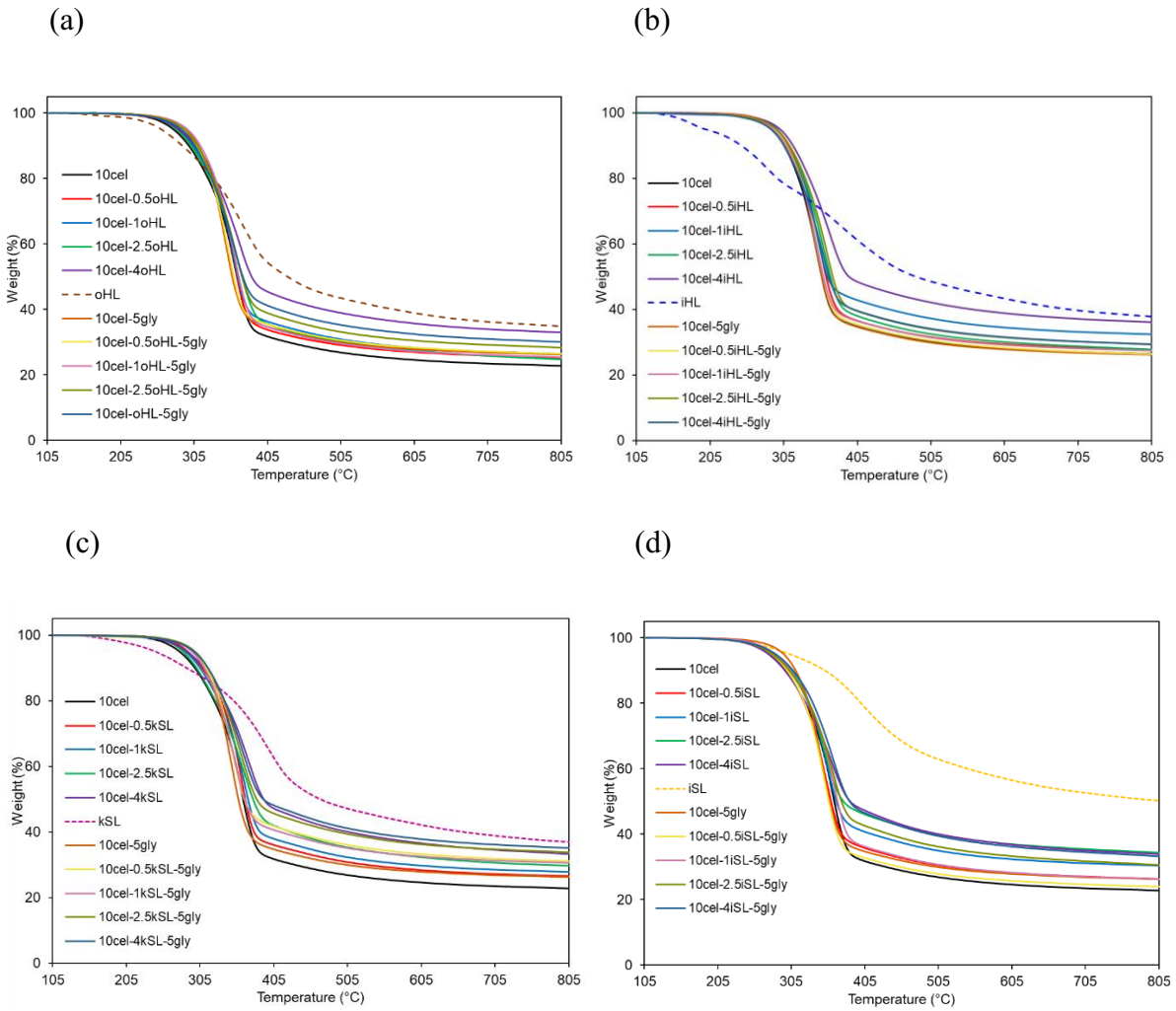


Figure 6.13: TGA curves of **cel-lig** and **cel-lig-gly** composite films at various lignin weight percent and different lignin types (a-b) hardwood lignin and (c-d) softwood lignin

T_{onset} values for the **cel-lig-gly** and **cel-gly** films were in the range 285 to 321 °C during the initial thermal event, demonstrating good thermal stability, as shown in Figure 6.13. A previous studies on cellulose films generated with Ioncell® technology from birch pulp exhibit the initiation of mass loss at temperatures ranging from 310 to 330 °C, which agreed with this finidng.[38] Another study on a series of corn starch bio-nanocomposites, plasticised with glycerol and lignin and reinforced with various amounts of cellulose nanocrystals (CNC), showed thermal degradation between 263 and 330°C. [39] The results indicate that the thermal stability of the fabricated films aligns with values documented in the literature.

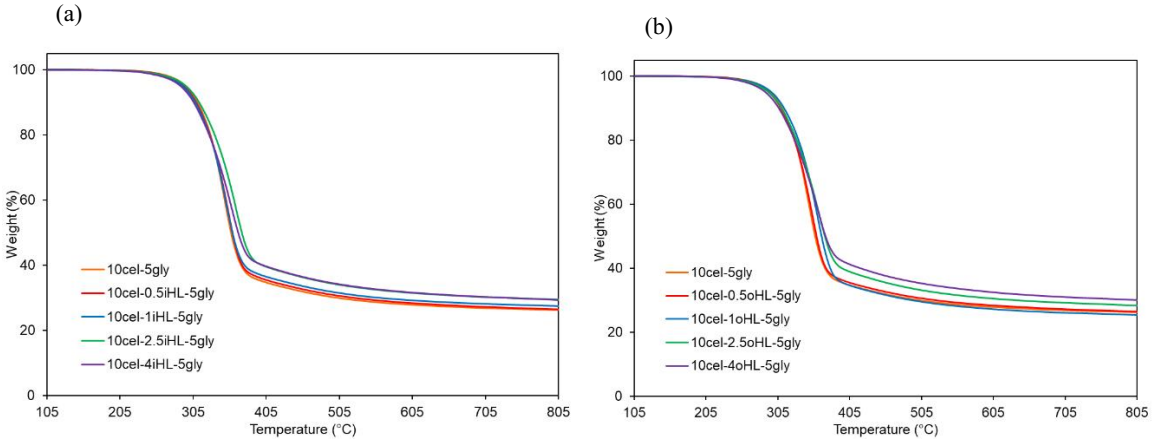
The main degradation of the **cel-lig** and **cel-lig-gly** film occurred between 300°C and 400°C, when a sharp decline signifies the fundamental thermal decomposition. T_{onset} is often associated with where the film begins to decompose significant amount at the main degradation region as tabulated in Table 6.6. This behaviour resembles that of composite fibres of cellulose mixed with organosolv or kraft lignin, which similarly demonstrate rapid thermal decomposition within the same temperature range.[33]

The T_{onset} of the majority of **cel–lig–gly** films showed a slight increase, with an average improvement of approximately 9 °C compared to the **cel–lig** films. These T_{onset} values correspond to the second thermal event rather than water loss. To our knowledge, there is limited literature reporting the effect of glycerol on T_{onset} for cellulose–lignin composite films, making direct comparisons difficult. The observed increase may indicate that glycerol contributes to structural stabilization of the composite films, though further studies are required to confirm this mechanism.

Although the primary application of these composite films is targeted toward plastic packaging, analysis of the residual weight provides valuable insights into their potential suitability for other applications. For example, carbon fiber production requires precursor materials with low ash content and high char yield to facilitate efficient melt-spinning and carbonization.[40] The residual weight at 800 °C for most **cel–lig** samples is significantly higher than that of the corresponding cel–lig–gly systems. For instance, **10cel-4iHL** exhibits a residual weight of 36.2%, which is higher than that of **10cel-4iHL-5gly** (29.3%). Similarly, **10cel-4oHL** shows a higher residual weight (33.0%) compared to **10cel-4oHL-5gly** (30.1%). In contrast, comparable residual weights were observed for **10cel-4iSL** (33.9%) and **10cel-4iSL-5gly** (33.2%). The lower residual weight observed in glycerol-containing samples can be attributed to the early-stage decomposition of glycerol. Glycerol is a small and simple molecule whose hydroxyl groups are more easily cleaved upon heating to give volatile products. In comparison, lignin possesses a more intricate structure composed of phenolic hydroxyl, carbonyl, and benzylic hydroxyl groups, which exhibit different thermal stabilities and contribute to higher char formation at elevated temperatures.[41]

Figure 6.14 is used to thoroughly discuss the thermal properties of **cel-lig-gly** in detail. **Cel-lig-gly** films with low lignin content exhibited higher T_{onset} compared to their corresponding lignin starting materials, with the exception of **iSL**. A similar trend is observed for the films without glycerol, indicating that the presence of glycerol does not substantially alter the relationship between lignin content and T_{onset}. The comparatively high thermal stability of **iSL** can be attributed to its broad molecular weight distribution, as reflected by its high polydispersity index (PDI). As demonstrated in Section 5.2.1, **iSL** exhibits the highest PDI (7.07) among all lignin samples investigated. Previous studies on *Miscanthus* lignins extracted via the ionosolv process using [DMBA][HSO_4] (80 wt%, a:b = 1.03:1) have shown that lignin degradation occurs over a wide temperature range, initiating at approximately 300 °C with the cleavage of aliphatic side chains, followed by the breakdown of more thermally stable C–C bonds at higher temperatures (370–400 °C).[40]

At low to moderate lignin loadings (0.5–2.5 wt%), the **cel–lig–gly** films exhibited a higher T_{onset} compared with the **10cel–5gly** control, particularly for films incorporating hardwood lignins such as **oHL** and **iHL**. In contrast, the film containing softwood kraft lignin (**10cel-0.5kSL-5gly**) showed an improvement in T_{onset} only at the lowest lignin concentration (0.5 wt%). The observed increase in T_{onset} is attributed to the higher content of aliphatic hydroxyl groups in hardwood lignins, which may contribute to enhanced thermal stabilization and allow these lignins to withstand higher heating rates.[42] Overall, the incorporation of lignin improved the thermal durability of the composite films by shifting the main thermal degradation event to higher temperatures.[39]



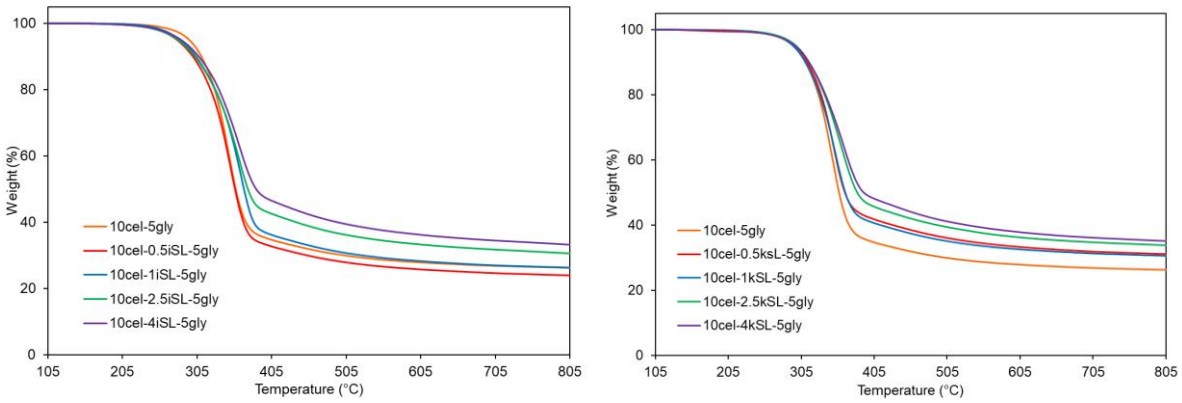


Figure 6.14: TGA curves of fabricated cellulose-lignin-glycerol films at various lignin weight percent and different lignin types (a-b) hardwood lignin and (c-d) softwood lignin

A similar trend in residual weight at 800 °C was observed for both **cel-lig** and **cel-lig-gly** films. For cellulose–hardwood lignin composites, the residual weight exhibited only minor variations with increasing lignin content. In contrast, cellulose–softwood lignin films showed a more pronounced increase in residual weight across all lignin loadings. Notably, composite films containing softwood lignin displayed higher residual weights at 800 °C, reaching 35.1% and 33.9% for **10cel-4kSL-5gly** and **10cel-4iSL-5gly**, respectively. By comparison, films incorporating hardwood lignin exhibited lower residual weights of 30.1% and 29.4% for **10cel-4oHL-5gly** and **10cel-4iHL-5gly**, respectively.

For **cel-lig** composite films without glycerol, all samples showed comparable residual weights, indicating limited dependence on lignin type in the absence of plasticizer. The higher residual weight observed in glycerol-containing films with softwood lignin is attributed to stronger interactions between glycerol and the lignin structure, which promote char formation and result in higher weight residues. Softwood lignin is characterized by a reduced content of β-O-4′ ether linkages and a more condensed structure, leading to a higher proportion of thermally stable C–C bonds.[42] **iSL** exhibited a high carboxylic –OH content (0.6 mmol g^{-1}) as determined by ^{31}P NMR in Section 5.2.5, indicating extensive structural cleavage during the ionosolv process. This structural feature contributes to improved thermal stability and increased residual weight following thermal degradation.

6.2.5 Water contact angle

The increase or decrease in water contact angle (WCA) of **cel-lig** and **cel-lig-gly** composite films is strongly dependent on the extent of glycerol integration within the cellulose–lignin matrix. In general, glycerol is a hydrophilic molecule and its effective incorporation into the matrix tends to decrease the WCA. However, when glycerol interaction with the matrix is limited, an increase in WCA may be observed.

For instance, the increased WCA observed in the **10cel-iHL-5gly** composite film (Figure 6.15(b)) can be attributed to the lack of glycerol interaction, as indicated by FTIR analysis (Section 6.2.2). This observation is further supported by the tensile results, which show a relatively low strain value, suggesting poor plasticization by glycerol. Literature reports on potato and corn starch films containing glycerol show WCA values ranging from 32° to 48°, confirming the strong hydrophilic effect of glycerol. This behavior is associated with the high number of hydroxyl (–OH) groups in glycerol, which are highly polar due to the large electronegativity difference between hydrogen and oxygen atoms.[43] Therefore, the absence or weak interaction of glycerol within the composite matrix can lead to an improvement (increase) in WCA. A similar trend is observed in most **10cel-oHL-5gly** composite films (Figure 6.15(a)), where increased WCA is associated with limited glycerol interaction, as evidenced by minimal changes in the FTIR OH and CH_2 bands. An exception is observed for **10cel-4oHL-5gly**, where broader OH and CH_2 bands indicate stronger glycerol interaction. This interpretation is supported by the slight reduction in WCA when comparing **10cel-4oHL-5gly** to **10cel-4oHL**.

In contrast to the previously discussed systems, a reduction in WCA was observed for the **10cel-kSL-5gly** composite films, indicating more effective glycerol incorporation within the matrix. This decrease in WCA is associated with the widening of the OH band observed in the FTIR spectra of **10cel-1kSL-5gly** and **10cel-2.5kSL-5gly**, suggesting enhanced hydrogen bonding interactions. Additionally, improvement in the CH_2 band for **10cel-0.5kSL-5gly** and **10cel-4kSL-5gly** further supports the presence of glycerol–polymer interactions. These spectral changes collectively indicate that the reduced WCA is a result of successful glycerol incorporation (Figure 6.15(d)).

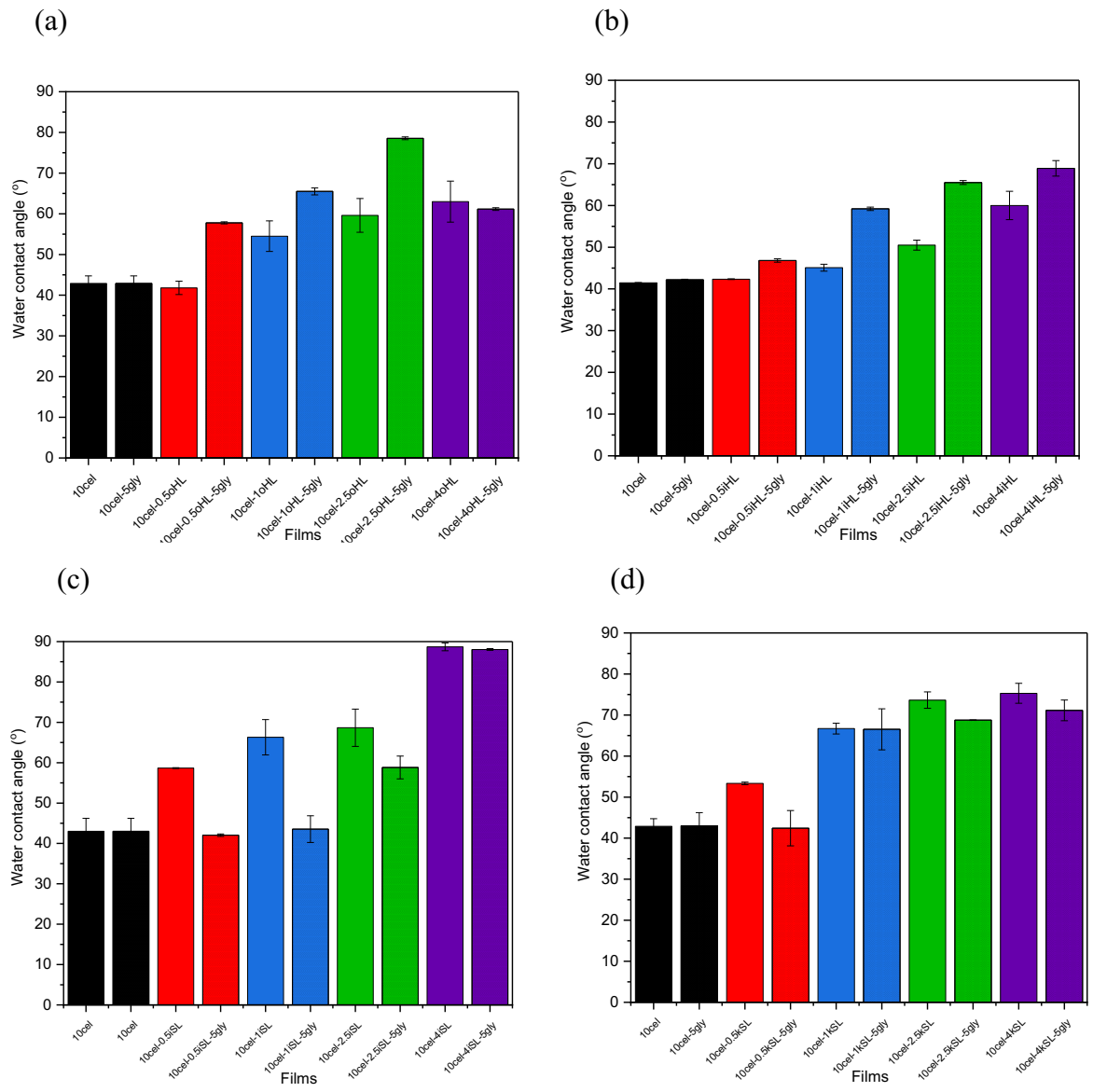


Figure 6.15: Water contact angle of **cel-lig** and **cel-lig-gly** films at various weight percent and different lignin types (a -b) hardwood lignin and (c-d) softwood lignin

Although glycerol integration was not distinctly identifiable in **10cel-iSL-5gly** by FTIR analysis, the mechanical properties provide supporting evidence. The highest strain (%) values observed for these films indicate increased flexibility, which is characteristic of effective plasticization by glycerol. Consequently, the presence of hydrophilic glycerol enhances polar interactions between the film surface and water molecules, leading to a decrease in WCA in **10cel-iSL-5gly.**

The following discussion on WCA for specific **cel-lig-gly** films is referred to Figure 6.16. The WCA of the **10cel-5gly** film was approximately 42.8°, indicating a moderately hydrophilic

surface. This value is comparable to the WCA of the **10cel** film (42.6°), with the marginal difference considered negligible when accounting for the associated standard error. The similarity in WCA suggests that the incorporation of glycerol at this concentration does not significantly alter the surface wettability of the cellulose matrix, implying limited glycerol enrichment or interaction at the film surface. This observation contrasts with findings reported for starch-based films, where increasing glycerol content (25%, 30%, and 35%) resulted in progressively lower WCAs of 49°, 44°, and 35°, respectively.[44] In those systems, the enhanced hydrophilicity was attributed to the high density of hydroxyl groups in glycerol, which readily interact with water molecules.

A clear increasing trend in WCA was observed with increasing lignin content. Specifically, the average WCA increased from 42.8° for the **10cel-5gly** film to 88.1° for the **10cel-4iSL-5gly** film, as illustrated in Figure 6.16. The enhancement in WCA with higher lignin loading is consistent with previous reports, indicating improved water resistance due to the inherently hydrophobic nature of lignin.[45] The incorporation of lignin appears to significantly reduce water absorption in the composite films by decreasing the water-holding capacity of the cellulose matrix. This effect is attributed to the formation of intermolecular interactions and crosslinking between lignin and cellulose, which effectively reduce the free volume available for water uptake and inhibit further swelling of the fibrous network structure.[45] To date, reported WCA values for **cel-lig-gly** composite films remain limited, as existing studies have predominantly focused on their mechanical, chemical, and thermal properties. Consequently, comparisons in this study are made primarily with related lignocellulosic composite films available in the literature, which nonetheless provide valuable context and insight into the observed wetting behavior.

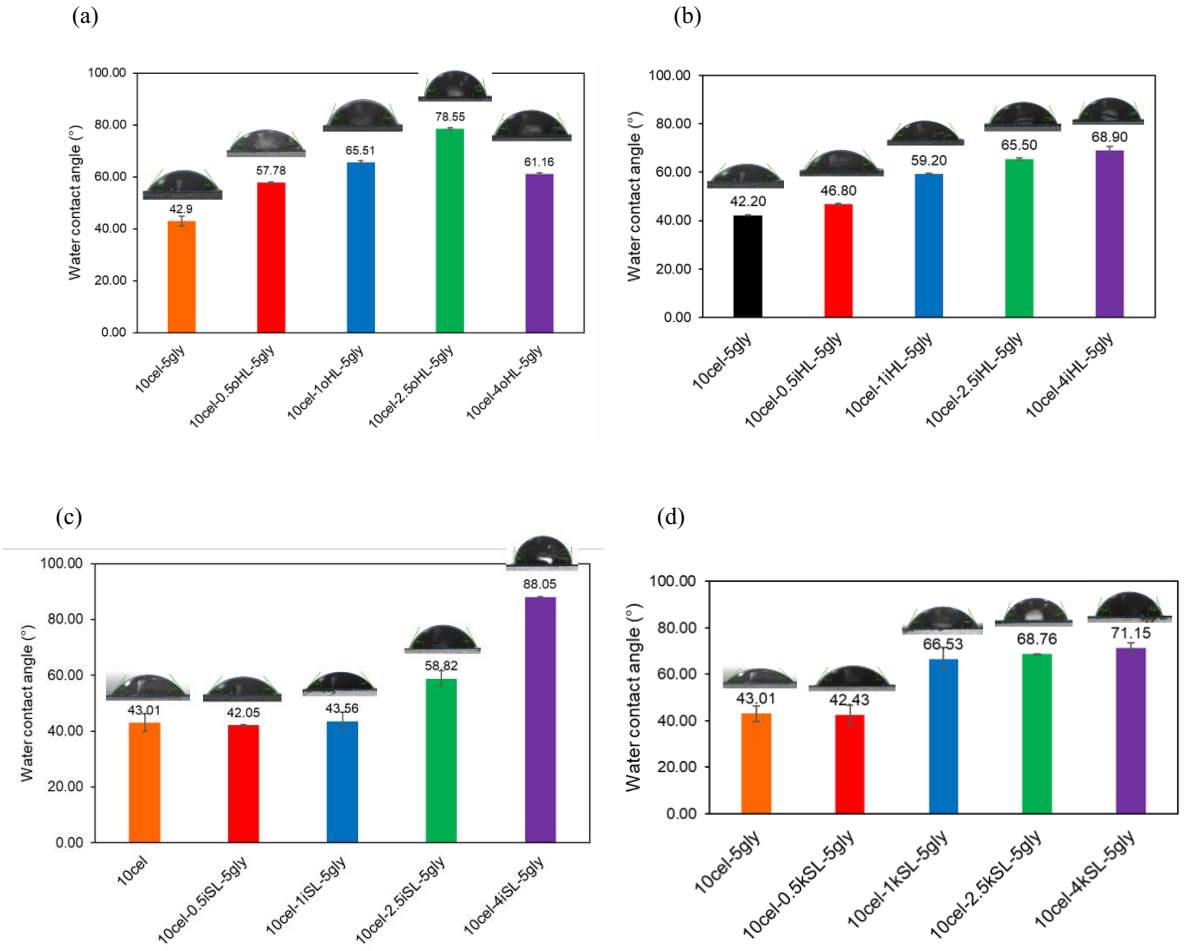


Figure 6.16: Water contact angle of cellulose-lignin-glycerol films at various weight percent and different lignin types (a-b) hardwood lignin and (c-d) softwood lignin

An interesting observation is the correlation between the WCA and the carboxylic hydroxyl (–COOH) content in lignin. A clear trend was observed in the series **10cel-iSL-5gly** > **10cel-oHL-5gly** > **10cel-kSL-5gly**, corresponding to carboxylic OH contents of 0.60, 0.18, and 0.15 mmol/g, respectively. The elevated WCA can be attributed to increased chemical heterogeneity arising from the introduction of carboxylic groups, which promote stronger and spatially non-uniform hydrogen-bonding interactions.[46] This trend is consistent with previous reports, where the addition of lignocellulose nanofibrils with varying lignin contents increased the WCA of nanopaper from 35° for the reference sample to 78° for the sample containing the highest lignin fraction.[46] Given that lignin is a highly complex, condensed macromolecule rich in aromatic groups and inherently less hydrophilic than cellulose, an increase in the advancing water contact angle with lignin content is expected. Furthermore, the observed increase in contact

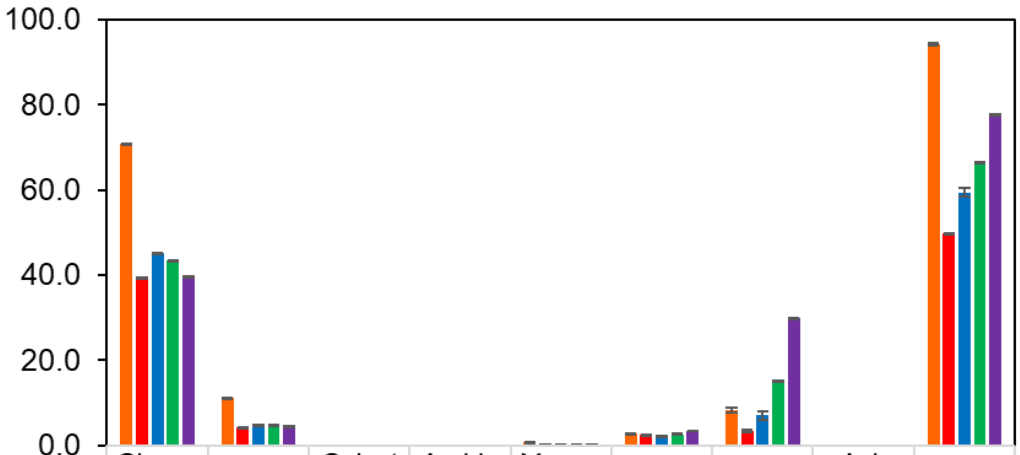
angle hysteresis (advancing θa – receding θr) with higher lignin content is not primarily due to surface roughness, but rather arises from the chemical heterogeneity introduced by the lignin. This finding underscores the role of carboxylic acid in improving surface wettability.

The effect of glycerol on lignin-containing films varies with lignin type, and mechanical properties provide a more reliable indicator of glycerol incorporation than FTIR, due to potential signal overlap. For **cel-oHL–gly** films (Figure 6.15a), most **cel–lig–gly** samples exhibited higher WCA than the corresponding **cel–lig** films, while % strain decreased in the majority of samples. This suggests limited glycerol incorporation, consistent with the high WCA values. In **cel-iHL–gly** films (Figure 6.15b), the FTIR did not show the characteristic OH band broadening or CH_2 band intensification, indicating incomplete glycerol incorporation; however, some samples displayed increased % strain, reflecting enhanced flexibility where glycerol was successfully incorporated, and WCA was generally higher than the equivalent **cel–lig** films. For **cel-iSL–gly** films (Figure 6.15c), most **cel–lig–gly** samples exhibited lower WCA than their **cel–lig** counterparts, consistent with glycerol reducing surface polarity. Finally, **cel-kSL–gly** films (Figure 6.15d), the scanned FTIR spectra confirmed successful glycerol incorporation through OH band broadening and CH_2 band intensification. Correspondingly, % strain increased, while WCA remained similar or slightly reduced compared to **cel–lig** films, indicating that glycerol enhanced flexibility without substantially altering surface hydrophilicity. Collectively, these observations indicate that % strain is a more reliable measure of glycerol incorporation than FTIR in lignin-containing films, and the effects of glycerol on WCA depend on both lignin type and the success of its incorporation.

6.2.6 Compositional analysis of cellulose-lignin-glycerol films

Compositional analysis (CA) was performed to quantify the cellulose and lignin content in the biomass, yielding experimentally determined values for comparison with theoretical formulations. **10cel-oHL-5gly** was selected for the CA experiment because it represents a hardwood lignin, serving as a replacement for **iHL** due to insufficient sample availability. Although data on the **10cel-iHL-5gly** film group would have been valuable, the main objective here is to quantify and compare the measured and theoretical values.

The overall mass recovery did not conform to the allowed range of 95–105%. The total contents for **10cel-0.5oHL-5gly**, **10cel-1oHL-5gly**, **10cel-2.5oHL-5gly**, and **10cel-4oHL-5gly** were significantly reduced, measuring 49.7%, 59.4%, 66.3%, and 77.8%, respectively as illustrated in Figure 6.17. The recovery of decreased mass was more significant in **cel-lig-gly** films compared to the **cel-lig** films addressed in Chapter 5. Glycerol has been suggested to greatly influence the acid hydrolysis by changing its enzymatic breakdown. Studies suggest that glycerol pretreatment can modify biomass components, leading to changes in enzyme activity and hydrolysis efficiency. While glycerol itself may not directly impede enzymatic breakdown, its presence and interaction with the substrate can alter the enzymatic process.[47] Despite the data's divergence from expectations, this data nonetheless offers significant insights into the composition of sugars, mainly in glucose form, and lignin.



	Glucose	Xylose	Galactose	Arabinose	Mannose	% ASL	% AIL	Ash residue	Total
10cel-5gly	70.7	11.2	0.0	0.0	0.8	2.9	8.3	0.0	94.2
10cel-0.5oHL-5gly	39.3	4.2	0.0	0.0	0.3	2.4	3.4	0.0	49.7
10cel-1oHL-5gly	45.1	4.7	0.0	0.0	0.4	2.2	7.0	0.0	59.4
10cel-2.5oHL-5gly	43.4	5.0	0.0	0.0	0.3	2.6	15.0	0.0	66.3
10cel-4oHL-5gly	39.7	4.6	0.0	0.0	0.3	3.3	29.9	0.0	77.8

Figure 6.17: Compositional analysis for selected films for cellulose-organosolv hardwood lignin incorporated with 5 wt.% glycerol

Glucose is the primary monosaccharide constituent of cellulose. The CA revealed that the control film, **10cel-5gly** sample comprised the greatest glucose content at 70.7%, whereas all other formulations integrated with lignin displayed significantly lower levels, between about

39% and 45%. The control film produced glucose levels comparable to those observed in prior research utilising lignocellulosic biomass subjected to dilute acid pretreatment and enzymatic hydrolysis. The yield of cellulose to glucose reached a maximum of 69.69% for mixed particulate biomass (particles <1000 μm) under batch conditions. This degree of hydrolysis is often desirable in methods intended to generate sugars from biomass.[48] The inclusion of lignin and glycerol markedly reduced glucose levels, presumably due to their disruption of acid hydrolysis efficacy. In a study, some lignin can interact with cellulases, leading to unproductive enzyme adsorption.[49] The results indicate that the matrix composition significantly impacts cellulose accessibility to hydrolytic enzymes, thereby influencing glucose release.

A similar pattern has been observed for xylose; a monosaccharide primarily sourced from the hemicellulose component of plant biomass. The maximum xylose content was seen in the **10cel-5gly** sample at 11.2%, whereas the remaining samples displayed lower amount, ranging from 4.2% to 5.0%. The incorporation of lignin and glycerol led to a decrease in xylose content too; however, the reduction was less significant than glucose. The percentage of xylose in the cellulose fraction can vary depending on the plant source and processing methods. Disagreement continues on the binding mechanism of hemicellulose; however, it is believed that the polysaccharides interact via hydrogen bonds. Other minor sugars, such as galactose, arabinose, and mannose, were identified solely at trace quantities in all CA. Mannose was the most consistently detected, but at low amounts of 0.3% to 0.8%, indicating negligible contributions from hemicellulosic breakdown under the examined conditions.

The lignin content was assessed regarding both acid-soluble lignin (ASL) and acid-insoluble lignin (AIL). The proportion of ASL shown minimal variation, varying from roughly 2% to 3% among the samples. The proportion of AIL exhibited a notable rise with elevated lignin concentration, escalating from 8.3% AIL in the **10cel-5gly** sample to 29.9% AIL in the **10cel-4oHL-5gly** formulation. Lignin derived from black carob tree sawdust, extracted via the soda-ethanosolv process which almost similar extraction process to **oHL**, exhibited an increase in extractive lignin concentration ranging from 30.7% to 36.2% AIL.[50] The value of cellulose combined with lignin in this study logically extends to a maximum of 29.9%. This study demonstrates that the incorporation of **oHL** leads to a significant amplification of the AIL fraction. AIL is the fraction of lignin that remains after a two-step acid hydrolysis process.[51]

The ash residue content was determined to be negligible (0%) in all samples, signifying the lack of detectable inorganic material residues. Cellulose derived from sugarcane bagasse reportedly contains 0.11% ash when subjected to hypochlorite-chlorite bleaching, attributable to the more pronounced reduction of silica by alkaline pulping compared to acid pulping.[52] Simultaneously, softwood kraft lignin was allegedly obtained with a free-ash content at pH 3, indicating complete protonation of the lignin.[27] A low ash detection ranging from 0.95 ± 0.02 to 1.18 ± 0.08 for hardwood and softwood lignin, primarily oxides in the form of ash.[25]

Ultimately, this CA cannot ascertain the theoretical value due to the underestimation of glucose content. Nevertheless, lignin exhibited a surprisingly tighter agreement with the measured value, differing by only 1.0 to 4.6% as shown in Table 6.7. According to Sluiter et al. (2010), who created the NREL approach, this procedure is essential for quantifying the structural carbohydrates and lignin in a solid biomass sample.[8] In contrast to these investigations, cellulose and lignin with glycerol were separated and subsequently combined physically. Utilising the appropriate pretreatment as recommended, CA would yield precise results and produce more accurate cellulose and lignin quantification.

Table 6.7: Cellulose-lignin-glycerol films measured and theoretical values

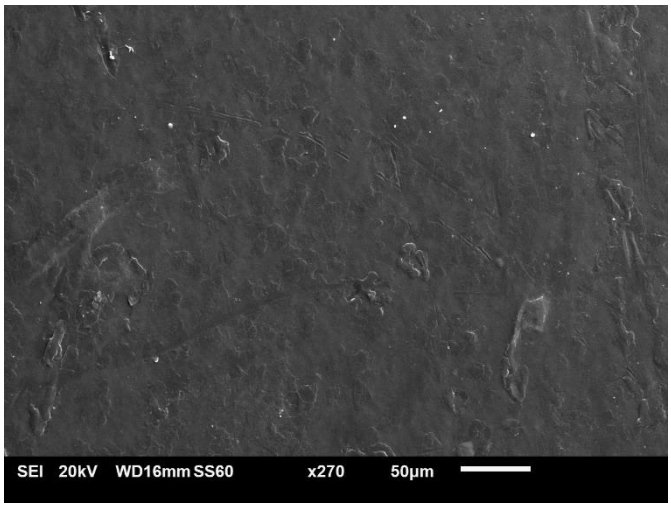
Sample	Measured		Theoretical	
	Cellulose (%)	Lignin (%) (AIL + ASL)	Cellulose (%)	Lignin (%)
10cel-5gly	82.7	11.2	100.0	0.0
10cel-0.5oHL-5gly	43.8	5.8	95.2	4.8
10cel-1oHL-5gly	50.2	9.2	90.9	9.1
10cel-2.5oHL-5gly	48.7	17.6	80.0	20.0
10cel-4oHL-5gly	44.6	33.2	71.4	28.6

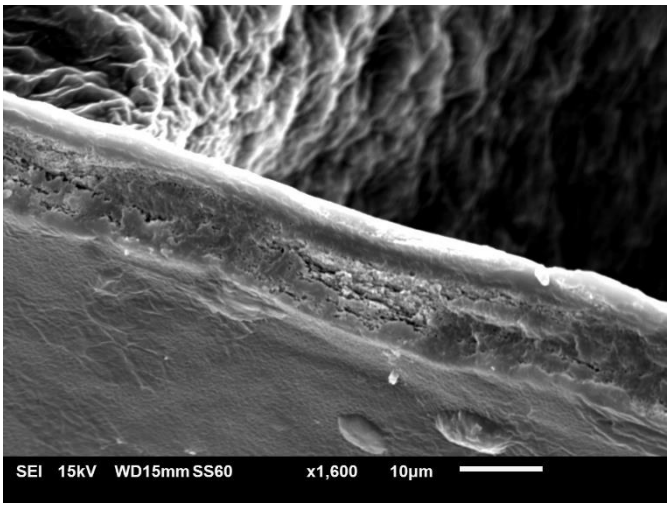
6.2.7 SEM for selected films

Scanning Electron Microscopy (SEM) was utilised to analyse the surface morphology and roughness of composite films, providing essential insights into their structural properties and mechanical performance. The **10cel-iHL-5gly** film group was chosen for comprehensive examination, with **10cel-2.5iHL-5gly** recognised as the formulation demonstrating superior mechanical qualities. This film was contrasted with **10cel-4iSL-5gly** to examine compositional

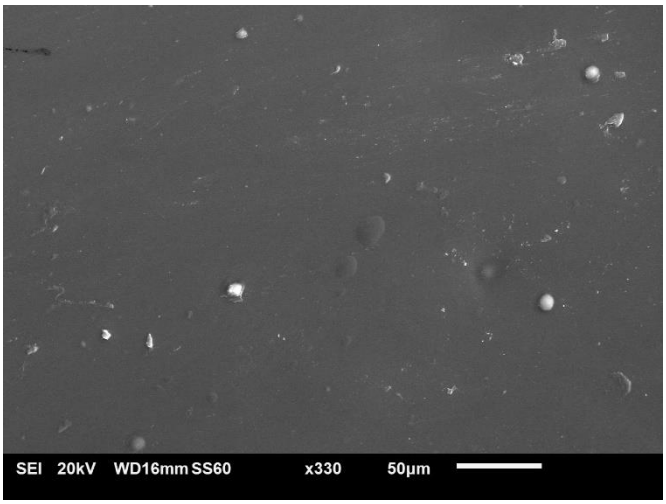
implications on mechanical performance. Significant disparities were noted between the two, as indicated by their mechanical parameters: **10cel-2.5iHL-5gly** had a tensile strength of 75.8 MPa, a strain at break of 1.2%, and a Young's modulus of 8.9 GPa, whereas **10cel-4iSL-5gly** exhibited values of 40.3 MPa, 1.6%, and 3.8 GPa, respectively. The disparities in mechanical performance are further clarified through the examination of the films' surface morphology acquired via SEM.

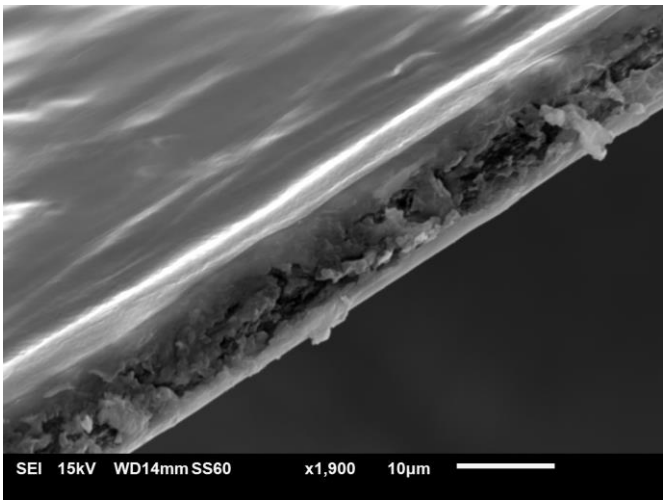
a) **10cel-0.5iHL-5gly** (left – surface morphology and right – cross section morphology)



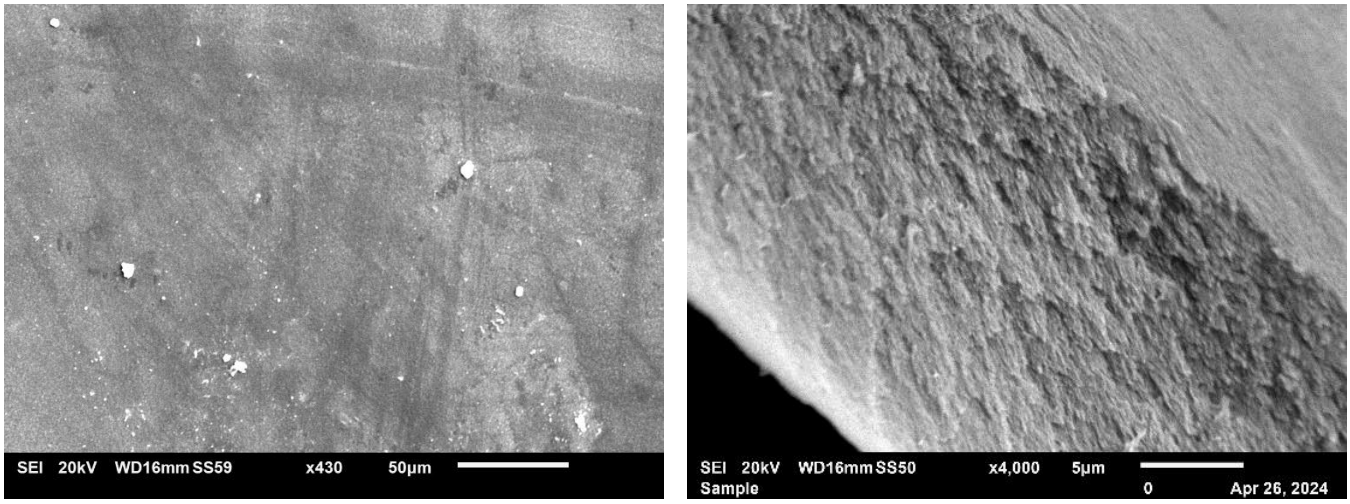


b) **10cel-1iHL-5gly** (left – surface morphology and right – cross section morphology)





c) **10cel-2.5iHL-5gly** (left – surface morphology and right – cross section morphology)



d) **10cel-4iHL-5gly** (left – surface morphology and right – cross section morphology)

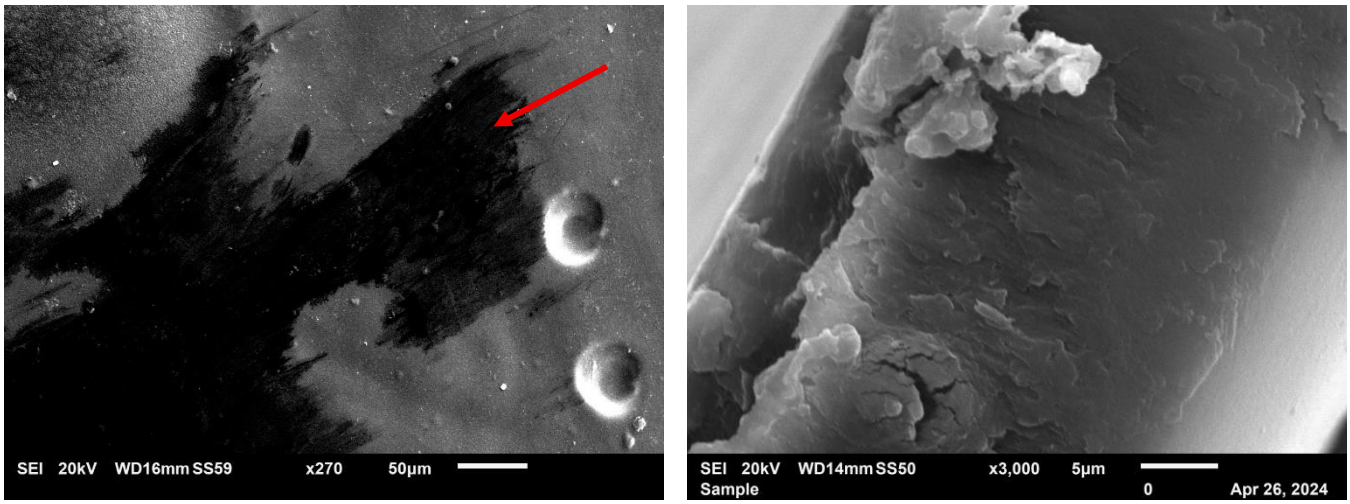


Figure 6.18: Surface morphology of all studied **10cel-iHL-5gly** films.

The surface morphology of the **10cel-iHL-5gly** film group was found to be relatively homogeneous as illustrated in Figure 6.18. Literature indicates that the addition of plasticisers can result in the development of micropores and lamellar structures inside polymer matrices. Cellulose acetate films with plasticisers like glycerol or sorbitol, together with alginate films containing 30% glycerol, demonstrated porous architectures due to these additions.[6, 53] It is hypothesised that glycerol's presence modifies the polymer network, resulting in internal morphological alterations and facilitating micropore development. In the current investigation, the films were dense and exhibited an absence of apparent porosity, possibly resulting from the

glycerol as an internal wetting and providing a bridge between cellulose and lignin molecules. This may explain why the **10cel-2.5iHL-5gly** film demonstrated enhanced tensile strength relative to other formulations. The dense, homogenous structure likely improves its capacity to disperse applied stress more efficiently, unlike porous structures that are more prone to crack initiation and propagation.

At 4 wt.% lignin loading, black patches indicated by red arrows in the SEM images were found in both the **10cel-4iHL-5gly** films, signifying the presence of lignin and implying its function as a co-binder within the cellulose composite matrix. This observation corresponds with the intermixing mechanisms suggested in previous research on lignocellulosic nanofibers with residual lignin for nanopaper fabrication as shown in Figure 6.19.[46] In these systems, amorphous lignin initially occupies the spaces between cellulose fibres; when subjected to high temperature and pressure (e.g., 100 °C and 220 bar), lignin softens and gets into the matrix, therefore joining the fibrils and forming a wood-like fiber–lignin composite. The cellulose-lignin films in this study were produced under milder conditions at temperatures between 70 and 100 °C and ambient pressure, yet SEM evidence indicates that lignin acts as a co-binder, enhancing the films' structural integrity by reinforcing the interfibrillar network.

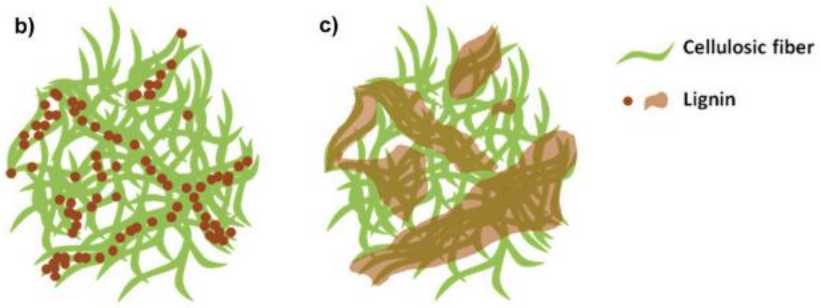
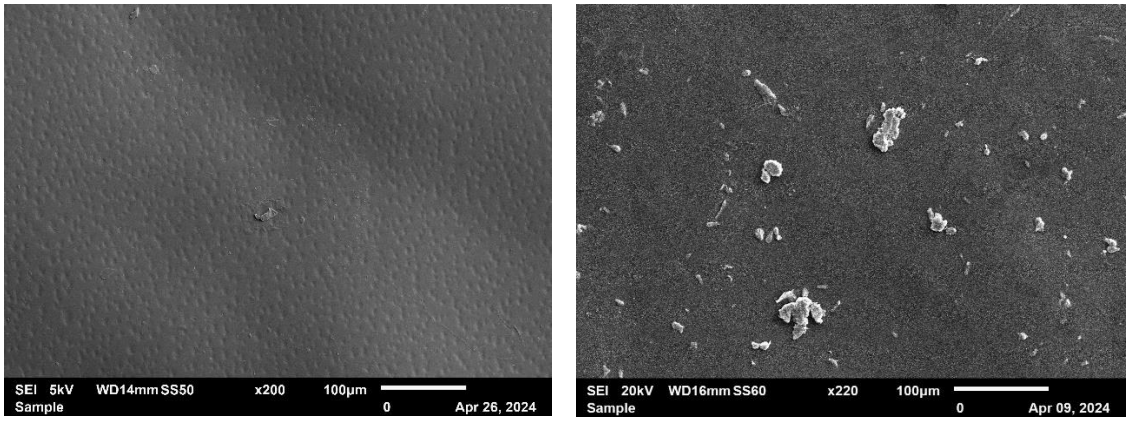


Figure 6.19: Proposed model to describe the location of the lignin within nanofibril suspensions and nanofibril after pressing. Image adopted from Rajo et. al[46]

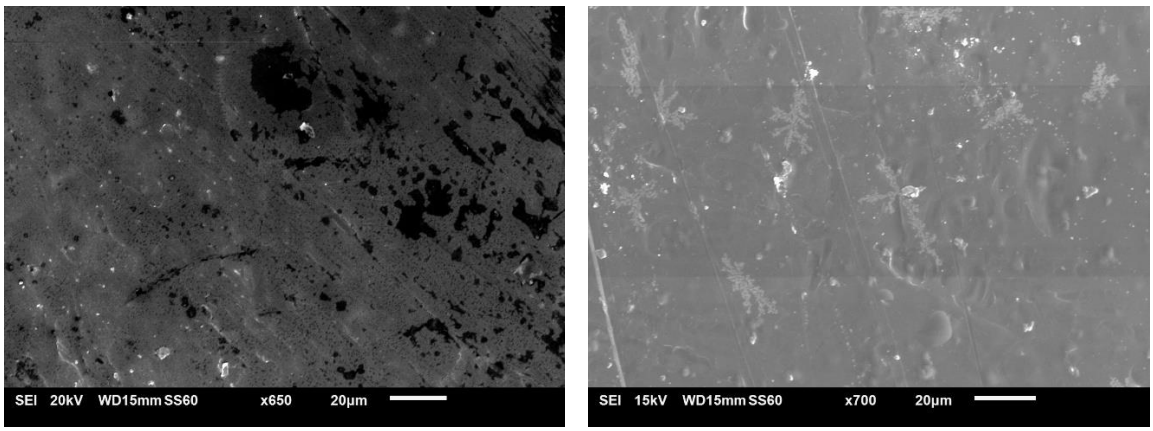
SEM images comparing films with and without glycerol under equivalent conditions for **cel-iSL** and **cel-iSL-5gly** are presented in Figure 6.20. A complete comparison was achieved for all formulations except at 1 wt.% **iSL**, for which the corresponding glycerol-containing film was unavailable due to sample unavailability. In general, glycerol-containing films (**10cel-iSL-5gly**) exhibit relatively smooth and compact surface morphologies, whereas films without

glycerol (**10cel-iSL**) display rougher surfaces with the presence of microbubbles (Figure 6.20 b–d). This observation is consistent with previous studies reporting that films produced without glycerol, including cellulose-lignin and cellulose-lignin-xylan composites sourced from softwood kraft lignin (e.g., pine), typically exhibit comparatively smooth surfaces.[54] In those studies, the lignin content was very low (0.02 and 0.04 wt.%). For the control film (**10cel**), surface indentations were observed, while the glycerol-containing film (**10cel-5gly**) appeared smoother but showed features that are likely attributable to undissolved cellulose, as the observed morphology closely resembles that of neat cellulose (Figure 5.1).

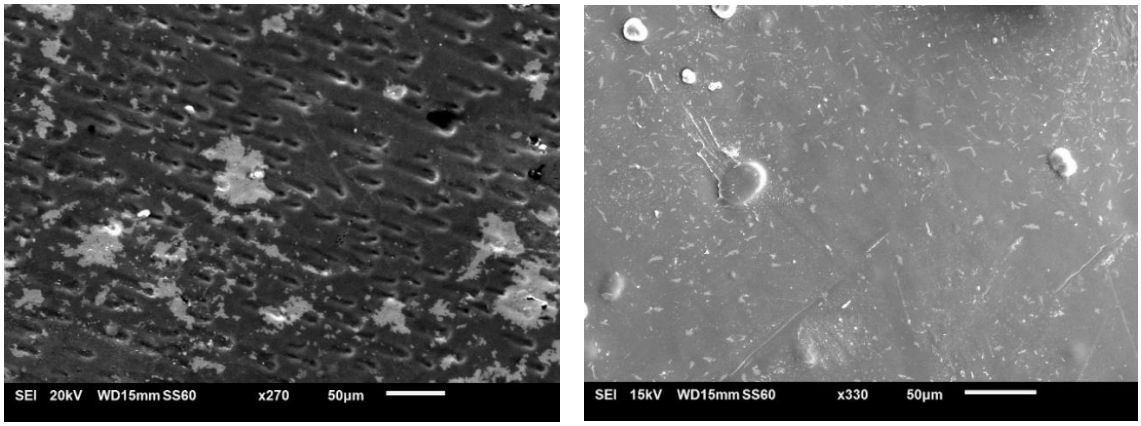
(a) **10cel** (left) and **10cel-5gly** (right)



(b) **10cel-0.5iSL** (left) and **10cel-0.5iSL-5gly** (right)



(c) **10cel-2.5iSL** (left) and **10cel-2.5iSL-5gly** (right)



(d) **10cel-4iSL** (left) and **10cel-10cel-4iSL-5gly** (right)

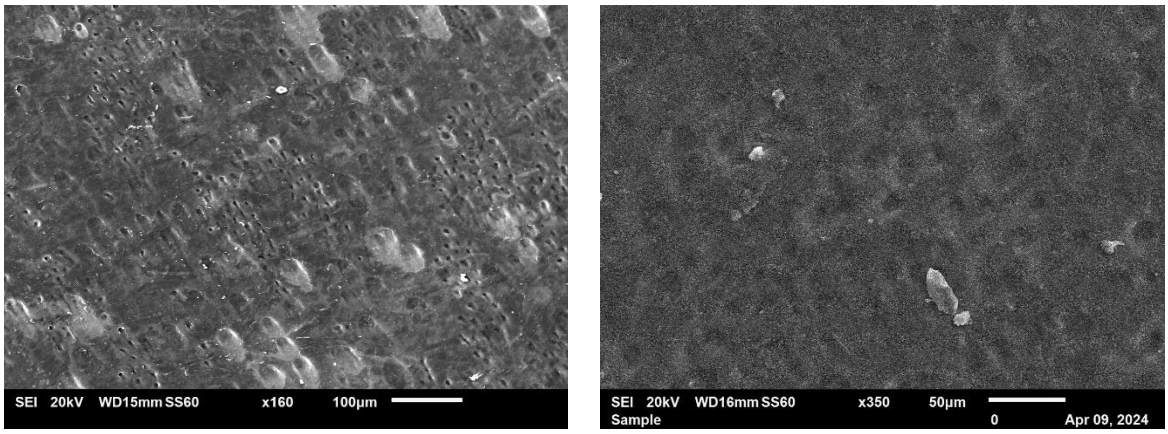


Figure 6.20: SEM images comparison of surface morphology for films with (left) and without glycerol (right) (**cel-iSL** vs. **cel-iSL-5gly**). The glycerol-containing counterpart at 1 wt.% iSL was unavailable.

6.2.8 Crystallinity for selected films

X-ray diffraction (XRD) was conducted to evaluate the crystallinity of the produced **cel-lig-gly** films. Due to the essentially amorphous characteristics of lignin, the films were expected to display a primarily amorphous structure. The XRD patterns elucidated the structural alterations caused by elevated lignin content, providing corroborative evidence for the observed trends in the mechanical characteristics of the films. To further clarify the superior characteristic of **10cel-iHL-5gly**, XRD observation exclusively analysed on this sample group.

Figure 6.21 demonstrates that all **10cel-iHL-5gly** films with varying lignin concentrations exhibit markedly reduced crystallinity compared to **cel** powder. The characteristic diffraction peaks of **cel** at 2θ = 15.7° and 22.3°, corresponding to the (101) and (002) planes, respectively, are significantly attenuated and broadened in the **10cel-iHL-5gly** films, indicating disruption of the ordered cellulose domains. Literature reports for cotton linter cellulose and cellulose nanocrystals (CNC) show diffraction peaks at 2θ = 14.4, 15.13, 17.09, 20.83, and 22.84◦, attributed to the diffraction planes (101), (10¯1), (021) and (002), respectively. [55] This corresponds to type I crystalline cellulose. In comparison, the **10cel-iHL-5gly** films retain weak reflections in similar 2θ regions, confirming the presence of cellulose I; however, the reduced peak intensity and increased amorphous background suggest decreased crystallite size and crystallinity due to lignin incorporation and film processing.

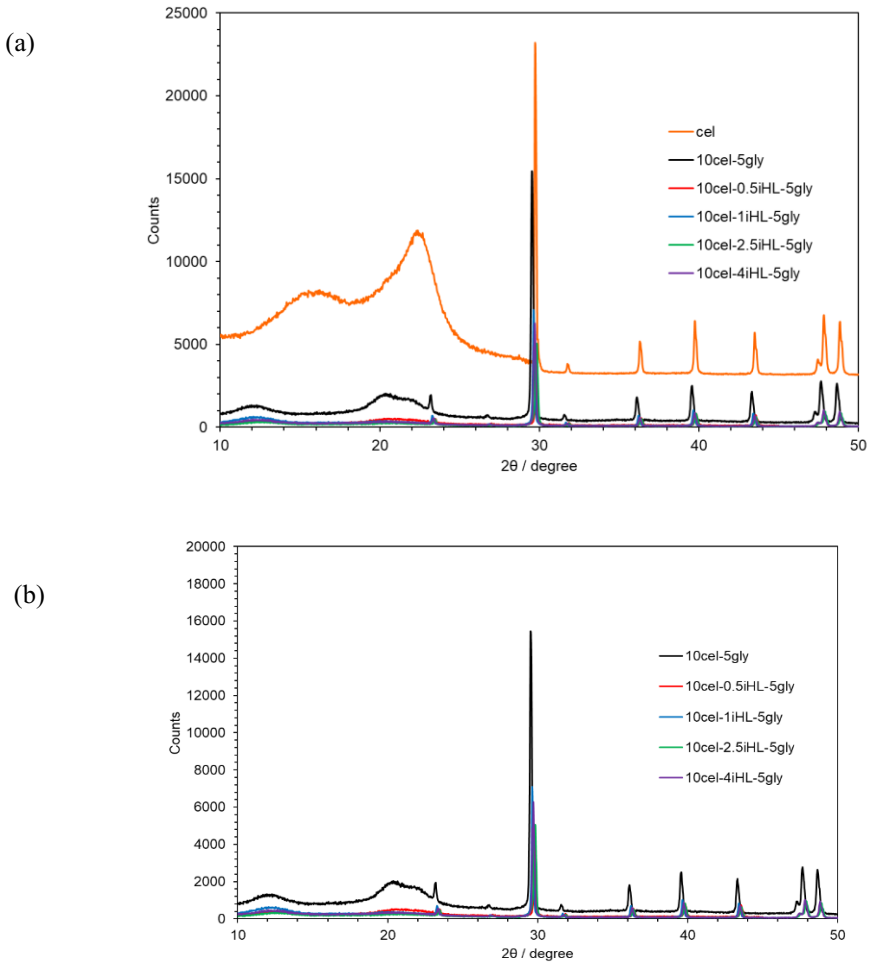


Figure 6.21: XRD patterns for (b) **10cel-iHL-5gly** films overlapped with (a) **cel** and **10cel-5gly**

The XRD patterns show a clear change from **cel** to **10cel**. The pronounced diffraction peak at 2θ ≈ 29.7°, associated with the (004) plane, is significantly diminished, along with several weaker peaks in the range of 31.7°–48.8°. These results indicate a substantial alteration of the cellulose crystalline structure during film regeneration. As described in the previous chapter, the XRD patterns of the **cel** and **10cel** samples exhibit multiple strong diffraction peaks that are absent in pure cellulose. These peaks are located at approximately 23.1°, 29.5°, 36.1°, 39.4°, 43.2°, and 47.5° (2θ) and do not correspond to the characteristic crystalline reflections of cellulose I. Comparison with standard diffraction patterns from the Crystallography Open Database shows that these peaks closely match those of the calcite phase of calcium carbonate ($CaCO_3$), indicating the presence of an additional inorganic crystalline phase.

All **10cel-iHL-5gly** films exhibit a predominantly amorphous structure, as shown in Figure 6.21(b). This observation is consistent with reports from the literature, where XRD patterns of composite films containing cellulose, starch, and lignin become largely amorphous after dissolution in the ionic liquid 1-allyl-3-methylimidazolium chloride ($[C_3C_1im]Cl$).[56] The pronounced reduction in crystallinity is attributed to the strong solubilizing capability of $[C_3C_1im]Cl$ and the formation of extensive intermolecular hydrogen bonding among cellulose, starch, and lignin.

Furthermore, a significant decrease in peak intensity at 21.2°, corresponding to the (021) plane, was detected for all **10cel-iHL-5gly** films at different lignin weight percentages. The reduction in peak intensity signifies a disordered structure attributable to the amorphous characteristics of lignin. This finding aligns with prior literature indicating that polyvinyl alcohol (PVOH)-lignin-tea tree oil composite films containing 1% glycerol had minor peak broadening, especially around 22°, implying intricate interactions among PVOH, cellulose, lignin, and tea tree oil.[57] The XRD peak broadening and reduced peak intensity observed in the **10cel-2.5iHL-5gly** sample suggest increased lattice strain, indicating internal distortion of the original cellulose crystallites after lignin addition, which contributes to the enhanced tensile strength

6.3 Conclusions

The aim of this chapter was to identify changes in the physical, chemical, thermal, and mechanical properties of **cel-lig** composite films upon the addition of glycerol. Structure–property interactions were evaluated through hydroxyl group content in lignin.

Chemical and mechanical properties confirmed the presence of glycerol in the films. Although its concentration was relatively low due to the washing process, glycerol did not act as a conventional plasticizer promoting wetting. Instead, it modulated the spatial arrangement of cellulose and lignin, producing a more ordered microstructure and enhanced mechanical strength.

Chemical modifications were observed through increased absorption in the O-H and C-H stretching region, indicating successful molecular interactions. The optimal glycerol content was 5 wt.%, with the **10cel-5gly** formulation showing high tensile strength (54.5 MPa), moderate strain at break (2.3%), and a balanced Young's modulus (6.4 GPa). The **10cel-2.5iHL-5gly** formulation exhibited the most significant mechanical improvement, with a tensile strength of 75.8 MPa, a strain of 1.2%, and a Young's modulus of 8.9 GPa, reflecting enhanced molecular alignment and interfacial contact facilitated by glycerol. SEM images confirmed a dense, homogeneous microstructure, while XRD peak broadening suggested increased amorphous content and lattice strain, contributing to higher tensile strength.

Hydroxyl group quantification clarified structure-property relationships. Higher phenolic OH content enhanced UV-blocking performance, whereas lower overall OH content correlated with improved mechanical strength, as seen in the **10cel-4oHL-5gly** formulation. High carboxylic OH content contributed to thermal stability; higher residual weight, and spatially heterogeneous hydrogen bonding, further stabilizing the films.

Overall, glycerol effectively modulates the **cel-lig** composite structure, enhancing mechanical performance while maintaining UV protection and thermal stability, demonstrating its potential as a functional additive in biopolymer films.

References

1 P. Ahokas, V. Kunnari, J. Majoinen, A. Harlin and M. Mäkelä, *ACS Sustain. Chem. Eng.*, 2025, **13**, 10771–10779.

2 P. Cazón, M. Vázquez and G. Velazquez, *Biomacromolecules*, 2019, **20**, 3115–3125.

3 V. Hospodarova, E. Singovszka and N. Stevulova, *Am. J. Anal. Chem.*, 2018, **09**, 303–310.

4 R. A. Syahputra, Z. Rani, R. Ridwanto, D. Miswanda and A. F. Pulungan, *Rasayan J. Chem.*, 2023, **16**, 648–682.

5 T. R. Fisher, G. Zhou, L. Huang and Y. Shi, *Phys. Chem. Chem. Phys.*, 2020, **22**, 2887–2907.

6 S. M. Gonçalves, D. C. dos Santos, J. F. G. Motta, R. R. dos Santos, D. W. H. Chávez and N. R. de Melo, *Carbohydr. Polym.*, 2019, **209**, 190–197.

7 E. C. Achinivu, R. M. Howard, G. Li, H. Gracz and W. A. Henderson, *Green Chem.*, 2014, **16**, 1114–1119.

8 A. Sluiter, B. Hames, R. Ruiz, C. Scarlata, J. Sluiter, D. Templeton and D. Crocker, *Natl. Renew. Energy Lab.*, 2008, 17.

9 M. Hassanpour, M. Abbasabadi, L. Gebbie, V. Setoa, J. Te and I. M. O. Hara, *ACS Sustain. Chem. Eng. 2020,* 2020, **8**, 10380–10388.

10 B. Zhang, F. Xie, T. Zhang, L. Chen, X. Li, R. W. Truss, P. J. Halley, J. L. Shamshina, T. McNally and R. D. Rogers, *Carbohydr. Polym.*, 2016, **146**, 67–79.

11 S. Hidayati, Zulferiyenni, U. Maulidia, W. Satyajaya and S. Hadi, *Heliyon*, 2021, **7**, e07799.

12 E. Brown, M. Abdelwahab, O. Valerio, M. Misra and A. K. Mohanty, *ACS Omega*, 2018, **3**, 3857–3867.

13 M. R. Abdollahi Moghaddam, M. A. Hesarinejad and F. Javidi, *Chem. Biol. Technol. Agric.*, 2023, **10**, 1–12.

14 J. H. Yan Cao, Huiquan Li, Yi Zhang, Jun Zhang, *J. Appl. Polym. Sci.*, 2010, **116**, 2658–2667.

15 E. Csiszár and S. Nagy, *Carbohydr. Polym.*, 2017, **174**, 740–749.

16 H. Sadeghifar, R. Venditti, J. Jur, R. E. Gorga and J. J. Pawlak, *ACS Sustain. Chem. Eng.*, 2017, **5**, 625–631.

17 X. Zhang, W. Liu, D. Sun, J. Huang, X. Qiu, Z. Li and X. Wu, *ChemSusChem*, 2020, **13**, 4974–4984.

18 Y. He, H. C. Ye, T. T. You and F. Xu, *Food Hydrocoll.*, 2023, **137**, 108355.

19 D. Wang, Y. Gu, S. Feng, W. Yang, H. Dai, H. Xiao and J. Han, *Green Chem.*, 2023, **25**,

9020–9044.

20 P. G. Seligra, C. Medina Jaramillo, L. Famá and S. Goyanes, *Carbohydr. Polym.*, 2016, **138**, 66–74.

21 M. Chen, F. Malaret, A. E. J. Firth, P. Verdía, A. R. Abouelela, Y. Chen and J. P. Hallett, *Green Chem.*, 2020, **22**, 5161–5178.

22 L. García-fuentevilla, F. Rubio-valle and R. Martín-sampedro, *Int. J. Biol. Macromol.*, 2022, **214**, 554–567.

23 I. Haq, P. Mazumder and A. S. Kalamdhad, *Bioresour. Technol.*, 2020, **312**, 123636.

24 N. Suderman, M. I. N. Isa and N. M. Sarbon, *Food Biosci.*, 2018, **24**, 111–119.

25 M. J. Suota, T. A. da Silva, S. F. Zawadzki, G. L. Sassaki, F. A. Hansel, M. Paleologou and L. P. Ramos, *Ind. Crops Prod.*, 2021, **173**, 114138.

26 B. Ahvazi, O. Wojciechowicz, T. M. Ton-That and J. Hawari, *J. Agric. Food Chem.*, 2011, **59**, 10505–10516.

27 T. V. Lourençon, F. A. Hansel, T. A. Da Silva, L. P. Ramos, G. I. B. De Muniz and W. L. E. Magalhães, *Sep. Purif. Technol.*, 2015, **154**, 82–88.

28 A. G. Margellou, P. A. Lazaridis, I. D. Charisteidis, C. K. Nitsos, C. P. Pappa, A. P. Fotopoulos, S. Van den Bosch, B. F. Sels and K. S. Triantafyllidis, *Appl. Catal. A Gen.*, 2021, **623**, 118298.

29 N. Giummarella, Y. Pu, J. Ragauskas and M. Lawoko, *Green Chem.*, 2019, **21**, 1573–1595.

30 ASTM D882-10, *Standard Test Method for Tensile Properties of Thin Plastic Sheeting*, 2014.

31 C. Huang, H. Y. Yu, L. Chen, B. Xue, Y. Shen, J. Shen and K. C. Tam, *Green Chem.*, 2023, **25**, 1453–1463.

32 S. J. Xiong, B. Pang, S. J. Zhou, M. K. Li, S. Yang, Y. Y. Wang, Q. Shi, S. F. Wang, T. Q. Yuan and R. C. Sun, *ACS Sustain. Chem. Eng.*, 2020, **8**, 5338–5346.

33 Y. Ma, S. Asaadi, L. S. Johansson, P. Ahvenainen, M. Reza, M. Alekhina, L. Rautkari, A. Michud, L. Hauru, M. Hummel and H. Sixta, *ChemSusChem*, 2015, **8**, 4030–4039.

34 Y. Zhou, Y. Han, J. Xu, W. Han, F. Gu, K. Sun, X. Huang and Z. Cai, *Int. J. Biol. Macromol.*, 2023, **232**, 123105.

35 S. Vincent, R. Prado, O. Kuzmina, K. Potter, J. Bhardwaj, N. D. Wanasekara, R. L. Harniman, A. Koutsomitopoulou, S. J. Eichhorn, T. Welton and S. S. Rahatekar, *ACS Sustain. Chem. Eng.*, 2018, **6**, 5903–5910.

36 H. Zhang, L. Deng, M. Yang, S. Min, L. Yang and L. Zhu, *Int. J. Mol. Sci.*, 2011, **12**, 3170–3181.

37 D. Maria V, C. Bernal and N. J. Francois, *J. Tissue Sci. Eng.*, 2016, **7**, 1000187.

38 E. González Carmona, I. Schlapp-Hackl, S. Jääskeläinen, M. Järvinen, K. Nieminen, D. Sawada, M. Hummel and H. Sixta, *Cellulose*, 2023, **30**, 11633–11648.

39 C. S. Miranda, M. S. Ferreira, M. T. Magalhães, W. J. Santos, J. C. Oliveira, J. B. A. Silva and N. M. José, *Mater. Today Proc.*, 2015, **2**, 63–69.

40 C. L. Chambon, V. Fitriyanti, P. Verdía, S. M. Yang, S. Hérou, M. M. Titirici, A. Brandt-Talbot, P. S. Fennell and J. P. Hallett, *ACS Sustain. Chem. Eng.*, 2020, **8**, 3751–3761.

41 M. Michelin, A. M. Marques, L. M. Pastrana, J. A. Teixeira and M. A. Cerqueira, *J. Food*

Eng., 2020, **285**, 110107.

42 P. Schlee, O. Hosseinaei, C. A. O'Keefe, M. J. M.-C. P. Grey and M.-M. Titrici, *J. Mater. Chem. A*, 2020, **8**, 23543–23554.

43 N. Pooja, S. Banik, I. Chakraborty, H. C. Sudeeksha, S. S. Mal, P. Srisungsitthisunti, A. Patil, K. K. Mahato and N. Mazumder, *Discov. Sustain.*, 2024, **5**, 467.

44 E. Basiak, A. Lenart and F. Debeaufort, *Polymers*, 2018, **10**, 412.

45 R. Tian, C. Wang, W. Jiang, S. Janaswamy, G. Yang, X. Ji and G. Lyu, *Small*, 2024, **20**, 1–13.

46 E. Rojo, M. S. Peresin, W. W. Sampson, I. C. Hoeger, J. Vartiainen, J. Laine and O. J. Rojas, *Green Chem.*, 2015, **17**, 1853–1866.

47 Y. Gong, Z. Chen, L. Zhang, P. Li, S. Zhang, J. Lin, W. Xiao, Y. Xu and Z. Liu, *Bioresour. Technol. Reports*, 2020, **11**, 100448.

48 A. Karapatsia, I. Pappas, G. Penloglou, O. Kotrotsiou and C. Kiparissides, *Bioenergy Res.*, 2017, **10**, 225–236.

49 Y. Yuan, B. Jiang, H. Chen, W. Wu, S. Wu, Y. Jin and H. Xiao, *Biotechnol. Biofuels*, 2021, **14**, 1–20.

50 E. P. Dagnino, L. R. Chiappero, V. V. Nicolau and E. R. Chamorro, *Chem. Eng. Res. Des.*, 2020, **155**, 66–79.

51 C. Sánchez, *Biotechnol. Adv.*, 2009, **27**, 185–194.

52 S. Shahine, S. El-Shorbani and M. El-Sadani, *J. Appl. Chem. Biotechnol.*, 1977, **27**, 608–610.

53 V. Jost, K. Kobsik, M. Schmid and K. Noller, *Carbohydr. Polym.*, 2014, **110**, 309–319.

54 T. J. Simmons, S. H. Lee, J. Miao, M. Miyauchi, T. J. Park, S. S. Bale, R. Pangule, J. Bult, J. G. Martin, J. S. Dordick and R. J. Linhardt, *Wood Sci. Technol.*, 2011, **45**, 719–733.

55 V. F. Lotfy and A. H. Basta, *Int. J. Biol. Macromol.*, 2025, **307**, 142124.

56 R. L. Wu, X. L. Wang, F. Li, H. Z. Li and Y. Z. Wang, *Bioresour. Technol.*, 2009, **100**, 2569–2574.

57 B. Abraham, N. Oladzadabbasabadi, H. Shakeela, C. Brennan, N. Mantri, N. P and B. Adhikari, *Int. J. Biol. Macromol.*, 2025, **309**, 142877.

Chapter 7: Conclusions and Outlook

7.1 Conclusions

Objective 1:

To develop and rigorously assess sustainable, low-cost synthesis pathways for $[C_2C_1im][OAc]$ utilizing simple green chemistry metrics and economic viability, thereby offering a quantitative standard for the holistic sustainability of ionic liquid production.

The ionic liquid $[C_2C_1im][OAc]$ was produced using three methods: (1) metathesis, (2) ion exchange, and (3) one-pot synthesis, to determine the most sustainable and environmentally benign approach. This specific ionic liquid is especially known for its efficacy in dissolving cellulose, making it an environmentally friendly dissolution process. The selection of raw materials and synthesis methods significantly impacts the results of green metrics assessments. The metathesis synthetic route utilizes silver acetate, which is expensive and environmentally detrimental, while the one-pot method requires lead (II) acetate trihydrate, a hazardous reagent that undermines the safety and sustainability of the process. Conversely, the ion exchange method employs comparatively benign chemicals; nonetheless, the significant water removal process through rotational evaporation may adversely affect its overall environmental sustainability. This study assesses each pathway according to essential green chemistry metrics, including atom economy (%AE), E-factor, and effective mass yield (%EMY), while also taking into account overall product yield and the cost per gram of $[C_2C_1im][OAc]$. These comparison evaluations aid in choosing a synthesis process that balances efficiency, environmental effect, and economic viability.

Key findings:

- The findings from a laboratory-scale study indicated that the ion exchange approach is the most advantageous for synthesizing $[C_2C_1im][OAc]$, due to the balance of environmental sustainability and economic efficiency. This pathway attained a %AE of 62.8%, an E-factor of 107.8, and an %EMY of 60.31%. The %AE and %EMY values were the highest among the three synthetic methods assessed, signifying effective

conversion of reactants into the target product. Nonetheless, the E-factor for the ion exchange approach was the highest, which is less favorable from a green chemistry standpoint, as a lower E-factor indicates reduced waste production and enhanced sustainability. The high E-factor is mainly due to the significant solvent consumption necessary, especially during the elimination of water, in contrast to the more straightforward metathesis method. Nevertheless, the ion exchange method continues to be the most promising method when evaluating both environmental implications and economic viability.

A recent investigation on the life cycle assessment (LCA) of lignocellulosic film production using [C_2C_1im][OAc] have confirmed that the fabrication of these films imposes high environmental burdens, primarily due to the energy-intensive steps such as ionic liquid synthesis and recovery. The synthesis of [C_2C_1im][OAc] via the dimethyl carbonate route was identified as a major contributor to the total global warming potential (GWP), with 1-ethylimidazole accounting for approximately 60% of the impact. During the dope solution preparation stage, [C_2C_1im][OAc] contributed about 79% to the total GWP. It is important to note that the environmental impact assessment is highly sensitive to the defined system boundaries and underlying assumptions. The conclusions drawn by the authors were based on the dimethyl carbonate inventory, which may not fully align with the scope of the present study. Therefore, a further investigation of the ion exchange synthesis route is recommended to confirm its environmental sustainability and economic feasibility.

Objective 2:

To devise and enhance a novel fabrication technique for reliable cellulose–lignin and cellulose–lignin–glycerol composite films.

To effectively produce homogeneous and flat cellulose-lignin composite films, every phase of the preparation process must be meticulously adjusted. This encompasses assessing the solubility of cellulose and lignin in [C_2C_1im][OAc], ensuring a comprehensive degassing of the dope solution to remove trapped air, executing an effective antisolvent washing procedure to eliminate residual ionic liquid, and choosing a suitable drying technique to maintain film

uniformity and structural integrity. These steps are essential for producing high-quality films appropriate for advanced material applications.

Key findings:

- The research demonstrated that elevating the cellulose content in the dope solution from 5 wt.% to 10 wt.% is crucial to satisfy the minimal film thickness criterion. Films generated from 5 wt.% cellulose-lignin solutions exhibited thicknesses under 10 μm, which is inadequate for film applications necessitating a minimum of 15 μm.

- Moreover, degassing the cellulose-lignin dope solution was essential for removing microbubbles that undermine film homogeneity. Degassing with an ultrasonic water bath at 70 °C and 80 W for 20–30 minutes proved to be as successful as passive degassing overnight by gravitational settling. The ultrasonic approach is advantageous due to its markedly decreased processing time while guaranteeing a bubble-free dope solution.

- A pivotal step in the film fabrication is the regeneration of the biopolymer matrix through the use of an antisolvent. This investigation identified water as the ideal antisolvent due to its efficacy in displacing [C_2C_1im][OAc], which can then be recovered by removing the water. This study provides a framework for determining optimal washing cycles using NMR, in contrast to prior research that utilized repeated antisolvent washing without clearly specifying the objective. It was established that pure cellulose (**cel**) films demand four washing cycles, whereas cellulose-lignin (**cel-lig**) films necessitate five cycles, each utilizing fresh deionised water. This approach guarantees the effective extraction of the ionic liquid from the films. The resulting **cel** and **cel-lig** films were proven to be free of residual [C_2C_1im][OAc] using FTIR and ^{1}H NMR spectroscopy, thereby proving the efficacy of the washing technique.

- Drying is a crucial factor in producing smooth, wrinkle-free films with uniform morphology. Regulated air drying under precise humidity levels markedly enhances film quality by decelerating capillary flow, thus improving structural homogeneity. The best results were achieved when films were dried in a sealed chamber at a consistent

relative humidity (RH) of 55–60% and cast onto glass substrates. This method produced an increased recovery area and improved reproducibility. Nevertheless, some **cel-lig** formulations demonstrated significant adherence to the glass surface, resulting in film deterioration upon removal. A practical alteration was implemented by placing short strips of parafilm to the substrate's margins. So, enabling easy detachment of the films without jeopardizing their integrity.

This study advances best practices in the production of **cel** and **cel-lig** films by implementing a more energy-efficient and environmentally sustainable approach. This work shows that good film casting can be accomplished at less harsh conditions, in contrast to earlier studies that prepare dope solutions at elevated temperatures, which may cause degradation of the ionic liquid and result in excessive energy use. The washing routine was refined to reduce antisolvent consumption and processing duration, adhering to green chemistry principles by decreasing solvent waste and energy expenditure.

The drying technique, especially the implementation of controlled humidity (55–60% RH), is based on existing literature with minor adjustments to meet the specific needs of these film systems. The process, including the selection of drying substrate and the optimization of washing cycles, fills gaps in existing film fabrication techniques, providing innovative procedural insights. The developed approach is appropriate for **cel** and **cel-lig** systems, although it is crucial to recognize its limitations. Differences in cellulose type, encompassing degrees of crystallinity and chemical alteration, might influence solubility and processability. Likewise, lignin's complexity and heterogeneous structure is determined by its source, extraction process, and solvent interaction introduces heterogeneity that may necessitate additional modification for wider applicability.

Objective 3:

To enhance the fundamental understanding of cellulose-lignin interactions through accurate measurement of hydroxyl groups in lignin and comprehensive compositional analysis, facilitating structure-property correlations in the resultant films.

The study thoroughly analyzed the physical, chemical, mechanical, and thermal properties of the initial materials of cellulose and lignin aiming to clarify their individual and collective impacts on composite film performance. The research of the synergistic interactions between cellulose and lignin was particularly significant, as demonstrated through compositional analysis and quantitative hydroxyl group profiling using ^{31}P NMR spectroscopy. This analysis elucidated the impact of molecular-level functionalities on the structural integrity and properties of the resultant films, establishing a significant foundation for the systematic design of bio-based materials with tailored functionalities.

Key findings:

- The physicochemical and thermal characterization of cellulose demonstrated features consistent with those documented in the literature. The lignin samples exhibited increased variability. All the technical lignin which are organosolv hardwood lignin (**oHL**), kraft softwood lignin (**kSL**), and ionosolv softwood lignin (**iSL**) demonstrated total soluble and insoluble lignin levels between 90.6% and 101.4%. Nevertheless, the self-synthesized ionosolv hardwood lignin (**iHL**) exhibited markedly reduced purity, including merely 60.1% lignin by weight. A comprehensive HSQC NMR analysis identified residual polymeric carbohydrates in **iHL**, as evidenced by signals associated with the C2/H2, C3/H3, and C5/H5 locations of β-D-glucopyranoside. This compositional analysis was recognized as a significant component affecting the qualities of the resultant **cel-lig** films, caused by differences in lignin actual yield.

- Further thermal decomposition studies corroborated the influence of lignin purity and structure on material performance. **Cel-lig** films with highly purified softwood lignin (**iSL**, ~99.9% lignin) demonstrated enhanced char yield with residual weight at 32.9 wt.%, owing to both the elevated purity and the inherent structural properties of softwood lignin. Significantly, its increased guaiacyl (G) unit concentration enhances cross-linking capability and facilitates char formation during pyrolysis. These findings highlight the significance of precise lignin quantification and structural characterization in forecasting and enhancing the functional qualities of bio-based composite materials.

- UV–Vis absorbance analysis revealed a significant correlation with lignin content, supported by compositional data indicating that softwood lignin consists of around 99.9% pure lignin, whereas hardwood lignin **iHL** includes only about 60.1 % lignin. The disparity in purity markedly affected the optical characteristics of the resultant films. Films containing softwood lignin demonstrated improved UV-blocking properties at a weight percent of only 2.5 wt. %, due to the elevated aromatic content and structural robustness of the lignin. These findings underscore the potential of cellulose–lignin composite films, especially those created with highly pure softwood lignin, for UV-resistant plastic packaging applications, where resilience to thermal degradation and UV exposure is essential.

- The measurement of hydroxyl groups by ^{31}P NMR yielded significant insights into the structure–property relationships of the utilized lignin. Significantly, hardwood lignins (**oHL** and **iHL**) demonstrated a greater total hydroxyl content than softwood lignins (**kSL** and **iSL**). Ionosolv-derived lignin, **iHL** from beech wood exhibited overestimated aliphatic hydroxyl content compared to organosolv-derived lignin, **oHL** primarily due to residual carbohydrate contamination, as previously indicated in HSQC NMR spectra. However, for high-purity lignin samples such as **kSL** and **iSL**, it was observed that a greater monomer sugar content including glucose, xylose, galactose, arabinose, and mannose in the CA correlated with a higher aliphatic hydroxyl content. The higher phenolic –OH content in **iSL** also suggested a greater degree of crosslinking within its structure, indicating a more stable and condensed network. This observation is further supported by the high thermal stability of **iSL**, with T_{onset} of 318.6 °C, which exceeds that of the other lignin types. These findings highlight that the lignin purity and sugar composition of lignin significantly influence its structural condensation and thermal stability.

- The differences in hydroxyl content greatly influenced the characteristics of the film. An increased hydroxyl content increased the miscibility of cellulose and lignin, resulting in improved dispersion and enhanced film integrity. This was evident in the studied films enhanced mechanical performance, notably improved tensile strength, especially in hardwood-based films with up to 2.5 wt.% lignin. Conversely, cellulose films combined with softwood lignin could withstand only up to 1 wt.% lignin before exhibiting brittleness, presumably due to diminished interfacial compatibility.

Improved miscibility was also apparent in surface morphology; for example, the **10cel–oHL** film displayed a smoother surface, while softwood lignin showed inferior dispersion, particularly at elevated lignin loadings, resulting in increased surface roughness and hydrophobicity. Contact angle studies confirmed this, with the **10cel–4iSL** film exhibiting the maximum water contact angle (WCA) of 88.7°, suggesting high surface roughness.

- Compositional analysis of **cel–lig** films accurately estimated lignin content, showing deviations of only 1.1– 4.9% from theoretical values. However, glucose recovery from cellulose was considerably lower than expected. The actual weight percentage of lignin strongly influenced film performance. For example, the **10cel–1iSL** film with actual 10.6 wt.% lignin exhibited tensile strength (54 MPa), moderate strain (1.7%), and a Young's modulus of 6.1 GPa. It also showed complete UVB-blocking capability and stable thermal degradation T_{onset} at 307.9 °C. The film's hydrophobicity improved, as reflected by a water contact angle of 66.3°. At higher lignin loading (19.5 wt.%) such as **10cel-2.5iSL**, the film became too brittle for mechanical testing. Overall, the results confirm that lignin incorporation enables **cel–lig** films with balanced mechanical strength, UV protection, and thermal stability.

Compositional analysis of lignin samples emerged as a vital determinant of the resultant film properties, with lignin content and residual carbohydrates in both cellulose and lignin markedly affecting the mechanical, thermal, and surface properties of the films. This study presents one of the initial systematic examinations of **cel-lig** composite films, filling an important gap in the literature and providing essential insights for the advancement of adjustable bio-based polymers designed for industrial use. However, glucose recovery from cellulose was lower in the regenerated **cel-lig** film composites. This deficiency underscores the necessity for supplementary pretreatment processes, such as enzymatic hydrolysis to the sample, to enhance cellulose conversion and for more precise film composition measurement.

Moreover, the number of hydroxyl groups plays a crucial role in film performance. It strongly influences hydrogen bonding interactions between cellulose and lignin, which in turn affect mechanical strength and surface wettability. Understanding these molecular interactions

establishes a basis for the systematic design of high-performance **cel–lig** films, tailored for specific functionality in fields such as packaging, coatings, and sustainable materials.

This study also identifies specific shortcomings, specifically with the methods of analysis utilised. For example, UV-Vis spectroscopy and water contact angle measurements may be performed over prolonged durations to evaluate the long-term stability and endurance of the films under environmental exposure. The biodegradability of the **cel-lig** films was not assessed in this study. This investigation would yield significant insights about their end-of-life behavior, particularly with sustainable packaging and waste management applications. Subsequent research should integrate these elements to enhance the empirical validation of the practical feasibility and ecological implications of these bio-based materials.

Objective 4:

To systematically clarify the function of glycerol as a plasticizer in modifying the mechanical properties and surface attributes of cellulose-lignin composites.

The main aim of this chapter was to incorporate plasticizers, particularly glycerol, into **cel-lig** composite films to improve their flexibility and hence broaden their applicability in plastic packaging. The resultant films underwent thorough assessment via physicochemical, thermal, and surface characterisation analysis. The impact of compositional analysis, specifically the type of lignin employed, on film qualities was methodically examined. This investigation offered enhanced understanding of the interactions between glycerol and the cellulose–lignin matrix, demonstrating significant enhancements in mechanical properties relative to unplasticized **cel–lig** films. The results emphasize the essential influence of lignin type and plasticizer compatibility on optimizing the performance of bio-based films for certain functional applications.

Key findings:

- The optimal glycerol concentration was established at 5 wt.%, yielding the most advantageous mechanical performance balance. The **10cel–5gly** formulation demonstrated the best tensile strength (54.5 MPa), a moderate elongation at break (2.3%), and a balanced Young's modulus (6.4 GPa), thus signifying appropriateness for certain applications such as composite films. Conversely, films with elevated glycerol contents (10 wt.% and 15 wt.%) exhibited excessive plasticization, resulting in diminished mechanical integrity and increased softness. These attributes restrict their applicability in structural or load-bearing contexts, highlighting the necessity of precise plasticizer optimization for material efficacy.

- Compositional study indicated that elevated glycerol concentrations resulted in a decrease in glucose yield and total sugar content, as measured by HPLC. At elevated glycerol concentrations (10 wt.% and 15 wt.%), only minor, indistinct peaks were detected in the chromatograms, signifying considerable interference with sugar identification. Significantly, at the optimal concentration of 5 wt.% glycerol, no leftover glycerol was observed in the produced film due to washing and subsequent dilution after acid hydrolysis in CA reduces the concentration to levels below the reliable detection limit of the detector. Even at this level, the total recoverable material decreased below the anticipated range. The low detection glycerol in the compositional analysis due to its degradation during concentrated acid hydrolysis and subsequent dilution. Accurate quantification of glycerol requires a separate experiment employing a glycerol-specific analytical method that avoids these steps.

- Despite the lack of plasticizer detected in CA, the lignin output continued to be a pivotal component affecting the performance of **cel–lig–gly** films. The UV-blocking properties were significantly associated with the lignin content. Films with softwood lignin showed enhanced UV-shielding properties relative to those with hardwood lignin, principally owing to their greater lignin content. The **10cel–iSL–5gly** and **10cel–kSL–5gly** films, incorporating 2.5 wt.% and 4 wt.% lignin respectively, exhibited remarkable UV protection, attaining total blocking of both UVA (320–400 nm) and UVB (280–320 nm) light. The results underscore the synergistic influence of lignin purity and

glycerol concentration in improving the functional efficacy of bio-based films, especially for UV-resistant packaging applications.

- Thermal testing demonstrated that **cel-gly** films containing softwood lignin displayed markedly greater residual mass post-pyrolysis, signifying enhanced char-forming relative to those made with hardwood lignin. The average residual mass for **cel-gly** films with hardwood and softwood lignin was 27.6% and 30.4%, respectively. The increased mass is due to the increased lignin weight percent as verified by CA, and the effect of lignin on the material's crystallinity. Lignin, especially from softwood sources, is thought to reduce crystalline areas in the cellulose matrix, therefore facilitating the generation of carbon-rich char during thermal decomposition. These findings emphasize the essential importance of precise lignin quantification in forecasting and customizing the thermal properties of bio-based composite films.

- This study determined that the addition of glycerol to cellulose-softwood lignin films decreased the water contact angle (WCA) in comparison to formulations hardwood **cel-lig-gly** films. This observation corresponds with mechanical properties which scored the highest % strain in **cel-iSL-gly** group, indicating that increased flexibility, which is characteristic of effective plasticization by glycerol. The presence of hydrophilic glycerol enhances polar interactions between the film surface and water molecules, leading to a decrease in WCA in **10cel-iSL-5gly**. Conversely, films with hardwood lignins such as **10cel–iHL–5gly** showed the lack of glycerol interaction at OH and CH_2 band, as indicated by FTIR analysis. This observation is further supported by the tensile results, which show a relatively low strain value, suggesting poor plasticization by glycerol. Therefore, the absence or weak interaction of glycerol within the composite matrix can lead to an improvement (increase) in WCA. These findings underscore the intricate relationship among lignin purity, hydroxyl functionality, and plasticizer compatibility from mechanical and chemical properties in influencing the surface properties of bio-based composite films.

- The overestimation of hydroxyl percentage seen in hardwood lignin (**iHL**) is due to cellulose impurities, leading to a low real lignin yield of merely 60.1%. Nonetheless,

the integration of **iHL** markedly enhanced the mechanical characteristics of **cel–lig–gly** films in comparison to those without glycerol. The films produced significantly enhanced tensile strength by as much as 120.1% containing 1 wt.% lignin. Of the formulations evaluated, the **10cel–2.5iHL–5gly** film demonstrated the most advantageous mechanical properties, with a tensile stress of 75.8 MPa, a strain at break of 1.2%, and a Young's modulus of 8.9 GPa. These improvements are likely attributable to glycerol's function in aiding the diffusion in lignin and cellulose chains, hence enhancing molecular alignment and interfacial contact before its elimination. This discovery highlights the important of plasticizer-mediated processing in enhancing the structural integrity of **cel-lig** based composite films.

- The compositional analysis of **cel–lig–gly** films indicated limitations in precisely ascertaining the theoretical component values, mainly attributable to the underestimating of glucose content, which aligns with findings related to **cel–lig** films. This underestimation is likely due to incomplete hydrolysis during analytical quantification. However, lignin quantification exhibited a far closer correlation with the theoretical values, with variances limited to 1.0% to 4.6%. This continuous agreement underscores the relative dependability of lignin estimation in compositional analysis, even with the inclusion of plasticizers like glycerol, and further corroborates the significance of lignin content as a crucial factor in assessing film composition and performance.

This study explores **cel-lig-gly** composite films with various types of lignin, addressing a significant gap in bio-polymer research. While **cel-lig** composites have been studied, there is a lack of research on films incorporating glycerol and the influence of lignin type on their properties, making this work a novel contribution. The findings provide novel insights into the subject, notably on the role and influence of plasticizers specifically glycerol on the structural, mechanical, and surface characteristics of cellulose–lignin films.

Nevertheless, specific limitations were recognized in this work, especially with the analytical methods employed for film characterization. Techniques such as UV–Vis spectroscopy, water

contact angle measurement, and compositional analysis may be improved for greater precision. Furthermore, subsequent research should concentrate on investigating more efficient methods for binding glycerol or other plasticizers to cellulose and lignin matrices to ensure success plasticiser incorporation. The biodegradability of the produced films, although crucial for sustainable material development, was not evaluated in this study and represents a significant area for future research.

7.2 Future work

Objective 1:

To develop and rigorously assess sustainable, low-cost synthesis pathways for $[C_2C_1im][OAc]$ utilizing simple green chemistry metrics and economic viability, thereby offering a quantitative standard for the holistic sustainability of ionic liquid production.

Simple green assessment techniques like the EA and EMY can offer a preliminary indication of the sustainability of a synthetic pathway. The most thorough method is to conduct a LCA on ion exchange route, which generally requires specialized software like ASPEN or comparable platforms. LCA provides a comprehensive assessment of the environmental effects throughout each phase of a product's lifecycle from cradle to grave. The software must have pertinent data for precise calculations. Nonetheless, performing such evaluations can markedly improve industrial practices by guiding decisions on raw materials, synthesis methods, and film manufacturing. The LCA of $[C_2C_1im][OAc]$ indicated that 1-methylimidazole contributed the most GWP.[1] The compound was synthesised using the dimethyl carbonate route. The next paragraph outlines the short- and long-term plans for the economic scalability of this compound. Other than that, future research could investigate alternative solvent systems that avoid the direct use of 1-ethylimidazole or imidazolium halide precursors. For instance, the ionic liquid 1,5-diazabicyclo[4.3.0]non-5-enium acetate, used in the Ioncell® process,[2] could be investigated for its ability to dissolve both cellulose and lignin as its precursor is not derived from an imidazolium ring. Such approaches may help to significantly reduce the overall GWP.

Economic Scalability and Future Outlook of [C_2C_1im][OAc] Synthesis

While the laboratory-scale assessment identifies the ion exchange pathway as the most balanced option due to its high score in green metrics, however, the primary driver of this high cost is the energy-intensive evaporation of water during purification. To transition this method from the laboratory to an economically viable industrial scale, several process intensification strategies can be implemented to drastically reduce the cost per gram of [C_2C_1im][OAc].

First, replacing conventional thermal rotary evaporation with low-energy membrane separation technologies, such as pervaporation, can drastically mitigate the energy costs associated with bulk water removal. Another options, transitioning from batch-wise ion exchange to a continuous fixed-bed resin column system optimizes solvent consumption, enables in-situ regeneration of the ion-exchange resin, and substantially lowers the overall E-factor.

To fully realize the industrial and environmental potential of this work, the development of [C_2C_1im][OAc] synthesis and its application in lignocellulosic biomass processing must be evaluated through a long-term developmental roadmap. Over a five-year horizon, engineering efforts should focus on designing a closed-loop solvent recycling system capable of recovering and reusing >95 % of the process water. Concurrently, executing a rigorous LCA and techno-economic analysis grounded in primary empirical data that is essential to precisely quantify utility costs and optimize heat integration for the ion-exchange pathway. Looking ahead to a ten-year timeline, the synthesis of [C_2C_1im][OAc] should be structurally integrated directly within lignocellulosic biorefineries. This co-location would eliminate the logistical overhead and packaging expenditures associated with bulk ionic liquid transport by establishing a continuous, on-site synthesis and immediate deployment loop.

Looking ahead to a twenty-year horizon, [C_2C_1im][OAc] is projected to mature into a commodity-scale green solvent, characterized by a completely closed-loop and near-zero-waste manufacturing framework. At this advanced stage of development, the process E-factor is anticipated to decline into single digits, driven by near-ideal thermodynamic efficiencies, fully automated continuous-flow synthesis, and the integration of renewable energy sources to

power the underlying dewatering systems. The robust economic viability established by these methodological advancements will enable ionic liquid-mediated biomass processing to widely displace conventional, hazardous volatile organic solvents (VOCs) on a global scale. Consequently, high-value biomaterials such as biodegradable lignocellulosic composite films will become highly cost-competitive with, and ecologically superior to, traditional petroleum-based polymers.

Objective 2:

To devise and enhance a novel fabrication technique for reliable cellulose–lignin and cellulose–lignin–glycerol composite films.

The methodology for fabricating **cel**, **cel-lig**, and **cel-lig-gly** films has been successfully established by a thorough examination of critical parameters, including component solubility, degassing, casting, and drying of the dope solutions, resulting in good quality films. However, variations in the solubility characteristics between cellulose and different lignin types presented issues, requiring modifications to the production process. In future work, a Design of Experiments (DOE) approach,[3] a statistical method used to identify relationships between input variables and system output could be implemented to gain a better understanding and optimize the solubility interactions between cellulose and lignin.

Because the solubility of cellulose and different lignin types varies significantly, experimental investigation is required to determine their solubility limits. Building on these results, a predictive modeling could be employed to estimate solubility and processing windows for various cellulose–lignin combinations. Empirical models and molecular dynamics (MD) simulations provide effective methods for determining solubility limits and informing formulation options.[4] Advanced computational approaches, particularly Graph Neural Networks (GNNs), offer substantial potential for improving solvent systems and processing conditions in sophisticated and large-scale predictions.[4] These predictive frameworks could facilitate the creation of cellulose-lignin films for sustainable packaging and provide a flexible platform for building material systems that meet various performance criteria across many industries.

Furthermore, the macromolecular architecture of cellulose specifically its molecular weight and degree of polymerization (DP) constitute a critical design parameter governing the mechanical performance of cellulose-lignin composite films. Prior work has demonstrated that high-DP cellulose (DP ≈ 800) dissolved in [C_2C_1im][OAc] requires a minimal solid loading of merely 0.08 wt.% to yield regenerated fibres exhibiting a remarkable tensile strength of 198 ± 25 MPa and a strain-to-failure of 2.8 ± 0.7%.[5] In contrast, the present study utilised microcrystalline cellulose (MCC PH101), which possesses a substantially lower DP range (70–400) dictated by the severity of the precursor acid hydrolysis. Consequently, prioritizing a high-molecular-weight cellulose precursor is imperative for optimizing tensile properties. Longer polymer chains facilitate dense topological entanglements and extensive, cumulative intermolecular hydrogen-bonding networks that robustly resist shear-induced chain sliding. Under tensile stress, the primary deformation mechanism shifts from simple intermolecular slippage to the stretching and ultimate scission of the polymer backbone's covalent bonds.

Objective 3:

To enhance the fundamental understanding of cellulose-lignin interactions through accurate measurement of hydroxyl groups in lignin and comprehensive compositional analysis, facilitating structure-property correlations in the resultant films.

Comprehensive characterization and testing are necessary to ensure the reliability and long-term performance of **cel-lig** films. One essential examination is to do the photodegradation behavior during extended exposure to sunshine, considering their UV-blocking properties. This evaluation can elucidate the resilience of the films under actual environmental circumstances. Surface wettability is a critical parameter. Water contact angle measurements with the sessile drop method, generally documented at a normal residence time of 2 seconds, yield preliminary insights. Extended observation over prolonged durations can provide a more profound comprehension of the material's behavior under wetting conditions. Moreover, in addition to water, which is frequently utilized, alternate wetting agents like ethanol and acetone should be examined to assess surface energy, hence enhancing application profiling. The water vapor permeability test using a gravimetric surface analyser (Dynamic Vapor Sorption) should be conducted to evaluate the capability of the **cel-lig** composite film to permit the transmission of water vapor through the material.

Biodegradability is an essential attribute, particularly as cellulose and lignin are fundamentally sourced from renewable and biodegradable materials. However, the rate and mechanism of degradation require a thorough investigation, which can be achieved using a UV-radiation or polymer weathering instruments. Comprehending degradation dynamics and determining suitable disposal methods are essential for efficient end-of-life waste management.

Compositional analysis is also crucial, especially when dealing with cellulose-lignin combinations dissolved in ionic liquids. The precise measurement of sugars and lignin may be difficult if hydrolysis is ineffective. Enzymatic hydrolysis, employing enzymes such cellulases that transform cellobiose into glucose, can enhance the precision of cellulose content assessment and offer a more reliable basis for compositional analyses.[6]

These comprehensive analyses will enhance scientific comprehension of lignocellulosic film properties particularly concerning biodegradability and environmental durability, while also offering industry stakeholders critical insights into the customization of these materials for specific applications.

Objective 4:

To systematically clarify the function of glycerol as a plasticizer in modifying the mechanical properties and surface attributes of cellulose-lignin composites.

In the quest to formulate efficient glycerol in cellulosic film, several methodologies are worth considerating. A viable technique entails utilizing plasticizer blends, such as urea–glycerol systems, in which urea breaks the crystalline areas of cellulose, hence improving glycerol's incorporation into biopolymers matrix.[7] Crosslinking methods using hydroxyl groups may additionally reinforce the matrix and improve film performance;[8] however, this necessitates further research.

The thorough characterisation of **cel-lig-gly** films must adhere to the methodology described in previous chapters, with necessary adjustments. Essential evaluations, including prolonged UV transmittance exposure and extended water contact angle measurements, are vital for assessing the environmental durability and surface characteristics of the films under actual settings, hence ensuring product reliability. Moreover, precise quantification of cellulose and lignin content in glycerol-modified films is reliant upon suitable pretreatment techniques. Employing techniques for CA, perhaps in conjunction with enzymatic digestion, can produce more accurate compositional data and guarantee result reproducibility.

These findings collectively create new opportunities for integrating glycerol into cellulose-lignin matrix, allowing researchers to enhance material formulations and improve comprehension of biopolymer interactions. This information serves as a basis for developing customized, bio-based plastic films that meet particular application needs and sustainability objectives for the sector.

7.3 References

1 R. Antonella, N. Pontillo, N. Mac Dowell, K. Lee, S. Chen, F. O. Diego and T. Welton, *RSC Sustain.*, 2025, **3**, 2301–2310.

2 M. Trogen, N. D. Le, D. Sawada, C. Guizani, T. V. Lourençon, L. Pitkänen, H. Sixta, R. Shah, H. O'Neill, M. Balakshin, N. Byrne and M. Hummel, *Carbohydr. Polym.*, 2021, **252**, 117133.

3 R. L. Wu, X. L. Wang, F. Li, H. Z. Li and Y. Z. Wang, *Bioresour. Technol.*, 2009, **100**, 2569–2574.

4 N. L. Mai and Y. M. Koo, *ACS Sustain. Chem. Eng.*, 2016, **4**, 541–547.

5 S. S. Rahatekar, A. Rasheed, R. Jain, M. Zammarano, K. K. Koziol, A. H. Windle, J. W. Gilman and S. Kumar, *Polymer (Guildf).*, 2009, **50**, 4577–4583.

6 X. Pan, N. Gilkes, J. Kadla, K. Pye, S. Saka, D. Gregg, K. Ehara, D. Xie, D. Lam and J. Saddler, *Biotechnol. Bioeng.*, 2006, **94**, 851–861.

7 M. Paluch, J. Ostrowska, P. Tyński, W. Sadurski and M. Konkol, *J. Polym. Environ.*, 2022, **30**, 728–740.

8 Y. Xie, Y. Pan and P. Cai, *Ind. Crops Prod.*, 2022, **176**, 114381.

Appendix

A1 ^{1}H NMR, ^{13}C NMR, MS and IR spectra of 1-Ethyl-3-methylimidazolium bromide

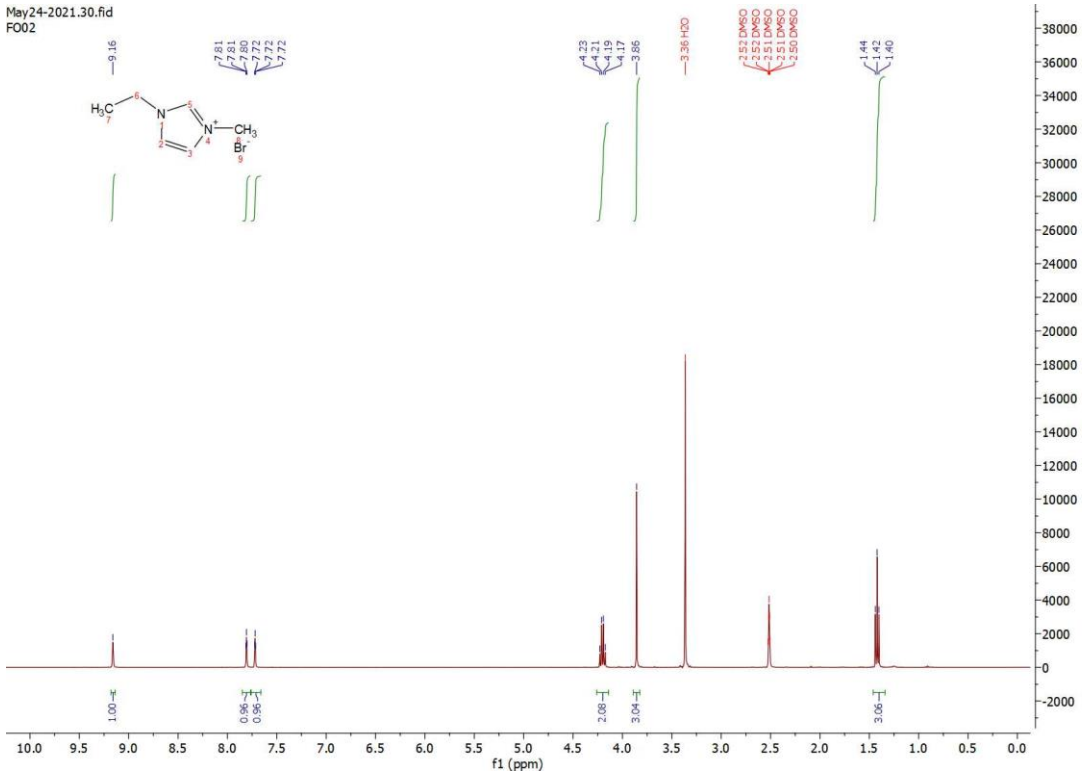


Figure 1 ^{1}H NMR spectra of 1-Ethyl-3-methylimidazolium bromide

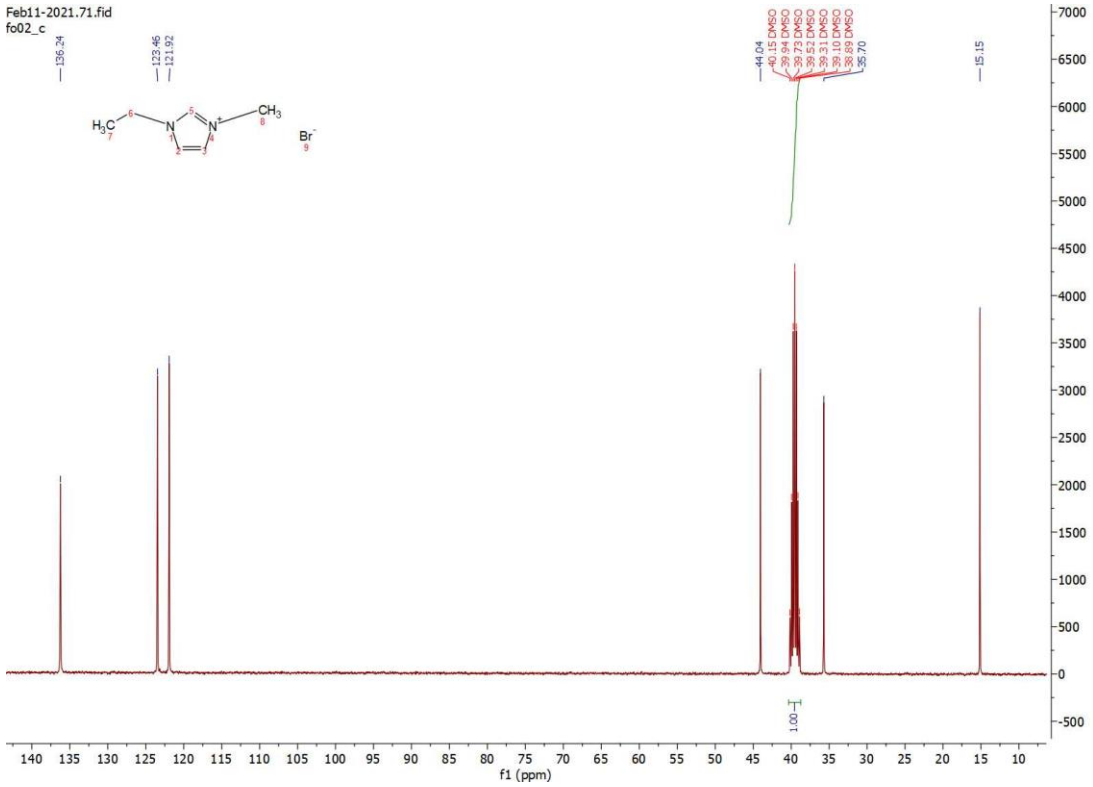


Figure 2 ^{13}C NMR spectra of 1-Ethyl-3-methylimidazolium bromide

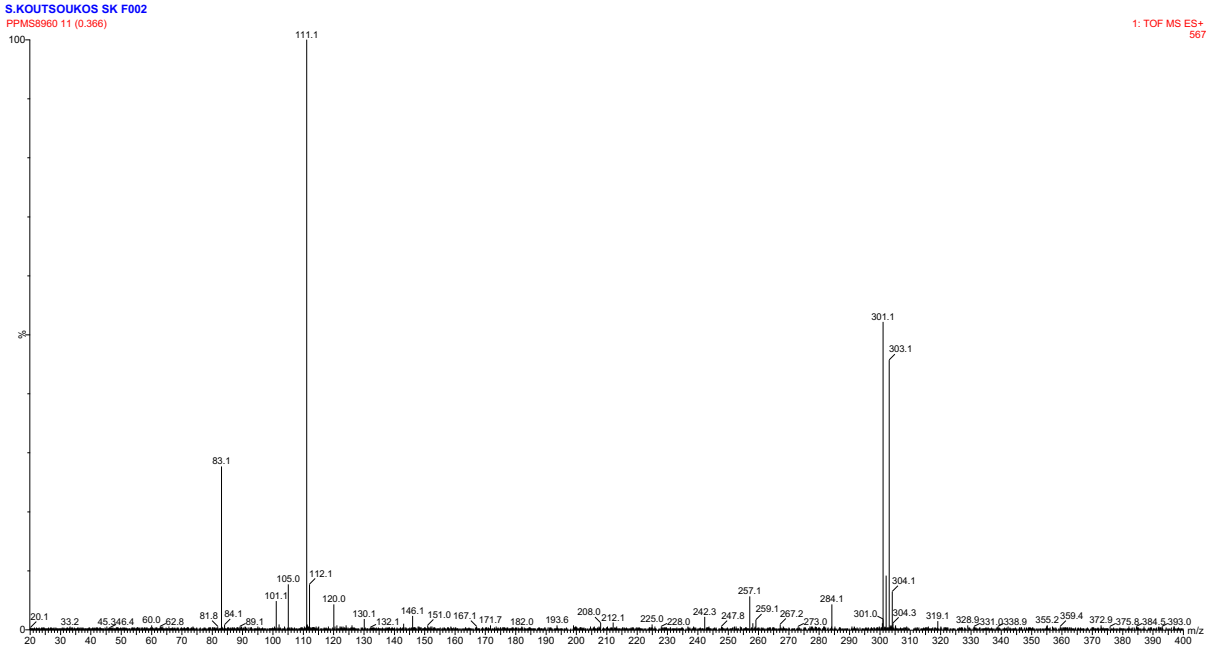


Figure 3 ES+MS spectra of 1-Ethyl-3-methylimidazolium bromide

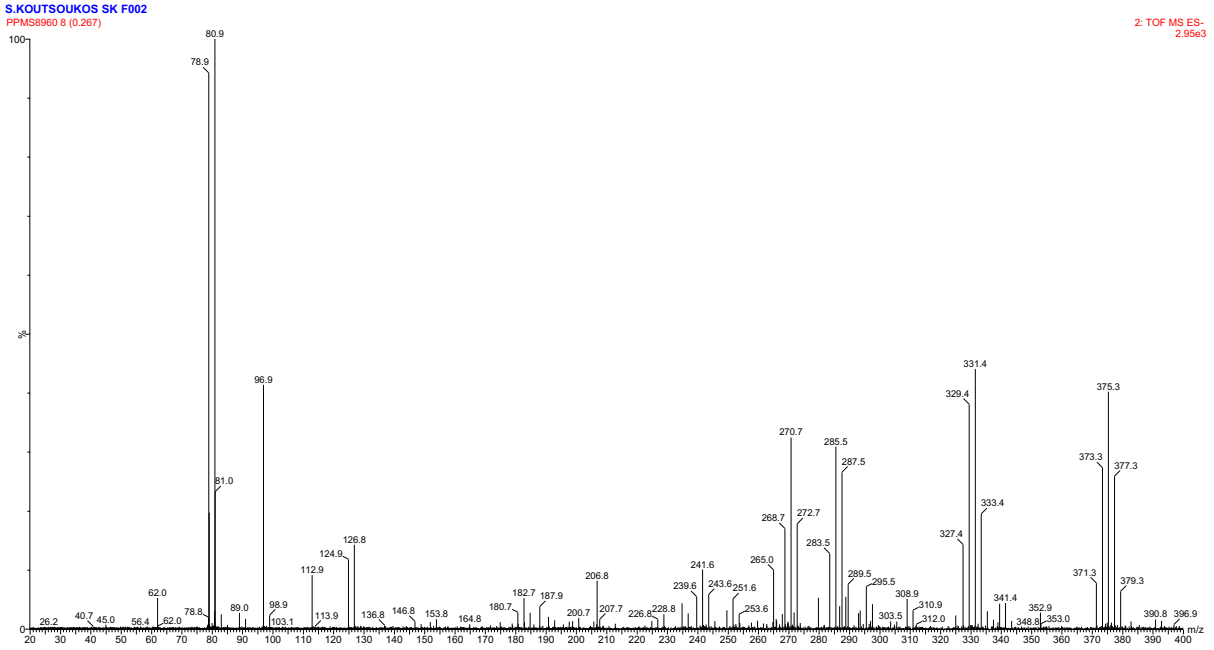


Figure 4 ES-MS spectra of 1-Ethyl-3-methylimidazolium bromide

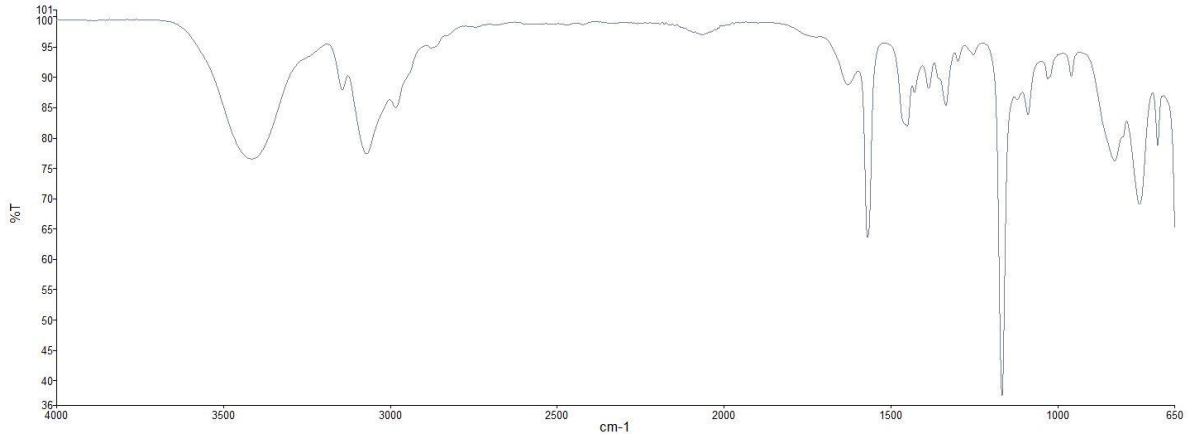


Figure 5 FTIR spectra of 1-Ethyl-3-methylimidazolium bromide

A2 ^{1}H NMR, ^{13}C NMR, MS and IR spectra of 1-Ethyl-3-methylimidazolium acetate via metathesis

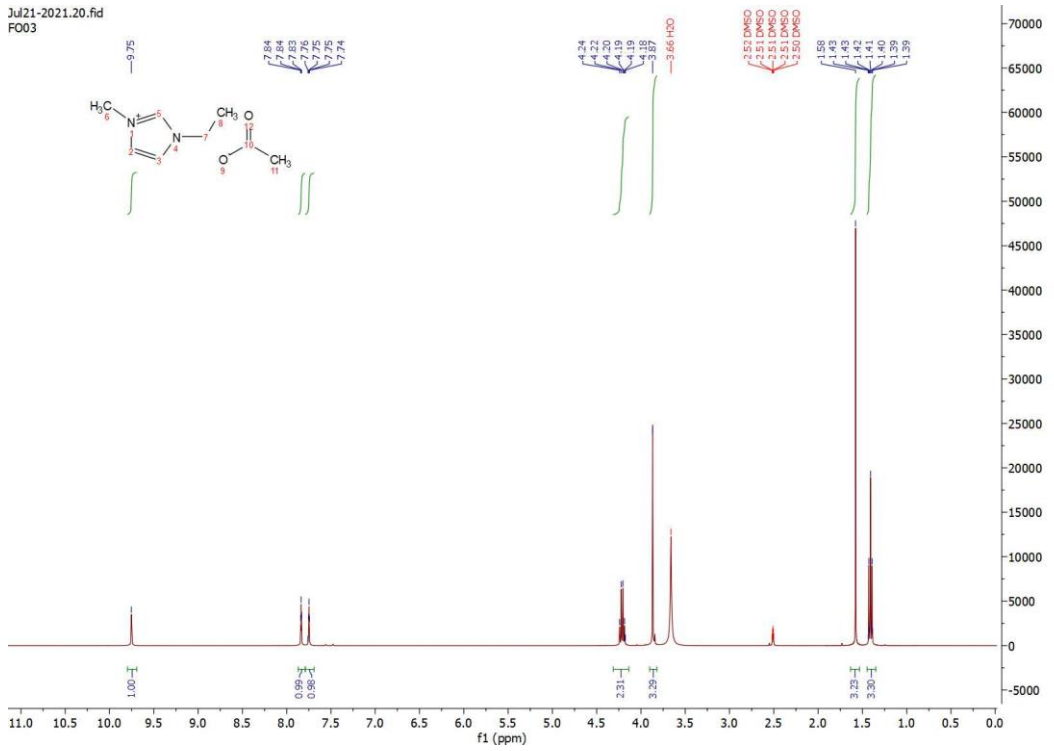


Figure 6 ^{1}H NMR spectra of 1-Ethyl-3-methylimidazolium acetate via metathesis

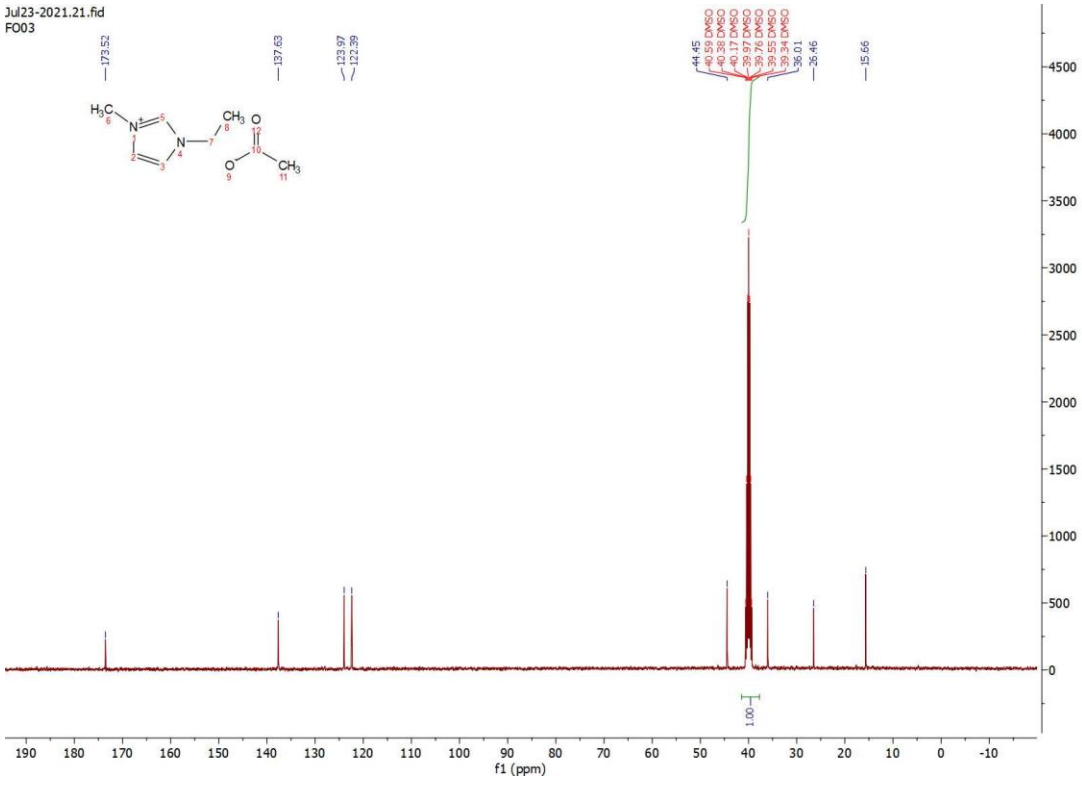


Figure 7 ^{13}C NMR spectra of 1-Ethyl-3-methylimidazolium acetate via metathesis

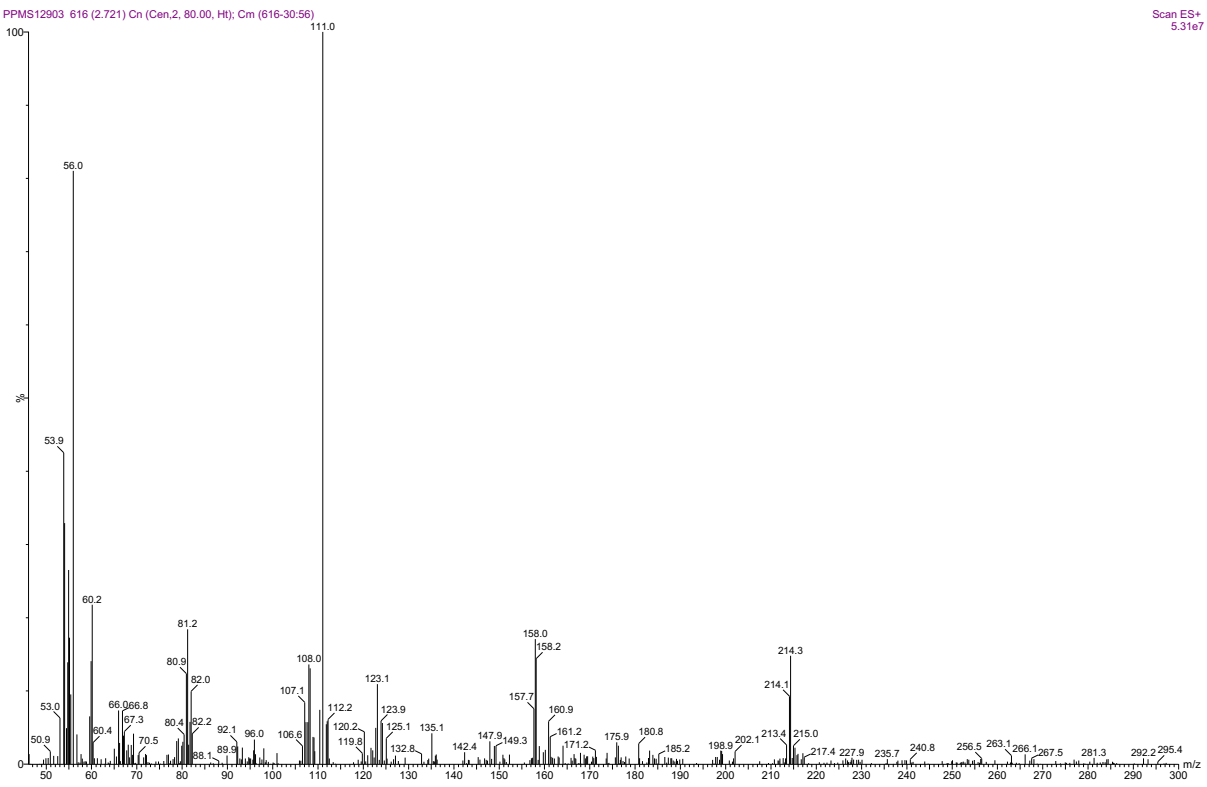


Figure 8 ES+MS spectra of 1-Ethyl-3-methylimidazolium acetate via metathesis

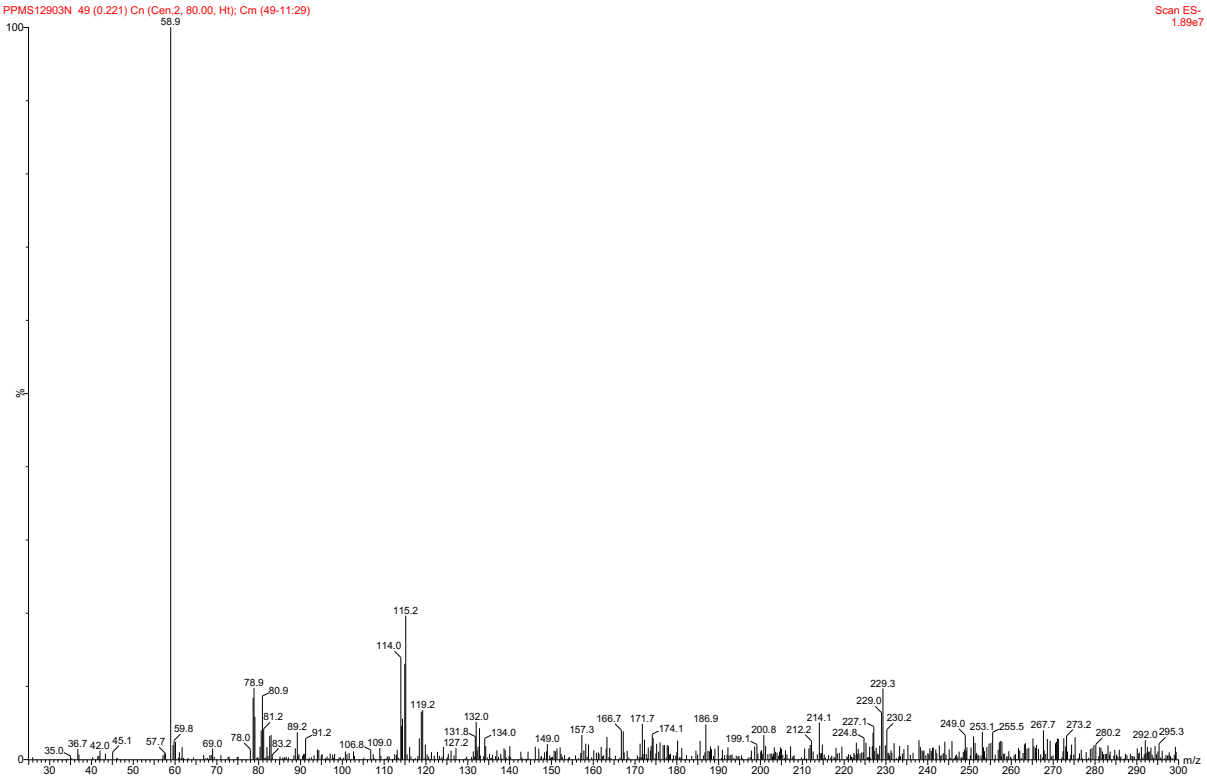


Figure 9 ES-MS spectra of 1-Ethyl-3-methylimidazolium acetate via metathesis

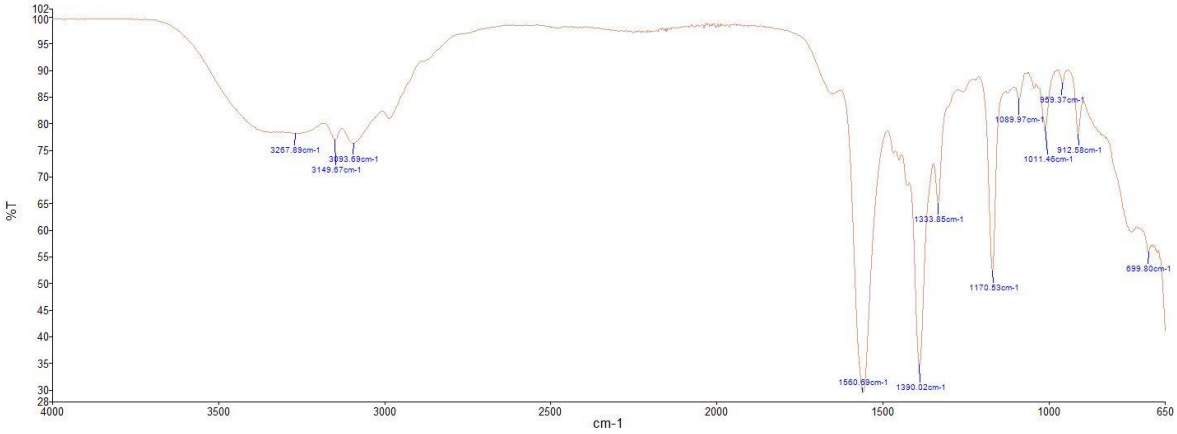


Figure 10 FTIR spectra of 1-Ethyl-3-methylimidazolium acetate via metathesis

A3 ^{1}H NMR, ^{13}C NMR, and IR spectra of 1-Ethyl-3-methylimidazolium acetate via ion exchange

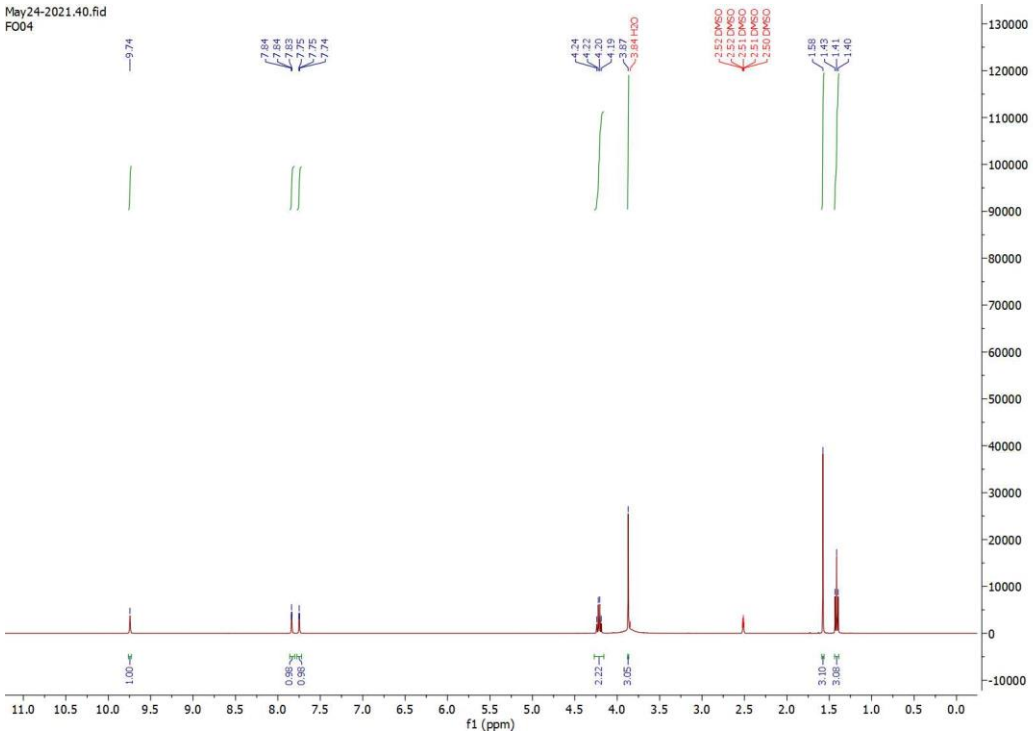


Figure 11 ^{1}H NMR spectra of 1-Ethyl-3-methylimidazolium acetate via ion exchange

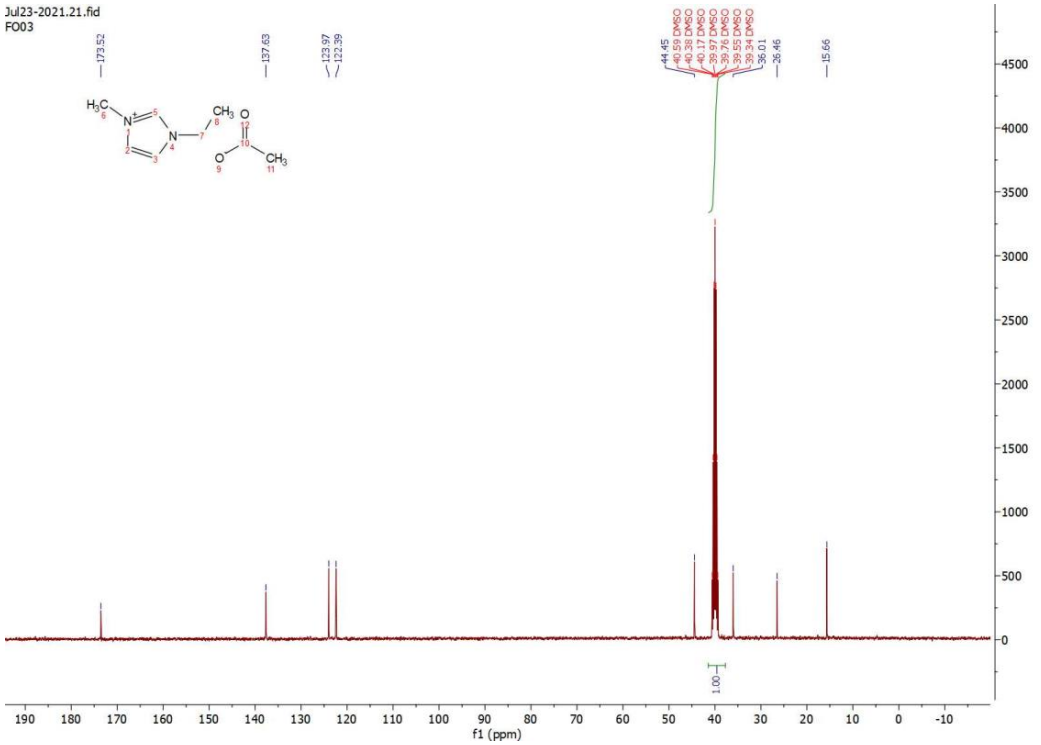


Figure 12 ^{13}C NMR spectra of 1-Ethyl-3-methylimidazolium acetate via ion exchange

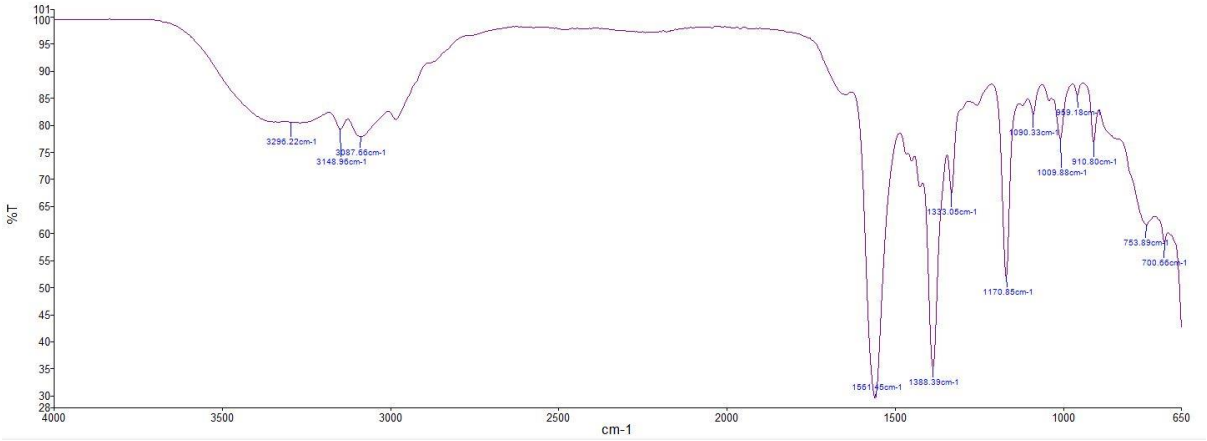


Figure 13 FTIR spectra of 1-Ethyl-3-methylimidazolium acetate via ion exchange

A4 ^{1}H NMR, ^{13}C NMR, and IR spectra of 1-Ethyl-3-methylimidazolium acetate synthesised via one-pot method

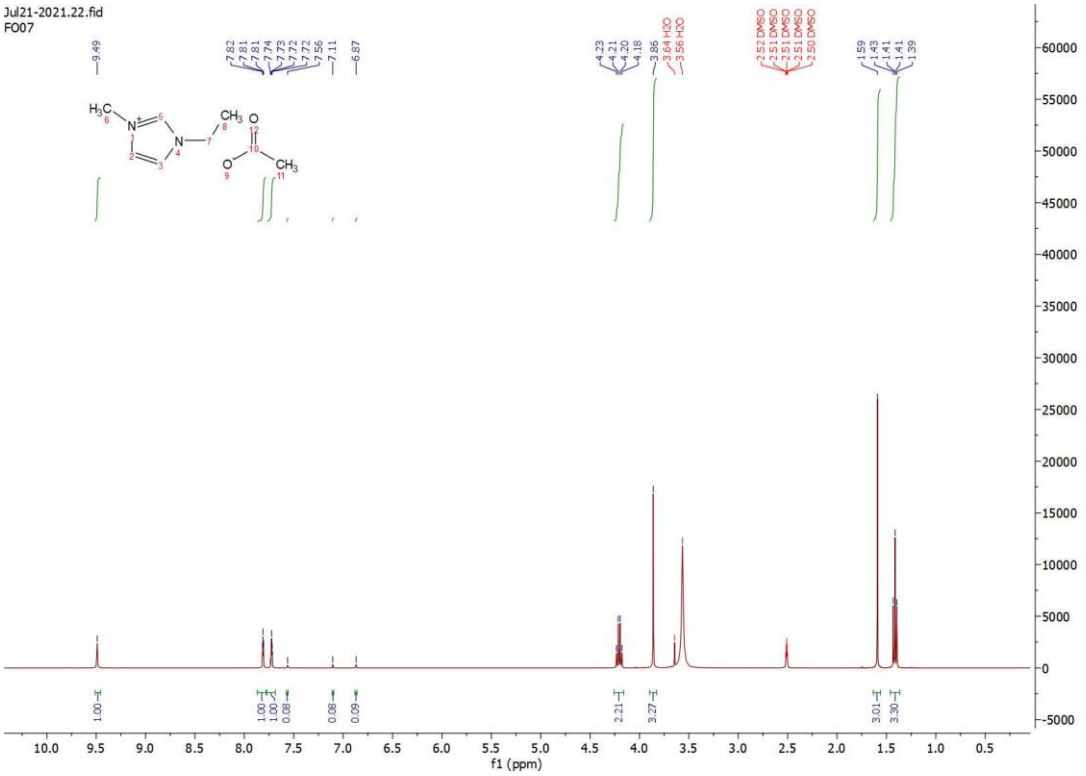


Figure 14: *^{1}H NMR spectra of 1-Ethyl-3-methylimidazolium acetate via one-pot method*

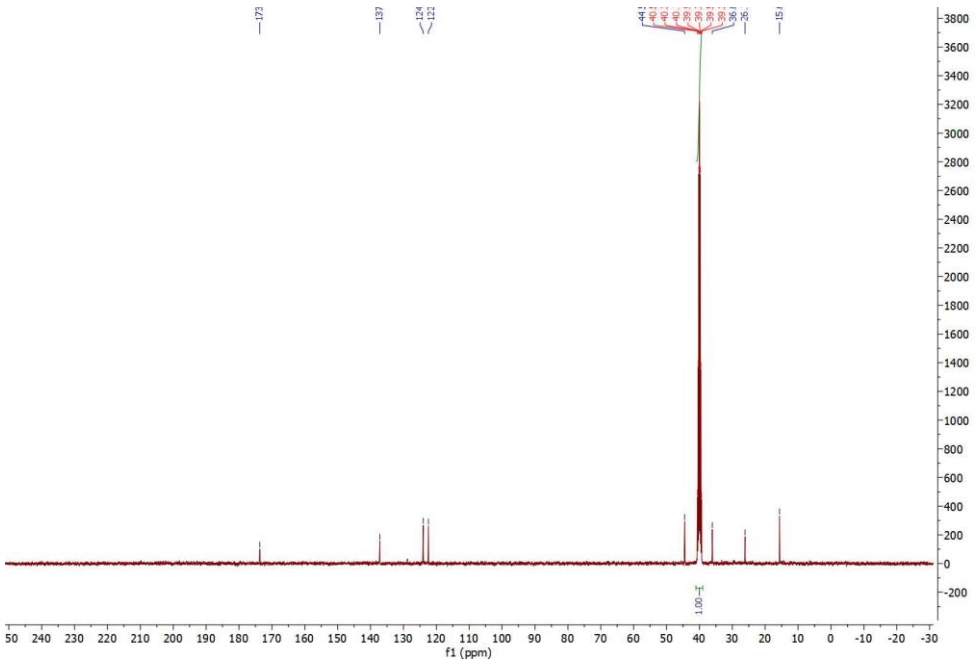


Figure 15 *^{13}C NMR spectra of 1-Ethyl-3-methylimidazolium acetate via one-pot method*

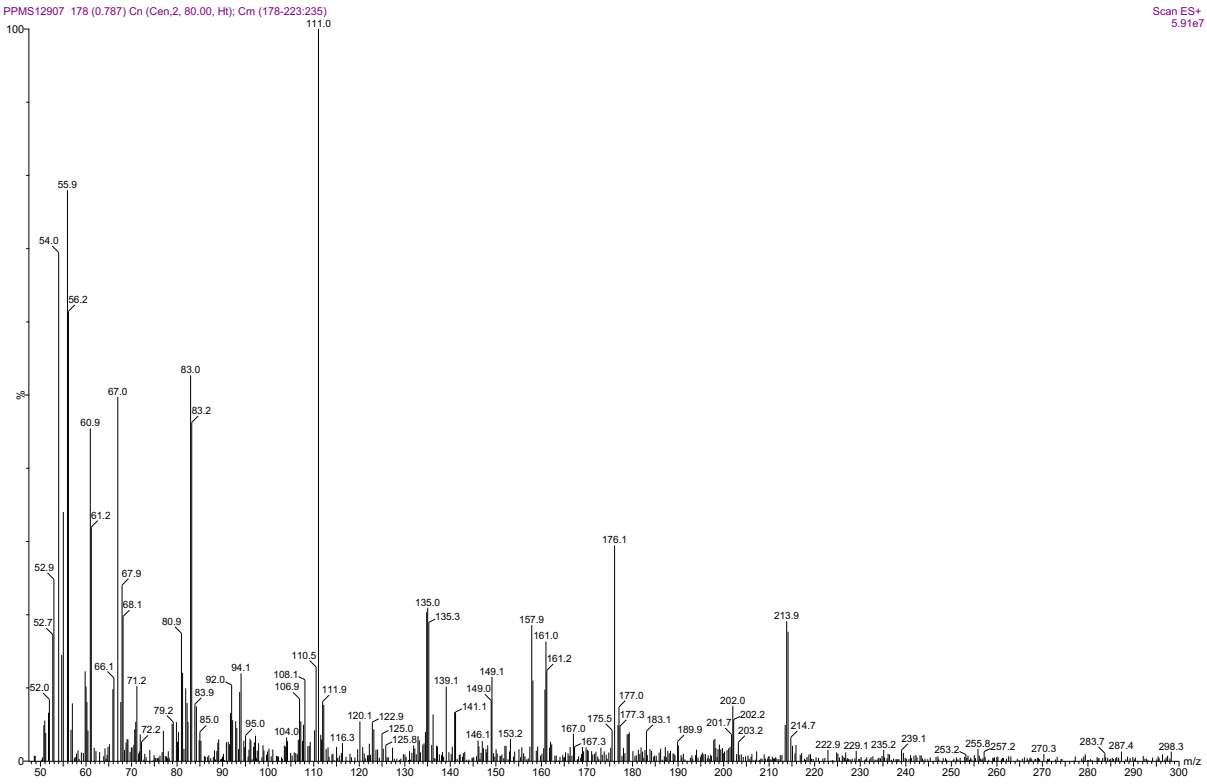


Figure 16 ES+MS spectra of 1-Ethyl-3-methylimidazolium acetate via one-pot method

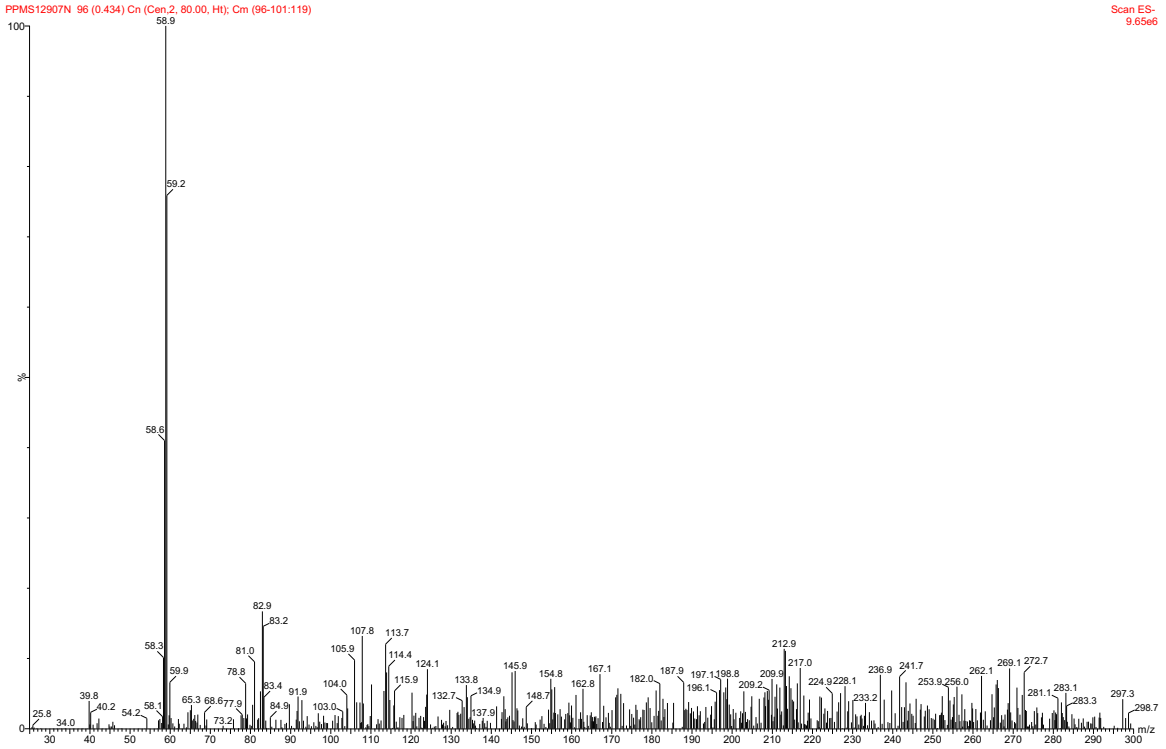


Figure 17 ES-MS spectra of 1-Ethyl-3-methylimidazolium acetate via one-pot method

A5 Green Metrics

Atom economy calculation

Atom economy is a theoretical measure defined strictly for the stoichiometric chemical reaction. Therefore, purification or isolation steps are excluded in the calculation.

Metathesis	C_2H_5Br + $C_4H_6N_2$ → M_w: 108.97 g/mol M_w: 82.10 g/mol $C_6H_{11}BrN_2$ + $AgC_2H_3O_2$ M_w: 191.07 g/mol M_w: 166.91 g/mol → $C_8H_{14}N_2O_2$ + AgBr M_w: 170.21 g/mol	AE = 170.21 x 100% 357.98 = 47.55 % Note: $C_6H_{11}BrN_2$ is an intermediate, therefore it is excluded in the calculation.
Ion Exchange	C_2H_5Br + $C_4H_6N_2$ → M_w: 108.97 g/mol M_w: 82.10 g/mol $C_6H_{11}BrN_2$ + OH- → M_w: 191.07 g/mol M_w:17.01 g/mol $C_6H_{11}N_2OH$ + CH_3COOH M_w: 60.05 g/mol → $C_8H_{14}N_2O_2$ + H_2O M_w: 170.21 g/mol	AE = 170.21 x 100 268.13 = 63.48 % Note: $C_6H_{11}BrN_2$ is an intermediate, therefore it is excluded in the calculation.
One-pot	$C_4H_6N_2$ + CH_3CH_2Br + M_w: 82.10 g/mol M_w: 108.97 g/mol Pb $(CH_3CO_2)_2.3H_2O$ → M_w: 379.33 g/mol $C_8H_{14}N_2O_2$ + $PbBr_2$ + $3H_2O$ M_w: 170.21 g/mol	AE = 170.21 x 100 570.40 = 29.84 %

E factor calculation

The E factor is calculated by dividing the total mass of waste by the total mass of the product.

To synthesize 10–15 grams of $[C_2C_1im]Br$ / $C_6H_{11}BrN_2$, the following compounds are required: 3.5 g of $NaHCO_3$, 67.34 g of H_2SO_4, 2 g of $MgSO_4$, 1 g of KOH, 27.1 g of EtOAc, and 94.3 g of MeCN.
Density water is 1 g /mL was used in this calculation.

Metathesis	C_2H_5Br + $C_4H_6N_2$ ↓ + 3.5 grams of $NaHCO_3$ (waste) 67.34 grams of H_2SO_4 (waste) 2 grams $MgSO_4$ (waste) 1 gram of KOH (waste) 27.1 g EtOAc: 94.3 g MeCN (waste) $C_6H_{11}BrN_2$ + $AgC_2H_3O_2$ ↓ + 30 mL H_2O (waste)	E factor = 230.87 g 11.52 g = 20.04

	$C_8H_{14}N_2O_2$ + AgBr 5.633 g (waste) 79 mmol [C_2C_1im][OAc] x 170.21 g/mol yielded 13.45 g 11.52 g / 13.45 g x 100 = 85.6 % yield	
Ion Exchange	C_2H_5Br + $C_4H_6N_2$ ↓ + 3.5 grams of $NaHCO_3$ (waste) 67.34 grams of H_2SO_4 (waste) 2 grams $MgSO_4$ (waste) 1 gram of KOH (waste) 27.1 g EtOAc: 94.3 g MeCN (waste) $C_6H_{11}BrN_2$ + OH- ↓ (200 mL H_2O pre-wash resin) (waste) $C_6H_{11}N_2OH$ + CH_3COOH ↓ 600 mL H_2O (waste) $C_8H_{14}N_2O_2$ + H_2O 2 g activated charcoal (waste) 15 g methanol (waste) 37 mmol [C_2C_1im][OAc] x 170.21 g/mol yielded 6.298 g. 5.353 g / 6.298 g x 100 = 85% yield	E factor = 1012.24 g / 5.35 g = 189.20
One-pot	$C_4H_6N_2$ + CH_3CH_2Br + $Pb(CH_3CO_2)_2.3H_2O$ ↓ 480 grams of EtOAc wash (waste) $C_8H_{14}N_2O_2$ + $PbBr_2$ + $3H_2O$ 18.35 g (waste) 2.7g (waste) 50 mmol [C_2C_1im][OAc] x 170.21 g/mol yielded 8.51 g. 7.2 g / 8.51 g x 100 = 84.7 % yield	E factor = 501.50 g / 7.20 g = 69.59

Effective Mass Yield

EMY is calculated by dividing the mass of the desired product by the mass of all non-benign materials and then multiplying the result by 100.

The weight of the starting material was calculated based on a 60% yield of [C_2C_1im]Br.

Metathesis	C_2H_5Br + $C_4H_6N_2$ → 14.24 g 10.73 g $C_6H_{11}BrN_2$ + $AgC_2H_3O_2$ 15.0 g 13.17 g → $C_8H_{14}N_2O_2$ + AgBr 11.52 g Total reactant leads to final product: (14.24+10.73+ 13.17) g = 38.14 g	EMY = 11.52 g x 100 38.14 g = 30.20 %
Ion Exchange	C_2H_5Br + $C_4H_6N_2$ → 6.65 g 5.10 g $C_6H_{11}BrN_2$ + OH- → 7.00 g $C_6H_{11}N_2OH$ + CH_3COOH 2.60 g → $C_8H_{14}N_2O_2$ + H_2O 5.79 g Total reactant leads to final product: (6.65 + 5.10 + 7.00) g = 18.75 g	EMY = 5.79 g x 100 18.75 g = 30.88 %
One-pot	$C_4H_6N_2$ + CH_3CH_2Br + 4.11 g 9.81 g Pb $(CH_3CO_2)_2.3H_2O$ → 9.48 g $C_8H_{14}N_2O_2$ + $PbBr_2$ + $3H_2O$ 7.20 g Total reactant leads to final product: (4.11 + 9.81 + 9.48) g = 23.40 g	EMY = 7.20 g x 100 23.4 g = 30.77 %

Cost Calculation

The price of the following starting materials might be fluctuating depending on current price.

Table 1 Estimation price of chemical used in synthesising [C_2C_1im][OAc]

Starting materials	**Company**	**Cost**	**Cost / g**
1-ethyl-3-methylimidazolium bromide, [C_2C_1im][Br^-]	Self-synthesis	£ 77.90 / 50 g	£ 1.558
Sulfuric acid (H_2SO_4, 95%)	Fischer Scientific	£ 89 / 4575 g	£ 0.019
Sodium hydrogen carbonate ($NaHCO_3$, >98%)	Fischer Scientific	£ 48.40 / 500g	£ 0.097
Magnesium sulfate ($MgSO_4$, >98%)	VWR Chemicals	£ 47 / 500 g	£ 0.094
1-Methylimidazole (>99%)	Sigma Aldrich	£ 81.70 / 500g	£ 0.163
1-bromoethane (C_2H_5Br, 98%)	Sigma Aldrich	£ 50.80 / 1470 g	£ 0.0345
Acetic acid (CH_3COOH,	Sigma Aldrich	£ 17.60 / 525 g	£ 0.034

99.8%)			
Lead (II) acetate trihydrate ($Pb(CH_3CO_2)_2.3H_2O$, 99.5%)	Sigma Aldrich	£ 59.80 / 50 g	£ 1.196
Acetonitrile (C_2H_3N, ≥99.9%)	VWR Chemicals	£ 187.55 / 1965 g	£ 0.0954
Ethyl acetate ($CH_3COOC_2H_5$, ≥99.5%)	VWR Chemicals	£ 76.40 / 2255 g	£ 0.016
Silver acetate ($AgC_2H_3O_2$, 99%)	Flurochem	£ 68 / 25 g	£ 2.72
Amberlyst™ A26, OH-form, ion-exchange resin	ACROS Organics	£ 243 / 1000 g	£ 0.243
Water	Thames Water	£ 138.18 / 1000 g	£ 1.38 x 10^{-4}

Purification of 10g $[C_2C_1im][Br^-]$	36.6 mL H_2SO_4 3.5 g $NaHCO_3$ 90 mL H_2O 2 g $MgSO_4$	Cost: £ 0.70 + £ 0.34+ £ 0.01 + £ 0.19 = £ 1.24 / 10 g £ 0.124 / 1 g (purfication of $[C_2C_1im][Br^-]$)
Metathesis	$C_6H_{11}BrN_2$ + $AgC_2H_3O_2$ 5.73 g 3.26 g → $C_8H_{14}N_2O_2$ + AgBr 4.31 g + 30 mL H_2O	Cost: £ 8.93 + £ 0.71 (purification) + £ 8.87 + £0.004 = £ 18.51 / 4.31 g £ 4.30 / 1 g $[C_2C_1im][OAc]$
Ion Exchange Resin	$C_6H_{11}BrN_2$ + OH- (resin) → 7 g 150 g $C_6H_{11}N_2OH$ + CH_3COOH 2.6 g → $C_8H_{14}N_2O_2$ + H_2O 5.78 g + 800 mL H_2O	Cost: £ 10.91 + £ 0.86 (purification) £ 36.45 + £ 0.08 + £ 0.11 = £ 48.50 / 5.787 g For 3 years running, approx. once per month application: £ 10.91(36 mth) + £ 0.86 (36 mth) + £ 36.45 + £ 0.08 (36 mth) + £ 0.11(36 mth) = £ 467.01 / 208.332 g £ 2.24 / 1 g $[C_2C_1im][OAc]$
One-pot	$C_4H_6N_2$ + CH_3CH_2Br + 4.11 g 9.81 g $Pb(CH_3CO_2)_2.3H_2O$ → 9.48 g $C_8H_{14}N_2O_2$ + $PbBr_2$ + $3H_2O$ 7.20 g + 600 mL EtOAc	Cost: £ 0.67 + £ 0.34 + £ 11.34 + £ 9.68 = £ 12.35/ 7.2 g £ 3.06 / 1 g $[C_2C_1im][OAc]$

A6 ^{1}H NMR, ^{13}C NMR, and IR spectra of commercial 1-Ethyl-3-methylimidazolium acetate

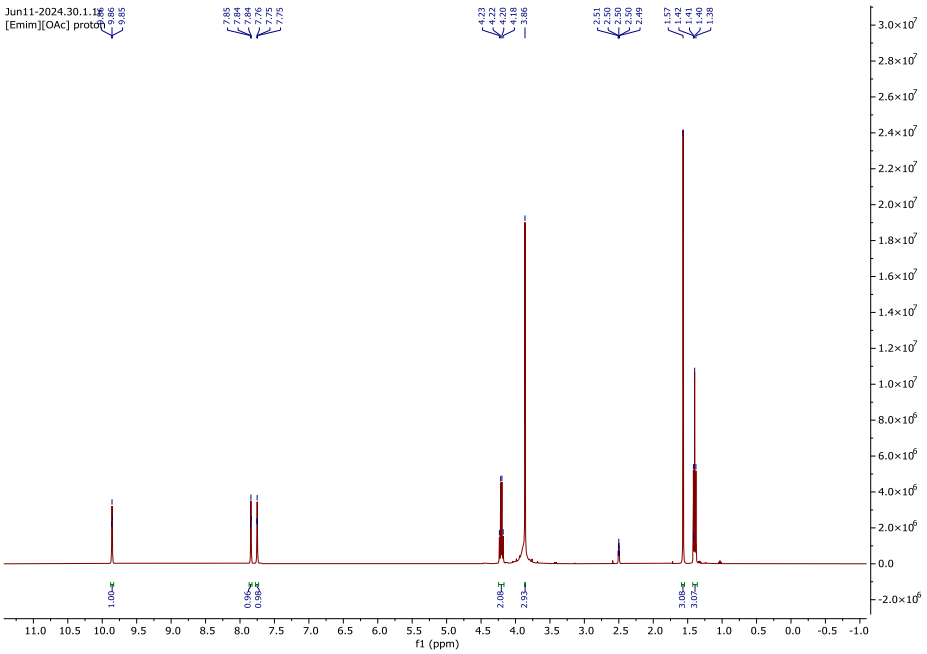


Figure 18 ^{1}H NMR spectra of 1-Ethyl-3-methylimidazolium acetate from commercial

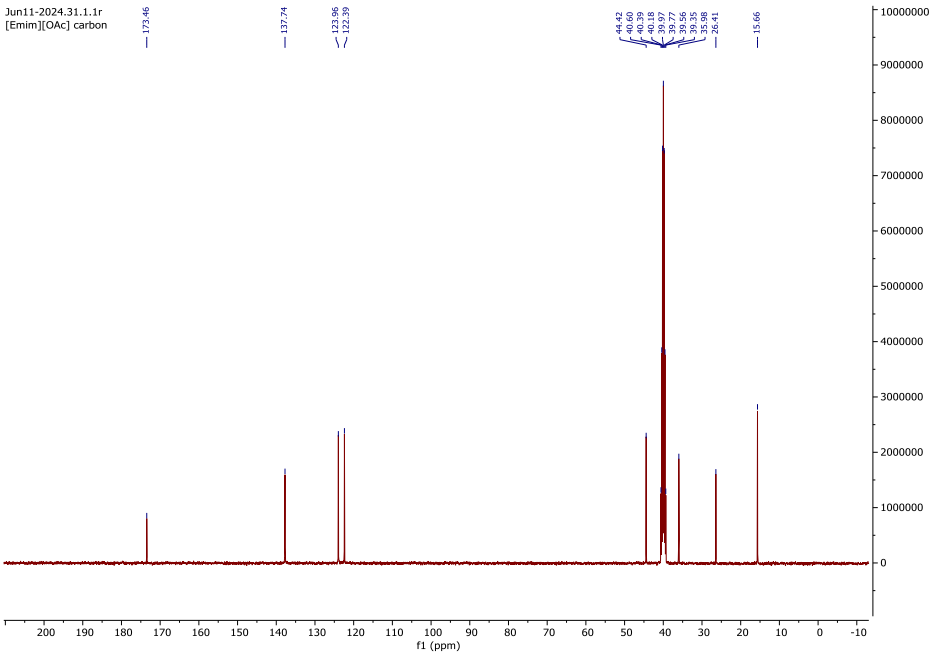


Figure 19 ^{13}C NMR spectra of 1-Ethyl-3-methylimidazolium acetate from commercial

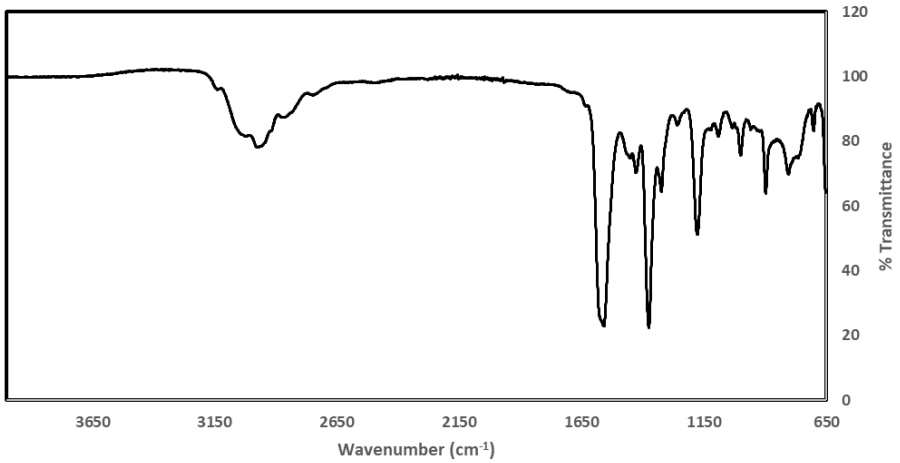


Figure 20 FTIR spectra of 1-Ethyl-3-methylimidazolium acetate from commercial

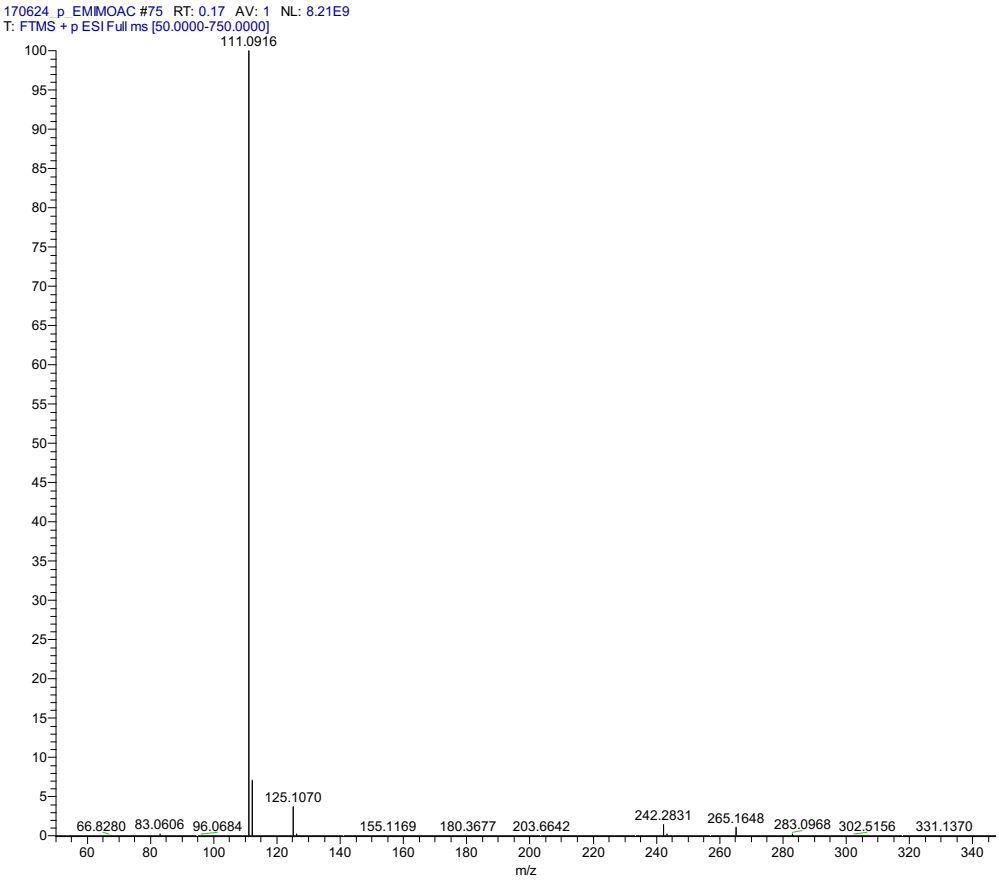


Figure 21 ES+MS spectra of 1-Ethyl-3-methylimidazolium acetate from commercial

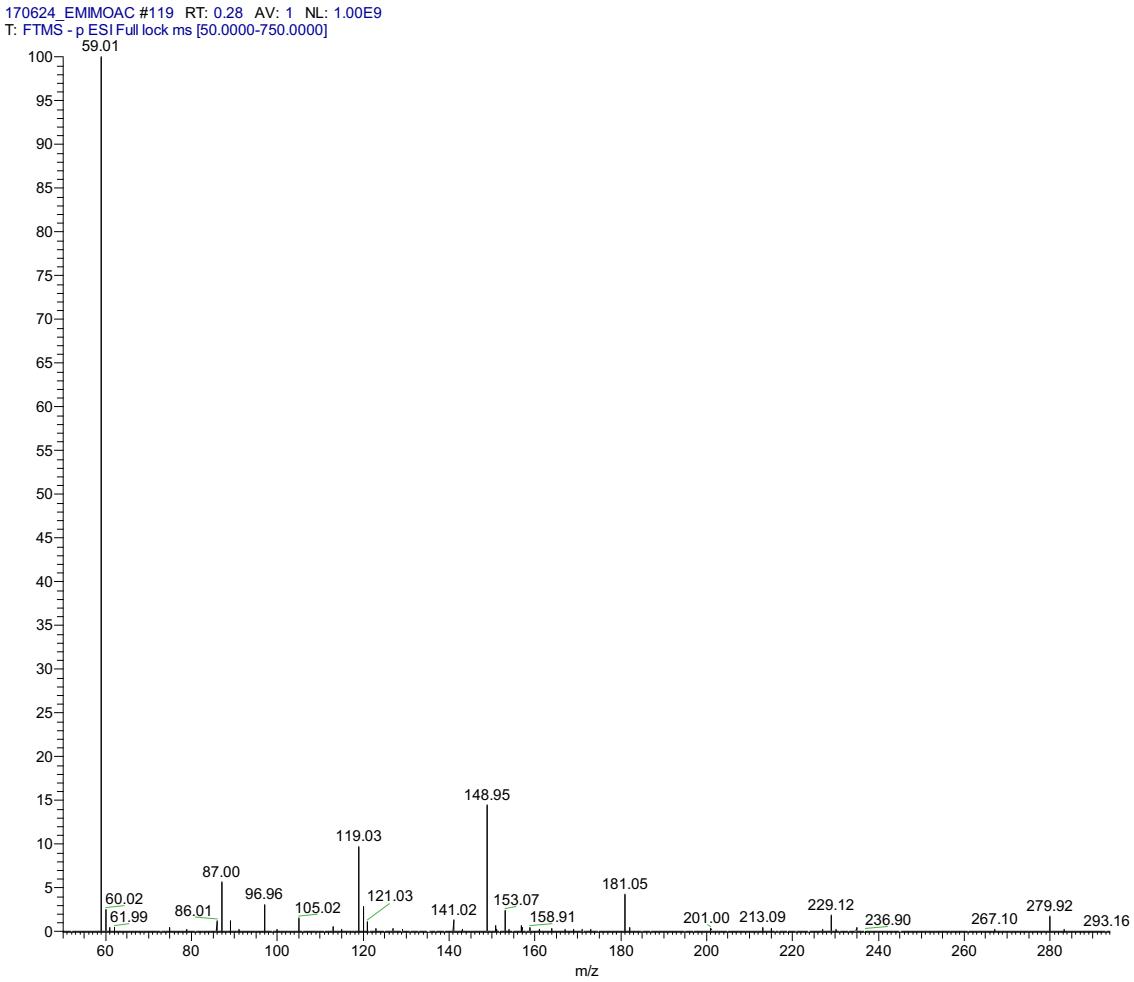


Figure 22 ES-MS spectra of 1-Ethyl-3-methylimidazolium acetate from commercial

A7 ^{1}H NMR, ^{13}C NMR, and MS spectra of N,N-dimethylbutylammonium hydrogen sulfate, [DMBA][HSO_4]

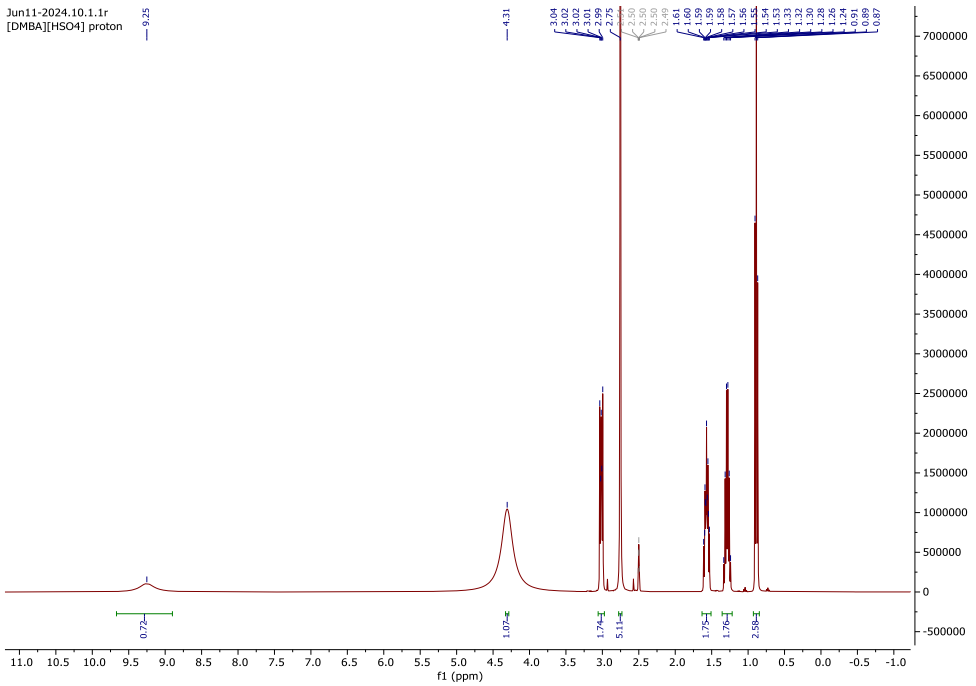


Figure 23 ^{1}H NMR spectra of [DMBA][HSO_4]

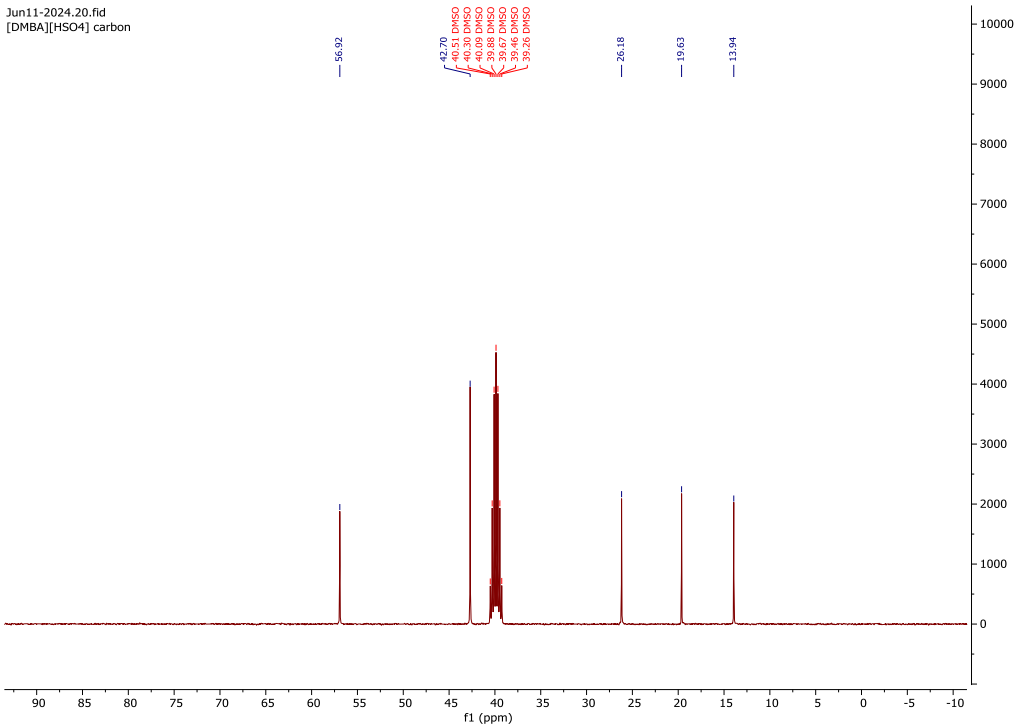


Figure 24 ^{13}C NMR spectra of [DMBA][HSO_4]

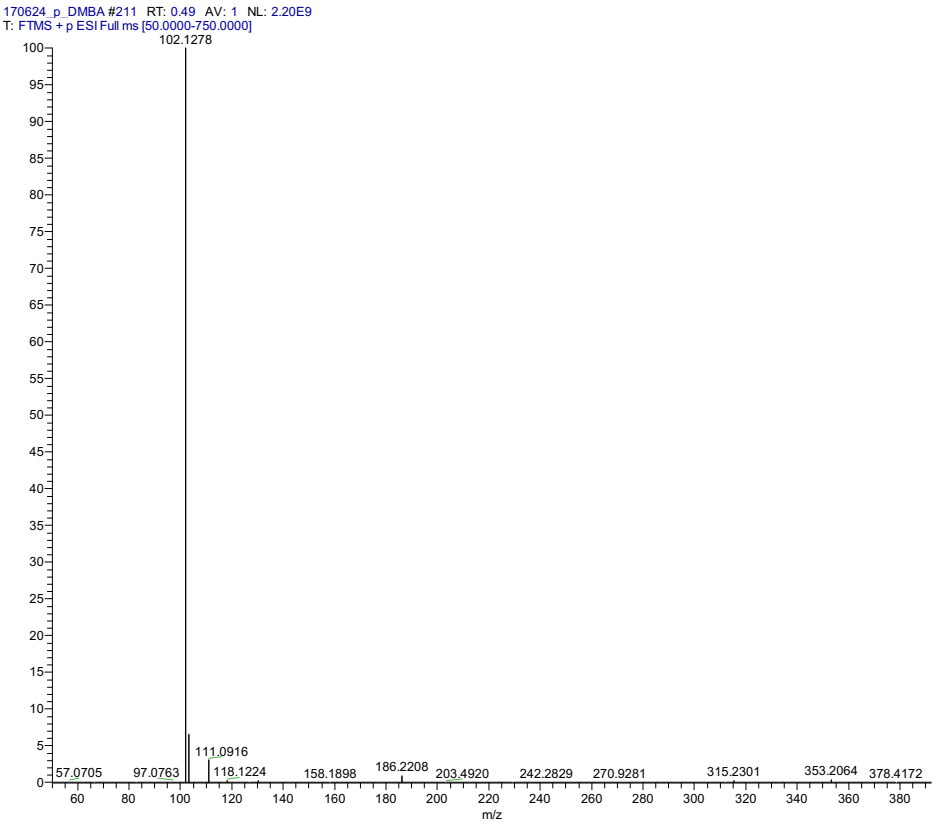


Figure 25 ES+MS spectra of [DMBA][HSO$_4$]

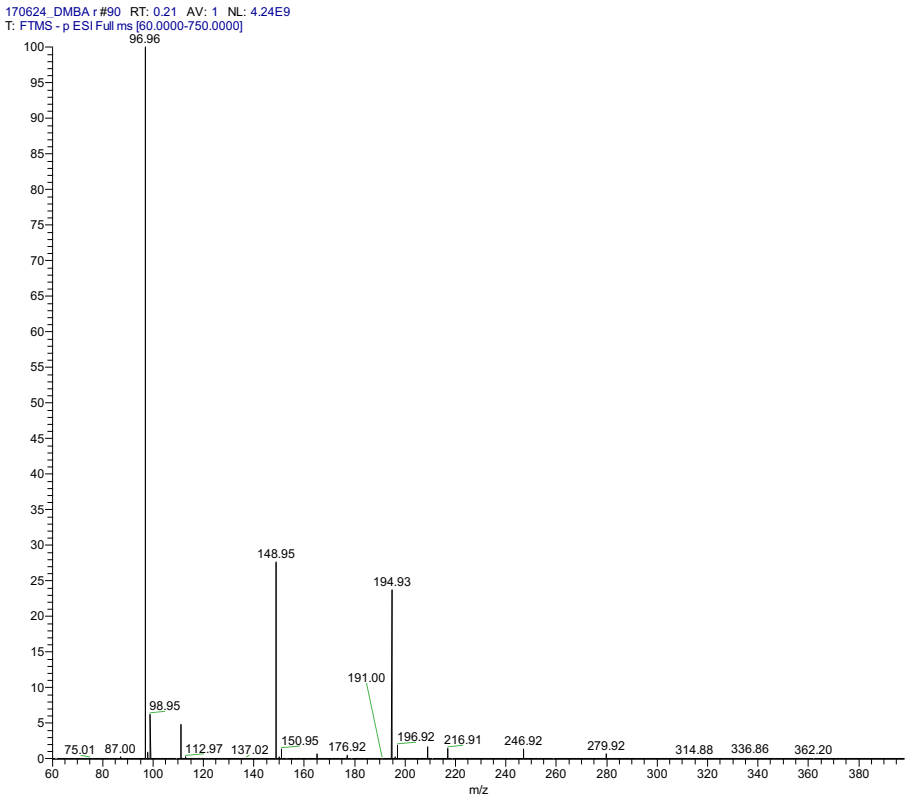


Figure 26 ES+MS spectra of [DMBA][HSO$_4$]